UNIVERSIDADE FEDERAL DO PARÁ
PROGRAMA DE PÓS-GRADUAÇÃO EM GEOLOGIA E GEOQUÍMICA
TESE APROVADA COM DISTINÇÃO
Instituto de Geociências

UNIVERSIDADE FEDERAL DO PARÁ
INSTITUTO DE GEOCIÊNCIAS
PROGRAMA DE PÓS-GRADUAÇÃO EM GEOLOGIA E GEOQUÍMICA

TESE DE DOUTORADO Nº 189

PETROLOGIA E EVOLUÇÃO CRUSTAL DA PORÇÃO SUL DO DOMÍNIO BACAJÁ, CRÁTON AMAZÔNICO: EVOLUÇÃO POLICÍCLICA DO MESOARQUEANO AO RIACIANO

Tese apresentada por:

ARTHUR SANTOS DA SILVA NERI
Orientador: Roberto Dall'Agnol (UFPA)

BELÉM - PARÁ
2025

Dados Internacionais de Catalogação na Publicação (CIP) de acordo com ISBD
Sistema de Bibliotecas da Universidade Federal do Pará
Gerada automaticamente pelo módulo Ficat, mediante os dados fornecidos pelo(a) autor(a)

N445p Neri, Arthur Santos da Silva.
Petrologia e evolução crustal da porção sul do Domínio Bacajá, Cráton Amazônico: evolução policíclica do Mesoarqueano ao Riaciano / Arthur Santos da Silva Neri. — 2025.
xxxv, 385 f. : il. color.

Orientador(a): Prof. Dr. Roberto Dall'agnol
Tese (Doutorado) - Universidade Federal do Pará, Instituto de Geociências, Programa de Pós-Graduação em Geologia e Geoquímica, Belém, 2025.

1. Petrologia. 2. Evolução Crustal. 3. Mesoarqueano. 4. Riaciano. 5. Domínio Bacajá. I. Título.

CDD 552

Universidade Federal do Pará
Instituto de Geociências
Programa de Pós-Graduação em Geologia e Geoquímica

PETROLOGIA E EVOLUÇÃO CRUSTAL DA PORÇÃO SUL DO DOMÍNIO BACAJÁ, CRÁTON AMAZÔNICO: EVOLUÇÃO POLICÍCLICA DO MESOARQUEANO AO RIACIANO

Tese apresentada por

ARTHUR SANTOS AS SILVA NERI

Como requisito parcial à obtenção do Grau de Doutor em Ciências na Área de GEOQUÍMICA E PETROLOGIA, Linha de Pesquisa EVOLUÇÃO CRUSTAL E METALOGÊNESE.

Data de Aprovação: 13 / 08 / 2025

Banca Examinadora:

Prof. Dr. Roberto Dall'Agnol
(Orientador-UFPA)

Profa. Dra. Maria de Lourdes da Silva Rosa
(Membro-UFS)

Profa. Dra. Lucia Travassos da Rosa-Costa
(Membro-CPRM)

Prof. Dr. Elson Paiva de Oliveira
(Membro-UNICAMP)

Prof. Dr. Moacir José Buenano Macambira
(Membro-UFPA)

A Lúcia e Airton

AGRADECIMENTOS

Esta tese é a realização de um sonho que cultivo desde muito, muito jovem, antes mesmo de saber o que significava ser um cientista. Para chegar até aqui, muitas pessoas e instituições me ajudaram ao longo desse caminho e todas elas serão devidamente agradecidas aqui.

Ao Instituto de Geociências (IG-UFPA) e Grupo de Pesquisa Petrologia de Granitoides (GPPG) pelo fornecimento da infraestrutura.

A Coordenação de Aperfeiçoamento de Pessoal de Nível Superior (CAPES) - Código de Financiamento 001 - pela concessão da bolsa de doutorado (No. 88887.643812/2021-00).

Ao Conselho Nacional de Desenvolvimento Científico e Tecnológico (CNPq) pelo suporte financeiro por meio da taxa de bancada de Roberto Dall'Agnol (304648- 2019-1).

Aos projetos de pesquisa "Conhecimento geológico para preservação do patrimônio natural e combate à mineração ilegal na Amazônia sul oriental" financiado pela Fundação Amazônica de Amparo a Estudos e Pesquisas (FAPESPA - E-2024/2285715) e "Evolução Arqueana-Proterozóica do Complexo Bacajaí e Aruanã, Domínio Bacajá - um segmento retrabalhado do paleocontinente Carajás?" financiado pelo CNPQ (408396/2023-7), ambos coordenados pela Gilmara Feio, pelo suporte financeiro e contribuição para o avanço do conhecimento sobre a geologia do Domínio Bacajá.

A Biblioteca Raimundo Montalvão do Instituto de Geociências pelas orientações de trabalhos acadêmicos.

Ao meu orientador, Roberto Dall'Agnol, com quem tive a oportunidade de colaborar durante o TCC, o que abriu caminho para que eu ingressasse no doutorado sob sua orientação. Agradeço o apoio, confiança e por sempre saber a melhor maneira de guiar jovens cientistas no mundo acadêmico. Foi ele quem reacendeu minha paixão por trabalhar com granitos, que havia sido levemente esquecida durante o mestrado, mas que nunca deixou de existir.

À Gilmara Feio e ao José de Arimatéia, sou grato por me proporcionarem essa área de pesquisa, na qual venho trabalhando desde o mestrado, por me acompanharem nas etapas de campo e por todo o suporte científico durante o desenvolvimento da dissertação e da tese. Um agradecimento mais do que especial à Gilmara, que sempre acreditou em mim desde o TCC, sendo minha maior incentivadora e colaboradora, e que, ao longo dos anos, se tornou também uma grande amiga.

Ao Elton Dantas, que deu o pontapé inicial nesta pesquisa quando eu ainda estava no mestrado e continuou participando ativamente do trabalho ao longo do doutorado, sempre trazendo contribuições essenciais para o desenvolvimento da tese.

À Alice Cunha, por todo o apoio e colaboração nessa longa jornada do doutorado que

percorremos juntos.

Ao Hilton Costi, pela receptividade e auxílio na obtenção de análises no Laboratório de Microscopia Eletrônica no Museu Paraense Emílio Goeldi.

Ao Nilson Botelho e ao Gabriel Fernandes, pelo suporte na obtenção de dados de química mineral no Laboratório de Microssonda da Universidade de Brasília.

Ao Kei Sato, pelo auxílio na obtenção e tratamento dos dados de U-Pb SHRIMP em zircão no Laboratório de Geocronologia de Alta Resolução da Universidade de São Paulo.

À Cláudia Passareli e Marly Babisnki pelo suporte na obtenção de dados de U-Pb em zircão e titanita e Sm-Nd em rocha total no CPGEO-USP.

Ao Valdecir Janasi, pela receptividade e suporte na obtenção de dados de ETR em minerais no laboratório de química ICP- USP.

Ao Marco Galarza, pelo auxílio na obtenção e tratamento dos dados de Lu-Hf em zircão no laboratório Pará-Iso-UFPA.

Aos técnicos IG-UFPA, pelo auxílio durante esses quatro anos, especialmente Joelma Lobo, Bruno Fernandes, Cleida Freitas e Joice Sousa. Estendo este agradecimento também aos técnicos do Instituto de Geociências da USP que me auxiliaram na obtenção de dados.

Ao projeto Clube do Pesquisador Mirim, uma iniciativa do Museu Paraense Emilio Goeldi. Participei do projeto dos 10 e 13 anos e foi ali que grande parte da curiosidade que me levou à carreira científica começou a se formar. Por isso, expresso minha gratidão ao Luiz Videira, coordenador do projeto, e à minha prima Alessandra Lima, que me apresentaram ao projeto. Além deles, aos instrutores que tive na época: Alcemir Aires, Hilma Guedes, Raquel Ferreira e Tâmara Pereira.

Aos meus pais, Lúcia e Airton, foram eles que me ensinaram que vencer por meio dos estudos é um caminho árduo, mas correto. Eles sempre foram meus maiores incentivadores, muitas vezes sem compreender completamente o que eu estava passando, mas sempre me oferecendo apoio incondicional em todos os âmbitos da minha vida. Apoiaram todas as minhas decisões: sair de casa aos 18 anos para estudar em Marabá-PA, aos 23 ir para Brasília-DF fazer o mestrado e, depois, retornar a Belém para o doutorado. Minha maior gratidão é a eles.

Ao meu irmão, Alex, e ao meu sobrinho, Antony, agradeço por todos os momentos essenciais de conversas, suporte e distrações.

As amizades construídas no PPGG-UFPA, especialmente Caio Mesquita e Ingrid Viana, os últimos dos moicanos, com quem tive o prazer de conviver e colaborar ao longo destes anos de doutorado. Além deles, agradeço também a todas e todos da sala 7: Luísa Barros, Yasmin Ferro, Fábio Pereira, Renata Veras, Renan Fernandes e Bruna Nogueira, que me acolheram

desde o início do doutorado e tornaram essa jornada mais tranquila.

À Nazaré Barbosa, pelo acolhimento, apoio, receptividade e ótimos momentos em São Paulo.

À Hévilla Gomes, por esses quase 30 anos de companheirismo.

À Andréia Milhomem, pela amizade e suporte mais que essencial ao longo dos anos.

As amizades fora do meio acadêmico, de longa ou curta data, que me proporcionaram momentos incríveis e estiveram ao meu lado ao longo do doutorado. Em especial: Jessé Santa Brígida, Gabriela Maués, Mário Penante, Bruna Lima, Tainara Nunes, Caio Reis, Laila Rocha, Jannifer Leão, Marcos Moraes, Patrícia Silva, Thaianny Trindade, Fábio Chaves, Neto Carvalho, Letícia Assunção, Antônio Portella e Adriano Oliveira.

À família Rocha pela receptividade e apoio em Marabá.

À Gicélia Gonçalvez, minha psicóloga, que me acompanha desde 2018 e tem me ajudado a levar a vida de maneira mais leve.

E, por fim, muito obrigado a todas as pessoas que, direta ou indiretamente, contribuíram para a realização deste sonho!

“I was afraid of this parade because I wanted so badly to be a part of it. So today, I’m marching for that part of me who was once too afraid to march, and for all the people who can’t march, the people living lives like I did. Today, I march to remember that I'm not just a 'me', but I’m also a 'we', and we march with pride.”
Lana e Lilly Wachowski

RESUMO

A integração de dados de campo, petrográficos, mineralógicos, geoquímicos, geocronológicos (U-Pb em zircão, monazita e titanita) e isotópicos (Sm-Nd em rocha total e Lu-Hf em zircão) na porção sul do Domínio Bacajá permitiu a identificação e caracterização de novas unidades de granitoides e charnockitos, previamente englobadas no Complexo Cajazeiras. Essas descobertas permitiram redefinir a estratigrafia da região e avançar no conhecimento sobre as condições de cristalização, origem e evolução das rochas magmáticas e metamórficas ortoderivadas. Um evento magmático riaciano de longa duração (~70 Ma) ocorreu na área com início em ~2,12 Ga e término em ~2,05 Ga. Neste evento foram cristalizados os granitos Bandeirante (2,12 Ga, $\varepsilon Hf_{(t)}$ = -6,5 a -4,6, $\varepsilon Nd_{(t)}$ = -3,40); Alto Rio Preto (2,10-2,06 Ga, $\varepsilon Hf_{(t)}$ = -10,2 a -6,3, $\varepsilon Nd_{(t)}$ = -8,96 a -2,80); os charnockitos Maravilha (2,09 Ga, $\varepsilon Hf_{(t)}$ = - 9,2 a -8,2, $\varepsilon Nd_{(t)}$ = -3,01 a -1,91) e Serra Azul (2,07 Ga, $\varepsilon Hf_{(t)}$ = -8,8 a -5,8, $\varepsilon Nd_{(t)}$ = -6,44 a -4,71); e granito Bernardino (2,05 Ga, $\varepsilon Nd_{(t)}$ = -6,71). Em termos geoquímicos, as unidades são cálcio-alcalinas e magnesianas (granitos Alto Rio Preto e Bernardino e Charnockito Serra Azul), e variam para cálcicas ou álcali-cálcicas e ferrosas (Granito Bandeirante e Charnockito Maravilha). Os granitoides são metaluminosos a fracamente peraluminosos, com exceção do granito Bernardino, que é fortemente peraluminoso. Os isótopos de Nd e Hf indicam uma fonte crustal com valores de épsilon fortemente negativos e idades modelo majoritariamente arqueanas, com grande diferença em relação às idades de cristalização, sugerindo longo período de residência crustal. Esses granitoides foram formados durante a colisão entre os domínios Bacajá e Carajás, durante a Orogenia Transamazônica, em um ambiente tardi- a pós-colisional. A delaminação da crosta espessada foi o provável mecanismo responsável pela fusão parcial da crosta para geração dos magmas. As assinaturas de Nd e Hf revelam uma compartimentação crustal coerente entre os domínios Bacajá, Lourenço, Carecuru (Cráton Amazônico) e Bauolé-Mossi (Cráton Oeste Africano), sugerindo que esses segmentos estiveram justapostos durante a amalgamação do supercontinente Columbia. O Granito Alto Rio Preto é composto por monzogranitos e restritos granodioritos-tonalitos com epidoto magmático. Ele foi colocado a pressões entre 0,4 e 0,7 GPa, cristalizou em temperaturas entre 949 e ~640 ºC, evoluiu sob condições oxidantes (NNO±0,5 a ±1), com teor inicial de H_2O <4 a 6 % em peso. A preservação do epidoto é atribuída a uma interação complexa entre altas pressões de geração, ambientes oxidantes e elevada quantidade de água no magma, somada à baixa densidade e viscosidade que facilitaram a rápida ascensão dos magmas (4-5 km/ano) através da crosta, impedindo a total dissolução do epidoto. A integração e dados de campo e petrográficos sugerem que esse granito representa uma intrusão sintectônica. Esse granito apresenta afinidade com as séries cálcio-

alcalinas de alto K. O magma parental da fácies monzograníticas foi gerado a partir da fusão por desidratação de fonte basáltica a 0,99 GPa e 865 °C deixando um resíduo anfibolítico. Eles representam um exemplo de granitoides formados pelo retrabalhamento crustal da crosta máfica inferior, não contribuindo para o crescimento crustal na zona de colisão entre os domínios Bacajá e Carajás. O Charnockito Maravilha é composto por duas associações petrográficas: (i) monzonito-granito-charnockito e (ii) granodiorito-monzogranito, que podem ou não conter ortopiroxênio e/ou faialita + quartzo de origem ígnea. A associação (i) cristalizou em temperaturas entre 1052 e ~680 ºC, e evoluiu em condições reduzidas (FMQ±0,5), com teor de água inicial no magma ≤3 wt%; a (ii) cristalizou em temperaturas entre 918 e ~680 °C, evoluiu em condições oxidantes (NNO±0,5), com teor inicial de água de ~ 3-4 wt%. Ambas as associações foram colocadas a pressões entre 0,3 e 0,6 GPa. O Charnockito Serra Azul é composto por tonalitos, granodioritos e granitos que podem ou não conter ortopiroxênio ígneo. Foi colocado a pressões entre 0,3 e 0,6 GPa, temperaturas entre 1078 e ~700 °C, evoluiu em condições oxidantes (NNO±0,7 a ±2) e com teor de água inicial de ~ 2 a 3 % em peso. Os dados termodinâmicos indicam que faialita é uma fase restrita a baixas pressões (≤0,3 GPa) e condições reduzidas (FMQ -2 a -0,6), mas que pode cristalizar em presença de teores significativos de água. Por outro lado, ortopiroxênio pode cristalizar a pressões variadas (0,1 a 1 GPa) em condições reduzidas a oxidadas (FMQ-2 a NNO+2,5) e com quantidades moderadas de água (~5,2 a 6,5 %). O Complexo Cajazeiras é composto por ortognaisses tonalíticos a monzograníticos cristalizados em 2,97-2,94 Ga, com posterior perda de Pb/metamorfismo em 2,80-2,81 Ga e 2,21-2,01 Ga. Na área estudada, apresentam afinidades geoquímicas com rochas sanukitoides *s.l.* (V ≥ 40 ppm, Cr ≥ 39 ppm, Ba+Sr >1400 ppm) representando o magmatismo sanukitoide mais antigo do Cráton Amazônico e o segundo mais antigo do mundo. Os isótopos de Nd e Hf (εNd(t) +0,65; εHf(t) +0,5 a +2,5) indicam contribuição juvenil e curto período de residência crustal com idades modelos muito próximas às de cristalização. A ocorrência de rochas sanukitoides sugere que o manto já estava metassomatizado no Mesoarqueano. Tais ortognaisses foram metamorfisados em fácies anfibolito superior a granulito. O pico do metamorfismo é marcado pela assembleia clinopiroxênio-anfibólio-biotita-quartzo-magnetita-ilmenita-líquido que marca início de fusão parcial, e foi formada a ~0,52–0,55 GPa/760–790 °C, por volta de 2,21 Ga; o resfriamento em direção ao *solidus* ocorreu entre 2,10 e 2,08 Ga, e o retrometamorfismo é marcado por anfibólio-biotita-quartzo-magnetita-ilmenita-H_2O, desenvolvido a ~0,40–0,48 GPa/600–650 °C, em torno de 2,01 Ga.

Palavras-chave: granitoides; charnockitos; sanukitoides; isótopos de Nd-Hf; Domínio Bacajá.

ABSTRACT

The integration of field, petrographic, mineralogical, geochemical, geochronological (U-Pb in zircon, monazite, and titanite), and isotopic data (Sm-Nd in whole rock and Lu-Hf in zircon) undertaken in the southern portion of the Bacajá Domain enabled the identification and characterization of new granitoid and charnockitic units previously encompassed within the Cajazeiras Complex. These discoveries allowed a redefinition of the regional stratigraphy and advancing the understanding of the crystallization conditions, origin, and evolution of magmatic and metamorphic orthoderived rocks. A long-lived Rhyacian magmatic event (~70 Ma) was recognized, beginning around 2.12 Ga and lasting until 2.05 Ga. During this interval, the following units were identified: Bandeirante (2.12 Ga, $\varepsilon Hf_{(t)}$ = -6.5 to -4.6, $\varepsilon Nd_{(t)}$ = -3.40); and Alto Rio Preto (2.10-2.06 Ga, $\varepsilon Hf_{(t)}$ = -10.2 to -6.3, $\varepsilon Nd_{(t)}$ = -8.96 -2.80) granites; Maravilha (2.09 Ga, $\varepsilon Hf_{(t)}$ = - 9.2 to -8.2, $\varepsilon Nd_{(t)}$ = -3.01 to -1.91) and Serra Azul (2.07 Ga, $\varepsilon Hf_{(t)}$ = -8.8 to -5.8, $\varepsilon Nd_{(t)}$ = -6.44 to -4.71) charnockites; Bernardino granite (2.05 Ga, $\varepsilon Nd_{(t)}$ = -6.71). Geochemically, the units are mostly high-K calc-alkaline and magnesian (Alto Rio Preto and Bernardino granites, Serra Azul charnockite), transitioning to calcic or alkali-calcic and ferroan (Bandeirante granite and Maravilha charnockite, respectively). They range from metaluminous to weakly peraluminous, except the Bernardino granite, which is strongly peraluminous. The Nd-Hf isotopic integration indicates a crustal source with strongly negative epsilon values and Archean model ages, with a marked contrast to crystallization ages, pointing to long crustal residence times. These granitoids were generated by the collision between the Bacajá and Carajás domains in a late- to post-collisional setting during the Transamazonian Orogeny. Crustal thickening and subsequent delamination are interpreted as the main mechanisms responsible for partial melting and generation of these magmas. The Nd-Hf isotopic signatures reveal a coherent crustal compartmentalization between the Bacajá, Carecuru and Lourenço (Amazonian Craton) and Bauolé-Mossi domains (West Africa Craton), suggesting that these segments were juxtaposed during the amalgamation of the Columbia supercontinent. The Alto Rio Preto granite is composed of epidote-bearing granites and granodiorites-tonalites. This granite was emplaced at pressures of 0.4-0.7 GPa and temperatures between 949 and ~640 ºC, evolved under oxidizing conditions (NNO±0.5 to ±1), with initial water contents of ~2-6 wt%. The preservation of magmatic epidote results of a complex interaction between generation and emplacement pressures, oxidizing conditions and water content in the magma, combined with low density and viscosity that facilitated rapid magma ascent (4-5 km/year) through the crust, preventing complete epidote dissolution. Field and petrographic data suggest that this granite represents a syntectonic intrusion, with geochemical affinities with high-K calc-alkaline series.

The parental magma of the monzogranitic facies was derived from dehydration melting of a basaltic source at 0.99 GPa and 865 °C leaving an amphibolite residuum. These granitoids represent an example of crustal reworking of lower mafic crust and do not contribute to net crustal growth in the collisional zone between the Bacajá and Carajás domains. The Maravilha charnockite comprises two petrographic associations: (i) monzonite-granite-charnockite and (ii) granodiorite-monzogranite, with or without igneous orthopyroxene and fayalite + quartz. The (i) association crystallized at temperatures between 1052 and ~680 °C, and evolved under reducing (FMQ±0.5), with ≤3 wt% initial water contents. The (ii) crystallized at temperatures between 918 and ~680 °C and evolved under oxidizing conditions (NNO±0.5), with ~4 wt% initial water contents. Both associations were emplaced at pressures between 0.3 and 0.6 GPa The Serra Azul charnockite consists of tonalites, granodiorites, and rare granites, with or without igneous orthopyroxene. These rocks were emplaced at pressures 0.3-0.6 GPa, temperatures between 1078 and ~700 ºC, and evolved under oxidizing conditions (NNO±0.7 to ±2), with initial water contents ~ 2-3 wt%. Thermodynamic data indicate that fayalite is restricted to low pressures (≤0.3 GPa) and reduced conditions (FMQ -2 to -0.6), but it can crystallize under water-rich conditions (2.3 to 6.2 wt%, possibly up to 9 wt%). In contrast, orthopyroxene can crystallize over a wide pressures range (0.1-1 GPa), from reduced to oxidizing conditions (FMQ-2 to NNO+2.5), and under moderate water contents (~5.2 to 6.5 wt%). The Cajazeiras Complex comprises tonalitic to monzogranitic orthogneisses crystallized at 2.97-2.94 Ga, followed by Pb-loss/metamorphism at 2.80–2.81 Ga and Paleoproterozoic metamorphism 2.21-2.01 Ga. These rocks show geochemical affinities with sanukitoid *s.l.*, representing the oldest sanukitoid magmatism in the Amazonian Craton and the second oldest worldwide. The Nd-Hf data (εNd(t) +0.65; εHf(t) +0.5 to +2.5) suggest a juvenile contribution and short crustal residence time, with model ages close to the crystallization age. The discovery of these rocks implies that the mantle was already metasomatized in the Mesoarchean and opens possibilities for the presence of other typical Archean rocks in the basement of the domain. These orthogneisses were metamorphosed under upper amphibolite to granulite facies. The metamorphic peak was marked by the assemblage clinopyroxene-amphibole-biotite-quartz-magnetite-ilmenite-melt, under conditions of ~0.52–0.55 GPa/760–790 °C at ~2.21 Ga. Cooling toward the *solidus* occurred at ~ 2.10-2.08 Ga, and retrograde metamorphism is represented by the amphibole-biotite-quartz-magnetite-ilmenite-H_2O assemblage, developed under ~0.40–0.48 GPa/600–650 °C at ~2.01 Ga.

Key-words: granitoids; charnockites; sanukitoids; Nd-Hf isotopes; Bacajá Domain.

LISTA DE ILUSTRAÇÕES

1 INTRODUÇÃO

Figura 1 - Localização e acesso a área de estudo 5

Figura 2 - (A) localização do Cráton Amazônico na Plataforma Sul-americana, (B) localização da Província Maroni-Itacaiúnas (Tassinari & Macambira 2004), (C) Mapa geológico regional simplificado do Domínio Bacajá (Barros 2023, Macambira *et al.* 2019, Macambira & Ricci 2015, 2019)..... 7

Figura 3 - Mapa de amostragem da área de estudo com a informação dos métodos aplicados contemplando os dados apresentados nesta tese, os dados da dissertação do autor e dados ainda não publicados. 26

2 RHYACIAN MAGMATISM AT THE SOUTHERN BACAJÁ DOMAIN: IMPLICATIONS FOR THE CRUSTAL EVOLUTION OF SE AMAZONIAN CRATON, BRAZIL

Figure 1 - (A) South American platform highlighting the Amazonian craton; (B) Amazonian craton showing the Maroni-Itacaiúnas province, according to Tassinari and Macambira (2004), and its Bacajá Domain (black rectangle); (C) simplified geological map of the Bacajá Domain modified after Vasquez and Rosa-Costa (2008), Macambira and Ricci (2015), Barros et al.(2023) and showing the proposed boundaries between the Bacajá Domain and Carajás province. The black rectangle in (C) corresponds to the study area (cf. Fig. 3)..... 40

Figure 2 - Summary of crystallization ages of the Rhyacian granitoids of the Bacajá Domain. References are the same as in the table 1..... 42

Figure 3 - Geological map of the study area showing the location of dated samples. 47

Figure 4 - Field aspects of the studied granitoids and charnockites. (A) interaction between coarse and medium-grained isotropic granites from the Bandeirante granite (B) interactions between the Alto Rio Preto granite and Serra Azul charnockite; (C) mylonitic biotite granodiorite from the Alto Rio Preto granite; (D) alignment of feldspar phenocrysts (magmatic flux structure) of the Maravilha charnockite; (E) bluish K-feldspar crystals from a sienite of the Maravilha charnockite;(F) oval-shaped mafic microgranular enclave in the Serra Azul charnockite; (G) igneous layering int biotite monzogranite of the Serra Azul charnockite; (H) metasedimentary enclave in a garnet-biotite granite of the Bernardino granite; (I) alignment of feldspar phenocrysts (magmatic flux structure) in the Bernardino granite showing a concordant leucogranitic vein. 50

Figure 5 - Main petrographic aspects of the studies granitoids and charnockites. (A) Biotite-amphibole leucosyenogranite of the Bandeirante granite showing remnants of clinopyroxene bordered by amphibole and opaque minerals and idiomorphic titanite crystals; (B) amphibole-biotite monzogranite of the Alto Rio Preto granite with hypidiomorphic granular texture and biotite bordering amphibole; (C) strongly deformed biotite granodiorite of the Alto Rio Preto granite, showing quartz ribbons and weakly pronounced mantle-core texture; (D) fayalite-pyroxene-amphibole syenogranite of the Maravilha charnockite exhibiting fayalite crystals in contact with quartz and with amphibole corona; (E) amphibole-biotite syenogranite showing coarse-grained hypidiomorphic granular texture, highlighting biotite lamellae with inclusions of early phases ;(F) pyroxene-amphibole-biotite tonalite of the Serra Azul charnockite showing remnants of ortho- and clinopyroxene bordered by amphibole; (G) pyroxene-amphibole-biotite granodiorite of the Serra Azul charnockite showing orthopyroxene crystals surrounded by amphibole; (H) garnet-biotite granodiorite of Bernardino granite with hypidiomorphic granular texture and fine biotite lamellae bordering plagioclase; (I) garnet-biotite granodiorite of Bernardino showing inclusion of hypidiomorphic garnet in a plagioclase phenocryst. Mineral abbreviations follow Whitney and Evans (2010)..... 51

Figure 6 - Chondrite normalized REE patterns (Boynton, 1984) and normalized multielement patterns (McDonough and Sun, 1995) 58

Figure 7 - Geochemical classification and magmatic series. (A) P-Q diagram (Debon and Fort, 1983); (B) AFM diagram (Irvine and Baragar, 1971); (C) Na-K-Ca diagram (trondhjemite field and trends Thd and CA = calc-alkaline of Barker and Arth, 1976; Luais and Hawkesworth, 1994); (D) SiO_2 vs Na_2O+K_2O – CaO diagram (Frost et al., 2001); (E) SiO_2 vs FeOt/(FeOt+MgO) diagram (Frost et al. 2001; Terentiev and Santosh, 2018); (F) ASI vs. A/NK (Frost et al., 2001) 61

Figure 8 - Tectonic discrimination diagrams. (A) Nb vs. Y diagram, (B) Nb/Zr vs. Zr diagram. Fields after Pearce et al., (1984); (C) DF1 vs.; DF2 ; (D) DF1 vs. DF2 (Verma et al., 2013) 62

Figure 9 - Representative CL (AA-03C, AA-76, AA-06A, AA-20) and BSE (ASM-01 and ASM-25) images from the analyzed zircons. 65

Figure 10 - SHRIMP U-Pb concordia plots for the studied granitoids and charnockites. (A) Bandeirante granite (AA-03C); (B) Alto Rio Preto granite (AA-76); (C) Maravilha charnockite (AA-06A); (D) Serra Azul charnockite (AA-20). Ellipses are colored

according to the unit color in the geological map from Figure 2; light gray ellipses were discarded for age calculations, and light blue ellipses represent inherited grains. 65

Figure 11 - LA-MC-ICP-MS U-Pb concordia plots for the studied granitoids. (A) Alto Rio Preto granite (ASM-01); (B) Bernardino granite (ASM-25 - zircon) in the histogram only zircon with ±10% were plotted; (C) Bernardino granite (ASM-25 - monazite); (D) Th vs. U diagram to distinguish magmatic vs. hydrothermal vs. metamorphic monazite (Piechoka et al., 2017). (E) Plot of time (Ma) vs. εHf for the Paleoproterozoic granitoids and charnockites from the study area, the gray shaded area represents the Hf data from northern Bacajá Domain (Magalhães et al., 2023), and the blue shaded area represents the Hf data from Archean and Orosirian Carajás Province (Marangoanha et al., 2019; Ribeiro-Silva et al., 2023; Teixeira et al., 2019). Ellipses are colored according to the unit color in the geological map from Figure 2; light gray ellipses were discarded for age calculations, and light blue ellipses represent inherited grains. 66

Figure 12 - $\varepsilon Nd_{(t)}$ vs. age (Ga) of samples from the studied granitoids and charnockites. The gray shaded area represents the Nd from the northeast, east, southeast, and central portion of the Bacajá Domain (with negative $\varepsilon Nd_{(t)}$), the red shaded area represents the Nd data from the extreme north of the domain (positive $\varepsilon Nd_{(t)}$ data). Data compiled from Macambira et al., (2009), Vasquez (2006), Vasquez and Rosa-Costa (2008), Magalhães et al., (2022), and Barros et al., (2023). 68

Figure 13 - (A) Map of Nd-T_{DM} model ages distribution in the Bacajá Domain based on whole-rock Sm-Nd istopic data from 107 samples of Archean to Rhyacian ages of felsic to intermediate compositions; (B) map of $\varepsilon Nd_{(t)}$ distribution in the Bacajá Domain based on 95 samples (excluding 12 samples of paragneisses used in the map in (A). Data from :Barros *et al.* (2023); Cristo (2018), Macambira *et al.* (2009), Magalhães *et al.* (2023), Neri *et al.* unpublished data, Vasquez and Rosa-Costa (2008) and references therein, Vasquez (2006).The black line in the southern region of the Bacajá Domain represents the proposed boundary with the Carajás Province (Correa *et al.* 2022). 73

Figure 14 - Proposed two-stage geodynamic model for the southern Bacajá Domain. (A) During 2.12–2.10 Ga, collision between the Archean Bacajá basement and island arcs accreted to the Carajás Province caused crustal thickening and high-temperature metamorphism, leading to the emplacement of syn-collisional granitoids. (B) Between 2.09–2.05 Ga, lithospheric delamination triggered asthenospheric upwelling

and partial melting of thickened Archean crust, generating post-collisional charnockites and peraluminous granitoids.. SLCM = subcontinental lithospheric mantle, O.C = oceanic crust, C.C = continental crust. 76

Figure 15 - Plot of time (Ma) vs. εHf for the Paleoproterozoic granitoids and charnockites from the Bacajá Domain, including the data from the studied area. For regional and global comparison, Hf data from selected Rhyacian terranes were compiled: Carecuru and Lourenço domains, and French Guiana from the Amazonian craton (Milhomen and Lafon, 2020, Queiroz, 2020); from Baoulé-Maossi domain, West Africa craton (Eglinger et al., 2017, Parra-Avila et al., 2018, Petterson et al., 2016). 80

3 MAGMATIC EPIDOTE AS A PROXY OF DEEP AND OXIDIZED MAGMATISM IN THE PALEOPROTEROZOIC BACAJÁ DOMAIN, SE AMAZONIAN CRATON

Figure 1 - (a) Amazonian craton and the location of the Bacajá Domain in the Maroni-Itacaiúnas Province (Tassinari and Macambira, 2004). (b) simplified geological map of the Bacajá Domain (Barros et al., 2007; Besser and Barros, 2015; Macambira and Ricci, 2015; Macambira et al., 2009; Vasquez and Rosa-Costa, 2008). (c) Geological map of the studied area (Neri et al., submitted). 122

Figure 2 - QAP and Q-A+P-M' diagrams (Le maitre 2002) for samples of the Alto Rio Preto granite 124

Figure 3 - Main petrographic aspects of the Alto Rio Preto granite. (a) mafic clot composed of amphibole, biotite, titanite and opaque minerals; (b) oval-shaped amphibole in mylonitic granite, surrounded by recrystallized biotite (bt3); (c) quartz with undulose extinction accompanied by subdiomorphic biotite (bt2). (d) fine grained titanite formed after biotite (ttn2); (e) magmatic epidote with straight contacts with biotite; (f) magmatic epidote forming coronitic texture in allanite; 126

Figure 4 – Classification diagrams for the analyzed mineral phases. (a, b) calcic amphibole classification after Leake et al. (1997); (c) Si vs. Fe/(Fe + Mg) compositional classification of biotite (Deer et al., 2013); (d) Fe/(Fe + Mg) vs. Al^{IV} compositional classification of biotite (Deer et al., 2013); (e) Mg vs. Al_t diagram for biotite (Nachit 1985); (f) (FeO + MnO)-(10*TiO_2)-MgO diagram with fields from Nachit et al. (2005) 127

Figure 5 – Classification diagrams for the analyzed mineral phases. (a) Ab–An–Or ternary diagram showing the plagioclase compositions (Deer et al., 2013); (b) histogram of compositional variation in the pistacite component ([Fe^{3+}/Fe^{3+}+Al]/100), in

molecular percentage (mol.%); (d) Al vs. Fe in titanite with fields from Aleinikoff et al. (2002); (c) F vs. Al in titanite (Kowallis et al., 2022); (e) Al/Fe density spectrum with fields of inherited igneous and recrystallized titanites (Scibiorski and Cawood, 2021) 128

Figure 6 - P-T pseudosection do the Alto Rio Preto granite at (a) 4 wt% H_2O, (b) 6 wt% H_2O of initial water in the system. Solid lines mark each phase stability field, the appearance is marked with the symbol (+) and disappearance with (-). Dashed lines mark the XAn in plagioclase (blue), XMg in amphibole (green), and Ti in the M2 site of biotite (red). Bellow the light grey dashed line, the minerals and melt co-exist with a free H_2O-rich fluid 132

Figure 7 - T/P-MH_2O for sample AA-76. (a) T-M_{H2O} at 0.64 GPa and ~ NNO+1; (b) T-M_{H2O} at 0.93 GPa and ~NNO+1; (c) P-M_{H2O} at 620 ºC and ~NNO+1; (d) P-MH_2O at 680 ºC and ~NNO+1. The plus (+) symbol marks the appearance of the phase, and the minus (-) the disappearance. The P-M_{H2O}/log$f$O2 must be read from the left to the right and from the bottom to the top. The phases highlighted at the top of the diagram are in all fields of the modeled ranges. 134

Figure 8 - T/P-Mlog$f$$O_2$ for sample AA-76. (a) T-Mlog$f$$O_2$ at 0.64 GPa; (b) T-MlogfO$_2$ at 0.93 GPa; (c) P-Mlog$f$$O_2$ at 620 ºC with 6 wt% H_2O; (d) P-Mlog$f$$O_2$ at 680 ºC with 6 wt% H_2O. The plus (+) symbol marks the appearance of the phase, and the minus (-) the disappearance. The P-M_{H2O}/log$f$$O_2$ must be read from the left to the right and from the bottom to the top. The phases highlighted in the tops of the diagram are in all fields of the modeled ranges. 135

Figure 9 - Estimative of crystallization parameters from Alto Rio Preto granite. (a) Fe/(Fe + Mg) vs Al^{IV} + Al^{VI} diagram for amphiboles from the studied rocks, with isobars from Anderson and Smith (1995), (b) Fe/(Fe+Mg) vs. Al^{IV} diagram showing the compositional variation of amphibole (the analyses in the high $f$$O_2$ field are from sample AA-76) fields after Anderson and Smith (1995), (c) Log$f$$O_2$ vs. temperature based on amphibole composition (Ridolfi et al., 2010), (d) Fe/(Fe+ Mg) vs. Al^{IV} + Al^{VI} diagram showing the compositional variation of biotites (ilmenite and magnetite series according to Anderson et al. (2008). The fields of comparison: from Seridó, Cahoeirinha-Salgueiro, Alto Pajeú and Macuraré terranes from Borborema Province, NE Brazil (Sial et al., 2008), Teixeira batholith, Borborema Province (Lima et al. 2021), and Agapur granitoids, India (Basak et al. 2019). 139

Figure 10 - Diagram showing the variation in the calculated magma viscosity from the Alto Rio Preto magmas as a function of temperature. Viscosity was calculated based on the model by Giordano et al. (2008). 142

Figure 11 - Textural aspects of the epidotes used in the dissolution kinetic study. The original shapes of the epidote crystals are indicated by the black lines, the orange lines delimit the current shape of the corroded crystals, the largest dimension. Line segments with an arrow point shows the maximum dissolution values used in kinetic study. (a-b) epidote crystals in the ABMzG facies with straight contacts with biotite and irregular contacts with quartzfeldspatic matrix; (c-d) epidote surrounding allanite cores in the BGrd facies with irregular contacts with quartzfeldspatic matrix. 145

Figure 12 - Magma nature inferences based on mineral chemistry data. (a) MgO vs FeO/(FeO + MgO) diagram for biotite showing the components present in the magma source (Zhao et al., 2012) ; (b) FeO–MgO–Al_2O_3 discrimination ternary diagram based on biotite composition (Abdel-Rahman, 1994); (c) Fe/(Fe+Mg) vs. Fe classification diagram showing trends for I-type and S-type granites defined from biotite composition (Villaseca et al., 2017); (d) Ca-Fe_T-Mg ternary diagram for the amphibole showing the components present in the magma source (Xie and Zhang, 1990) 148

4 DEHYDRATION MELTING OF BASALTIC CRUST TO GENERATE RHYACIAN HIGH-K CALC-ALKALINE GRANITES, SE AMAZONIAN CRATON: IMPLICATIONS FOR CRUSTAL REWORKING IN COLLISIONAL OROGENS

Figure 1 - (a) Amazonian craton and the location of the Bacajá Domain in the Maroni-Itacaiúnas Province (Tassinari and Macambira, 2004). (b) simplified geological map of the Bacajá Domain (Barros et al., 2007; Besser and Barros, 2015; Macambira and Ricci, 2015; Macambira et al., 2009; Vasquez and Rosa-Costa, 2008). (c) Geological map of the studied area (Neri et al., submitted). 174

Figure 2 - Field aspects of the Alto Rio Preto granite. (a) oval-shaped mafic enclaves in the contact zone between the granite and the Serra Azul charnockite; (b) late granitic veins concordant with the regional foliation; (c) low plunge mineral stretching lineation; (d) isotropic biotite monzogranite; (e) alignment of K-feldspars phenocrystals indicating magmatic flux structures; (f) centimetric shear-bands developed in the granite; (g) S-C structures with sinistral shear sense; (h) plagioclase

σ-porphyroclast with dextral shear sense in mylonitic granitoid; (i) tectonic banding juxtaposing mylonites and ultramylonites. 180
Figure 3 - QAP and Q-A+P-M' diagrams (Le Maitre 2002) for samples of the Alto Rio Preto granite 181
Figure 4 - Microstructural features of the Alto Rio Preto granite's low-grade (a–e) and medium-grade (f–i) mylonites. (a) Idiomorphic to subidiomorphic aggregates of amphibole, biotite, and titanite. (b) Late-magmatic fractures in plagioclase. (c) Crystal-plastic deformation in plagioclase, evidenced by comminution into tiny new grains. (d) Quartz with undulose extinction, highlighting the recovery process. (e) Deformed quartz with undulose extinction and lobate contacts, showing incipient recrystallization by bulging. (f) Plagioclase porphyroclast exhibiting deformation by "kinking." (g) Core-mantle structures in K-feldspar porphyroclasts formed by bulging recrystallization. (h) Flame-perthite in K-feldspar. (i) Quartz recrystallized by subgrain rotation 183
Figure 5 - Harker diagram (SiO_2 vs major elements) of the Alto Rio Preto granite 188
Figure 6 - Harker diagram (SiO_2 vs trace elements) of the Alto Rio Preto granite..... 189
Figure 7 - Chondrite normalized REE patterns (Boynton, 1984) and normalized multielement patterns (McDonough and Sun, 1995) of the distinct facies of the Alto Rio Preto granite. (a-b) ABMzG, (c-d) BMzG, (e-f) BGrd. 190
Figure 8 - Geochemical classification and magmatic series. (a) P-Q diagram (Debon and Fort, 1983); (b) A/NK vs. A/CNK (Shand, 1943); (c) SiO_2 vs Na_2O+K_2O – CaO diagram (Frost et al., 2001); (d) SiO_2 vs FeOt/(FeOt+MgO) diagram (Frost et al. 2001) (F) K_2O vs. SiO_2 (Peccerillo and Taylor, 1976); (f) Rb vs. Y+Nb (Pearce, 1984)..... 191
Figure 9 - Representative CL images for zircon and BSE images for titanite from of the Alto Rio Preto granite. Zircon CL images for sample AA-76 are from Neri et al. (submitted) 193
Figure 10 – (a-b) SHRIMP U-Pb concordia plots for zircons. (c-d) LA-ICP-MS concordia plots for titanite. Zircon data for sample AA-76 (a) are from Neri et al. (submitted).... 193
Figure 11 - Geochemical insights into petrogenesis. (a) source dagram Al_2O_3/(FeOt+MgO) vs. 3CaO vs. 5(K_2O/Na_2O) (Laurent et al., 2014); CaO + FeOt +MgO + TiO_2 vs. CaO/ (FeOt + MgO + TiO_2) (Patiño Douce, 1999b); (c) FeOt vs. Nb + Zr + Y (Laurent et al., 2014); (d) Y vs. Sr/Y..... 197

Figure 12 - Pseudosection of an average basalt composition (Condie 1993). The red circle represents the P-T conditions at which melt composition was extracted, and the trace elements were calculated. 200

Figure 13 - Trace element modeling for the generation of the Alto Rio Preto granite magmas. (a) Amphibole-biotite monzogranite (AA-76). (b) Biotite granodiorite (AA-45). 202

Figure 14 - (a) La vs. La/Sm, (b) Th vs. Th/Nd with trends for partial melting and fractional crystallization defined by Schiano et al. (2010)..... 203

5 WATER, REDOX, AND COMPOSITIONAL CONTROLS ON ORTHOPYROXENE AND FAYALITE STABILITY IN RHYACIAN IGNEOUS CHARNOCKITES, BACAJÁ DOMAIN, SE AMAZONIAN CRATON: INSIGHTS FROM MINERAL CHEMISTRY AND THERMODYNAMIC MODELING

Figure 1 - (a) The Amazonian craton, highlighting the Maroní-Itacaiúnas Province. (b) regional map of the Bacajá Domain (modified after (Vasquez and Rosa-Costa 2008; Macambira and Ricci 2015; Barros et al. 2023). (c) geological map of the studied area with the location of the studied samples 230

Figure 2 - Field aspects of the Maravilha (a-c) and Serra Azul (d-f) charnockites. (a) isotropic biotite-amphibole quartz monzonite. (b) coarse-grained fayalite-pyroxene-amphibole syenogranite. (c) equigranular medium-grained pyroxene-amphibole-biotite granodiorite (sample AA-109; cf. modeling). (d) medium-grained pyroxene-amphibole-biotite tonalite (sample AA-20;cf. modeling). (e) alignment of mafic minerals in the clinopyroxene-biotite tonalite. (f) alignment of mafic minerals in the biotite monzogranite facies 231

Figure 3 - QAP and Q-A+P-M’ diagrams for representative samples of the Maravilha and Serra Azul charnockites (Fields of Le Maitre et al., 2002) 234

Figure 4 - Microscopic features of the Maravilha (a-f) and Serra Azul (g-i) charnockites. (a) fayalite with straight contacts with quartz and rimmed by amphibole in FAPSG. (b) mafic clot in FAPSG composed of amphibole, fayalite, and inverted pigeonite. (c) symplectic intergrowth of biotite + quartz after amphibole in BAMz. (d) grunerite enclosed by hastingsitic amphibole in BAMz. (e) idiomorphic orthopyroxene in straight contact with quartz and feldspars in the matrix of BPMzG. (f) elongated orthopyroxene accompanied by amphibole and biotite in BPMzG. (g) amphibole associated with biotite and orthopyroxene in PABTn. (h) subidiomorphic orthopyroxene crystal surrounded by late-magmatic biotite in PABGrd. (i) subidiomorphic orthopyroxene crystals associated with plagioclase in the matrix234

Figure 5 - Classification diagrams for olivine, pyroxenes and amphiboles from Maravilha and Serra Azul charnockites. (a) Olivine composition plotted in the Fo-Lrn-Fa diagram. (b) Pyroxene compositions plotted in the En-Wo-Fs classification diagram (fields after Morimoto *et al*. 1988). (c) $Mg/(Mg + Fe^{2+})$ versus Si diagram for amphiboles with $Ca_B \geq 1.50$, $(Na + K)A \geq 0.50$, and $Ti < 0.50$. (d) $Mg/(Mg + Fe^{2+})$ versus Si diagram for amphiboles with $Ca_B \geq 1.50$, $(Na + K)A < 0.50$, and $Ca_A < 0.50$..... 236

Figure 6 - Classification diagrams for biotite and plagioclase from Maravilha and Serra Azul charnockites. (a) Si vs. Fe/(Fe + Mg) diagram (Deer et al., 2013). (b) Fe/(Fe + Mg) x Al^{IV} diagram (Deer et al., 1992). (c) Mg x Alt diagram (Nachit, 1985); (d) (FeO + MnO)-(10*TiO2)-MgO diagram with fields from Nachit et al. (2005). (e) and (f) Ab-An-Or diagram for feldspars (Deer et al., 2013)..... 237

Figure 7 - P-T pseudosection for the reduced variety of the Maravilha charnockite at (a) 1 wt%, (b) 2 wt%, (c) 3 wt%, and (d) 4 wt% of initial H_2O in the system. Solid lines mark each phase stability field; the beginning of crystallization is marked with the symbol (+) and its end with (-). (d) dashed lines mark the XMg of orthopyroxene (yellow) and XAn in plagioclase (blue). The light grey dashed lines indicate water saturation. 241

Figure 8 - T/P-M_{H2O} and T/P-M$logfO_2$ for the reduced Maravilha charnockite (sample AA-09). (a) T-M_{H2O} at 0.5 GPa and ~NNO. (b) P-M_{H2O} at 820 ºC and ~NNO. (c) T-M$log\mathit{f}O_2$ for 4 wt% H_2O. (d) P-M$log\mathit{f}O_2$ for 4 wt% H_2O at 820 ºC. The plus (+) symbol marks the appearance of the phase, and the minus (-) its disappearance. The vertical striped lines mark the upper limit of fayalite and orthopyroxene stability. Dashed areas indicate inconclusive stability fields for fayalite and orthopyroxene. These uncertain domains probably reflect limitations in the thermodynamic dataset resolution, and should be interpreted with caution. The P-M_{H2O}/$log\mathit{f}O_2$ must be read from the left to the right and from the bottom to the top 243

Figure 9 - P-T pseudosection for the oxidized variety of the Maravilha charnockite at (a) 1 wt%, (b) 2 wt%, (c) 3 wt%, and (d) 4 wt% of initial H_2O in the system. Solid lines mark each phase stability field; the beginning of crystallization is marked with the symbol (+) and its end with (-); and the dashed light-pink line represents the limit of titanite, experimental phase not observed in natural samples. (d) dashed lines mark the XMg of orthopyroxene (yellow) and biotite (red). The light grey dashed lines indicate water saturation. 245

Figure 10 - T/P-M_{H2O} and T/P-MlogfO_2 for the oxidized Maravilha charnockite (sample AA-109). (a) T-M_{H2O} at 0.5 GPa and ~NNO. (b) P-M_{H2O} at 820 ºC and ~NNO. (c) T-$M_{log fO2}$ for 4 wt% H_2O. (d) P-MlogfO_2 for 4 wt% H_2O at 820 ºC. The plus (+) symbol marks the appearance of the phase, and the minus (-) its disappearance. The vertical striped lines mark the upper limit of orthopyroxene stability. The P-M_{H2O}/logfO_2 must be read from the left to the right and from the bottom to the top..... 247

Figure 11 - P-T pseudosection of the Serra Azul charnockite at (a) 1 wt%, (b) 2 wt%, (c) 3wt%, and (d) 4 wt% of initial H_2O in the system. Solid lines mark each phase stability field; the beginning of crystallization is marked with the symbol (+) and its end with (-); the dashed light-pink line represents the limit of titanite, experimental phase not observed in natural samples. (b, c) dashed lines mark the XMg of orthopyroxene (yellow), green (amphibole), and biotite (red). The light grey dashed lines indicate water saturation 249

Figure 12 - T/P-M_{H2O} and T/P-MlogfO_2 for the Serra Azul charnockite (sample AA-20). (a) T-M_{H2O} at 0.5 GPa and ~NNO. (b) P-M_{H2O} at 850 ºC and ~NNO. (c) T-MlogfO_2 at 3 wt% H_2O. (d) P-MlogfO_2 at 3 wt% H_2O and 850 ºC. The plus (+) symbol marks the appearance of the phase, and the minus (-) is the disappearance. The vertical striped lines mark the upper limit of orthopyroxene stability. The P-M_{H2O}/logfO_2 must be read from the left to the right and from the bottom to the top 251

Figure 13 - Estimative of crystallization parameters from Maravilha and Serra Azul charnockites. (a) Fe/(Fe+Mg) vs. Al^{IV} diagram showing the compositional variation of amphibole (fields after Anderson and Smith 1995). (b) Fe/(Fe+ Mg) vs. Al^{IV} + Al^{VI} diagram showing the compositional variation of biotites (ilmenite and magnetite series according to Anderson et al. 2008). (c) LogfO_2 vs. temperature based on amphibole composition (Ridolfi et al. 2010). (d) XMg vs. Al/2 in orthopyroxene; fields of igneous and metamorphic pyroxenes are after Zhao et al. (2023). Fields for comparison in (a) and (b) are from Red Mountain Pluton (Anderson et al. 2003), Sherman batholith (Frost et al. 1999), Rio Seco charnockite (Felix et al. 2020); Café enderbite (Marangoanha et al., 2022); and Igarapé Gelado suite (Mesquita et al., 2025) 258

6 THE OLDEST SANUKITOID *s.l.* MAGMATISM IN THE AMAZONIAN CRATON REVEALS MANTLE-CRUST INTERACTIONS DURING THE MESOARCHEAN IN THE BACAJÁ DOMAIN

Figure 1 - (A) Amazonian craton and the location of the Bacajá Domain in the Maroni-Itacaiúnas Province (Tassinari and Macambira, 2004). (B) simplified geological map of the Bacajá Domain (Barros et al., 2007; Besser and Barros, 2015; Macambira and Ricci, 2015; Macambira et al., 2009; Vasquez and Rosa-Costa, 2008). (C) Geological map of the studied area. The white star symbol near the Cruzeiro do Sul village (AA-142) represents the 3.01 Ga orthogneiss dated by Macambira et al. (2007)..... 290

Figure 2 - Field (A to D) and microscopic (E, F) aspects of the Cajazeiras complex. (a) compositional layering parallel to stromatic leucosomes; (B) foliation highlighted by the alignment of mafic and felsic minerals; (C) amphibolite enclave in metatexitic orthogneiss. Leucosome accumulation at the enclave's border; (D) centimetric injected granitic leucosome; (E) interlayered levels of aligned ferromagnesian minerals alternated with quartz-feldspathic levels; (F) coronitic texture of clinopyroxene (core) and amphibole (rim). Abbreviations follows Whitney and Evans (2010). 291

Figure 3 - Major-element geochemistry of the orthogneisses of the Cajazeiras Complex. (A) MALI index ([Na_2O + K_2O] – CaO) vs. SiO2 diagram (Frost et al. 2001); (B) A/CNK vs. A/NK; (C) FeOt / (FeOt + Mg) vs. SiO_2 (Frost et al. 2001, modified by Terentiev and Santosh, 2018); (D) sum of “mafic” oxides (FeOt + MgO + MnO + TiO2) vs. SiO2; (E) Al_2O_3/(FeOt + MgO) vs. CaO/(Na_2O + K_2O); (F) Ternary source diagram 2A/CNK vs. Na_2O/K_2O vs. 2FMSB, fields are the same as Laurent et al. (2014 and references therein). For comparison are shown the fields of Amazonian craton sanukitoids (Rio Maria suite, Oliveira et al., 2011; Ourilândia and Tucumã suites, Ribeiro-Silva et al., 2023), sanukitoids *s.l.*, TTG and Bt-granite from Pietersburg block and Limpopo belt (Laurent et al., 2014). 292

Figure 4 - Trace-element geochemistry of the Cajazeiras complex. (A) Sr/Y vs. Ba/Rb ratios; (B) HFSE (represented by Zr) vs. transition element (represented by V) concentrations; (C) REE patterns normalized according to Boynton (1984); (D) multi-element patterns normalized according to McDonough and Sun (1995)..... 293

Figure 5 - (A) concordia diagram of the sample ASM-22 (tonalitic orthogneiss); (B) concordia diagram for sample AA-144A (granodioritic orthogneiss), zircon scale bar is 100 µm; (C) εHf(t) vs T (Ma).; (D) εNd(t) vs. T(Ga). Data from the Aruanã complex are from Magalhães et al. (2023) and those of the tonalitic gneiss from Macambira et al., (2009). The fields of Carajás Crust in (C) are summarized from Marangoanha et al. (2019) and Ribeiro-Silva et al. (2023); and in (D) are from Feio et al. (2013). 295

Figure 6 - Petrogenetic diagrams for the orthogneisses of the Cajazeiras Complex. (A) Ternary 1/Er vs. (Ba+Sr)/1000 vs. Er discriminant source (Heilimo *et al.*, 2010); (B) Source discriminant diagram for Archean granitoids (Laurent et al., 2014); (C) Nb/La vs. La/Yb diagram (after Smith et al., 1999); (D) discriminant Nb/Y vs. La/Yb diagram of mantle metasomatism agents (Martin *et al.*, 2009); (E) $(Hf/Sm)_N$ versus $(Nb/La)_N$ diagram (after La Flèche et al., 1998); (F) Nb/Ta vs. Nb/Zr diagram (Sun et al., 2020). Depleted-mantle (DM, Workman and Hart, 2005), average-TTG (Martin et al., 2005), sediment-derived melts (Barth et al., 2000). 296

Figure 7 - Multi-dimensional diagrams based on ln-transformed ratios of immobile trace elements for the discrimination of acid rocks (Verma et al., 2013). (A) DF1 vs. DF2., (B) DF1 vs. DF2. 298

7 TITANITE PETROCHRONOLOGY OF GARNET-FREE ORTHOGNEISSES FROM THE BASEMENT OF BACAJÁ DOMAIN, SE AMAZONIAN CRATON: INSIGHTS INTO METAMORPHIC EVOLUTION WITHOUT GARNET CONTROL

Figure 1 - (a) Amazonian craton and the location of Maroni-Itacaiúnas Province (Tassinari and Macambira, 2004). (b) simplified map of the Bacajá Domain (modified after Barros et al., 2023; Macambira and Ricci, 2015; Macambira et al., 2009; Vasquez and Rosa-Costa, 2008). (c) Geological map of the studied area (Neri et al., submitted). The withe star symbol near the Vila Cruzeiro do Sul represents the orthogneiss crystallized at 3009 ± 27 Ma and metamorphosed at 2074 ± 8 Ma (Macambira et al., 2007). 326

Figure 2 - Hand specimen and plane polarized transmitted light photomicrographs of sample ASM -22 (a, c, d), and AA-144A (b, e, f). (c) amphibole coronas around clinopyroxene; (d), alignment of amphibole in straight contact with titanite alternating with quartzfeldspatic levels; (e) medium-grainer amphibole with clinopyroxene core, medium-grained allanite associated with amphibole; (f) association of titanite with biotite. 330

Figure 3 - Classification diagrams for the analyzed mineral phases. (a) Pyroxene compositions showing En-Wo-Fs classification diagram after (Morimoto et al., 1988); (b) amphibole classification (Leake; et al., 1997); $Mg/(Mg + Fe^{2+})$ versus Si diagram based on $Ca_B \geq 1.50$, $(Na + K)_A < 0.50$, and $Ca_A < 0.50$; (c) compositional classification of biotite after (Deer et al., 2013); (f) Ab–An–Or ternary diagram showing the plagioclase compositions 331

Figure 4 - Si vs. Ti in amphibole diagram with metamorphic facies boundaries (after Liao et al. 2021). Amphibole compositions from Cajazeiras orthogneiss indicate transition from high-temperature amphibolite to granulite facies. Ultra-high temperature granulite facies (UHT); high temperature granulite facies (HT-GT); high-temperature amphibolite facies (HAM) 332

Figure 5 - (a) Pseudosection of sample ASM-22 calculated with GeoPs 3.5 (Xiang and Connolly, 2022); (b) pseudosection contoured by selected mineral isopleths to define a P-T path. 334

Figure 6 - Chondrite-normalized REE patterns of (a-b) clinopyroxene, (c-d) amphibole, normalized to the chondrite values of McDonough and Sun (1995). 335

Figure 7 - Chondrite-normalized REE patterns titanite from sample ASM-22 (a) and AA-144A (b); (c) Sr vs. Y diagram for both samples; (d) box plot of Zr concentration in both samples. Normalized to the chondrite values after McDonough and Sun (1995). 337

Figure 8 - U-Pb wheterill plots for titanite data from samples ASM-22 (a), and AA-144A (b); (c) U-Pb and REE data of zircon rims from sample ASM-22; (d) U-Pb from sample AA-144A. gray ellipses were discarded for age calculations. Scale bar in figura a and b are 100 μm; blue circles indicate REE spots (25 μm), and red circles U-Pb spots (20 μm)..... 338

Figure 9 - Summary of titanite and zircon U-Pb data from the Cajazeiras orthogneiss..... 343

Figure 10 - P-T-t trajectories for the clinopyroxene-amphibole-biotite tonalitic orthogneiss (ASM-22). The titanite ages are from the two analyzed samples in this study. (1) P-T path from high-pressure aluminous granulite from the studied area (Neri et al., in press). Metamorphic facies grid for metabasaltic rocks and geothermal gradients from Bucher and Frey (2002); CM – Contact metamorphism, Grn – Granulite, Amp – Amphibolite, Gsc – Greenschist, Sgsc – Subgreenschist, Bsc - Blueschist..... 344

9 CONCLUSÕES

Figura 1 - Sumário dos eventos magmáticos e metamórficos registrados na área de estudo (acrescidos dos dados de Neri *et al.* submetido, Silva 2021, Macambira *et al.* 2007 e dados não publicados do autor). CG = cinturão granulítico, Cmp= complexo; Grn = granito; Chn = charnockito. 367

Figura 2 - Blocos diagramas mostrando a evolução sugerida para evolução arqueana do Domínio Bacajá e norte da Província Carajás. (A) 3,0-2,94 Ga; (B)2,84-2,80 Ga; (C) 2,75-2,50 Ga (sem escala)..... 370

Figura 3 - Blocos diagramas mostrando a evolução sugerida para evolução Riaciana do sul do Domínio Bacajá e norte da Província Carajás. (A) 2,23-2,16 Ga; (B)2,12-2,10 Ga; (C) 2,10-2,06 Ga (sem escala). 371

LISTA DE TABELAS

1 INTRODUÇÃO

Tabela 1 - Síntese dos dados geocronológicos das rochas ígneas e metamórficas ortoderivadas do Domínio Bacajá 8

Tabela 2 - Síntese geocronológica das rochas paraderivadas e migmatitos associados do Domínio Bacajá 11

2 RHYACIAN MAGMATISM AT THE SOUTHERN BACAJÁ DOMAIN: IMPLICATIONS FOR THE CRUSTAL EVOLUTION OF SE AMAZONIAN CRATON, BRAZIL

Table 1 - Summary of crystallization ages from Rhyacian granitoids from Bacajá Domain... 40

Table 2 - Summary of field and petrographic aspects of the granitoids and charnockites of the southern Bacajá Domain 52

Table 3 - Representative whole-rock geochemical analyses of the Rhyacian granites and charnockites from the southern Bacajá Domain 55

Table 4 - Summary of geochemical data of the Rhyacian granitoids from the southern Bacajá Domain..... 59

Table 5 - Sm-Nd isotopic data from the granitoids and charnockites of the southern Bacajá Domain..... 67

3 MAGMATIC EPIDOTE AS A PROXY OF DEEP AND OXIDIZED MAGMATISM IN THE PALEOPROTEROZOIC BACAJÁ DOMAIN, SE AMAZONIAN CRATON

Table 1 - Summary of crystallization conditions of the Alto Rio Preto granite determined by mineral chemistry data 140

Table 2 - estimation of magma transport rate based on kinetic dissolutions of magmatic epidotes from the Alto Rio Preto granite 145

Table 3 - Comparison between the main crystallization parameters of epidote-bearing granites 150

4 DEHYDRATION MELTING OF BASALTIC CRUST TO GENERATE RHYACIAN HIGH-K CALC-ALKALINE GRANITES, SE AMAZONIAN CRATON: IMPLICATIONS FOR CRUSTAL REWORKING IN COLLISIONAL OROGENS

Table 1 - Whole-rock chemical composition of representative samples of the Alto Rio Preto granite 186

Table 2 - Modeling of major and trace elements for the generation of Rhyacian granites via dehydration melting of basaltic crust 201

5 WATER, REDOX, AND COMPOSITIONAL CONTROLS ON ORTHOPYROXENE AND FAYALITE STABILITY IN RHYACIAN IGNEOUS CHARNOCKITES, BACAJÁ DOMAIN, SE AMAZONIAN CRATON: INSIGHTS FROM MINERAL CHEMISTRY AND THERMODYNAMIC MODELING

Table 1 - Summary of P-T conditions for studied charnockites based on conventional and machine learning thermobarometry 259

Table 2 - Comparison between the main crystallization parameters of selected charnockites 264

6 THE OLDEST SANUKITOID s.l. MAGMATISM IN THE AMAZONIAN CRATON REVEALS MANTLE-CRUST INTERACTIONS DURING THE MESOARCHEAN IN THE BACAJÁ DOMAIN

Table 1 - Nd isotopes data from the studied orthogneisses 294

7 TITANITE PETROCHRONOLOGY OF GARNET-FREE ORTHOGNEISSES FROM THE BASEMENT OF BACAJÁ DOMAIN, SE AMAZONIAN CRATON: INSIGHTS INTO METAMORPHIC EVOLUTION WITHOUT GARNET CONTROL

Table 1 - Summary of petrography, geochronology, and metamorphic conditions of the Cajazeiras Complex 342

SUMÁRIO

AGRADECIMENTOS ..... **v**
RESUMO ..... **ix**
ABSTRACT ..... **xi**
LISTA DE ILUSTRAÇÕES ..... **xiii**
LISTA DE TABELAS ..... **xxvii**
1 INTRODUÇÃO **1**
1.1 APRESENTAÇÃO 1
1.2 ESTRUTURA DA TESE 2
1.3 LOCALIZAÇÃO E ACESSO 4
1.4 GEOLOGIA REGIONAL 5
1.4.1 Embasamento metamórfico 12
1.4.1.1 Mesoarqueano 12
1.4.1.2 Neoarqueano 13
1.4.1.3 Unidades paraderivadas 14
1.4.2 Magmatismo neoarqueano a sideriano 14
1.4.3 Greenstone belts 15
1.4.3.1 Sequência Três Palmeiras 15
1.4.3.2 Outras associações supracrustrais 15
1.4.4 Magmatismo riaciano (colisional) 16
1.4.4.1 Magmatismo Pré-Colisional 16
1.4.4.2 Magmatismo Sin-Colisional 16
1.4.4.3 Magmatismo Tardi-Colisional 17
1.4.5 Magmatismo orosiriano (pós-colisional) 18
1.5 PROBLEMÁTICA E JUSTIFICATIVA 18
1.6 OBJETIVOS 22
1.7 MATERIAIS E MÉTODOS 23
1.7.1 Pesquisa bibliográfica 23
1.7.2 Uso de Inteligência Artificial 24
1.7.3 Mapeamento geológico e amostragem 24
1.7.4 Petrografia 26
1.7.5 Química mineral 27
1.7.6 Litogeoquímica 28
1.7.7 Modelamento termodinâmico 28
1.7.8 Modelamento geoquímico 30

1.7.9 Elementos terras raras em minerais 30
1.7.10 Geocronologia U-Pb 30
1.7.11 Lu-Hf em zircão 32
1.7.12 Sm-Nd em rocha total 34
2 RHYACIAN MAGMATISM AT THE SOUTHERN BACAJÁ DOMAIN: IMPLICATIONS FOR THE CRUSTAL EVOLUTION OF SE AMAZONIAN CRATON, BRAZIL **35**
2.1 INTRODUCTION 37
2.2 GEOLOGICAL SETTING 38
2.3 METHODOLOGY 43
2.3.1 Fieldwork and lithostratigraphic classification 43
2.3.2 Whole-rock geochemistry 43
2.3.3 U-Pb geochronology 43
2.3.4 Hf isotopes on zircon 45
2.3.5 Whole-rock Nd isotopes 46
2.4 RESULTS 46
2.4.1 Geology and petrography 46
2.4.1.1 Bandeirante granite 46
2.4.1.2 Alto Rio Preto granite 46
2.4.1.3 Maravilha charnockite 48
2.4.1.4 Serra Azul charnockite 48
2.4.1.5 Bernardino granite 48
2.4.2 Geochemistry 54
2.4.2.1 Major and trace elements 54
2.4.2.1.1 Bandeirante granite 54
2.4.2.1.2 Alto Rio Preto granite 54
2.4.2.1.3 Maravilha charnockite 57
2.4.2.1.4 Serra Azul charnockite 57
2.4.2.1.5 Bernardino granite 57
2.4.2.2 Geochemical classification and magmatic series 59
2.4.3 U-Pb geochronology and Hf isotopes on zircon 62
2.4.3.1 Bandeirante granite 62
2.4.3.2 Alto Rio Preto granite 63
2.4.3.3 Maravilha charnockite 63
2.4.3.4 Serra Azul charnockite 64

2.4.3.5 Bernardino granite 64
2.4.4 Nd isotopes 66
2.5 DISCUSSION 68
2.5.1 Timing magmatic events in the southern Bacajá Domain 68
2.5.2 Geochemical affinities of the studied rocks: geological and tectonic implications 69
2.5.3 Rhyacian crustal evolution of the southern Bacajá Domain: implications for its tectonic setting 71
2.5.3.1 Geodynamic model for the southern Bacajá Domain 74
2.5.3.2 A comparison between the Bacajá Domain with the Carajás province and an evaluation of their limits 76
2.5.4 Brief comparison with Rhyacian granitoid magmatism in Paleoproterozoic orogens and implications for Columbia assembly 78
2.6 CONCLUSIONS 81
3 MAGMATIC EPIDOTE AS A PROXY OF DEEP AND OXIDIZED MAGMATISM IN THE PALEOPROTEROZOIC BACAJÁ DOMAIN, SE AMAZONIAN CRATON 116
3.1 INTRODUCTION 119
3.2 GEOLOGICAL SETTING OF THE STUDIED GRANITE 119
3.3 METHODS 123
3.4 RESULTS 123
3.4.1 Petrography and mineral chemistry 123
3.4.2 Crystallization phase equilibria 128
3.4.2.1 Experimental background on epidote and amphibole stability 128
3.4.2.2 Modeling parameters 128
3.4.2.3 Amphibole-biotite monzogranite 129
3.5 DISCUSSION 135
3.5.1 Thermodynamic modeling uncertanties 135
3.5.2 Crystallization parameters 135
3.5.2.1 Temperature 136
3.5.2.2 Pressure 137
3.5.2.3 Oxygen fugacity 137
3.5.2.4 Water content 137
3.5.2.5 Magma density 140
3.5.2.6 Magma viscosity 140
3.5.3 Origin and stability magmatic epidote: role of P-T-fO_2-H_2O 142
3.5.4 Controls on epidote preservation during magma ascent 143
3.5.5 Magma ascent rates 143

3.5.6 Magma affinity and source characteristics 146
3.5.7 The petrogenetic significance of epidote-granites in orogenic settings 148
3.6 CONCLUSIONS 151
4 DEHYDRATION MELTING OF BASALTIC CRUST GENERATES RHYACIAN HIGH-K CALC-ALKALINE GRANITES IN THE BACAJÁ DOMAIN, SE AMAZONIAN CRATON 170
4.1 INTRODUCTION 172
4.2 GEOLOGICAL SETTING 172
4.3 METHODS 175
4.3.1 Fieldwork and petrography 175
4.3.2 Geochemistry 175
4.3.3 Thermodynamic and trace element modelling 175
4.3.4 Zircon and titanite U-Pb geochronology 176
4.4 RESULTS 178
4.4.1 Geological and structural aspects 178
4.4.2 Petrography 181
4.4.2.1 Modal classification 181
4.4.2.2 Microtextural and microstructural features 181
4.4.2.3 Deformational Aspects 181
4.4.2.3.1 Low-grade domain 182
4.4.2.3.2 Medium-grade domain 182
4.4.3 Whole-rock geochemistry 184
4.4.3.1 Major and trace elements 184
4.4.3.2 Geochemical classififcation and magmatic series 190
4.4.4 U-Pb geochronology 191
4.5 DISCUSSION 194
4.5.1 Meaning of U-Pb ages 194
4.5.2 Petrogenesis 194
4.5.2.1 Assessment of element mobility 194
4.5.2.2 Magma source 195
4.5.2.3 Phase equilibria and trace element modeling 197
4.5.2.4 Thermodynamic-geochemical modeling uncertanties 202
4.5.3 Magmatic evolution 203
4.5.4 Magma emplacement and deformation 203
4.5.5 Implications for magmatism in collisional settings 204

4.6 CONCLUSIONS 205

5 WATER, REDOX, AND COMPOSITIONAL CONTROLS ON ORTHOPYROXENE AND FAYALITE STABILITY IN RHYACIAN IGNEOUS CHARNOCKITES, BACAJÁ DOMAIN, SE AMAZONIAN CRATON: INSIGHTS FROM MINERAL CHEMISTRY AND THERMODYNAMIC MODELING 225

5.1 INTRODUCTION 227

5.2 GEOLOGICAL SETTING OF STUDIED CHARNOCKITES 228

5.3 ANALYTICAL METHODS 231

5.4 RESULTS 232

5.4.1 Petrography and mineral chemistry 232

5.4.1.1 Maravilha charnockite 232

5.4.1.2 Serra Azul charnockite 235

5.4.2 Crystallization phase equilibria 238

5.4.2.1 Experimental constraints on orthopyroxene and fayalite stability 238

5.4.2.2 Modeling strategy and parameters 238

5.4.2.3 Reduced Maravilha charnockite 239

5.4.2.4 Oxidized Maravilha charnockite 243

5.4.2.5 Serra Azul charnockite 247

5.5 DISCUSSION 251

5.5.1 Characteristics of orthopyroxene and fayalite and origin of the studied charnockites 251

5.5.2 Thermodynamic modeling: limitations and reliability 253

5.5.3 Crystallization parameters 254

5.5.3.1 Temperature 254

5.5.3.2 Pressure 255

5.5.3.3 Oxygen fugacity 256

5.5.3.4 Water content 257

5.5.4 The effects of P-T-fO_2-H_2O and melt composition on orthopyroxene and fayalite stability in metaluminous magmas 260

5.5.5 Comparison with other igneous charnockites 261

5.5.6 Global implications for charnockite magmatism 265

5.6 CONCLUSIONS 265

6 THE OLDEST SANUKITOID *s.l.* MAGMATISM IN THE AMAZONIAN CRATON REVEALS MANTLE-CRUST INTERACTIONS DURING THE MESOARCHEAN IN THE BACAJÁ DOMAIN 285

6.1 INTRODUCTION 287

6.2 GEOLOGICAL SETTING 288

6.3 RESULTS 288
6.3.1 Field aspects and petrography 288
6.3.2 Geochemistry 292
6.3.3 Zircon U-Pb-Hf isotopes 293
6.3.4 Nd isotopes 294
6.4 DISCUSSION 295
6.4.1 Petrogenesis 295
6.4.2 Tectonic setting and regional implications 297
6.4.3 Mantle metasomatism and crustal growth in the Archean 299
6.5 CONCLUSIONS 299
7 TITANITE PETROCHRONOLOGY OF GARNET-FREE ORTHOGNEISSES FROM THE BASEMENT OF BACAJÁ DOMAIN, SE AMAZONIAN CRATON: INSIGHTS INTO METAMORPHIC EVOLUTION WITHOUT GARNET CONTROL 321
7.1 INTRODUCTION 323
7.2 GEOLOGICAL SETTING 323
7.3 ANALYTICAL METHODS 327
7.3.1 Petrography and mineral chemistry 327
7.3.2 In-situ trace elements LA-ICP-MS 327
7.3.3 U-Pb geochronology 327
7.4 RESULTS 328
7.4.1 Petrography and mineral chemistry 328
7.4.2 P-T conditions 331
7.4.2.1 Mineral thermobarometry 331
7.4.2.1.1 Amphibole 331
7.4.2.1.2 Titanite 332
7.4.2.2 Phase equilibria modeling 332
7.4.3 Trace element mineral chemistry of rock-forming minerals 335
7.4.4 Titanite petrochronology 335
7.5 DISCUSSION 339
7.5.1 Significance of REE patterns, trace elements, and U-Pb ages 339
7.5.2 Zr-in-titanite temperatures 339
7.5.3 P-T-t evolution and regional implications 340
7.6 CONCLUSIONS 346
8 ATIVIDADES FUTURAS 363
9 CONCLUSÕES 364
REFERÊNCIAS 372

APÊNDICE A 384

1 INTRODUÇÃO

1.1 APRESENTAÇÃO

A configuração atual do Cráton Amazônico resultou de uma série de processos orogenéticos acrescionários e/ou colisionais ocorridos durante o Paleoproterozoico e Mesoproterozoico, os quais foram responsáveis por amalgamar fragmentos de crosta ao núcleo arqueano estável, denominado Província Carajás (Santos *et al.* 2006, Tassinari & Macambira 2004). Durante o Paleoproterozoico, um dos principais eventos que ocorreu no Cráton foi a Orogenia Transamazônica, entre ~2,26-1,95 Ga (Hurley *et al.* 1967, Vanderhaeghe *et al.* 1998, Delor *et al.* 2003, Kroonenberg *et al.* 2016, Rosa-Costa *et al.* 2006, Kroonenberg 2019).

O Domínio Bacajá está situado na Província Maroní-Itacaiunas (Tassinari & Macambira 2004) ou Transamazonas (Santos *et al.* 2006), no Escudo Brasil Central. Geograficamente, localiza-se na região Norte do Brasil e sul do Estado Pará, abrangendo uma área com cerca de 104.866 km^2. É considerado por diversos autores um orógeno colisional paleoproterozoico (Vasquez & Rosa-Costa 2008, Vasquez 2006, Vasquez *et al.* 2005, Macambira *et al.* 2009, Barros *et al.* 2023), com uma evolução complexa que se estende desde o Mesoarqueano até o Riaciano (Magalhães *et al.* 2023, Macambira *et al.* 2007, Vasquez & Rosa-Costa 2008, Vieira *et al.* 2022). Sua evolução está intimamente ligada à Orogenia Transamazônica, que foi responsável pelo retrabalhamento de fragmentos de crosta arqueana, hoje preservadas como janelas do embasamento ao longo do domínio (Magalhães *et al.* 2023, Macambira *et al.* 2007, Vasquez & Rosa-Costa 2008, Vieira *et al.* 2022), além de gerar extenso magmatismo paleoproterozoico, desde o Sideriano até o Riaciano, e processos associados de sedimentação, deformação, mineralização, metamorfismo e fusão parcial (Souza *et al.* 2003, Macambira *et al.* 2004, Barros *et al.* 2007, Vasquez & Rosa-Costa 2008, Cristo 2018, Corrêa *et al.* 2019, Corrêa 2020, Magalhães *et al.* 2023).

Durante muitos anos, o Domínio Bacajá foi alvo de poucos estudos em comparação às províncias adjacentes, como Carajás, o que se reflete diretamente na escassez de dados geológicos que possibilitem a compreensão da origem e evolução daquele domínio.

Recentemente, a porção sul do domínio, tema da pesquisa, vem sendo alvo de novos estudos (Almeida *et al.* 2016, Barbosa *et al.* 2016, Feio *et al.* 2016, Félix-Silva *et al.* 2016, Sousa *et al.* 2016, Motta *et al.* 2019, Silva 2021, Correa *et al.* 2022), voltados à compreensão da sua geologia e da definição do seu limite com a Província Carajás. Nessa região afloram rochas do Complexo Cajazeiras, Cinturão Granulítico Novolândia e Rochas Supracrustais 01 (Félix-Silva *et al.* 2016, Silva 2021, Vasquez & Rosa-Costa 2008). Estudos preliminares sugerem que o Complexo Cajazeiras é constituído de variedades de rochas granitoides

intercaladas com rochas metamórficas (granulitos de alta pressão, orto- e paragnaisses) (Almeida *et al.* 2016, Barbosa *et al.* 2016, Félix-Silva *et al.* 2016). Por outro lado, o Cinturão granulítico Novolândia é constituído de rochas de alto grau metamórfico (granulitos e migmatitos) com protólitos ortoderivados máficos, félsicos e paraderivados que foram metamorfisados em fácies granulito a granulito de temperatura ultra alta (Almeida *et al.* 2016, Barbosa *et al.* 2016, Félix-Silva *et al.* 2016, Sousa *et al.* 2016, Silva 2021). De toda forma, a porção sul do domínio ainda representa uma das áreas de menor conhecimento geológico de todo o domínio, com carência significativa de dados das referidas unidades/complexos, que são muito heterogêneas e precisam ser mais bem compreendidas.

Nesse contexto, essa tese apresenta um conjunto robusto e inédito de dados de campo, petrográficos, mineralógicos, geoquímicos, geocronológicos e isotópicos de granitoides, charnockitos e ortognaisses aflorantes na porção sul do Domínio Bacajá. Esses dados foram organizados em diferentes artigos com a finalidade de esclarecer os processos magmáticos e metamórficos que foram responsáveis pela formação da crosta atualmente exposta na área de estudo.

1.2 ESTRUTURA DA TESE

Esta tese é apresentada na forma de agregação de artigos científicos. Dessa forma, a primeira Seção (1) é introdutória e inclui a apresentação da pesquisa, localização da área de estudo, geologia regional, a formulação dos problemas, os objetivos traçados para resolvê-los e os materiais e métodos utilizados para alcançá-los. O corpo central da tese apresenta seis artigos apresentados na forma de seções (Seções 2, 3, 4, 5, 6 e 7), submetidos ou a serem submetidos a periódicos internacionais com fator de impacto (FI) $\geq$ 2,5. A seção seguinte (Seção 8) apresenta a programação futura para o andamento da pesquisa e a seção final (Seção 9) sintetiza os principais resultados obtidos a partir dos artigos e da tese como um todo. Os artigos estão organizados na seguinte ordem:

Artigo 1: ***Rhyacian magmatism at the Bacajá-Carajás boundary: implications for the crustal evolution of the SE Amazonian Craton and Columbia assembly***

Este artigo, submetido à revista *Precambrian Research* (FI: 3,2), apresenta os aspectos geológicos, petrográficos, geoquímicos, geocronológicos e isotópicos (Nd-Hf) dos diversos granitoides aflorantes na área de estudo. Os novos dados permitiram a individualização de diferentes unidades, previamente englobadas no Complexo Cajazeiras, contribuindo para elucidar a evolução crustal da porção sul do Domínio Bacajá, suas relações com a Província Carajás, suas implicações para o segmento sudeste do Cráton Amazônico e correlação com

outros orógenos desenvolvidos durante a assembleia do supercontinente Columbia.

Artigo 2: ***Magmatic epidote as a proxy of deep and oxidized magmatism in the Paleoproterozoic Bacajá Domain, SE Amazonian Craton***

Este artigo, submetido à revista *Lithos* (FI: 2,5), discute as composições mineralógicas, as condições de cristalização (P, T, fO_2 e H_2O), viscosidade e densidade do Granito Alto Rio Preto. A integração entre termobarometria clássica, *machine learning*, modelamento termodinâmico e estudo de dissolução de epidoto permitiu definir a história de cristalização, determinar as condições de formação e estabilidade de epidoto magmático e estabelecer as taxas de ascensão dos magmas, contribuindo para uma melhor compreensão de processos magmáticos profundos no Domínio Bacajá e permitindo estabelecer semelhanças com granitos similares em outros orógenos do mundo.

Artigo 3: ***Dehydration melting of basaltic crust generates Rhyacian high-K calc-alkaline granites in the Bacajá Domain, SE Amazonian Craton***

Neste artigo, submetido à revista *Journal of the Geological Society* (FI: 3,0), são discutidos os aspectos geológicos, estruturais, geoquímicos e geocronológicos do Granito Alto Rio Preto. A integração desses dados permitiu inferir os processos petrogenéticos e a evolução magmática do granito, além de contribuir para um melhor entendimento sobre sua estruturação e colocação e as implicações para o magmatismo em orógenos colisionais.

Artigo 4: ***Water, redox, and compositional controls on orthopyroxene and fayalite stability in Rhyacian igneous charnockites, Bacajá Domain, SE Amazonian Craton: insights from mineral chemistry and thermodynamic modeling***

Neste artigo, submetido à revista *Contributions to Mineralogy and Petrology* (FI: 3,5), são discutidas as composições mineralógicas e as condições de cristalização (P, T, fO_2 e H_2O) de duas unidades charnockíticas distintas, utilizando geotermobarometria clássica, *machine learning* e modelamento termodinâmico. A combinação dessas metodologias permitiu determinar a trajetória de cristalização, estabelecer as condições de formação dessas rochas e avaliar a influência da variação de parâmetros como fugacidade de oxigênio e teor de água na estabilidade do ortopiroxênio e faialita.

Artigo 5: ***The oldest sanukitoid s.l. magmatism in the Amazonian Craton reveals Mesoarchean mantle-crust interactions in the Bacajá Domain***

Este artigo, submetido à seção de *Short Communications* da revista *Gondwana Research* (FI: 8,6), apresenta dados geoquímicos, geocronológicos e isotópicos (Nd-Hf) da ocorrência mais antiga de magmatismo sanukitoide *s.l.* no Cráton Amazônico e a segunda mais antiga do mundo. São discutidos os processos petrogenéticos e as implicações da presença de rochas com

assinatura sanukitoide na evolução do Domínio Bacajá, bem como suas consequências para o crescimento crustal e o metassomatismo do manto no Mesoarqueano.

Artigo 6: ***Titanite petrochronology of garnet-free orthogneisses from the basement of Bacajá Domain, SE Amazonian Craton: insights into metamorphic evolution without garnet control***

Este artigo, ainda se encontra em preparação e poderá ser submetido à revista *Lithos* (FI: 2,5). Ele apresenta dados petrográficos, termobarométricos, modelamento termodinâmico e petrocronologia de titanita, integrados à química mineral (elementos maiores, traços e terras raras) dos minerais formadores de rocha. São discutidas as condições do metamorfismo que afetou o Complexo Cajazeiras bem como a relação entre a distribuição de elementos terras raras na titanita e nos minerais como anfibólio e clinopiroxênio na ausência de granada.

1.3 LOCALIZAÇÃO E ACESSO

A área de estudo possui aproximadamente 1.660 km² e está localizada no sudeste do estado do Pará, na região de fronteira entre os municípios de Marabá, São Félix do Xingu, Novo Repartimento e Itupiranga. A região abrange as folhas topográficas Rio Bernadino (SB.22-X-C-I) e Rio Cajazeiras (SB.22-X-C-II). Partindo de Belém, o acesso pode ser feito por via terrestre ou aérea até a cidade de Marabá. A partir de Marabá, o deslocamento até a área de estudo é realizado por via terrestre (Fig. 1), seguindo pela Rodovia Transamazônica (BR-230), em direção a Itupiranga, até o quilômetro oito da rodovia. A partir desse ponto, o trajeto continua pela Estrada do Rio Preto, percorrendo-se cerca de 180 km até a Vila Cruzeiro do Sul. O acesso aos afloramentos a partir daquela Vila é realizado por meio de vicinais não pavimentadas e trilhas transitáveis.

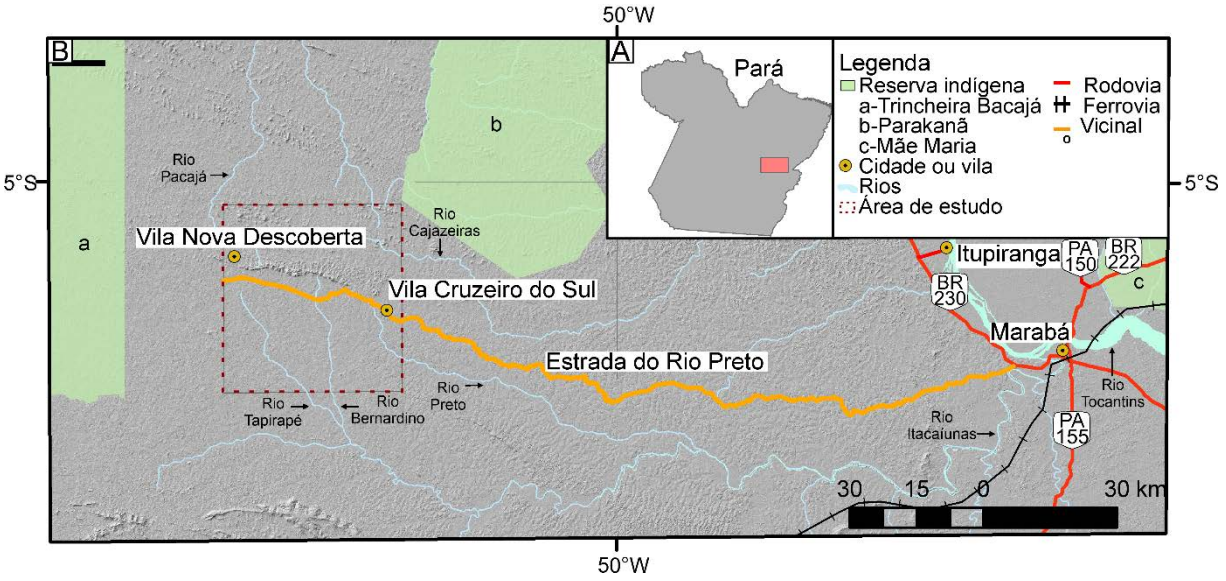


Figura 1 - Localização e acesso a área de estudo.

1.4 GEOLOGIA REGIONAL

O Domínio Bacajá (Fig. 2) está localizado na porção oriental do Cráton Amazônico, na Província Maroni-Itacaiúnas (Tassinari & Macambira 2004) ou Transamazonas (Santos *et al.* 2006). Ele é recoberto por rochas sedimentares fanerozoicas da Bacia do Amazonas e da Sub-Bacia de Cametá, ao norte. A oeste, as rochas vulcânicas e os granitos do Domínio Iriri-Xingu recobrem e cortam as unidades do Domínio Bacajá. No entanto, a presença de janelas de embasamento no Domínio Iriri-Xingu e a continuidade para o oeste da assinatura aeromagnetométrica do Domínio Bacajá sugerem a sua extensão nesse sentido. A leste, cavalgamentos marcam o limite tectônico entre o Domínio Bacajá e o Cinturão Araguaia (Vasquez & Rosa-Costa 2008). Ao sul, os limites propostos com a Província Carajás ainda são incertos. Alguns autores sugerem que ele seja marcado pela Zona de cisalhamento Buritirama (Faraco *et al.* 2006), ou posicionado logo abaixo dessa zona (Vasquez & Rosa-Costa 2008), enquanto outros sugerem que esse limite estaria mais a norte (Correa *et al.* 2022).

Quanto à evolução tectônica do Domínio Bacajá, existem duas principais correntes interpretativas. A primeira baseia-se principalmente em estudos geocronológicos, isotópicos, estruturais e geofísicos, e propõe que, durante a Orogenia Transamazônica, ocorreu a colisão entre os blocos Carajás e Bacajá. Esse evento teria sido responsável por retrabalhar fragmentos de crosta meso- a neoarqueana e sideriana, representando o embasamento e/ou arcos magmáticos que foram amalgamados à crosta arqueana de Carajás (Faraco *et al.* 2006, Barros *et al.* 2007, Macambira *et al.* 2007, Vasquez & Rosa-Costa 2008). Além disso, durante os estágios colisionais entre o Riaciano e o Orosiriano, também ocorreu intensa atividade magmática e metamórfica.

Por outro lado, Motta *et al.* (2019) propuseram duas novas hipóteses para a evolução do Domínio Bacajá, com base principalmente em levantamentos geofísicos associados a dados geocronológicos e isotópicos. A primeira hipótese considera que a crosta arqueana dos blocos Carajás e do sul do Domínio Bacajá formava um único segmento crustal que teria colidido com o Domínio Rio Maria no Mesoarqueano. Nesse contexto, a Zona de Cisalhamento Cinzento seria uma estrutura pré-existente que foi (re-)ativada durante a Orogenia Transamazônica. A segunda hipótese admite que os domínios Carajás e Bacajá compartilharam uma história arqueana, até o momento não totalmente compreendida, que teria ocorrido entre a colisão Carajás-Rio Maria e a Orogenia Transamazônica. Nessa hipótese, a crosta de Carajás seria formada pela justaposição entre os proto-domínios Carajás e Bacajá, e o processo de cratonização teria ocorrido ao longo da Zona de Cisalhamento Cinzento em algum momento antes da Orogenia Transamazônica. Tais autores também especulam que a separação entre Carajás e o proto-Bacajá poderia ter ocorrido devido à formação do rifte intracontinental, que originou a Bacia Carajás durante o Neoarqueano (~2,75 Ga).

No projeto do mapa geológico e de recursos naturais do estado do Pará (Vasquez & Rosa-Costa 2008), as unidades e complexos que compõem o Domínio Bacajá foram agrupados em diferentes associações litotectônicas, conforme os modelos aceitos para a evolução do Domínio Bacajá. Dessa forma, assumindo que o pico da colisão ocorreu por volta de 2,11 Ga (Vasquez 2006), com base em dados geocronológicos (monazita e zircão), os granitoides foram classificados em pré-, sin-, tardi- e pós-colisionais. No entanto, estudos petrocronológicos em monazita de granulitos da porção oeste do Domínio e na área de estudo (Corrêa 2020; Neri *et al.* submetido) sugerem que o pico do metamorfismo se deu entre 2,23 Ga e 2,17 Ga, e seria, portanto, mais antigo do que o proposto por Vasquez (2006) e Vasquez & Rosa-Costa (2008). Fica evidente, portanto, que a compartimentação estratigráfica e a evolução tectônica do Domínio Bacajá, desde o Arqueano até o Orosiriano, são bastante complexas e permanecem controversas. Todavia, como ainda não existe uma nova proposta de compartimentação consistente para a totalidade do domínio, neste trabalho serão seguidas, em linhas gerais, as recomendações de Vasquez & Rosa-Costa (2008). Os dados geocronológicos disponíveis do Domínio Bacajá estão dispostos nas tabelas 1 e 2.

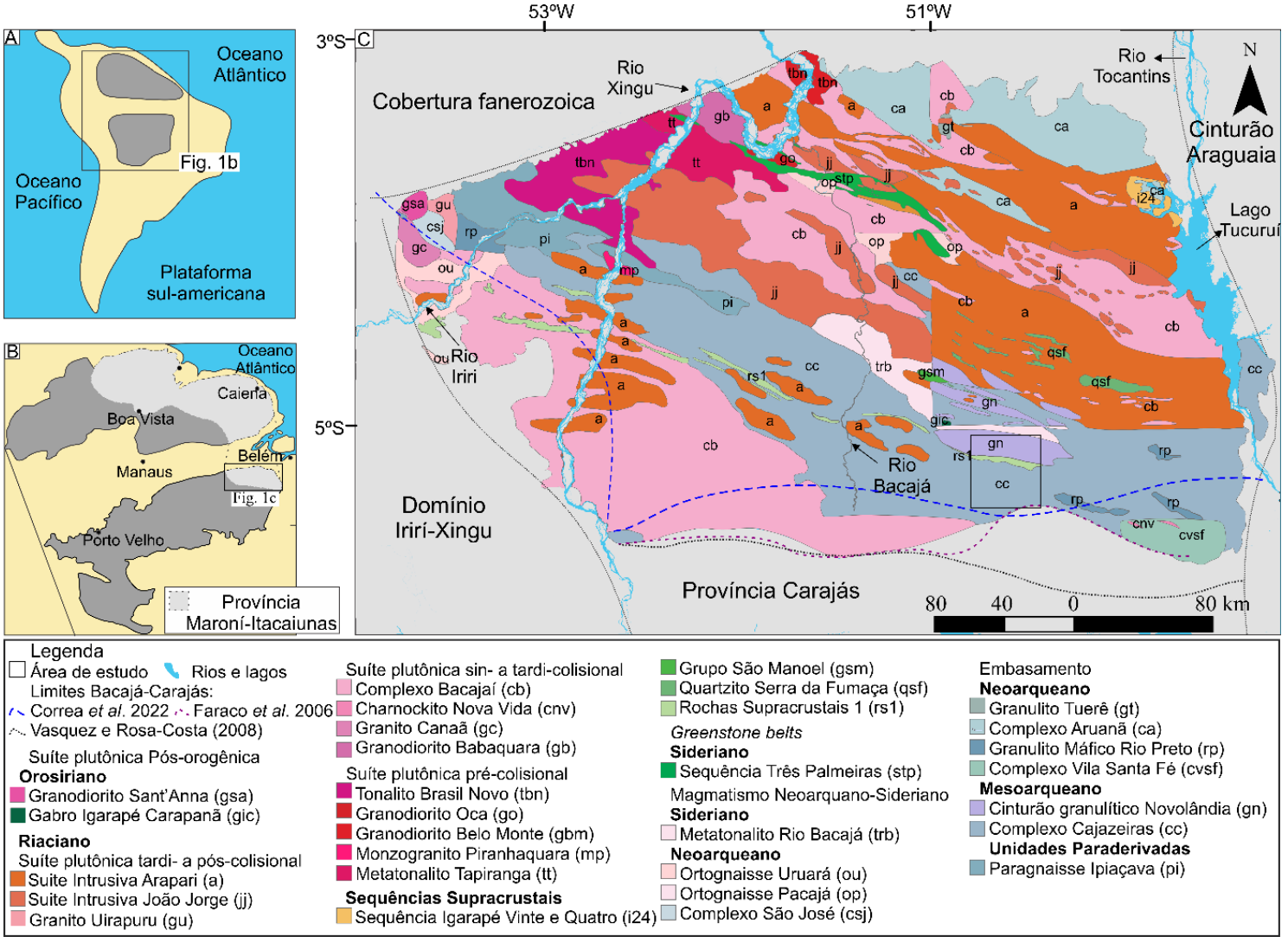


Figura 2 - (A) localização do Cráton Amazônico na Plataforma Sul-americana, (B) localização da Província Maroni-Itacaiúnas (Tassinari & Macambira 2004), (C) Mapa geológico regional simplificado do Domínio Bacajá (Barros 2023, Macambira *et al.* 2019, Macambira & Ricci 2015, 2019).

Tabela 1 - Síntese dos dados geocronológicos das rochas ígneas e metamórficas ortoderivadas do Domínio Bacajá

Período	Unidade	Litologia	Amostra	Método/mineral analisado	Idade C (Ma)	Idade M (Ma)	Ref.
Riaciano	Granodiorito Sant'ana	Granodiorito	-	Evaporação de Pb, Zrn	1986±5	-	12
		Granodiorito	-		2483±11*	-	12
		Granodiorito	-		2086±5 *	-	12
		Biotita Monzogranito	CVM-21	U-Pb, LA-ICP-MS, Zrn	2124±7	-	17
	Granito Bernardino	Granada-biotita granodiorito	ASM-25	U-Pb, LA-ICP-MS, Mnz	2052.3±5.4	-	20
	Charnockito Serra Azul	Enderbito	AA-20	U-Pb, SHRIM, Zrn	2062.5±8.8	-	20
	-	Quartzo diorito	-	Evaporação de Pb, Zrn	2071±3	-	10
	Suíte intrusiva João Jorge	Granodiorito	EM-55	U-Pb LA-ICP-MS, zrn	2062±22	-	19
		Titanita-biotita granodiorito	MCM55	Evaporação de Pb, Zrn	2076±6	-	13
		Alcali-feldspato sienito	-	Evaporação de Pb, Zrn	2076±2	-	16
		-	EM-49	Evaporação de Pb, Zrn	2077±5	-	15
		Biotita monzogranito	MVD-06B	Evaporação de Pb, Zrn	2077±2	-	11
					2097±7*	-	9
					2115±9*	-	9
					2219±3*	-	9
	Granito Felício Turvo	-	-		2069±6	-	8
		Monzogranito	MDM02	Evaporação de Pb, Zrn	2085±4	-	2
	Suíte Intusiva Arapari	Charnockito	PR-32	Evaporação de Pb, Zrn	2059±4	-	16
		Jotunito	MVD94	Evaporação de Pb, Zrn	2070±3	-	11
		Quartzo monzodiorito	-		2072±4	-	16
		Charnoenderbito	PMM-01	Evaporação de Pb, Zrn	2079±3	-	6
					2824±22*	-	6
					2613±8*	-	6
					2415±10*	-	6
					2157±3*	-	6
		Granodiorito	EM-55	U-Pb LA-ICP-MS, zrn	2080±16	-	19
		Charnockito	PR-29B	Evaporação de Pb, Zrn	2088±2	-	15
		Charnockito	EM-116	Evaporação de Pb, Zrn	2540±14*	-	16
	Granito Alto Rio Preto	Biotita monzogranito	AA-46	U-Pb, SHRIMP, Zrn	2067±4.9	-	20
					2589±6*	-	20
					3202±28*	-	20
				U-Pb, LA-ICP-MS, Ttn	2067±9.3		20
		Biotita granodiorito	ASM-01	U-Pb LA-ICP-MS, zrn	2076±12	-	20

				2295±28*	-	20
	Afibólio-biotita monzogranito	AA-76	U-Pb, SHRIMP, Zrn	2098±11	-	20
			U-Pb, LA-ICP-MS, Ttn	2068±9.9		20
Charnockito Maravilha	Anfibolio-biotita sienogranito	AA-06A	U-Pb SHRIMP, Zrn	2089±12	-	20
Monzogranito Belo Monte	-	MO36	U-Pb SHRIMP, Zrn	2086±5	-	7
Granodiorito Babaquara	biotita-hornblenda granodiorito	MVD102	Evaporação de Pb, Zrn	2102±3	-	10
Granito Canãa	Granitoide	MVD-26A	Evaporação de Pb, Zrn	2104±5	-	9
				2121±5*	-	9
				2139±5*	-	9
				2156±7*	-	9
Complexo Bacajaí	Charnockito	PMM-06	Evaporação de Pb, Zrn	2094±4	-	6
	Metatonalito	EM-100	U-Pb LA-ICP-MS, Zrn	2094±11	-	19
	Charnockito	PMM-20A	Evaporação de Pb, Zrn	2084±2	-	6
				2108±5*	-	6
				2436±3*	-	6
	Enderbito	-		2090±6	-	15
	Monzogranito	PR-170	U-Pb LA-ICP-MS, Zrn	2103±21	-	19
	Monzogranito	-	U-Pb SHRIMP, Zrn	2113±3	-	1
	Monzogranito	FB-148	Evaporação de Pb, Zrn	2112±8	-	16
	Charnoenderbito	TF-45	U-Pb SHRIMP, Zrn	2113+35/-33	-	1
				2673±2*	-	1
	Enderbito	PMM-09C	Evaporação de Pb, Zrn	2114±3	-	6
		PMM-09C	Evaporação de Pb, Zrn	2573±2*	-	6
Granito Bandeirante	Anfibólio sienogranito	AA-03C	U-Pb SHRIMP, Zrn	2116±11	-	20
Metatonalito Tapiranga	Metatonalito	MVD103A	Evaporação de Pb, Zrn	2133±10	-	8
Monzogranito Piranhaquara	Monzogranito	MVD115B	U-Pb SHRIMP, Zrn	2147±5	-	11
Granodiorito Oca	Quartzomonzodiorito	MVD125A	U-Pb SHRIMP, Zrn	2160±3	-	11
Granitoides Riacianos indiferenciados	Granodiorito	-	Evaporação de Pb, Zrn	2154±2	-	2
	Monzogranito	-	Evaporação de Pb, Zrn	2191±2	-	2
	Leucogranodiorito	-	Evaporação de Pb, Zrn	2077±3	-	2
Tonalito Brasil Novo	Monzogranito	M0-32	U-Pb SHRIMP, Zrn	2182±6	-	3
	Granitoide	MVD-05	Evaporação de Pb, Zrn	2215±2	-	9
				2524±5*	-	9
	Sienogranito	MVD-	Evaporação de Pb, Zrn	2209±2	-	12

27E

Sideriano	*Greenstone belt* Três Palmeiras	metalapili-tufo dacítico	MVD39	Evaporação de Pb, Zrn	2452±3	-	10
		Metavulcanoclástica	PVG-08	U-Pb LA-ICP-MS, Zrn	2419±49	-	14
		Metavulcanoclástica	PVG-08	Evaporação de Pb, Zrn	2410±11	-	14
		Metandesito	PVG-05	Evaporação de Pb, Zrn	2417±4	-	14
		Metandesito	-	Evaporação de Pb, Zrn	2359±2	-	2
	Metatonalito Rio Bacajá	Metatonalito	TF-42	U-Pb SHRIMP, Zrn	2313±9	-	1
		Metatonalito	MVD134A	U-Pb SHRIMP, Zrn	2338±5	-	12
	Quartzomonzodiorito	Quartzomonzodiorito	MDM01	Evaporação de Pb, Zrn	2439±4	-	2
					2457±5*	-	2
	Ortognaisse tonalítico	Ortognaisse tonalítico	PMM-04B	U-Pb SHRIMP, Zrn	2482±11	2073±11	6
	Ortognaisse Uruará	Gnaisse quartzo diorítico	MVD04B	Evaporação de Pb, Zrn	2440±7	-	9
		Gnaisse Granodiorítico	MVD54	U-Pb SHRIMP, Zrn	2487±13	-	11
		Gnaisse Granodiorítico	MVD54		2521±14*	-	11
		Gnaisse Granodiorítico	MVD54		2548±6*	-	11
		Tonalito	MO15	U-Pb SHRIMP, Zrn	2503±10	-	7
		Tonalito	MO15	U-Pb SHRIMP, Zrn	2581±6*	-	7
	Ortognaisse tonalítico	Ortognaisse tonalítico	PMM-02A	U-Pb SHRIMP, Zrn	2554±39	2108±5	6
Neoarqueano	Complexo São José	Biotita tonalito	CVM-33	U-Pb, LA-ICP-MS, Zrn	2502±6	-	17
	Ortognaisse Pacajá	Gnaisse tonalítico	PR-125	Evaporação de Pb, Zrn	-	2195± 3	12
		-	-	Evaporação de Pb, Zrn	2671±3	-	4
	Complexo Aruanã	Veio granítico	PR-21A	U-Pb, LA-ICP-MS, Zrn		2122±18	15
		Monzogranito	FB 99	Evaporação de Pb, Zrn	2585±4,6	-	16
		Gnaisse granodiorítico	-	Evaporação de Pb, Zrn	2606±4	-	12
		Ortognaisse	-	U-Pb, LA-ICP-MS, Zrn	2630±15	-	19
	Granulito Máfico Rio Preto	Granulito Máfico		Evaporação de Pb, Zrn	2628±3	2072±3	12
Mesoaqruano	Cinturão Granulítico Novolândia	Granulito Máfico	ASM-13	U-Pb, LA-ICP-MS, Zrn		2090±, 1921±16	18
		Granulito Máfico	ASM-34B	U-Pb, LA-ICP-MS, Zrn		2035±14	18
	Complexo Cajazeiras	Ortognaisse	MJ-21	U-Pb SHRIMP, Zrn	3009±27	2074±8	3
		Ortognaisse tonalítico	ASM-22	U-Pb, LA-ICP-MS, Zrn	2970.4±9.2 2812±12**	2210±13 - 2074±14	20
				U-Pb, LA-ICP-MS, Ttn	-	2017±16	20
		Ortognaisse granodiorítico	AA-144A	U-Pb, LA-ICP-MS, Zrn	2940±12 2807.4±7.5* *	1962± 11	20
				U-Pb, LA-ICP-MS, Ttn	-	2012±9.2	20
		Gnaisse granodiorítico	-	Evaporação de Pb, Zrn	2942±4	-	12
		Granodiorito	-	U-Pb SHRIMP, Zrn	2057±7	-	5

Baseada na Tab. 2.6 de Vasquez & Rosa-Costa (2008) acrescida de novas informações da literatura. Fontes: 1 - Faraco *et al.* (2006), 2- Macambira *et al.* (2009), 3 - Macambira *et al.* (2007), 4 - Macambira *et al.* (2004), 5 - Macambira *et al.* (2003), 6 – Macambira *et al.* (2022), 7 – Santos (2003), 8 – Souza *et al.* (2003), 9 - Vasquez *et al.* (2005), 10- Vasquez (2006), 11 - Vasquez *et al.* (2008), 12 - Vasquez & Rosa-Costa (2008), 13- Barros *et al.* (2007), 14 - Cristo (2018) e Macambira & Amireault (2025), 15 - Macambira & Ricci (2015), 16 - Besser & Barros (2015) e Barros *et*

al. (2023), 17 – Vieira *et al.* (2022), 18 – Silva AS (2021 e dados não publicados) e 19- Magalhães *et al.* (2023), 20 - este trabalho. C = cristalização, M = metamorfismo. * herança, ** abertura do sistema devido a metamorfismo e/ou perda de chumbo.

Tabela 2 - Síntese geocronológica das rochas paraderivadas e migamatitos associados do Domínio Bacajá

Unidade	Litologia	Amostra	Método	Fácies Metamórficas	Idade D	Idade M	Ref.
-	Paragnaisse pelítico	PM-23B	U-Pb, SHRIMP, mnz	Anfibolito alto a granulito	-	2062±8	6
	Veio leucogranítico	PM-23A	Sm-Nd, TIMS, grt	-	-	1962±15	22
		PM-23A	Evaporação de Pb, TIMS, zrn	-	-	2075±2*	6
Granulito Novolândia	Paragnaisse	MJ-24	U-Pb, SHRIMP, mnz	Anfibolito alto a granulito	-	2064±4	3
	Opx-Grt resíduo granulítico	ASM-09A	U-Pb, LA-ICP-MS, zrn	Granulito de UHT	3320±31 a 2608±18	2075±13	18
			U-Pb, LA-ICP-MS, mnz	Granulito de UHT	-	2044±10	18
	Grt-Sil resíduo granulítico	ASM-19A	U-Pb, LA-ICP-MS, zrn	Granulito	2758±7 a 2310±8	2163±5 e 2139±5	18
			U-Pb, LA-ICP-MS, mnz	Granulito	-	2052±7	18
	Grt-Sil leucossoma	ASM-19B	U-Pb, LA-ICP-MS, zrn	-	-	2186±17 e 2104±7	18
	Granulito Félsico	ASM-10	U-Pb, LA-ICP-MS, Zrn	Granulito	-	2094±9	18
Granulitos de alta pressão	Ky-Sil-Grt-Crd gnaisse	ASM-26	U-Pb, LA-ICP-MS, Zrn	Granulito de HP	-	2043.9±9.9	23
			U-Pb, LA-ICP-MS, Mnz			2044±5	
			U-Th-Pb, Microssonda Eletrônica, Mnz			2225±8 Ky	23
						2205±16 Grt	23
						2193±6 Mtx	23
Paragnaisse Ipiaçava	Gnaisse pelítico migmatítico	MVD-21	Sm-Nd, grt	Granulito	-	2024.6±1.9	10
			U-Pb, SHRIMP, zrn		-	2109.0±8.7	10
			U-Pb, ID-TIMS, zrn		-	2278.9±4.8	10
	Metapsamito	MVD40	U-Pb, SHRIMP, zrn	Anfibolito alto a granulito	3122±25 a 2290±5.9	-	10
			Sm-Nd, TIMS, grt		-	2208±24	10
			Evaporação de Pb, zrn		3135±4 a	2074±3	10

					2391±8	
Gnaisse pelítico migmatítico	MVD26 B	U-Pb, SHRIMP, mnz	Anfibolito alto a granulito	-	2123±4.8 N	10
				-	2071±3.5 N + B	10
				-	2057±3.3 B	10
Migmatito pelítico	MVD34 A	U-Pb, SHRIMP, mnz	Anfibolito alto a granulito	-	2073.3±2 B	10
				-	2132.9±4 .6 N	10
		U-Pb, SHRIMP, zrn		-	2147.3±7 ,4	10
Crd-grt-bt gnaisse	BCJ-10	U-Th-Pb, Microssonda Eletrônica, Mnz	Granulito	-	2185±4,5 9 Th	22
				-	2231±1,4 5 Y	22
Sil-crd-grt-bt gnaisse	BCJ-11	U-Th-Pb, Microssonda Eletrônica, Mnz	Granulito	-	2147±2,6 7 Th	22
				-	2219±1,7 1 Y	22

Fontes: o número de referências segue o padrão da tabela 1. 21 – Corrêa (2020), 22 – Monteiro (2006), 23 - Neri *et al.* (submetido). Idade D = fontes detríticas, Idade M = idade de metamorfismo, *cristalização de leucossoma. Grt = granada, mnz = monazita, zrn = zircão, UHT = temperatura ultra alta, HP = alta pressão. N = núcleo, B = Borda, Y = domínio rico em ítrio e associado ao crescimento de monazita na fase progressiva do metamorfismo, Th = domínio de monazita rico em tório, cristalizado a partir do fundido.

1.4.1 Embasamento metamórfico

1.4.1.1 Mesoarqueano

O **Complexo Cajazeiras** é constituído por granulitos e migmatitos de composição tonalítica a granítica, com evidências de retrometamorfismo em fácies anfibolito a xisto verde. Sua distribuição no Domínio Bacajá é ampla (Fig. 2), predominando em uma extensa faixa que se estende da porção sul até o noroeste do domínio. Os litotipos exibem bandamento tectono-composicional com bandas largas, realçado por níveis e/ou corpos máficos alternados com bandas félsicas (Vasquez & Rosa-Costa, 2008 e referências ali contidas). Esse bandamento apresenta mergulho de alto ângulo a vertical, geralmente associado a zonas de cisalhamento transcorrente sinistral (Ricci 2006b; Vasquez & Rosa-Costa 2008, Macambira *et al.* 2020) As idades de cristalização variam entre 2,94 e 3,01 Ga, enquanto o metamorfismo está registrado por volta de 2,07 Ga (Macambira *et al.* 2003; Vasquez & Rosa-Costa 2008, cf. Tabela 1).

O **Cinturão granulítico Novolândia** é composto por granulitos félsicos, aluminosos e máficos, com migmatitos associados, além de ocorrências subordinadas de formações

ferríferas bandadas e serpentinitos (Ricci 2006a; Silva 2021). Essa unidade é representada por diversos corpos alongados segundo o trend NW–SE, localizados na porção sudeste do domínio (Fig. 2). Apresenta foliação paralela à direção regional NW–SE, e, localmente, N–S. Granulitos aluminosos são característicos dessa unidade e registraram metamorfismo em fácies granulito de temperatura ultra alta, com temperaturas atingindo 934 ± 16 °C e pressões de 8,25 ± 0,1 kbar (Silva 2021). As rochas félsicas apresentam idades de cristalização em torno de 2,93 Ga e 2,74 Ga, as máficas entre 2,07–2,03 Ga, enquanto as rochas aluminosas contêm zircões provavelmente detríticos com idades variando do Arqueano ao Proterozoico (Silva 2021, dados não publicados). Todas essas litologias registraram metamorfismo entre 2,16 e 2,03 Ga (Macambira *et al.* 2007; Silva 2021).

1.4.1.2 Neoarqueano

O **Granulito Máfico Rio Preto** é formado por granulitos máficos e ortognaisses ocasionalmente migmatizados. Ocorre na porção sudeste do domínio, como corpos estreitos alongados segundo a direção WNW–ESE. Cristalizou em 2,6 Ga e foi metamorfisado em 2,07 Ga (Vasquez & Rosa-Costa 2008).

O **Complexo Aruanã** ocorre como uma extensa faixa com direção WNW–ESE, na porção mais setentrional do domínio. É composto por metagranitoides e ortognaisses de composições tonalíticas a monzo- e sienograníticas, contendo enclaves de granulitos máficos e anfibolitos (**Anfibolito Armenzinho**) de caráter subalcalino, toleítico e com assinatura tipo MORB (Besser & Barros 2015). De acordo com a proximidade às zonas de cisalhamento, as rochas exibem desde foliação incipiente até bandamento gnáissico e foliação milonítica bem desenvolvidos, com estruturas orientadas segundo NW–SE e mergulhos verticalizados. São rochas cálcio-alcalinas, de médio a alto potássio, variando de magnesianas a ferrosas. Apresentam idades de cristalização entre 2,59 e 2,61 Ga (Besser & Barros 2015, Magalhães *et al.* 2023, Vasquez & Rosa-Costa 2008), e metamorfismo estimado em 2,12 Ga (Macambira & Ricci 2015,Besser & Barros 2015, Magalhães *et al.* 2023, Vasquez & Rosa-Costa 2008)

O **Granulito Tuerê** é constituído por granulitos máficos, félsicos e ortognaisses de composição granítica a granodiorítica, variavelmente migmatizados, que formam dois corpos orientados segundo o *trend* NW–SE, englobados pelo Complexo Aruanã. O metamorfismo é de baixa pressão, com temperaturas em torno de 850 °C (Macambira e Ricci 2015).

O **Ortognaisse Pacajá** é formado por ortognaisses tonalíticos a graníticos migmatizados, que ocorrem como corpos elípticos alongados segundo a direção WNW–ESE, envolvidos pelo embasamento granulítico (Vasquez & Rosa-Costa 2008). Apresenta idade de

cristalização de 2,63 Ga (Macambira *et al.* 2004) e migmatização em 2,19 Ga (Vasquez & Rosa-Costa 2008).

O **Complexo Vila Santa Fé** é composto por ortognaisses de composição tonalítica a granodiorítica, granulitizados e migmatizados, além de lentes intercaladas de anfibolitos e/ou granulitos máficos. Forma um corpo na porção sudoeste do domínio, englobando as rochas do Charnockito Nova Vida. Apresenta idades de metamorfismo/migmatização entre 2,10 e 2,06 Ga (Macambira *et al.* 2007, Tavares 2015, Tavares & Silva 2015).

1.4.1.3 Unidades paraderivadas

O **Paragnaisse Ipiaçava** ocorre como dois corpos aflorantes na porção oeste do Domínio Bacajá ou como megaxenólitos no Granito Canãa. É constituído por paragnaisses pelíticos a psamíticos migmatizados, com lentes de silimanita quartzitos e granulitos máficos. Apresenta foliação concordante com o *trend* regional NW-SE ou, localmente, N-S. Foi metamorfisado em fácies granulito de média a baixa pressão com condições de P entre 6,7-5,3 kbar e T de 785-795 ºC (Corrêa, 2020b). As idades indicam um metamorfismo de longa duração entre 2,25-2,05 Ga (Vasquez 2006, Corrêa 2020) e fontes detríticas com idades que variam entre 3,13-2,47 Ga (Vasquez 2006).

Os **Granulitos de alta pressão** ocorrem como lentes restritas ou como enclaves em rochas granitoides na porção sul do domínio (Neri *et al*. submetido). São constituídos por cianita granulitos variavelmente migmatizados que apresentam foliação concordante com o *trend* regional NW-SE. Foram metamorfisados em fácies granulito de alta pressão, possuem uma trajetória P-T horária com pico metamórfico entre 9,8 e 13,2 kbar a 790–820 °C por volta de 2,21–2,23 Ga. Após o pico, ocorreu uma descompressão quase isotérmica em condições de 4,1–5,7 kbar a 755–815 °C, por volta de 2,19 Ga. Posteriormente, a evolução foi marcada por um resfriamento isobárico em temperatura de 740–780 °C e pressão de 3,6–5,1 kbar, em cerca de 2,04 Ga (Neri *et al.* submetido).

1.4.2 Magmatismo neoarqueano a sideriano

O **Complexo São José** é constituído por biotita-tonalitos levemente peraluminosos, cálcio-alcalinos de médio a alto teor de potássio, predominantemente ferrosos, com afinidade com granitos do tipo I. Cristalizou em 2,50 Ga (Vieira *et al.* 2022a)

O **Ortognaisse Uruará** é composto por metatonalitos e metagranodioritos, com subordinados metamonzogranitos e metaquartzo-dioritos, ocasionalmente migmatizados. Apresenta bandamento gnáissico com direção NE e eixos de dobras mergulhando para SW,

(Vasquez & Rosa-Costa 2008). Cristalizou entre 2,49 a 2,44 Ga (Santos 2003, Vasquez & Rosa-Costa 2008, Vasquez *et al.* 2005).

O **Metatonalito Rio Bacajá** é composto por metatonalitos e metamonzogranitos que formam um corpo orientado segundo NW–SE, intrusivo na Sequência Três Palmeiras. O bandamento possui direção NW e mergulho subvertical, com dobras cujos eixos mergulham para WNW (Vasquez & Rosa-Costa 2008). Suas rochas forneceram idades prováveis de cristalização de 2,34 Ga e 2,31 Ga (Faraco *et al.* 2006, Vasquez & Rosa-Costa 2008).

1.4.3 Greenstone belts

1.4.3.1 Sequência Três Palmeiras

A **Sequência Três Palmeiras** é representada por sucessões metavulcanossedimentares metamorfisadas em fácies xisto-verde a anfibolito. É composta por anfibolitos ortoderivados, rochas metavulcanoclásticas, metavulcânicas ácidas a intermediárias, metaplutônicas máficas a intermediárias, rochas metassedimentares e formações ferríferas bandadas (João & Vale 1987, Faraco *et al.* 2006, Besser & Barros 2015, Macambira & Ricci 2015). Os anfibolitos e as rochas metavulcânicas são subalcalinos, toleíticos a cálcio-alcalinos, e apresentam características semelhantes às rochas geradas em cadeias meso-oceânicas (Macambira *et al.* 2019). As idades de cristalização das rochas metavulcânicas variam entre 2,40 e 2,35 Ga (Macambira *et al.* 2009, Cristo 2018), enquanto as metavulcanoclásticas apresentam idades entre 2,45 e 2,41 Ga (Vasquez 2006, Cristo 2018).

1.4.3.2 Outras associações supracrustrais

Outras sequências supracrustais ocorrem no domínio de forma subordinada e permanecem pobremente caracterizadas. Em geral, essas unidades foram metamorfisadas em fácies xisto-verde a anfibolito. Dentre elas, destacam-se: **Sequência Rochas Supracrustais 01** e **Quartzito Serra da Fumaça**, que ocorrem como corpos lenticulares orientados segundo a direção WNW–ESE e são constituídos, respectivamente, por quartzitos, xistos e formações ferríferas bandadas (Oliveira *et al.* 1994, Souza 1995, Faraco *et al.* 2005) e por quartzitos micáceos e quartzitos com porfiroblastos de granada (Macambira *et al.* 2019). **Sequência São Manoel**, composta por talco-xistos, hornblenditos, anfibolitos, biotita-xistos e muscovita-quartzitos (Macambira *et al.* 2019, Souza 1995, Souza & Kotschoubey 2005). **Sequência Igarapé Vinte e Quatro**, que forma um corpo de direção WNW–ENE, composto por antofilita-xistos, talco-xistos, serpentinitos, esteatitos e outras rochas hidrotermalizadas de fundo oceânico, bem como micaxistos e formações ferríferas bandadas (Macambira & Ricci 2015).

1.4.4 Magmatismo riaciano (colisional)

1.4.4.1 Magmatismo Pré-Colisional

O **Tonalito Brasil Novo** forma um batólito constituído por tonalitos e granodioritos, com ocorrências subordinadas de monzogranitos e sienogranitos. O corpo apresenta orientação NW–SE e é recortado por zonas de cisalhamento com a mesma direção (Santos 2003, Vasquez & Rosa-Costa 2008). Forneceu idades entre 2,21-2,18 Ga direção (Santos 2003, Vasquez *et al.* 2005, Vasquez & Rosa-Costa 2008).

O **Granodiorito Oca** forma dois plútons intrusivos na **Sequência Três Palmeiras** e é constituído por granodioritos e tonalitos, com quartzo monzodioritos subordinados. As rochas preservam texturas ígneas, e faixas miloníticas estão restritas às bordas dos plútons. A alteração hidrotermal é intensa e está associada à ocorrência de mineralizações auríferas (Jorge João & Vale 1987, Vasquez & Rosa-Costa 2008). Forneceu idade de 2,16 Ga (Vasquez 2006).

O **Granodiorito Belo Monte** é representado por um plúton composto por granodioritos e monzogranitos. As texturas ígneas estão preservadas, embora em algumas porções as rochas apresentem foliação com direção E–W e mergulhos subverticais, além de bandamento local (Vasquez & Rosa-Costa 2008). Apresenta idade de cristalização de 2,15 Ga (Macambira *et al.* 2003).

O **Monzogranito Piranhaquara** é constituído por monzogranitos e leucogranitos. Forma um plúton sigmoidal intrusivo no **Paragnaisse Ipiaçava** e no **Complexo Cajazeiras**, com orientação NW–SE. A foliação segue a direção NW com mergulhos altos e o corpo é cortado por zonas de cisalhamento transcorrente de direção NW–SE (Vasquez & Rosa-Costa 2008). Cristalizou em 2,15 Ga (Vasquez *et al.* 2008)

O **Metatonalito Tapiranga** é composto por tonalitos e granodioritos e forma um batólito irregular com orientação segundo o trend regional NW–SE (Vasquez & Rosa-Costa 2008). Apresenta idade de cristalização de 2133 ± 10 Ma, com uma população de zircões mais jovens (2055 ± 6 Ma), interpretada como resultado de um evento de migmatização (Vasquez 2006b).

1.4.4.2 Magmatismo Sin-Colisional

O **Granito Canaã** é composto por monzogranitos, com ocorrências subordinadas de granodioritos e tonalitos. Forma um plúton intrusivo no **Ortognaisse Uruará**, no **Paragnaisse Ipiaçava** e no **Granulito Máfico Rio Preto**. O corpo apresenta orientação NNW–SSE e, em geral, suas rochas são isotrópicas, exibindo apenas foliação magmática incipiente. São

levemente peraluminosas, ferrosas e apresentam afinidade com granitos do tipo I, cálcio-alcalinos de alto potássio (Vieira *et al.* 2022). Foram cristalizadas em 2,10 G (Vasquez *et al.* 2005).

O **Granodiorito Babaquara** é constituído por granodioritos e subordinados leucogranitos. Forma um corpo intrusivo no **Metatonalito Tapiranga** e no **Complexo Bacajaí**. O corpo está orientado segundo o trend regional NW–SE, e as rochas apresentam foliação incipiente, concordante com essa direção (Vasquez & Rosa-Costa 2008). Cristalizou em 2,10 Ga (Vasquez & Rosa-Costa 2008).

O **Complexo Bacajaí** é composto predominantemente por enderbitos e charnoenderbitos, com ocorrências subordinadas de charnockitos, jotunitos e mangeritos. Forma diversos plútons e batólitos orientados segundo NW–SE a WNW–ESE, distribuídos ao longo da porção norte do Domínio Bacajá. É intrusivo na **Sequência Três Palmeiras** e é cortado pelas suítes **Arapari** e **João Jorge**. Preserva estruturas magmáticas primárias. As rochas apresentam assinatura geoquímica cálcio-alcalina de baixo a médio potássio, e variam de magnesianas a ferrosas, de cálcicas a cálcio-alcalinas, bem como de metaluminosas a fracamente peraluminosas (Besser & Barros 2015, Macambira & Ricci 2015, Macambira *et al.* 2019, Macambira *et al.* 2022; Vasquez & Rosa-Costa 2008). As idades de cristalização são sobrepostas dentro do erro analítico: nas margens do rio Iriri variam entre 2,08 e 2,12 Ga (Macambira *et al.* 2022), na região da Folha Rio Bacajá, foi obtida idade de 2,11 Ga (Besser & Barros 2015), e na porção norte da Folha Tucuruí, entre 2,09 e 2,10 Ga (Magalhães *et al.* 2023).

O **Charnockito Nova Vida** é composto por charnockitos e enderbitos, englobados pelo **Complexo Vila Santa Fé**. As rochas são localmente deformadas e metamorfisadas em fácies anfibolito (Tavares 2015; Tavares & Silva 2015).

1.4.4.3 Magmatismo Tardi-Colisional

A **Suíte Intrusiva Arapari** é composta por charnockitos e charnoenderbitos, além de monzogranitos e tonalitos, com subordinados monzodioritos. Forma diversos batólitos e stocks orientados segundo NW–SE, localizados na porção central do domínio. Apresenta contatos tectônicos com o **Complexo Bacajaí** e com a **Sequência Três Palmeiras**. As rochas são metaluminosas a fracamente peraluminosas, cálcio-alcalinas de alto potássio e variam de magnesianas a levemente ferrosas. As idades de cristalização variam entre 2,08 Ga e 2,06 Ga

A **Suíte Intrusiva João Jorge** é constituída por monzogranitos, sienogranitos e subordinados granodioritos, além de subordinados sienitos e monzonitos. Apresenta foliação magmática incipiente, com foliação milonítica local de direção NW. As rochas são

metaluminosas a levemente peraluminosas, cálcio-alcalinas de alto potássio, transicionais entre magnesianas e ferrosas, e exibem afinidade com granitos do tipo A. Suas idades de cristalização também variam entre 2,08 Ga e 2,06 Ga (Besser & Barros 2015, Macambira *et al.* 2019, Macambira *et al.* 2001, Magalhães *et al.* 2023, Souza *et al.* 2003, Vasquez *et al.* 2005).

O **Granito Uirapuru** é formado por monzogranitos, com subordinados sienogranitos e granodioritos. Forma um plúton orientado segundo o trend regional NW–SE, com foliação acompanhando essa mesma direção. As rochas são levemente metaluminosas a peraluminosas, com afinidades alcalinas a shoshoníticas, e apresentam características compatíveis com granitos do tipo A oxidados (Vieira *et al.* 2022).

1.4.5 Magmatismo orosiriano (pós-colisional)

Esse magmatismo é extremamente restrito e ocorre predominantemente na porção oeste do Bacajá na região limítrofe com o Domínio Iriri-Xingu. Na definição inicial de Vasquez & Rosa-Costa (2008), esse magmatismo foi interpretado como pertencente a uma fase pós-colisional da Orogênese Transamazônica no Domínio Bacajá devido principalmente a sua assinatura isotópica de Nd (εNd(t) -8,99 e T_{DM} 2,83 Ga) que se assemelha as assinaturas de outras unidades do domínio (Vasquez 2006, Vasquez & Rosa-Costa 2008). Todavia, dados mais recentes sugerem idades modelos arqueanas também para o Iriri-Xingu (cf., Semblano *et al.* 2016). Portanto, nota-se que esse magmatismo pós-colisional relacionado à evolução do Bacajá deve ser reavaliado.

O **Granodiorito Sant'Ana** é composto por granodioritos e tonalitos com raros leucomonzogranitos. Apresenta foliação magmática incipiente. São meta- a peraluminosos com afinidade cálcio-alcalina alto-K a shoshonítica, tem caraterísticas semelhantes aos granitos tipo-A e por vezes com granitos tipo I. Forneceram idades de cristalização distintas de 1,98 Ga (Vasquez *et al.* 2005) e 2,12 Ga (Vieira *et al.* 2022).

O **Gabro Igarapé Carapanã** forma um corpo máfico circular de aproximadamente 5 km de diâmetro, bastante homogêneo, que ocorre no sudoeste da Folha Repartimento (Macambira *et al.* 2019).

1.5 PROBLEMÁTICA E JUSTIFICATIVA

A área selecionada para este estudo localiza-se na porção sul do Domínio Bacajá, região que vem sendo alvo de crescente interesse geológico e geofísico nos últimos anos (Motta *et al.* 2019, Costa *et al.* 2020, Silva 2021, Correa *et al.* 2022, Neri *et al.* submetido). Embora os trabalhos recentes tenham fornecido informações importantes, sobretudo sobre o metamorfismo

e as características geofísicas da crosta, ainda persistem grandes lacunas no conhecimento geológico dessa parte do domínio, especialmente no que tange à sua arquitetura crustal, evolução magmática e metamórfica, e relação com domínios adjacentes.

As principais rochas aflorantes na região são tradicionalmente agrupadas no Complexo Cajazeiras, no Cinturão Granulítico Novolândia e na unidade informal Rochas Supracrustais 01 (Vasquez & Rosa-Costa 2008). Estudos mais recentes (Almeida *et al.* 2016, Félix-Silva *et al.* 2016; Silva 2021) revelaram que tanto o Complexo Cajazeiras quanto o Cinturão Novolândia são substancialmente mais complexos do que inicialmente se supunha. Enquanto o Complexo Novolândia já possui descrição petrográfica, metamórfica e geocronológica mais robusta (Silva 2021), o Complexo Cajazeiras permanece pobremente caracterizado. Evidências geológicas recentes (Almeida *et al.* 2016; Félix-Silva *et al.* 2016; Silva 2021) sugerem que este último é composto por diferentes litotipos de origens ígnea e metamórfica, englobados de forma heterogênea em um mesmo complexo. Isso indica que sua individualização é fundamental para o avanço no entendimento da geologia local, além de permitir correlações mais precisas com outras áreas do Domínio Bacajá, como a Província Carajás e com orógenos coevos em outros crátons.

O embasamento arqueano no Domínio Bacajá é notavelmente diverso, com rochas cujas idades de cristalização variam do Mesoarqueano (3,01–2,94 Ga, Macambira *et al.* 2007; Vasquez & Rosa-Costa 2008) ao Neoarqueano (2,67–2,50 Ga, Macambira *et al.* 2009, Magalhães *et al.* 2023, Vieira *et al.* 2022). Além da ampla dispersão de idades, observa-se também uma significativa heterogeneidade isotópica com rochas de assinaturas juvenis e outras com assinaturas crustais (Macambira *et al.* 2009, Magalhães *et al.* 2023), ainda pouco compreendida. O Complexo Cajazeiras, considerado como a porção mais exumada do embasamento, é constituído por granulitos e migmatitos, com idades de cristalização entre 3,01 e 2,94 Ga e metamorfismo em 2,07 Ga (Macambira *et al.* 2007; Vasquez & Rosa-Costa 2008). Apesar dessas idades pontuais, a caracterização petrográfica, mineralógica, geoquímica e isotópica é limitada, o que dificulta o entendimento de sua gênese, evolução e condições metamórficas, além de impossibilitar a sua correlação com terrenos arqueanos típicos da Amazônia ou de outros crátons.

Outro problema de escala regional envolve a definição do limite entre o Domínio Bacajá e a Província Carajás. Motta *et al.* (2019) sugerem que a porção sul do Bacajá pode representar crosta exumada da Província Carajás, enquanto Correa *et al.* (2022) propõem um novo limite mais ao norte do que o definido anteriormente por Faraco *et al.* (2005). No entanto, essas propostas baseiam-se majoritariamente em interpretações geofísicas e a ausência de dados

geológicos detalhados na porção sul do Bacajá impede a validação dessas hipóteses, reforçando a necessidade de investigações geológicas para o refinamento desse limite.

Em um contexto mais amplo, a compreensão da evolução de orógenos paleoproterozoicos, como o Domínio Bacajá, é essencial para as reconstruções do supercontinente Columbia (e.g., Meert & Santosh 2017, Johansson *et al.* 2022, Zhao *et al.* 2002). Estudos anteriores sugerem que os crátons Amazônico e Oeste Africano estiveram conectados durante a amalgamação desse supercontinente paleoproterozoico (por ex., Meert & Santosh 2017, Grenholm *et al.* 2019, Johansson *et al.* 2022). No entanto, os estudos comparativos entre domínios paleoproterozoicos do Cráton Amazônico e do Cráton Oeste Africano concentram-se majoritariamente no Escudo das Guianas, especialmente nos domínios Caicuru e Lourenço (ex., Milhomem-Neto & Lafon, 2020, Rosa-Costa *et al.* 2025 e referências contidas neles), o que limita a compreensão sobre a relação do Domínio Bacajá com os demais terrenos. Assim, investigações detalhadas sobre a origem, evolução e compartimentação do Domínio Bacajá têm o potencial de contribuir significativamente para o refinamento dos modelos de acoplamento cratônico e para a avaliação do papel do Cráton Amazônico na nucleação e estabilização de Columbia.

Do ponto de vista petrológico, a determinação das condições de cristalização e propriedades físicas de magmas, como pressão (P), temperatura (T), fugacidade de oxigênio (fO_2), teor de água (H_2O), densidade (ρ) e viscosidade (η) é um desafio marcante. Embora técnicas clássicas de termobarometria sejam amplamente utilizadas para tais estimativas, a aplicação de modelagem termodinâmica a rochas ígneas ainda é relativamente recente (Mesquita *et al.* 2025, Zhao *et al.* 2017). Essa abordagem, tradicionalmente voltada ao estudo de rochas metamórficas, tornou-se viável com os recentes avanços em softwares de modelagem e bancos de dados internamente consistentes para rochas ígneas (Holland *et al.* 2018). A integração entre termobarometria clássica e modelagem termodinâmica pode, portanto, fornecer informações fundamentais sobre os processos magmáticos. No Domínio Bacajá, que foi palco de extenso magmatismo granitoide e charnockítico, estudos com esse enfoque ainda são inexistentes, impedindo o avanço na compreensão das condições de cristalização dessas rochas e avaliação da estabilidade de minerais chaves como ortopiroxênio, faialita e epidoto com a variação dos parâmetros P-T-fO_2-H_2O, bem como a comparação com outras rochas semelhantes em outras regiões do mundo.

Outro ponto crítico é a compreensão do comportamento da titanita, mineral acessório presente em diversas rochas ígneas e metamórficas da área de estudo. A titanita tem se mostrado um excelente indicador de processos geocronológicos, mineralógicos e isotópicos (Bonamici *et*

al. 2015, Kowallis *et al.* 2022, Scibiorski & Cawood 2022). Seu estudo é especialmente relevante em áreas onde sua ocorrência se dá tanto em rochas não metamorfisadas quanto em rochas afetadas por metamorfismo, como é o caso da região investigada. A análise da titanita permitirá avaliar o grau de recristalização das rochas, diferenciar domínios com metamorfismo ransamazônico de domínios preservados e compreender sua interação com outros minerais portadores de elementos terras raras.

É evidente que avanços expressivos na caracterização das rochas magmáticas e rochas ortoderivadas félsicas ainda são necessários, tendo em vista a escassez de trabalhos realizados na região. Assim, a caracterização das principais litologias e unidades em termos petrográficos, mineralógicos, geoquímicos, geocronológicos e isotópicos fornecerá os dados indispensáveis para que a geologia da região seja mais bem compreendida e que as incógnitas sobre a porção sul do Domínio Bacajá sejam esclarecidas, permitindo assim a correlação do domínio com províncias adjacentes, bem como com outros orógenos coevos em outros crátons. Em paralelo, serão aprofundadas diversas questões mineralógicas e petrológicas de interesse global.

Entre os principais questionamentos existentes, destacam-se:

1. Na área de estudo, o Complexo Cajazeiras existe efetivamente ou deverá ser desmembrado em diferentes unidades?
2. Qual a natureza das séries magmáticas e as idades do magmatismo granitoide presente na área? Qual o posicionamento estratigráfico dessas rochas? Qual é assinatura geoquímica dos diferentes granitoides e quais seriam as prováveis fontes dos seus magmas?
3. Qual é a composição química dos minerais constituintes das rochas charnockíticas e granitoides e em quais condições (P, T, fO_2 e H_2O) elas foram cristalizadas?
4. Como a variação dos parâmetros P, T, fO_2 e H_2O afetam a estabilidade a estabilidade do ortopiroxênio, faialita e epidoto magmáticos?
5. É possível estimar a taxa de ascensão dos magmas portadores de epidoto magamático?
6. Qual a relação entre o magmatismo com a deformação impressa nas rochas? Essa deformação ocorreu durante a colocação dos corpos ou foi posterior?
7. Qual a relação temporal e genética entre o magmatismo e o metamorfismo de alto grau registrado na região?

8. Qual a idade de cristalização e metamorfismo dos ortognaisses presentes na área? Qual a sua assinatura geoquímica e comportamento isotópico? A qual associação arqueana típica eles se assemelham?

9. Quais foram as condições de P-T do metamorfismo que atingiu os ortognaisses? Em que ambiente tectônico essas rochas foram metamorfisadas? Qual a fonte de calor responsável pelo metamorfismo?

10. Como a titanita se comportou durante os processos de cristalização, deformação e metamorfismo que atingiram a região? É possível identificar diferentes fases de crescimento da titanita? Como o padrão de elementos terras raras de titanita se relacionam com os padrões dos demais minerais presentes nas rochas?

11. Qual a idade e o papel das rochas supracrustais na evolução da porção sul do domínio? Seriam elas correlatas aos *greenstones* localizados na porção norte?

12. Quando se deu a formação da crosta exposta no sul do Domínio Bacajá, como se deu sua evolução e qual seu papel na evolução geológica da área situada atualmente na interface entre o Domínio Bacajá e a Província Carajás? Trata-se de uma crosta juvenil ou retrabalhada?

13. Qual a relação entre o Domínio Bacajá e outros orógenos coevos nos crátons Amazônico e do Oeste Africano?

14. As associações litológicas da região sul do Domínio Bacajá são similares em termos geoquímicos, geocronológicos e isotópicos às que ocorrem na porção norte da Província Carajás?

15. O limite entre os domínios Bacajá e Carajás está situado nas proximidades da área de estudo?

1.6 OBJETIVOS

O objetivo principal dessa tese é definir as assinaturas geoquímicas, a composição mineralógica, as condições de (re)cristalização, as idades, o comportamento isotópico e a origem do magmatismo granitoide, das rochas charnockíticas e dos ortognaisses da porção sul do Domínio Bacajá. Em uma escala regional, o conhecimento gerado deverá contribuir para esclarecer a evolução tectônica do Domínio Bacajá e das suas relações com a Província Carajás e outras regiões da Província Maroni-Itacaiúnas. Por outro lado, em uma escala global, deverá contribuir para melhor compreensão do magmatismo em orógenos paleoproterozoicos e suas relações com o metamorfismo, bem como na elucidação das conexões do Domínio Bacajá com outros orógenos coevos.

Para alcançar esses propósitos, foram estabelecidos os seguintes objetivos específicos:

1. Caracterizar as variedades petrográficas das rochas presentes na área e sua distribuição espacial;
2. Determinar a assinatura geoquímica e tipologia dos granitoides, charnockitos e ortognaisses, e no caso das rochas ígneas, avaliar possíveis processos de diferenciação magmática;
3. Determinar a composição química dos minerais e estimar os parâmetros físico-químicos de cristalização (P, T, fO_2, H_2O, ρ e η) para charnockitos e granitos com epidoto magmático;
4. Realizar modelamento termodinâmico das litologias portadoras de ortopiroxênio, faialita e epidoto magmáticos, determinar a sequência e condições de cristalização e compará-las com os resultados obtidos a partir de geotermobarômetros clássicos;
5. Calcular o tempo de dissolução dos epidotos magmáticos e determinar as taxas de ascensão dos magmas na crosta;
6. Determinar as condições de pressão e temperatura do metamorfismo que atingiu os ortognaisses;
7. Definir idades de cristalização de granitoides, charnockitos bem como de formação dos protólitos e de metamorfismo para os ortognaisses;
8. Definir a idade de separação do manto de possíveis fontes dos magmas geradores dos granitoides, charnockitos e ortognaisses e avaliar a participação de fontes crustais e/ou mantélicas nas suas origens;
9. Situar a granitogênese e o metamorfismo no contexto geológico do Domínio Bacajá e do Cráton Amazônico, bem como comparar com os de outros terrenos contemporâneos do mundo.

1.7 MATERIAIS E MÉTODOS

1.7.1 Pesquisa bibliográfica

Ao longo de todo desenvolvimento da tese foi realizado levantamento bibliográfico acerca da geologia arqueana e paleoproterozoica do Domínio Bacajá, com foco na sua granitogênese e metamorfismo, bem como nas rochas portadoras de ortopiroxênio. Além disso, também estão sendo pesquisadas associações similares de rochas em outros crátons do mundo com destaque para os arqueanos e paleoproterozoicos.

Paralelamente, foram realizadas pesquisas sobre as metodologias utilizadas durante a

pesquisa (geoquímica de rochas graníticas e metamórficas, química mineral de minerais formadores de rocha e acessórios, modelamento termodinâmico, isótopos de Sm-Nd em rocha total, U-Pb em zircão e titanita e Lu-Hf em zircão).

Ademais, foram consultados e sumarizados os trabalhos realizados anteriormente na área de estudo. Eles resultam essencialmente de mapeamentos geológicos, trabalhos de conclusão de curso e resumos de congresso realizados por alunos e professores da UNIFESSPA, além da dissertação do autor que foi realizada em parte da área de estudo.

1.7.2 Uso de Inteligência Artificial

Trechos desta tese redigidos em inglês foram revisados quanto à gramática, ortografia e fluidez por meio de ferramentas de Large Language Models (LLMs), como Grammarly e ChatGPT. O uso desta ferramenta restringiu-se à melhoria da escrita de textos elaborados pelo autor e não interferiu na formulação dos dados, interpretações ou conclusões científicas apresentadas neste trabalho.

1.7.3 Mapeamento geológico e amostragem

Parte da área de estudo já havia sido previamente mapeada por duas turmas da disciplina Mapeamento Geológico II da UNIFESSPA, nos anos de 2013 e 2014. Os dados de campo gerados e as lâminas resultantes dessas atividades serviram como base para o planejamento do desenvolvimento da pesquisa.

Foram realizadas quatro etapas de campo com a participação do autor. A primeira ocorreu de 7 a 11 de julho de 2019, como parte do trabalho de mestrado do autor (campo 1 - C1, sigla ASM), contando com a presença do então orientador, agora colaborador, Elton Luiz Dantas (Universidade de Brasília - UnB) e da colaboradora Gilmara Regina Lima Feio (Universidade Federal do Sul e Sudeste do Pará - UNIFESSPA). Nessa campanha, foram visitados 37 pontos, dos quais 35 foram amostrados para o desenvolvimento da dissertação. O material remanescente dessa atividade foi posteriormente aproveitado para a presente tese.

A segunda etapa de campo (campo 2 - C2, sigla AA) ocorreu durante o doutorado, entre 3 e 10 de novembro de 2021, com a participação do colaborador José de Arimatéia Costa de Almeida (UFPA). O objetivo principal foi examinar afloramentos, reamostrar as principais litologias da área e visitar novos pontos ainda não mapeados. Durante essa campanha, foram visitados 81 pontos, dos quais 78 foram amostrados.

A terceira etapa (campo 3 - C3, sigla ASD) foi realizada de 17 a 30 de agosto de 2022, em parceria com a doutoranda Alice Cunha da Silva (docente da UNIFESSPA), que também

desenvolve pesquisa na região sob a orientação do pesquisador Vinícius Tieppo Meira (Universidade de Campinas -UNICAMP). O foco principal dessa campanha foi o mapeamento em escala de detalhe do Cinturão Granulítico Novolândia, objeto de estudo da referida doutoranda. Foram visitados 85 pontos, porém apenas 27 amostras foram coletadas para a presente tese.

A quarta e última etapa de campo (campo 4 – C4, sigla AA) ocorreu entre 3 e 9 de setembro de 2023, com o objetivo de complementar o mapeamento e a amostragem da porção sul da área de estudo, além de realizar verificações em pontos previamente selecionados. Durante essa campanha, foram visitados 67 pontos, dos quais 58 foram amostrados.

Ao todo, considerando as quatro etapas de campo, foram visitados 270 pontos, com um total de 198 pontos amostrados. Todos os pontos visitados estão indicados na Figura 3.

Em todas as campanhas, o mapeamento foi realizado na escala de 1:100.000, utilizando como base imagens de radar Alos Palsar (resolução espacial de 12 m), imagens de satélite CBERS e levantamentos aerogeofísicos (magnetometria e aerogamaespectrometria) do projeto Anapu-Tuere, gerados pela CPRM e disponíveis no portal GeoSGB (https://geosgb.sgb.gov.br). Esses dados foram previamente processados em ambiente SIG.

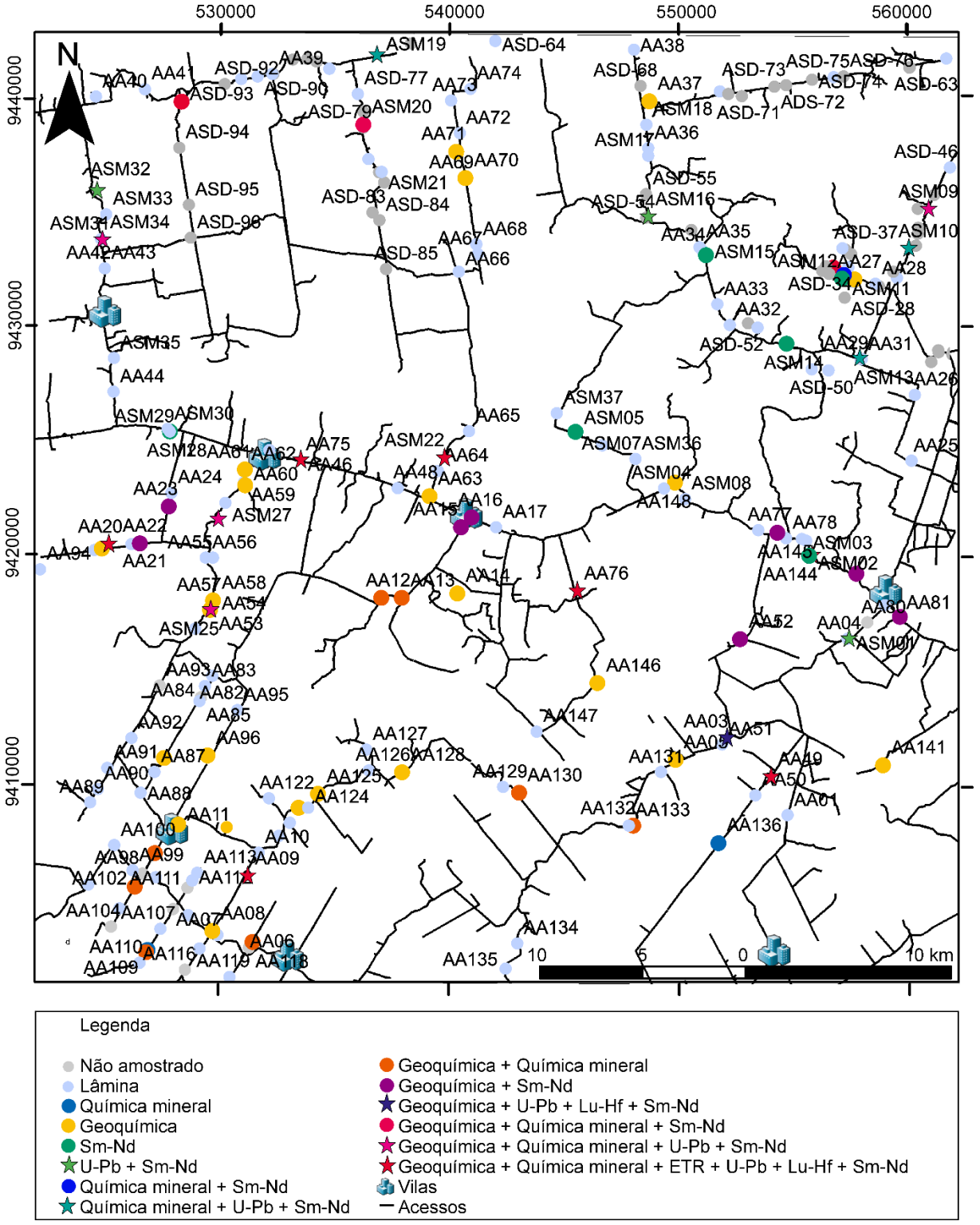


Figura 3 - Mapa de amostragem da área de estudo com a informação dos métodos aplicados contemplando os dados apresentados nesta tese, os dados da dissertação do autor e dados ainda não publicados.

1.7.4 Petrografia

Inicialmente, foi realizada a caracterização petrográfica mesoscópica das amostras de mão, com observações dos principais aspectos visíveis a olho nu ou com auxílio de lupa de mão, tais como cor, estrutura, textura e mineralogia. A partir dessa etapa, foram selecionadas

amostras para a confecção de lâminas polidas na Oficina de Laminação da Faculdade de Geologia do IG-UFPA. As lâminas foram analisadas em microscópio óptico Zeiss no laboratório de Suscetibilidade Magnética do PPGG e no laboratório de Petrografia da Pós-Graduação (LabPetro).

Durante a descrição microscópica, foi realizada a identificação sistemática dos minerais, bem como a análise detalhada das texturas magmáticas, deformacionais e metamórficas, com base em Passchier & Trouw (2005), Sawyer (2008), Trouw *et al.* (2009), Vernon (2005). O estudo de dissolução do epidoto foi realizado seguindo a metodologia proposta por Sial *et al.* (2008), detalhadamente descrita no artigo 2. As siglas dos minerais seguem o modelo proposto por Whitney & Evans (2010).

No total, foram confeccionadas cerca de 250 lâminas, abrangendo amostras de todas as etapas de campo. Além disso, um acervo com aproximadamente 60 lâminas provenientes de mapeamentos anteriores foi revisado quanto à sua petrografia.

As composições modais foram determinadas por meio do contador de pontos automático Stageledge, Endeeper, com uma contagem média de 1800 a 2000 pontos por lâmina para rochas ígneas e de 1000 a 1500 pontos para rochas metamórficas, utilizando uma malha de 0,4 mm. Rochas muito grossas, porfiríticas de grão grosso e altamente deformadas não foram submetidas a essa metodologia, sendo classificadas com base na composição química. A nomenclatura das rochas seguiu as recomendações das Subcomissões de Nomenclatura de Rochas Ígneas e Metamórficas da International Union of Geological Sciences (IUGS) (Fette & Desmons 2014, Le Maitre 2002).

1.7.5 Química mineral

Foram realizadas observações texturais por imagens de elétrons retroespalhados (ERE), análises pontuais semiquantitativas e mapas composicionais em lâminas polidas previamente selecionadas com base no estudo petrográfico. As análises foram conduzidas no Laboratório de Microscopia Eletrônica de Varredura (LME) do Museu Paraense Emílio Goeldi (MPEG), utilizando um microscópio eletrônico de varredura (MEV) Tescan Mira3, equipado com canhão FEG e detector EDS (Dispersive Energy Spectroscopy) Oxford modelo x-act, operando com o software Aztec. As análises pontuais e os mapas composicionais por EDS foram obtidos com uma voltagem de aceleração de 17,5 kV e uma distância de trabalho de 15 mm. Com base nas observações de amostras representativas, foram definidas as seções para análises em microssonda eletrônica.

A análise quantitativa da composição química dos minerais foi realizada em 16 lâminas

no Laboratório de Microssonda Eletrônica (LABSON) da Universidade de Brasília (UnB), utilizando uma microssonda JEOL JXA-8230, equipada com cinco espectrômetros. As análises foram conduzidas sob as seguintes condições operacionais: voltagem aceleradora de 15 kV, corrente de 10 a 20 nA, tempo de aquisição de 10 s e diâmetro do feixe variando entre 1 e 5 nm. Os padrões utilizados para calibração do instrumento foram andradita (Ca e Fe), microclina (Si, Al e K), olivina (Mg), albita (Na), pirofanita (Ti e Mn), vanadinita (V e Cl), óxido de níquel (Ni), trióxido de cromo (Cr) e celestita (Sr). Os minerais analisados incluíram faialita, piroxênios, anfibólio, biotita, titanita, epidoto, plagioclásio e óxidos de Fe-Ti.

1.7.6 Litogeoquímica

Foram realizadas análises geoquímicas de rocha total em 57 amostras representativas da área de estudo. As amostras selecionadas foram inicialmente britadas em britadores de mandíbula primários e secundários na Oficina de Preparação de Amostras (OPA) e, em seguida, pulverizadas no gral de ágata, no Laboratório de Sedimentologia (IG-UFPA), ou em moinho de carbeto de tungstênio, na Oficina de Laminação (IG-UFPA).

As análises foram conduzidas no laboratório comercial ALS Geochemistry Ltda. Os elementos maiores e menores (SiO_2, TiO_2, Al_2O_3, Fe_2O_3t, MgO, CaO, MnO, Na_2O, K_2O e P_2O_5) foram determinados por Espectrometria de Emissão Atômica com Plasma Indutivamente Acoplado (ICP-AES). Já os elementos-traço (Ba, Rb, Sr, Zr, Nb, Y, Hf, Ta, Ga, Cs, Sn, Th, U, V, W, Cr), incluindo os elementos terras raras (La, Ce, Pr, Nd, Sm, Eu, Gd, Tb, Dy, Ho, Er, Tm, Yb e Lu), foram analisados por Espectrometria de Massa com Plasma Indutivamente Acoplado (ICP-MS).

Uma descrição detalhada dos métodos analíticos e dos limites de detecção está disponível no site do laboratório (www.alsglobal.com/br).

1.7.7 Modelamento termodinâmico

O modelamento termodinâmico foi realizado utilizando o software GeoPS, versão 3.3 ou 3.5 (Xiang & Connolly 2022). Para o modelamento de cristalização e fusão parcial em rochas ígneas, foi empregada uma base de dados internamente consistente e modelos de atividade-composição (a-X) de Holland *et al.* (2018), no sistema NCKFMASHTO (Na_2O–CaO–K_2O–FeO–MgO–Al_2O_3–SiO_2–H_2O–TiO_2–Fe_2O_3). O estado de oxidação dos magmas foi estimado com base no software fO_2Melt Holland *et al.* (2018), considerando os dados de química mineral e de rocha total.

O modelamento foi aplicado de duas formas distintas. No segundo artigo, ele foi

utilizado para definir as condições de fusão necessárias à geração de um líquido semelhante aos magmas parentais do Granito Alto Rio Preto, seguindo a metodologia proposta por Semprich *et al.* (2015). O procedimento seguiu as seguintes etapas:

1. Realização do modelamento termodinâmico de uma possível rocha-fonte sob condições de pressão e temperatura adequadas para a origem dos magmas primários da unidade estudada.
2. Determinação das isolinhas composicionais de SiO_2 e MgO, que são excelentes indicadores de diferenciação magmática, e comparação desses valores com os dos magmas primários.
3. Seleção de um ponto específico no qual as composições do líquido gerado mais se assemelham às dos magmas parentais.
4. Extração, nesse ponto, das informações necessárias para o modelamento de elementos-traço, incluindo: composição do líquido gerado, fração de fusão, minerais residuais, suas composições e porcentagens em volume (%).

Devido à grande quantidade de dados gerados em formato de planilha Excel, foi desenvolvido um código VBA (Visual Basic for Applications) para automatizar a seleção do líquido mais semelhante ao magma parental.

No terceiro e quarto artigos o modelamento foi empregado para determinar as condições de cristalização de amostras representativas do Granito Alto Rio Preto e dos charnockitos Maravilha e Serra Azul, respectivamente.

Foram elaborados três tipos de pseudoseções, sendo elas:

1. Pressão-Temperatura (P-T): em que pressão e temperatura variam, utilizadas para inferir a sequência e as condições de cristalização.
2. Temperatura-Composição (T-M_{H_2O}/logfO_2): em que a temperatura e a composição (água ou fugacidade de oxigênio) variam a uma pressão fixa.
3. Pressão-Composição (P-M_{H_2O}/logfO_2): em que a pressão e a composição (água ou fugacidade de oxigênio) variam a uma temperatura fixa.

As duas últimas pseudoseções foram utilizadas para avaliar o efeito da variação composicional nas fases minerais.

O modelamento termodinâmico também foi empregado para determinar as condições do metamorfismo registrado nos ortognaisses aflorantes na área de estudo. Para isso, foi utilizado o GeoPS, mas com uma base de dados distinta, mais adequada à composição dos ortognaisses analisados. Nesse caso, foi empregada a base de dados de Holland & Powell (2011), também no sistema NCKFMASHTO. Os modelos a-X estão apresentados no artigo 6.

1.7.8 Modelamento geoquímico

Após a identificação do líquido mais semelhante ao magma parental em termos de elementos maiores no modelamento termodinâmico (Seção 1.7.7), as informações foram validadas por meio da modelagem de elementos-traço, utilizando planilhas do Microsoft Excel®. Esse procedimento tem como objetivo selecionar coeficientes de partição mineral/líquido (Kd) adequados, garantindo um bom ajuste gráfico para os principais elementos-traço. Os valores de Kd utilizados na modelagem foram obtidos a partir do banco de dados online disponível em: https://kdd.earthref.org/KdD/.

Para os modelos de fusão, foi empregada a equação de fusão parcial em equilíbrio de Wilson (1989):

$$\frac{CL}{C0} = \frac{1}{D(1-f)}\left(\frac{1}{D} - 1\right)$$

- C_L e C_0 são as concentrações dos elementos-traço no líquido e na fonte, respectivamente,
- F é a fração em peso do líquido formado,
- D é o coeficiente de distribuição total para os sólidos residuais no momento da remoção do líquido do sistema.

1.7.9 Elementos terras raras em minerais

Os minerais titanita, anfibólio e clinopiroxênio foram analisados via LA-ICP-MS para determinação de elementos-traço e terras raras no Laboratório de Química-ICP do IGC-USP. As análises foram conduzidas em um espectrômetro de massa com analisador quadrupolo iCapQ (Thermo), acoplado a um sistema de laser CETAC LSX-213 G2+. As condições operacionais do laser foram: fluência de 3 J/cm², frequência de 6 Hz e *spot* de 25 μm para titanita e 50 μm para anfibólio e clinopiroxênio. A aquisição e o processamento dos dados foram realizados em blocos de 120 análises, intercaladas com padrões e brancos de limpeza. O padrão primário utilizado foi o NIST SRM 612, enquanto os materiais de referência secundários foram NIST SRM 610, USGS BCR-1 e USGS BHVO-2G. O processamento dos dados do sinal resolvido no tempo foi realizado com o software Glitter (Griffin *et al.* 2008). Os valores do padrão interno foram determinados com base nos dados de química mineral para titanita, anfibólio e clinopiroxênio.

1.7.10 Geocronologia U-Pb

Foram realizadas análises de U-Pb em zircão, titanita e monazita utilizando os sistemas

LA-MC-ICP-MS (*laser ablation multi-collector inductively coupled plasma mass spectrometry*) no Laboratório de Estudos Geodinâmicos e Ambientais (LEGA-UnB) e no Centro de Pesquisas em Geocronologia e Geoquímica Isotópica (CEPGeo-USP), além do sistema SHRIMP IIe (*Sensitive High Resolution Ion Microprobe*) no Laboratório de Geocronologia de Alta Resolução (GEOLAB-USP). No total, foram analisados grãos de zircão de nove amostras (três via LA-ICP-MS da etapa de campo 1, cinco via SHRIMP IIe da etapa de campo 2 e uma via LA-ICP-MS da etapa de campo 4), quatro de titanita (uma do campo 1, duas do campo 2 e uma do campo 4, todas via LA-ICP-MS) e uma de monazita (campo 1, via LA-ICP-MS). Sempre que possível, foram datados zircão e titanita ou monazita da mesma amostra. Informações detalhadas sobre a localização e descrições das amostras estão nos artigos 1, 3, 5 e 6.

Os concentrados de zircão, titanita e monazita foram extraídos a partir de 5-10 kg de rocha, que foram trituradas, moídas e peneiradas. A separação dos minerais pesados foi realizada com auxílio de bateia e, posteriormente, com um separador magnético isodinâmico Frantz (tipo barreira magnética). A seleção final foi feita manualmente sob lupa binocular, e os minerais foram montados em resina epóxi, polidos para expor os centros dos cristais e posteriormente analisados por imagens de elétrons retroespalhados (ERE) em um microscópio eletrônico de varredura QUANTA 450 – FEI. Essas etapas foram realizadas no Laboratório de Estudos Geodinâmicos, Geocronológicos e Ambientais (LEGGA) da UnB.

Três amostras (ASM-01, ASM-22 e ASM-25) foram analisadas via U-Pb por LA-MC-ICP-MS em zircão e monazita no LEGGA-UnB, utilizando um espectrômetro Thermo Finnigan Neptune multi-coletor acoplado a um sistema de ablação a laser Nd-YAG 213 nm NewWave. Os parâmetros do equipamento foram fluência de 3,81-3,85 J/cm², frequência de 10 Hz e spot de ~25 μm. O padrão primário utilizado foi o GJ-1 (609 Ma, Jackson *et al.* 2004), enquanto o padrão secundário foi o 19950 (Wiedenbeck *et al.* 1995). As análises de monazita foram realizadas com um espectrômetro Thermo-Fischer Element XR de alta resolução acoplado a um sistema de ablação a laser 193 nm Iridia (ArF), com fluência de 3,0 J/cm², frequência de 20 Hz e spot de ~15 μm. O padrão primário foi o Itambé (Gonçalves *et al.* 2016) e o secundário, o Steenkampskraal (Knoper *et al.* 2000). A interferência de chumbo comum (204Pb) foi corrigida pelo monitoramento das massas 202Hg e 204Pb (204Hg+204Pb). A redução dos dados foi feita com os softwares Iolite v4.0 (Paton *et al.* 2011) e VisualAge (Petrus & Kamber, 2012).

A preparação da segunda e terceira levas de amostras seguiu os mesmos procedimentos, mas foi realizada na Oficina de Preparação de Amostras (OPA) e no Laboratório de Preparação Mineral (LPM) do IG-UFPA. As imagens de catodoluminescência (CL) e ERE, utilizadas para

observar aspectos texturais dos cristais (estrutura interna, sobrecrescimentos, fraturas e inclusões), foram obtidas antes das análises U-Pb em cinco amostras (AA-03C, AA-06A, AA-20, AA-46 e AA-76) no GEOLAB-USP.

As análises via SHRIMP seguiram o protocolo adotado pelo GEOLAB (Del Lama *et al.* 2008, Stern 1998, Williams 1997). Os padrões utilizados foram SL 13 (U = 238 ppm, (Sato *et al.* 2014) e TEMORA2 (416,78 ± 0,33 Ma, Black *et al.* 2004), com análises realizadas na proporção 5:1. Os pontos de análise foram selecionados em áreas de ~25 μm de diâmetro, evitando fraturas, inclusões e evidências de metamictização. A redução dos dados foi feita com o software SQUID (Ludwig, 2009), e as idades foram calculadas no programa Isoplot 4.15 (Ludwig 2008), com erros das razões isotópicas a 1σ e das elipses de idade a 2σ (absoluto). A seleção dos cristais de zircão para cálculo das idades seguiu os critérios: (a) conteúdo de chumbo comum (^{204}Pb), excluindo análises com $^{204}Pb/^{206}Pb > 0,0004$, (b) precisão analítica, descartando razões isotópicas com erro > 3,0%, e (c) grau de discordância, priorizando valores próximos de zero.

Além disso, titanita de quatro amostras (AA-46, AA-76, AA-144A, ASM-22) e zircão de uma (AA-144A) foram analisadas via LA-ICP-MS no CEPGeo-USP, utilizando um espectrômetro Thermo Finnigan Neptune multi-coletor acoplado a um sistema de ablação a laser Excimer 193 nm Ar–F. Os padrões primários utilizados foram GJ-1 (609 Ma, Jackson *et al.* 2004) e BLR-1 (1047±0,7 Ma, Aleinikoff *et al.* 2007) para zircão e titanita, respectivamente, enquanto os padrões secundários foram Plešovice (337.13±0.37 Ma, Sláma *et al.* 2008) e Khan (522±2.2 Ma, Heman 2009), respectivamente. As condições analíticas incluíram taxa de repetição de 6 Hz, fluência do laser de 8,9 e 8,55 J/m² e spot de 25 e 20 μm, para zircão e titanita respectivamente. O fluxo de gases incluiu 16 L/min de Ar para o plasma, 0,80 L/min de Ar auxiliar e ~1 L/min de He na célula de amostra. A correção de interferência utilizou o valor $^{202}Hg/^{204}Hg = 4,350360$. A redução dos dados foi realizada com macros internas do laboratório no Microsoft Excel. Diagramas de concórdia, histogramas, probabilidades relativas e médias ponderadas foram gerados no Isoplot 4.15 (Ludwig 2008).

1.7.11 Lu-Hf em zircão

As análises de isótopos de Hf em zircão foram realizadas no Laboratório de Geologia Isotópica (Pará-Iso) do Instituto de Geociências da UFPA. As análises foram feitas utilizando o sistema LA-MC-ICP-MS modelo Neptune, marca Thermo Finnigan, equipado com uma sonda laser Nd:YAG 213nm, modelo LSX-213 G2 da marca CETAC. Foram realizadas análises em cinco amostras previamente datadas por U-Pb (AA-03C, AA-06A, AA-20, ASM-01 e ASM-

22).

Os parâmetros analíticos para operação do ICP-MS envolveram: 16,0 l/min de fluxo de gás argônio resfriador, 0,7 a 0,8 l/min de gás argônio auxiliar, 1,2 a 1,3 l/min de gás argônio de arraste, 1200 W de potência, -2000 de extração, com análise em modo estático em baixa resolução, utilizando oito coletores de Faraday. O diâmetro de spot do laser foi de 40 a 50 µm. Durante as análises, o fluxo de gás hélio (He), responsável pelo transporte do material de ablação para o ICP-MS, variou de 450 a 500 ml/min, com frequência de 10 Hz e tempo total de ablação de aproximadamente 60 segundos. Utilizou-se uma potência de 50%, que forneceu uma densidade de energia de 4-5 J/cm^2 e permitiu obter um sinal da ordem de 1 a 3 volts para ^{178}Hf.

O zircão Mud Tank (731±1 Ma, Horstwood *et al.*, 2016) foi utilizado como material de referência para a razão ^{176}Hf/^{177}Hf. A sequência de análises intercalou três análises na amostra e uma no zircão de referência, para possibilitar as correções de interferências isobáricas dos isótopos Lu e Yb na massa 176. Os isótopos de Lu, Hf e Yb foram medidos concomitantemente, com base nas razões isotópicas ^{173}Yb/^{171}Yb, ^{179}Hf/^{177}Hf, ^{175}Lu/^{177}Hf e ^{176}Hf/^{177}Hf. As interferências isobáricas do ^{176}Lu e ^{176}Yb foram corrigidas utilizando uma equação que envolve um fator de fracionamento de massa (β) para Lu e Yb, com base na intensidade dos sinais observados nos isótopos livres de interferência ^{175}Lu e ^{173}Yb, normalizados a partir de suas abundâncias isotópicas aceitas: ^{176}Lu/^{175}Lu = 0,026549 (Chu *et al.* 2002) e ^{176}Yb/^{173}Yb = 0,786956 (Thirlwall and Anczkiewicz, 2004). O fator β (Hf, Yb e Lu) foi calculado para cada medida realizada, uma vez que seu valor depende diretamente da razão medida entre os isótopos de interesse.

Para corrigir o fracionamento isotópico gerado pelo equipamento durante as análises, de acordo com a lei exponencial (Russell *et al.* 1978), as razões isotópicas de Yb foram normalizadas assumindo valor de 1,12346 para ^{173}Yb/^{171}Yb (Thirlwall & Anczkiewicz, 2004) e as razões isotópicas de Hf foram normalizadas utilizando valor de 0,7325 para a razão ^{179}Hf/^{177}Hf (Patchett & Tatsumoto, 1980). Para a realização destes cálculos de correção e obtenção dos valores corrigidos das razões ^{176}Hf/^{177}Hf e ^{176}Lu/^{177}Hf de cada ponto analisado. Os dados brutos foram processados em macro Microsoft Excel, sendo selecionados aproximadamente 40 valores de um total de 60 dados integrados de 1,049 s/ponto (Milhomem Neto and Lafon, 2019).

Planilhas de Excel foram utilizadas para calcular as idades-modelo dois estágios ou crustais (Hf-$_{TDM}^{C}$) e os parâmetros épsilon háfnio (ƐHf) no tempo, assim como para gerar os diagramas de evolução do Hf vs tempo. Foi utilizada a constante de decaimento λ^{176}Lu de 1,867x10-11 anos^{-1} (Söderlund *et al.* 2004), razão ^{176}Lu/^{177}Hf de 0,015 para o valor médio da

crosta continental (Griffin *et al.* 2002) e razões $^{176}Lu/^{177}Hf$ e $^{176}Hf/^{177}Hf$ atuais para o Reservatório Uniforme Condrítico (CHUR) de 0,0336 e 0,282785 (Bouvier *et al.* 2008) e para o manto empobrecido (DM) de 0,0388 e 0,28325 (Andersen *et al.* 2009), respectivamente.

1.7.12 Sm-Nd em rocha total

As análises de Sm-Nd em rocha total foram realizadas em dezoito amostras (apresentadas nos artigos 1 e 5) no LEGGA-UnB, utilizando o espectrômetro de massa Finnigan MAT 262, conforme a metodologia descrita por Gioia & Pimentel (2000). Foram utilizadas 50 mg de rocha pulverizada, as quais foram misturadas com uma solução spike de $^{149}Sm–^{150}Nd$ e dissolvidas em cápsulas de Savillex. A extração de Sm e Nd seguiu a técnica de troca catiônica, utilizando uma coluna de teflon contendo resina L-N spec (HDEHP–ácido dietilhexílico fosfórico suportado em pó PTFE). O Sm e o Nd separados foram depositados em filamentos de Re e analisados em modo estático no espectrômetro. A precisão das razões Sm/Nd e $^{143}Nd/^{144}Nd$ é superior a ± 0,5% (2σ) e ± 0,005% (2σ), respectivamente, com base em repetições de análises de padrões internacionais de rocha (BHVO-1 e BCR-1). A razão $^{143}Nd/^{144}Nd$ foi normalizada para $^{146}Nd/^{144}Nd$ igual a 0,7219, e a constante de decaimento utilizada foi $6{,}54 \times 10^{-12}$ a^{-1}. O valor das idades-modelo T_{DM} foi calculado utilizando o modelo de De Paolo (1981).

Três amostras foram analisadas no CPGEO-USP (apresentadas no artigo 5) utilizando o MC-ICP-MS do modelo Neptune Plus Thermo Scientífic, conforme a metodologia interna do laboratório. Previamente as análises, os ácidos utilizados são purificados em destiladores sub-boiling DST-1000 ®Savillex e garrafas de destilação sub-boiling ®Savillex, a baixas temperaturas. Cerca de 50 mg de rocha pulverizada foram dissolvidos por digestão ácida, utilizando-se em etapas distintas HNO_3 + HF e HCl em um béquer de teflon (®Savillex), à temperatura de 100º C em um “clean box”. Para cada amostra as análises de Nd e Sm são efetuadas, respectivamente, 120 e 45 medições e a incerteza é calculada para 2σ. As razões isotópicas $^{143}Nd/^{144}Nd$ foram normalizadas para o valor de $^{146}Nd/^{144}Nd = 0{,}7219$ (De Paolo, 1981).

2 RHYACIAN MAGMATISM AT THE SOUTHERN BACAJÁ DOMAIN: IMPLICATIONS FOR THE CRUSTAL EVOLUTION OF SE AMAZONIAN CRATON, BRAZIL

Arthur Santos da Silva Neri

Roberto Dall'Agnol

Elton Luiz Dantas

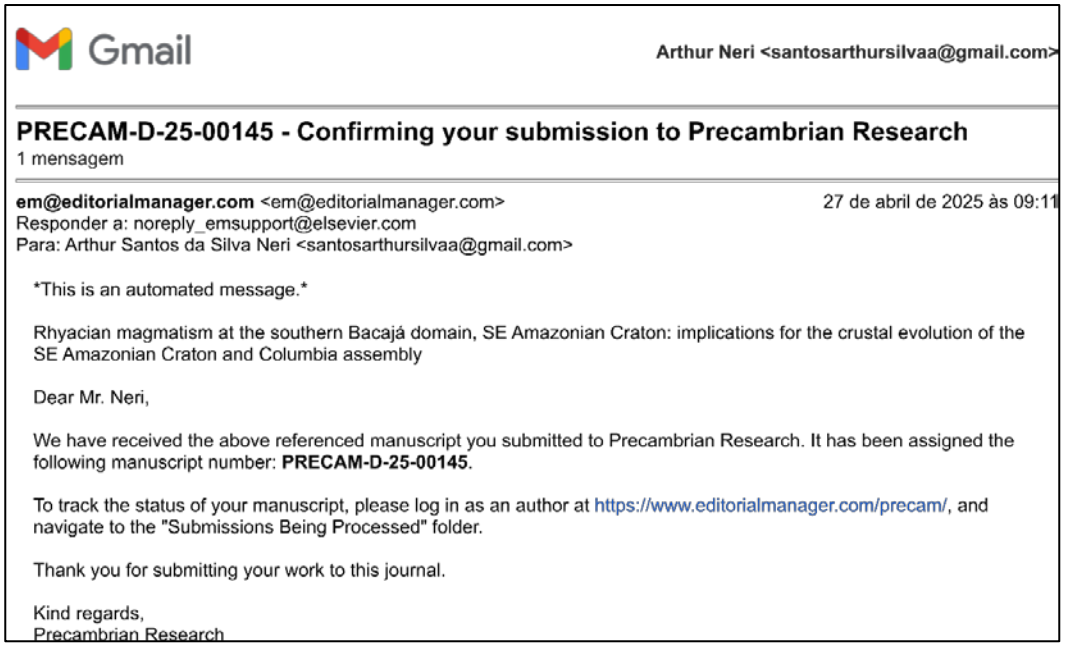
Gilmara Regina Lima Feio

José de Arimatéia Costa de Almeida

Marco Antonio Galarza

Submetido à *Precambrian Research* como *research article* em 27/04/2025 e em processo de revisão em 18/05/2025.

Devido aos direitos autorais da *Precambrian Research*, a formatação, citações e referências bibliográficas desta seção seguem o padrão requerido pela revista.



Gmail Arthur Neri <santosarthursilvaa@gmail.com>

PRECAM-D-25-00145 - Confirming your submission to Precambrian Research

1 mensagem

em@editorialmanager.com <em@editorialmanager.com> 27 de abril de 2025 às 09:11
Responder a: noreply_emsupport@elsevier.com
Para: Arthur Santos da Silva Neri <santosarthursilvaa@gmail.com>

This is an automated message.

Rhyacian magmatism at the southern Bacajá domain, SE Amazonian Craton: implications for the crustal evolution of the SE Amazonian Craton and Columbia assembly

Dear Mr. Neri,

We have received the above referenced manuscript you submitted to Precambrian Research. It has been assigned the following manuscript number: **PRECAM-D-25-00145**.

To track the status of your manuscript, please log in as an author at https://www.editorialmanager.com/precam/, and navigate to the "Submissions Being Processed" folder.

Thank you for submitting your work to this journal.

Kind regards,
Precambrian Research

Rhyacian magmatism at the southern Bacajá Domain, SE Amazonian Craton: implications for the crustal evolution of the SE Amazonian Craton and Columbia assembly

Arthur Santos da Silva Neri [a*], Roberto Dall'Agnol [a, b, c], Elton Luiz Dantas [d], Gilmara Regina Lima Feio [e], José de Arimatéia Costa de Almeida [a, b], Marco Antonio Galarza[a]

[a] Programa de pós-graduação em Geologia e Geoquímica, Instituto de Geociências (IG), Universidade Federal do Pará (UFPA), Rua Augusto Corrêa, 01, Belém-PA, Brazil. CEP 66075-110.

[b] Grupo de Pesquisa Petrologia de Granitoides IG – UFPA.

[c] Instituto Tecnológico Vale, Belém-PA, Brazil.

[d] Laboratório de Estudos Geocronológicos, Geodinâmicos e Ambientais, Universidade de Brasília, Brasília-DF, Brazil**.** CEP 70910-900.

[e] Universidade Federal do Sul e Sudeste do Pará (UNIFESSPA), Marabá-PA, Brazil.

*Corresponding author: santosarthursilvaa@gmail.com

ABSTRACT: Collisional orogenesis represents one of the most complex geodynamic processes, leading to the formation of diverse granitoids, including charnockites and strongly peraluminous granites. The coexistence of I-A, and S-type granites in these settings reflects crustal thickening and the intense thermal conditions of orogenic belts. However, the nature, timing and tectonic setting of the Rhyacian magmatism in SE Amazonian Craton remain poorly understood. This study focusses on this gap by integrating geological mapping, petrography, whole-rock geochemistry, U-Pb geochronology, and Nd-Hf isotopic studies conducted in the southern portion of the Bacajá Domain, a Paleoproterozoic collisional orogen in the SE Amazonian craton. Our results identify previously unrecognized Rhyacian granitic and charnockitic, formerly assigned to the Measoarchean Cajazeiras complex: (i) 2.12 Ga high-K calc-alkaline Bandeirante granite (2.12 Ga, $\varepsilon Hf_{(t)}$ = -6.5 to -4.6, $\varepsilon Nd_{(t)}$ = -3.40); (ii) 2.09 Ga to 2.06 Ga calc-alkaline to high-K calc-alkaline Alto Rio Preto granite ($\varepsilon Hf_{(t)}$ = -10.2 to -6.3, $\varepsilon Nd_{(t)}$ = -8.96 -2.80); (iii) 2.09 Ga ferroan Maravilha charnockite ($\varepsilon Hf_{(t)}$ = - 9.2 to -8.2, $\varepsilon Nd_{(t)}$ = -3.01 to -1.91); (iv) 2.06 Ga magnesian Serra Azul charnockite ($\varepsilon Hf_{(t)}$ = -8.8 to -5.8, $\varepsilon Nd_{(t)}$ = -6.44 to -4.71); and (v) 2.05 Ga strongly peraluminous Bernardino granite ($\varepsilon Nd_{(t)}$ = -6.71).Overlapping ages suggests a prolonged magmatic activity (~70 Ma). These rocks

are mostly calc-alkaline and magnesian but vary to calcic or alkali-calcic/ferroan. Whole-rock geochemistry, zircon U-Pb-Hf, and whole-rock Nd isotopes point to a collisional origin for the magmatic rocks with extensive reworking of Archean sources and limited mantle contribution. We propose a two-stage geodynamic model: (1) collision between the Archean Bacajá basement and pre-collisional island arcs with the Carajás Province (~2.12-2.10 Ga), leading to significant crustal thickening and generation of small syn-collisional plutons; (2) the thickened crust becomes unstable, leading to crustal delamination and the generation of late- to post-collisional magmas (2.09-2.05 Ga). Compiled zircon U-Pb-Hf reveals crustal reworking and juvenile input patterns similar to the Guiana Shield and West African Craton, supporting the hypothesis of their juxtaposition during Columbia assembly.

Keywords: granitoids, charnockites, geochemistry, Nd-Hf isotopes, Paleoproterozoic, supercontinent.

2.1 INTRODUCTION

The Paleoproterozoic Era (2.5-1.6 Ga) is recognized as a period of intense tectonic activity, marked by major episodes of crustal growth and continental emergence (Cawood et al., 2013; Rino et al., 2004). During this Era, especially throughout the Rhyacian and Orosirian periods, several collisional and/or accretionary belts developed on a global scale, contributing the formation of the Columbia supercontinent (Zhao et al., 2002).

The assembly and breakup of supercontinents occurred multiple times throughout Earth's geological history, having significant impacts on climate, life, and lithospheric evolution (e,g., D'Agrella-Filho et al., 2016; Meert, 2002; Nance et al., 2014; Rogers and Santosh, 2002; Zhao et al., 2002). The reconstruction of the earliest supercontinents relies on several proxies, such as paleomagnetic data and magmatic and metamorphic events (Chaves, 2021; Hou et al., 2008; Meert, 2012; Volante and Kirscher, 2024; Wu et al., 2020).

Collisional orogenic belts are a ubiquitous feature in the supercontinent assembly and defining and comparing these belts are essential for reconstructing the supercontinents (Zhao et al., 2004, 2002b). Within these belts, diverse magmatic rocks form as a result of complex interaction between crustal and mantle materials in distinct tectonic settings and at different orogenic stages, from pre-collisional to post-collisional (Bruno et al., 2021; Eglinger et al., 2017; Klein et al., 2020; Saboia et al., 2020; Wu et al., 2020). Therefore, understanding the processes that lead to the formation of the

magmatic rocks, their sources, and tectonic settings plays a key role in elucidating the evolution of individual belt and their relationships with coeval belts worldwide (Grenholm et al., 2019a).

The Bacajá Domain is a collisional orogen developed during a regional Paleoproterozoic orogenetic event in the Amazonian Craton, known as the Transamazonian Orogeny (e.g., Macambira et al., 2020; Vasquez, 2006; Vasquez and Rosa-Costa, 2008). This event took place between 2.26 and 1.95 Ga (e.g., Grenholm et al., 2019b; Hurley et al., 1967; Kroonenberg et al., 2016; Rosa-Costa et al., 2025), and was responsible for reworking Archean fragments, which are now preserved as basement inliers, as well as for extensive orogenic magmatism and metamorphism between 2.23 to 2.05 Ga (e..g., Barros et al., 2023; Macambira et al., 2022, 2009; Magalhães et al., 2023; Vasquez et al., 2008, 2005). While geological data are available for the western and northern sectors of the domain, the southern portion remains poorly constrained due to a lack of geochemical, geochronological and isotopic data. This limitation hinders a precise understanding of the tectonic evolution of the southern Bacajá Domain, its correlation with the northern sector and its potential relationship with the adjacent Carajás Province. p. In fact, some previous studies have proposed that the southern Bacajá may represent a exhumed Carajás crust (Correa et al., 2022; Motta et al., 2019), highlighting the need for further investigation to clarify their relationship.

In this context, the present study integrates geological mapping, petrography, geochemistry, U-Pb geochronology, and Nd-Hf isotopes on several granitoids and charnockitic units in the southern Bacajá Domain, close to its boundary with the Archean Carajás Province. The resulting dataset provides a more consistent understanding of the Rhyacian magmatism in the Bacajá Domain and helps clarify its crustal evolution and relationship with the Carajás domain. Furthermore, the results offer new insights into its correlation with other coeval orogens developed during the Columbia assembly in Amazonian and West Africa cratons.

2.2 GEOLOGICAL SETTING

The Maroni-Itacaiúnas province (Fig. 1) is the main province established during the Paleoproterozoic (Rhyacian-Orosirian) in the Amazonian craton (Santos et al., 2006; Tassinari and Macambira, 2004). It extends from the northern Guiana shield, covering part of Venezuela, French Guiana, Suriname, and the Amapá state of Brazil, to the Bacajá Domain in the southeastern Amazon region and includes several subduction-related and collisional orogenic belts (Fraga et al., 2024; S. B. Kroonenberg et al., 2016; Ledru et al.,

1994; Macambira et al., 2020; Rosa-Costa et al., 2003, 2006, 2025; Vanderhaeghe et al., 1998).

The Bacajá Domain (Fig. 1c) represents the southeastern extension of the Maroni-Itacaiúnas Province into the Central Brazil Shield. It is predominantly composed of Rhyacian to Orosirian granitoids related to orogenic magmatism (Vasquez, 2006; Vasquez et al., 2008; Vasquez and Rosa-Costa, 2008), together with Archean and Siderian fragments reworked during the Transamazonian Orogeny between ca. 2.26 and 1.99 Ga (Cordani et al., 2000; Hurley et al., 1967).

The Bacajá basement comprises two lithotectonic associations: (i) Archean metamorphic complexes composed of granulites and orthogneisses with Mesoarchean (3000±2 Ma and 2943±4 Ma; Macambira et al., 2007; Vasquez and Rosa-Costa, 2008), or Neoarchean protoliths (2671±3 Ma; Vasquez and Rosa-Costa, 2008); and (ii) a late Neoarchean granite-gneiss-migmatite association crystallized at 2503±10 Ma (Macambira et al., 2003; Macambira et al., 2004). In the first association, aluminous granulites and paragneiss occur as small lenses or enclaves within the Archean orthoderived rocks. These units contain detrital zircon populations with ages ranging from the Mesoarchean to the Paleoproterozoic (3.14-2.47 Ga, Macambira et al., 2007; Vasquez, 2006). Associated with this basement, Siderian juvenile greenstone belts and related rocks are also exposed, including acid volcanic rocks crystallized between 2452±3 Ma and 2359±3 Ma (Macambira et al., 2009; Macambira et al., 2003; Vasquez, 2006).

The Paleoproterozoic orogenic magmatism includes several distinct episodes, as proposed by Vasquez and Rosa-Costa (2008): (i) pre-collisional magmatism dated from 2215±2 Ma to 2133±10 Ma; (ii) the syn- to late-collisional magmatism dated from 2114±3 Ma to 2102±3 Ma; (iii) late- to post-collisional magmatism dated from 2086±5 Ma to 2069±6 Ma; and (iv) the post-collisional magmatism dated at 1986±5 Ma (Tab. 1, Fig. 2).

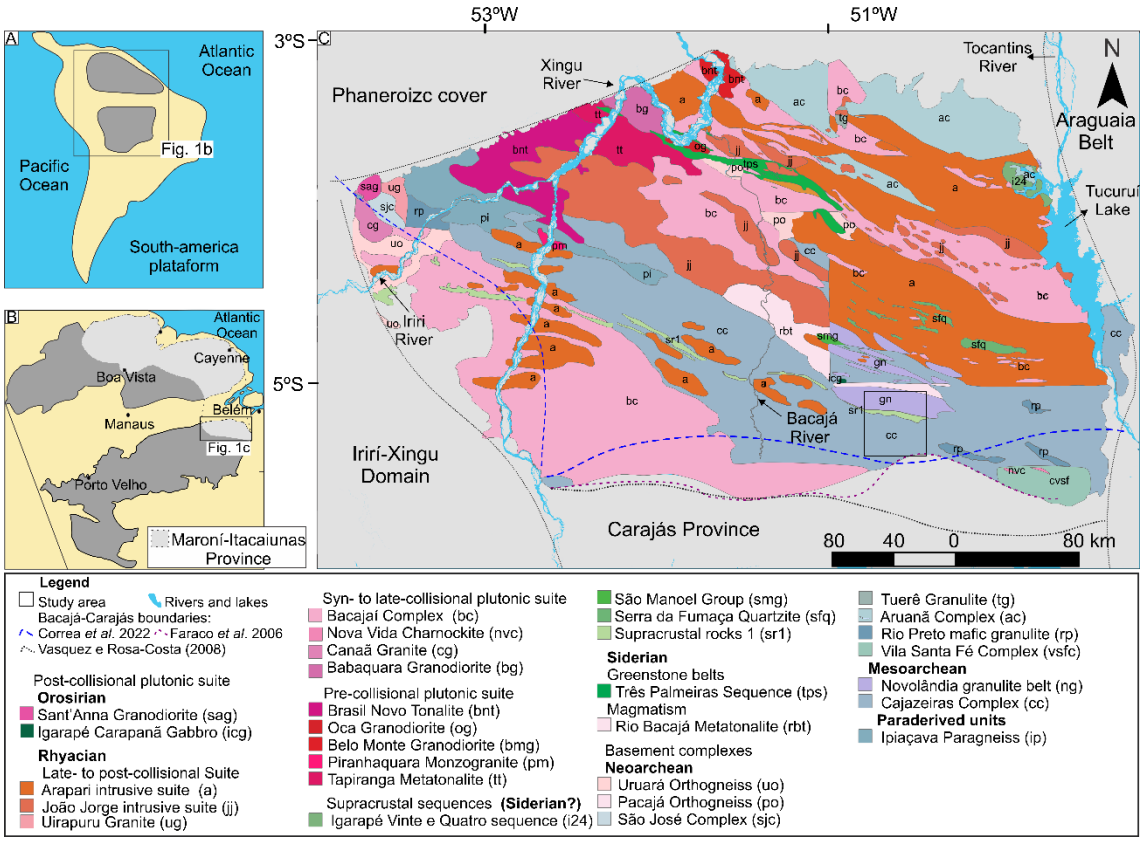


Figure 1 - (A) South American platform highlighting the Amazonian craton; (B) Amazonian craton showing the Maroni-Itacaiúnas province, according to Tassinari and Macambira (2004), and its Bacajá Domain (black rectangle); (C) simplified geological map of the Bacajá Domain modified after (Vasquez and Rosa-Costa, 2008, Macambira and Ricci, 2015, Barros et al., 2023) and showing the proposed boundaries between the Bacajá Domain and Carajás province. The black rectangle in (C) corresponds to the study area (cf. Fig. 3).

Table 1 - Summary of crystallization ages from Rhyacian granitoids from Bacajá Domain

Unit	Lithology	Sample	Method	Analyzed Mineral	Age (Ma)	Ref.
Sant'ana granodiorite	Granodiorite	-	Pb-evaporation	Zircon	1986±5	8
		-	Pb-evaporation	Zircon	2483±11*	8
		-	Pb-evaporation	Zircon	2086±5 *	8
	Monzogranite	CVM-21	U-Pb, LA-ICP-MS	Zircon	2124±7	14
Bernardino granite	Monzogranite	ASM-25	U-Pb LA-ICP-MS	Monazite	2052.3±5.4	16
Serra Azul charnockite	Tonalite	AA-20	U-Pb SHRIMP	Zircon	2062.5±8.8	16
João Jorge intrusive suíte	Granodiorite	EM-55	U-Pb LA-ICP-MS	Zircon	2062±22	15
	Granodiorite	MCM55	Pb-evaporation	Zircon	2076±6	6
	Alcali-feldspar syenite	-	Pb-evaporation	Zircon	2076±2	11
	-	EM-49	Pb-evaporation	Zircon	2077±5	12
	Monzogranite	MVD-06B	Pb-evaporation	Zircon	2077±2	5
		MVD-06B	Pb-evaporation	Zircon	2097±7*	5
		MVD-06B	Pb-evaporation	Zircon	2115±9*	5
		MVD-06B	Pb-evaporation	Zircon	2219±3*	5

Felício Turvo granite	-	-	Pb-evaporation	Zircon	2069±6	2
	Monzogranite	MDM02	Pb-evaporation	Zircon	2085±4	10
Undifferentiated grainitoids	Leucogranodiorite	MCM-48	Pb-evaporation	Zircon	2077±3	10
	Quartz-diorite	MVD-46A	Pb-evaporation	Zircon	2071±3	5
Arapari intrusive suite	Charnockite	PR-32	Pb-evaporation	Zircon	2059±4	11
	Jotunite	MVD94	Pb-evaporation	Zircon	2070±3	7
	Quartz-monzodiorite	-	Pb-evaporation	Zircon	2072±4	11
	Charnoenderbite	PMM-01	Pb-evaporation	Zircon	2079±3	13
		PMM-01	Pb-evaporation	Zircon	2157±3*	13
		PMM-01	Pb-evaporation	Zircon	2415±10*	13
		PMM-01	Pb-evaporation	Zircon	2613±8*	13
		PMM-01	Pb-evaporation	Zircon	2824±22*	13
	Granodiorite	EM-55	U-Pb LA-ICP-MS	Zircon	2080±16	15
	-	MO36	U-Pb SHRIMP	Zircon	2086±5	1
	Charnockite	PR-29B	Pb-evaporation	Zircon	2088±2	12
Alto Rio Preto granite	Granodiorite	ASM-01	U-Pb LA-ICP-MS	Zircon	2076±12	16
		ASM-01	U-Pb LA-ICP-MS	Zircon	2295±28	16
	Monzogranite	AA-76	U-Pb SHRIMP	Zircon	2098±11	16
Maravilha charnockite	Syenogranite	AA-06A	U-Pb SHRIMP	Zircon	2089±12	16
Babaquara granodiorite	Granodiorite	MVD102	Pb-evaporation	Zircon	2102±3	5
Canãa granite	Granitoid	MVD-26A	Pb-evaporation	Zircon	2104±5	3
		MVD-26A	Pb-evaporation	Zircon	2121±5*	3
		MVD-26A	Pb-evaporation	Zircon	2139±5*	3
		MVD-26A	Pb-evaporation	Zircon	2156±7*	3
Bacajaí complex	Charnockite	PMM-20A	Pb-evaporation	Zircon	2084±2	13
		PMM-20A	Pb-evaporation	Zircon	2108±5*	13
		PMM-20A	Pb-evaporation	Zircon	2436±3*	13
	Enderbite	EM-97	Pb-evaporation	Zircon	2090±6	12
	Charnockite	PMM-06	Pb-evaporation	Zircon	2094±4	13
	Metatonalite	EM-100	U-Pb LA-ICP-MS	Zircon	2094±11	15
	Monzogranite	PR-170	U-Pb LA-ICP-MS	Zircon	2103±21	12
	Monzogranite	-	U-Pb SHRIMP	Zircon	2113±3	4
	Monzogranite	FB-148	Pb-evaporation	Zircon	2112±8	11
	Charnoenderbite	TF-45	U-Pb SHRIMP	Zircon	2113+35/-33	4
		TF-45	U-Pb SHRIMP	Zircon	2673±2*	4
	Enderbite	PMM-09C	Pb-evaporation	Zircon	2114±3	13
			Pb-evaporation	Zircon	2573±2*	13
Bandeirante granite	Monzogranite	AA-03C	U-Pb SHRIMP	Zircon	2116±11	16
Tapiranga metatonalite	Metatonalite	MVD103A	U-Pb SHRIMP	Zircon	2133±10	7
		MVD103A	U-Pb SHRIMP	Zircon	2337±11*	7
Piranhaquara monzogranite	Monzogranite	MVD115B	U-Pb SHRIMP	Zircon	2147±5	7

Belo Monte granodiorite	Granodiorite	-	Pb-evaporation	Zircon	2154±2	8
Oca granodiorite	Quartz-monzodiorite	MVD125 A	U-Pb SHRIMP	Zircon	2160±3	7
Undifferentiated grainitoids	Monzogranite	-	Pb-evaporation	Zircon	2191±2	10
Brasil Novo tonalite	Monzogranite	M0-32	U-Pb SHRIMP	Zircon	2182±6	1
	Granitoid	MVD-05	Pb-evaporation	Zircon	2215±2	3
	Granitoid	MVD-05	Pb-evaporation	Zircon	2524±5*	3
	Syenogranite	MVD-27E	Pb-evaporation	Zircon	2209±2	7

References: 1 - Santos (2003), 2 - Souza et al., (2003), 3 - Vasquez et al., (2005), 4 - Faraco et al., (2006), 5 - Vasquez (2006), 6 - Barros et al., (2007), 7 - Vasquez et al., (2008), 8 -Vasquez and Rosa-Costa (2008 and references therein), 9 - Macambira et al., (2007), 10 - Macambira et al., (2009), 11 -Barros et al., (2023), 12 - Macambira and Ricci (2015) 13 - Macambira et al., (2022), 14 - Vieira et al., (2022), 15 - Magalhães et al., (2023), 16 - this work. * inheritance

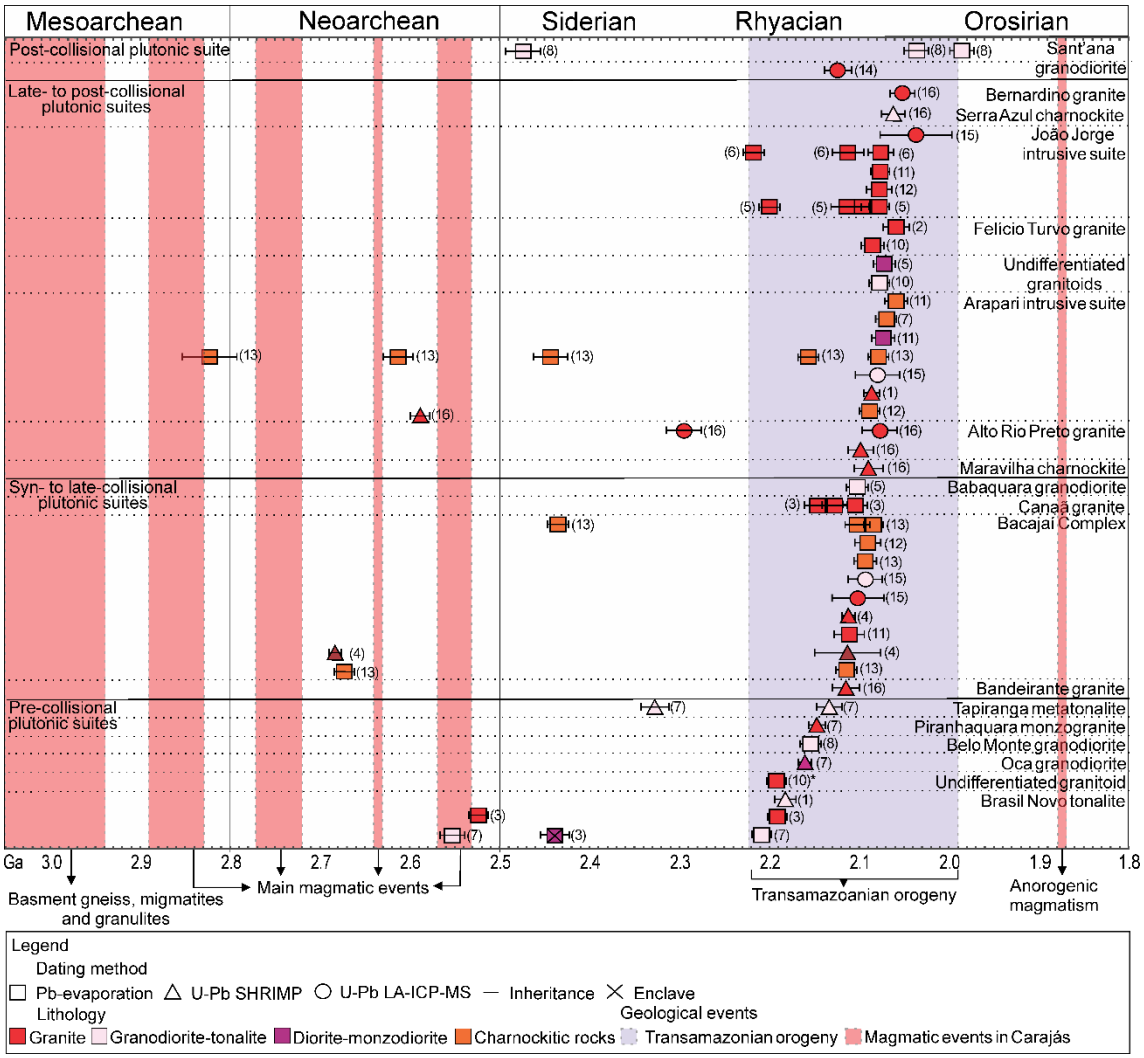


Figure 2 - Summary of crystallization ages of the Rhyacian granitoids of the Bacajá Domain. References are the same as in the table 1.

2.3 METHODOLOGY

2.3.1 Fieldwork and lithostratigraphic classification

The fieldwork was conducted in four campaigns from 2019 to 2023 in southeast Pará state, North of Brazil. Geophysical data (surveys of the Brazilian Geological Survey) and petrographic and geochemical studies supported the fieldwork.

The lithostratigraphic classification of the studied granitoids follows the recommendations of the Brazilian Guide to Stratigraphic Classification (Petri et al., 1986) and the International Subcommission on Stratigraphic Classification (Murphy and Salvador, 1999) of the International Union of Geological Sciences (IUGS).

2.3.2 Whole-rock geochemistry

Forty-three chemical analyses of representative samples from the studied rocks were conducted at ALS laboratories. Major element concentrations were determined using inductively coupled plasma emission spectrometry (ICP-AES), while trace elements, including rare earth elements, were analyzed by inductively coupled plasma–mass spectrometry (ICP–MS) following the ME-MS81d protocol. This method employs lithium borate fusion to ensure total digestion of the sample, including resistate phases, prior to analysis. Detailed information on analytical procedures and detection limits is available at https://www.alsglobal.com.

2.3.3 U-Pb geochronology

Zircon and monazite were separated using standard rock crushing and heavy mineral separation techniques. Grains were individually selected, picked, and mounted in epoxy resin. Grain mounts were polished to expose the grain centers. Backscatter electron images (BSE) and cathodoluminescence (CL) for zircon were performed with a QUANTA 450 – FEI scanning electron microscope (SEM) at the Laboratório de Estudos Geodinâmicos, Geocronológicos e Ambientais (LEGGA) from UnB with the following conditions: 10 nA, 20kV, 13.8 mm working distance.

Zircon and monazite U-Pb analyses were carried out in the Laboratório de Estudos Geodinâmicos, Geocronológicos e Ambientais (LEGGA) of the Universidade de Brasília (UnB), Brazil, following the laboratory's standard procedures (Bühn et al., 2009). The analyses in zircon were carried out using a Neptune Series High-Resolution Multicollector ICP-MS coupled with laser ablation system Nd-YAG 213nm NewWave. Instrument setup parameters were 3,81-3,85 and 2,67-2,70 J/cm2 laser fluence for zircon and monazite, respectively, 10 Hz, ~25 μm spot size. U-Pb zircon data were standardized using GJ-1 (reference 609.5 ± 1.5 Ma, Jackson et al., 2004) as a primary standard and

tested using the zircon Plešovice (337.13 ± 0.37 Ma, Sláma et al., 2008),Wiedenbeck et al., 1995) as a secondary standard. External errors were calculated with the error propagation of individual measurements of GJ-1 and each spot's measurements.

The analyses in monazite were performed using a Thermo Finnigan Element XR high-resolution single-collector sector field ICP-MS coupled to a 193 nm Iridia (ArF) laser ablation system that was used to measure the masses of interest. The laser ablation system is equipped with a Cobalt dual-volume chamber. The mass spectrometer was tuned to improve U and Pb sensitivity while minimizing oxide production prior to each analytical session. Each spot's analysis was measured in 10 s of background measurement followed by 20 s of sample acquisition. A triple detection mode (SEM+Faraday) was used to measure each mass (202, 204, 206, 207,208, 232, 238) by sweeping the electrostatic sector on each mass. The analyses used a spot diameter of 15 µm, with a repetition rate of 20 Hz, and a laser fluence of 3.0 J cm-2. The Itambé monazite (Gonçalves et al., 2016) was used as primary standard the Steenkampskraaal (Knoper et al., 2000; Liu et al., 2012) as a secondary one. Itambé monazite were used for quality control. Excess variance on the primary calibrant was propagated on each analytical point. Systematic uncertainty of ca. 1% is propagated on each final age. No common lead correction was applied. Ages are quoted at 2σ. Raw data for both zircon and monazite was processed on Iolite 4.0 (Paton et al., 2011) as a time-resolved signal, and individual signal inspection was done with the assistance of the VizualAge (Petrus and Kamber, 2012). Data correction included blank subtraction and LIEF correction using an exponential plus linear model. For density plots of detritral zircon grains only analyses in a range of ±10% of concordance was used.

The SHRIMP IIe system at GeoLab/USP consists of a mass spectrometer coupled to an ion microprobe with high sensitivity and resolution that uses a collimated and accelerated beam of primary ions (O^{2-}) to reach a target where secondary ions are generated from a 30 µm spot. The secondary ions are accelerated through the equipment, and the $^{254}UO^{+}$, $^{206}Pb^{+}$, $^{207}Pb^{+}$, $^{208}Pb^{+}$, $^{238}U^{+}$, $^{254}ThO^{+,}$ and $^{196}Zr_2O^{+}$ isotopes generated by the sample are measured successively. Its instrumental performance and analytical procedures are documented by Sato et al. (2014) and references therein: (i) primary beam → Kohler aperture = 120 µm; spot size = 30 µm; beam density of O^{2-} ions = 2.5–7.0 ηA (depending on brightness aperture); (ii) secondary beam → source aperture = 80 µm; mass resolutions for $^{196}Zr_2O$, ^{206}Pb, ^{207}Pb, ^{208}Pb, ^{238}U, ^{248}ThO and ^{254}UO ranging from 5,000 to 5,500 (1%), and residuals <0.025. The corrections required by the technique are made by analyzing unknown materials and reference materials to determine specific calibration

factors (Black et al., 2004). Thus, during execution, for every five analyses on material of unknown age, one analysis is performed on the reference standard.

The Temora-2 reference zircon (416.78 ± 0.33 Ma; Black et al., 2004) was used for standard isotopic ratios, and the SL13 zircon (238 ppm; Sato et al., 2014) was used for reference of the concentration of U. The corrections for common lead were performed with ^{204}Pb, according to the isotopic evolution model of Stacey and Kramers (1975). Data reduction was performed in SQUID 1.6 software (Ludwig, 2009), while data processing and diagram generation were carried out in Isoplot 4.15 (Ludwig, 2003).. The errors of the isotope ratio were 1σ (%), and those of the age ellipses were 2σ (absolute). Concordia diagrams and density plots were done using Isoplot/Ex (Ludwig, 2003).

2.3.4 Hf isotopes on zircon

The Lu-Hf analyses on zircon were performed using an LA–MC–ICP–MS at the Pará-Iso (UFPA). Following the laboratory procedures described in Milhomem and Lafon (2019). The laser-induced elemental fractionation and instrumental mass discrimination were corrected using the isotopic ratios of the GJ-1 zircon (608.5 ± 1.5 Ma; Jackson et al., 2004), while the Mud Tank zircon (732 ± 1 Ma; Black and Gulson, 1978; Horstwood et al., 2016) was analyzed as a secondary reference material.

Data were collected in static mode for 60s of ablation with a spot size of 40-50 µm laser spots comprising most of the previous U-Pb spots or near them, but always in the same zircon domain. The Lu, Hf, and Yb isotopes were concomitantly measured from isotope ratios $^{173}Yb/^{171}Yb$, $^{179}Hf/^{177}Hf$, $^{175}Lu/^{177}Hf$ and $^{176}Hf/^{177}Hf$. The isobaric interferences of ^{176}Lu and ^{176}Yb were corrected using an equation that involved a mass fractionation factor (β) for Lu and Yb and the intensity of the signals observed in the interference-free isotopes ^{175}Lu and ^{173}Yb, normalized from their isotopic abundances $^{176}Lu/^{175}Lu = 0.026549$ (Chu et al., 2002) and $^{176}Yb/^{173}Yb = 0.786956$ (Thirlwall and Anczkiewicz, 2004). For the correction of the isotopic fractionation caused by the equipment during the analyses, according to the exponential law (Russell et al., 1978), the Yb isotope ratios were normalized, assuming a value of 1.12346 for $^{173}Yb/^{171}Yb$ (Thirlwall and Anczkiewicz, 2004). The Hf isotope ratios were normalized using a value of 0.7325 for $^{179}Hf/^{177}Hf$ (Patchett and Tatsumoto, 1980). The mass bias behavior of Lu was assumed to be identical to that of Yb. To calculate $\varepsilon Hf_{(t)}$ and two-stage model ages (Hf-T_{DM}^{C}), the decay constant λ_{176Lu} of $1.867x10^{-11}$ years^{-1} (Söderlund et al., 2004) was used, as well as a $^{176}Lu/^{177}Hf$ ratio of 0.015 as an average value for the continental crust (Griffin et al., 2002) and present-day $^{176}Lu/^{177}Hf$ of 0.0336 and $^{176}Hf/^{177}Hf$ ratios of

0.282785 for the chondritic uniform reservoir (CHUR) (Bouvier et al., 2008) and $^{176}Lu/^{177}Hf$ ratios of 0.0388 and $^{176}Hf/^{177}Hf$ of 0.28325 for the depleted mantle (DM) (Andersen et al., 2009).

2.3.5 Whole-rock Nd isotopes

The procedures used in the LEGGA-UnB for whole-rock Nd isotopes are described by Gioia and Pimentel (2000). The analyses were carried out using the mass spectrometer MAT Finnigan MAT 262 (ID-TIMS). The whole rock powders (~50 mg) were mixed with a spike ^{149}Sm-^{150}Nd and dissolved in Savillex capsules. The Sm and Nd extraction follows the cationic exchange using Teflon columns with L-N spec resin (HDEHP– diethyl hexyl phosphoric acid supported on PTFE powder). Sm and Nd were placed in a rhenium filament and measured in static mode. The Sm/Nd and $^{143}Nd/^{144}Nd$ precision are higher than ± 0.5% (2σ) and ± 0.005% (2σ), respectively, based on repeated analyses in international rock standards (BHVO-1 and BCR-1).

2.4 RESULTS

2.4.1 Geology and petrography

2.4.1.1 Bandeirante granite

The Bandeirante granite comprises two elongated stocks located in the central and southwestern portion of the study area (Fig. 3, 4a). It includes amphibole monzogranites (Fig. 5a), amphibole-biotite monzogranites, and leucosyenogranites. Mafic microgranular enclaves are rare. The Bernardino granite intrudes the southwestern stock of the Bandeirante granite. Leucogranitic veins concordant with foliation are common. Shear zones define its contact with the Serra Azul charnockite.

Away from shear zones (the stock in the center of the area), the unit is composed by non-deformed rocks that preserve primary magmatic textures (Fig. 4a, Tab. 2). However, in proximity to the shear zones (southeastern stock), the granite is strongly deformed (Tab. 2). The foliation is defined by the alignment of mafic minerals and concordant leucogranite veins, which follow the regional NW-SE to NNW-SSE trend, dipping moderately to NE.

2.4.1.2 Alto Rio Preto granite

The Alto Rio Preto granite consists of two elongated and coalescent plutons, as well as a small stock, that corps out near the center of the mapped area along the Rio Preto road (Fig. 3, 4b, c). It comprises amphibole-biotite and biotite-bearing granites, with subordinate granodiorites and tonalites (Fig. 5b, c). Sparse microgranular mafic and high-pressure granulite xenoliths may occur. The granite is intruded by the Bernardino granite

(Fig. 3, 4a, Tab. 2). In the southeast of the area, interactions between the Alto Rio Preto granite and Serra Azul charnockite were observed (Fig. 4b). Leucogranitic veins concordant with foliation are common, and quartz and epidote veins crosscut the granite. Regional shear zones define its contact with the Cajazeiras Complex (Fig. 3).

The deformation that affected the granite is heterogeneous. Away from the Misteriosa Shear Zone, the rocks preserve primary magmatic features, including aligned feldspar crystals that define a NW-SE magmatic flux. However, close to the shear zone, the granite displays mylonitic to ultra-mylonitic textures, and its original fabric is partially or totally obliterated (Fig 4c). The foliation displays a WNW-ESE to NW-SE trend with moderate to steep, locally subvertical, dips towards NE or SW. It is associated with shallowly plunging mineral stretching lineation.

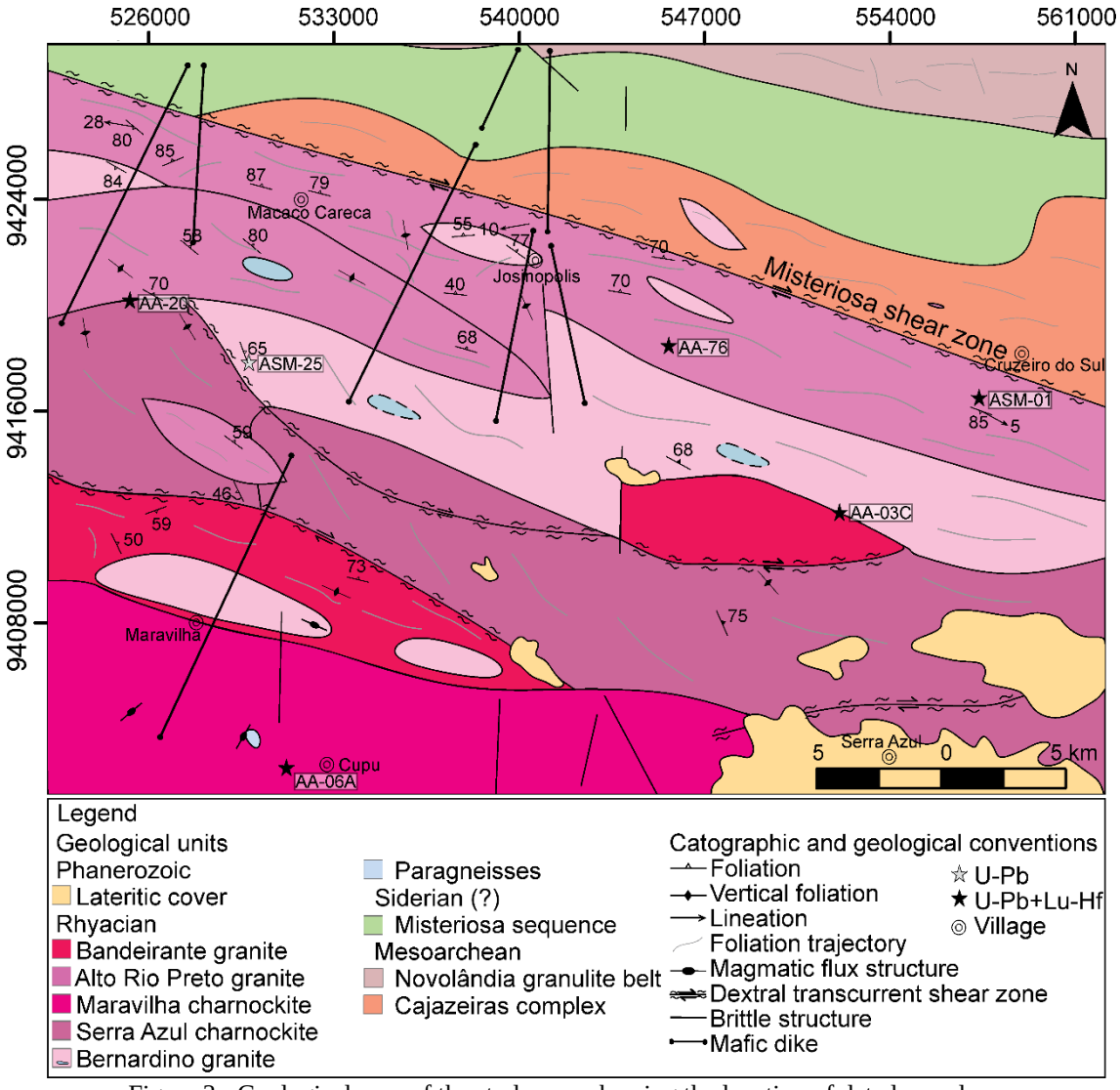


Figure 3 - Geological map of the study area showing the location of dated samples.

2.4.1.3 Maravilha charnockite

The Maravilha charnockite occurs as a batholith in the southwestern portion of the study area, near the Maravilha and Cupu villages (Fig. 3, 4d, e). It comprises orthopyroxene-bearing charnockites, charnoenderbites, and rare fayalite-bearing charnockites (Fig. 5d), with subordinate amphibole-biotite granites (Fig. 5e) and granodiorites, and, more rarely, quartz syenites to quartz monzonites (Fig. 4d; Tab. 2). Locally, it contains enclaves of paragneisses and rare mafic microgranular enclaves.

The batholith consists predominantly of weakly to non-deformed rocks that preserve primary magmatic textures. These are characterized by NW-SE magmatic flux structures marked by the alignment of feldspar phenocrysts (Fig. 4d).

2.4.1.4 Serra Azul charnockite

The Serra Azul charnockite forms an elongated batholith extending from WNW to ESE across the central-southern portion of the mapped area (Fig. 3, Fig. 4f, g). It comprises both orthopyroxene-bearing (Fig. 5f) and orthopyroxene-free tonalites and granodiorites (Fig. 5g), as well as rare biotite granites. Amphibolite enclaves (Fig. 4f, Tab. 2) are a common feature of this unit. Leucogranitic veins commonly crosscut the charnockite. Field observation reveals interactions with Alto Rio Preto granite (Fig. 4b), direct contact with other units were not observed; however, it is inferred that major shear zone mark the contact with the Bandeirante granite.

The deformation that affected the charnockite is heterogeneous, it may sometimes preserve an isotropic character, with local igneous banding (Fig. 4 g), however close to the shear zones it is strongly deformed, typically exhibiting a pervasive NW-SE foliation with moderate to sub-vertical dips towards NE; the foliation is highlighted by the alignment of mafic minerals.

2.4.1.5 Bernardino granite

The main body of the Bernardino granite is exposed in the central portion of the study area, with smaller stocks occurring to the north and southwest (Fig. 3, 4h, i). The main body forms an elongated pluton composed of garnet-bearing and garnet-free peraluminous granites, along with rare granodiorites (Fig. 5h, i). Metasedimentary enclaves are common and represent a distinct feature of this unit (Fig. 4h, Tab. 2). The granite intrudes the Alto Rio Preto granite, Bandeirante granite, and Cajazeiras complex. Regional shear zones locally define contacts with the Serra Azul charnockite.

Away from the shear zones, the Bernardino granite preserves primary magmatic fabrics characterized by the alignment of feldspar phenocrysts (Fig. 4i). In the proximity

to shear zones, foliation follows the regional trend WNW-ESSE to NW-SE, with steep to sub-vertical dips toward SW.



Figure 4 - Field aspects of the studied granitoids and charnockites. (A) interaction between coarse and medium-grained isotropic granites from the Bandeirante granite (B) interactions between the Alto Rio Preto granite and Serra Azul charnockite; (C) mylonitic biotite granodiorite from the Alto Rio Preto granite; (D) alignment of feldspar phenocrysts (magmatic flux structure) of the Maravilha charnockite; (E) bluish K-feldspar crystals from a sienite of the Maravilha charnockite;(F) oval-shaped mafic microgranular enclave in the Serra Azul charnockite; (G) igneous layering int biotite monzogranite of the Serra Azul charnockite; (H) metasedimentary enclave in a garnet-biotite granite of the Bernardino granite; (I) alignment of feldspar phenocrysts (magmatic flux structure) in the Bernardino granite showing a concordant leucogranitic vein.

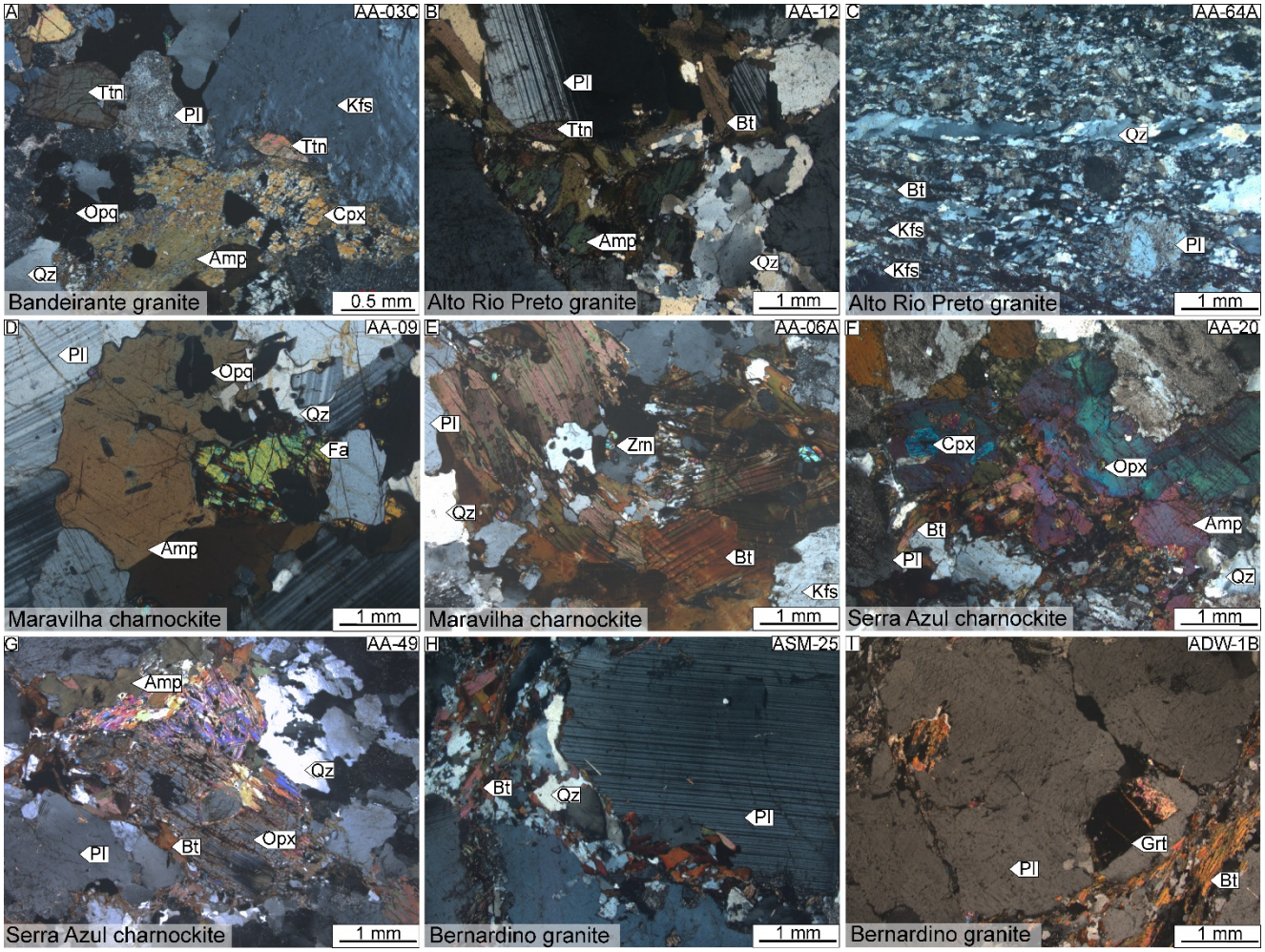


Figure 5 - Main petrographic aspects of the studies granitoids and charnockites. (A) Biotite-amphibole leucosyenogranite of the Bandeirante granite showing remnants of clinopyroxene bordered by amphibole and opaque minerals and idiomorphic titanite crystals; (B) amphibole-biotite monzogranite of the Alto Rio Preto granite with hypidiomorphic granular texture and biotite bordering amphibole; (C) strongly deformed biotite granodiorite of the Alto Rio Preto granite, showing quartz ribbons and weakly pronounced mantle-core texture; (D) fayalite-pyroxene-amphibole syenogranite of the Maravilha charnockite exhibiting fayalite crystals in contact with quartz and with

amphibole corona; (E) amphibole-biotite syenogranite showing coarse-grained hypidiomorphic granular texture, highlighting biotite lamellae with inclusions of early phases ;(F) pyroxene-amphibole-biotite tonalite of the Serra Azul charnockite showing remnants of ortho- and clinopyroxene bordered by amphibole; (G) pyroxene-amphibole-biotite granodiorite of the Serra Azul charnockite showing orthopyroxene crystals surrounded by amphibole; (H) garnet-biotite granodiorite of Bernardino granite with hypidiomorphic granular texture and fine biotite lamellae bordering plagioclase; (I) garnet-biotite granodiorite of Bernardino showing inclusion of hypidiomorphic garnet in a plagioclase phenocryst. Mineral abbreviations follow Whitney and Evans (2010).

Table 2 - Summary of field and petrographic aspects of the granitoids and charnockites of the southern Bacajá Domain

South Bacajá magmatism		Field data	Petrography				
Unit	Age (Ga)	Field and structural aspects	Petrographic classification	Textural aspects	Varietal minerals	Accessory minerals	Secondary minerals
Bandeirante granite	2.12	Composed of two elongated stocks; Magmatic flux structures; Magmatic to tectonic foliation NW-SE oriented with moderate to steep dips Sparse mafic enclaves;	Monzogranites and syenogranites	Medium-grained equigranular texture Locally porphyritic texture with medium-grained matrix Magmatic fabrics Low-temperature deformation microstructures	(1) Amp (2) Amp + Bt	Ttn, Zrn, Ep, Ap, Opq, ± Rt, ± Cpx	Ser, Chl, Ep
Alto Rio Preto granite	2.10-2.07	Composed of two coalescent plutons and a stock; Subparallel magmatic to tectonic foliation with NW-SE to WNW-ESE direction and moderate to high dips; Mineral stretching lineation with WNW-ESE trend and low plunges; Shear bands and complex folds Dextral shear sense Rotated porphyroclasts and S-C foliations	Monzogranite to granodiorite	Medium equigranular texture Heterogranular texture with medium-grained matrix Porphyritic to porphyroclastic texture with medium-grained matrix Magmatic to mylonitic fabrics medium to high-grade deformation microstructures	(1) Amp + Bt (2) Bt	Zrn, Apt, Opq, ± Aln, ± Ep, ± Rt, ± Ttn	Chl, Ser, Ep, Ms, Cb,

		Sparse mafic enclaves; Leucogranitic veins;					
Maravilha charnockite	2.09	Elongated batholith Magmatic flux structures with NW-SE direction; Host mega enclaves of aluminous granulites and sparse mafic enclaves;	Charnockites, charnoenderbites, and granites with subordinate (quartz)-syenites and gabbros	Megaporphyritic texture with medium- to coarse-grained matrix Medium- to very coarse-grained equigranular texture Magmatic fabrics Absent to low-grade temperature deformational microstructures	(1) Fa + Opx + Cpx + Amp (2) Opx + Cpx + Amp + Bt (2) Opx + Bt (3) Amp + Bt	Zrn, Ap, Opq, ± Aln	Act, Chl, Ms, Ser
Serra Azul charnockite	2.06	Occurs as an elongated batholith; Tectonic foliation with NW-SE direction and high dips; Compositional banding, complex folds, and mylonitization features; Mafic enclaves;	Charnockites, charnoenderbites, enderbites, and granites	Medium-grained equigranular texture Porphyroclastic texture Mylonitic fabrics Low to moderate-temperature deformation microstructures	(1) Opx + Amp +Bt (2) Opx ± Cpx + Bt (3) Cpx + Bt (3) Bt	Zrn, Ep, Opq	Chl, Ser, Ep, Opq
Bernardino granite	2.05	Occur as an elongated pluton and small stocks intruded in other units; Magmatic to tectonic foliation with NW-SE direction and moderate to high dips; Metasedimentary enclaves;	Monzogranites to granodiorites	Medium- to coarse-grained equigranular texture Porphyritic texture with medium-grained matrix Magmatic and mylonitic fabrics low-grade temperature deformation microstructures	(1) Bt	Grt, Zrn, Mnz, Ap, Opq, ± Ms	Chl, Ep, Ms, Cb ± Rt

*when epidote (ep) is shown in the accessory mineral column, it implies that it is of magmatic origin

2.4.2 Geochemistry

This section presents the results of forty-three whole-rock geochemistry (Tab. 3 and 4, Table S1) of the studied magmatic rocks. These data are used to highlight the main geochemical features of the granitoids and charnockites in the southern Bacajá Domain, distinguish their magmatic series, and illustrate the behavior of trace elements, including rare earth elements (REE).

2.4.2.1 Major and trace elements

2.4.2.1.1 Bandeirante granite

The Bandeirante granite displays moderate to high silica contents (66.7-76.8 wt%), variable K_2O/Na_2O ratios (0.4-1.06), low Mg# (22-36), and metaluminous to slightly peraluminous character (0.91 < A/CNK <1.06). The trace element composition reveals low to high LILE (Ba+Rb+Sr+Cs = 326-3221 ppm), moderate to high HFSE contents (Zr+Hf+Nb+Ta = 115-370 ppm), and low to medium Sr/Y ratios (2-78). On chondrite-normalized REE and multielement diagrams (Fig. 6a, b), the rocks shows slightly variable negative Eu anomalies (Eu/Eu* = 0.15–0.75,), except for one outlier (AA-05, Eu/Eu* = 4.04), which shows impoverishment in all REE except europium, likely due to post-magmatic processes. the rocks exhibit moderate LREE/HREE fractionation [$(La/Yb)_N$ = 5-39)], and Nb, P, and Ti negative anomalies.

2.4.2.1.2 Alto Rio Preto granite

The Alto Rio Preto granite shows moderate to high silica contents (67-76.1 wt%), variable K_2O/Na_2O ratios (0.6-1.5), low Mg# (23-41), and metaluminous to slightly peraluminous character (0.96 < A/CNK <1.07). The rocks display high LILE (1093-2354 ppm), moderate HFSE (118-271 ppm), and variable Sr/Y ratios (7-136). In chondrite-normalized REE and multielement diagrams (Fig. 6c, d), the rocks show slightly positive to variable negative Eu anomalies (Eu/Eu* = 0.38–1.2), with moderate LREE/HREE fractionation [$(La/Yb)_N$ = 19–64] and one outlier (127). Negative Ba, Nb, P, and Ti negative anomalies are also observed.

Table 3 - Representative whole-rock geochemical analyses of the Rhyacian granites and charnockites from the southern Bacajá Domain.

Unit	Bandeirante granite			Alto Rio Preto granite			Maravilha charnockite			Serra Azul charnockite			Bernardino granite		
Sample	AA-03A	AA03C	AA-123	AA-76	AA-21	AA-46	AA-102	AA-06A	AA-09	AA-20	AA-49	AA-128	AA-146	AA-11	AA-53
Variety	AMzG	LSG	ABSG	ABGrd	ABMzG	BGrd	BAQMzn	ABSG	FPASG	PABTn	PABGrd	BMzG	BrG	BrG	BrG
SiO_2	66.7	72.5	76.2	67	73.1	72.2	65.7	66.8	70	60.4	70.3	70.5	67.8	69.1	71.4
TiO_2	0.42	0.2	0.16	0.66	0.35	0.26	0.52	0.61	0.51	0.82	0.56	0.43	0.68	0.89	0.33
$Al2O_3$	14.80	15.1	12.95	14.65	13.85	14.55	17.55	14.15	14.7	16	14	14.55	15.7	14.15	13.95
FeOt	4.47	2.00	1.78	4.71	2.47	2.07	3.65	3.62	3.95	6.51	4.34	3.64	4.64	4.71	3.18
MnO	0.1	0.04	0.04	0.07	0.06	0.03	0.05	0.06	0.06	0.11	0.05	0.06	0.06	0.06	0.06
MgO	1.41	0.31	0.32	1.78	0.87	0.49	0.5	1.02	0.43	2.76	1.65	1.25	1.52	1.03	1.08
CaO	2.93	2.14	1.13	3.35	2.21	2.18	3.54	2.25	2.3	5	2.36	2.17	2.31	2.2	1.87
Na_2O	3.71	3.54	3.36	3.21	2.96	4.07	3.47	2.8	3.18	3.84	3.16	3.25	2.94	2.65	3.13
K_2O	4.41	5.7	4.45	3.38	4.44	3.12	4.9	5.05	5.73	2.01	3.24	4.24	3.58	4.53	3.05
P_2O_5	0.17	0.12	0.03	0.17	0.09	0.06	0.14	0.19	0.15	0.25	0.03	0.15	0.08	0.33	0.06
LOI	0.84	0.98	0.61	0.94	0.95	0.67	1.12	0.95	0.14	1.65	0.96	0.81	0.98	1.02	1.45
Total	100.71	>102.00	101.28	100.6	101.79	100.1	101.99	98.1	101.85	100.14	101.35	101.89	100.95	101.35	100.06
Ba	1560	2530	401	996	1175	1100	3530	1400	1935	252	1010	3430	1000	1120	1005
Rb	96.2	116	249	128	135	121	94.5	202	149.5	108	73.1	79.1	136	194.5	89.7
Sr	456	574	123	321	291	449	462	253	236	263	323	515	238	193.5	262
Zr	352	130	106	250	150	175	548	300	440	235	246	415	197	385	195
Nb	7.63	3.25	5.58	11.95	5.49	8.48	15.95	16.4	19.4	9.35	13.2	4.68	11.9	18.95	6.08
Y	60.9	29.7	72.1	30.8	12	12.4	18.4	24.4	30.8	22.6	11.6	7.8	28.8	36.7	16.1
Hf	9.05	3.61	3.39	6.31	4.03	4.75	12.45	7.73	10.65	6	5.76	9.52	5.7	10.1	5.29
Ta	1	0.6	0.3	0.8	0.4	1.2	0.9	1.4	1.3	0.8	1	0.3	1.1	1.4	0.7
Ga	18	16.2	18	19.6	16.2	19.6	22.7	17.4	18.8	23.4	20.2	16	20.9	16.2	14.8
Cs	1.1	1.12	0.62	1.76	0.89	1.45	0.33	2.8	0.3	2.15	0.89	0.46	2.43	3.53	0.95
Sn	11.6	5	0.7	2	1.3	1.5	<0.5	2	0.7	3.7	1.4	1.9	1.6	3.5	1.3
Th	17.05	3.4	8.64	22.3	5.24	25.6	2.09	13.7	10.8	1.84	4.36	14.25	30.9	23	9.48
U	4.18	1.21	2.99	1.41	1.19	3.25	0.42	3.12	0.86	1.27	1.26	0.38	3.35	2.41	1.88

V	63	29	16	75	32	14	29	50	21	131	68	52	115	61	50
Cr	59	8	50	26	68	12	30	65	11	56	43	49	80	32	75
La	82.7	19.7	33.8	82.7	30.4	48.7	35.9	63.7	87.9	22.2	28.6	73.9	71.7	78.6	25.5
Ce	181.5	46	54.8	166	51.9	88.7	71.2	128.5	175	47.1	56.2	127	137	164	47.4
Pr	22.6	6.08	7.63	18.2	5.36	9.07	8.65	14.65	19.25	6.09	6.32	12.45	14.75	18.5	4.81
Nd	92	26.5	30.7	65.1	18.6	30.2	33.5	53.3	70	26.4	23.8	40.1	46.8	70.3	16.4
Sm	17.2	5.53	7.01	11.7	3.01	4.57	6.95	9.15	11.45	6.5	4.72	5.73	8.78	13.2	2.83
Eu	2.57	1.35	0.84	1.3	1.05	0.9	2.58	1.52	2.22	1.13	1.34	1.29	1.52	1.7	1.05
Gd	16.55	5.42	10	9.26	2.46	3.49	5.27	7.47	8.91	6.45	3.75	2.65	6.23	10.25	2.63
Tb	2.03	0.69	1.44	1.2	0.3	0.5	0.65	0.89	1.18	0.87	0.42	0.33	0.9	1.37	0.39
Dy	12.3	3.62	9.59	6.91	1.62	2.34	3.87	5.06	6.14	4.91	2.26	1.34	5.21	7.4	2.58
Ho	2.22	0.79	2.18	1.21	0.32	0.5	0.72	0.95	1.2	0.87	0.43	0.26	1.1	1.29	0.55
Er	5.76	2.04	6.23	2.97	0.71	1.02	1.92	2.29	3.3	2.18	1.12	0.94	3.3	3.86	1.77
Tm	0.82	0.27	0.8	0.37	0.12	0.14	0.23	0.3	0.44	0.33	0.13	0.1	0.4	0.51	0.23
Yb	4.91	1.69	4.73	2.48	0.62	0.73	1.71	1.88	2.88	1.92	0.96	0.54	2.66	3.33	1.52
Lu	0.6	0.2	0.66	0.31	0.09	0.12	0.29	0.35	0.4	0.23	0.18	0.08	0.38	0.49	0.23
ΣREE	443.76	119.9	170.4	369.7	116.6	191.0	173.4	290.0	390.3	127.2	130.2	266.7	300.7	374.8	107.9
Σ LREE	398.57	105.16	134.78	345	110.32	182.14	158.78	270.82	365.82	109.42	120.98	260.47	280.55	346.3	97.99
Ba+Sr	2016	3104	524	1317	1466	1549	3992	1653	2171	515	1333	3945	1238	1313.5	1267
Mg#	36.0	22	24	40	39	30	20	33	16	43	40	38	37	28	38
$(La/Yb)_N$	11.36	7.9	4.8	22.5	33.1	45.0	14.2	22.8	20.6	7.8	20.1	92.3	18.2	15.9	11.3
Eu/Eu*	0.47	0.75	0.31	0.38	1.18	0.69	1.30	0.56	0.67	0.53	0.97	1.01	0.63	0.45	1.18

2.4.2.1.3 Maravilha charnockite

The Maravilha charnockite shows moderate to high silica contents (62.1-76.9 wt%), high K_2O/Na_2O ratios (0.9-1.9), and low Mg# (14-34). It is metaluminous to slightly peraluminous (0.94 < A/CNK <1.03), with moderate to high LILE (940-4087 ppm), high HFSE (162-577 ppm), and low Sr/Y ratios (7-37). In chondrite-normalized REE and multielement diagrams (Fig. 6e, f), the rocks display variable negative Eu anomalies (Eu/Eu* = 0.23–0.81), with two anomalous values (1.3 and 2.09). LREE/HREE fractionation is low to moderate [$(La/Yb)_N$ = 14-38], with an isolated value of 74. Pronounced negative Nb, Ta, P, and Ti are also present.

2.4.2.1.4 Serra Azul charnockite

The Serra Azul charnockite shows a wide silica range range (58.5-72.4 wt%), low to moderate K_2O/Na_2O ratios (0.4-1.3), and moderate to high Mg# (32-52). The rocks are metaluminous to slightly peraluminous (0.86 < A/CNK <1.08). (Fig. 6f). Trace element concentrations show moderate to high LILE (625-4025 ppm), variable HFSE (61-430 ppm), and variable Sr/Y ratios (12-112). In chondrite-normalized REE and multielement diagrams (Fig. 6g, h), most samples show absence or discrete Eu negative anomalies (Eu/Eu* = 0.83-1.01), with a few showing distinct negative (0.53) or apparent positive anomalies (1.51 and 2.54*). The highest outlier (AA-132, Eu/Eu* = 2.54) show REE depletion except for europium, which likely results in an artificially high Eu/Eu* ration, probably due to post-magmatic processes. LREE/HREE fractionation is highly variable [$(La/Yb)_N$ = 8–92)], and slight negative Nb, P, and Ti anomalies are present.

2.4.2.1.5 Bernardino granite

The Bernardino granite shows moderate to high silica contents (64-71.4 wt%), variable K_2O/Na_2O ratios (0.6-1.7), and low to moderate Mg# (28-44). The granite is strongly peraluminous (Fig. 6e, ASI > 1.1). Trace element composition show relatively homogeneous LILE (1148-2239 ppm), moderate to high HFSE (179-415 ppm), and low Sr/Y ratios (5-34). In chondrite-normalized REE and multielement diagrams (Fig. 5i, j), the rocks show slightly positive (Eu/Eu* = 1.11–1.18) to moderate negative Eu anomalies (Eu/Eu* = 0.45–0.70), low LREE/HREE fractionation [$(La/Yb)_N$ = 11-18, outlier 98)]. Pronounced negative anomalies in Nb, P, and Ti are consistently observed.

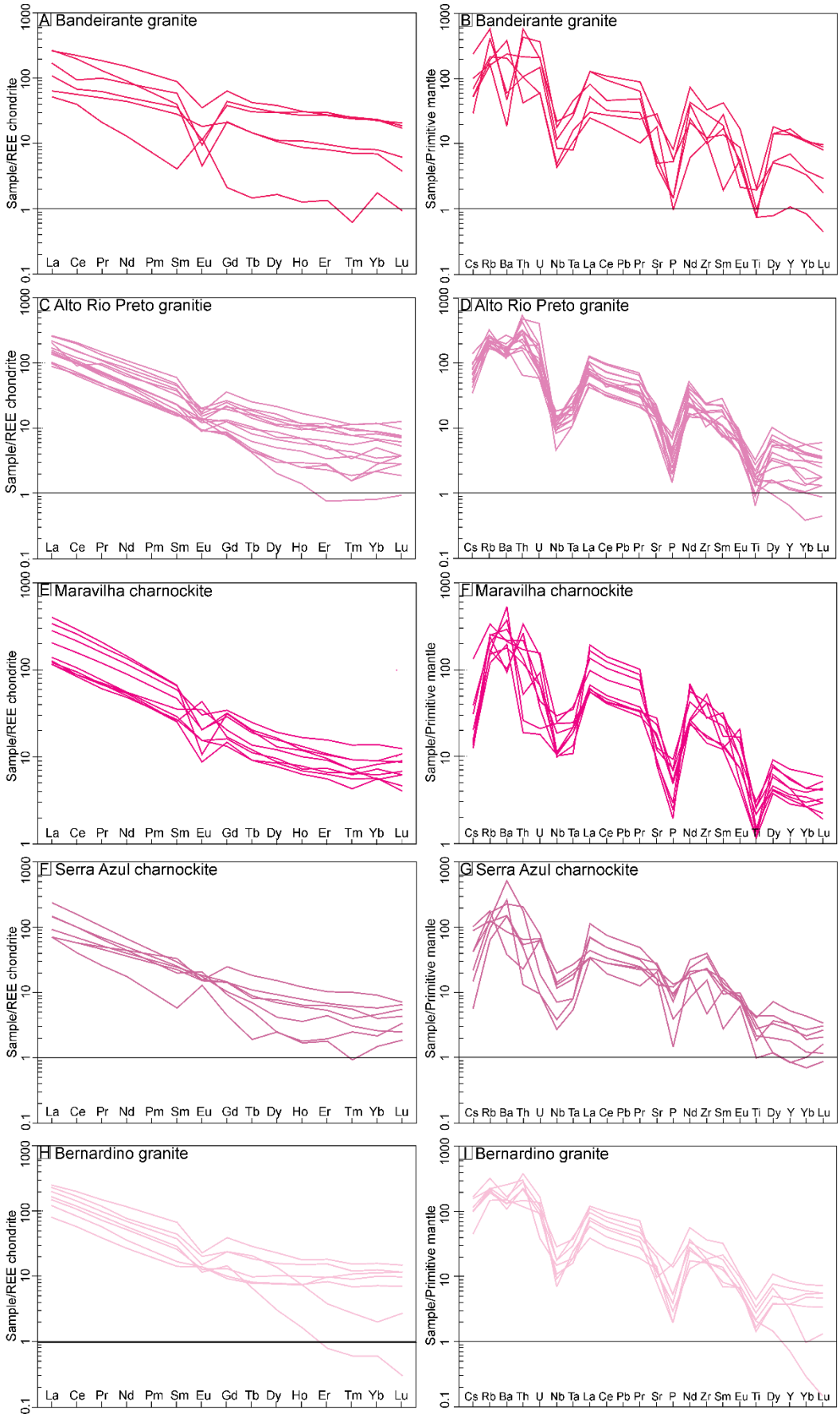


Figure 6 - Chondrite normalized REE patterns (Boynton, 1984) and normalized multielement patterns (McDonough and Sun, 1995).

Table 4 - Summary of geochemical data of the Rhyacian granitoids from the southern Bacajá Domain

	Bandeirante granite	Alto Rio Preto granite	Maravilha charnockite	Serra Azul charnockite	Bernardino granite
Geochemical signature	Calc-alkaline to alkali-calcic Ferroan	Calc-alkaline to calcic Magnesian	Alkali-calcic Ferroan	Calc-alkaline to calcic Magnesian	Calc-alkaline Magnesian (strongly peraluminous)
Number of Samples	6	14	9	7	7
SiO_2 (Median/Avg/2SD)	66.7-76.8 (73.7/72.3/9.09)	67-76.1 (72.4/71.9/5.78)	62.1-76.9 (69.9/69.8/9.41)	58.5-72.4 (66.3/66.4/10.53)	64.1-71.4 (70.3/69.2/5.09)
A/CNK (Median/Avg/2SD)	0.91-1.06 (11.04/1.01/0.13)	0.96-1.06 (1.02/1.02/0.06)	0.94-1.03 (1.00/0.99/0.06)	0.86-1.08 (0.97/0.98/0.16)	1.07-1.34 (1.11/1.15/0.73)
ASI (Median/Avg/2SD)	0.93-1.07 (1.05/1.02/0.12)	0.98-1.07 (1.03/1.03/0.05)	0.95-1.04 (1.02/1.00/0.06)	0.88-1.08 (0.99/1.00/0.15)	1.09-1.35 (1.12/1.17/0.74)
Fe# (median/Avg/2SD)	0.76-0.87 (0.85/0.82/0.10)	0.72-0.86 (0.76/0.78/0.09)	0.77-0.91 (0.81/0.84/0.12)	0.62-0.79 (0.74/.073/0.11)	0.69-0.82 (0.75/0.75/0.44)
K_2O/Na_2O (Median/Avg/2SD)	0.4-1.06 (1.25/1.16/0.84)	0.6-1.5 (1.12/1.09/0.54)	0.9-1.9 (1.41/1.42/0.76)	0.4-1.3 (0.66/0.75/0.63)	0.6-1.7 (1.02/1.08/0.75)
Mg* (Median/Avg/2SD)	22-36 (25-27/14)	23-40 (36/34/12)	14-34 (30/25/18)	32-52 (38/40/14)	28-44 (38/37/18)
Sr/Y (Median/Avg/2SD)	2-78 (6/19/60)	7-68 (136*) (19/27/37)	7-37 (15/18/21)	12-112 (40/54/72)	5-34 (130*) (12/15/47)
$(La/Yb)_N$ (Median/Avg/2SD)	5-39 (9.6/16.6/27.9)	19-64 (127*) (27.2/33.2/27.2)	14-38 (74*) (20.6/28/36.6)	8-92 (36.1/40.7/62.2)	11-18 (98*/268*) (14.6/28.3/68.0)
Eu/Eu* (Median/Avg/2SD)	0.15-0.75 4.04* (0.39/0.98/3.02)	0.38-0.83 (1.18*) (0.69/0.65/0.33)	0.23-0.81 (1.3*-2.09*) (0.67/0.81/1.12)	0.53-1.51 2.54* (097/1.18/1.34)	0.45-1.18 (0.63/0.73/0.73)
∑REE (Median/Avg/2SD)	62-444 (205.8/228.9/283.9)	117-370 (185.9/210.9/159.9)	157-506 (189.4/277.4/275.7)	74-267 (130.2/151.8/124.3)	108-375 (206.4/227.7/172.6)
Σ LILE (Median/Avg/2SD)	326-3221 (1312/1506/2179)	1093-2354 (1483/1510/625)	940-4087 (1760/2043/2032)	625-4025 (1571/1836/2194)	1148-1512 (2239*) (1339/1334/685)
ΣHFSE (Median/Avg/2SD)	115-370 (139/201/226)	118-271 (193/194/92)	162-577 (310/332/287)	61-430 (251/258/247)	179-415 (207/238/156)

outliers, Mg# ($MgO_{mol}/(FeO+MgO)_{mol}$, LILE (=Ba+Rb+Sr+Cs), HFSE (=Zr+Hf+Nb+Ta), Eu/Eu = Eu/ $\sqrt{[(Sm_N)*(Gd)_N]}$, chondrite-normalized values from Boyton (1984). The 2SD refers to the average value.

2.4.2.2 Geochemical classification and magmatic series

The P-Q diagram (Debon and Le Fort, 1983) shows that the studied rocks exhibit limited compositional variation, plotting predominantly in the monzogranite and granodiorite fields, with subordinate occurrences of tonalites, syenogranites, quartz monzonites, and quartz syenites (Fig 6a). Samples from the Bandeirante granite are mostly concentrated in the monzogranite field. Samples from the Alto Rio Preto granite

cluster within the monzogranite and granodiorite fields, some approaching the syenogranite field. The Maravilha charnockite exhibits a wider compositional range, with samples distributed mainly in the monzogranite and syenogranite fields, and subordinately in the granodiorite, quartz syenite, and quartz monzonite fields. The Serra Azul charnockite primarily plots within the granodiorite field, with subordinate samples in the tonalite and monzogranite fields. The Bernardino granite displays predominantly granodioritic to monzogranitic composition, with a single syenogranitic sample.

All units follow a calc-alkaline trend in AFM diagram (Fig 6b, Irvine and Baragar, 1971) and in K-Na-Ca ternary diagrams (Fig.6c, Barker and Arth, 1976; Luais and Hawkesworth, 1994). In the modified alkali-lime index (MALI = $Na_2O + K_2O$-CaO) vs. SiO_2 diagram (Fig. 7d; fields of Frost et al., 2001), the samples range from calcic to calc-alkaline (e.g., Alto Rio Preto granite and Serra Azul charnockite) or are dominantly calc-alkaline (e.g., Bandeirante and Bernardino granites), or even alkali-calcic (e.g., Maravilha charnockite).

In the Fe* vs. SiO_2 diagram (Fig. 7e, Frost et al., 2001), the Alto Rio Preto granite plots essentially in the magnesian field (moderate-Mg), with some samples near the magnesian-ferroan boundary. In contrast, the Bandeirante granite and Maravilha charnockite fall predominantly within the ferroan field, with a few exceptions plotting in the magnesian field. The Serra Azul charnockite and Bernardino granite are primarily magnesian (moderate-Mg) with few exceptions in the ferroan (Bernardino granite) and high-Mg (Serra Azul charnockite) fields.

In the A/NK vs. ASI (Fig. 7g, Frost et al., 2001), most samples plot along the transition from metaluminous to slightly peraluminous compositions. The Bernardino granite, however, stands out due to its strongly peraluminous character (Fig. 7f).

In the Y vs. Nb (Fig. 7a; fields of Pearce et al., 1984), most of the samples fall within the volcanic arc granite (VAG) + syn-collisional granite (syn-COLG) fields Two sample from the Bandeirante granite in the ocean-ridge granite (ORG) field, while three others (from the same granite), along with samples from the the Maravilha charnockite and Bernardino granite, fall in the within-plate granite (WPG) field. In the Y+Nb vs. Rb diagram (Fig. 8b; fields of Pearce et al., 1984), all units, except for the Bandeirante granite, plot in the volcanic arc field or along its boundary with the syn-collisional field (e.g., Alto Rio Preto granite). In The multi-dimensional diagrams based on ln-transformed ratios of immobile trace elements from Verma et al. (2013), most samples plot in the collisional field (Fig. 8c), or along the transition from the collisional field to continental

arc field (Fig. 8d). These geochemical discrimination diagrams suggest predominantly collision related magmatic setting for the studied units.

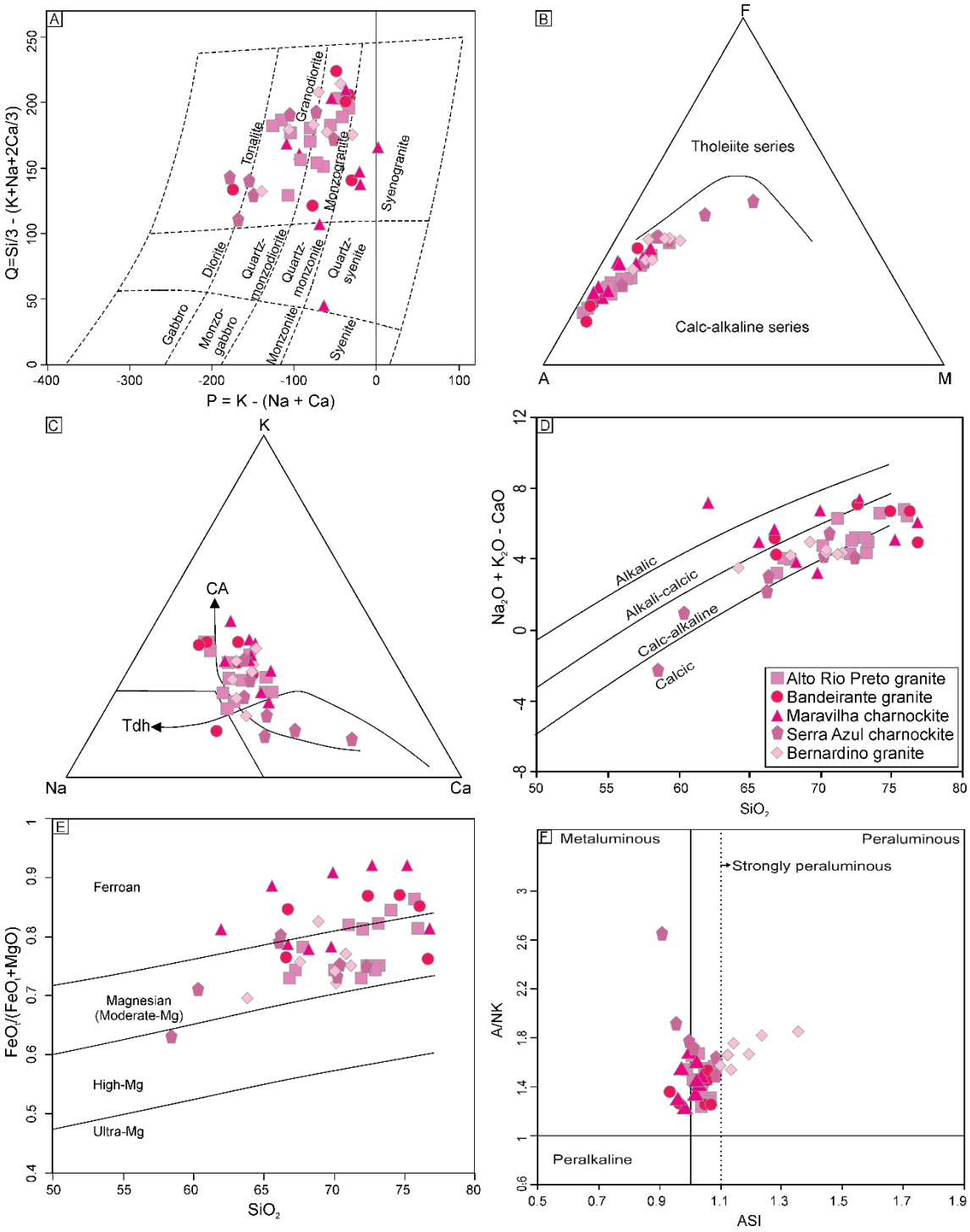


Figure 7 - Geochemical classification and magmatic series. (A) P-Q diagram (Debon and Fort, 1983); (B) AFM diagram (Irvine and Baragar, 1971); (C) Na-K-Ca diagram (trondhjemite field and trends Thd and CA = calc-alkaline of Barker and Arth, 1976; Luais and Hawkesworth, 1994); (D) SiO_2 vs Na_2O+K_2O – CaO diagram (Frost et al., 2001); (E) SiO_2 vs FeOt/(FeOt+MgO) diagram (Frost et al. 2001; Terentiev and Santosh, 2018); (F) ASI vs. A/NK (Frost et al., 2001).

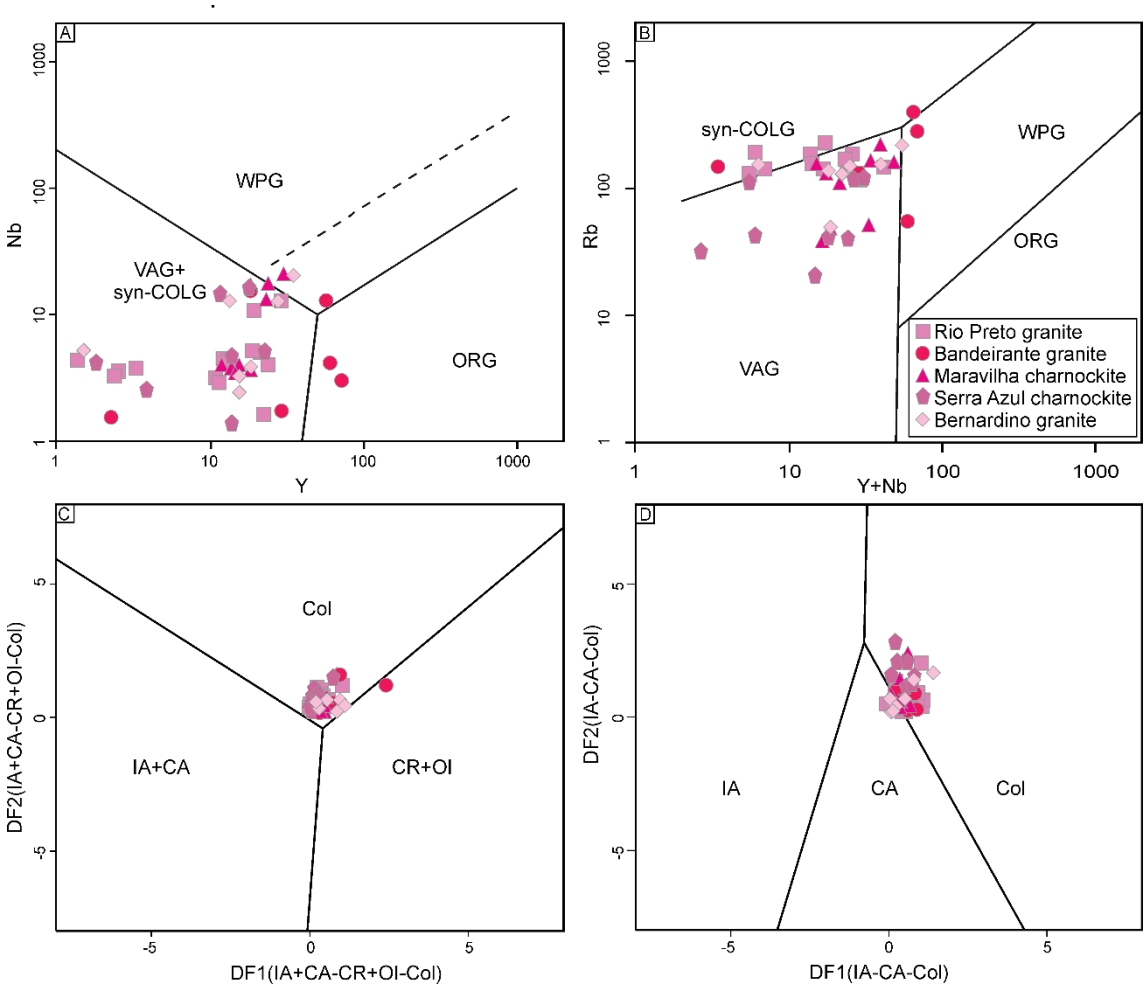


Figure 8 - Tectonic discrimination diagrams. (A) Nb vs. Y diagram, (B) Nb/Zr vs. Zr diagram. Fields after Pearce et al., (1984); (C) DF1 vs.; DF2 ; (D) DF1 vs. DF2 (Verma et al., 2013).

2.4.3 U-Pb geochronology and Hf isotopes on zircon

We selected representative samples of the Bandeirante granite (AA-03C), Alto Rio Preto granite (ASM-01 and AA-76), Maravilha (AA-06A) and Serra Azul (AA-20) charnockites and Bernardino granite (ASM-25), totaling six samples. One sample from each unit were also analyzed for Hf isotopes, except the one from the peraluminous Bernardino granite, which yielded variable and complex U-Pb ages. The isotopic data are available in Supplementary material 2 and 3. The available geochronological data of the granitoids from the Bacajá Domain, including the new results presented in this study, are summarized in Fig. 2 and Tab. 1.

2.4.3.1 Bandeirante granite

A leucosyenogranite sample (AA-03C) from the Bandeirante granite was dated via SHRIMP. The zircon grains are pale brown to pinkish, euhedral to subhedral, and long prismatic with lengths ranging from 220 to 450 μm. Cathodoluminescence (CL) images reveal medium to low luminescence, typically with faint to regular oscillatory

zoning (Fig. 9). Twelve zircon grains yielded an upper intercept age of 2120±24 Ma (MSWD = 2.9). Excluding discordant analysis, four grains provided a concordia age of 2116±11 Ma (Fig. 10a, MSWD = 0.108). Th/U ratios range from 0.16 to 0.58 (Tab. S2).

Zircon Hf isotopes were obtained from ten spots (Fig. 11e), showing subchondritic εHf(t) values ranging from -6.5 to -4.6, with Mesoarchean Hf-T_{DM}^{c} ages ranging from 3.0 to 3.1 Ga.

2.4.3.2 Alto Rio Preto granite

One sample was dated via SHRIMP: an amphibole-biotite granodiorite (AA-76). The zircon grains are pale to dark brown, euhedral, short to long prismatic, with lengths between 100 to 330 μm. CL images typically show low luminescence associated with regular oscillatory zoning. Some zircon grains display high-luminescence cores and low luminescence rims. Minor opaque and apatite inclusions are common (Fig. 9).

For sample AA-76, twelve spot analyses revealed that most zircons are strongly discordant. Six grains define an upper intercept of 2098±11 Ma (Fig. 10b, MSWD = 1.9) and a lower intercept of 312±61 Ma (MSWD = 1.9). Th/U ratios varies from 0.21 to 1.02 (Tab.S3).

Another sample was dated via LA-ICP-MS: a biotite monzogranite (ASM-01). Zircon grains are pale brown, are euhedral, with prismatic terminations, and locally rounded, with lengths between 135 and 350 μm and elongation ratios between 2:1 and 4:1. BSE images show typical oscillatory zoning and local resorption (Fig. 9). Fifty-three analyses were performed in 32 zircons. Most analyses are discordant and define an upper intercept age of 2099±18 Ma (Fig. 11a, MSWD = 3.9), with Th/U ratios ranging from 0.20-0.39 (Tab. S6). Excluding highly discordant data, three zircons yielded a concordia age of 2076±12 Ma (Fig. 11a, MSWD = 2.0). One concordant grain yielded a $^{207}Pb/^{206}Pb$ apparent age 2295±28 Ma, interpreted as inherited.

Zircon Hf isotopes (9 spots, Fig. 11e), show subchondritic εHf(t) values from -10.2 to -6.3, with Meso- to Paleoarchean crustal model ages (Hf-T_{DM}^{c}) ranging from 3.2 to 3.3 Ga.

2.4.3.3 Maravilha charnockite

One sample of amphibole-biotite syenogranite (AA-06A) was dated via SHRIMP. Zircon grains are colorless to pale brown, euhedral, and long prismatic, ranging from 140 to 540 μm, with elongation rations between 2:1 to 4:1. CL images reveal regular oscillatory zoning with medium to high luminescence, and rare convoluting zoning (Fig. 9).

Twelve spots on twelve zircon grains provided a discordia with an upper intercept at 2082±20 Ma (Fig. 10c, MSWD = 0.47). The ten most concordant zircons (±3%) yield a concordia age of 2089±12 Ma (Fig. 10d, MSWD = 0.72). Th/U ratios range from 0.18 to 0.38 (Tab. S4).

Zircon Hf isotopes (10 spots, Fig. 11e) yield subchondritic εHf(t) values from -9.2 to -8.2, with early Mesoarchean Hf-T_{DM}^{c} model ages around 3.2 Ga.

2.4.3.4 Serra Azul charnockite

One sample of clinopyroxene-amphibole-biotite tonalite (AA-20) was dated via SHRIMP. The zircons are colorless to dark brown, short to long prismatic with elongation ratios of 2:1 to 3:1, and lengths ranging from 150 to 490 μm. CL images show oscillatory-zoned cores with medium to low luminesce, surrounded by homogeneous rims with similar responses (Fig. 9).

Fifteen spot analyses on thirteen zircons grains dated both cores and rims , with no significant age difference. Twelve analyses defined a discordia with an upper intercept of 2062±8.8 Ma (Fig. 10d, MSWD = 1.02). Th/U ratios range from 0.23 to 0.75 (Tab. S6).

Zircon Hf isotopes (10 spots, Fig. 11e) yield subchondritic $\varepsilon Hf_{(t)}$ values from -8.8 to -5.8 and early Mesoarchean Hf-T_{DM}^{c} models ages between 3.0 and 3.2 Ga.

2.4.3.5 Bernardino granite

One garnet-biotite granodiorite (ASM-25) was dated via LA-ICP-MS. The zircons are pale to dark brown, subhedral to anhedral, and high variability in shape and size. Two textural types were identified in BSE-imagens: (i) cores with blurred oscillatory zoning with homogeneous rims and (ii) structureless crystals.

Eighty analyses were performed on 52 zircons. Most results are highly discordant. Type-I cores yielded $^{207}Pb/^{206}Pb$ apparent ages ranging from 2726±16 Ma to 2252±19 Ma (within ±10% of concordance). Type-I rims and type-II crystals provided a series of concordant crystals from 2175±23 Ma to 2003±12 Ma, with Th/U ratios of 0.07-2.46 (Tab. S7). Due to the large spread along the concordia, a precise crystallization age could not be defined (Fig. 10b).

Given the highly complex zircon behavior, monazite grains were also selected for U-Pb dating, as they represent the best alternative to date Precambrian peraluminous granites (Piechocka et al., 2017) and S-type granites in general. The monazite are yellowish to greenish, subhedral, and commonly rounded. Thirty analyses performed on thirty grains yielded a discordia with an upper intercept age of 2052±5 Ma (Fig. 10c,

MSWD =1.3). Th/U ratios range between 30.8 and 194.8, consistent with the field of igneous monazite (Piechocka et al., 2017, Fig. 10d).

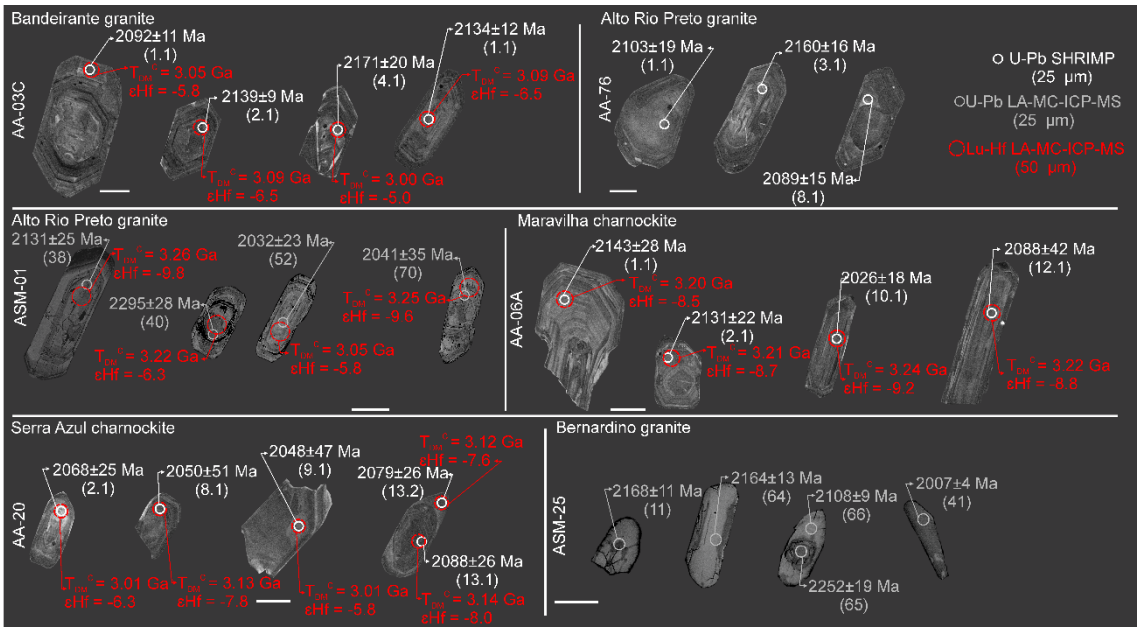


Figure 9 - Representative CL (AA-03C, AA-76, AA-06A, AA-20) and BSE (ASM-01 and ASM-25) images from the analyzed zircons.

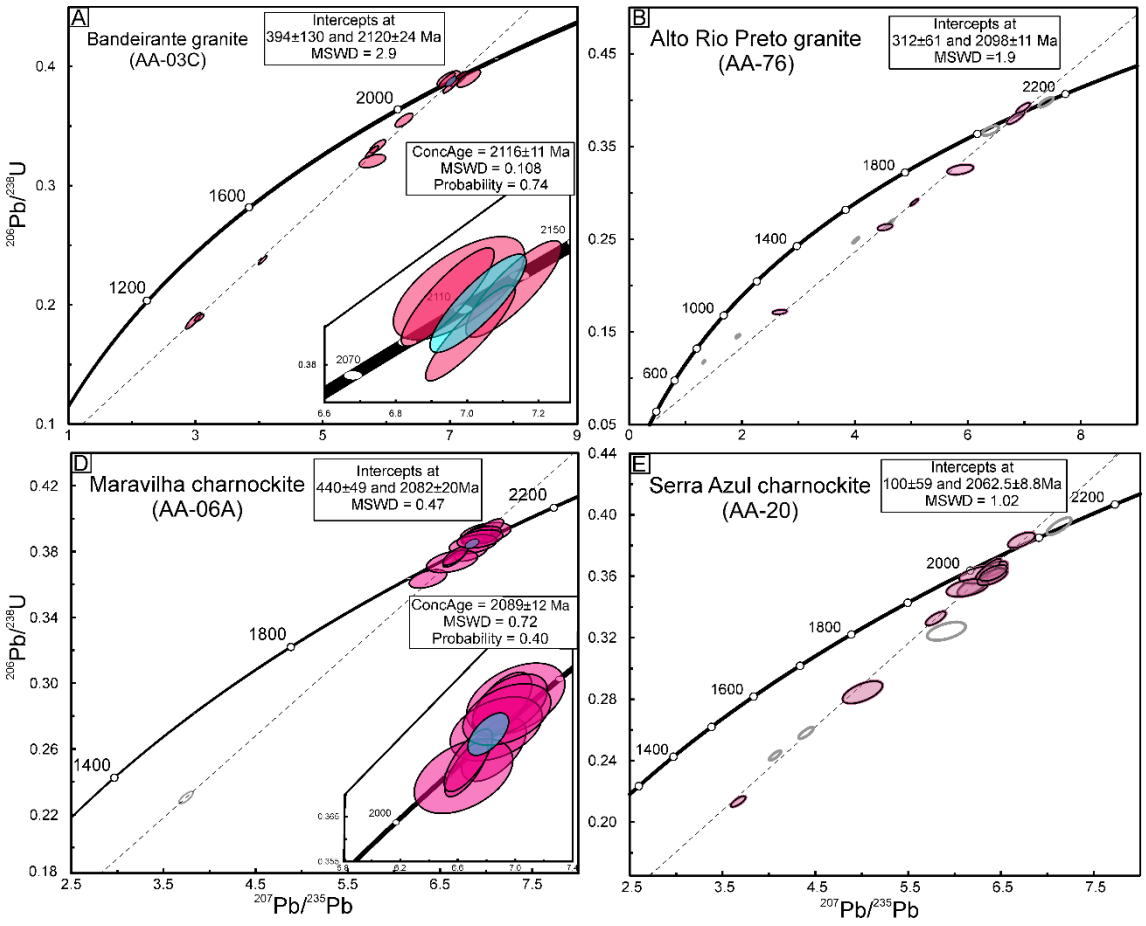


Figure 10 - SHRIMP U-Pb concordia plots for the studied granitoids and charnockites. (A) Bandeirante granite (AA-03C); (B) Alto Rio Preto granite (AA-76); (C) Maravilha charnockite (AA-06A); (D) Serra Azul charnockite (AA-20). Ellipses are colored according to the unit color in the geological map from

Figure 2; light gray ellipses were discarded for age calculations, and light blue ellipses represent inherited grains.

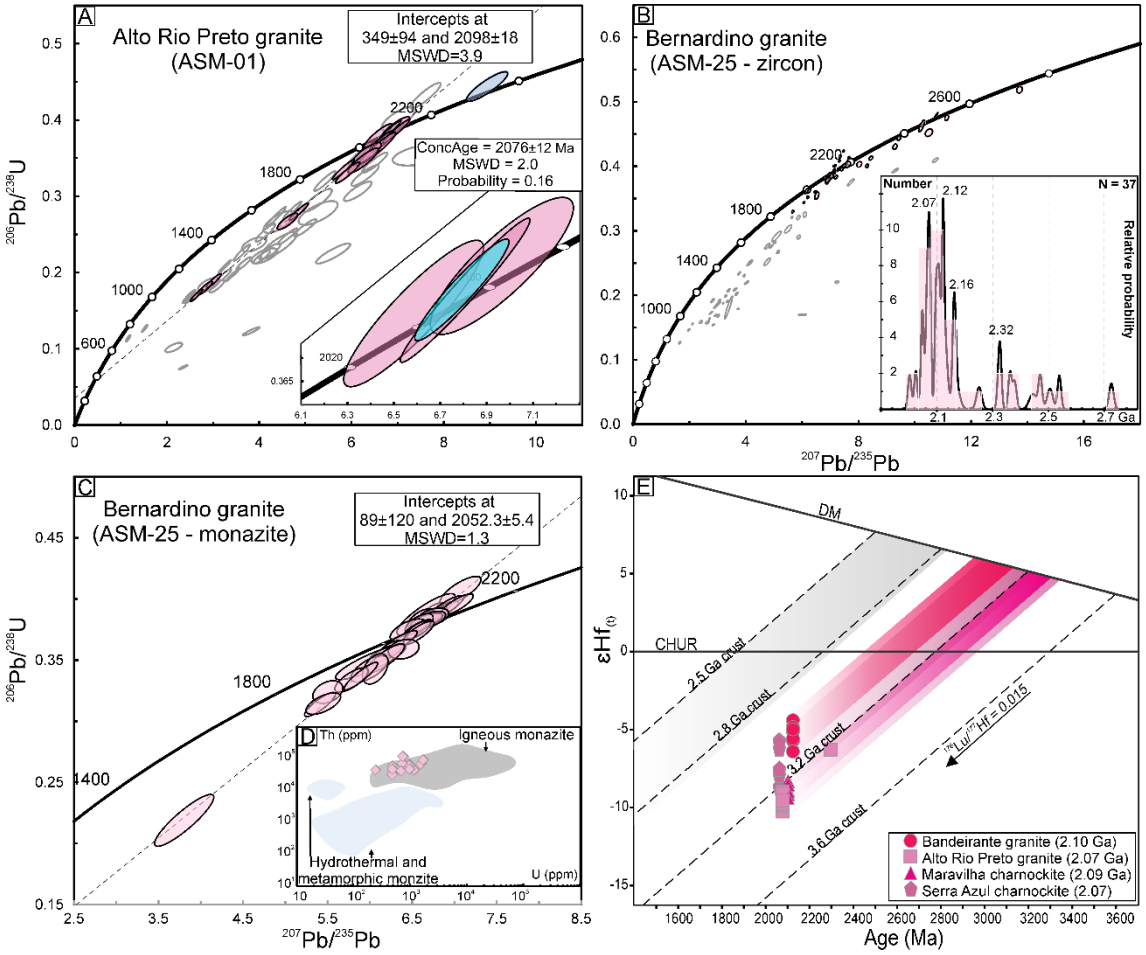


Figure 11 - LA-MC-ICP-MS U-Pb concordia plots for the studied granitoids. (A) Alto Rio Preto granite (ASM-01); (B) Bernardino granite (ASM-25 - zircon) in the histogram only zircon with ±10% were plotted; (C) Bernardino granite (ASM-25 - monazite); (D) Th vs. U diagram to distinguish magmatic vs. hydrothermal vs. metamorphic monazite (Piechoka et al., 2017). (E) Plot of time (Ma) vs. εHf for the Paleoproterozoic granitoids and charnockites from the study area, the gray shaded area represents the Hf data from northern Bacajá Domain (Magalhães et al., 2023), and the blue shaded area represents the Hf data from Archean and Orosirian Carajás Province (Marangoanha et al., 2019; Ribeiro-Silva et al., 2023; Teixeira et al., 2019). Ellipses are colored according to the unit color in the geological map from Figure 2; light gray ellipses were discarded for age calculations, and light blue ellipses represent inherited grains.

2.4.4 Nd isotopes

Twenty-six whole-rock Sm-Nd isotopic compositions were determined for representative samples from all the studied units (Table 5, Fig. 12). The analyzed samples reveal a wide spectrum of crustal signatures with $\varepsilon Nd_{(t)}$ values ranging from -8.96 to -1.91, while T_{DM} model ages vary between 2.48 and 2.90 Ga. The $^{147}Sm/^{144}Nd$ ratios, span from 0.0656 to 0.1531, which is expected, given the wide silica range (Tab. 5).

The Bandeirante granite (2.11 Ga) plots in an intermediate field with $\varepsilon Nd_{(t)}$ values of -3.40 and Neoarchean T_{DM} ages of 2.74 Ga.

The Alto Rio Preto granite (2.10-2.07 Ga) exhibits the most evolve isotopic signatures, with $\varepsilon Nd_{(t)}$ values as low as -8.96 (sample AA-16) and T_{DM} ages up to ranging

from Neoarchean 2.56 Ga (sample AA-76) to Mesoarchean 2.90 Ga (sample AA-16). Within this units, isotopic heterogeneity is observed, with $\varepsilon Nd_{(t)}$ differences up to six epsilon units (-2.84, sample AA-52).

The Maravilha charnockites (2.09) displays a more radiogenic $\varepsilon Nd_{(t)}$ values, up to -1.91 (sample AA-06A) and younger T_{DM} ages from Neoarchean (2.59 Ga, sample AA-09) to Siderian (2.48 Ga, sample AA-08B).

The Serra Azul charnockite (2.06 Ga) display an evolved isotopic signature with consistent $\varepsilon Nd_{(t)}$ values from -4.71 (sample AA-20) to -6.41 (sample AA-02), with T_{DM} Neoarchean T_{DM} ages (2.60-2.75 Ga).

The Bernardino granite (2.05 Ga) displays $\varepsilon Nd_{(t)}$ a value of -6.71 and Neoarchean T_{DM} age of 2.7 Ga. These values are comparable to those observed in the more evolved portions of the Alto Rio Preto and Serra Azul units.

Table 5 - Sm-Nd isotopic data from the granitoids and charnockites of the southern Bacajá Domain.

Sample	Lithology	Sm (ppm)	Nd (ppm)	$^{147}Sm/^{144}Nd$	$^{143}Nd/^{144}Nd$ (±2)	f(Sm/Nd)	εNd(0)	εNd(t)	T_{DM} (Ga)	T_{DM2} (Ga)
Bandeirante granite (2.11 Ga)*										
AA-03C	ALSG	4.669	22.392	0.1260	0.511483(8)	-0.36	-22.53	-3.40	2.74	
Alto Rio Preto granite (2.10 Ga)*										
AA-23	BSG	4.816	29.813	0.0977	0.511056(4)	-0.50	-30.86	-4.16	2.63	-
AA-52	ABMzG	9.257	52.995	0.1056	0.511233(4)	-0.46	-27.41	-2.84	2.57	-
AA-76	ABMzG	9.660	62.411	0.0936	0.511036(10)	-0.52	-31.25	-3.45	2.56	-
ASM-02	BMzG	21.927	129.266	0.1025	0.511127(11)	-0.48	-29.47	-4.45	2.65	
Alto Rio Preto granite (2.07 Ga)*										
AA-16	BTon	1.837	11.899	0.0933	0.510772(14)	-0.53	-36.40	-8.96	2.90	
AA-46	BMzG	4.422	28.661	0.0933	0.510949(7)	-0.53	-32.95	-5.47	2.67	
ASM-01	BGrd	5.725	34.743	0.0996	0.511040(10)	-0.49	-31.17	-5.38	2.70	
ASM-23	BMzG	6.694	60.243	0.0672	0.510580(7)	-0.66	-40.15	-5.74	2.58	2.68
ASM-28	BMzG	5.013	46.228	0.0656	0.510640(17)	-0.67	-42.49	-7.67	2.68	2.83
Maravilha charnockite (2.09 Ga)*										
AA-06A	ABSG	9.565	53.565	0.1079	0.511319(10)	-0.45	-25.73	-1.91	2.56	
AA-08B	PBGrd	5.124	30.329	0.1021	0.511189(10)	-0.48	-28.27	-3.01	2.48	
AA-09	PASG	11.960	74.261	0.0974	0.511158(3)	-0.51	-28.87	-2.34	2.59	
Serra Azul charnockite (2.07 Ga)*										
AA-15A	ABTon	4.515	23.286	0.1172	0.511318(7)	-0.40	-25.75	-4.74	2.75	
AA-20	PABTon	6.828	26.951	0.1531	0.511807(7)	-0.22	-16.21	-4.71	3.18	2.60
AA-02	OBGrd	3.273	24.159	0.0819	0.510745(10)	-0.58	-36.93	-6.44	2.68	
AA-49	OABGrd	4.690	25.597	0.1108	0.511221(10)	-0.44	-27.64	-4.81	2.72	
Bernardino granite (2.05 Ga)*										
AA-22	CGBGrd	3.014	20.121	0.0905	0.510863	-0.54	-34.62	-6.71	2.72	

*Age used for calculating εNd(t)

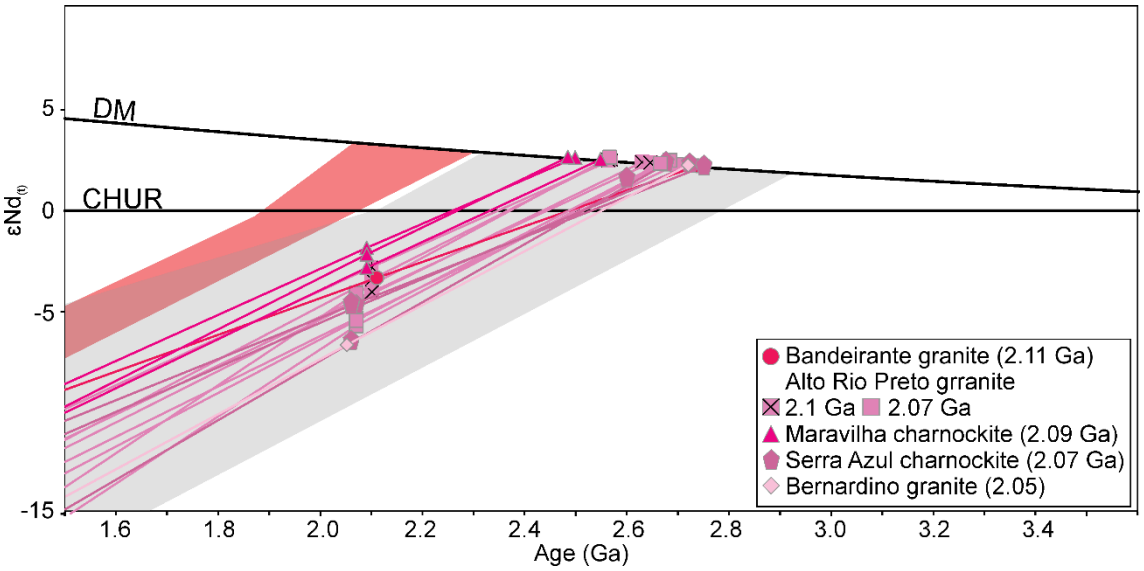


Figure 12 - $\varepsilon Nd_{(t)}$ vs. age (Ga) of samples from the studied granitoids and charnockites. The gray shaded area represents the Nd from the northeast, east, southeast, and central portion of the Bacajá Domain (with negative $\varepsilon Nd_{(t)}$), the red shaded area represents the Nd data from the extreme north of the domain (positive $\varepsilon Nd_{(t)}$ data). Data compiled from Macambira et al., (2009), Vasquez (2006), Vasquez and Rosa-Costa (2008), Magalhães et al., (2022), and Barros et al., (2023).

2.5 DISCUSSION

2.5.1 Timing magmatic events in the southern Bacajá Domain

The ages obtained for Paleoproterozoic granitoids in the southern Bacajá Domain do not significantly differ from the previously reported ages within the domain (Tab. 1). The overlapping crystallization ages among the studied magmatic rocks suggest a long-lived magmatic episode from 2.12 Ga to 2.05 Ga, representing approximately 70 Ma of continuous magmatic activity. This event was responsible for the formation of the granites (Bandeirante, Alto Rio Preto and Bernardino) and charnockites (Maravilha and Serr Azul) exposed in the study area.

In addition to this major magmatic event, several inherited zircons were identified within the studied units. In the Bernardino granite, the zircon age spectra range from Neoarchean (2.72 Ga) to Paleoproterozoic (2.01 Ga). The Paleoproterozoic ages broadly correspond to the crystallization ages from Rhyacian and Siderian magmatic rocks in the Bacajá Domain (Tab. 1), suggesting a proximal source for the inherited zircon crystals. The older Archean zircons grains imply a contribution from ancient crustal components to the sedimentary protolith of the Bernardino granite.

In the biotite granodiorite facies of the Alto Rio Preto granite, xenocryst zircon core ranging with 2.2 Ga was also identified. These cores may represent xenocrysts captured from the wall-rocks during magma ascent, suggesting a polycyclic evolution for the Alto Rio Preto granite.

All dated units exhibit lower intercept ages between 303 and 440 Ma, albeit with significant analytical uncertainties. These discrepancies may reflect errors associated with regressions derived from mixed zircon populations or, more likely, variable discordance within the zircon grains themselves. Regardless, the lower intercepts point to isotopic disturbance, most probably due to Pb loss during younger geological events. This disturbance is interpreted as consequence of tectonic, magmatic, or metamorphic events related to the Neoproterozoic to Early Cambrian orogenesis along the margins of the Amazonian Craton (Fonseca et al., 2004; Freitas et al., 2024), similar to what has been observed in several granitoids from the Carajás Province and São Luis Craton (Feio et al., 2013; Klein et al., 2012).

2.5.2 Geochemical affinities of the studied rocks: geological and tectonic implications

The magmatism described in the southern Bacajá Domain includes both orthopyroxene-free granitoids and orthopyroxene-bearing or fayalite-bearing charnockites, which vary in age and geochemical signature.

The granitoids, primarily monzogranites and granodiorites, include the Bandeirante, Alto Rio Preto, and Bernardino granites, all of which show affinity with the calc-alkaline series (see section 4.3). Calc-alkaline magmatism is widespread throughout the Bacajá Domain (Barros et al., 2023; Besser and Barros, 2015; Macambira and Ricci, 2015; Vieira et al., 2022). Among them, the Bernardino is distinct due to its strongly peraluminous character, suggesting a significant sedimentary contribution to its parental magma. It represents the first strongly peraluminous granite described in the Bacajá Domain.

In contrast, the charnockites units include the Maravilha and Serra Azul charnockites. The first comprises (quartz) monzonites to syenites, charnockites, and granites with ferroan or A-type affinity (Rajesh et al., 2011; Zhao et al., 2023), characterizes by high $FeO_t/(FeO_t+MgO)$ ratios (>0.80) and enrichment in HFSE. The latter, on the other hand, consist of enderbites, charnoenderbites, and rare granites with magnesian or I-type affinities (Rajesh et al., 2011; Zhao et al., 2023), based on lower FeOt/(FeOt+MgO) rations (<0.80) and lower HFSE contents. Rhyacian charnockite are also widespread in the Bacajá Domain and are generally more akin to the Serra Azul charnockite in their magnesian/I-type nature, as seen in the Bacajaí complex and Arapari suite (Macambira et al., 2019; Macambira and Ricci, 2015). Units with A-type affinity are more restricted in the domain and, when present, typically lack orthopyroxene and/or

fayalite + quartz in their mineralogy, such as in the João Jorge suite and Uirapuru granite (Besser and Barros, 2015; Macambira and Ricci, 2015; Vieira et al., 2022).

The geochemical features of all the studied units point to a collisional tectonic setting (see section 4.2). Therefore, determining the specific stage of the collision at which each magmatic unit was generated relies primarily on their geochemical contrasts and ages. Based on the classification of Vasquez and Rosa-Costa (2008), the Bandeirante granite and the older facies of the Alto Rio Preto granite would correspond to syn- to late-collisional magmatism, while the Maravilha and Serra Azul charnockites, the younger facies of the Alto Rio Preto granite, and the Bernardino granite would fall into the late- to post-collisional category. However, recent petrochronological data (Corrêa et al., 2019; Neri et al., in press; Silva, 2021) suggest that the metamorphic peak in the Bacajá Domain may be at least 100 Ma older than previously expected, indicating that the framework proposed by Vasquez and Rosa-Costa (2008) may need to be revised. Although a complete reassessment of the timing and meaning in the tectonic cycle of all magmatic events of the Bacajá Domain is beyond the scope of this paper, some constraints regarding the tectonic evolution of the area may be addressed based on our data.

The geochemical diversity of the studied granitoids points to complex processes leading to their formation. On the other hand, there is no evidence of marked differences in the tectonic setting of the studied area, and admitting a common setting, this would imply that the granitoids are probably derived from distinct sources (section 4.2). It is common in collisional orogens to observe the spatial association of compositionally diverse granitoids (e.g., Collins et al., 2020; Regelous et al., 2021). This is evident in the southern Bacajá Domain, where S-type like granitoids (Bernardino granite), calc-alkaline I-type like granitoids (Bandeirante granite, Alto Rio Preto granite, and Serra Azul charnockite), and A-type like granitoids (Maravilha charnockite) occur is close spatial association.

The dominance of Rhyacian calc-alkaline granites and charnockites, with more restricted A-type like charnockites, demonstrates that the southern Bacajá Domain shares geochemical and tectonic similarities with other regions of the domain (Barros et al., 2023; Macambira et al., 2019; Macambira and Ricci, 2015), and with other coeval formed in the Columbia supercontinent is both Amazonian and West Africa cratons (Milhomem Neto and Lafon, 2020; Parra-Avila et al., 2019; Vianna et al., 2020). This scenario contrast with earlier interpretation, which assumed that Mesoarchean metamorphic complexes were the dominant lithologies in the southern Bacajá Domain (Vasquez and

Rosa-Costa, 2008).

2.5.3 Rhyacian crustal evolution of the southern Bacajá Domain: implications for its tectonic setting

Integrated U-Pb and Nd-Hf isotopes indicate that the crust from the southern Bacajá Domain has been present at least since the late Paleoarchean (ca. 3.3-2.9 Ga) and was strongly reworked in the Rhyacian (2.12-2.05 Ga) resulting in widespread granitoid and charnockite magmatism and high-grade metamorphism (Neri et al., in press; Silva, 2021). The Rhyacian granitoids and charnockites display moderately to strongly negative $\varepsilon Nd_{(t)}$ and $\varepsilon Hf_{(t)}$ values, suggesting that the Paleoproterozoic crust in the study area is not juvenile and lack significant mantle contribution to its origin. Instead, it was primarily derived from the reworking of pre-existing Archean crust, likely similar to the regional basement (Macambira et al., 2007).The Mesoarchean rocks exposed in the northern part of the studied area (Fig. 3) may represent remnants of this Archean crust.

The Nd model ages pattern reveal a broad period of crustal extraction from Mesoarchean to early Siderian (2.90-2.48 Ga), with a major peak in the Neoarchean (2.75-2.56 Ga). Isotopic heterogeneities are observed among the different granitoids and charnockites (section 4.4) and even within the same unit (e.g., Alto Rio Preto granite), suggesting complex petrogenetic processes, possibly involving crustal assimilation or magma mixing processes.

Although all units exhibit negative $\varepsilon Nd_{(t)}$ values, some display relatively more radiogenic compositions (e.g., Maravilha charnockite), which may reflect derivations from less evolved crustal. In contrast, the Hf-T_{DM}^{c} model ages are significantly older, suggesting crustal extraction predominantly during the late Paleoarchean to early Mesoarchean (3.3-3.0 Ga). The discrepancy between Nd and Hf model ages is attributed to methodological differences: Nd model ages for whole-rock samples are average model ages, whereas Hf model ages of individual grains in a zircon population may better represent multiple sources contributing during magma formation (Nebel et al., 2007; Roberts and Spencer, 2015). These discrepancies are often observed in magmatic rocks from the Maroni-Itacaiúnas and Carajás provinces (Milhomem-Neto and Lafon, 2019; Rosa-Costa et al., 2025; Teixeira et al., 2019).

The gap between T_{DM} and crystallization ages implies prolonged crustal residence times, up to 1.1 Ga, for the protoliths of the studied granites and charnockites (section 4.3, 4.4). The interpretation is further supported by the presence of inherited Archean zircon grains (Tab. 1; Fig. 2, 10, 11), indicating an Archean crustal contribution to the

Rhyacian magmatism.

Compiled Nd-Hf data across the entire Bacajá Domain reveals isotopic heterogeneity in different regions of the domain (Fig. 11e, 12). In the northwestern sector, along the Iriri, Xingu, and Bacajá rivers, as well as in the central-southern region west of the study area (Fig. 1), Rhyacian granitoids and charnockites (2.2 to 2.07 Ga) generally exhibit slightly to strongly negative $\varepsilon Nd_{(t)}$ associated with Archean model ages (Fig. 13a and b), indicating a dominant crustal source for those rocks (Macambira et al., 2004, 2003; Monteiro, 2006; Vasquez, 2006; Vasquez and Rosa-Costa, 2008). In contrast, in the extreme northern domain, Rhyacian granitoids (2.2-2.06 Ga) display either positive or slightly negative $\varepsilon Nd_{(t)}$, with Siderian to Rhyacian model ages, as well as variable positive and negative $\varepsilon Hf_{(t)}$ values (Fig. 11e, 12, 13a and b). This positive isotopic signatures both isotopic systems implies a mantle influence to the genesis of these rocks (Barros et al., 2023; Magalhães et al., 2023). Additionally, their model ages are often close to the crystallization ages, especially in the central-northern sector (Barros et al., 2023), suggesting short periods of crustal residence.

In summary, although the Rhyacian crystallization ages (Tab. 1) are similar across various magmatic units in the Bacajá Domain, they do not always share similar isotopic behavior. The northwestern and southern sectors exhibits consistently negative $\varepsilon Nd_{(t)}$ and $\varepsilon Hf_{(t)}$ values, indicating a predominately crustal origin for their magmatic rocks. In contrast, the northern and northeastern sectors display more juvenile isotopic signatures, with positive $\varepsilon Nd_{(t)}$ and $\varepsilon Hf_{(t)}$, suggesting a greater mantel contribution to their origin or derivation from crustal sources with short residence times (e.g., early Rhyacian or Siderian material).

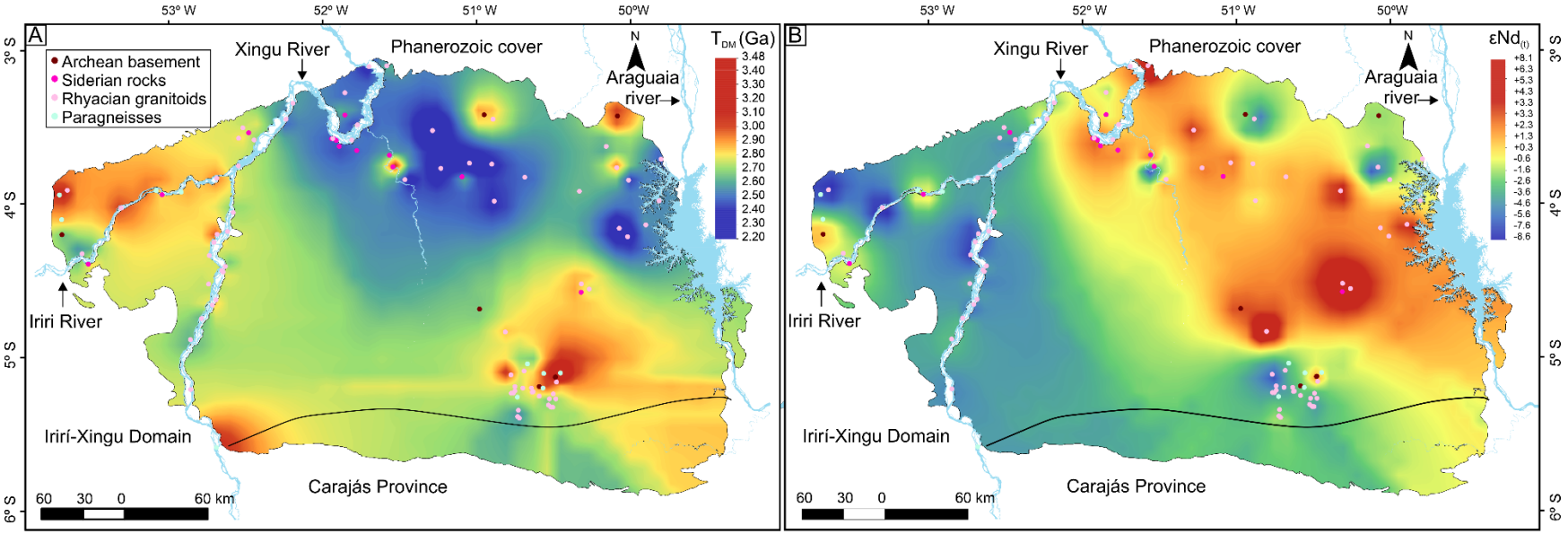


Figure 13 - (A) Map of Nd-T_{DM} model ages distribution in the Bacajá Domain based on whole-rock Sm-Nd istopic data from 107 samples of Archean to Rhyacian ages of felsic to intermediate compositions; (B) map of $\varepsilon Nd_{(t)}$ distribution in the Bacajá Domain based on 95 samples (excluding 12 samples of paragneisses used in the map in (A). Data from:Barros et al., (2023); Cristo (2018); Macambira et al., (2009); Magalhães et al., (2023); Neri et al., unpublished data, Vasquez and Rosa-Costa (2008) and references therein, Vasquez (2006).The black line in the southern region of the Bacajá Domain represents the proposed boundary with the Carajás Province (Correa et al., 2022).

2.5.3.1 Geodynamic model for the southern Bacajá Domain

Considering the integrated geochemical, geochronological, and isotopic data, a complex evolutionary history is inferred for the Bacajá Domain, involving diverse Archean fragments (basement inliers) that were reworked during the Paleoproterozoic orogenesis. This history includes the formation of multiple Rhyacian arc components accompanied by intricate episodes of sedimentation, deformation, magmatism, and metamorphism (Macambira et al., 2022, 2009, 2004, 2001; Magalhães et al., 2023; Vieira et al., 2022). In the northern region, a two-sided subduction-related setting has been proposed based on geochemistry and isotopic data in the pre- to syn-collisional suites (Barros et al., 2023).

Focusing on the southern region, it is clear the dominance of high-K calc-alkaline granites and ferroan to magnesian charnockites. These lithologies are generally emplaced in arc and post-collision settings following an episode of crustal thickening (e.g., Jiang et al., 2002; Laurent et al., 2014; Lu et al., 2013). The geological, geochemical, and isotopic features of the studied units are consistent with a collisional tectonic setting, during which extensive crustal reworking occurred (Fig. 8, 11e, 12).

A continental collision between the Bacajá basement and the Carajás Province may have caused crustal thickening of the continental lithosphere in the contact zone, as put in evidence by geophysical data that suggest the crust in this region extends up to ~46 km (Albuquerque et al., 2017; Correa et al., 2022). In this context, lithospheric delamination is a plausible tectonic trigger for the initiation of partial melting of the crust to produce these potassic magmas at the same time (Couzinié et al., 2014; Laurent et al., 2014a, 2014b). Other proposed mechanisms, such as slab break-off, also described during late- to post-collisional periods, could explain the dominant high-K affinity of these granitoids but fail to explain their large lateral spatial extent (Eglinger et al., 2017).

The timing of metamorphic events is also crucial, as these events often serve as robust indicator of major tectonic episodes (Brown, 2007; Brown and Johnson, 2018). In the studied area, high-pressure metamorphism in aluminous granulites peaked at 2.21~2.23 Ga, followed by an isothermal decompression at 2.19 Ga and later isobaric cooling at 2.05 in a marking a subduction to collisional setting (Neri et al., in press). The onset of (ultra)-high-temperature granulite metamorphism probably occurred at 2.16-2.13 Ga, with cooling stages at 2.09-2.05 Ga (Silva, 2021)Clique ou toque aqui para inserir o texto.. These time constraints suggest that the oldest granitoids (e.g., Bandeirante granite and early facies of the Alto Rio Preto granite) crystallized shortly after peak high-

temperature metamorphism, whereas the youngest units (e.g., Maravilha and Serra Azul charnockite, youngest facies of the Alto Rio Preto and Bernardino granites) were emplace during lates isobaric cooling of both high-temperature and high-pressure metamorphism.

A two-step geodynamic evolution for the southern region is proposed considering all obtained data (Fig. 14):

I) 2.12-2.10 Ga: collision between the Archean Bacajá basement and island arcs with the Carajás province leads to crustal thickening and reworking of the older crust. This stage results in the emplacement of calc-alkaline syn-collisional plutons represented by the Bandeirante granite and oldest rocks of the Alto Rio Preto granite.

II) 2.09-2.05 Ga: following crustal thickening, the lower crust becomes gravitationally unstable, triggering lithospheric delamination and asthenosphere upwelling. This thermal perturbation induces the partial melting of preexisting Archean igneous and sedimentary crust, generating diversified late- to post-colisional granitoids and charnockites (Maravilha and Serra Azul charnockites, youngest rocks of the Alto Rio Preto granite and Bernadino granite).

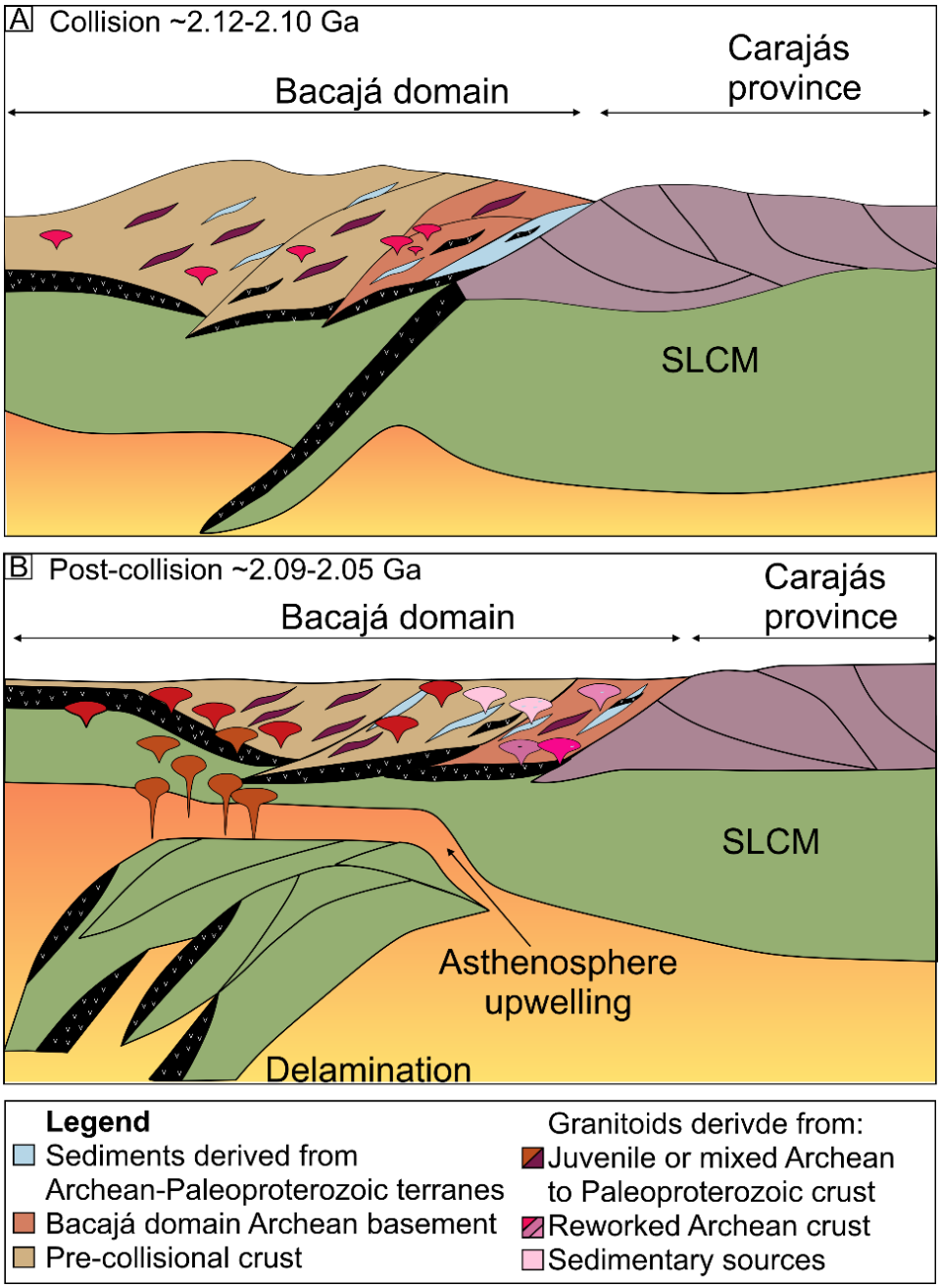


Figure 14 - Proposed two-stage geodynamic model for the southern Bacajá Domain. (A) During 2.12–2.10 Ga, collision between the Archean Bacajá basement and island arcs accreted to the Carajás Province caused crustal thickening and high-temperature metamorphism, leading to the emplacement of syn-collisional granitoids. (B) Between 2.09–2.05 Ga, lithospheric delamination triggered asthenospheric upwelling and partial melting of thickened Archean crust, generating post-collisional charnockites and peraluminous granitoids.. SLCM = subcontinental lithospheric mantle, O.C = oceanic crust, C.C = continental crust.

2.5.3.2 A comparison between the Bacajá Domain with the Carajás province and an evaluation of their limits

The exact location of the boundary between the Bacajá Domain and Carajás province remains controversial. Recent studies, based mainly on geophysical data (Correa et al., 2022; Motta et al., 2019), suggest that the southern portion of the Bacajá Domain

may represent an exhumated Carajás crust, with the boundary located farther north than previously indicated by Faraco et al. (2006) and Vasquez and Rosa-Costa (2008). In this context, the detailed geological mapping, whole rock and isotope geochemistry, and geochronology presented in this study for a representative portion of the southern Bacajá Domain shed lights on key aspects of its crustal evolution and contribute to a better understanding of its relationship with the Carajás province.to support this, we will briefly compare the information available from northern Carajás and southern Bacajá.

The Carajás Basin, located in the northernmost portion of the Carajás Province, is mainly composed of Neoarchean supracrustal units, dominated represented by mafic to intermediate volcanic rocks and banded iron formations (Gibbs et al., 1986; Machado et al., 1991; Teixeira and Eggler, 1994; Vasquez and Rosa-Costa, 2008; Wirth et al., 1986). Mafic-ultramafic intrusions and Neoarchean and Paleoproterozoic A-type granites intersect these units(Barbosa Teixeira et al., 2018; Barros et al., 2009; Dall'Agnol et al., 2005a; Machado et al., 1991; Sardinha et al., 2006; Souza et al., 1996; Toledo et al., 2023). The Archean units are partially covered by the extensive sedimentary sequence of the Águas Claras Formation (Nogueira et al., 1995). Granulites and migmatites occur only south of the Carajás basin in the Mesoarchean Canaã dos Carajás terrane (Marangoanha et al., 2019; Silva et al., 2021; Vasquez and Rosa-Costa, 2008).

In contrast, the southern Bacajá Domain is composed of a diverse metamorphic basement composed of ortho- and paragneisses and granulites of Mesoarchean age (3.0-2.94 Ga; Cajazeiras Complex), and Neoarchean (2.60 Ga, Rio Preto mafic granulite) Ga, all metamorphosed under amphibolite to granulite facies during the Rhyacian (2.16-2.07 Ga) (Macambira et al., 2007; Silva, 2021; Vasquez and Rosa-Costa, 2008). Supracrustal sequences in Bacajá are interpreted as Siderian greenstone belt sequences (Faraco et al., 2006; Vasquez and Rosa-Costa, 2008). During the Rhyacian (~2.2-2.05 Ga), intense magmatic activity led to the emplacement of diverse granitoids and charnockites (Macambira et al., 2019; Macambira and Ricci, 2015; Macambira et al., 2007; Vasquez and Rosa-Costa, 2008).

There are some remarkable contrasts between both tectonic domains: (1) There is no equivalent on Bacajá to the huge Neoarchean metavolcanosedimentary sequences and to the significant occurrences of banded-iron formations seen in Carajás; (2) The notable concentration of Cu (IOCG) and Fe deposits in Carajás (DOCEGEO, 1988; Melo et al., 2017; Schutesky and de Oliveira, 2020; Trunfull et al., 2020) has no correspondence in Bacajá; (3) The intense, voluminous, and diverse Rhyacian magmatic associations

dominant in southern Bacajá as described in this work are not registered in Carajás; (4) The Rhyacian metamorphic event identified in Bacajá was not identified so far in Carajás; (5) No U-Pb crystallization age ca. 2.2-2.05 Ga have been reported in the Carajás so far; the few ~2.0 Ga ages are found especially in mineral deposits (Ar-Ar in micas and amphibole, U-Pb in apatite and monazite), are interpreted as deformation or hydrothermal overprints on older protolithes (Campo-Rodriguez et al., 2025 and references therein); (6) The Orosirian within plate granites of the Serra dos Carajás suite or similar (Dall'Agnol et al., 2005b; Santos et al., 2023; Teixeira et al., 2018) are absent in Bacajá; (7) while Mesoarchean granulitic rocks in both tectonic domains, the Chicrin-Cateté and Ouro-Verde granulites that occur in Carajás show a TTG-type affinity and were formed at 3.06-2.93 Ga and affected by metamorphism at the Mesroarchean (2.89-2.85 Ga) (Marangoanha et al., 2019; Pidgeon et al., 2000; Silva et al., 2021), while the Cajazeiras Complex of Bacajá Domain, despite their similar Mesoarchean protolithes ages, was reworked during the Rhyacian metamorphism (Macambira et al., 2007).

Based on the observed differences in dominant lithologies, their time of formation, and the geologic evolution of the two domains, it is concluded that the studied area, a representative part of the southern Bacajá Domain, does not represent an exhumated fragment of Carajás crust. Still, the Bacajá-Carajás collision seems to have played a critical role in the hydrothermal and deformational events in the Carajás province (Campo-Rodriguez et al., 2025; Tavares et al., 2018).

2.5.4 Brief comparison with Rhyacian granitoid magmatism in Paleoproterozoic orogens and implications for Columbia assembly

Paleoproterozoic supercontinent reconstructions often position the Amazonian and West Africa Craton adjacent to each other, linked by an extensive long-lived orogenic system active during the Rhyacian to early Orosirian (e.g., Meert and Santosh, 2017; D'Agrella-Filho et al., 2016; Zhao et al., 2002). This configuration is supported by the overlapping geological and isotopic affinities between the two cratons (Kroonenberg et al., 2016). To better understand their tectonic relationship during Columbia assembly, we compare zircon U-Pb-Hf isotopic data from the Bacajá Domain with selected Paleoproterozoic terranes of the Amazonian and West Africa cratons.

In the eastern part of the Guiana shield (Amazonian Craton), the Lourenço and Carecuru domains are compose predominantly of Rhyacian granitoids formed in arc-related and potentially collisional settings (Barreto et al., 2013; Rosa-Costa et al., 2014 Rosa-Costa et al., 2006). Although their tectonic evolution still debated, both domains

flank the Archean Amapá block and exhibit spatial isotopic patterns consistent with varying degrees of crustal reworking (Milhomem-Neto and Lafon, 2020; Rosa-Costa et al., 2025 and references therein). For the Lourenço domain, two distinct sectors were identified based on Nd-Hf isotope data: (i) in southeast French Guiana (northwestern of Lourenço domain), far from the Archean margin of the Amapá Block, the magmatic rocks display suprachondritic zircon $\varepsilon Hf_{(t)}$ and whole-rock $\varepsilon Nd_{(t)}$ suggesting juvenile contributions with Rhyacian and Neoarchean model ages; (ii) in the south and northwestern, closer to the margin of the Amapá Block the magmatic rocks revealed subchondritic Nd-Hf values with older model ages(Paleo- to Mesoarchean), consistent with strong crustal reworking. A similar pattern is seen in the Carecuru domain, where most rocks are characterized by suprachondritic Hf-Nd isotopic signatures with Neoarchean model ages, but also include some more evolved components (Milhomem-Neto and Lafon, 2020).

The southern portion of the West Africa Craton also presents evidences for a comparable tectonic scenario. The Baoulé-Mossi domain, situated east of the Archean Kénéma-Man nucleus, was affected by widespread Rhyacian magmatism (2265 to 2095 Ma), which evolved from arc-related to collisional regimes (Eglinger et al., 2017; Parra-Avila et al., 2017; Perret et al., 2025). Isotopic data show a similar spatial trend: in the proximity of the Archean Kénéma-Man domain, the granitoids display less radiogenic $\varepsilon Hf_{(t)}$, suggesting an intense crustal reworking in the Archean margin. In contrast, far away from that domain, the rocks tend to reveal more radiogenic $\varepsilon Hf_{(t)}$, suggesting a mantellic contribution to their origin, although rocks with crustal signatures were also found, reflecting varying degrees of crustal recycling (Eglinger et al., 2017; Parra-Avila et al., 2018; Petersson et al., 2018, 2016).

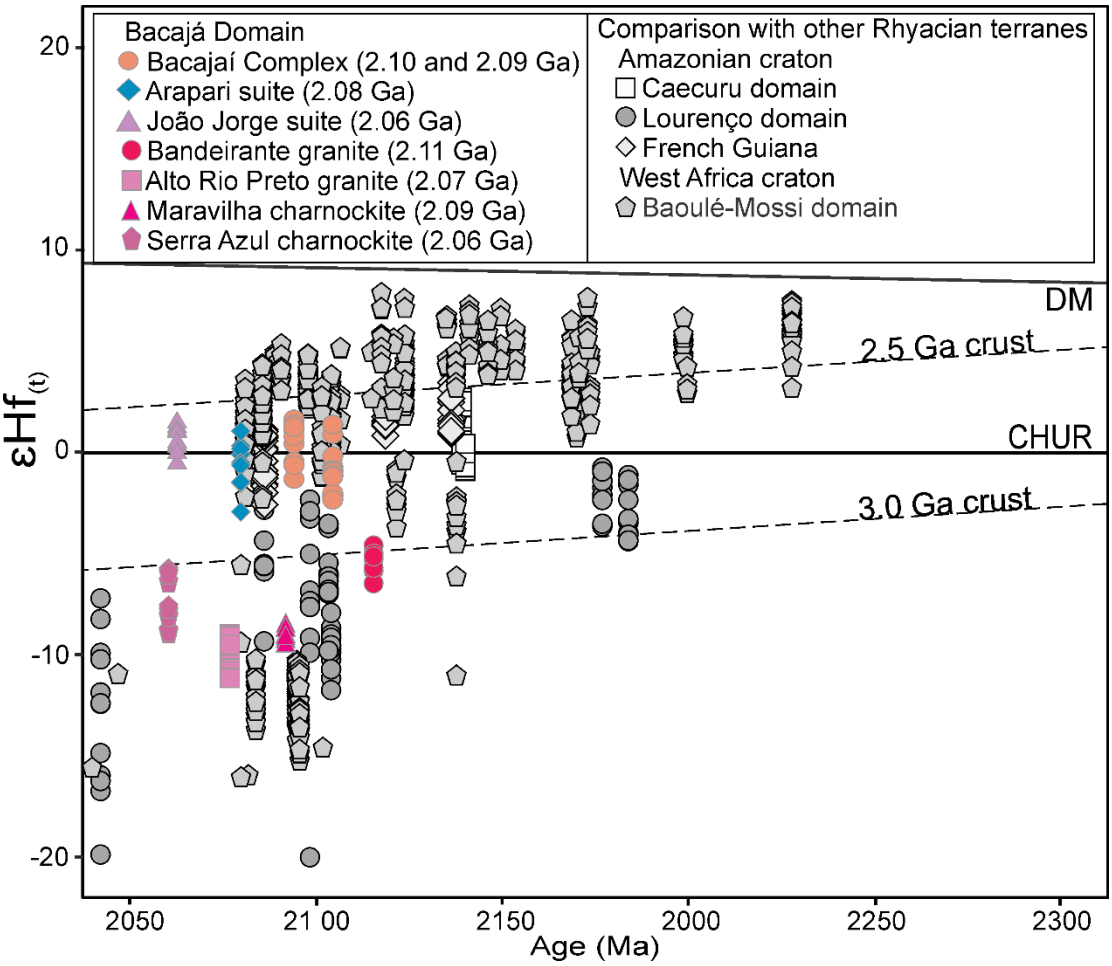


Figure 15 - Plot of time (Ma) vs. εHf for the Paleoproterozoic granitoids and charnockites from the Bacajá Domain, including the data from the studied area. For regional and global comparison, Hf data from selected Rhyacian terranes were compiled: Carecuru and Lourenço domains, and French Guiana from the Amazonian craton (Milhomen and Lafon, 2020, Queiroz, 2020); from Baoulé-Maossi domain, West Africa craton (Eglinger et al., 2017, Parra-Avila et al., 2018, Petterson et al., 2016).

In the Bacajá Domain, the newly acquired Hf isotopic dataset reveals an analogous spatial distribution of $\varepsilon Hf_{(t)}$ values among Rhyacian granitoids and charnockites (Fig. 14). Units emplaced near the border of the Carajás province (this work) are marked by subchondritic $\varepsilon Hf_{(t)}$ values (down to -10), implying strong reworking of preexisting crustal sources with early Mesoarchean to late Paleoarchean model ages. Conversely, units emplaced in the northern portion, distant from the main Archean landmass, display more juvenile $\varepsilon Hf_{(t)}$ values, ranging from slightly negative to strongly positive, suggesting involvement of mantle-derived components (Magalhães et al., 2023).

The identified trend is show in Fig. 15, which shows εHf(t) versus age for zircon grains in the Bacajá and the compared terranes from Guiana Shield and West Africa cratons. In all regions, the spatial variation in isotopic signatures closely correlated with the distance from the adjacent Archean blocks (Carajás, Amapá and Kénéma-Man).

These features strongly suggest that Rhyacian magmatic systems in these two cratons developed in analogous geodynamic settings related to subduction and collisional tectonics (Eglinger et al., 2017; Milhomem-Neto and Lafon, 2020; Rosa-Costa et al., 2025).

The compilation of U-Pb-Hf zircon data from the Bacajá Domain and selected Paleoproterozoic terranes in the Amazonian and West Africa cratons revealed strong similarities between them. The Rhyacian magmatic rocks are not only coeval but isotopically comparable. This convergence supports the hypothesis that these two cratons were once juxtaposed during the Columbia supercontinent assembly (Johansson et al., 2022; Meert and Santosh, 2017b; Zhao et al., 2002). Moreover, the systematic isotopic variation observed in these domains provides new geodynamic constraints for this reconstruction, indicating that the accretion of juvenile arc and their collision with Archean margins played a critical role in the growth and stabilization during the Rhyacian.

Although the presence of multiple isotopic sources and complex tectonic settings has been previously recognized in Columbia related magmatism (Eglinger et al., 2017; Grenholm et al., 2019; Kroonenberg et al., 2016; Wane et al., 2018), this study reinforces that these characteristics are not random. Instead, they reflect large-scale processes that took place along the margins of at least two major cratons. In this sense, the Bacajá Domain offers geochronological and isotopic evidence that strengthens existing models of Amazonian-West Africa proximity during Columbia assembly and provides a framework for future refinements of paleogeographic reconstruction.

2.6 CONCLUSIONS

1. Integrated geological mapping, petrography, geochemistry, U-Pb geochronology, and Nd-Hf isotopic data revealed previously unrecognized, compositionally distinct Rhyacian granitoids and charnockites in the southern portion of the Bacajá Domain, near its boundary with the Carajás Province.
2. The southern Bacajá Domain recorded a long-lived magmatic episode between 2.12 and 2.05, spanning ca. 70 Ma. This event is represented by the Bandeirante, Alto Rio Preto and Bernardino granites, as well as the Maravilha and Serra Azul charnockites.
3. These magmatic rocks were emplaced in a collisional tectonic setting, resulting from the convergence of between the Mesoarchean basement fragments and island arcs of the Bacajá Domain with the Archean Carajás Province.

4. The sources of the Rhyacian magmas are linked pre-existing Mesoarchean to Paleoarchean crust (2.9-3.3 Ga Hf-T_{DM}^{c}), with prominent crustal extraction events during the Mesoarchean to Neoarchean. Their negative $\varepsilon Nd_{(t)}$ and $\varepsilon Hf_{(t)}$ values indicate that Rhyacian granitoids and charnockites are not juvenile and lack significant mantellic influence in their origin and are derived from the reworking of pre-existing Archean crust, most likely from the Mesoarchean basement of the domain.

5. Substantial contrasts in lithological composition, timing of curst formation and overall geological evolution were observed when comparing the Bacajá and Carajás domains. These differences support the conclusion that the studied region, a representative part of the southern Bacajá Domain, does not represent an exhumated fragment of the Carajás crust.

6. The Bacajá Domain and correlative Paleoproterozoic belts in Amazonia and West Africa cratons share Rhyacian ages and show systematic Nd–Hf isotopic zonation. Crustal reworking dominates near Archean margins, while juvenile magmatism prevails in distal areas. This spatial pattern, observed across cratons, supports their juxtaposition during Columbia assembly and highlights Bacajá's role in global Paleoproterozoic crustal evolution.

ACKNOWLEDGMENTS

This paper is part of the first author's PhD thesis developed at the Instituto de Geociências, UFPA. The authors acknowledge UNIFESSPA students and staff for their previous work in the studied area and for shared information; K. Sato and C. J. S. Mesquita for their support during the SHRIMP analysis. RD acknowledges CNPq (Proc. 304648-2019-1). This study was financed in part by the Coordenação de Aperfeiçoamento de Pessoal de Nível Superior - Brasil (CAPES) - Finance Code 001 (No. 88887.643812/2021-00).

REFERENCES

Albuquerque, D.F., França, G.S., Moreira, L.P., Assumpção, M., Bianchi, M., Barros, L.V., Quispe, C.C., Oliveira, M.E., 2017. Crustal structure of the Amazonian Craton and adjacent provinces in Brazil. J South Am Earth Sci 79, 431–442. https://doi.org/10.1016/j.jsames.2017.08.019

Barbosa Teixeira, M.F., Dall'Agnol, R., Schneider Santos, J.O., Carvalho de Oliveira, D.,

Lamarão, C.N., McNaughton, N.J., 2018. Crystallization ages of Paleoproterozoic A-type granites of Carajás province, Amazon craton: Constraints from U-Pb geochronology of zircon and titanite. J South Am Earth Sci 88, 312–331. https://doi.org/10.1016/j.jsames.2018.08.020

Barker, F., Arth, J.G., 1976. Generation of trondhjemitic-tonalitic liquids and Archean bimodal trondhjemite-basalt suites. Geology 4, 596. https://doi.org/10.1130/0091-7613(1976)4<596:GOTLAA>2.0.CO;2

Barros, C.E. de M., Besser, M.L., Gouvêa Vasconcellos, E.M., 2023. Voluminous Paleoproterozoic plutonic belt of the Bacajá Domain in Amazon Craton: Petrology, geotectonic setting and Pb–Pb zircon evaporation ages. J South Am Earth Sci 130, 104491. https://doi.org/10.1016/j.jsames.2023.104491

Barros, C.E.M., Macambira, M.J.B., Santos, M.C.C., Silva, D.C.C., Palmeira, L.C.M., Sousa, M., 2007. Estruturas sinmagmáticas e idade de zircão de granitos (evaporação de Pb) paleoproterozóicos da parte leste do Domínio Bacajá, Província Maroni-Itacaiúnas. Revista Brasileira de Geociências 37, 293–304. https://doi.org/10.25249/0375-7536.2007373293304

Barros, C.E.M., Sardinha, A.S., de Oliveira Barbosa, J. d. P., Macambira, M.J.B., Barbey, P., Boullier, A.-M., 2009. Structure, petrology, geochemistry and zircon U/Pb and Pb/Pb geochronology of the synkinematic Archean (2.7 ga) A-type granites from the Carajás metallogenic Province, northern Brazil. The Canadian Mineralogist 47, 1423–1440. https://doi.org/10.3749/canmin.47.6.1423

Besser, M.L., Barros, C.E.M., 2015. Geologia e recursos minerais da Folha Rio Bacajá - SA.22-Y-D-VI, Estado do Pará. CPRM.

Black, L.P., Gulson, B.L., 1978. The age of the Mud Tank carbonatite, strangways range, northern Territory. BMR Journal of Australian Geology and Geophysics 3, 227–232.

Black, L.P., Kamo, S.L., Allen, C.M., Davis, D.W., Aleinikoff, J.N., Valley, J.W., Mundil, R., Campbell, I.H., Korsch, R.J., Williams, I.S., Foudoulis, C., 2004. Improved 206Pb/238U microprobe geochronology by the monitoring of a trace-element-related matrix effect; SHRIMP, ID–TIMS, ELA–ICP–MS and oxygen isotope documentation for a series of zircon standards. Chem Geol 205, 115–140. https://doi.org/10.1016/j.chemgeo.2004.01.003

Bouvier, A., Vervoort, J.D., Patchett, P.J., 2008. The Lu–Hf and Sm–Nd isotopic composition of CHUR: Constraints from unequilibrated chondrites and implications for the bulk composition of terrestrial planets. Earth Planet Sci Lett 273, 48–57.

https://doi.org/10.1016/j.epsl.2008.06.010

Boynton, W. V, 1984. Cosmochemistry of the Rare Earth Elements: Meteorite Studies. https://doi.org/10.1016/B978-0-444-42148-7.50008-3

Brown, M., 2007. Metamorphic conditions in orogenic belts: A record of secular change. Int Geol Rev 49, 193–234. https://doi.org/10.2747/0020-6814.49.3.193

Brown, M., Johnson, T., 2018. Secular change in metamorphism and the onset of global plate tectonics. American Mineralogist 103, 181–196. https://doi.org/10.2138/am-2018-6166

Bruno, H., Heilbron, M., de Morisson Valeriano, C., Strachan, R., Fowler, M., Bersan, S., Moreira, H., Motta, R., Almeida, J., Almeida, R., Carvalho, M., Storey, C., 2021. Evidence for a complex accretionary history preceding the amalgamation of Columbia: The Rhyacian Minas-Bahia Orogen, southern São Francisco Paleocontinent, Brazil. Gondwana Research 92, 149–171. https://doi.org/10.1016/j.gr.2020.12.019

Bühn, B., Pimentel, M.M., Matteini, M., Dantas, E.L., 2009. High spatial resolution analysis of Pb and U isotopes for geochronology by laser ablation multi-collector inductively coupled plasma mass spectrometry (LA-MC-ICP-MS). An Acad Bras Cienc 81, 99–114. https://doi.org/10.1590/s0001-37652009000100011

Campo-Rodriguez, Y.T., Ciobanu, C.L., Gilbert, S., Wade, B., Cook, N.J., Schutesky, M.E., Ehrig, K., 2025. Coupled Lu-Hf and U-Pb apatite geochronology of Jatobá orebody supports ~ 2.5 Ga metamorphism in deep shear zones from southern Copper Belt, Carajás Domain, Brazil. Precambrian Res 421, 107753. https://doi.org/10.1016/j.precamres.2025.107753

Cawood, P.A., Hawkesworth, C.J., Dhuime, B., 2013. The continental record and the generation of continental crust. Geol Soc Am Bull 125, 14–32. https://doi.org/10.1130/B30722.1

Chaves, A.O., 2021. Columbia (Nuna) supercontinent with external subduction girdle and concentric accretionary, collisional and intracontinental orogens permeated by large igneous provinces and rifts. Precambrian Res 352, 106017. https://doi.org/10.1016/j.precamres.2020.106017

Chu, N.-C., Taylor, R.N., Chavagnac, V., Nesbitt, R.W., Boella, R.M., Milton, J.A., German, C.R., Bayon, G., Burton, K., 2002. Hf isotope ratio analysis using multi-collector inductively coupled plasma mass spectrometry: an evaluation of isobaric interference corrections. J Anal At Spectrom 17, 1567–1574.

https://doi.org/10.1039/b206707b

Collins, W.J., Huang, H.-Q., Bowden, P., Kemp, A.I.S., 2020. Repeated S–I–A-type granite trilogy in the Lachlan Orogen and geochemical contrasts with A-type granites in Nigeria: implications for petrogenesis and tectonic discrimination. Geological Society, London, Special Publications 491, 53–76. https://doi.org/10.1144/SP491-2018-159

Cordani, U.G., Sato, K., Teixeira, W., Tassinari, C.G., Basei, M.A.S., 2000. Crustal evolution of the South American Platform. Tectonic Evolution of South America 19–40.

Corrêa, L.C., Meira, V.T., Vasquez, M.L., 2019. Metamorfismo dos paragnaisses da região oeste do Domínio Bacajá, estado do Pará: dados preliminares, in: 16º Simpósio de Geologia Da Amazonia. Sociedade Brasileira de Geologia, Manaus, pp. 626–630.

Correa, R.T., Vidotti, R.M., Guedes, V.J.C.B., Scandolara, J.E., 2022. Mapping the Thermal Structure of the Amazon Craton to Constrain the Tectonic Domains. J Geophys Res Solid Earth 127. https://doi.org/10.1029/2021JB023025

Couzinié, S., Moyen, J.-F., Villaros, A., Paquette, J.-L., Scarrow, J.H., Marignac, C., 2014. Temporal relationships between Mg-K mafic magmatism and catastrophic melting of the Variscan crust in the southern part of Velay Complex (Massif Central, France). Journal of GEOsciences 69–86. https://doi.org/10.3190/jgeosci.155

Cristo, L.C.F., 2018. Estudo petrográfico e isotópico (Pb-Pb, U-Pb e Sm-Nd) de rochas metavulcânicas, mineralizações auríferas e rochas granitoides relacionadas ao greenstone belt Três Palmeiras, Volta Grande do Xingu, Domínio Bacajá. Universidade Federal do Pará.

D'Agrella-Filho, M.S., Bispo-Santos, F., Trindade, R.I.F., Antonio, P.Y.J., 2016. Paleomagnetism of the Amazonian Craton and its role in paleocontinents. Brazilian Journal of Geology 46, 275–299. https://doi.org/10.1590/2317-4889201620160055

Dall'Agnol, R., Teixeira, N.P., Rämö, O.T., Moura, C.A.V., Macambira, M.J.B., de Oliveira, D.C., 2005. Petrogenesis of the Paleoproterozoic rapakivi A-type granites of the Archean Carajás metallogenic province, Brazil. Lithos 80, 101–129. https://doi.org/10.1016/j.lithos.2004.03.058

Debon, F., Fort, P. Le, 1983. A chemical–mineralogical classification of common plutonic rocks and associations. Trans R Soc Edinb Earth Sci 73, 135–149. https://doi.org/10.1017/S0263593300010117

DOCEGEO, R.D.G. e M.S.A., 1988. Revisão litoestratigráfica da Província Mineral de Carajás - litoestratigrafia e principais depósitos minerais., in: Congresso Brasileiro de Geologia. Belém, pp. 11–54.

Eglinger, A., Thébaud, N., Zeh, A., Davis, J., Miller, J., Parra-Avila, L.A., Loucks, R., McCuaig, C., Belousova, E., 2017. New insights into the crustal growth of the Paleoproterozoic margin of the Archean Kéména-Man domain, West African craton (Guinea): Implications for gold mineral system. Precambrian Res 292, 258–289. https://doi.org/10.1016/j.precamres.2016.11.012

Faraco, M.T.L., Vale, A.G., Santos, J.O.S., Luzardo, R., Ferreira, A. l., Oliveira, M.A., Marinho, P.A.C., 2006. Levantamento geológico da região ao norte da Província Carajás in: Souza. Contribuições a Geologia da Amazônia.

Feio, G.R.L., Dall'Agnol, R., Dantas, E.L., Macambira, M.J.B., Santos, J.O.S., Althoff, F.J., Soares, J.E.B., 2013. Archean granitoid magmatism in the Canaã dos Carajás area: Implications for crustal evolution of the Carajás province, Amazonian craton, Brazil. Precambrian Res 227, 157–185. https://doi.org/10.1016/j.precamres.2012.04.007

Fonseca, M.A., de Oliveira, C.G., Evangelista, H.J., 2004. The Araguaia Belt, Brazil: Part Of A Neoproterozoic Continental-Scale Strike-Slip Fault System. Journal of the Virtual Explorer 17. https://doi.org/10.3809/jvirtex.2004.00107

Fraga, L.M., Cordani, U., Maria Dreher, A., Sato, K., Joaquim Reis, N., Nadeau, S., De Roever, E., Kroonenberg, S., Camara Maurer, V., 2024. Early Orosirian belts of the central Guiana Shield, northern Amazonian Craton: U-Pb geochronology and tectonic implications. Precambrian Res 407, 107362. https://doi.org/10.1016/j.precamres.2024.107362

Freitas, G.B.F., Meira, V.T., Cioffi, C.R., Rocha, B.C., Luvizotto, G.L., Vervoort, J., da Trindade, R.I.F., 2024. Metamorphic and geochronological constraints on the final assembly of West Gondwana: an Ediacaran-Cambrian collisional setting in the northern Araguaia Orogen, central Brazil. Int Geol Rev 66, 31–53. https://doi.org/10.1080/00206814.2023.2262695

Frost, B.R., Barnes, C.G., Collins, W.J., Arculus, R.J., Ellis, D.J., Frost, C.D., 2001. A Geochemical Classification for Granitic Rocks. Journal of Petrology 42, 2033–2048. https://doi.org/10.1093/petrology/42.11.2033

Gibbs, A.K., Wirth, K.R., Hirata, W.K., OLSZEWSKI JR., W.J., 1986. AGE AND COMPOSITION OF THE GRÃO PARÁ GROUP VOLCANICS, SERRA DOS

CARAJÁS. Revista Brasileira de Geociências 16, 201–211. https://doi.org/10.25249/0375-7536.1986201211

Gioia, S.M.C.L., Pimentel, M.M., 2000. The Sm-Nd isotopic method in the Geochronology Laboratory of the University of Brasília. An Acad Bras Cienc 72, 218–245. https://doi.org/10.1590/s0001-37652000000200009

Gonçalves, G.O., Lana, C., Scholz, R., Buick, I.S., Gerdes, A., Kamo, S.L., Corfu, F., Marinho, M.M., Chaves, A.O., Valeriano, C., Nalini, H.A., 2016. An assessment of monazite from the Itambé pegmatite district for use as U–Pb isotope reference material for microanalysis and implications for the origin of the "Moacyr" monazite. Chem Geol 424, 30–50. https://doi.org/10.1016/j.chemgeo.2015.12.019

Grenholm, M., Jessell, M., Thébaud, N., 2019a. A geodynamic model for the Paleoproterozoic (ca. 2.27–1.96 Ga) Birimian Orogen of the southern West African Craton – Insights into an evolving accretionary-collisional orogenic system. Earth Sci Rev 192, 138–193. https://doi.org/10.1016/j.earscirev.2019.02.006

Griffin, W.L., Wang, X., Jackson, S.E., Pearson, N.J., O'Reilly, S.Y., Xu, X., Zhou, X., 2002. Zircon chemistry and magma mixing, SE China: In-situ analysis of Hf isotopes, Tonglu and Pingtan igneous complexes. Lithos 61, 237–269. https://doi.org/10.1016/S0024-4937(02)00082-8

Horstwood, M.S.A., Košler, J., Gehrels, G., Jackson, S.E., McLean, N.M., Paton, C., Pearson, N.J., Sircombe, K., Sylvester, P., Vermeesch, P., Bowring, J.F., Condon, D.J., Schoene, B., 2016. Community-Derived Standards for LA-ICP-MS U-(Th-)Pb Geochronology – Uncertainty Propagation, Age Interpretation and Data Reporting. Geostand Geoanal Res 40, 311–332. https://doi.org/10.1111/j.1751-908X.2016.00379.x

Hou, G., Santosh, M., Qian, X., Lister, G.S., Li, J., 2008. Configuration of the Late Paleoproterozoic supercontinent Columbia: Insights from radiating mafic dyke swarms. Gondwana Research 14, 395–409. https://doi.org/10.1016/j.gr.2008.01.010

Hurley, P M, Almeida, F.F.M., Melcher, G.C., Cordani, U.G., Rand, J., Kawashita, K., Vandoros, P., Pinson, W.H., Fairbairn, H.W., 1967. Test of continental drift by means of radiometric ages. Science (1979) 495–500.

Irvine, T.N., Baragar, W.R.A., 1971. A Guide to the Chemical Classification of the Common Volcanic Rocks. Can J Earth Sci 8, 523–548. https://doi.org/10.1139/e71-055

Jackson, Simon E., Pearson, N.J., Griffin, W.L., Belousova, E.A., 2004. The application

of laser ablation-inductively coupled plasma-mass spectrometry to in situ U-Pb zircon geochronology. Chem Geol 211, 47–69. https://doi.org/10.1016/j.chemgeo.2004.06.017

Jiang, Y.-H., Jiang, S.-Y., Ling, H.-F., Zhou, X.-R., Rui, X.-J., Yang, W.-Z., 2002. Petrology and geochemistry of shoshonitic plutons from the western Kunlun orogenic belt, Xinjiang, northwestern China: implications for granitoid geneses. Lithos 63, 165–187. https://doi.org/10.1016/S0024-4937(02)00140-8

Johansson, Å., Bingen, B., Huhma, H., Waight, T., Vestergaard, R., Soesoo, A., Skridlaite, G., Krzeminska, E., Shumlyanskyy, L., Holland, M.E., Holm-Denoma, C., Teixeira, W., Faleiros, F.M., Ribeiro, B. V., Jacobs, J., Wang, C., Thomas, R.J., Macey, P.H., Kirkland, C.L., Hartnady, M.I.H., Eglington, B.M., Puetz, S.J., Condie, K.C., 2022. A geochronological review of magmatism along the external margin of Columbia and in the Grenville-age orogens forming the core of Rodinia. Precambrian Res 371, 106463. https://doi.org/10.1016/j.precamres.2021.106463

Klein, E.L., Lopes, E.C.S., Rodrigues, J.B., Souza-Gaia, S.M., Cordani, U.G., 2020. Rhyacian and Neoproterozoic magmatic associations of the Gurupi Belt, Brazil: Implications for the tectonic evolution, and regional correlations. Geoscience Frontiers 11, 2243–2269. https://doi.org/10.1016/j.gsf.2020.02.016

Klein, E.L., Rodrigues, J.B., Lopes, E.C.S., Soledade, G.L., 2012. Diversity of Rhyacian granitoids in the basement of the Neoproterozoic-Early Cambrian Gurupi Belt, northern Brazil: Geochemistry, U–Pb zircon geochronology, and Nd isotope constraints on the Paleoproterozoic magmatic and crustal evolution. Precambrian Res 220–221, 192–216. https://doi.org/10.1016/j.precamres.2012.08.007

Knoper, M., Armstrong, R.A., Andreoli, M.A.G., Ashwal, L., 2000. The Steenkampskraal monazite vein: a subhorizontal stretching shear zone indicating extensional collapse of Namaqualand at 1033 Ma? Journal of African Earth Sciences 31, 38–38.

Kroonenberg, S. B., Roever, E.W.F. De, Fraga, L.M., Reis, N.J., Faraco, T., Lafon, J.M., Cordani, U., Wong, T.E., 2016. Paleoproterozoic evolution of the Guiana Shield in Suriname: A revised model. Geologie en Mijnbouw/Netherlands Journal of Geosciences 95, 491–522. https://doi.org/10.1017/njg.2016.10

Laurent, O., Martin, H., Moyen, J.F., Doucelance, R., 2014a. The diversity and evolution of late-Archean granitoids: Evidence for the onset of “modern-style” plate tectonics between 3.0 and 2.5Ga. Lithos 205, 208–235. https://doi.org/10.1016/j.lithos.2014.06.012

Laurent, O., Rapopo, M., Stevens, G., Moyen, J.F., Martin, H., Doucelance, R., Bosq, C., 2014b. Contrasting petrogenesis of Mg–K and Fe–K granitoids and implications for post-collisional magmatism: Case study from the Late-Archean Matok pluton (Pietersburg block, South Africa). Lithos 196–197, 131–149. https://doi.org/10.1016/j.lithos.2014.03.006

Ledru, P., Johan, V., Milési, J.P., Tegyey, M., 1994. Markers of the last stages of the Palaeoproterozoic collision: evidence for a 2 Ga continent involving circum-South Atlantic provinces. Precambrian Res 69, 169–191. https://doi.org/10.1016/0301-9268(94)90085-X

Liu, Z.-C., Wu, F.-Y., Yang, Y.-H., Yang, J.-H., Wilde, S.A., 2012. Neodymium isotopic compositions of the standard monazites used in U Th Pb geochronology. Chem Geol 334, 221–239. https://doi.org/10.1016/j.chemgeo.2012.09.034

Lu, Y.-J., Kerrich, R., Mccuaig, T.C., Li, Z.-X., Hart, C.J.R., Cawood, P.A., Hou, Z.-Q., Bagas, L., Cliff, J., Belousova, E.A., Tang, S.-H., 2013. Geochemical, Sr-Nd-Pb, and Zircon Hf-O Isotopic Compositions of Eocene-Oligocene Shoshonitic and Potassic Adakite-like Felsic Intrusions in Western Yunnan, SW China: Petrogenesis and Tectonic Implications. Journal of Petrology 54, 1309–1348. https://doi.org/10.1093/petrology/egt013

Luais, B.A., Hawkesworth, C.J., 1994. The Generation of Continental Crust: An Integrated Study of Crust-Forming Processes in the Archaean of Zimbabwe. Journal of Petrology 35, 43–94. https://doi.org/10.1093/petrology/35.1.43

Ludwig, K.R., 2003. isoplot Excell version 3.0. A geochronological toolkit for Microsoft Excel,.

Macambira, E.M.B., Ricci, P.D.F., Anjos, G.A., 2019. Geologia e recursos minerais da Folha Repartimento - SB.22-X-A. CPRM.

Macambira, E.M.B., Ricci, P.S.F., 2015. Geologia e recursos minerais da Folha Tucuruí – SA.22-Z-C, Estado do Pará, 1st ed. CPRM.

Macambira, M.J.B., Barros, C.E., Cristina, D., Silva, C., Santos, C.C., 2001. Novos dados geológicos e geocronológicos para a região ao norte da Província de Carajás ; evidências para o estabelecimento do limite Arqueano- Paleoproterozóico no sudeste do Cráton Amazônico, in: VII Simpósio de Geologia Da Amazônia. SBG, pp. 818–821.

Macambira, M.J.B., Pinheiro, V.L., Armstrong, R.A., 2007. A fronteira Arqueano-Paleoproterozoico no SE do Cráton Amazônico: abrupta no tempo, suave na

tectônica?, in: X Simpósio de Geologia Da Amazônia. pp. 97–100.

Macambira, M. J. B., Silva, D.C.C., Barros, C.E.M., Scheller, T., 2003. New isotope evidences confirming the existence of a paleoproterozoic terrain in the region at the north of the Carajas Mineral Province, in: IV South American Symposium on Isotope Geology. Salvadaro, Brazil, pp. 205–206.

Macambira, M. J. B., Silva, D.C.C., Vasquez, M.L., Barros, C.E.M., 2004. Investigação do limite Arqueano-Paleoproterozoico ao norte da Província Carajás, Amazônia Oriental, in: 42º Congresso Brasileiro de Geologia. Araxá.

Macambira, M.J.B., Teixeira, W., Vasquez, M.L., 2020. O Cráton Amazônico e suas províncias geocronológicas: o legado de Umberto Cordani., in: Geocronologia e Evolução Tectônica Do Continente Sul-Americano: A Contribuição de Umberto Giuseppe Cordani,. pp. 47–62.

Macambira, M.J.B., Vasquez, M.L., Monteiro, P.C., Armstrong, R.A., 2022. Neoarchean to Rhyacian crustal records along the Middle Xingu River area, Amazonian craton. Brazilian Journal of Geology 52. https://doi.org/10.1590/2317-4889202220220017

Macambira, M. J. B., Vasquez, M.L., Silva, D.C.C., Galarza, M.A., Barros, C.E.M., Camelo, J.F., 2009. Crustal growth of the central-eastern Paleoproterozoic domain, SW Amazonian craton: Juvenile accretion vs. reworking. J South Am Earth Sci 27, 235–246. https://doi.org/10.1016/j.jsames.2009.02.001

Machado, N., Lindenmayer, Z., Krogh, T.E., Lindenmayer, D., 1991. U-Pb geochronology of Archean magmatism and basement reactivation in the Carajás area, Amazon shield, Brazil. Precambrian Res 49, 329–354. https://doi.org/10.1016/0301-9268(91)90040-H

Magalhães, L.B., Macambira, M.J.B., Macambira, E.M.B., dos Santos Freire Ricci, P., 2023. Crustal growth in the northeast portion of the Rhyacian Bacajá Domain, SE Amazonian craton, based on U-Pb, Lu-Hf, and Sm-Nd data. Brazilian Journal of Geology 53. https://doi.org/10.1590/2317-4889202320220068

Marangoanha, B., de Oliveira, D.C., Dall'Agnol, R., 2019. The Archean granulite-enderbite complex of the northern Carajás province, Amazonian craton (Brazil): Origin and implications for crustal growth and cratonization. Lithos 350–351, 105275. https://doi.org/10.1016/j.lithos.2019.105275

McDonough, W.F., Sun, S. -s., 1995. The composition of the Earth. Chem Geol 120, 223–253. https://doi.org/10.1016/0009-2541(94)00140-4

Meert, J.G., 2012. What's in a name? The Columbia (Paleopangaea/Nuna)

supercontinent. Gondwana Research 21, 987–993. https://doi.org/10.1016/j.gr.2011.12.002

Meert, J.G., 2002. Paleomagnetic Evidence for a Paleo-Mesoproterozoic Supercontinent Columbia. Gondwana Research 5, 207–215. https://doi.org/10.1016/S1342-937X(05)70904-7

Meert, J.G., Santosh, M., 2017. The Columbia supercontinent revisited. Gondwana Research 50, 67–83. https://doi.org/10.1016/j.gr.2017.04.011

Melo, G.H.C., Monteiro, L.V.S., Xavier, R.P., Moreto, C.P.N., Santiago, E.S.B., Dufrane, S.A., Aires, B., Santos, A.F.F., 2017. Temporal evolution of the giant Salobo IOCG deposit, Carajás Province (Brazil): constraints from paragenesis of hydrothermal alteration and U-Pb geochronology. Miner Depos 52, 709–732. https://doi.org/10.1007/s00126-016-0693-5

Milhomem, J.M.N., Lafon, J.M., 2019. Zircon U-Pb and Lu-Hf isotope constraints on Archean crustal evolution in Southeastern Guyana Shield. Geoscience Frontiers 10, 1477–1506. https://doi.org/10.1016/j.gsf.2018.09.012

Milhomem-Neto, J.M., Lafon, J.-M., 2020. Crustal growth and reworking of Archean crust within the Rhyacian domains of the southeastern Guiana Shield, Brazil: Evidence from zircon U–Pb–Hf and whole-rock Sm–Nd geochronology. J South Am Earth Sci 103, 102740. https://doi.org/10.1016/j.jsames.2020.102740

Monteiro, P.C., 2006. Investigação do limite entre os domínios geocronológicos da região do Médio Xingu, Sudeste do Cráton Amazônico.

Motta, J.G., Filho, C.R. de S., Carranza, E.J.M., Braitenberg, C., 2019. Archean crust and metallogenic zones in the Amazonian Craton sensed by satellite gravity data. Sci Rep 9. https://doi.org/10.1038/s41598-019-39171-9

Murphy, M.A., Salvador, A., 1999. International Subcommission on Stratigraphic Classification of IUGS, International Commission on Stratigraphy; International stratigraphic guide; an abridged version. Episodes 22, 255–271.

Nance, R.D., Murphy, J.B., Santosh, M., 2014. The supercontinent cycle: A retrospective essay. Gondwana Research 25, 4–29. https://doi.org/10.1016/j.gr.2012.12.026

Nebel, O., Nebel-Jacobsen, Y., Mezger, K., Berndt, J., 2007. Initial Hf isotope compositions in magmatic zircon from early Proterozoic rocks from the Gawler Craton, Australia: A test for zircon model ages. Chem Geol 241, 23–37. https://doi.org/10.1016/j.chemgeo.2007.02.008

Neri, A. S. S., Dantas, E. L., Peixoto, E. I. N., Fuck, R. A., Feio, G. R. L.; Luvizotto, G.

L., Silva, A. C, Almeida, J. A. C., 2025. Filling the missing gap of high-pressure granulite metamorphism in the Amazonian Craton. Terra Nova, *in press.*

Nogueira, A.C.R., Truckenbrodt, W., Pinheiro, R.V.L., 1995. Formação Águas Claras, Pré- Cambriano da Serra dos Carajás. Redescrição e redefinição. Boletim do Museu Paraense Emílio Goeldi, 177–197.

Parra-Avila, L.A., Baratoux, L., Eglinger, A., Fiorentini, M.L., Block, S., 2019. The Eburnean magmatic evolution across the Baoulé-Mossi domain: Geodynamic implications for the West African Craton. Precambrian Res 332, 105392. https://doi.org/10.1016/j.precamres.2019.105392

Parra-Avila, L.A., Belousova, E., Fiorentini, M.L., Eglinger, A., Block, S., Miller, J., 2018. Zircon Hf and O-isotope constraints on the evolution of the Paleoproterozoic Baoulé-Mossi domain of the southern West African Craton. Precambrian Res 306, 174–188. https://doi.org/10.1016/j.precamres.2017.12.044

Parra-Avila, L.A., Kemp, A.I.S., Fiorentini, M.L., Belousova, E., Baratoux, L., Block, S., Jessell, M., Bruguier, O., Begg, G.C., Miller, J., Davis, J., McCuaig, T.C., 2017. The geochronological evolution of the Paleoproterozoic Baoulé-Mossi domain of the Southern West African Craton. Precambrian Res 300, 1–27. https://doi.org/10.1016/j.precamres.2017.07.036

Patchett, P.J., Tatsumoto, M., 1980. Hafnium isotope variations in oceanic basalts. Geophys Res Lett 7, 1077–1080. https://doi.org/10.1029/GL007i012p01077

Paton, C., Hellstrom, J., Paul, B., Woodhead, J., Hergt, J., 2011. Iolite: Freeware for the visualisation and processing of mass spectrometric data. J Anal At Spectrom 26, 2508–2518. https://doi.org/10.1039/c1ja10172b

Pearce, J.A., Harris, N.B.W., Tindle, A.G., 1984. Trace Element Discrimination Diagrams for the Tectonic Interpretation of Granitic Rocks. Journal of Petrology 25, 956–983. https://doi.org/10.1093/petrology/25.4.956

Perret, J., Jessell, M.W., Masurel, Q., Hayman, P.C., Thébaud, N., Baratoux, L., Kouamélan, A., Eglinger, A., André-Mayer, A.-S., Koffi, A.Y., Dia, I., Koné, J., Davis, J., Wane, O., Amponsah, P.O., Naba, S., Vanderhaeghe, O., 2025. Review of Paleoproterozoic tectonics in the southern West African Craton: Insights from multi-disciplinary data integration. Precambrian Res 422, 107707. https://doi.org/10.1016/j.precamres.2025.107707

Petersson, A., Scherstén, A., Gerdes, A., 2018. Extensive reworking of Archaean crust within the Birimian terrane in Ghana as revealed by combined zircon U-Pb and Lu-

Hf isotopes. Geoscience Frontiers 9, 173–189. https://doi.org/10.1016/j.gsf.2017.02.006

Petersson, A., Scherstén, A., Kemp, A.I.S., Kristinsdóttir, B., Kalvig, P., Anum, S., 2016. Zircon U–Pb–Hf evidence for subduction related crustal growth and reworking of Archaean crust within the Palaeoproterozoic Birimian terrane, West African Craton, SE Ghana. Precambrian Res 275, 286–309. https://doi.org/10.1016/j.precamres.2016.01.006

Petri, S., Coimbra, A.M., Amaral, G., Ojeda, H.A.O., Fúlfaro, V.J., Ponçano, W.L., 1986. Código Brasileiro de Nomenclatura Estratigráfica Guia de Nomenclatura Estratigráfica. Revista Brasileira de Geociências 16, 370–415.

Petrus, J.A., Kamber, B.S., 2012. VizualAge: A Novel Approach to Laser Ablation ICP-MS U-Pb Geochronology Data Reduction. Geostand Geoanal Res 36, 247–270. https://doi.org/10.1111/j.1751-908X.2012.00158.x

Pidgeon, R.T., Macambira, M.J.B., Lafon, J.-M., 2000. Th–U–Pb isotopic systems and internal structures of complex zircons from an enderbite from the Pium Complex, Carajás Province, Brazil: evidence for the ages of granulite facies metamorphism and the protolith of the enderbite. Chem Geol 166, 159–171. https://doi.org/10.1016/S0009-2541(99)00190-4

Piechocka, A.M., Gregory, C.J., Zi, J.-W., Sheppard, S., Wingate, M.T.D., Rasmussen, B., 2017. Monazite trumps zircon: applying SHRIMP U–Pb geochronology to systematically evaluate emplacement ages of leucocratic, low-temperature granites in a complex Precambrian orogen. Contributions to Mineralogy and Petrology 172, 63. https://doi.org/10.1007/s00410-017-1386-5

Rajesh, H.M., Santosh, M., Yoshikura, S., 2011. The Nagercoil Charnockite: a Magnesian, Calcic to Calc-alkalic Granitoid Dehydrated during a Granulite-facies Metamorphic Event. Journal of Petrology 52, 375–400. https://doi.org/10.1093/petrology/egq084

Regelous, A., Scharfenberg, L., De Wall, H., 2021. Origin of S-, A- and I-Type Granites: Petrogenetic Evidence from Whole Rock Th/U Ratio Variations. Minerals 11, 672. https://doi.org/10.3390/min11070672

Ribeiro-Silva, L., Oliveira, D.C., Toro, M.A.G., do Nascimento, A.C., Marangoanha, B., Marques, G.T., 2023. Zircon U–Pb–Hf isotope and geochemical constraints on the petrogenesis and tectonic setting of Mesoarchean granitoids from the Carajás province, Amazonian craton, Brazil. Precambrian Res 398, 107204.

https://doi.org/10.1016/j.precamres.2023.107204

Rino, S., Komiya, T., Windley, B.F., Katayama, I., Motoki, A., Hirata, T., 2004. Major episodic increases of continental crustal growth determined from zircon ages of river sands; implications for mantle overturns in the Early Precambrian. Physics of the Earth and Planetary Interiors 146, 369–394. https://doi.org/10.1016/j.pepi.2003.09.024

Roberts, N.M.W., Spencer, C.J., 2015. The zircon archive of continent formation through time. Geological Society, London, Special Publications 389, 197–225. https://doi.org/10.1144/SP389.14

Rogers, J.J.W., Santosh, M., 2002. Configuration of Columbia, a Mesoproterozoic Supercontinent. Gondwana Research 5, 5–22. https://doi.org/10.1016/S1342-937X(05)70883-2

Rosa-Costa, L.T., Chaves, C.L., Klein, E.L., 2014. Geologia e recursos minerais da folha Rio Araguari-NA. 22-YB: estado do Amapá. CPRM.

Rosa-Costa, Lúcia T, Lafon, J.M., Delor, C., 2006. Zircon geochronology and Sm-Nd isotopic study: Further constraints for the Archean and Paleoproterozoic geodynamical evolution of the southeastern Guiana Shield, north of Amazonian Craton, Brazil. Gondwana Research 10, 277–300. https://doi.org/10.1016/j.gr.2006.02.012

Rosa-Costa, Lúcia T., Lafon, J.M., Delor, C., 2006. Zircon geochronology and Sm–Nd isotopic study: Further constraints for the Archean and Paleoproterozoic geodynamical evolution of the southeastern Guiana Shield, north of Amazonian Craton, Brazil. Gondwana Research 10, 277–300. https://doi.org/10.1016/j.gr.2006.02.012

Rosa-Costa, L.T., Lafon, J.-M., Milhomem Neto, J.M., Pinto, J.A.E., 2025. An overview of Rhyacian continental magmatic arcs of the southeastern Guiana Shield, Amazonian Craton. J South Am Earth Sci 159, 105504. https://doi.org/10.1016/j.jsames.2025.105504

Rosa-Costa, L.T., Ricci, P., Lafon, J., Vazquez, M.L., Carvalho, J., Klein, E., Macambira, E., 2003. Geology and geochronology of Archean and Paleoproterozoic domains of southwestern Amapa and northwestern Para, Brazil, southeastern Guiana shield. Géologie de la France 101–120.

Russell, W.A., Papanastassiou, D.A., Tombrello, T.A., 1978. Ca isotope fractionation on the Earth and other solar system materials. Geochim Cosmochim Acta 42, 1075–

1090. https://doi.org/10.1016/0016-7037(78)90105-9

Saboia, A.M., Gouveia de Oliveira, C., Dantas, E.L., Scandolara, J.E., Cordeiro, P., Rodrigues, J.B., Cordeiro de Sousa, I.M., 2020. The 2.26 to 2.18 Ga Arc-Related Magmatism of the Almas-Conceição do Tocantins Domain: An Early Stage of the São Francisco Paleocontinent Assembly in Central Brazil. J South Am Earth Sci 104, 102757. https://doi.org/10.1016/j.jsames.2020.102757

Santos, J.O.S., 2003. Geotectônica dos Escudos das Guianas e Brasil-Central. Geologia, Tectônica e Recursos Minerais do Brasil.

Santos, J.O.S., Hartmann, L.A., Faria, M.S., Riker, S.R., Miguel, M., Almeida, M.E., Mcnaughton, N.J., 2006. a Compartimentação Do Cráton Amazonas Em Províncias : Avanços Ocorridos No Período 2000-2006, in: IX Simpósio de Geologia Da Amazônica. Sociedade Brasileira de Geologia, Belém.

Santos, R.F.S., Oliveira, D.C. de, Marangoanha, B., Galarza, M.A., Santos, M.R., 2023. Geochemistry, zircon U-Pb geochronology and Lu-Hf isotopes of the Manda Saia granite: Petrological affinity and magma source of evolved A-type granites from the Carajás province, southeastern Amazonian craton, Brazil. Lithos 462–463, 107412. https://doi.org/10.1016/j.lithos.2023.107412

Sardinha, A.S., Barros, C.E. de M., Krymsky, R., 2006. Geology, geochemistry, and U–Pb geochronology of the Archean (2.74Ga) Serra do Rabo granite stocks, Carajás Metallogenetic Province, northern Brazil. J South Am Earth Sci 20, 327–339. https://doi.org/10.1016/j.jsames.2005.11.001

Sato, K., Tassinari, C.C.G., Basei, M.A.S., Siga Júnior, O., Onoe, A.T., Souza, M.D. de, 2014. Sensitive High Resolution Ion Microprobe (SHRIMP IIe/MC) of the Institute of Geosciences of the University of São Paulo, Brazil: analytical method and first results. Geologia USP. Série Científica 14, 3–18. https://doi.org/10.5327/Z1519-874X201400030001

Schutesky, M.E., de Oliveira, C.G., 2020. From the roots to the roof: An integrated model for the Neoarchean Carajás IOCG System, Brazil. Ore Geol Rev 127, 103833. https://doi.org/10.1016/j.oregeorev.2020.103833

Silva, A.S., 2021. Metamorfismo de UHT e HP no Domínio Bacajá, Cráton do Amazonas (Master's dissertation). Universidade de Brasília, Brasília.

Silva, M.A.D., Monteiro, L.V.S., Santos, T.J.S., Moreto, C.P.N., Sousa, S.D., Faustinoni, J.M., Melo, G.H.C., Xavier, R.P., Toledo, B.A.M., 2021. Mesoarchean migmatites of the Carajás Province: From intra-arc melting to collision. Lithos 388–389, 106078.

https://doi.org/10.1016/j.lithos.2021.106078

Sláma, J., Košler, J., Condon, D.J., Crowley, J.L., Gerdes, A., Hanchar, J.M., Horstwood, M.S.A., Morris, G.A., Nasdala, L., Norberg, N., Schaltegger, U., Schoene, B., Tubrett, M.N., Whitehouse, M.J., 2008. Plešovice zircon — A new natural reference material for U–Pb and Hf isotopic microanalysis. Chem Geol 249, 1–35. https://doi.org/10.1016/j.chemgeo.2007.11.005

Söderlund, U., Patchett, P.J., Vervoort, J.D., Isachsen, C.E., 2004. The 176Lu decay constant determined by Lu–Hf and U–Pb isotope systematics of Precambrian mafic intrusions. Earth Planet Sci Lett 219, 311–324. https://doi.org/10.1016/S0012-821X(04)00012-3

Souza, V.S., Macambira, M.J.B., Kotschoubey, B., 2003. Idade de zircão do granito Felício Turvo, graimpo de ouro do Manelão, região do Bacajá (PA): implicações tectônicas, in: VIII Simpósio de Geologia Da Amazônia.

Souza, Z.S., Dall"Agnol, R., Althoff, F.J., Leite, A.A.S., 1996. Carajás Mineral Province: geological, geochronological and tectonic contrasts on the Archean evolution of the Rio Maria granite – greenstone terranes and the Carajás Block., in: Symposium Archaean Terranes of the South American Platform. SBG, Brasília, pp. 31–32.

Stacey, J.S., Kramers, J.D., 1975. Approximation of terrestrial lead isotope evolution by a two-stage model. Earth Planet Sci Lett 26, 207–221. https://doi.org/10.1016/0012-821X(75)90088-6

Tassinari, C.C.G., Macambira, M.J.B., 2004. A evolução tectônica do Craton Amazônico, in: Mantesso-Neto, V., Bartorelli, A., Carneiro, C.D.R., Brito Neves, B.B. (Eds.), Geologia Do Continente Sul Americano: Evoluc¸ Ão Da Obra de Fernando Flávio Marques Almeida. São Paulo, pp. 471–486.

Tavares, F.M., Trouw, R.A.J., da Silva, C.M.G., Justo, A.P., Oliveira, J.K.M., 2018. The multistage tectonic evolution of the northeastern Carajás Province, Amazonian Craton, Brazil: Revealing complex structural patterns. J South Am Earth Sci 88, 238–252. https://doi.org/10.1016/j.jsames.2018.08.024

Teixeira, J.B.G., Eggler, D.H., 1994. Petrology, geochemistry, and tectonic setting of Archean basaltic and dioritic rocks from the N4 iron deposit, Serra dos Carajás, Pará, Brazil. Acta Geologica Leopoldensia. 17, 71–114.

Teixeira, M.F.B., Dall'Agnol, R., Santos, J.O.S., Kemp, A., Evans, N., 2019. Petrogenesis of the Paleoproterozoic (Orosirian) A-type granites of Carajás Province, Amazon Craton, Brazil: Combined in situ Hf O isotopes of zircon. Lithos 332–333,

1–22. https://doi.org/10.1016/j.lithos.2019.01.024

Teixeira, M.F.B., Dall'Agnol, R., Schneider Santos, J.O., Carvalho de Oliveira, D., Lamarão, C.N., McNaughton, N.J., 2018. Crystallization ages of Paleoproterozoic A-type granites of Carajás province, Amazon craton: Constraints from U-Pb geochronology of zircon and titanite. J South Am Earth Sci 88, 312–331. https://doi.org/10.1016/j.jsames.2018.08.020

Thirlwall, M.F., Anczkiewicz, R., 2004. Multidynamic isotope ratio analysis using MC–ICP–MS and the causes of secular drift in Hf, Nd and Pb isotope ratios. Int J Mass Spectrom 235, 59–81. https://doi.org/10.1016/j.ijms.2004.04.002

Toledo, P.I. de F., Moreto, C.P.N., Monteiro, L.V.S., de Melo, G.H.C., Matos, F.M.V., Xavier, R.P., Carvalho, J.A., Filho, C.A.M., Navarro, M.S., de Carvalho Lana, C., 2023. Breaking up the temporal link between granitic magmatism and iron oxide-copper–gold (IOCG) deposits in the Carajás Mineral Province, NW Brazil. Miner Depos. https://doi.org/10.1007/s00126-023-01224-5

Trunfull, E.F., Hagemann, S.G., Xavier, R.P., Moreto, C.P.N., 2020. Critical assessment of geochronological data from the Carajás Mineral Province, Brazil: Implications for metallogeny and tectonic evolution. Ore Geol Rev 121. https://doi.org/10.1016/j.oregeorev.2020.103556

Vanderhaeghe, O., Ledru, P., Thiéblemont, D., Egal, E., Cocherie, A., Tegyey, M., Milési, J.-P., 1998. Contrasting mechanism of crustal growth. Precambrian Res 92, 165–193. https://doi.org/10.1016/S0301-9268(98)00074-6

Vasquez, M. L., 2006. Geocronologia em zircão, monazita e granada e isótopos de Nd das associações litológicas da porção oeste do Domínio Bacajá: evolução crustal da porção meridional da Província Maroni-Itacaiúnas – Sudeste Do Cráton Amazônico. Universidade Federal do Pará.

Vasquez, M.L., Macambira, M.J.B., Armstrong, R.A., 2008. Zircon geochronology of granitoids from the western Bacajá Domain, southeastern Amazonian craton, Brazil: Neoarchean to Orosirian evolution. Precambrian Res 161, 279–302. https://doi.org/10.1016/j.precamres.2007.09.001

Vasquez, M.L., Macambira, M.J.B., Galarza, M.A., 2005. Granitoides Transamazônicos da região Iriri-Xingu, Pará – novos dados geológicos e geocronológicos, in: Contribuições a Geologia Da Amazônia. CPRM, p. 16.

Vasquez, M L.;, Rosa-Costa, L.T.;, 2008. Geologia e Recursos Minerais do Estado do Pará : Sistema de Informações Geográficas – SIG : texto explicativo dos mapas

Geológico e Tectônico e de Recursos Minerais do Estado do Pará, 1st ed. Brazilian Geological Service, CPRM.

Verma, S.P., Pandarinath, K., Verma, S.K., Agrawal, S., 2013. Fifteen new discriminant-function-based multi-dimensional robust diagrams for acid rocks and their application to Precambrian rocks. Lithos 168–169, 113–123. https://doi.org/10.1016/j.lithos.2013.01.014

Vianna, S.Q., Lafon, J.M., Milhomem Neto, J.M., Silva, D.P.B., Barros, C.E. de M., 2020. U–Pb geochronology, Nd–Hf isotopes, and geochemistry of Rhyacian granitoids from the Paleoproterozoic Lourenço domain (Brazil), southeastern Guiana Shield. J South Am Earth Sci 104, 102937. https://doi.org/10.1016/j.jsames.2020.102937

Vieira, C., Amaral, W., Holanda Santos, F., 2022a. Petrography, geochemistry and zircon U-Pb geochronology of the Siderian-Rhyacian granitoids of NW Bacajá Domain, Amazonian Craton. Journal of the Geological Survey Of Brazil 5. https://doi.org/10.29396/jgsb.2022.v5.n3.1

Volante, S., Kirscher, U., 2024. Metamorphic turnover at 2 Ga related to two-stage assembly of Columbia. Sci Rep 14, 6483. https://doi.org/10.1038/s41598-024-56691-1

Wane, O., Liégeois, J.-P., Thébaud, N., Miller, J., Metelka, V., Jessell, M., 2018. The onset of the Eburnean collision with the Kenema-Man craton evidenced by plutonic and volcanosedimentary rock record of the Masssigui region, southern Mali. Precambrian Res 305, 444–478. https://doi.org/10.1016/j.precamres.2017.11.008

Wirth, K.R., Gibbs. A. K., Olszewski Jr, W.J., 1986. U-Pb zircon ages of the Grão Pará group and Serra dos Carajás granite, Pará, Brazil. . Revista Brasileira de Geociências 16, 195–200.

Whitney, D.L. and Evans, B.W. 2010. Abbreviations for names of rock-forming minerals. American Mineralogist, 95, 185–187, https://doi.org/10.2138/am.2010.3371

Wu, G., Yang, S., Meert, J.G., Xiao, Y., Chen, Y., Wang, Z., Li, X., 2020. Two phases of Paleoproterozoic orogenesis in the Tarim Craton: Implications for Columbia assembly. Gondwana Research 83, 201–216. https://doi.org/10.1016/j.gr.2020.02.009

Zhao, G., Cawood, P.A., Wilde, S.A., Sun, M., 2002. Review of global 2.1-1.8 Ga orogens: Implications for a pre-Rodinia supercontinent. Earth Sci Rev 59, 125–162. https://doi.org/10.1016/S0012-8252(02)00073-9

Zhao, G., Sun, M., Wilde, S.A., Li, S., 2004. A Paleo-Mesoproterozoic supercontinent: assembly, growth and breakup. Earth Sci Rev 67, 91–123. https://doi.org/10.1016/j.earscirev.2004.02.003

Zhao, K., Xu, X., Klemd, R., He, Z., Zhang, X., 2023. A review of the genetic mechanisms generating igneous charnockite: CO2 flushing and crystal-melt segregation in mushy reservoirs. Earth Sci Rev 237, 104295. https://doi.org/10.1016/j.earscirev.2022.104295

SUPPLEMENTARY MATERIAL 1 – GEOCHEMICAL DATA

Table S 1 - Whole-rock geochemical data for the studied granitoids and charnockites.

Sample	AA-05	AA-123	AA-03C	AA-125	AA-03A	AA-76	AA-52	AA-12	AA-45	AA-58	AA-63A	AA-16	AA-46	AA60	AA-21	AA-19	AA-13	AA-23	AA-61	AA-14A
Unit	Bandeirante granite					Alto Rio Preto granite														
Variety	AMzG	BGrd	BMzG	ABSG	LMzG	ABGrd	ABGrd	ABMzG	BMzG	BMzG	BMzG	BTn	BGrd	BMzG	ABMzG	BGrd	ABMzG	BSG	BSG	BSG
SiO_2	66.7	66.8	74.8	76.2	76.8	67	67.4	67.9	70.2	70.3	71.2	72.1	72.2	72.5	73.1	73.3	73.4	74.2	75.9	76.1
TiO_2	0.42	0.39	0.15	0.16	0.15	0.66	0.55	0.37	0.44	0.42	0.34	0.28	0.26	0.3	0.35	0.29	0.38	0.18	0.13	0.2
Al_2O_3	14.8	15.95	12.85	12.95	13.25	14.65	14.3	17.2	14.3	14.3	15.2	14.9	14.55	14.25	13.85	14.85	14.3	12.95	12.9	13.4
FeOt	4.47	3.91	1.69	1.78	1.06	4.71	3.91	2.80	3.34	3.56	2.59	2.59	2.07	2.06	2.47	2.29	2.80	1.58	1.46	2.34
MnO	0.1	0.1	0.05	0.04	0.02	0.07	0.06	0.05	0.06	0.02	0.03	0.02	0.03	0.03	0.06	0.04	0.06	0.04	0.03	0.03
MgO	1.41	0.73	0.26	0.32	0.34	1.78	1.38	0.8	1.18	1.4	0.59	0.98	0.49	0.7	0.87	0.51	0.95	0.3	0.24	0.55
CaO	2.93	2.72	1	1.13	1.89	3.35	3.01	3.63	2.41	2.28	2.06	2.43	2.18	2.1	2.21	2.52	2.5	1.16	1.12	1.32
Na_2O	3.71	5.12	3.44	3.36	3.02	3.21	3.13	3.82	3.52	3.33	3.81	4.2	4.07	3.7	2.96	4.03	3.18	3.32	3.44	3.47
K_2O	4.41	1.83	4.25	4.45	3.82	3.38	3.9	3.81	3.6	3.41	4.52	2.5	3.12	3.62	4.44	2.81	4.32	4.45	4.51	4.27
P_2O_5	0.17	0.11	0.03	0.03	0.02	0.17	0.14	0.1	0.15	0.11	0.08	0.07	0.06	0.03	0.09	0.04	0.1	0.04	0.03	0.05
LOI	0.84	0.9	0.79	0.61	1.05	0.94	0.94	0.69	0.82	0.6	0.45	0.83	0.67	0.89	0.95	0.9	0.79	0.6	0.53	0.63
Total	100.71	99.02	99.54	101.28	101.74	100.6	99.35	101.74	100.54	100.38	101.33	101.34	100.1	100.55	101.79	101.98	>102.00	99.12	100.55	>102.00
Ba	1560	122.5	311	401	1360	996	1305	1775	1045	1700	1080	865	1100	796	1175	898	1155	919	802	782
Rb	96.2	101.5	344	249	128.5	128	147.5	112.5	161	135	123	113	121	110	135	100.5	157.5	195.5	134	163.5
Sr	456	99.5	88.5	123	361	321	352	465	311	402	340	380	449	336	291	393	298	178.5	155.5	259
Zr	352	296	122	106	116	250	242	256	181	171	187	187	175	176	150	192	145	143	111	140
Nb	7.63	14.4	11.9	5.58	2.87	11.95	9.72	7.49	9.5	9.72	7.15	8.1	8.48	6.06	5.49	10.2	5.97	8.21	3.03	6.72
Y	60.9	18.5	58.5	72.1	4.6	30.8	19.6	24.7	22.1	3.1	6.8	2.8	12.4	4.9	12	20.2	11.5	14	23.5	5.2
Hf	9.05	9.08	4.29	3.39	3.43	6.31	6.38	6.59	4.94	4.17	5.13	4.78	4.75	4.94	4.03	5.37	3.99	4.57	3.44	4.1
Ta	1	1.1	1.7	0.3	0.4	0.8	0.7	0.8	0.9	0.7	0.6	1.1	1.2	0.5	0.4	0.6	0.8	0.8	0.4	0.5
Ga	18	25.3	20	18	13.6	19.6	18.3	19.8	20.6	18.2	18.3	18.4	19.6	16.6	16.2	17.9	16.1	14.4	16.3	16.5
Cs	1.1	2.12	4.98	0.62	1.47	1.76	1.38	1.44	2.94	2.09	1.37	2.13	1.45	0.72	0.89	1.05	1.66	1.99	1.68	1.16
Sn	11.6	2.1	3.3	0.7	1.2	2	2.6	1.7	2.2	3	1.3	2.8	1.5	1.4	1.3	0.9	1.7	2.5	1.8	0.8

Th	17.05	46.2	34.4	8.64	8.39	22.3	25.9	16.5	13.6	24.6	22.4	12.55	25.6	43.8	5.24	34.8	18.6	25.3	14.8	38.2
U	4.18	4.01	7.32	2.99	1.17	1.41	1.53	1.45	2.37	0.78	1.76	1.2	3.25	3.93	1.19	2.73	2	3.69	3.84	8.12
V	63	31	13	16	14	75	54	36	48	40	32	25	14	26	32	15	38	11	15	19
Cr	59	41	51	50	10	26	30	12	30	73	16	54	12	53	68	9	38	9	9	137
La	82.7	83.5	52.9	33.8	16.2	82.7	80.6	68.1	53.1	51.8	45.5	32.1	48.7	42.5	30.4	67.9	42.4	46	64.1	27.6
Ce	181.5	160	77.2	54.8	32.2	166	159	122.5	98.6	96.6	79.6	58.7	88.7	79.5	51.9	125	82.1	82.2	72.9	54.9
Pr	22.6	16.15	12.4	7.63	2.59	18.2	16.45	13.6	11.4	10.35	7.84	5.99	9.07	8.39	5.36	13.45	8.84	8.63	12.1	5.84
Nd	92	54	49.9	30.7	7.7	65.1	57.9	50.6	37.9	35.5	26.3	19.7	30.2	28	18.6	45.6	30.1	28.7	40.7	21.1
Sm	17.2	7.76	11.5	7.01	0.79	11.7	9.35	8.76	7.32	5.66	3.17	3.21	4.57	3.69	3.01	7.78	4.43	4.53	6.32	3.36
Eu	2.57	0.33	0.69	0.84	0.87	1.3	1.22	1.49	1.12	0.86	0.99	0.7	0.9	0.68	1.05	0.95	1.03	0.66	1.47	0.67
Gd	16.55	5.59	11.55	10	0.55	9.26	6.49	6.79	5.51	3.85	1.99	2.06	3.49	2.16	2.46	5.65	3.25	3.28	5.02	2.24
Tb	2.03	0.69	1.66	1.44	0.07	1.2	0.78	0.93	0.89	0.32	0.21	0.2	0.5	0.21	0.3	0.68	0.39	0.46	0.75	0.23
Dy	12.3	3.48	9.67	9.59	0.53	6.91	4.21	5.28	4.52	0.99	0.97	0.66	2.34	1.08	1.62	3.51	2.17	2.84	3.64	1.07
Ho	2.22	0.63	1.95	2.18	0.09	1.21	0.72	0.83	0.86	0.12	0.21	0.1	0.5	0.18	0.32	0.68	0.42	0.5	0.78	0.18
Er	5.76	1.7	5.64	6.23	0.28	2.97	1.84	2.49	2.18	0.17	0.59	0.16	1.02	0.48	0.71	2.14	1.13	1.36	2.22	0.57
Tm	0.82	0.23	0.78	0.8	0.02	0.37	0.25	0.3	0.25	0.02	0.05	<0.01	0.14	0.06	0.12	0.37	0.11	0.18	0.32	0.05
Yb	4.91	1.46	4.75	4.73	0.37	2.48	1.72	1.88	1.42	0.13	0.58	0.17	0.73	0.45	0.62	2.44	1.05	1.38	1.81	0.46
Lu	0.6	0.12	0.55	0.66	0.03	0.31	0.23	0.25	0.2	0.01	0.12	0.03	0.12	0.06	0.09	0.41	0.12	0.17	0.24	0.09
ΣREE	443.8	335.6	241.1	170.4	62.3	369.7	340.8	283.8	225.3	206.4	168.1	123.8	191.0	167.4	116.6	276.6	177.5	180.9	212.4	118.4
ΣLREE	398.57	321.74	204.59	134.78	60.35	345	324.52	265.05	209.44	200.77	163.4	120.4	182.14	162.76	110.32	260.68	168.9	170.72	197.59	113.47
(La/Yb)n	11.4	38.6	7.5	4.8	29.5	22.5	31.6	24.4	25.2	268.6	52.9	127.3	45.0	63.7	33.1	18.8	27.2	22.5	23.9	40.5
Eu/Eu*	0.47	0.15	0.18	0.31	4.04	0.38	0.48	0.59	0.54	0.56	1.21	0.83	0.69	0.74	1.18	0.44	0.83	0.52	0.80	0.75
Mg#	36	25	22	24	36	40	39	34	39	41	29	40	30	38	39	28	38	25	23	30

Table S 1 cont - Whole-rock geochemical data for the studied granitoids and charnockites.

Sample	AA-119A	AA-102	AA-06A	AA-08D	AA-109	AA-09	AA-08A	AA-97	AA-08B	AA-15A	AA-20	AA-130	AA-02	AA-49	AA-128	AA-132	AA-54A	AA-146	AA-11	AA-22	AA-58	AA-141	AA-53
Unit	Maravilha charnockite									Serra Azul charnockite							Bernardino granite						
Variety	BAQSn	BAQMzn	ABSG	PABMzG	PABGrd	FPASG	ASG	BAMzG	PBMzG	ABTn	PABTn	PBGrd	PBGrd	PABGrd	BMzG	PABGrd	BGrd	MBMzg	BMzg	BMzg	BMzG	BMzg	MBMzg
SiO_2	62.1	65.7	66.8	68.3	69.9	70	72.8	75.3	76.9	58.5	60.4	66.2	66.3	70.3	70.5	72.4	64.1	67.8	69.1	70.3	70.3	71.1	71.4
TiO_2	0.3	0.52	0.61	0.43	0.44	0.51	0.27	0.24	0.23	0.87	0.82	0.37	0.66	0.56	0.43	0.2	0.55	0.68	0.89	0.43	0.42	0.29	0.33
Al_2O_3	19.3	17.55	14.15	14.25	15.25	14.7	13.65	13.7	13.75	14.8	16	15.8	16.6	14	14.55	14.85	16.5	15.7	14.15	14.65	14.3	15.55	13.95
FeOt	2.94	3.65	3.62	3.46	3.89	3.95	2.35	2.11	1.96	7.52	6.51	4.15	4.67	4.34	3.64	2.15	4.96	4.64	4.71	4.36	3.56	2.92	3.18
MnO	0.05	0.05	0.06	0.06	0.07	0.06	0.03	0.03	0.04	0.13	0.11	0.06	0.08	0.05	0.06	0.04	0.02	0.06	0.06	0.08	0.02	0.06	0.06
MgO	0.71	0.5	1.02	1.02	1.12	0.43	0.22	0.2	0.47	4.58	2.76	1.15	1.22	1.65	1.25	0.75	2.22	1.52	1.03	1.56	1.4	0.89	1.08
CaO	3.13	3.54	2.25	3.09	3.49	2.3	1.5	2.17	1.79	6.35	5	4.05	3.96	2.36	2.17	2.61	3.12	2.31	2.2	1.62	2.28	2.48	1.87
Na_2O	4.23	3.47	2.8	3.46	3.54	3.18	3.01	2.85	3.53	2.39	3.84	4.44	4.25	3.16	3.25	3.75	4.18	2.94	2.65	2.64	3.33	3.83	3.13
K_2O	5.96	4.9	5.05	3.33	3.04	5.73	5.82	4.29	4.2	1.58	2.01	1.64	2.64	3.24	4.24	2.86	2.42	3.58	4.53	3.35	3.41	2.9	3.05
P_2O_5	0.1	0.14	0.19	0.11	0.1	0.15	0.06	0.04	0.05	0.28	0.25	0.18	0.2	0.03	0.15	0.08	0.29	0.08	0.33	0.04	0.11	0.04	0.06
LOI	1.5	1.12	0.95	0.59	0.46	0.14	0.8	0.52	0.57	1.55	1.65	1.15	0.68	0.96	0.81	0.88	1.39	0.98	1.02	1.95	0.6	0.93	1.45
Total	100.97	101.99	98.1	98.66	101.92	101.85	100.96	101.77	>102.00	99.53	100.14	99.83	101.95	101.35	101.89	101.05	100.45	100.95	101.35	101.61	100.38	101.44	100.06
Ba	2460	3530	1400	1185	1295	1935	1435	680	615	559	252	973	1505	1010	3430	1735	718	1000	1120	866	1700	877	1005
Rb	121.5	94.5	202	90.7	71.8	149.5	152.5	101.5	144.5	75.6	108	38.3	101.5	73.1	79.1	58.3	133	136	194.5	116	135	123	89.7
Sr	548	462	253	337	364	236	172.5	158	185.5	451	263	560	319	323	515	415	466	238	193.5	164	402	285	262
Zr	437	548	300	173	184	440	290	289	149	50	235	369	235	246	415	162	253	197	385	178	171	170	195
Nb	6.51	15.95	16.4	7.33	6.94	19.4	12.2	6.73	7.34	8.7	9.35	2.52	7.7	13.2	4.68	1.79	11.85	11.9	18.95	7.26	9.72	4.6	6.08
Y	14.7	18.4	24.4	15.6	13.8	30.8	23.4	18.5	12.1	14	22.6	13.9	3.6	11.6	7.8	3.7	13.9	28.8	36.7	19.1	3.1	16.1	16.1
Hf	11.15	12.45	7.73	4.42	4.91	10.65	7.15	6.86	4.38	1.52	6	8.4	6.38	5.76	9.52	4.1	5.95	5.7	10.1	5.11	4.17	3.84	5.29
Ta	0.5	0.9	1.4	0.7	0.7	1.3	0.8	0.4	0.8	0.7	0.8	0.3	0.6	1	0.3	0.2	1.5	1.1	1.4	0.6	0.7	0.9	0.7
Ga	24.7	22.7	17.4	17.4	19.4	18.8	18.2	17.9	16.2	17.4	23.4	19.5	15.5	20.2	16	16.2	23.8	20.9	16.2	16.6	18.2	18.2	14.8
Cs	0.82	0.33	2.8	0.43	0.28	0.3	0.31	0.26	0.65	1.88	2.15	0.12	0.9	0.89	0.46	0.31	3.3	2.43	3.53	2.13	2.09	2.16	0.95

Sn	0.8	<0.5	2	0.8	<0.5	0.7	0.5	<0.5	0.8	2.1	3.7	0.9	0.8	1.4	1.9	0.6	7	1.6	3.5	1.7	3	3.6	1.3
Th	4.17	2.09	13.7	9.45	1.5	10.8	17.45	21	26.8	5.28	1.84	3.93	16.65	4.36	14.25	1.05	18.35	30.9	23	17.4	24.6	11.95	9.48
U	1.84	0.42	3.12	1.31	0.36	0.86	1.31	0.72	2.88	1.33	1.27	0.19	1.57	1.26	0.38	0.19	2.11	3.35	2.41	1.77	0.78	2.75	1.88
V	16	29	50	44	49	21	9	11	20	180	131	61	79	68	52	23	72	115	61	70	40	34	50
Cr	27	30	65	57	43	11	7	35	11	152	56	45	73	43	49	40	91	80	32	69	73	46	75
La	39.5	35.9	63.7	43.2	36	87.9	106.5	125.5	37.9	22.2	22.2	45	45.7	28.6	73.9	22	62.8	71.7	78.6	47.3	51.8	38.5	25.5
Ce	70.8	71.2	128.5	84.9	67.8	175	208	237	76.6	47	47.1	81.8	81.5	56.2	127	32.8	118	137	164	88.7	96.6	68	47.4
Pr	8.3	8.65	14.65	9.41	7.39	19.25	22.5	25.5	8.37	5.66	6.09	8.44	8.01	6.32	12.45	3.18	12.2	14.75	18.5	8.94	10.35	7.09	4.81
Nd	32.3	33.5	53.3	33.3	29.1	70	80.9	86.3	30.5	21.5	26.4	30	26.5	23.8	40.1	10.5	42.1	46.8	70.3	31.8	35.5	21.9	16.4
Sm	4.97	6.95	9.15	5.64	5.25	11.45	12.85	12.95	4.91	4.4	6.5	4.98	3.86	4.72	5.73	1.13	7.45	8.78	13.2	5.12	5.66	3.35	2.83
Eu	3.18	2.58	1.52	1.14	1.13	2.22	1.5	0.78	0.64	1.11	1.13	1.16	1.51	1.34	1.29	0.95	1.13	1.52	1.7	0.96	0.86	1.04	1.05
Gd	4.35	5.27	7.47	4.18	3.45	8.91	8.25	8.1	3.81	3.72	6.45	3.67	2.41	3.75	2.65	1.16	6.21	6.23	10.25	3.48	3.85	2.44	2.63
Tb	0.57	0.65	0.89	0.53	0.43	1.18	0.97	0.93	0.43	0.52	0.87	0.39	0.25	0.42	0.33	0.09	1	0.9	1.37	0.47	0.32	0.38	0.39
Dy	2.8	3.87	5.06	3.1	2.71	6.14	5.32	4.17	2.5	3	4.91	2.49	0.79	2.26	1.34	0.8	4.48	5.21	7.4	3.35	0.99	2.53	2.58
Ho	0.56	0.72	0.95	0.52	0.5	1.2	0.86	0.85	0.45	0.57	0.87	0.46	0.13	0.43	0.26	0.12	0.54	1.1	1.29	0.73	0.12	0.54	0.55
Er	1.39	1.92	2.29	1.55	1.32	3.3	2.19	2	1.18	1.44	2.18	1.32	0.41	1.12	0.94	0.38	0.81	3.3	3.86	2.07	0.17	2.09	1.77
Tm	0.21	0.23	0.3	0.2	0.18	0.44	0.3	0.23	0.14	0.2	0.33	0.18	0.08	0.13	0.1	0.03	0.09	0.4	0.51	0.36	0.02	0.3	0.23
Yb	1.3	1.71	1.88	1.51	1.18	2.88	1.88	1.15	1.16	1.2	1.92	0.84	0.45	0.96	0.54	0.31	0.43	2.66	3.33	2.39	0.13	2.11	1.52
Lu	0.22	0.29	0.35	0.2	0.13	0.4	0.28	0.2	0.15	0.21	0.23	0.14	0.11	0.18	0.08	0.06	0.09	0.38	0.49	0.38	0.01	0.32	0.23
ΣREE	170.5	173.4	290.0	189.4	156.6	390.3	452.3	505.7	168.7	112.7	127.2	180.9	171.7	130.2	266.7	73.5	257.3	300.7	374.8	196.1	206.4	150.6	107.9
ΣLREE	159.05	158.78	270.82	177.59	146.67	365.82	432.25	488.03	158.92	101.87	109.42	171.38	167.08	120.98	260.47	70.56	243.68	280.55	346.3	182.82	200.77	139.88	97.99
(La/Yb)n	20.5	14.2	22.8	19.3	20.6	20.6	38.2	73.6	22.0	12.5	7.8	36.1	68.5	20.1	92.3	47.8	98.5	18.2	15.9	13.3	268.6	12.3	11.3
Eu/Eu*	2.09	1.30	0.56	0.72	0.81	0.67	0.45	0.23	0.45	0.84	0.53	0.83	1.51	0.97	1.01	2.54	0.51	0.63	0.45	0.70	0.56	1.11	1.18
Mg#	30	20	33	34	34	16	14	14	30	52	43	33	32	40	38	38	44	37	28	39	41	35	38

SUPPLEMENTARY MATERIAL 2 – U-Pb GEOCHRONOLOGY

Table S 2 - U-Pb SHRIMP data on zircon for sample AA-03C (Bandeirante granite).

Location - 552046/9412076					Isotopic ratios									Apparent ages				
Spot	U (ppm)	Th (ppm)	Th/U	^{206}Pbc (%)	^{238}U/^{206}Pb	1σ (%)	^{207}U/^{206}Pb	1σ (%)	^{207}Pb/^{235}U	1σ (%)	^{206}Pb/^{238}U	1s (%)	ρ	^{207}Pb/^{206}Pb	1σ (%)	^{206}Pb/^{208}U	1σ (%)	%conc
AA-03C-1.1	443	99	0.22	0.38	2.57	1.1	0.130	0.61	6.9	1.2	0.389	1.1	±20	2092	0.32	2117	±10	-1
AA-03C-2.1	544	257	0.47	0.69	2.60	1.1	0.132	0.52	7.0	1.2	0.384	1.1	±20	2129	0.20	2096	±9	+2
AA-03C-7.1	566	75	0.13	1.05	2.57	1.1	0.133	0.66	7.1	1.2	0.390	1.1	±20	2134	0.32	2122	±10	+1
AA-03C-12.1	275	49	0.18	1.36	2.56	1.1	0.130	1.32	7.0	1.7	0.390	1.1	±21	2095	0.43	2123	±21	-2
AA-03C-3.1	1630	621	0.38	2.04	3.04	1.0	0.127	0.58	5.8	1.2	0.329	1.0	±18	2061	0.14	1832	±8	+13
AA-03C-4.1	123	71	0.58	0.79	2.56	1.2	0.136	1.13	7.3	1.7	0.390	1.2	±24	2171	0.36	2124	±16	+3
AA-03C-5.1	2016	332	0.16	1.52	4.20	1.0	0.123	0.47	4.0	1.1	0.238	1.0	±13	2007	0.18	1376	±6	+35
AA-03C-6.1	839	386	0.46	2.88	5.28	1.1	0.117	1.07	3.1	1.5	0.190	1.1	±12	1909	0.17	1119	±10	+45
AA-03C-8.1	325	122	0.38	3.97	3.12	1.1	0.131	2.09	5.8	2.4	0.321	1.1	±19	2105	0.27	1795	±14	+17
AA-03C-10.1	433	140	0.32	1.58	2.81	1.1	0.128	1.02	6.3	1.5	0.355	1.1	±19	2072	0.25	1960	±16	+6
AA-03C-11.1	641	229	0.36	1.51	5.35	2.4	0.115	1.30	3.0	2.7	0.187	2.4	±26	1878	1.53	1104	±25	+45
AA-03C-13.1	385	63	0.16	1.21	3.00	1.1	0.127	0.92	5.9	1.4	0.333	1.1	±18	2063	0.39	1854	±11	+12

Table S 3 - U-Pb SHRIMP data on zircon for sample AA-76 (Alto Rio Preto granite).

Location - 545527/9418493					Isotopic ratios									Apparent ages				
Spot	U (ppm)	Th (ppm)	Th/U	^{206}Pbc (%)	^{238}U/^{206}Pb	1σ (%)	^{207}U/^{206}Pb	1σ (%)	^{207}Pb/^{235}U	1σ (%)	^{206}Pb/^{238}U	1s (%)	ρ	^{207}Pb/^{206}Pb	1σ (%)	^{206}U/^{208}Pb	1σ (%)	%conc
AA-76-1.1	140	79	0.56	0.98	2.62	1.5	0.130	1.09	6.9	1.9	0.381	1.5	0.82	2103	±19	2083	±27	+1
AA-76-4.1	524	175	0.33	0.24	3.45	1.1	0.126	0.55	5.1	1.2	0.290	1.1	0.89	2050	±10	1642	±16	+23
AA-76-5.1	1488	608	0.41	0.39	3.74	1.1	0.125	0.40	4.6	1.2	0.268	1.1	0.94	2032	±7	1529	±15	+28
AA-76-7.1	96	98	1.02	1.83	3.07	1.4	0.131	2.93	5.9	3.2	0.325	1.4	0.42	2111	±51	1816	±21	+16
AA-76-8.1	223	108	0.49	0.87	2.55	1.1	0.129	0.88	7.0	1.4	0.392	1.1	0.79	2089	±15	2132	±21	-2
AA-76-10.1	1316	62	0.05	0.81	5.83	1.1	0.113	3.73	2.7	3.9	0.172	1.1	0.29	1847	±68	1021	±11	+48
AA-76-11.1	392	143	0.37	2.66	3.80	1.1	0.125	2.13	4.5	2.4	0.263	1.1	0.45	2030	±38	1506	±15	+29

AA-76-2.1	956	298	0.31	0.61	6.88	1.0	0.096	1.12	1.9	1.5	0.145	1.0	0.68	1549	±21	875	±9	+46
AA-76-3.1	273	147	0.54	0.49	2.51	1.1	0.135	0.90	7.4	1.4	0.398	1.1	0.78	2160	±16	2159	±20	+0
AA-76-6.1	203	150	0.74	0.98	2.72	1.2	0.126	1.49	6.4	1.9	0.367	1.2	0.61	2048	±26	2016	±20	+2
AA-76-9.1	659	135	0.21	0.27	4.02	1.0	0.117	0.49	4.0	1.2	0.249	1.0	0.91	1911	±9	1432	±13	+28
AA-76-12.1	1113	274	0.25	0.36	8.49	1.0	0.081	0.74	1.3	1.3	0.118	1.0	0.81	1232	±15	718	±7	+44

Table S 4 - U-Pb SHRIMP data for sample AA-06A (Maravilha charnockite).

Location - 531023/9402536					Isotopic ratios									Apparent ages				
Spot	U (ppm)	Th (ppm)	Th/U	^{206}Pbc(%)	^{238}U/^{206}Pb	1σ(%)	^{207}U/^{206}Pb	1σ(%)	^{207}Pb/^{235}U	1σ(%)	^{206}Pb/^{238}U	1σ(%)	ρ	^{207}Pb/^{206}Pb	1σ(%)	^{206}Pb/^{208}U	1σ(%)	%conc
AA-06A-1.1	117	79	0.68	2.57	2.555	1.4	0.1298	2.9	7.00	3.2	0.391	1.4	0.4	2095	±51	2129	±25	-2
AA-06A-2.1	180	114	0.63	1.05	2.631	1.2	0.1307	1.8	6.85	2.2	0.380	1.2	0.6	2108	±31	2076	±22	+2
AA-06A-3.1	139	116	0.83	1.03	2.563	1.2	0.1284	1.6	6.91	2.0	0.390	1.2	0.6	2076	±28	2124	±22	-3
AA-06A-4.1	235	127	0.54	1.36	2.751	1.3	0.1272	2.3	6.38	2.6	0.364	1.3	0.5	2060	±40	1999	±22	+3
AA-06A-5.1	153	117	0.76	0.91	2.536	1.2	0.1297	1.2	7.05	1.7	0.394	1.2	0.7	2093	±22	2143	±21	-3
AA-06A-6.1	185	88	0.48	0.79	2.563	1.2	0.1294	2.2	6.96	2.5	0.390	1.2	0.5	2090	±38	2123	±21	-2
AA-06A-7.1	540	208	0.38	0.81	4.340	1.3	0.1180	1.0	3.75	1.7	0.230	1.3	0.8	1926	±18	1337	±16	+34
AA-06A-8.1	179	111	0.62	1.88	2.600	1.2	0.1294	2.8	6.87	3.1	0.385	1.2	0.4	2090	±50	2098	±22	-0
AA-06A-9.1	121	88	0.73	1.38	2.673	1.5	0.1287	3.1	6.64	3.4	0.374	1.5	0.4	2080	±54	2049	±26	+2
AA-06A-10.1	324	71	0.22	0.54	2.661	1.1	0.1285	1.0	6.66	1.5	0.376	1.1	0.7	2078	±18	2057	±20	+1
AA-06A-11.1	439	78	0.18	0.45	2.648	1.2	0.1281	1.1	6.67	1.7	0.378	1.2	0.7	2073	±20	2065	±22	+0
AA-06A-12.1	179	42	0.24	1.08	2.578	1.2	0.1298	2.7	6.94	2.9	0.388	1.2	0.4	2095	±47	2113	±21	-1

Table S 5 - U-Pb SHRIMP data for sample AA-20 (Serra Azul charnockite).

Location - 524968/9420338					Isotopic ratios									Apparent ages				
Spot	U (ppm)	Th (ppm)	Th/U	^{206}Pbc(%)	^{238}U/^{206}Pb	1σ(%)	^{207}U/^{206}Pb	1σ(%)	^{207}Pb/^{235}U	1σ(%)	^{206}Pb/^{238}U	1σ(%)	ρ	^{207}Pb/^{206}Pb	1σ(%)	^{206}Pb/^{208}U	1σ(%)	%conc
AA20-1.1	319	83	0.26	0.87	2.607	1.1	0.1271	1.4	6.73	1.8	0.384	1.1	0.6	2059	±25	2093	±19	-2
AA20-2.1	402	234	0.58	1.17	2.741	1.1	0.1278	1.4	6.43	1.8	0.365	1.1	0.6	2068	±25	2005	±20	+4

AA20-3.1	565	213	0.38	0.48	3.006	1.1	0.1265	1.1	5.80	1.5	0.333	1.1	0.7	2050	±19	1851	±18	+11
AA20-4.1	314	100	0.32	2.06	3.084	1.5	0.1323	2.4	5.91	2.9	0.324	1.5	0.5	2128	±43	1810	±24	+17
AA20-5.1	878	417	0.48	0.35	4.686	1.3	0.1247	1.2	3.67	1.8	0.213	1.3	0.8	2025	±20	1247	±15	+42
AA20-6.1	823	235	0.29	0.09	3.876	1.2	0.1237	0.9	4.40	1.5	0.258	1.2	0.8	2010	±16	1480	±16	+29
AA20-7.1	446	202	0.45	0.55	2.828	1.5	0.1271	1.6	6.20	2.2	0.354	1.5	0.7	2059	±28	1952	±25	+6
AA20-8.1	288	201	0.70	0.37	2.769	1.3	0.1265	2.9	6.30	3.2	0.361	1.3	0.4	2050	±51	1987	±22	+4
AA20-9.1	338	128	0.38	0.85	2.836	1.3	0.1263	2.7	6.14	3.0	0.353	1.3	0.5	2048	±47	1947	±23	+6
AA20-10.1	649	484	0.75	0.33	2.741	1.5	0.1266	0.9	6.37	1.8	0.365	1.5	0.9	2052	±15	2005	±26	+3
AA20-10.2	234	72	0.31	0.31	2.547	1.2	0.1317	1.0	7.13	1.5	0.393	1.2	0.8	2120	±17	2135	±21	-1
AA20-11.1	614	291	0.47	1.41	3.514	2.1	0.1277	2.8	5.01	3.5	0.285	2.1	0.6	2067	±50	1614	±30	+25
AA20-12.1	835	193	0.23	0.52	4.110	1.0	0.1212	0.7	4.07	1.3	0.243	1.0	0.8	1974	±13	1404	±13	+32
AA20-13.1	470	197	0.42	0.34	2.780	1.2	0.1293	1.6	6.41	2.0	0.360	1.2	0.6	2088	±29	1981	±21	+6
AA20-13.2	467	208	0.44	0.48	2.760	1.2	0.1286	1.5	6.42	1.9	0.362	1.2	0.6	2079	±26	1993	±20	+5

Table S 6 - U-Pb LA-ICP-MS data on zircon for sample ASM-01 (Alto Rio Preto granite).

Location - 557318/9416429						radiogenic ratios					apparent ages						
Spot number	^{206}Pb mV	U[1] (ppm)	Th/U	^{206}Pb/^{204}Pb	1s (%)	^{207}Pb/^{235}U	2s (%)	^{206}Pb/^{238}U	2s (%)	Rho	^{207}Pb/^{206}Pb	2s (abs)	^{206}Pb/^{238}U	2s (abs)	^{207}Pb/^{235}U	2s	% conc[3]
#07	0.014	304	1.14	8485	134.1	7.6052	3.5	0.43182	3.2	0.90	2074	29	2314	62	2185	32	111.6
#08	0.023	546	0.39	81477	41.4	7.0213	4.3	0.40166	3.2	0.75	2067	49	2177	59	2114	38	105.3
#40	0.019	357	1.55	1403	61.6	8.9449	4.1	0.44410	3.6	0.88	2295	28	2369	71	2332	37	103.2
#70	0.025	618	0.39	33543	39.6	6.5848	3.7	0.37950	3.4	0.90	2041	25	2074	60	2057	33	101.6
#25	0.016	366	0.51	4273	47.5	6.9652	3.6	0.38965	3.1	0.85	2103	26	2121	55	2107	32	100.9
#37	0.027	682	0.22	12431	35.3	6.8069	3.4	0.38446	3.3	0.97	2088	24	2097	58	2087	30	100.4
#38	0.014	357	0.20	3913	40.8	6.9766	3.4	0.38540	3.3	0.97	2131	25	2101	60	2108	31	98.6
#13	0.011	269	0.43	3690	39.4	6.6808	3.5	0.37279	3.2	0.91	2110	29	2042	56	2070	31	96.8
#52	0.029	764	0.74	18047	31.7	6.1641	3.2	0.35488	3.1	0.97	2032	23	1958	53	1999	28	96.3
#20	0.023	582	0.23	2711	28.4	6.5758	4.9	0.36338	4.6	0.95	2125	26	1997	79	2055	43	94.0
#71	0.028	782	0.27	4030	35.2	6.3369	4.1	0.35600	3.4	0.83	2093	32	1963	57	2023	36	93.8
#53	0.015	423	0.55	5774	62.2	6.2672	4.3	0.34709	3.8	0.89	2115	35	1921	64	2014	38	90.8

#14	0.026	731	0.40	7085	59.5	5.8314	3.3	0.33528	3.2	0.96	2055	24	1864	51	1951	29	90.7
#69	0.011	278	0.64	7076	80.0	5.4265	3.5	0.31986	3.3	0.94	2003	26	1789	52	1889	30	89.3
#23	0.032	864	0.14	3449	41.7	6.1569	3.2	0.34036	3.2	0.98	2120	23	1888	52	1998	28	89.1
#61	0.019	578	0.25	4785	55.5	5.9264	3.7	0.33128	3.4	0.94	2101	30	1845	55	1965	32	87.8
#12	0.020	537	0.37	1142	99.6	6.5053	3.4	0.34408	3.2	0.92	2203	28	1906	52	2047	31	86.5
#65	0.007	192	0.68	754	92.3	6.2959	3.9	0.32728	3.4	0.88	2217	31	1825	54	2018	34	82.3
#41	0.021	490	0.22	465	81.4	7.5031	6.6	0.35413	3.2	0.48	2381	60	1954	54	2171	59	82.1
#73	0.012	383	0.30	6954	74.7	4.3670	4.0	0.27315	3.9	0.97	1903	24	1557	54	1706	33	81.8
#55	0.021	629	0.29	12880	89.2	4.7196	3.5	0.28166	3.3	0.97	1963	25	1600	47	1770	29	81.5
#47	0.024	737	0.25	2700	204.7	5.2641	4.9	0.29478	4.1	0.85	2073	42	1665	61	1862	42	80.3
#54	0.023	806	0.21	3217	72.4	4.8661	3.5	0.27992	3.3	0.95	2046	26	1591	47	1796	30	77.8
#62	0.037	1305	0.54	13810	20.9	4.4297	6.2	0.26643	4.4	0.71	1959	41	1522	60	1716	50	77.7
#24	0.007	169	0.30	666	91.5	6.1364	4.0	0.30646	3.4	0.85	2298	35	1723	51	1995	35	75.0
#51	0.006	195	0.24	4690	93.0	4.1362	4.2	0.25210	3.8	0.91	1937	33	1449	50	1661	35	74.8
#28	0.013	400	0.26	1776	92.8	4.6219	3.9	0.26732	3.2	0.83	2041	31	1527	44	1753	33	74.8
#10	0.019	582	0.18	1012	69.7	5.2774	6.6	0.27810	4.6	0.70	2195	39	1581	64	1862	55	72.0
#72	0.015	563	0.17	2368	51.1	3.8904	5.6	0.23689	3.3	0.58	1941	49	1370	40	1611	45	70.6
#21	0.023	921	0.30	5047	33.5	3.6254	4.0	0.22606	3.8	0.95	1910	26	1314	46	1555	32	68.8
#49	0.018	1461	0.43	17960	56.5	1.1614	3.4	0.11384	3.0	0.89	1027	29	695	20	783	19	67.7
#22	0.006	168	0.52	601	90.3	4.9986	3.9	0.25860	3.6	0.92	2240	31	1483	48	1819	34	66.2
#34	0.006	176	0.48	890	98.6	4.6164	3.7	0.24739	3.5	0.94	2182	27	1425	45	1752	31	65.3
#27	0.020	888	0.33	5820	54.6	3.2560	3.5	0.20788	3.4	0.98	1878	24	1217	37	1470	27	64.8
#63	0.013	543	0.41	855	34.9	4.4272	7.2	0.23593	6.0	0.83	2178	56	1365	74	1714	59	62.7
#11	0.034	1397	0.32	723	114.9	4.2279	4.4	0.22762	3.7	0.84	2171	38	1322	44	1679	37	60.9
#09	0.019	767	0.25	1074	109.7	3.6660	3.5	0.21183	3.2	0.91	2038	25	1238	36	1564	28	60.8
#67	0.011	434	0.43	590	85.4	4.1103	5.6	0.22190	3.6	0.65	2157	46	1292	43	1656	46	59.9
#26	0.023	873	0.13	857	225.1	4.0535	3.6	0.22018	3.2	0.87	2146	32	1283	37	1645	30	59.8

#42	0.010	433	0.22	1702	113.0	3.2302	4.1	0.19549	3.8	0.92	1945	28	1151	40	1464	32	59.2
#56	0.007	286	0.35	1625	94.8	3.0282	4.3	0.18950	4.0	0.93	1891	30	1119	41	1414	33	59.2
#66	0.012	546	0.17	2139	61.8	2.9051	6.5	0.18390	4.0	0.62	1865	49	1088	40	1380	47	58.3
#19	0.011	516	0.35	4614	129.0	2.4818	4.5	0.16849	4.2	0.93	1752	28	1004	39	1266	32	57.3
#64	0.015	767	0.27	2612	104.6	2.8372	4.5	0.17985	4.0	0.90	1867	27	1066	40	1363	32	57.1
#06	0.021	956	0.13	1717	27.7	3.4331	3.8	0.19740	3.7	0.98	2037	24	1161	39	1512	30	57.0
#35	0.017	1286	0.38	7136	126.0	1.5197	3.2	0.12667	3.0	0.94	1370	28	769	22	938	20	56.1
#05	0.019	1033	0.45	2600	99.6	2.5052	3.9	0.16679	3.6	0.91	1791	33	994	33	1273	29	55.5
#33	0.009	419	0.15	2772	107.0	2.6493	4.2	0.17016	3.9	0.95	1857	27	1013	37	1314	31	54.5
#39	0.019	810	0.20	804	95.6	3.0870	4.3	0.18212	3.8	0.87	2004	31	1078	37	1429	33	53.8
#48	0.004	144	0.64	233	103.8	5.6037	5.4	0.22493	4.8	0.88	2659	39	1308	57	1916	47	49.2
#36	0.014	1028	0.36	289	108.2	2.1485	6.9	0.10173	5.0	0.72	2393	52	624	30	1164	48	26.1
#50	0.005	342	0.24	128	99.0	3.8281	3.9	0.12294	3.7	0.93	3021	25	747	26	1598	32	24.7
#68	0.018	2082	0.13	145	86.9	2.3516	3.3	0.07572	3.1	0.94	3010	24	470	14	1228	24	15.6

Following http://www.plasmage.org/recommendations

[1] concentration uncertainty c.20%

[2] data not corrected for common-Pb

[3] Concordance calculated as (^{206}Pb-^{238}U age/^{207}Pb-^{235}U age)*100

Decay constants of Jaffey et al. (1971) used

bd = below detection; #N/A = not available

Uncertainties quoted without components related to systematic error unless otherwise stated

Total systematic uncertainties (s_{sys}): ^{206}Pb/^{238}U = 1.0%, ^{207}Pb/^{206}Pb = 0.55% (2s)

Table S 7 - U-Pb LA-ICP-MS data on zircon for sample ASM25- (Bernardino granite).

Location - 529649/9417676							radiogenic ratios					apparent ages						
Session	Spot number	^{206}Pb (cps)	U [1] (ppm)	Th/U	$^{206}Pb/^{204}Pb$	1s (%)	$^{207}Pb/^{235}U$	2s (%)	$^{206}Pb/^{238}U$	2s (%)	Rho	$^{207}Pb/^{206}Pb$	2s (abs)	$^{206}Pb/^{238}U$	2s (abs)	$^{207}Pb/^{235}U$	2s (abs)	% conc [3]
1	#28	478952	572	1.46	10867	59.4	7.4843	0.4	0.42401	0.3	0.24	2065	7	2279	5	2171	3	110.4
1	#30	461414	551	0.68	36317	35.4	7.3613	0.4	0.41571	0.4	0.35	2066	9	2241	8	2156	4	108.4
1	#32	355804	385	1.15	2634	103.2	7.3401	0.3	0.40871	0.4	0.47	2076	7	2209	8	2153	3	106.4
2	#13	287421	321	0.07	19987	24.3	7.6772	0.3	0.41399	0.3	0.22	2122	7	2233	6	2194	3	105.2
2	#34	340650	395	0.64	9115	33.4	7.1870	0.3	0.40128	0.3	0.34	2071	7	2175	6	2135	3	105.0
2	#18	341976	404	0.42	11148	30.8	7.1460	0.3	0.40044	0.3	0.15	2072	7	2171	6	2130	2	104.8
2	#29	172456	173	1.68	17847	19.7	10.7694	0.5	0.47929	0.7	0.96	2471	13	2523	16	2503	5	102.1
1	#66	420930	481	0.60	14370	41.1	7.1562	0.5	0.39465	0.4	0.41	2108	9	2144	8	2131	4	101.7
1	#34	251585	260	0.38	8676	42.4	6.8220	0.5	0.38194	0.7	0.41	2057	12	2085	12	2088	5	101.4
1	#79	321543	375	1.85	84965	29.9	6.9205	0.7	0.38495	0.7	0.83	2078	7	2099	13	2100	6	101.0
2	#10	318060	404	0.48	1154	372.8	7.0082	0.8	0.38724	0.7	0.57	2099	13	2110	12	2112	7	100.5
1	#11	310293	383	0.21	3251	19.5	7.6173	1.2	0.40284	1.0	0.35	2174	23	2182	19	2186	11	100.4
1	#64	400060	456	0.53	8533	52.9	7.4996	0.8	0.40065	0.7	0.50	2164	13	2172	13	2172	8	100.4
1	#29	203446	205	1.45	3876	61.4	9.4531	0.6	0.44432	0.7	0.37	2362	12	2370	14	2383	6	100.3
2	#30	86933	92	1.17	5100	39.8	10.2589	0.9	0.46271	1.6	0.79	2445	27	2448	34	2457	8	100.2
2	#48	355948	439	0.95	5948	19.0	7.1715	0.3	0.39005	0.4	0.22	2124	8	2123	7	2133	3	100.0
1	#61	334576	356	0.69	5834	59.9	6.9972	0.4	0.38264	0.4	0.30	2097	8	2088	7	2111	4	99.6
1	#27	408018	560	0.45	22998	56.2	6.9709	1.0	0.38599	1.0	0.56	2116	17	2104	18	2107	9	99.5
1	#42	260970	334	2.05	3252	104.9	6.1792	0.9	0.36219	0.9	0.75	2003	12	1992	16	2001	8	99.5
1	#75	308210	391	1.50	606	584.3	7.4288	0.6	0.39622	0.6	0.22	2165	11	2151	11	2164	5	99.4
2	#11	205602	266	0.45	4702	136.5	7.0557	0.9	0.38534	1.0	0.46	2124	18	2101	19	2118	8	98.9
1	#50	175371	189	2.46	4543	39.2	6.9258	0.7	0.38129	0.9	0.36	2105	17	2082	17	2101	6	98.9
1	#60	196726	157	0.75	1286	235.1	13.7274	0.6	0.51902	0.8	0.18	2726	16	2695	18	2731	6	98.9
1	#15	152908	153	0.29	22254	28.1	11.1440	0.5	0.47551	0.7	0.29	2539	12	2507	15	2535	5	98.7
1	#58	267283	331	0.29	2814	146.0	6.8981	0.7	0.37758	1.0	0.15	2119	20	2065	19	2098	6	97.4

1	#62	314212	391	0.36	7579	74.0	6.9324	1.0	0.37896	0.9	0.54	2129	17	2071	16	2102	9	97.3
1	#57	206730	194	1.04	9158	39.8	9.3105	0.7	0.43069	0.8	0.35	2379	15	2308	16	2369	6	97.1
1	41	164910	165	2.92	18140	63.5	8.0433	0.9	0.40328	0.9	0.28	2252	19	2183	16	2235	8	97.0
2	#28	349816	443	0.40	1868	3.2	7.2163	0.6	0.38346	0.6	0.49	2160	10	2092	10	2138	6	96.9
1	#76	167081	158	2.88	1819	139.6	10.5143	1.0	0.45240	1.1	0.32	2506	20	2405	22	2480	10	96.0
1	#25	404772	479	3.73	35715	38.2	8.4555	0.6	0.41297	0.6	0.43	2323	12	2228	12	2281	6	95.9
2	#41	381087	494	0.89	69539	31.6	6.2163	0.5	0.35229	0.5	0.19	2046	11	1945	8	2007	4	95.1
1	#26	351683	493	1.26	3011	7.3	6.4861	0.5	0.36054	0.4	0.31	2102	11	1985	8	2044	5	94.4
2	#47	244283	274	1.17	4075	50.3	8.3227	0.5	0.40083	0.6	0.39	2328	11	2173	11	2266	4	93.3
2	#46	365170	484	0.63	104764	24.1	6.0791	0.4	0.34399	0.3	0.33	2048	8	1906	6	1987	4	93.1
2	#12	136419	184	1.39	10285	60.3	6.5370	0.9	0.35459	1.3	0.50	2134	21	1955	22	2050	8	91.7
1	#47	330012	442	2.17	3799	41.1	5.6849	0.5	0.33018	0.5	0.40	2025	11	1839	8	1929	5	90.8
2	#33	244826	326	0.39	3799	57.2	7.7286	1.3	0.37514	1.2	0.91	2320	14	2053	21	2199	12	88.5
2	#45	276014	403	0.77	2400	77.0	5.6389	0.4	0.32089	0.4	0.36	2038	8	1794	7	1922	4	88.0
1	#77	248946	346	1.15	4966	13.8	5.8699	0.8	0.32047	0.8	0.52	2103	14	1792	13	1956	7	85.2
2	#09	195190	297	2.35	84523	69.4	6.0980	0.8	0.32501	1.0	0.23	2166	20	1817	15	1989	7	83.9
1	#73	527659	637	0.75	7133	114.0	9.3042	1.0	0.39328	0.7	0.87	2557	7	2138	14	2368	9	83.6
1	#14	233489	266	0.39	1274	3.5	10.7278	0.7	0.40937	0.7	0.76	2709	8	2211	13	2499	7	81.6
1	#09	226949	348	0.19	4159	39.0	5.5075	1.9	0.30269	1.6	0.76	2105	22	1704	25	1900	16	80.9
2	#13	223953	393	0.16	7936	49.0	5.0935	2.7	0.29139	2.3	0.89	2038	22	1647	34	1831	24	80.8
2	#14	211960	348	0.59	667	430.4	4.7652	1.7	0.27598	1.4	0.85	2009	16	1570	19	1776	15	78.2
1	#31	464855	811	0.38	4844	45.0	5.0369	0.7	0.28210	0.5	0.62	2088	11	1602	8	1828	7	76.7
1	#17	446819	668	0.33	15707	35.0	4.9019	1.0	0.27553	0.8	0.85	2054	9	1569	11	1802	8	76.4
1	#59	249709	408	0.50	396	697.9	4.1928	0.9	0.25164	0.9	0.79	1931	11	1448	13	1673	8	75.0
1	#12	366905	717	0.21	3954	97.0	4.1261	1.7	0.24952	1.3	0.88	1928	14	1436	17	1658	14	74.5
1	#46	321857	624	1.22	3624	15.6	4.1644	0.8	0.25191	0.7	0.55	1971	12	1448	9	1666	7	73.5
1	#78	378473	794	2.75	20327	36.5	3.7624	1.0	0.23401	0.8	0.86	1895	9	1355	10	1584	8	71.5

1	#80	252867	432	2.18	1809	5.0	5.8769	0.8	0.29022	0.8	0.43	2304	16	1642	12	1957	7	71.3
2	#16	331719	581	0.09	797	2.7	5.1482	0.8	0.26724	0.8	0.63	2206	12	1527	12	1844	7	69.2
2	#49	214477	422	1.46	32356	33.1	3.9420	0.6	0.23047	0.7	0.38	1991	13	1337	9	1622	5	67.1
1	#82	195617	321	1.82	1201	11.7	4.7645	2.0	0.25191	1.9	0.82	2157	20	1448	25	1776	17	67.1
1	#48	198162	423	1.00	12713	53.7	2.8215	1.7	0.19156	1.4	0.83	1727	16	1129	14	1361	13	65.4
1	#16	304173	625	0.28	13388	35.6	3.3861	1.3	0.20750	1.0	0.76	1897	15	1215	11	1500	11	64.1
2	#25	519564	1165	0.77	1220	2.7	3.6202	1.5	0.20888	1.0	0.82	2014	14	1222	12	1550	12	60.7
1	#33	304045	666	1.05	3925	10.1	3.0631	1.2	0.19147	1.0	0.80	1862	13	1129	11	1423	9	60.6
2	#50	233368	547	0.88	2622	14.8	3.2903	0.8	0.19900	0.7	0.55	1930	14	1170	8	1478	6	60.6
1	#49	444170	833	0.52	1042	3.3	4.0284	1.5	0.21955	1.0	0.84	2122	16	1279	12	1638	12	60.3
1	#45	337070	1106	0.33	2329	6.1	2.1097	0.8	0.15560	0.7	0.40	1620	16	932	6	1152	6	57.5
2	#31	248927	660	1.25	2298	11.9	2.9852	3.3	0.18501	2.3	0.94	1954	19	1105	11	1400	28	56.5
1	#10	357055	866	0.13	487	350.2	2.7615	1.7	0.17280	1.0	0.92	1837	17	1027	10	1342	13	55.9
1	#74	278690	685	0.45	2550	6.9	3.6665	1.2	0.20206	1.1	0.68	2121	15	1186	12	1563	10	55.9
2	#44	497470	1253	0.03	868	2.4	3.1965	0.5	0.18770	0.5	0.34	1985	11	1109	5	1456	4	55.9
1	#63	281720	614	0.61	1290	4.2	3.3528	0.9	0.19053	0.6	0.56	2036	13	1124	6	1493	7	55.2
1	#44	232942	837	7.76	2369	16.7	1.9759	1.5	0.14633	1.0	0.69	1600	21	880	9	1106	11	55.0
2	#15	201132	493	0.18	2012	36.0	3.3899	3.3	0.18095	7.9	0.94	2039	22	1061	84	1494	30	52.1
1	#43	156061	532	2.25	999	6.8	2.4043	1.7	0.15855	1.2	0.47	1826	30	949	11	1245	13	51.9
2	#26	184864	647	0.01	4212	37.5	1.6563	1.8	0.12642	1.2	0.60	1501	26	767	9	991	11	51.1
2	#32	316921	945	0.35	1010	2.8	2.7165	1.0	0.16335	0.8	0.86	1945	15	975	7	1332	7	50.1
1	#41	405507	1265	2.39	1657	3.7	2.9267	1.1	0.16912	0.8	0.79	2053	11	1007	8	1388	8	49.1
2	#42	216369	679	0.49	1310	10.0	2.6409	1.9	0.15797	1.2	0.61	1950	27	945	11	1310	14	48.5
1	#81	199172	578	0.75	529	4.8	3.0244	1.0	0.16816	1.0	0.70	2094	16	1002	10	1413	8	47.8
2	#43	324805	832	0.97	452	1.2	3.7344	0.7	0.17874	0.4	0.23	2336	12	1060	4	1578	6	45.4
1	#18	358804	1028	0.47	477	1.4	2.8518	1.0	0.15411	0.6	0.67	2143	13	924	5	1369	8	43.1
2	#27	372712	778	1.83	124	1.3	7.2384	0.7	0.22036	0.7	0.19	3086	18	1284	8	2142	6	41.6

2	#17	308775	902	0.91	98	1.7	6.0092	1.9	0.16986	0.6	0.24	3209	30	1011	6	1975	17	31.5

Following http://www.plasmage.org/recommendations

[1] concentration uncertainty c.20%

[2] data not corrected for common-Pb

[3] Concordance calculated as (^{206}Pb-^{238}U age/^{207}Pb-^{235}U age)*100

Decay constants of Jaffey et al. (1971) used

bd = below detection; #N/A = not available

Uncertainties quoted without components related to systematic error unless otherwise stated

Total systematic uncertainties (s_{sys}): ^{206}Pb/^{238}U = 1.0%, ^{207}Pb/^{206}Pb = 0.55% (2s)

Table S 8 - U-Pb LA-ICP-MS data on monazite for sample ASM-25 (Bernardino granite).

Location - 529649/9417676						Isotopic ratios								Apparente ages						
Identifier	^{206}Pb	Uppm	Th/U	^{206}Pb/^{204}Pb	1s%	^{207}Pb/^{235}U	2s%	^{206}Pb/^{238}U	2s%	Rho	^{208}Pb/^{232}Th	1s%	^{207}Pb/^{206}Pb	2s (abs)	^{206}Pb/^{238}U	2s (abs)	^{207}Pb/^{235}U	2s (abs)	^{208}Pb/^{232}Th	2s (abs)	% conc
30	195446	297	171.0	-9423.502464	-5.556329547	7.0795	2.8	0.40706	2.3	0.77	0.10244	0.6	2017	32	2200	45	2118	26	1971	23	109.1
13	808533	1524	44.2	-67506.30821	-3.704589451	6.7743	1.6	0.39139	1.2	0.67	0.10319	0.6	2000	21	2128	22	2080	14	1985	22	106.4
5	210685	343	114.5	-14721.57671	-9.726747253	6.6729	4.2	0.38751	3.6	0.85	0.09433	1.4	1995	39	2107	66	2060	38	1821	49	105.6
2	478060	931	80.1	-59234.83802	-6.390016832	6.6043	1.8	0.38414	1.7	0.64	0.10097	0.6	1988	26	2094	31	2057	16	1944	21	105.3
6	771375	1475	43.9	-42971.34714	-8.434244027	6.9054	1.8	0.39267	1.2	0.74	0.10018	0.6	2028	23	2134	22	2097	16	1930	24	105.2
21	529450	1023	65.7	-29798.39575	-5.574043493	6.7311	2.3	0.38697	1.5	0.81	0.10089	0.6	2004	25	2107	27	2072	20	1942	23	105.1
8	775648	1286	40.1	-38279.46041	-12.48755529	6.8880	2.8	0.39230	2.3	0.88	0.09996	0.5	2032	25	2132	42	2099	27	1926	19	104.9
3	545870	1035	75.0	-67680.67735	-10.56450455	7.0397	2.2	0.39568	1.8	0.82	0.10082	0.7	2058	24	2147	33	2112	20	1941	26	104.3
11	393663	831	158.6	-21948.32221	-7.314911594	6.7554	2.2	0.38568	1.5	0.39	0.10302	1.1	2020	39	2102	28	2078	20	1981	40	104.0
27	526635	1043	68.7	-55067.17734	-8.188046811	6.6756	2.3	0.38238	1.4	0.66	0.10073	0.9	2013	32	2087	25	2066	21	1939	32	103.7
20	334357	535	84.6	-71900.97747	-6.50380662	6.6977	2.5	0.38266	1.6	0.60	0.09993	1.0	2021	36	2095	32	2069	22	1925	38	103.7
12	330637	526	70.1	-22726.3987	-6.819199917	6.5898	2.1	0.37992	1.8	0.62	0.09891	0.7	2006	33	2075	32	2056	18	1906	26	103.5
26	161319	266	194.8	-109017.2828	-7.019049768	6.4606	2.7	0.37461	2.0	0.60	0.09978	0.6	2001	40	2050	36	2037	25	1922	23	102.4

7	855251	1679	47.3	-45783.64725	-7.533751361	6.5774	2.0	0.37697	1.4	0.84	0.09685	0.6	2015	20	2061	25	2053	18	1868	21	102.3
9	403248	790	103.5	-38226.3298	-5.842227904	6.5774	1.7	0.37506	1.5	0.69	0.09661	0.6	2028	23	2052	28	2053	16	1864	22	101.2
28	268979	530	127.6	-17719.75259	-5.484551335	6.5769	2.4	0.37242	2.1	0.83	0.09461	0.6	2044	23	2038	38	2051	21	1827	23	99.7
4	446179	750	64.4	-70091.67484	-6.861767742	6.3447	2.9	0.36439	2.2	0.86	0.09625	0.6	2018	26	2002	39	2021	26	1857	20	99.2
23	561235	1071	50.1	-168663.5222	-3.873613246	6.2605	2.0	0.35935	1.6	0.67	0.09554	0.5	2017	28	1978	28	2010	18	1844	17	98.1
1	275335	529	103.9	-26709.0933	-5.833425938	6.1937	2.7	0.35550	1.8	0.76	0.09385	0.5	2007	31	1965	33	1998	23	1813	18	97.9
22	795944	1856	57.1	-70804.62902	-8.639821971	6.0148	5.6	0.34835	3.3	0.87	0.09051	1.9	1977	59	1924	56	1966	50	1750	62	97.3
18	356462	804	168.3	-20629.99033	-10.55114854	6.4074	2.3	0.35917	1.8	0.25	0.09213	1.2	2053	47	1977	32	2031	21	1781	42	96.3
25	574332	1069	51.3	3306173.358	18.7688477	6.1955	2.9	0.35175	2.7	0.83	0.09299	0.7	2039	30	1941	46	2000	26	1797	23	95.2
17	254659	553	172.4	-15019.4863	-5.507538458	6.0020	3.0	0.34301	2.6	0.66	0.08797	1.3	2020	40	1899	43	1971	26	1704	41	94.0
29	871337	2159	63.3	-32120.67223	-18.77161417	6.0694	2.0	0.34301	3.0	0.44	0.10211	1.7	2043	50	1900	50	1985	18	1965	63	93.0
10	363440	774	123.5	-37175.50139	-5.842896133	5.7897	2.8	0.33395	2.4	0.73	0.08583	1.1	2006	36	1854	40	1937	25	1664	36	92.5
16	869530	1997	49.8	-49987.63453	-6.693969385	5.8997	2.8	0.33711	2.7	0.91	0.08672	1.0	2023	21	1870	46	1956	25	1681	32	92.5
14	146519	272	178.7	-12142.53012	-5.124288627	5.5083	2.6	0.32406	2.3	0.35	0.08641	0.6	1978	52	1809	38	1900	23	1675	19	91.4
24	674426	1354	33.3	-319092.1427	-10.94124788	5.4156	2.8	0.31385	2.6	0.85	0.08500	0.7	2004	26	1758	40	1884	25	1649	22	87.7
15	564678	1084	40.0	-36431.24347	-7.554044811	5.4555	3.1	0.31456	2.3	0.62	0.08358	0.9	2011	43	1762	36	1890	27	1622	27	87.6
19	602618	1358	30.8	-31447.34355	-50.22552297	3.8082	7.5	0.21905	7.9	0.89	0.07591	4.1	2027	63	1273	94	1584	63	1477	116	62.8

SUPPLEMENTARY MATERIAL 3 – Lu-Hf isotopes on zircon

Table S 9 - Lu-Hf isotopic data on zircon by LA-MC-ICP-MS. *Calculated from the ratio $^{176}Lu/^{177}Hf$ = 0.015, the average value of the continental crust (Griffin et al., 2002).

Spot ID	t_{U-Pb} (Ma)	$^{176}Hf/^{177}Hf$	2SE	$^{176}Lu/^{177}Hf$	2SE	$^{176}Yb/^{177}Hf$	2SE	$^{178}Hf/^{177}Hf$	2SE	$\varepsilon_{Hf}(0)$	$^{176}Hf/^{177}Hf_{(t)}$	$\varepsilon_{Hf}(t)$	$\varepsilon_{Hf}(t)$ 2SE	T_{DM}^{C} (Ga)*
Amp Leucosyenogranite (AA-03C)														
1	2116	0.281297	0.000022	0.000757	0.000020	0.020341	0.000715	1.467220	0.000031	-52.6	0.281267	-5.8	0.17	3.1
2	2116	0.281317	0.000033	0.001680	0.000049	0.049911	0.003581	1.467228	0.000044	-51.9	0.281249	-6.5	0.21	3.1
3	2116	0.281356	0.000022	0.001358	0.000048	0.040553	0.002392	1.467250	0.000042	-50.5	0.281301	-4.6	0.17	3.0
4	2116	0.281348	0.000021	0.001420	0.000031	0.043056	0.001559	1.467260	0.000041	-50.8	0.281291	-5.0	0.12	3.0
7	2116	0.281321	0.000043	0.001796	0.000050	0.050607	0.006651	1.467263	0.000060	-51.8	0.281248	-6.5	0.20	3.1
8	2116	0.281323	0.000031	0.001006	0.000076	0.028113	0.002984	1.467265	0.000032	-51.7	0.281283	-5.3	0.41	3.0
9	2116	0.281337	0.000028	0.001650	0.000040	0.044610	0.004034	1.467274	0.000036	-51.2	0.281270	-5.7	0.16	3.0
10	2116	0.281327	0.000017	0.000629	0.000021	0.017588	0.000688	1.467236	0.000039	-51.6	0.281301	-4.6	0.17	3.0
11	2116	0.281323	0.000021	0.000816	0.000008	0.025187	0.000437	1.467248	0.000044	-51.7	0.281290	-5.0	0.06	3.0
12	2116	0.281370	0.000020	0.002079	0.000060	0.059973	0.006621	1.467237	0.000034	-50.0	0.281286	-5.1	0.16	3.0
Bt Granite (ASM-01)														
8	2076	0.281238	0.000068	0.000854	0.000066	0.036059	0.004268	1.467253	0.000047	-54.7	0.281204	-9.0	2.13	3.2
13	2076	0.281224	0.000024	0.000564	0.000066	0.027640	0.002733	1.467217	0.000044	-55.2	0.281202	-9.1	1.11	3.2
20	2076	0.281210	0.000037	0.000843	0.000058	0.037648	0.003746	1.467192	0.000057	-55.7	0.281177	-10.0	1.44	3.3
25	2076	0.281191	0.000030	0.000551	0.000041	0.026342	0.001660	1.467214	0.000036	-56.4	0.281170	-10.2	0.82	3.3
37	2076	0.281214	0.000068	0.000900	0.000069	0.046075	0.005252	1.467133	0.000075	-55.5	0.281179	-9.9	1.58	3.3
38	2076	0.281200	0.000106	0.000446	0.000059	0.018560	0.002981	1.467296	0.000134	-56.0	0.281182	-9.8	2.65	3.3
52	2076	0.281225	0.000055	0.000616	0.000062	0.028578	0.002296	1.467294	0.000108	-55.2	0.281200	-9.1	0.98	3.2
70	2076	0.281216	0.000033	0.000698	0.000078	0.033738	0.002896	1.467217	0.000042	-55.5	0.281188	-9.6	1.12	3.3
40	2295	0.281199	0.000039	0.001428	0.000067	0.070584	0.006032	1.467253	0.000054	-56.1	0.281136	-6.3	0.83	3.2
Amp-Bt Syenogranite (AA-06A)														

1	2093	0.281228	0.000020	0.000505	0.000006	0.015494	0.000173	1.467248	0.000036	-55.1	0.281208	-8.5	0.13	3.2
2	2093	0.281221	0.000021	0.000524	0.000013	0.016273	0.000601	1.467253	0.000042	-55.3	0.281200	-8.7	0.23	3.2
3	2093	0.281232	0.000033	0.000805	0.000067	0.025798	0.002729	1.467282	0.000048	-54.9	0.281200	-8.8	0.75	3.2
5	2093	0.281242	0.000021	0.000851	0.000042	0.026821	0.001113	1.467242	0.000044	-54.6	0.281208	-8.5	0.44	3.2
6	2093	0.281243	0.000022	0.000852	0.000022	0.025450	0.000666	1.467288	0.000052	-54.5	0.281209	-8.4	0.24	3.2
8	2093	0.281247	0.000018	0.000830	0.000088	0.025370	0.002892	1.467217	0.000038	-54.4	0.281214	-8.2	0.89	3.2
9	2093	0.281219	0.000019	0.000653	0.000022	0.020006	0.000571	1.467253	0.000044	-55.4	0.281193	-9.0	0.32	3.2
10	2093	0.281221	0.000022	0.000859	0.000061	0.026715	0.002023	1.467251	0.000034	-55.3	0.281187	-9.2	0.68	3.2
11	2093	0.281258	0.000032	0.001248	0.000058	0.036142	0.003687	1.467245	0.000065	-54.0	0.281208	-8.5	0.85	3.2
12	2093	0.281233	0.000019	0.000906	0.000021	0.029342	0.000684	1.467264	0.000060	-54.9	0.281197	-8.8	0.23	3.2
Px-Amp-Bt Tonalite (AA-20)														
1	2061	0.281331	0.000015	0.000766	0.000015	0.037904	0.001136	1.467230	0.000035	-51.4	0.281301	-5.9	0.17	3.0
2	2061	0.281317	0.000026	0.000705	0.000050	0.034418	0.003545	1.467256	0.000051	-51.9	0.281289	-6.3	0.51	3.0
7	2061	0.281231	0.000017	0.000314	0.000025	0.014971	0.000938	1.467207	0.000041	-54.9	0.281219	-8.8	0.77	3.2
8	2061	0.281265	0.000014	0.000438	0.000025	0.020537	0.000714	1.467251	0.000035	-53.7	0.281248	-7.8	0.51	3.1
9	2061	0.281322	0.000016	0.000452	0.000023	0.021593	0.000925	1.467202	0.000047	-51.7	0.281304	-5.8	0.34	3.0
10.1	2061	0.281247	0.000020	0.000171	0.000015	0.007693	0.000386	1.467214	0.000066	-54.4	0.281240	-8.1	0.76	3.1
10.2	2061	0.281269	0.000024	0.001215	0.000044	0.058429	0.001515	1.467249	0.000050	-53.6	0.281222	-8.7	0.39	3.2
11	2061	0.281326	0.000042	0.000643	0.000052	0.031206	0.005583	1.467282	0.000069	-51.6	0.281301	-5.9	0.53	3.0
13.1	2061	0.281251	0.000026	0.000229	0.000020	0.010145	0.000407	1.467215	0.000048	-54.2	0.281242	-8.0	0.77	3.1
13.2	2061	0.281273	0.000019	0.000512	0.000042	0.024771	0.001580	1.467229	0.000036	-53.5	0.281253	-7.6	0.69	3.1

3 MAGMATIC EPIDOTE AS A PROXY OF DEEP AND OXIDIZED MAGMATISM IN THE PALEOPROTEROZOIC BACAJÁ DOMAIN, SE AMAZONIAN CRATON

Arthur Santos da Silva Neri

Roberto Dall'Agnol

Gilmara Regina Lima Feio

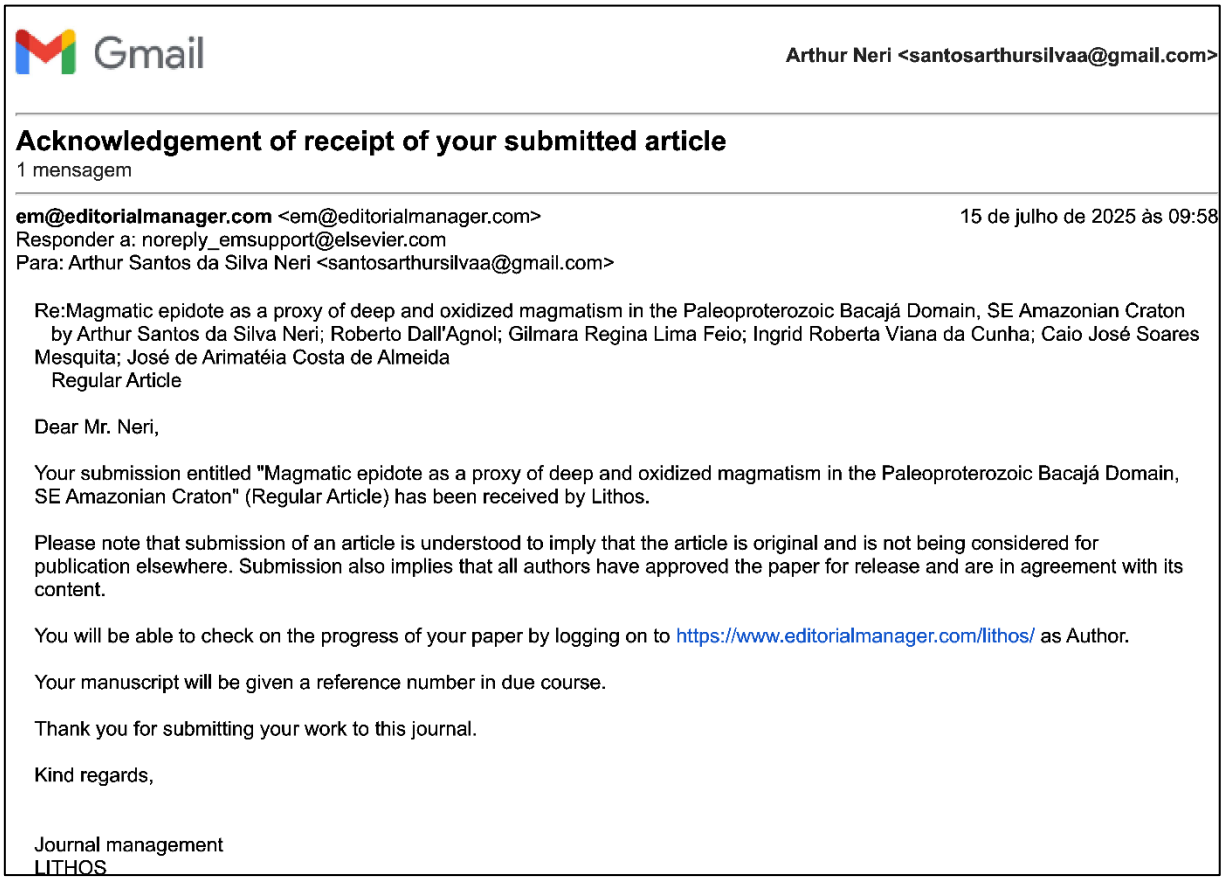
Ingrid Roberta Viana da Cunha

Caio José Mesquita Soares

José de Arimatéia Costa de Almeida

Submetido à *Lithos* como *regular article* em 15/07/25 e em processo de revisão em 18/07/2025.

Respeitando as normas da revista *Lithos* a formatação, citações e referências bibliográficas desta seção seguem o padrão requerido pela revista.



Gmail — Arthur Neri <santosarthursilvaa@gmail.com>

Acknowledgement of receipt of your submitted article

1 mensagem

em@editorialmanager.com <em@editorialmanager.com> 15 de julho de 2025 às 09:58
Responder a: noreply_emsupport@elsevier.com
Para: Arthur Santos da Silva Neri <santosarthursilvaa@gmail.com>

Re:Magmatic epidote as a proxy of deep and oxidized magmatism in the Paleoproterozoic Bacajá Domain, SE Amazonian Craton
by Arthur Santos da Silva Neri; Roberto Dall'Agnol; Gilmara Regina Lima Feio; Ingrid Roberta Viana da Cunha; Caio José Soares Mesquita; José de Arimatéia Costa de Almeida
Regular Article

Dear Mr. Neri,

Your submission entitled "Magmatic epidote as a proxy of deep and oxidized magmatism in the Paleoproterozoic Bacajá Domain, SE Amazonian Craton" (Regular Article) has been received by Lithos.

Please note that submission of an article is understood to imply that the article is original and is not being considered for publication elsewhere. Submission also implies that all authors have approved the paper for release and are in agreement with its content.

You will be able to check on the progress of your paper by logging on to https://www.editorialmanager.com/lithos/ as Author.

Your manuscript will be given a reference number in due course.

Thank you for submitting your work to this journal.

Kind regards,

Journal management
LITHOS

Magmatic epidote as a proxy of deep and oxidized magmatism in the Paleoproterozoic Bacajá Domain, SE Amazonian Craton

Arthur Santos da Silva Neri [a, b*], Roberto Dall'Agnol [a, b, c], Gilmara Regina Lima Feio [d, e], Ingrid Roberta Viana da Cunha [b, f], Caio José Mesquita Soares [b.] José de Arimatéia Costa de Almeida [a, b]

[a] Programa de pós-graduação em Geologia e Geoquímica, Instituto de Geociências (IG), Universidade Federal do Pará (UFPA), Rua Augusto Corrêa, 01, Belém-PA, Brazil. CEP 66075-110.

[b] Grupo de Pesquisa Petrologia de Granitoides IG – UFPA.

[c] Instituto Tecnológico Vale, Belém-PA, Brazil.

[d] Grupo de Mineralogia e Petrologia, Instituto de Geociências e Engenharias (IGE), Universidade Federal do Sul e Sudeste do Pará (UNIFESSPA), Marabá, PA, CEP 68505080, Brazil.

[e] Programa de Pós-Graduação em Propriedade Intelectual e Transferência de Tecnologia para a Inovação (UNIFESSPA).

[f] Present address: Universidade Federal do Oeste do Pará (UFOPA), Rua Ver. José de Sousa Andrade, Juruti - PA, Brazil. CEP 68170-000.

*Corresponding author

ABSTRACT: Magmatic epidote is a key indicator of crystallization conditions in granitic magmas; it is often used as a monitor of oxygen fugacity and pressure conditions. This study investigates the epidote-bearing high-K calc-alkaline Alto Rio Preto granite (2.10-2.07 Ga), located in the Bacajá Domain, SE Amazonian Craton. Petrography, mineral chemistry, and thermodynamic modelling were integrated to constrain the P-T-fO_2-H_2O conditions of crystallization and the epidote stability. Three distinct facies were identified in the granite: amphibole-biotite monzogranite, biotite monzogranite, and biotite granodiorite. Amphibole is classified as magnesium-hastingsite to ferroedenite, with minor tschermakite and ferrohornblende. Biotite is Mg-rich (Fe/(Fe+Mg) ~ 0.60). Textural and compositional evidence (Ps = 28-35, low TiO_2) supports a magmatic origin for epidote. Titanite compositions point to an inherited igneous to recrystallized origin. Plagioclase composition varies from oligoclase to andesine The distinct facies were emplaced at 0.4-0.7 GPa and evolved under oxidizing conditions (NNO±0.5 to ±1), with moderate to high initial water contents (<4-6wt% H_2O). Thermodynamic modelling suggest that epidote stability is favored by high-pressure, restricted to near-solidus

temperatures, high H_2O, and mildly oxidizing conditions. Low magma density and viscosity favored rapid ascent (epidote partial dissolution 2-3 years and magma transport rate of 5-4 km/year), enhancing epidote preservation. Mineral chemistry suggests a calc-alkaline I-type affinity with predominantly crustal source for the Alto Rio Preto magmas. These results provide new insights into deep, oxidized, and water-rich magmatic process in Paleoproterozoic orogenic settings.

Keywords: magmatic epidote; granite crystallization; phase equilibria modeling; Rhyacian magmatism; Bacajá Domain

3.1 INTRODUCTION

Granites and granodiorites make up almost 70% of the upper continental crust and represent key records of crustal evolution (Rudnick and Gao, 2003; Wedepohl, 1995). These rocks can be generated from distinct sources and in a wide range of tectonic settings (Brown, 2013; Moyen, 2020). Understanding the conditions under which granitic magmas crystallize, such as pressure (P), temperature (T), redox conditions (fO_2) and water (H_2O) content, is essential for constraining magma evolution, geochemical affinities and source characteristics. In this context, the mineral chemistry of mafic and accessory phases provides a powerful tool for estimating these intensive parameters and magmatic affinities (Nachit 1985; Hollister et al. 1987; Schmidt 1992; Holland and Blundy 1994; Anderson and Smith 1995; Nachit et al. 2005; Ridolfi et al. 2010).

Amphibole and biotite composition are sensitive to variations in P, T, fO_2, and H_2O in the crystallizing magma (Nachit 1985; Abdel-Rahman 1994; Dall'Agnol et al. 1999, 2017; Putirka 2016; Silva et al. 2020; Cunha et al. 2016). Likewise, accessory mineral such as epidote, titanite and Fe-Ti oxides can retain information about these parameters (Cunha et al., 2021; Sial et al., 2008, 1999; Sousa et al., 2022; Zen and Hammarstrom, 1984)

Although epidote was first recognized as a magmatic mineral by Keyes (1892), its petrogenetic importance was only confirmed by experimental data almost a century later by Naney (1983). This and subsequent experimental and mineral chemistry studies demonstrated that epidote can crystallize in granitic magmas over a wide pressure range (> 0.3-1.0 GPa), with its stability strongly dependent on oxygen fugacity and melt compositions (Dawes and Evans 1991; Schmidt and Thompson 1996; Sial et al. 1999; Schmidt and Poli 2004). Other studies also highlighted that epidote dissolution in granitic magmas is relatively fast, implying that its preservation in these magmas depends on rapid

upward migration (Brandon et al., 1996; Sial et al., 1999). Therefore, epidote represents an important accessory phase, used to estimate the emplacement pressure, redox state and ascension rate of magmas (Cunha et al., 2021; Lima et al., 2021; Nascimento et al., 2023; Schmidt and Poli, 2004; Schmidt and Thompson, 1996; Sial et al., 1999; Zen and Hammarstrom, 1984).

In this study, we investigate the crystallization conditions and epidote stability in the Rhyacian high-K calc-alkaline epidote-bearing Alto Rio Preto granite located in the Bacajá Domain, SE Amazonian craton. The integration of petrography, mineral chemistry, and thermodynamic modelling allow us to infer the P–T–fO_2–H_2O conditions during crystallization and explore the implication of magmatic epidote stability for understanding the granite genesis and evolution.

3.2 GEOLOGICAL SETTING OF THE STUDIED GRANITE

The Maroni-Itacaiúnas Province was established during the Rhyacian-Orosirian in the Amazonian craton (Santos et al., 2006; Tassinari and Macambira, 2004) and includes several granulite-gneiss belts. The Bacajá Domain (Fig. 1b) is an extension of the Maroni-Itacaiúnas Province in the Brazil Central shield. This domain is composed of Archean and Siderian fragments reworked during the Transamazonian Orogeny between ca. 2.26 and 1.99 Ga, (Cordani et al., 2000; Hurley et al., 1967), and Rhyacian to Orosirian granitoids related to orogenic magmatism (Vasquez, 2006; Vasquez et al., 2008; Vasquez and Rosa-Costa, 2008).

The Paleoproterozoic orogenic magmatism is divided into: (i) pre-collisional magmatism dated from 2215±2 Ma to 2133±10 Ma; (ii) the syn- to late-collisional magmatism dated from 2114±3 Ma to 2102±3 Ma; (iii) late- to post-collisional magmatism dated from 2086±5 Ma to 2069±6 Ma; and (iv) the post-collisional magmatism dated at 1986±5 Ma (Vasquez and Rosa-Costa 2008, and references therein).

The Alto Rio Preto granite is in the southern portion of the Bacajá Domain, close to the boundary with the Carajás Province. It consists of two coalescent plutons (ca. 250 km^2) and a small stock, elongated according to the regional trend WNW-ESE, intruded into the Mesoarchean Cajazeiras complex. To the north, it is limited by the Serra Misteriosa transcurrent shear zone, while to the south, it is in contact with Serra Azul charnockite and Bernardino granite. Magmatic to solid-state fabrics were recognized in the granite, defined by WNW-ESE to NW-SE foliation planes, concordant with the regional trend, with moderate to subvertical dips towards mostly NE and subordinately SW, associated with shallow plunging mineral stretching lineation mostly towards E

(Neri et al., submitted a, b).

Neri et al. (submitted a, b) conducted a detailed geological, geochemical, geochronological, and isotopic study in the Alto Rio Preto granite. These authors defined the granite as a classical magnesian (Frost et al., 2001), high-K calc-alkaline granite, composed of two independent magmas crystallized between 2.10-2.07 Ga: (i) amphibole-biotite monzogranite (ABMzG) that evolved to biotite monzogranite (BMzG) via fractional crystallization; and (ii) biotite granodiorite-tonalite. These magmas are products of crustal reworking of Archean sources of basaltic composition that experienced dehydration melting at the lower crust, without significant input of juvenile components, as highlighted by negative $\varepsilon Nd_{(t)}$ and $\varepsilon Hf_{(t)}$. The granite was formed in a late to post-collisional setting, probably triggered by crustal delamination and asthenosphere upwelling.

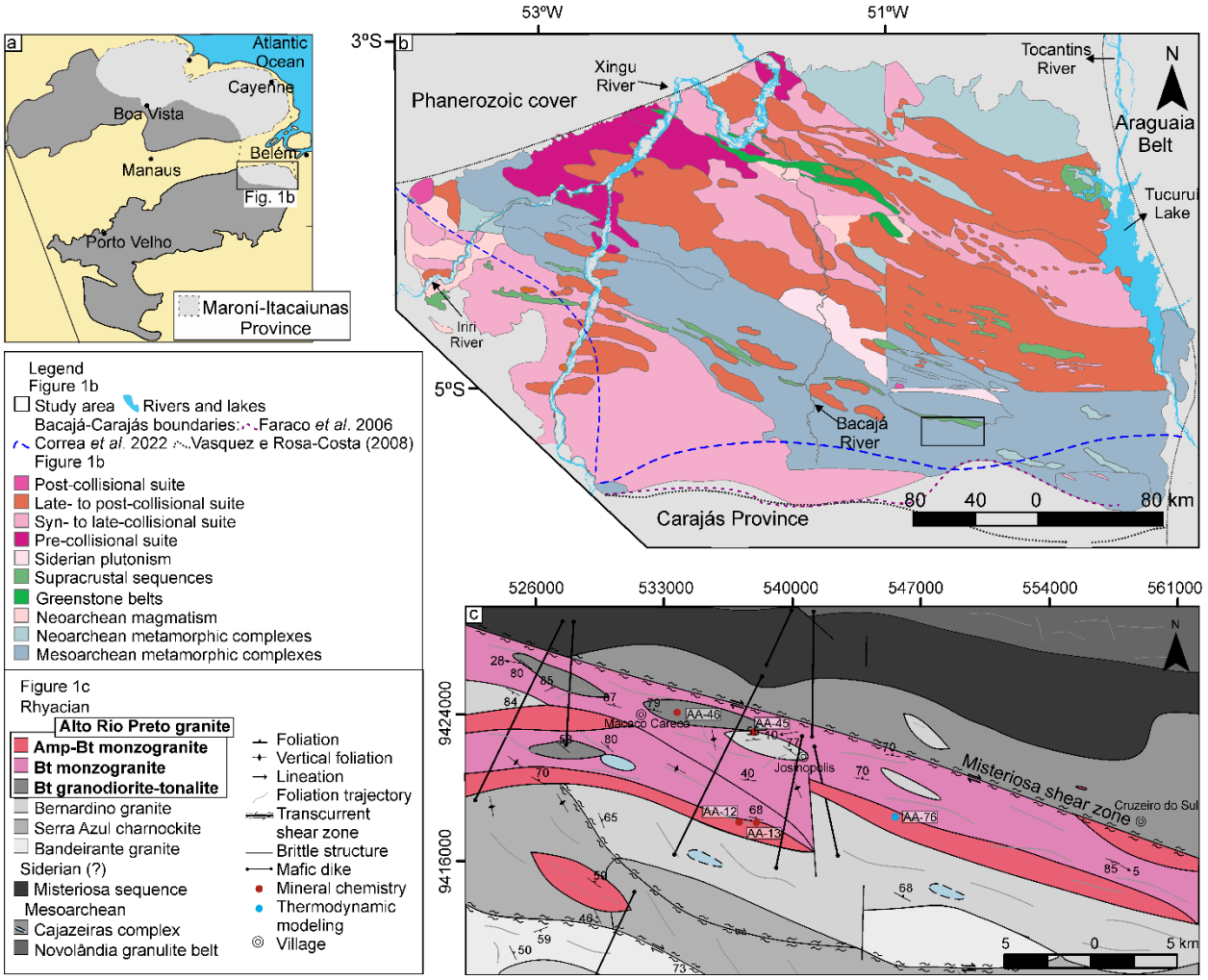


Fig. 1. (a) Amazonian craton and the location of the Bacajá Domain in the Maroni-Itacaiúnas Province (Tassinari and Macambira, 2004). (b) simplified geological map of the Bacajá Domain (Barros et al., 2007; Besser and Barros, 2015; Macambira and Ricci, 2015; Macambira et al., 2009; Vasquez and Rosa-Costa, 2008). (c) Geological map of the studied area (modified from Neri et al., submitted).

3.3 METHODS

Petrography was performed using a Zeiss Axio Imager.A2M microscope at IG-UFPA. Modal analysis was conducted using an automatic point counter (Stageled) coupled with the Hardlegde software by Endeeper. A total of ~1800-2000 points were counted per sample in a grid of 0.4 mm (Tab. S1), which were then used to classify the rock samples according to the Subcommission on the Systematics of Igneous Rocks of the International Geological Sciences (Le Maitre 2002).

Five representative samples were selected for mineral chemistry analyses. The analyzed minerals were amphibole, biotite, plagioclase, titanite, and epidote. Polished thin sections were submitted to wavelength dispersive spectroscopy (WDS) quantitative analyses at the Laboratório de Microssonda (LABSON) from Universidade de Brasília (UnB), using a JEOL JXA-8230 electron microprobe analyzer. Analyses were performed under the following operating conditions: a column accelerating voltage of 15 kV, a current of 10-20 nA, an analysis time of 10 s, and a spot size of 1-5 nm. The standards used for instrument calibration were andradite (Ca and Fe), microcline (Si, Al, and K), olivine (Mg), albite (Na), pyrophanite (Ti and Mn), vanadinite (V and Cl), nickel oxide (Ni), chromium trioxide (Cr), and Celestine (Sr). Mineral abbreviations follows Whitney and Evans (2010).

3.4 RESULTS

3.4.1 Petrography and mineral chemistry

According to the modal classification (Fig. 3), the Alto Rio Preto granite was divided into three facies: (i) amphibole-biotite monzogranite (ABMzG); (ii) biotite monzogranite (BMzG); and (iii) biotite granodiorite-tonalite (BGrd). They are rocks that vary in color from light gray to pink depending on the proportion of essential and mafic minerals. They show medium- to coarse-grained heterogranular to equigranular with local porphyroclastic textures.

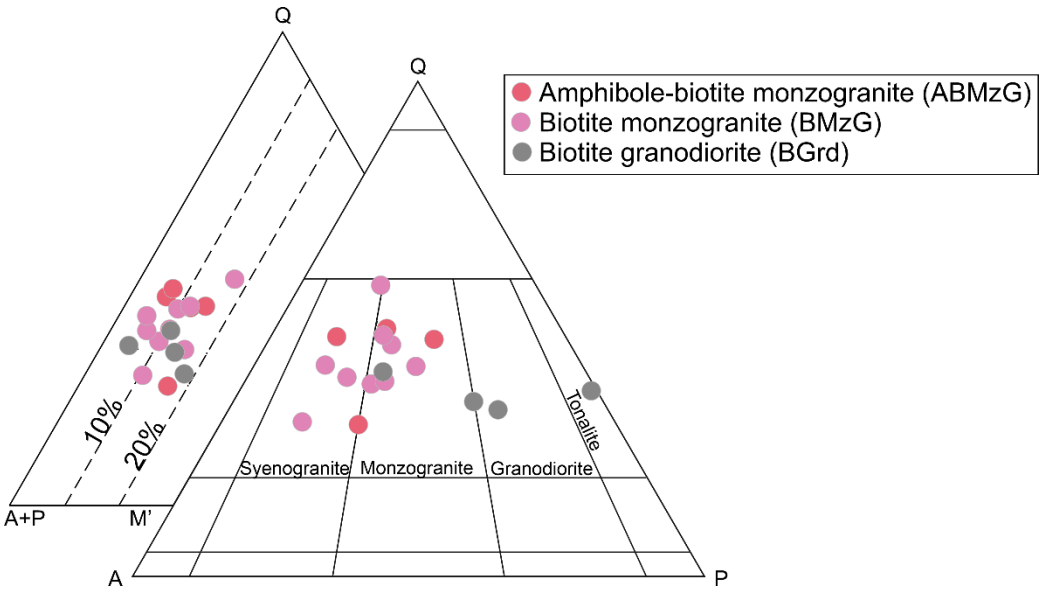


Fig. 2. QAP and Q-A+P-M' diagrams (Le maitre 2002) for samples of the Alto Rio Preto granite.

The granitoids are predominantly leucocratic (M' = 9.15-21.4), with rare hololeucocratic varieties (M' = 4.8). They are composed of varying proportions of quartz, K-feldspar, and plagioclase, with biotite ± amphibole as the main mafic minerals. Primary accessory minerals include titanite, allanite, epidote, zircon, and opaques (magnetite + ilmenite); while muscovite, chlorite, carbonate, and epidote are the secondary ones (Tab. S1).

Amphibole crystals are medium- to fine-grained, exhibiting subdiomorphic to idiomorphic textures in undeformed samples (Fig. 3a). In contrast, in mylonitic samples, they may appear as xenomorphic, oval-shaped crystals (Fig. 3b). Amphibole typically occurs in mafic clots with biotite and titanite. The analyzed amphiboles show no significant compositional variation between samples; they are calcic s and classified as magnesio-hastingsite and ferroedenite [$(Ca + Na)_B \geq 1.00$ and $Na_B < 0.50$], with minor tschermakite and ferrohornblende (Fig. 4a, b, Leake et al. 1997, Tab. S2)

Biotite occurs in three main textural types: (i) in the ABMzG facies, it forms idiomorphic to subdiomorphic crystals that crystallized after amphibole during late-magmatic stages (Fig. 3a); (ii) in all three granite facies, it also appears as subdiomorphic to xenomorphic crystals aligned with the foliation (Fig. 3b, c, d); (iii) in mylonitic to ultramylonitic rocks, it occurs as fully recrystallized xenomorphic crystals (Fig. 3b). Biotite displays a restricted Fe/(Fe+Mg) ratios, generally near ~0.60 (Tab. S2), being classified as Mg-biotite (Fig. 4c, d). In the Al vs. Mg diagram (Fig. 4e, Nachit 1985), biotite compositions display sub-alkaline to calc-alkaline affinity. The FeO+MnO vs. $10*TiO_2$ vs. MgO diagram (Fig. 4f, fields of Nachit et al. 2005) biotite from monzogranite

facies plot within the primary magmatic field. In contrast, biotites from granodiorite facies vary from primary to reequilibrated.

Four distinct epidote texture types were observed: (i) fine-grained, subdiomorphic to xenomorphic crystals, with straight contact with amphibole and biotite (Fig. 3e); (ii) fine-grained subdiomorphic crystals forming coronas around allanite (Fig. 3f); (iii) fine-grained xenomorphic crystals along biotite cleavage planes; and (iv) xenomorphic crystals with sinuous contacts with plagioclase. Only the first two types were analyzed, the analyses yielded low TiO_2 (<0.16 wt%, Tab. S3), the 'pistacite' component (Ps = molar $[Fe^{3+}/(Fe^{3+} + Al)] * 100$) values range from 28 to 35 (Tab. S3, Fig.5b). The combination of textural evidence, low TiO_2 and pistacite content suggests that the analyzed epidotes are from magmatic origin (Evans and Vance, 1987; Pandit et al., 2014; Tulloch, 1979).

Three distinct titanite textural types were identified: (i) fine- to medium-grained idiomorphic to subdiomorphic crystals, with straight contacts with amphibole and biotite, commonly in mafic clots; (ii) fine-grained xenomorphic crystals forming after biotite and amphibole (Fig. 3b); and (iii) coronitic, fine-grained xenomorphic titanite surrounding ilmenite grains. Titanite major element-compositions do not vary significantly between textural types and samples (Tab. S3). Their Fe/Al ratios (0.23 to 0.45) plot in the transition field between igneous and metamorphic titanite (Fig. 5c). Some exhibit fluorine enrichment (Fig. 5d). The Al/Fe ratios range (2.24-4.34 in ABMzG; 1.35-3.89 in BGrd; Tab. S3) suggests compositions typical of inherited igneous or recrystallized crystals (Scibiorski and Cawood, 2022).

Plagioclases and K-feldspar occur as fine- to coarse-grained idiomorphic to subdiomorphic (Fig. 3a, e, f). In deformed rocks, they are xenomorphic and exhibit oval shapes (Fig. 3b, c). Microcline commonly exhibit perthitic exsolution textures and tartan twinning. Quartz is fine- to medium-grained, typically recrystallized into sub-grains and new grains. Bulbous myrmekite intergrowths are observed near the borders of microcline crystals and in microfractures. Plagioclase compositions do not vary significantly between samples in the same facies (Tab. S4, Fig 5a), ranging from oligoclase to andesine (An_{28-33}) in monzogranitic facies, and is oligoclase in the granodiorite facies (An_{24-29}). Single crystals usually show normal zoning, with a rim-ward decrease of anorthite content.

Zircon, apatite, and opaques form fine-grained idiomorphic inclusions in other phases. Allanite forms fine- to medium-grained idiomorphic to subdiomorphic crystals

that can show epidote coronas (Fig. 3f).

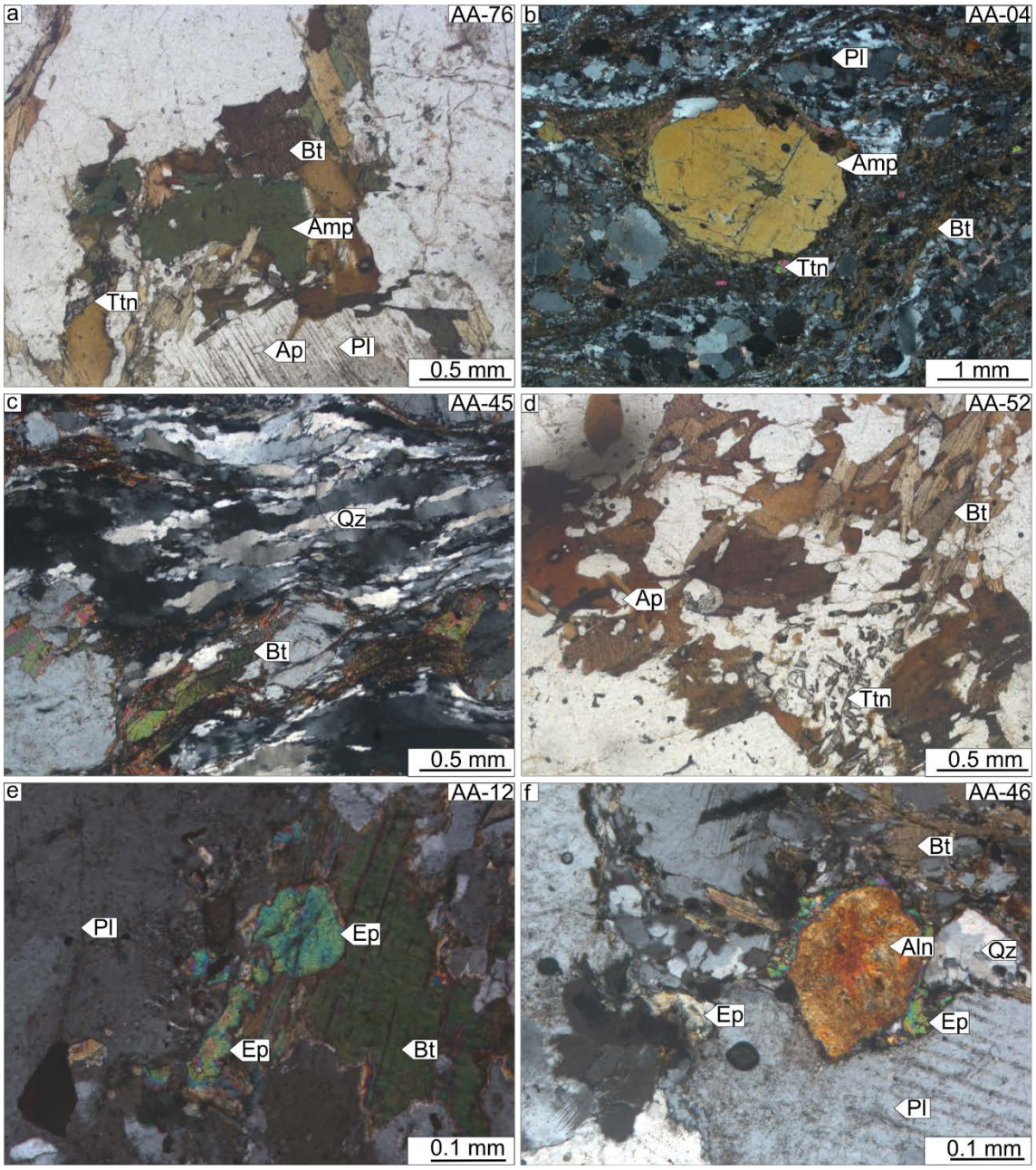


Fig. 3. Main petrographic aspects of the Alto Rio Preto granite. (a) mafic clot composed of amphibole, biotite, titanite and opaque minerals; (b) subdiomorphic amphibole in mylonitic granite, surrounded by recrystallized biotite (bt3); (c) quartz with undulose extinction accompanied by subdiomorphic biotite (bt2). (d) fine grained titanite formed after biotite (ttn2); (e) magmatic epidote with straight contacts with biotite; (f) magmatic epidote forming coronitic texture in allanite.

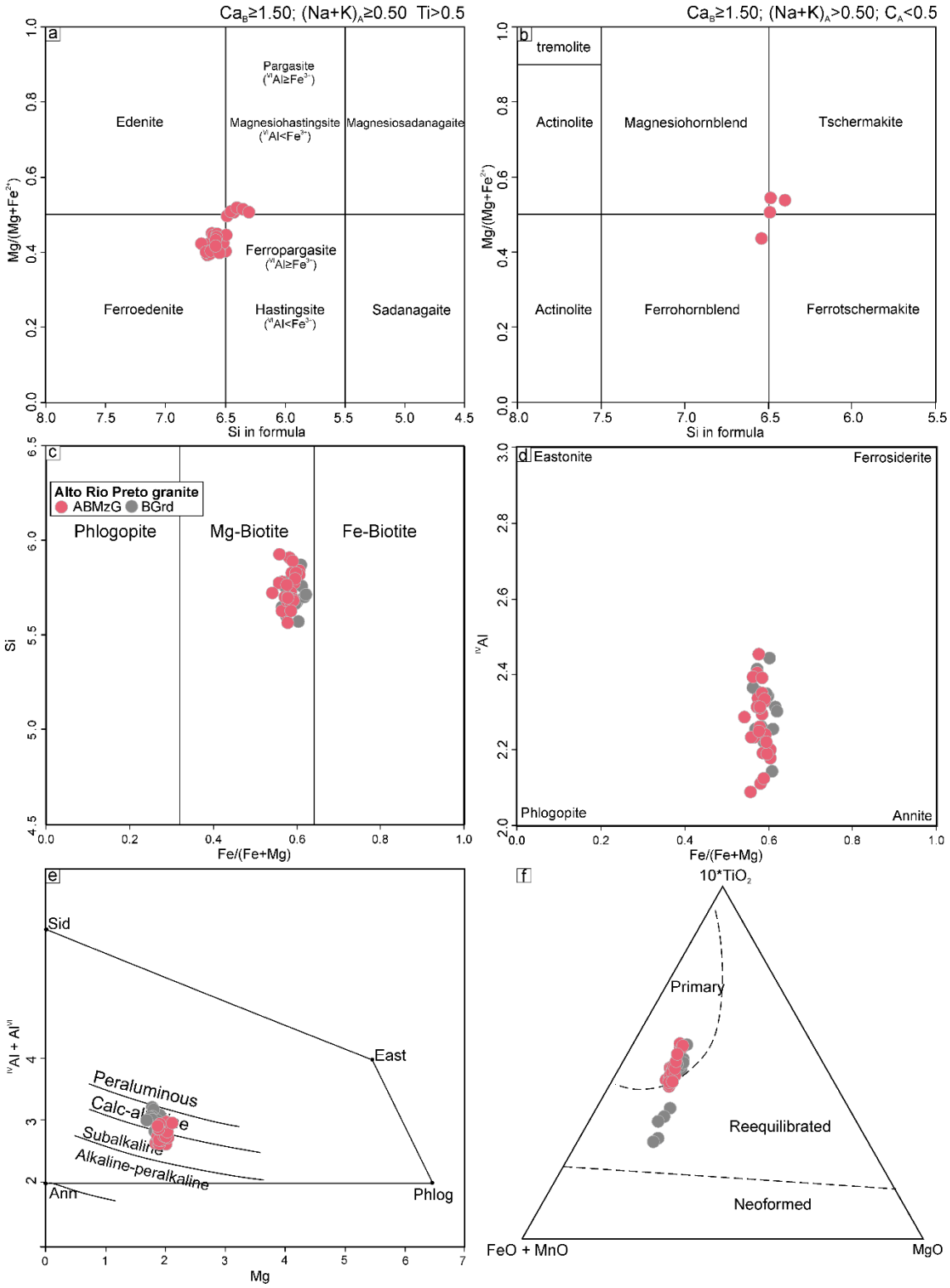


Fig. 4. Classification diagrams for the analyzed mineral phases. (a, b) calcic amphibole classification after Leake et al. (1997); (c) Si vs. Fe/(Fe + Mg) compositional classification of biotite (Deer et al., 2013); (d) Fe/(Fe + Mg) vs. Al^{IV} compositional classification of biotite (Deer et al., 2013); (e) Mg vs, Al_t diagram for biotite (Nachit 1985);(f) (FeO + MnO)-(10*TiO_2)-MgO diagram with fields from Nachit et al. (2005).

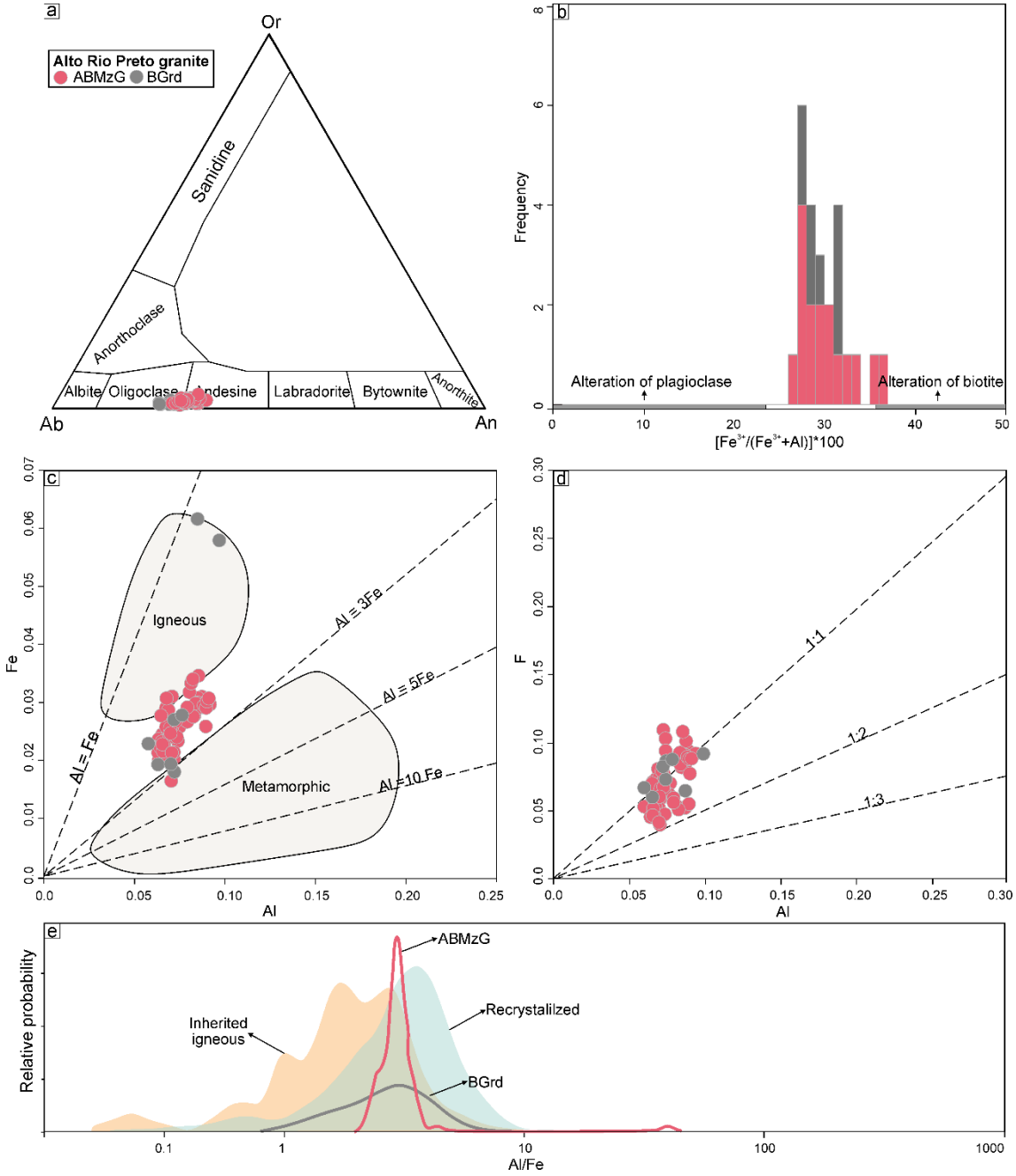


Fig. 5. Classification diagrams for the analyzed mineral phases. (a) Ab–An–Or ternary diagram showing the plagioclase compositions(Deer et al., 2013); (b) histogram of compositional variation in the pistacite component ([Fe^{3+}/Fe^{3+}+Al]/100), in molecular percentage (mol.%); (d) Al vs. Fe in titanite with fields from Aleinikoff et al. (2002); (c) F vs. Al in titanite (Kowallis et al., 2022); (e) Al/Fe density spectrum with fields of inherited igneous and recrystallized titanites (Scibiorski and Cawood, 2021).

3.4.2 Crystallization phase equilibria

3.4.2.1 Experimental background on epidote and amphibole stability

The stability of magmatic epidote is controlled by distinct variables, which include pressure, temperature, magma composition, and oxygen fugacity (Liou, 1973; Schmidt and Thompson, 1996; Poli and Schmidt, 2004; Schmidt and Poli, 2004). Experimental data indicate that epidote is stable above 0.3 GPa, however the minimum pressures may

vary depending on whole-rock composition and redox state (Schmidt and Poli, 2004). In granodiorite and tonalitic magmas, epidote is stable at 0.8 to 1.0 GPa in near solidus temperatures (Liou, 1973; Naney, 1983; Schmidt and Poli, 2004). On the other hand, in water-saturated granitic compositions a minimum pressure of 0.6 GPa is required for epidote crystallization (Crawford and Hollister, 1982; Liou, 1973)

Oxygen fugacity exerts a major influence on epidote stability: it can crystallize in pressure as low as 0.3 GPa in oxidizing conditions near the Hematite–Magnetite (HM) buffer, but in less oxidized environments near the Nickel–Nickel Oxide (NNO) buffer a minimum pressure of 0.5 GPa in necessary for epidote to be stable (Naney 1983; Schmidt and Thompson 1996). Overall, epidote stability increases toward more oxidizing conditions, with its magmatic stability lying mainly between the Fayalite–Magnetite-Quartz (FMQ) and HM buffers (Liou, 1973; Schmidt and Poli, 2004; Schmidt and Thompson, 1996).

Concerning amphibole, which is one of the main mafic minerals in the Alto Rio Preto granite together with biotite, experimental data point that a minimum of 5 wt.% H_2O at 0.4 GPa, or 7–9 wt.% H_2O at 0.96 GPa is required for amphibole be the ferromagnesian liquidus phase and prevent orthopyroxene formation (Naney 1983; Prouteau and Scaillet 2003).

3.4.2.2 Modeling parameters

Crystallization phase equilibria modeling was carried out with GeoPS version 3.5 (Xiang and Connolly, 2022), using the internally consistent dataset and activity-composition (a-X) models of Holland et al. (2018) in the KNCFMASHTO (K_2O–Na_2O–CaO–FeO–MgO–Al_2O_3–SiO_2–H_2O–TiO_2–Fe_2O_3) designed for igneous rocks in near-dry and wet conditions. The oxidation state of the magma was determined using the software fO_2Melt (Holland et al. 2018), considering the calculated $\log fO_2$ estimated from amphibole and biotite compositions (Anderson et al. 2008; Ridolfi et al. 2010) and whole-rock FeO/(FeO+MgO) ratios (Neri et al., submitted a, b).

The different facies of the Alto Rio Preto granite appear to have crystallized under relatively similar pressure, temperature, and redox conditions, with changes only in water content (section 5.1). For this reason, the modelling was focused on the sample AA-76 (ABMzG), which shows the best-preserved mineral assemblage. This sample also has the lowest SiO_2 and highest MgO, and is therefore interpreted as the most primitive composition, likely representing the parental magma of the monzogranitic magma of the Alto Rio Preto granite.

Given the presence of magmatic epidote and the absence of orthopyroxene, modeling was conducted over a pressure range of 0.2 to 1.0 GPa, using initial H_2O of 4 wt% and 6 wt%. These values are consistent with mineral thermobarometry constraints and experimental data from rocks with similar compositions.

To evaluate the effects of varying water content and redox state on epidote stability, T-$M_{H2O/}O(\log fO2)$ were calculated at fixed pressure at 0.64 and 0.93 GPa; while the P-$M_{H2O/}O(\log fO2)$ were calculated at 620 and 680 ºC. These values were obtained by the lower and upper limits of epidote stability without garnet in the P-T pseudosection (Fig. 6). The normalized molar proportion used for modelling is shown in Tab. S5.

3.4.2.3 Amphibole-biotite monzogranite

Pseudosections for sample AA-76, an amphibole-biotite monzogranite, indicate that melt H_2O content, temperature, and pressure exert strong influence on phase stability. The liquidus temperature decreases from ~1000 ºC (at 4 wt% H_2O, Fig. 6a) to ~960 ºC (at 6 wt%, Fig. 6b), in contrast, the solidus temperatures decrease with increasing pressure. In both calculations, plagioclase is the liquidus phase followed by magnetite and ilmenite. The calculated plagioclase composition near the liquidus is enriched in anorthite (An = ~0.86, 960 ºC) compared to the most calcic composition detected in the natural sample (An = 0.33, 640 ºC at 0.65 GPa, Fig. 6b).

The crystallization sequence slightly differs with water content. At 4 wt% (Fig. 6a), orthopyroxene is the first ferromagnesian phase to crystallize, with stability between ~920 to 780 ºC. Amphibole begins to crystallize at ~860 ºC, becoming unstable near the solidus at high pressures (i.e., 0.68 GPa), biotite crystallizes shortly after (~800 º) and remains stable to near solidus temperatures. At 6 wt% (Fig. 6b), orthopyroxene is absent, and amphibole becomes the liquidus ferromagnesian silicate, in a temperature range of ~880 ºC down to the solidus, becoming unstable in pressures >0.66 GPa, shortly after epidote crystallization. The XMg (Mg/(Mg+Fe) in amphibole indicates crystallization temperatures from 840 to 780 ºC at 0.65 GPa (Fig. 6b).

Biotite stability is relatively insensitive to H_2O content, initiating at ~800 ºC in both systems and remaining sable until the solidus. The Ti_{M2} contents in biotite indicates crystallization over the range ~760-730 ºC (at 0.65 GPa and 6 wt%, Fig. 6b).

Epidote is a near solidus and high-pressure phase becoming stable only above 0.66 and 0.64 GPa at 4 and 6 wt% H_2O, respectively. The crystallization of epidote in both systems is slightly coincident with the amphibole out curves.

Titanite and rutile exhibit mutually exclusive stability fields: rutile is stable at

higher pressures, while titanite is stable at lower pressures, consistent with experimental data in granitoids (Angiboust and Harlov, 2017). With increasing H_2O, titanite's stability field shrinks while that of rutile enlarges.

K-feldspar and quartz stability strongly depends on water content and pressure; their stability shifts to lower temperature with increasing water and decreasing pressure. This feature is more accentuated in K-feldspar that becomes a near solidus phase at 6 wt% (Fig. 6b).

Garnet is stable only at a high-pressure and high-temperature conditions (>0.93 GPa and ~760-885ºC at 6 wt%), while muscovite is a high-pressure near solidus phase (>0.72 GPa).

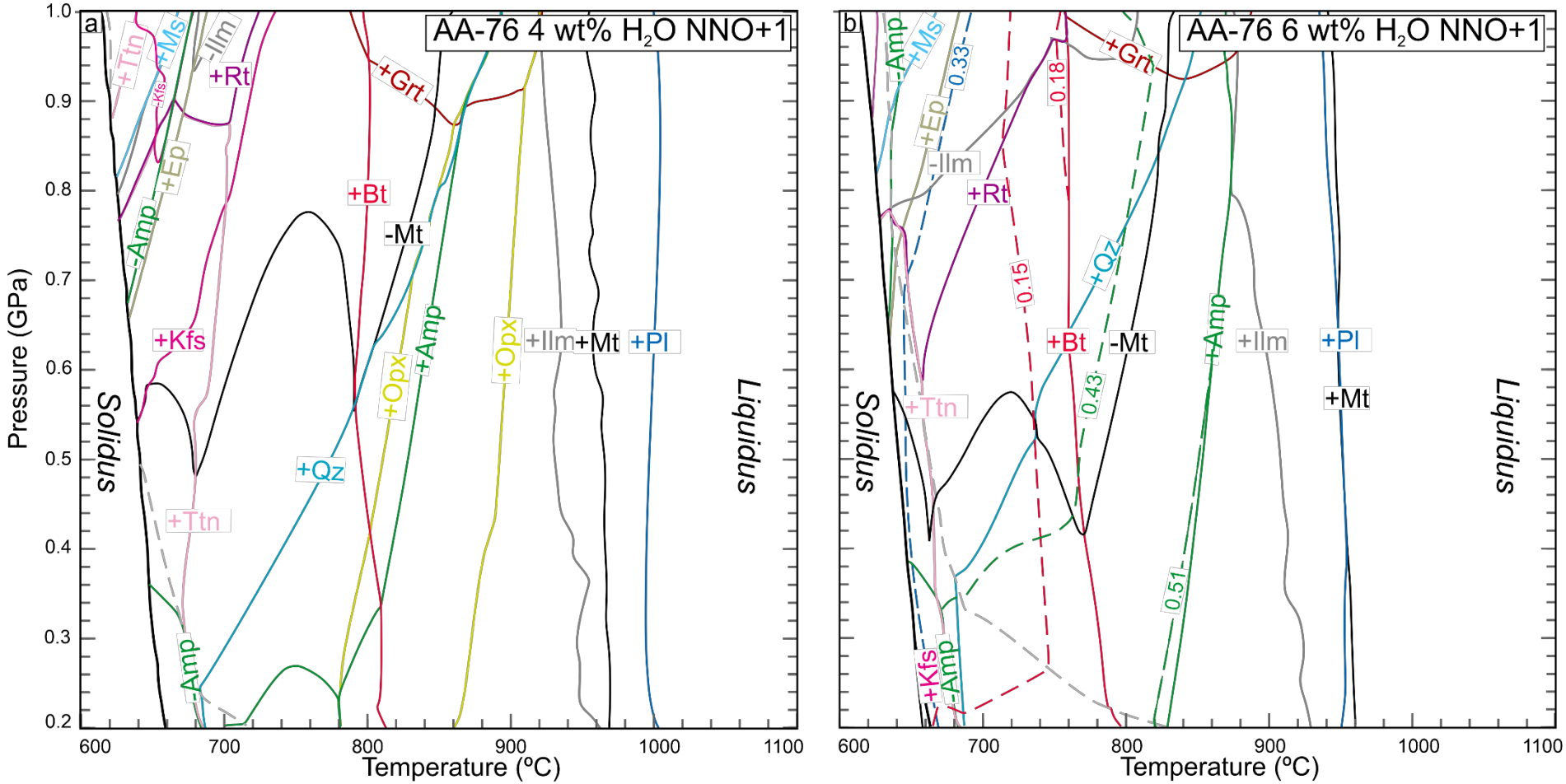


Fig 6. P-T pseudosection do the Alto Rio Preto granite at (a) 4 wt% H_2O, (b) 6 wt% H_2O of initial water in the system. Solid lines mark each phase stability field, the appearance is marked with the symbol (+) and disappearance with (-). Dashed lines mark the XAn in plagioclase (blue), XMg in amphibole (green), and Ti in the M2 site of biotite (red). Bellow the light grey dashed line, the minerals and melt co-exist with a free H_2O-rich fluid.

The T/P-M_{H2O} modeling (Fig. 7a-d) indicates that both pressure and water content exert a strong influence on epidote stability. Under sub-saturated (1 wt% H_2O) to water-saturated conditions (9 wt%), epidote stability increases with both increasing water content and pressure. At 0.64 GPa (Fig. 7a), epidote appears as near solidus phase, crystallizing only at 638ºC and above ~4.8 H_2O wt%. In contrast, at 0.93 GPa (Fig. 7b), epidote is stable throughout the modeled range from 668 ºC (1 wt%) to a maximum of ~678 ºC with 5.9 wt%. In the P-M_{H2O} diagram at 620 ºC (Fig. 7c), the solidus occurs at relatively high pressure (~0.89 GPa); and, under these conditions, epidote remains stable across the full range of water content. In contrast, at 680 ºC (Fig. 7d), epidote is stable only above ~0.93 GPa and become unstable at ~7wt% H_2O.

As observed in the P-T diagram titanite and rutile are incompatible and rutile prevails under higher pressures, and titanite in lower ones. Amphibole is stable at lower pressures (0.64 GPa) and higher temperature conditions (680 ºC), while at higher pressures (0.93 GPa) its stability increases with increasing water content (i.e., 664 ºC at 1 wt% and 636 ºC at 9 wt%). K-feldspar stability is favored in low water conditions, becoming unstable above ~4.8-5.0 wt% in all modeled ranges. Plagioclase, quartz, and biotite stability are not influenced by water content and are stable throughout the modeled range.

Changing the redox conditions from reduced (NNO-1.5) to strongly oxidized (NNO+2.5), important constraints about epidote stability can be identified (Fig. 8a-d). At 0.64 GPa, epidote appear as a near-solidus phase, crystallizing only below 636 ºC and becoming unstable under more oxidizing conditions, disappearing above NNO+0.2 (Fig. 8a). At higher pressure (at 0.93 GPa, Fig. 8b), epidote is stable across a broader range, crystallizing from reduced (NNO-1.5, 644 ºC) to oxidized conditions (NNO+2.5, 654 ºC). In the P-M$\log fO2$ diagram, epidote is stable across the entire modeled range (Fig. 8c, d). At 620 ºC, epidote is stable above ~0.89 GPa. At higher temperatures (680 ºC), its stability shifts to lower pressures towards more oxidizing conditions, from 1.0 GPa at NNO-1.5 to 0.97 GPa at NNO+2.5.

Titanite and rutile display a similar behavior compared to the other diagrams, they are mutually exclusive, rutile usually being stable towards more oxidizing conditions (Fig. 8a-d). Amphibole is unstable in low pressures and temperature conditions, and at higher temperature and pressure redox state does no significantly influence its stability. Biotite, quartz, and plagioclase are not affected by changing in the redox conditions, being stable throughout the modeled range.

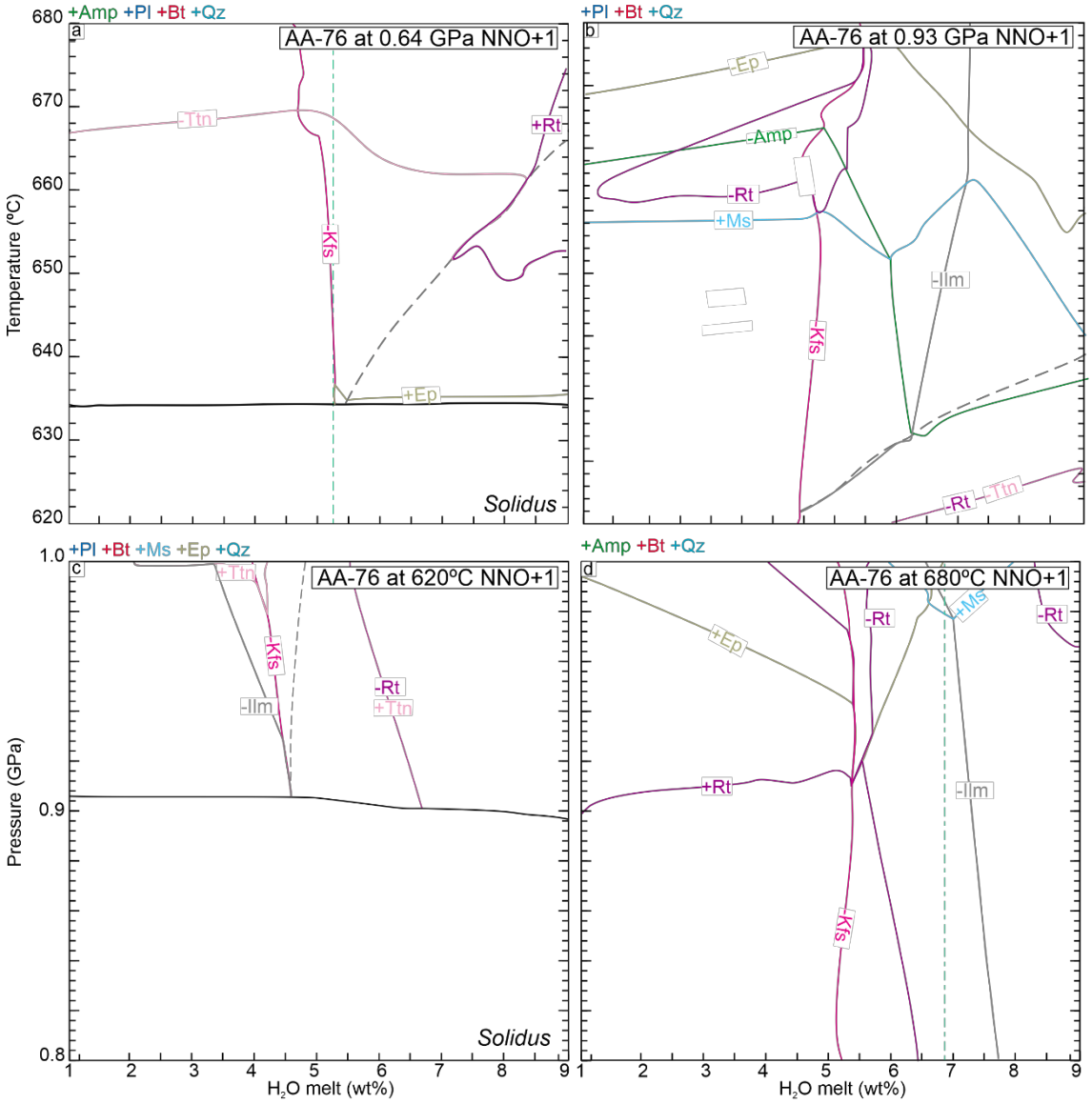


Fig 7. T/P-MH_2O for sample AA-76. (a) T-M_{H2O} at 0.64 GPa and ~ NNO+1; (b) T-M_{H2O} at 0.93 GPa and ~NNO+1; (c) P-M_{H2O} at 620 ºC and ~NNO+1; (d) P-MH_2O at 680 ºC and ~NNO+1. The plus (+) symbol marks the appearance of the phase, and the minus (-) the disappearance. The P-$M_{H2O/log fO2}$ must be read from the left to the right and from the bottom to the top. The phases highlighted at the top of the diagram are in all fields of the modeled ranges.

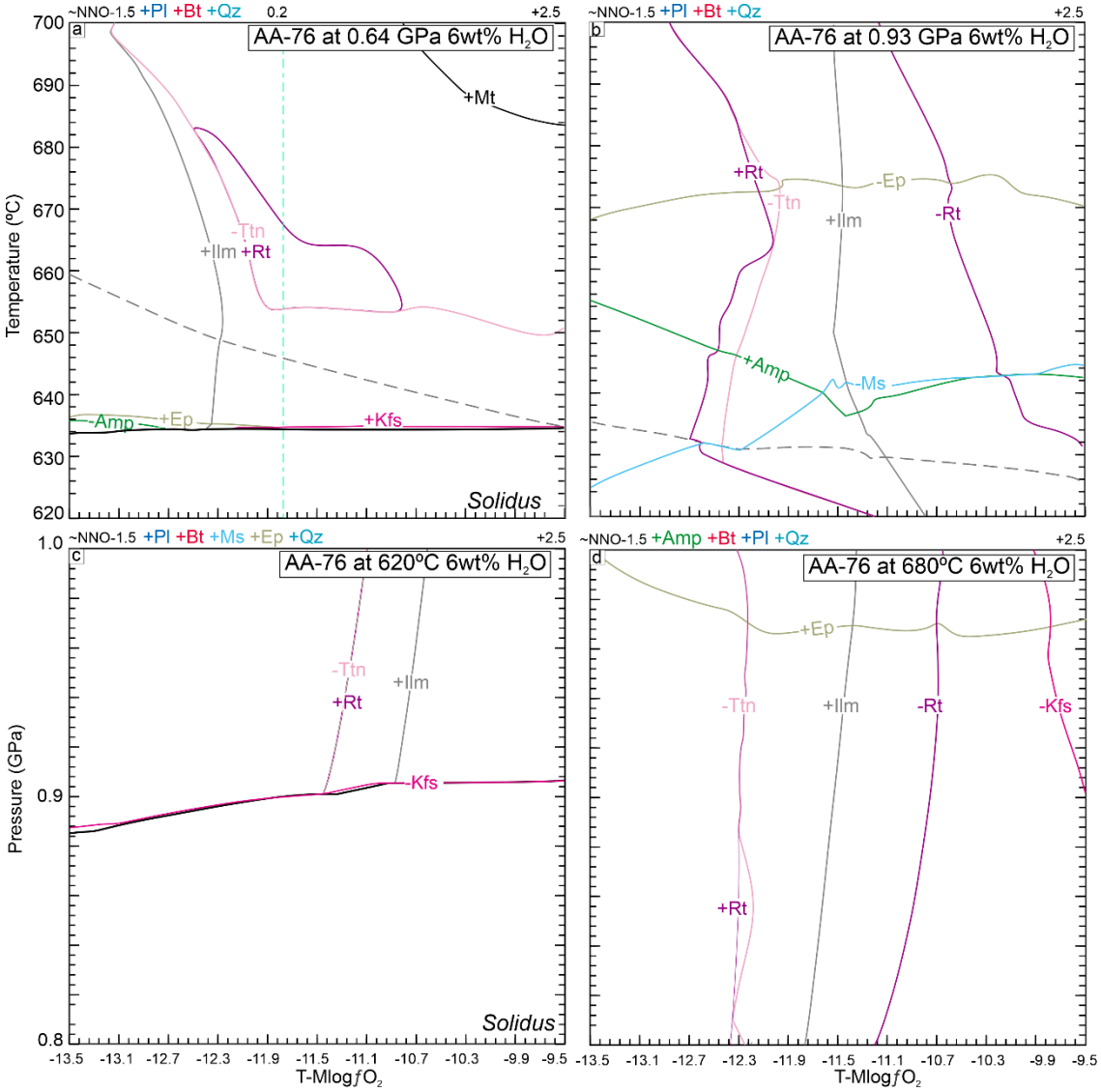


Fig. 8. T/P-Mlog$f$O2 for sample AA-76. (a) T-Mlog$f$O2 at 0.64 GPa; (b) T-MlogfO2 at 0.93 GPa; (c) P-Mlog$f$O2 at 620 ºC with 6 wt% H_2O; (d) P-Mlog$f$O2 at 680 ºC with 6 wt% H_2O. The plus (+) symbol marks the appearance of the phase, and the minus (-) the disappearance. The P-$M_{H2O/logfO2}$ must be read from the left to the right and from the bottom to the top. The phases highlighted in the tops of the diagram are in all fields of the modeled ranges.

3.5 DISCUSSION

3.5.1 Thermodynamic modeling uncertanties

Prior to addressing any interpretation based on thermodynamic modelling data, it is necessary to understand the uncertainty inherent to the method. Thermodynamic modeling has been widely applied to the understanding of metamorphic rocks with distinct compositions, and even for igneous rocks derived from melting of sedimentary sources (Wang et al., 2023; Zhao et al., 2017) using the well stablished internally consistent dataset of Holland and Powell (2011). In contrast, the application of this methodology to metaluminous igneous rocks is less common (Mesquita et al., 2025), mostly because of the limitations on the models of Holland and Powell (2011) for these

compositions. However, the new internally consistent dataset of Holland et al. (2018) provided consistent models to address the evolution of igneous rocks of distinct compositions (peridotite do granite) in a wide P-T-H_2O range (0.0001-7.0 GPa, 650º C to peridotite liquidus, 0.8-15 wt% H_2O). Although some inconsistencies may arise from these models, given some assumed simplifications compared to the natural systems (Holland et al. 2018), it is safe to affirm that the modeling performed in this study can provide geological consistent information into igneous crystallization of the studied granites.

3.5.2 Crystallization parameters

Crystallization parameters were estimated using whole-rock geochemistry compiled from Neri et al. (submitted b), mineral chemistry of selected phases (amphibole, biotite, and plagioclase), and thermodynamic modelling. All amphibole calculations were performed using the WinAmptb programs (Yavuz and Döner, 2017). The summary of P-T-fO_2-X_{H2O} obtained is given in Tab. 1.

It is also worth noting that although the granite is deformed, we selected the least deformed samples to perform the analyses. Therefore, the data obtained here represent the magmatic compositions of its phases and can be used to infer the crystallization conditions.

3.5.2.1 Temperature

The apatite saturation thermometer (Harrison and Watson 1984) yielded high temperatures from 930 to 882 ºC (ABMzG) and 950 to 877 ºC (BGrd). These results are consistent with those obtained using the machine-learning whole-rock thermometer (Weber and Blundy 2024), which produced temperatures between 930 to 877 ºC (ABMzG) and 898 to 853 ºC (BGrd). The amphibole-plagioclase thermometer (Holland and Blundy, 1994), also provided high-temperatures between 980 and 842 ºC. The thermodynamic modelling provided slightly higher liquidus temperatures from 1000 ºC (4 wt% H_2O) to 960 ºC (6 wt%). In contrast, the zircon saturation thermometer (Harrison and Watson 1984) yielded lower temperatures: 814 to 770 ºC (ABMzG) and 792-790 ºC (BGrd). Temperature progressively decreases when using thermometers based on calcic-amphibole compositions from 839 to 751 ºC (Putirka 2016) and 908 to 834 ºC (Ridolfi et al., 2010). These values overlap or are slightly higher than the amphibole stability field obtained in the thermodynamic modelling (~880-680 ºC, Fig. 6b). The machine-learning thermometer based on biotite composition (Li and Zhang, 2022) returned the lowest temperatures estimates, between 751 to 766 ºC (ABMzG), and slightly higher values in

the granodioritic facies, ranging from 762 to 792 ºC. The values from monzogranitic facies broadly overlaps with the temperatures obtained in the thermodynamic modelling using the Ti_{M2} contents in biotite (760-730 ºC).

3.5.2.2 Pressure

For the amphibole-bearing facies, using rim compositions the Al-in-amphibole geobarometers (Schmidt 1992; Anderson and Smith 1995) yielded consistent pressures estimated from 0.3 to 0.66 GPa. In contrast, the calibration by Mutch et al. (2016) provided slightly lower pressures (0.35-0.49 GPa), while the Ridolfi et al. (2010) barometer yielded even lower values (0.2-0.32 GPa). The graphic barometer (Anderson and Smith 1995) suggest pressure between 0.5 and 0.7 GPa (Fig. 9a). The machine learning barometer based on biotite composition (Li and Zhang 2022) provided pressures estimates broadly comparable to those from amphibole, ranging from 0.36 to 0.71 (ABMzG) and 0.58 to 0.77 (BGrd) GPa. The thermodynamic modelling indicates a minimum pressure of ~0.64 GPa for epidote crystallization which is similar to the higher values obtained by mineral thermobarometry.

In the granodioritic facies, the lack of amphibole hinders a precise pressure estimation. However, both whole-rock (Weber and Blundy 2024) and biotite-based barometers (Li and Zhang 2022) provided consistent values from 0.55 to 0.58 GPa (whole-rock) and 0.54-0.77 GPa (biotite composition), suggesting emplacement at similar or slightly higher pressures compared to the monzogranitic facies.

Geological and geochronological evidence supports an intrusive relationship between the granite and Cajazeiras complex, which records metamorphic conditions ranging from amphibolite to granulite facies. The garnet-free orthogneiss suggest a minimum peak-pressure of ca. 0.55-0.52 GPa and retrograde reequilibration at 0.40-0.46 GPa (Neri et al., submitted c). Additionally, the granite host enclaves of aluminous high-pressure granulites (Neri et al., submitted c) that register peak conditions at ca. 1.1 GPa, consistent with pressures from the generation of the magmas of the ABMzG facies (Neri et al., submitted b).

Taken together, mineral barometry, thermodynamic modelling and geological evidence indicate emplacement pressures of 0.4-0.7 GPa for the two facies of the Alto Rio Preto granite.

3.5.2.3 Oxygen fugacity

Quantitative estimates of the oxygen fugacity are mostly based on the Fe/(Fe + Mg) ratio of amphibole and biotite, as these phases tend to incorporate more Mg in their

structure with increasing fO_2 (Anderson and Smith 1995; Anderson et al. 2008; Cunha et al. 2016; Dall'Agnol et al. 2017; Silva et al. 2020).

Oxygen fugacity estimates derived from Fe/(Fe+Mg) ratios of amphibole indicate a transition between high and intermediate fO_2 (Fig. 9b). To further quantify redox conditions, LogfO_2 values were calculated using the formulations by Ridolfi et al. (2010), coupled with amphibole temperatures by the same authors. In the LogfO_2 vs. temperature diagram (Fig. 9c), the analyzed amphibole plot at or slightly above the NNO buffer. Biotite compositions also support oxidizing conditions. In the total Al vs. Fe/(Fe+Mg) diagram, biotite plots in the fields of magnetite-series granites (Fig. 9d), further indicating the crystallization from an oxidized melt.

Further qualitative inferences about the redox state can be based on the presence of magmatic epidote and titanite, both stable under relatively high fO_2 (Schmidt and Thompson, 1996). Additionally, whole-rock geochemistry reveals low FeO/(FeO+MgO) ratios (Neri et al., submitted), consistent with magnesian and oxidized magmas.

Taken together, the mineralogical and geochemical indicators suggest that the Alto Rio Preto granite crystallized under moderately to strongly oxidizing conditions, likely at NNO±0.5 to NNO+1.

3.5.2.4 Water content

Experimental data suggest that a minimum of 4 wt% H_2O is required for amphibole stability in granitic magmas (Dall'Agnol et al., 1999; Scaillet et al., 2016). Other studies indicate that 5 wt% H_2O at 0.4 GPa or 7–9 wt.% at 0.96 are necessary for amphibole to be the silicic liquidus phase and inhibit pyroxene formation (Naney 1983; Prouteau and Scaillet 2003). The Alto Rio Preto granite is dominated by biotite and amphibole and no trace of orthopyroxene or clinopyroxene was observed in petrographic analyses. Combined with emplacement pressure estimates between 0.4 and 0.7 GPa, this suggests that the initial water in the monzogranitic facies must have been ≥ 5 wt%. In contrast, the absence of amphibole in the BMzG and granodioritic facies implies water content below 4 wt%.

To further constrain the water content at the time of amphibole crystallization, the amphibole hygrometer of Ridolfi et al. (2010) was applied (Tab. 1), yielding values from 5.35 to 7.93 H_2O wt% (Tab. 1). Since water concentration increases during crystallization, these values likely reflect the H_2O content at the time of amphibole crystallization. Given that amphibole is not the earliest crystallized phase (section 4.2), the initial water must have been lower than the hygrometer estimates.

In the thermodynamic modeling the pseudosection with an initial 6 wt% H_2O content provided the best match between the modeled assemblages and the natural sample. Therefore, a reasonable value of 6 wt% is inferred to represent the initial water in the amphibole-biotite monzogranitic facies.

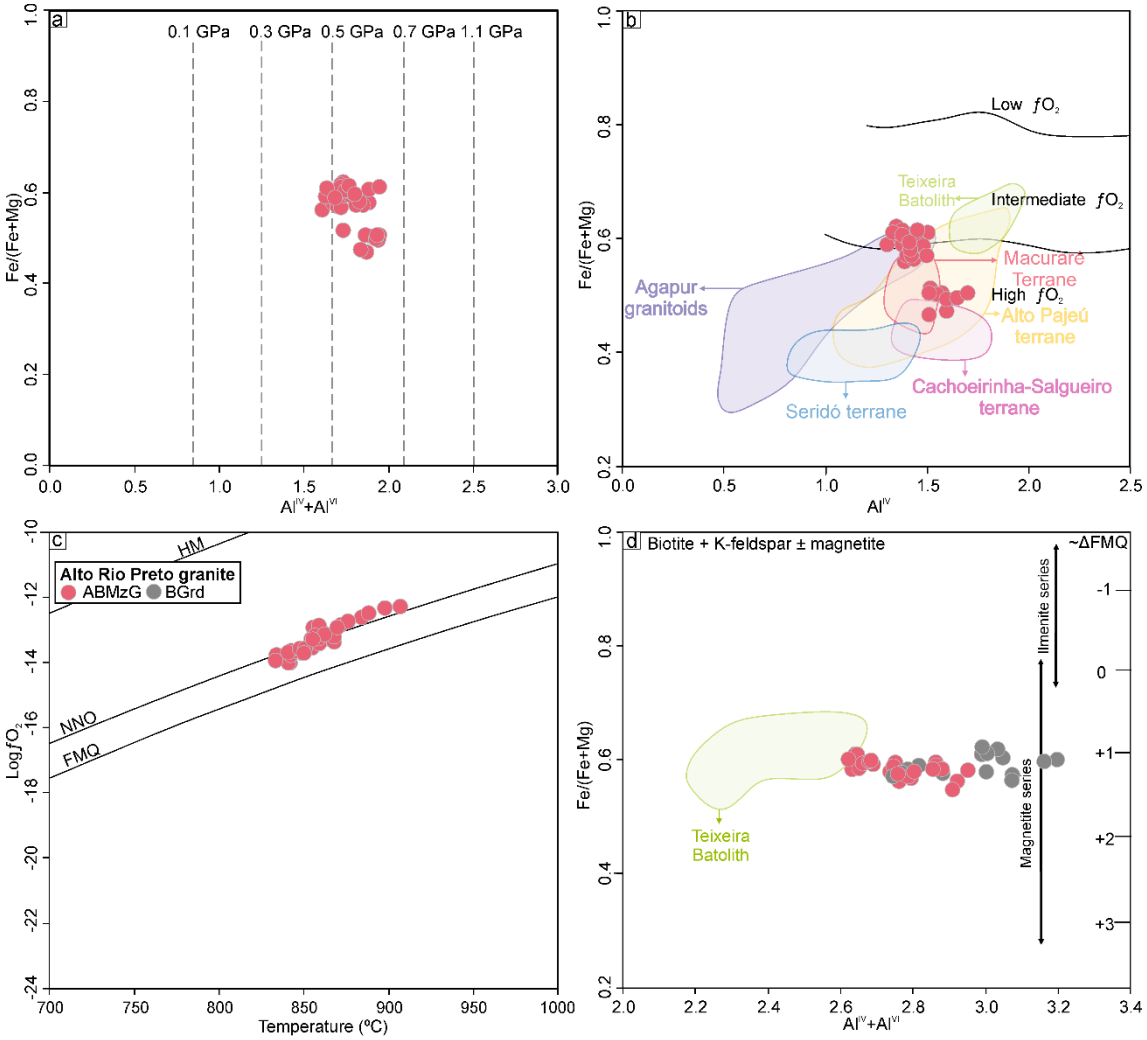


Fig. 9. Estimative of crystallization parameters from Alto Rio Preto granite. (a) Fe/(Fe + Mg) vs Al^{IV} + Al^{VI} diagram for amphiboles from the studied rocks, with isobars from Anderson and Smith (1995), (b) Fe/(Fe+Mg) vs. Al^{IV} diagram showing the compositional variation of amphibole (the analyses in the high fO_2 field are from sample AA-76; fields after Anderson and Smith 1995), (c) LogfO_2 vs. temperature based on amphibole composition (Ridolfi et al., 2010), (d) Fe/(Fe+ Mg) vs. Al^{IV} + Al^{VI} diagram showing the compositional variation of biotites (ilmenite and magnetite series according to Anderson et al. 2008). The fields for comparison: from Seridó, Cahoeirinha-Salgueiro, Alto Pajeú, and Macuraré terranes from Borborema Province, NE Brazil (Sial et al., 2008), Teixeira batholith, Borborema Province (Lima et al. 2021), and Agapur granitoids, India (Basak et al. 2019).

Table 1. Summary of crystallization conditions of the Alto Rio Preto granite determined by mineral chemistry data.

Facies	Amphibole-biotite monzogranite			Biotite granodiorite	
Sample	AA-76	AA-12	AA-13	AA-45	AA-46*
Temperature (ºC)					
Harrison and Watson (1984) - Ap	930	882	937	949	877
Watson and Harrison (1983) - Zrn	809	814	770	790	792
Weber and Blundy (2024) - Whole-rock	930	890	877	898	853
Holland and Blundy (1994) – Amp-Pl	907-950	842-877	949-980	-	-
Putirka (2016) Amp	773-839	751-782	778-795	-	-
Ridolfi et al.(2010) Amp	835-908	834-866	851-869	-	-
Li and Zhang (2022) Bt	751-766	755-767	818-796	781-796	762-796
Pressure (GPa)					
Schmidt (1992) - Amp	0.48-0.63	0.51-0.63	0.49-0.5	-	-
Anderson and Smith (1995) - Amp	0.33-0.51	0.29-0.66	0.38-0.46	-	-
Ridolfi et al. (2010) - Amp	0.20-0.32	0.22-0.32	0.21-0.25	-	-
Mutch et al. (2016) - Amp	0.35-0.49	0.37-0.49	0.35-0.41	-	-
Li (2022) - Bt	0.34-0.61	0.38-0.67	0.37-0.71	0.58-0.76	0.54-0.77
Weber and Blundy (2024) – Whole-rock	0.61	0.73	0.59	0.58	0.55
Oxygen fugacity					
Ridolfi et al. (2010) logfO_2	-13.69 to -12.21	-13.92 to -13.18	-13.72 to -13.22	-	-
Water content (wt%)					
Ridolfi et al. (2010)	5.35 to 7.21	6.19 to 7.93	5.40-6.47	<4	<4

*Biotites from sample AA-46 are classified as reequilibrated (Fig. 4f), yet their analyses provided similar results if compared to primary biotites from the sample AA-45.

3.5.2.5 Magma density

Magma density was calculated for sample AA-76 (Fig. S1). The results show a clear increase in density with progressive magma crystallization, assuming no significant fractionation, with the variation of density being directly controlled by melt proportion. At liquidus temperatures (930 ºC), the magma density is ~2.34 g/cm^3 (0.65 GPa). These values are significantly lower than the typical density of middle to lower continental crust, which ranges from 3.0 to 3.2 g/cm^3 (Jaupart and Mareschal, 2010), where the Alto Rio Preto granite magmas were generated (Neri et al., submitted b).

3.5.2.6 Magma viscosity

Magma viscosity was estimated using the non-Arrhenius, Newtonian model (Giordano et al., 2008), which accounts for the effects of melt composition, H_2O, and F on the viscosity of silicate magmas. The viscosity (η, in Pa·s) is expressed by the following equation:

$$\mathrm{VTF}\ [\log \eta\ = \mathrm{A} + \mathrm{B}/\ \mathrm{T}\ (\mathrm{K}) - \mathrm{C})]$$

where A is the upper temperature limit for the viscosity of all silica melts, which is - 4.55 (±0.2), and B and C are compositional-dependent parameters calibrated from over 1770 experimental measurements conducted at 1 bar and elevated pressures, including hydrous melts. The A parameter reflects the convergence of silicate melts to a low viscosity at super-liquidus temperatures due to the high degree of melt depolymerization. The B and C parameters incorporate the influence of 17 major element oxides and their interactions, including volatile components, allowing the model to capture viscosity variations across more 15 log units (10^{-1} to 10^{15} Pa s) for a wide range of magma compositions (Giordano et al., 2008),

Given that the Rio Preto granitoids have compositional affinities with calc-alkaline to high-K calc-alkaline granitoids, this model is appropriate to estimates the order of magnitude of melt viscosity, provided temperature and H_2O content are well constrained.

Viscosity was calculated for samples with available whole-rock geochemistry (Tab. S6) and either thermodynamic modeling or mineral thermobarometry calculations. The relevant liquidus and solidus temperatures, along with initial H_2O melt contents, were derived from pseudosection modeling and mineral thermobarometric constraints.

The calculated viscosity of each sample is listed in Tab. S7, and its variation as a function of temperature is shown in Fig. 10. The amphibole-biotite monzogranitic magma has the lowest silica content and highest water content, resulting in the lowest viscosity at the liquidus ~$10^{2.9}$ Pa s (AA-76), ~$10^{3.5}$ Pa s (AA-12), and ~$10^{3.4}$ Pa s (AA-13). The granodioritic magma has higher silica content, lower water and modal ferromagnesian minerals, which result in the highest viscosity at the liquidus ~$10^{4.7}$ Pa s (AA-45) and ~$10^{5.7}$ Pa s (AA-46). In both facies, the viscosity increases with increasing silica content and decreasing temperature.

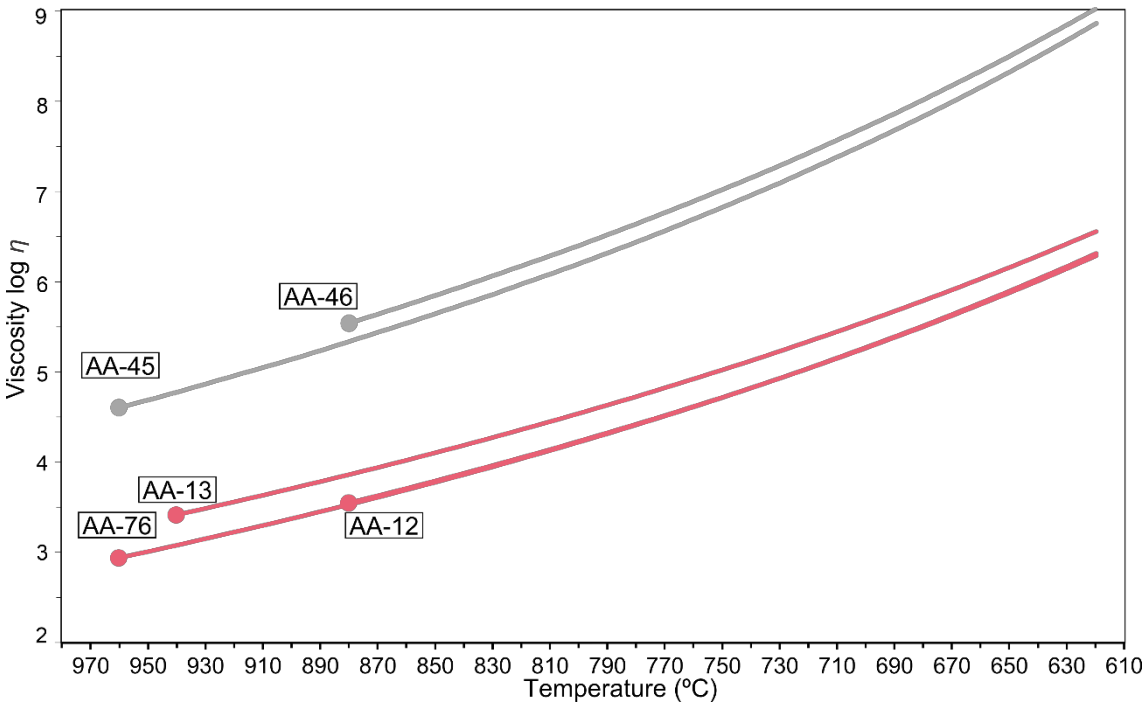


Fig. 10. Diagram showing the variation in the calculated magma viscosity from the Alto Rio Preto magmas as a function of temperature. Viscosity was calculated based on the model by Giordano et al. (2008). Gray lines correspond to the BGrd facies, while dark-pink are related to ABMzG facies.

3.5.3 Origin and stability magmatic epidote: role of P-T-*f*O_2-H_2O

To assess the magmatic origin of epidote, petrography, textures, associated mineral assemblages, and chemical compositions must be considered (Cunha et al., 2021; Pandit et al., 2014). In the Alto Rio Preto granite, epidote display straight contacts with amphibole and biotite (Fig. 3e) or form a coronitic texture after allanite (Fig. 3f). Moreover, chemical composition of epidote shows low TiO_2 and pistacite content (Ps = 25-35). Although some overlapping between magmatic and hydrothermal epidote can occur (Pandit et al., 2014), the combination of textural and chemical data supports a magmatic origin for the epidote from Alto Rio Preto granite.

Magmatic epidote can be originated through peritectic hornblende resorption without completely consuming the hornblende in the system, decreasing only its abundance proportionally to the modal increase in biotite + epidote (Schmidt and Poli 2004 and references therein). The following equilibrium appears to control epidote stability in granitoids (Schmidt and Poli, 2004):

$$Ca_2(Mg,Fe,Al)_5(Al,Si)_8O_{22}(OH)_2 + KAlSi_3O_8 + NaAlSi_3O_8 + Fe_3O_4 + H_2O \rightarrow$$
$$Ca_2Al_3Si_3O_{12}(OH) + K(Mg,Fe)_3AlSi_3O_{10}(OH)_2 + SiO_2$$

hornblend + K-feldspar + plagioclase + magnetite + H_2O = epidote + biotite + quartz

(Schmidt and Poli, 2004)

A distinct origin can be constrained for epidote, when it exhibits textural evidence

consistent with the concomitant formation with magmatic biotite (Fig. 3). This relationship can be explained by the peritectic reaction:

$$NaAlSi_3O_8 + Ca_2(Mg,Fe,Al)_5(Al,Si)_8O_{22}(OH)_2 + melt \rightarrow K(Mg,Fe)_3AlSi_3O_{10}(OH)_2 + Ca_2Al_3Si_3O_{12}(OH)$$

plagioclase + amphibole + melt = biotite + epidote (Sial et al., 1999)

Magmatic epidote can also be originated by the epitaxial growth after allanite, due to magma impoverishment in rare earth elements during crystallization, which inhibits allanite crystallization and enables epidote growth (Dawes and Evans, 1991; Giere and Sorensen, 2004). In this scenario, epidote would result from the coupled substitution:

$REE^{3+} + Fe^{2+} \rightleftharpoons Ca^{+2}\ Fe^{+3}$ (Giere and Sorensen 2004 and references therein)

Our essays of thermodynamic modelling in the Alto Rio Preto granite constrained the stability of epidote and suggests that it relies on a complex interaction between pressure, melt H_2O content, and redox conditions, similar to what was observed in previous experimental studies (e.g., Liou 1973; Naney 1983; Schmidt and Poli 2004). A minimum pressure of 0.64 GPa is necessary for epidote to crystallize at 6 wt% of initial water, and its stability field significantly expands at higher presses (e.g., 0.93 GPa); in both conditions epidote is a near-solidus phase. In the lower pressure limit (0.64 GPa), its stability strongly depends on water content and redox conditions, being stable only above 4.8 wt% H_2O and becoming unstable above NNO+0.2. In contrast, at the upper pressure limit (0.93 GPa), epidote is stable from 1 to 9 wt% H_2O and from reduced (NNO-1.5) to oxidizing conditions (NNO+2.5).

Altogether, the thermodynamic data indicates that epidote stability in the modeled composition is favored under high-pressure, water-rich and moderately to strongly oxidizing conditions, which fairly agree with previous experimental data (e.g., Schmidt and Poli, 2004).

3.5.4 Controls on epidote preservation during magma ascent

Epidote is a phase easily resorbed during magma ascent or under decompression, especially if ascent is slow (Brandon et al., 1996; Schmidt and Poli, 2004; Sial et al., 1999; Zen and Hammarstrom, 1984). Therefore, the presence of magmatic epidote in rocks emplaced at relatively low pressures suggests that they derived of magmas that were likely generated at greater depths and experience rapid transport in the crust to prevent complete epidote dissolution (e.g., Cunha et al. 2021). In this scenario, density and viscosity of the magmas exert a strong influence on epidote preservation, given that these physical properties are the main parameters that control magma ascent rate (Browne and

Szramek, 2015; Giordano et al., 2008; Schulze et al., 1996; Wang et al., 2023).

Magma density calculations for monzogranitic facies (AA-76) yielded values of ca. 2.34 g/cm³ at liquidus temperatures that is significantly lower than the average density of the lower continental crust (3.0–3.2 g/cm³; Jupart and Mareschal 2010), where these magmas were formed (Neri et al. submitted b). This density contrast between the source region and the generated magma suggests that the Alto Rio Preto magmas were buoyant enough to efficiently ascent through the crust to be emplaced at shallower crustal levels.

Complementary to density, the melt viscosity also plays a critical role in controlling magma ascent rate. The model of Giordano et al. (2008) indicates low viscosity values at liquidus conditions ($10^{2.9}$ to $10^{3.5}$ Pa s), for monzogranitic facies. These values, combined with relatively low silica content (Tab. S5) and elevated H_2O content (6 wt%), are decisive for rapid ascent rates that are essential for preservation of epidote. In contrast, the granodiorite facies displays higher viscosity at liquidus temperatures (~$10^{4.7}$ to ~$10^{5.7}$ Pa s) associated with higher silica contents and lower water content, suggesting more evolved and less mobile magmas, with less favorable conditions for epidote preservation. This can explain the common occurrence in these rocks of epidote as coronas surrounding allanite and very rare isolate crystals.

Altogether, the physical and chemical properties of the Alto Rio Preto magmas, which includes medium to high water content, oxidizing conditions, low density and viscosity, coupled with ascent through shear zones, provided favorable conditions not only for epidote crystallization but also allowed a fast ascent of its magma that avoid complete resorption of epidote crystals and favored its preservation in the Alto Rio Preto granite.

3.5.5 Magma ascent rates

Epidote dissolution kinetics is directly related to changes in intensive crystallization parameters during magma rise and emplacement, that can induce destabilization and complete dissolution of epidote crystals (Schmidt and Poli, 2004). In this sense, the magma transport rates can be estimated based on the degree of epidote dissolution (Brandon et al., 1996; Cunha et al., 2021; Pandit et al., 2014; Sial et al., 2008, 1999).

The emplacement pressure of the granite is a key variable to calculate the magma transport rate (Brandon et al., 1996). As discussed in section 5.1, the Alto Rio Preto magmas were emplaced at 0.4-0.7 GPa. We assumed a mean value of 0.64 for both magmas, which is consistent with the minimum pressure of epidote crystallization in

thermodynamic modeling (section 4.2).

Considering the equations proposed by Brandon et al. (1996), and the methodological criteria detailed by Sial et al. (2008) (Sup. Material 6), an average time of epidote partial dissolution is ~2 and ~3 years and transport rates of ~5423 and ~4178 m/year were estimated for monzogranitic and granodioritic magmas, respectively (Fig. 11, Tab. 2).

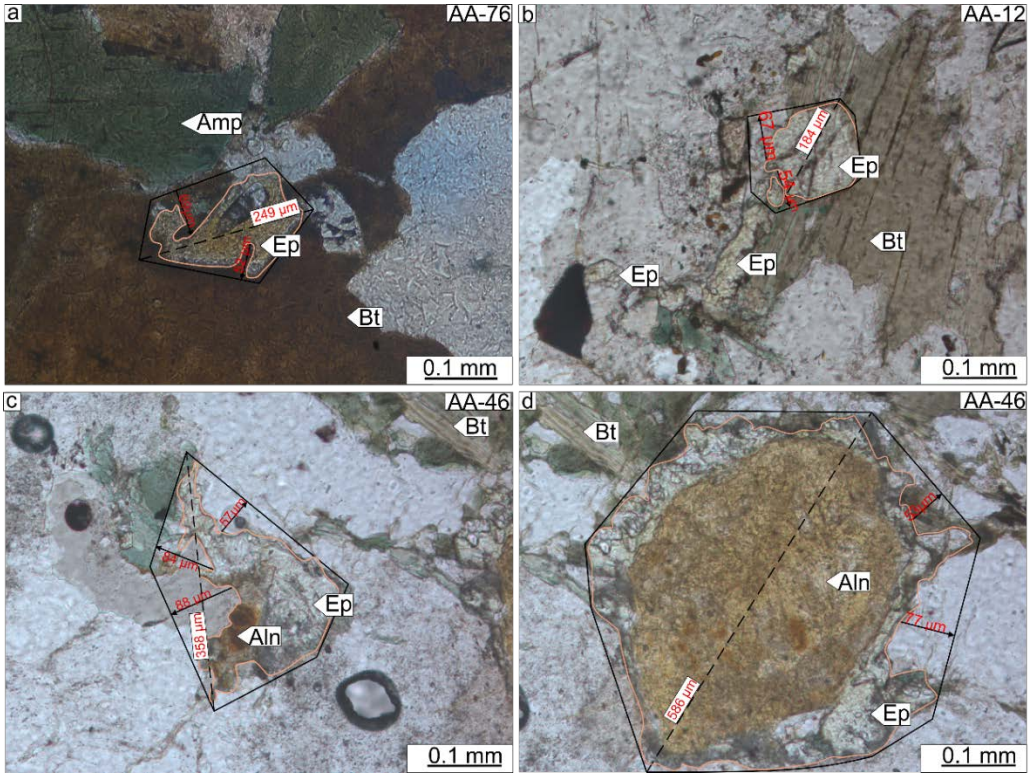


Fig. 11. Textural aspects of the epidotes used in the dissolution kinetic study. The original shapes of the epidote crystals are indicated by the black lines, the orange lines delimit the current shape of the corroded crystals, the largest dimension. Line segments with an arrow point shows the maximum dissolution values used in kinetic study. (a-b) epidote crystals in the ABMzG facies with straight contacts with biotite and irregular contacts with quartzfeldspatic matrix; (c-d) epidote surrounding allanite cores in the BGrd facies with irregular contacts with quartzfeldspatic matrix.

Table 2. estimation of magma transport rate based on kinetic dissolutions of magmatic epidotes from the Alto Rio Preto granite.

Amphibole-biotite monzogranite				
Sample	Grain width (µm)	Maximum width of dissolution (µm)	Partial dissolution time (years)	Rate of upward transport (m/year)
AA-76				
Spot 1	249	52	1.7	7002
Spot 2		69	1.3	3977
AA-12				
Spot 1	184	67	2.8	4218
Spot 2		56	1.8	6493
Average			2	5423

Biotite granodiorite				
A-46				
Spot 1	586	53	1.8	6741
Spot 2		77	3.8	3194
Spot 3	530	57	2.1	5828
Spot 4		84	4.5	2683
Spot 5		88	4.9	2445
Average			3	4178

The epidote dissolution is controlled by multiple factors, such as composition, water content, density, and viscosity of the host magmas, and conduit width (Brandon et al., 1996; Cunha et al., 2021; Nascimento et al., 2023; Sial et al., 1999). Additionally, the relationships of epidote crystals with other minerals in the rock are also relevant: if epidote crystals are fully or partially enclosed by amphibole and biotite, the dissolution tends to be slower if compared to crystals in contact with the residual melt (Cunha et al., 2021).

Considering these variables, the differences in the dissolution kinetics and ascent rates between the two magmas of the Alto Rio Preto granite can be related to the compositional differences between the two magmas. Compared with the granodioritic magma, the monzogranitic magma has lower viscosity and higher water content resulting in higher ascent rates and, in it, epidote crystals are often showing straight contacts with biotite (Fig. 11a, b). In contrast, in the granodioritic rock, epidote crystals were in direct contact with residual melt (now represented by felsic minerals; Fig. 11c, d), being more intensely corroded and showing irregular outlines. Conduit width might have played a secondary role, as the two magmas coexist in the field, they probably were emplaced and deformed together, probably ascending through similar conduits.

Based on geological and structural data, Neri et al. (submitted b) concluded that the Alto Rio Preto granite represents a syntectonic intrusion, which deformation began in the magmatic stage and perpetuated to solid-state deformation. The magma ascent and emplacement were facilitated by regional transcurrent shear zones, similar to other syntectonic magmatic epidote-bearing granites in the northern Bacajá Domain (Barros et al., 2023). This rapid ascent enough for epidote preservation were probably possible through conduit flow/dyke mechanism (Petford et al., 2000).

3.5.6 Magma affinity and source characteristics

The compositions of ferromagnesian phases such as amphibole and biotite are widely recognized as an effective tool to constrain magma nature and affinities (Abdel-

Rahman, 1994; Nachit, 1985; Villaseca et al., 2017; Xie and Zhang, 1990; Zhao et al., 2012). To infer the nature of the Alto Rio Preto magmas, both minerals were used

In the MgO vs. FeO/FeO+MgO) diagram (Zhao et al., 2012), biotite compositions plot in the crustal field (Fig. 11a). In the Al_2O_3–MgO–FeO ternary diagram (Abdel-Rahman 1994), biotites compositions indicate moderate Mg enrichment relative to Al and Fe, plotting within the field of calc-alkalic orogenic suites (Fig. 11b). Furthermore, the progressive increase of Fe and Fe/(Fe+Mg) ratios in biotite defines compositional trend typical of I-type granitoids (Fig. 11c, fields of Villaseca et al. 2017). Amphibole compositions suggest transition from crustal to crustal-mantle sources (Fig. 11d, fields of Xie and Zhang 1990).

These results are in accord with whole-rock geochemistry data from the Alto Rio Preto granite (Neri et al., submitted b), which classify the granite as metaluminous to slightly peraluminous and calc-alkaline to high-K calc-alkaline in character, indicative of I-type affinity. Furthermore, the mentioned authors concluded that the Alto Rio Preto magmas were generated by dehydration melting of a basaltic lower crust, without significant input of juvenile components as highlighted by strongly negative $\varepsilon Nd_{(t)}$ and $\varepsilon Hf_{(t)}$ values.

Taken together, the mineral chemistry, whole-rock geochemistry and isotopic data (Neri et al. submitted a, b) converge to a dominant crustal source for the Alto Rio Preto magmas, with limited juvenile input. This interpretation is supported by the very sparse occurrence of mafic microgranular enclaves (MME), which are restricted to the margins of the intrusion (Neri et al., submitted b).

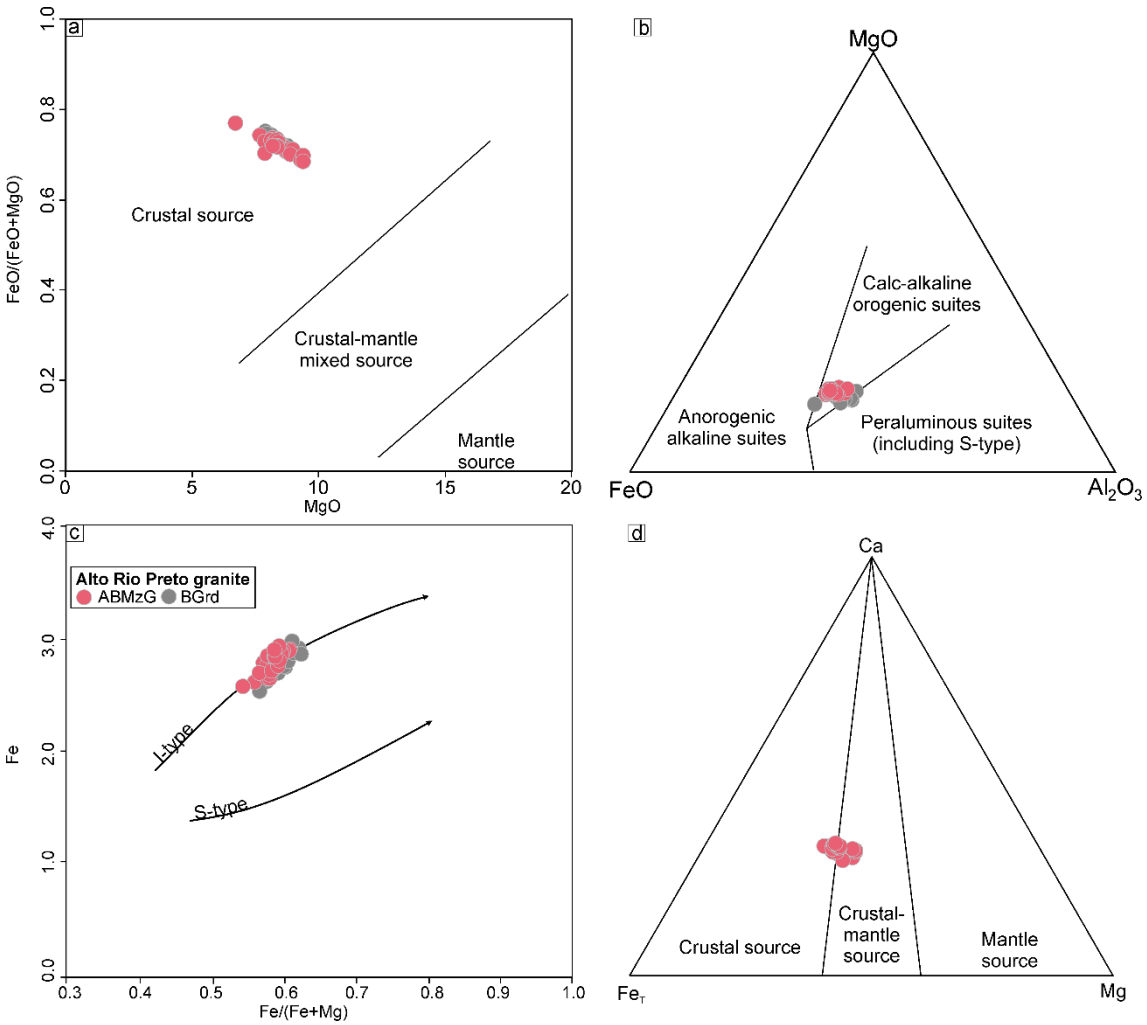


Fig. 12. Inferences of magma nature of the Alto Rio Preto granite based on mineral chemistry data. (a) MgO vs FeO/(FeO + MgO) diagram for biotite indicating the nature of the magma source(Zhao et al., 2012) ; (b) FeO–MgO–Al_2O_3 discrimination ternary diagram based on biotite composition (Abdel-Rahman, 1994); (c) Fe/(Fe+Mg) vs. Fe classification diagram showing trends for I-type and S-type granites defined from biotite composition (Villaseca et al., 2017); (d) Ca-Fe_T-Mg ternary diagram for the amphibole indicating the nature of the magma source (Xie and Zhang, 1990).

3.5.7 The petrogenetic significance of epidote-granites in orogenic settings

The occurrence of magmatic epidote in granitoids provides valuable insights into physicochemical conditions and tectonic settings in which deep-seated magmas were generated and crystallized (Cunha et al., 2021; Lima et al., 2021; Nascimento et al., 2023; Sial et al., 2008). As indicated by several experimental studies, mineral chemistry data and the new thermodynamic approach presented in this work, the preservation of magmatic epidote is a product of a complex combination of high-pressure, hydrous and oxidizing conditions coupled with rapid ascent rates (Dawes and Evans, 1991a; Schmidt and Poli, 2004; Schmidt and Thompson, 1996; Zen and Hammarstrom, 1984). These conditions are not commonly observed in different geological settings and the record of magmatic epidote is relatively rare due to epidote kinetic instability during magma ascent

(Brandon et al., 1996). In this context, epidote-bearing granitoids are not only a great marker on crystallization and magma ascent conditions but also provides a window into the processes that occur in deep regions of the continental crust.

Epidote-granites have been described throughout the geological record, from the Archean to Mesozoic (Cunha et al., 2021; Nascimento et al., 2023; Sial et al., 1999). Epidote-bearing granitoids have been described in the Borborema Province, NE Brazil (Lima et al., 2021; Sial et al., 2008), and in the Agapur region, Central India (Basak et al. 2019). In the Borborema, Neoproterozoic granites from the Seridó, Cachoeirinha-Salgueiro, Alto Pajeú, Macuraré terranes and the Teixeira batholith contains calcic amphibole (magnesiohastingsite to ferroedenite) and record emplacement pressures between 0.35 to 0.85 GPa (Tab. 3). These granitoids evolved under oxidizing conditions, with amphibole Fe/(Fe+Mg) ratios similar or slightly lower than those of the Alto Rio Preto granite. The Grenvillian Agapur granitoids also contain calcic amphibole (magnesiohornblende and ferroedenite) with variable Fe/(Fe+Mg) ratios (0.35 to 0.6, with higher values similar with the Alto Rio Preto granite), and record slightly lower pressures (0.12 to 0.48 GPa, Tab. 3) compared to the other mentioned granites. In summary, despite the differences in age and emplacement pressures, these granitoids crystallized from hydrous, calc-alkaline to high-K calc alkaline magmas, under moderately to strongly oxidizing conditions, consistent with epidote crystallization in magmatic environments and share key features with the Alto Rio Preto granite.

The similarities observed between the granitoids from different ages and tectonic settings selected for comparison highlight that magmatic epidote can be used as a diagnostic mineral to identify deep, oxidized, and hydrous magmatism in orogenic crust.

Table 3. Comparison between the main crystallization parameters of epidote-bearing granites.

	Temperature (ºC)			Pressure (GPa)			fO_2	H_2O content	Reference
Alto Rio Preto granite ABMzG	842-980[1] 751-782[2] 835-869[3]			0.29-0.66[a] 0.48-0.63[b] 0.35-0.61[c]			Oxidized NNO+0.5 to +1	6 wt%	this study
BGrd	762-796[3]	-	-	0.55-0.77[d]	-	-	Oxidized NNO+0.5	<4 wt%	this study
Seridó	650-700[1]	-	-	0.35-0.45 [a]	-	-	Oxidized	-	Sial et al. (2008)
Cachoeirinha-Salgueiro	650-810[1]	-	-	0.45-0.8 [a]	-	-	Oxidized	-	Sial et al. (2008)
Alto-Pajeú	650-760[1]	-	-	0.5-.85 [a]	-	-	Oxidized	-	Sial et al. (2008)
Macuraré	655-670[1]	-	-	0.5-0.65 [a]	-	-	Oxidized	-	Sial et al. (2008)
Teixeira batholith	717-778[2]	-	-	0.39-0.6[a] 0.4-0.6[b]		-	Oxidized Above FMQ	-	Lima et al. (2021)
Agarpur granitoids	753-783[3]	-	-	0.12-0.48[c]	-	-	Oxidized NNO+2	-	Basak et al. (2019)

Thermometers: [1]Holland and Blundy (1994) – amphibole-plagioclase; [2]Putirka (2016) – amphibole; [3]Ridolfi et al. (2010) – amphibole; [3]Li and Zhang (2022) – biotite;

Barometers: [a]Anderson and Smith (1995); [b]Schmidt (1992); [c]Mutch et al. (2016); [d]Li and Zhang (2022)

ABMzG = amphibole-biotite monzogranite; BGrd = biotite granodiorite.

3.6 CONCLUSIONS

The integration of mineral chemistry and thermodynamic modeling applied to the Alto Rio Preto granite led to the following conclusions:

1- The amphiboles of the Alto Rio Preto granite are classified as magnesio-hastingsite and ferroedenite with minor tschermakite and ferrohornblende. Biotite compositions do not significantly vary between distinct facies; they are classified as Mg-biotites with Fe/(Fe+Mg) ratios between 0.56 and 0.63. Plagioclase varies from oligoclase to andesine. Epidote texture and composition points to a magmatic origin (Ps=27-35). Titanite composition approaches those of inherited igneous and recrystallized grains.

2- The granite was emplaced at pressures between 0.4 to 0.7 GPa and evolved in oxidizing conditions probably at NNO±0.5 to NNO±1. The initial water content in the amphibole-bearing monzogranitic facies was probably 6 wt%, while in the biotite monzogranite and granodiorite facies it was lower (<4 wt%).

3- Epidote stability is favored by high-pressure, moderate to high-H_2O, and oxidizing conditions, being restricted to near-solidus temperatures. The preservation of magmatic epidote is also favored by low density and viscosity of the magma, that allows its rapid ascent in the crust.

4- Epidote dissolution kinetics suggest rapid ascent of the Alto Rio Preto magmas at a rate of ca. 5 and 4 km/year for monzogranitic and granodioritic magmas, respectively. These contrasts result from slight differences in the composition of parental magma, water content, and viscosity.

5- The chemistry of biotite and amphibole suggest an affinity with I-type orogenic calc-alkaline suites derived from crustal sources with limited to absent mantellic influence.

6- The presence of magmatic epidote in rocks with distinct ages and tectonic setting highlights its role as key mineral to identify deep and oxidized crystallization environments.

ACKNWOLEDGMENTS

This paper is part of the first author's PhD thesis developed at the Instituto de Geociências, UFPA. The authors acknowledge UNIFESSPA students and staff for their previous work in the studied area and for shared information; N.F Botelho, G. Fernandes for their assistance with EPMA analyses. This research received financial support from CNPq

(R. Dall'agnol – 304648-2019-1; G.R.L. Feio - 408396/2023-7) and FAPESPA (G.R.L. Feio E-2024/2285715). This study was also financed in part by the Coordenação de Aperfeiçoamento de Pessoal de Nível Superior - Brasil (CAPES) - Finance Code 001 (A.S.S. Neri - No. 88887.643812/2021-00).

REFERENCES

Abdel-Rahman, A.-F.M., 1994. Nature of Biotites from Alkaline, Calc-alkaline, and Peraluminous Magmas. Journal of Petrology 35, 525–541. https://doi.org/10.1093/petrology/35.2.525

Aleinikoff, J.N., Wintsch, R.P., Fanning, C.M., Dorais, M.J., 2002. U–Pb geochronology of zircon and polygenetic titanite from the Glastonbury Complex, Connecticut, USA: an integrated SEM, EMPA, TIMS, and SHRIMP study. Chem Geol 188, 125–147. https://doi.org/10.1016/S0009-2541(02)00076-1

Anderson, J L, Barth, A.P., Wooden, J.L., Mazdab, F., 2008. Thermometers and Thermobarometers in Granitic Systems. Rev Mineral Geochem 69, 121–142. https://doi.org/10.2138/rmg.2008.69.4

Anderson, J.L., Smith, D.R., 1995. The effects of temperature and fO2 on the Al-in-hornblende barometer. American Mineralogist 80, 549–559. https://doi.org/10.2138/am-1995-5-614

Angiboust, S., Harlov, D., 2017. Ilmenite breakdown and rutile-titanite stability in metagranitoids: Natural observations and experimental results. American Mineralogist 102, 1696–1708. https://doi.org/10.2138/am-2017-6064

Barros, C.E. de M., Besser, M.L., Vasconcellos, E.M.G., 2023. Voluminous Paleoproterozoic plutonic belt of the Bacajá Domain in Amazon Craton: Petrology, geotectonic setting and Pb–Pb zircon evaporation ages. J South Am Earth Sci 130, 104491. https://doi.org/10.1016/j.jsames.2023.104491

Barros, C.E. de M., Macambira, M.J.B., Santos, M.C. da C., Silva, D.C.C., Palmeira, L.C.M., Sousa, M.M., 2007. Estruturas sinmagmáticas e idade de zircão de granitos (evaporação de Pb) paleoproterozóicos da parte leste do domínio Bacajá, Província Maroni-Itacaiúnas. Revista Brasileira de Geociências 37, 293–304. https://doi.org/10.25249/0375-7536.2007373293304

Basak, A., Goswami, B., Singha, A., Das, S., Bhattacharyya, C., 2019. Magmatic Epidote in the Grenvillian Granitoids of North Purulia Shear Zone, Chhotanagpur Gneissic Complex, India and its Significance. Curr Sci 117, 298.

https://doi.org/10.18520/cs/v117/i2/298-303

Besser, M.L., Barros, C.E.M., 2015. Geologia e recursos minerais da Folha Rio Bacajá - SA.22-Y-D-VI, Estado do Pará. CPRM, Belém.

Brandon, A.D., Creaser, R.A., Chacko, T., 1996. Constraints on Rates of Granitic Magma Transport from Epidote Dissolution Kinetics. Science (1979) 271, 1845–1848. https://doi.org/10.1126/science.271.5257.1845

Brown, M., 2013. Granite: From genesis to emplacement. Geol Soc Am Bull 125, 1079–1113. https://doi.org/10.1130/B30877.1

Browne, B., Szramek, L., 2015. Rates of Magma Ascent and Storage, in: The Encyclopedia of Volcanoes. Elsevier, pp. 203–214. https://doi.org/10.1016/B978-0-12-385938-9.00009-2

Cordani, U.G., Sato, K., Teixeira, W., Tassinari, C.G., Basei, M.A.S., 2000. Crustal evolution of the South American Platform. Tectonic Evolution of South America 19–40.

Crawford, M.L., Hollister, L.S., 1982. Contrast of metamorphic and structural histories across the work channel lineament, Coast Plutonic Complex, British Columbia. J Geophys Res Solid Earth 87, 3849–3860. https://doi.org/10.1029/JB087iB05p03849

Cunha, I.R.V. da, Dall'Agnol, R., Feio, G.R.L., 2016. Mineral chemistry and magnetic petrology of the Archean Planalto Suite, Carajás Province – Amazonian Craton: Implications for the evolution of ferroan Archean granites. J South Am Earth Sci 67, 100–121. https://doi.org/10.1016/j.jsames.2016.01.007

Cunha, I.R.V., Dall'Agnol, R., Scaillet, B., de Sousa, L.A.M., 2021. Magmatic epidote in Archean granitoids of the Carajás Province, Amazonian craton, and its stability during magma rise and emplacement. J South Am Earth Sci 112, 103570. https://doi.org/10.1016/j.jsames.2021.103570

Dall'Agnol, R., da Cunha, I.R.V., Guimarães, F.V., de Oliveira, D.C., Teixeira, M.F.B., Feio, G.R.L., Lamarão, C.N., 2017. Mineralogy, geochemistry, and petrology of Neoarchean ferroan to magnesian granites of Carajás Province, Amazonian Craton: The origin of hydrated granites associated with charnockites. Lithos 277, 3–32. https://doi.org/10.1016/j.lithos.2016.09.032

Dall'Agnol, R., Scaillet, B., Pichavant, M., 1999. An Experimental Study of a Lower Proterozoic A-type Granite from theEastern Amazonian Craton, Brazil. Journal of Petrology 40, 1673–1698. https://doi.org/10.1093/petrology/40.11.1673

Dawes, R.L., Evans, B.W., 1991. Mineralogy and geothermobarometry of magmatic epidote-bearing dikes, Front Range, Colorado. Geol Soc Am Bull 103, 1017–1031. https://doi.org/10.1130/0016-7606(1991)103<1017:MAGOME>2.3.CO;2

Deer, W.A., Howie, R.A., Zussman, J., 2013. An Introduction to the Rock-Forming Minerals. Mineralogical Society of Great Britain and Ireland. https://doi.org/10.1180/DHZ

Evans, B.W., Vance, J.A., 1987. Epidote phenocrysts in dacitic dikes, Boulder County, Colorado. Contributions to Mineralogy and Petrology 96, 178–185. https://doi.org/10.1007/BF00375231

Frost, B.R., Barnes, C.G., Collins, W.J., Arculus, R.J., Ellis, D.J., Frost, C.D., 2001. A Geochemical Classification for Granitic Rocks. Journal of Petrology 42, 2033–2048. https://doi.org/10.1093/petrology/42.11.2033

Giere, R., Sorensen, S.S., 2004. Allanite and Other REE-Rich Epidote-Group Minerals, in: Epidotes. De Gruyter, pp. 431–494. https://doi.org/10.1515/9781501509599-013

Giordano, D., Russell, J.K., Dingwell, D.B., 2008. Viscosity of magmatic liquids: A model. Earth Planet Sci Lett 271, 123–134. https://doi.org/10.1016/j.epsl.2008.03.038

Harrison, T.M., Watson, E.B., 1984. The behavior of apatite during crustal anatexis: Equilibrium and kinetic considerations. Geochim Cosmochim Acta 48, 1467–1477. https://doi.org/10.1016/0016-7037(84)90403-4

Holland, T., Blundy, J., 1994. Non-ideal interactions in calcic amphiboles and their bearing on amphibole-plagioclase thermometry. Contributions to Mineralogy and Petrology 116, 433–447. https://doi.org/10.1007/BF00310910

Holland, T.J.B., Green, E.C.R., Powell, R., 2018. Melting of Peridotites through to Granites: A Simple Thermodynamic Model in the System KNCFMASHTOCr. Journal of Petrology 59, 881–900. https://doi.org/10.1093/petrology/egy048

Holland, T.J.B., Powell, R., 2011. An improved and extended internally consistent thermodynamic dataset for phases of petrological interest, involving a new equation of state for solids. Journal of Metamorphic Geology 29, 333–383. https://doi.org/10.1111/j.1525-1314.2010.00923.x

Hollister, L.S., Grissom, G.C., Peters, E.K., Stowell, H.H., Sisson, V.B., 1987. Confirmation of the empirical correlation of Al in hornblende with pressure of solidification of calc-alkaline plutons. American Mineralogist 72, 231–239.

Hurley, P.M., Almeida, F.F.M., Melcher, G.C., Cordani, U.G., Rand, J., Kawashita, K., Vandoros, P., Pinson, W.H., Fairbairn, H.W., 1967. Test of continental drift by means of radiometric ages. Science (1979) 495–500.

Jaupart, C., Mareschal, J.-C., 2010. Heat Generation and Transport in the Earth. Cambridge University Press. https://doi.org/10.1017/CBO9780511781773

Keyes, C.R., 1892. Epidote as a primary component op eruptive rocks. Geol Soc Am Bull 4, 305–312. https://doi.org/10.1130/GSAB-4-305

Kowallis, B.J., Christiansen, E.H., Dorais, M.J., Winkel, A., Henze, P., Franzen, L., Mosher, H., 2022. Variation of Fe, Al, and F Substitution in Titanite (Sphene). Geosciences (Basel) 12, 229. https://doi.org/10.3390/geosciences12060229

Leake;, B.E., Woolley;, A.R., Arps;, C.E.S., Birch;, W.D., Gilbert;, M.C., Grice;, J.D., Hawthorne;, F.C., Kato;, A., Kisch;, H.J., Krivovichev;, V.G., Linthout;, K., Laird;, J., Mandarino;, J.A., Maresch;, W. V, Nickel;, E.H., Rock;, N.M.S., Youzhi, Schumacher;, J.C., Smith;, D.C., Stephenson;, N.C.N., Ungaretti;, L., Whittaker;, E.J.W., Guo, Y., 1997. Nomenclature of amphiboles; Report of the Subcommittee on Amphiboles of the International Mineralogical Association, Commission on New Minerals and Mineral Name. American Mineralogist 82, 1019–1037.

Li, X., Zhang, C., 2022. Machine Learning Thermobarometry for Biotite-Bearing Magmas. J Geophys Res Solid Earth 127. https://doi.org/10.1029/2022JB024137

Lima, B.T.A., Ferreira, V.P., Ardila, D.H., Neves, C.H.F.S., Sial, A.N., 2021a. Crystallization conditions of the Carmo stock, NE Brazil: Implications for magmatic epidote-bearing granitoids petrogenesis. J South Am Earth Sci 110, 103427. https://doi.org/10.1016/j.jsames.2021.103427

Lima, J.V. de, Guimarães, I. de P., Neves, S.P., Santos, I.D., Brainer, C.C.G., Dantas, E.L., 2021b. Mineral chemistry constrains on crystallization conditions and petrological evolution of the Teixeira Batholith granitoids, Borborema Province, NE Brazil. J South Am Earth Sci 112, 103577. https://doi.org/10.1016/j.jsames.2021.103577

Liou, J.G., 1973. Synthesis and Stability Relations of Epidote, Ca2Al2FeSi3O12 (OH). Journal of Petrology 14, 381–413. https://doi.org/10.1093/petrology/14.3.381

Macambira, E.M.B., Ricci, P.S.F., 2015. Geologia e recursos minerais da Folha Tucuruí – SA.22-Z-C, Estado do Pará, 1st ed. CPRM, Belém.

Macambira, M.J.B., Amireault, S., 2025. Isotopic study (U Pb, Sm Nd, and Pb Pb) of rocks and auriferous mineralizations from the Volta Grande do Xingu deposits,

Bacajá Domain, Amazonian craton. J Geochem Explor 274, 107767. https://doi.org/10.1016/j.gexplo.2025.107767

Macambira, M.J.B., Vasquez, M.L., Silva, D.C.C., Galarza, M.A., Barros, C.E.M., Camelo, J.F., 2009. Crustal growth of the central-eastern Paleoproterozoic domain, SW Amazonian craton: Juvenile accretion vs. reworking. J South Am Earth Sci 27, 235–246. https://doi.org/10.1016/j.jsames.2009.02.001

Magalhães, L.B., Macambira, M.J.B., Macambira, E.M.B., dos Santos Freire Ricci, P., 2023. Crustal growth in the northeast portion of the Rhyacian Bacajá Domain, SE Amazonian craton, based on U-Pb, Lu-Hf, and Sm-Nd data. Brazilian Journal of Geology 53. https://doi.org/10.1590/2317-4889202320220068

Neri, A.S.S., Dall'Agnol, R., Dantas, E.L., Feio, G.R.L., Almeida, J.A.C., Galarza, M.A., Rhyacian magmatism in the southern Bacajá Domain: Implications for the crustal evolution of SE Amazonian Craton, Brazil. Precambrian Research. manuscript submitted for publication b.

Neri, A.S.S., Dall'Agnol, R., Feio, G.R.L., Almeida, J.A.C. Dehydration melting of basaltic crust to generate Rhyacian high-K calc-alkaline granites, SE Amazonian Craton. Journal of the Geological Soci*ety*, manuscript submitted for publication a.

Neri A.S.S., Dantas E.L., Peixoto E.I.N., Fuck R.A., Feio G.R.L., Luvizotto G.L., Silva A.C., Almeida J.A.C. 2025. The missing record of high-pressure granulite metamorphism in the Amazonian Craton. Terra Nova. manuscript submitted for publication c.

Le Maitre, R.W. 2002. Igneous Rocks: A Classification and Glossary of Terms, Geological Magazine. Cambridge University Press. https://doi.org/10.1017/CBO9780511535581

Moyen, J.-F., 2020. Granites and crustal heat budget. Geological Society, London, Special Publications 491, 77–100. https://doi.org/10.1144/SP491-2018-148

Mutch, E.J.F., Blundy, J.D., Tattitch, B.C., Cooper, F.J., Brooker, R.A., 2016. An experimental study of amphibole stability in low-pressure granitic magmas and a revised Al-in-hornblende geobarometer. Contributions to Mineralogy and Petrology 171, 85. https://doi.org/10.1007/s00410-016-1298-9

Nachit, H., 1985. Composition chemique des biotites et typologie magmatique des granitoids. Comtes Rendus Hebdomadaires de l'Academie des Sciences 813–181.

Nachit, H., Ibhi, A., Abia, E.H., Ohoud, M. Ben, 2005. Discrimination between primary magmatic biotites, reequilibrated biotites and neoformed biotites. Comptes Rendus.

Géoscience 337, 1415–1420. https://doi.org/10.1016/j.crte.2005.09.002

Naney, M T, 1983. Phase equilibria of rock-forming ferromagnesian silicates in graniic systems. Am J Sci 283, 993–1033.

Nascimento, A.C. do, Oliveira, D.C. de, Gabriel, E.O., Marangoanha, B., Ribeiro da Silva, L., Aleixo, E. da C., 2023. Mineral chemistry of the Água Limpa suite: Insights into petrological constraints and magma ascent rate of Mesoarchean sanukitoids from the Sapucaia terrane (Carajás Province, southeastern Amazonian Craton, Brazil). J South Am Earth Sci 132, 104683. https://doi.org/10.1016/j.jsames.2023.104683

Neri, A.S.S., Dall'Agnol, R., Dantas, E.L., Feio, G.R.L., Almeida, J.A.C., Galarza, M.A., Rhyacian magmatism in the southern Bacajá Domain: Implications for the crustal evolution of SE Amazonian Craton, Brazil. *Precambrian Research*, manuscript submitted for publication a.

Neri, A.S.S., Dall'Agnol, R., Almeida, J.A.C., & Feio, G.R.L., Dehydration melting of basaltic crust to generate Rhyacian high-K calc-alkaline granites, SE Amazonian Craton: Implications for crustal reworking in collisional orogens. *Journal of the Geological Society*, manuscript submitted for publication b.

Pandit, D., Panigrahi, M.K., Moriyama, T., 2014. Constrains from magmatic and hydrothermal epidotes on crystallization of granitic magma and sulfide mineralization in Paleoproterozoic Malanjkhand Granitoid, Central India. Geochemistry 74, 715–733. https://doi.org/10.1016/j.chemer.2014.04.008

Petford, N., Cruden, A.R., McCaffrey, K.J.W., Vigneresse, J.-L., 2000. Granite magma formation, transport and emplacement in the Earth's crust. Nature 408, 669–673. https://doi.org/10.1038/35047000

Prouteau, G., Scaillet, B., 2003. Experimental Constraints on the Origin of the 1991 Pinatubo Dacite. Journal of Petrology 44, 2203–2241. https://doi.org/10.1093/petrology/egg075

Putirka, K., 2016. Amphibole thermometers and barometers for igneous systems and some implications for eruption mechanisms of felsic magmas at arc volcanoes. American Mineralogist 101, 841–858. https://doi.org/10.2138/am-2016-5506

Ridolfi, F., Renzulli, A., Puerini, M., 2010. Stability and chemical equilibrium of amphibole in calc-alkaline magmas: an overview, new thermobarometric formulations and application to subduction-related volcanoes. Contributions to Mineralogy and Petrology 160, 45–66. https://doi.org/10.1007/s00410-009-0465-7

Rudnick, R.L., Gao, S., 2003. Composition of the Continental Crust, in: Treatise on Geochemistry. Elsevier, pp. 1–64. https://doi.org/10.1016/B0-08-043751-6/03016-4

Santos, J.O.S., Hartmann, L.A., Faria, M.S., Riker, S.R., Miguel, M., Almeida, M.E., Mcnaughton, N.J., 2006. a Compartimentação Do Cráton Amazonas Em Províncias : Avanços Ocorridos No Período 2000-2006, in: IX Simpósio de Geologia Da Amazônica. Sociedade Brasileira de Geologia, Belém.

Scaillet, B., Holtz, F., Pichavant, M., 2016. Experimental Constraints on the Formation of Silicic Magmas. Elements 12, 109–114. https://doi.org/10.2113/gselements.12.2.109

Schmidt, Max W, 1992. Amphibole composition in tonalite as a function of pressure: an experimental calibration of the Al-in-hornblende barometer. Contributions to Mineralogy and Petrology 110, 304–310. https://doi.org/10.1007/BF00310745

Schmidt, M.W., Poli, S., 2004. Magmatic Epidote. Rev Mineral Geochem 56, 399–430. https://doi.org/10.2138/gsrmg.56.1.399

Schmidt, M.W., Thompson, A.B., 1996. Epidote in calcalkaline magmas; an experimental study of stability, phase relationships, and the role of epidote in magmatic evolution. American Mineralogist 81, 462–474. https://doi.org/10.2138/am-1996-3-420

Schulze, F., Behrens, H., Holtz, F., Roux, J., Johannes, W., 1996. The influence of H2O on the viscosity of a haplogranitic melt. American Mineralogist 81, 1155–1165. https://doi.org/10.2138/am-1996-9-1014

Scibiorski, E.A., Cawood, P.A., 2022. Titanite as a petrogenetic indicator. Terra Nova 34, 177–183. https://doi.org/10.1111/ter.12574

Sial, A.N., Toselli, A.J., Saavedra, J., Parada, M.A., Ferreira, V.P., 1999. Emplacement, petrological and magnetic susceptibility characteristics of diverse magmatic epidote-bearing granitoid rocks in Brazil, Argentina and Chile. Lithos 46, 367–392. https://doi.org/10.1016/S0024-4937(98)00074-7

Sial, A.N., Vasconcelos, P.M., Ferreira, V.P., Pessoa, R.R., Brasilino, R.G., Morais Neto, J.M., 2008. Geochronological and mineralogical constraints on depth of emplacement and ascencion rates of epidote-bearing magmas from northeastern Brazil. Lithos 105, 225–238. https://doi.org/10.1016/j.lithos.2008.04.002

Silva, A.S. da, Feio, G.R.L., Alves, J.P.S., Dall'Agnol, R., Almeida, J. de A.C. de, Gomes, A.C.B., 2020. Mineralogy, petrology, and origin of the Pedra Branca Suite: a

tonalitic-trondhjemitic association with high Zr, Ti and Y, Carajás Province, Amazonian Craton. Brazilian Journal of Geology 50. https://doi.org/10.1590/2317-4889202020190093

Sousa, L.A.M. de, Dall'Agnol, R., Cunha, I.R.V. da, Silva, F.F. da, Oliveira, D.C. de, 2022. Magnetic petrology of the Neoarchean granitoids in the Vila Jussara Suite, Carajás Province, Amazonian Craton. Brazilian Journal of Geology 52. https://doi.org/10.1590/2317-4889202220210071

Tassinari, C.C.G., Macambira, M.J.B., 2004. A evolução tectônica do Craton Amazônico, in: Mantesso-Neto, V., Bartorelli, A., Carneiro, C.D.R., Brito Neves, B.B. (Eds.), Geologia Do Continente Sul Americano: Evoluc¸ Ão Da Obra de Fernando Flávio Marques Almeida. São Paulo, pp. 471–486.

Tulloch, A.J., 1979. Secondary Ca-Al silicates as low-grade alteration products of granitoid biotite. Contributions to Mineralogy and Petrology 69, 105–117. https://doi.org/10.1007/BF00371854

Vasquez, M L, 2006. Geocronologia em zircão, monazita e granada e isótopos de Nd das associações litológicas da porção oeste do Domínio Bacajá: evolução crustal da porção meridional da Província Maroni-Itacaiúnas – Sudeste Do Cráton Amazônico. Universidade Federal do Pará.

Vasquez, M.L., Macambira, M.J.B., Armstrong, R.A., 2008. Zircon geochronology of granitoids from the western Bacajá Domain, southeastern Amazonian craton, Brazil: Neoarchean to Orosirian evolution. Precambrian Res 161, 279–302. https://doi.org/10.1016/j.precamres.2007.09.001

Vasquez, M. L.;, Rosa-Costa, L.T.;, 2008. Geologia e Recursos Minerais do Estado do Pará : Sistema de Informações Geográficas – SIG : texto explicativo dos mapas Geológico e Tectônico e de Recursos Minerais do Estado do Pará, 1st ed. Brazilian Geological Service, CPRM, Belém.

Vieira, C., Amaral, W., Santos, F.H., 2022. Petrography, geochemistry and zircon U-Pb geochronology of the Siderian-Rhyacian granitoids of NW Bacajá Domain, Amazonian Craton. Journal of the Geological Survey Of Brazil 5. https://doi.org/10.29396/jgsb.2022.v5.n3.1

Villaseca, C., Ruíz-Martínez, V.C., Pérez-Soba, c., 2017. Magnetic susceptibility of Variscan granite-types of the Spanish Central System and the redox state of magma. Geologica Acta 15, 379–394.

Wang, B., Wei, C., Tian, W., 2023. Ultrahigh-Temperature Anatexis of Greywackic

Granulites Generates Peraluminous Charnockites in the Jining Complex, North China Craton. Journal of Petrology 64. https://doi.org/10.1093/petrology/egad030

Watson, E.B., Harrison, T.M., 1983. Zircon saturation revisited: temperature and composition effects in a variety of crustal magma types. Earth Planet Sci Lett 64, 295–304. https://doi.org/10.1016/0012-821X(83)90211-X

Weber, G., Blundy, J., 2024. A Machine Learning-Based Thermobarometer for Magmatic Liquids. Journal of Petrology 65. https://doi.org/10.1093/petrology/egae020

Wedepohl, K.H., 1995. The composition of the continental crust. Geochim Cosmochim Acta 59, 1217–1232. https://doi.org/10.1016/0016-7037(95)00038-2

Whitney, D.L. and Evans, B.W. 2010. Abbreviations for names of rock-forming minerals. American Mineralogist, 95, 185–187, https://doi.org/10.2138/am.2010.3371

Xiang, H., Connolly, J.A.D., 2022. GeoPS: An interactive visual computing tool for thermodynamic modelling of phase equilibria. Journal of Metamorphic Geology 40, 243–255. https://doi.org/10.1111/jmg.12626

Xie, Y.W., Zhang, Y.Q., 1990. Peculiarities and genetic significance of hornblende from granite in the Hengduanshan region. Acta Min 10, 35–45.

Yavuz, F., Döner, Z., 2017. WinAmptb : A Windows program for calcic amphibole thermobarometry. Periodico di Mineralogia 86. https://doi.org/https://doi.org/10.2451/2017PM710

Zen, E., Hammarstrom, J.M., 1984. Magmatic epidote and its petrologic significance. Geology 12, 515. https://doi.org/10.1130/0091-7613(1984)12<515:MEAIPS>2.0.CO;2

Zhao, K., Xu, X., Erdmann, S., 2017. Crystallization conditions of peraluminous charnockites: constraints from mineral thermometry and thermodynamic modelling. Contributions to Mineralogy and Petrology 172, 26. https://doi.org/10.1007/s00410-017-1344-2

Zhao, K.-D., Jiang, S.-Y., Yang, S.-Y., Dai, B.-Z., Lu, J.-J., 2012. Mineral chemistry, trace elements and Sr–Nd–Hf isotope geochemistry and petrogenesis of Cailing and Furong granites and mafic enclaves from the Qitianling batholith in the Shi-Hang zone, South China. Gondwana Research 22, 310–324. https://doi.org/10.1016/j.gr.2011.09.010

SUPPLEMENTARY MATERIAL 1 – TABLES

Table S 1. Modal analyses of the Alto Rio Preto granite samples.

	Amphibole-biotite monzogranite					Amphibole-biotite monzogranite							BGrd-tonalite			
Lithology	ABMzG	ABSG	ABMzG	ABMzG	ABMzG	BMzG	BMzG	BMzG	BMzG	BSG	BSG	BSG	Bton	BMzG	BGrd	BMzG
Samples	AA-12	AA-13	AA-21	AA-52	AA-76	AA-14A	AA-24A	AA-63A	AA-64	AA-23	AA-61	AA-62	AA-16	AA-19	AA-45	AA-46
Quartz	23.17	37.55	41.5	26.65	38.85	39.5	39.7	30	42.05	35.6	38.55	25.45	29.95	31.5	25.72	34.25
Plagioclase	35.06	10.25	20.3	29.95	16.45	20	17.4	19.95	11.25	17.05	12.75	13.15	50.3	40.35	36.78	19.4
K-feldspar	20.06	31.6	26.75	32.9	23.95	26.85	26.5	28.05	19.65	38.3	41.3	46	1.9	20	16.06	31.45
Amphibole	5.39	3.7	0.3	1.35	2.85	-	-	-	-	-	-	-	-	-	-	-
Biotite	15.28	11.6	8.5	7.85	16	12.65	15.25	20.2	22.1	8.35	6.75	13.45	15.9	4.95	21.28	11.6
Muscovite	-	-	-	-	-	0.2	0.25	-	-	-	0.05	-	0.55	-	-	0.25
Titanite	0.06	0.45	-	0.05	0.4	-	0.15	0.25	0.7	0.05	-	-	-	-	0.06	0.2
Allanite	0.39	x	-	-	0.15	0.05	0.05	x	0.2	0.15	-	-	-	-	-	0.2
Epidote	0.17	0.2	x	0.15*	0.15	0.05	0.1	x	0.15	0.05	-	-	-	x	-	0.2
Zircon	0.06	x	x	0.05	x	x	0.05	0.2	0.15	0.05	0.05	0.05	0.15	0.05	0.06	0.05
Opaque	0.17	0.1	0.05	0.05	0.15	0.05	0.15	0.45	0.61	0.05	0.15	0.2	0.25	0.1	0.06	0.05
Apatite	0.06	0.15	-	0.3	0.25	0.3	0.15	0.35	0.05	0.25	0.3	0.1	0.05	x	x	0.3
Clorite	0.06	x		x	0.15	0.1	0.05	0.1	1.1	0.05	0.15	0.25	x	0.1	x	0.5
Sericite	0.11	3.85	1.40	0.65	0.65	0.15	0.2	0.25	2.85	x	0.1	1.35	0.75	2.8	x	1.55
Carbonate	-	0.10	-	0.05	0.15	-	-	0.05	0.05	-	-	0.05	0.3	0.1	-	-
F Minerals	78.69	83.55	89.95	90.15	79.9	86.7	84.05	78.25	75.8	90.95	92.75	85.8	83.5	94.65	78.62	86.9
M minerals 100%	21.35	15.95	8.8	9.45	19.6	12.85	15.6	20.7	23.4	8.65	6.85	13.6	16.6	5	21.4	12.25
Q	29.60	47.29	46.87	49.02	49.02	45.74	47.50	38.47	57.64	39.15	41.64	30.08	36.46	34.30	32.74	40.25
A	44.78	39.80	22.92	30.22	30.22	31.09	31.69	35.96	26.93	42.11	44.59	54.37	61.23	24.01	20.44	36.96
P	25.62	12.91	30.21	20.76	20.76	23.16	20.81	25.57	15.43	18.74	13.77	15.54	2.31	41.69	46.82	22.80
M'	21.29	15.75	8.75	9.00	19.35	12.6	15.2	20.25	22.75	8.6	6.7	13.45	15.7	4.8	21.4	11.95

- not observed in the thin section; x -observed, but not counted

Table S 2. Representative compositions of amphibole and biotite from the Alto Rio Preto granite.

Mineral	Amphibole				Biotite							
Facies	ABMzG				ABMzG				BGrd			
Sample	AA-76		AA-12		AA-76		AA-12		AA-45		AA-46	
Analyses	C4.7	C4.4	C3.1	C4.2	C1.3	C3.1	C1.2	C2.2	C1.4	C2.2	C4.1	C4.4
Texture	rim	core	rim	core	core	core	core	core	core	core	core	core
SiO_2	42.45	43.07	42.39	42.40	36.18	36.75	37.47	37.15	37.48	36.73	37.11	37.23
TiO_2	1.62	1.54	1.80	1.56	3.49	2.84	2.48	2.57	2.86	3.02	1.51	2.40
Al_2O_3	11.01	10.62	9.32	9.38	15.30	14.31	14.36	14.65	15.46	17.17	16.81	16.60
Fe_2O_3*	4.27	5.18	1.45	3.28	-	-	-	-	-	-	-	-
FeO*	15.19	15.15	19.22	17.70	20.79	21.82	22.32	22.02	21.27	20.56	22.71	22.35
MgO	8.92	8.48	7.52	7.64	0.27	0.24	0.33	0.31	8.41	8.47	7.76	7.52
MnO	11.30	10.69	11.70	11.09	8.89	8.74	8.32	8.27	0.25	0.29	0.29	0.25
CaO	0.46	0.46	0.50	0.45	0.02	0.00	0.03	0.03	0.10	0.09	0.00	0.05
Na_2O	1.63	1.74	1.18	1.35	0.07	0.11	0.27	0.08	0.13	0.12	0.10	0.06
K_2O	1.40	1.31	1.24	1.29	9.65	9.50	9.49	9.52	9.73	9.24	9.89	9.34
F	0.45	0.51	0.19	0.42	0.08	0.10	0.14	0.13	0.50	0.68	0.42	0.26
Cl	0.10	0.08	0.12	0.10	0.34	0.37	0.51	0.41	0.25	0.24	0.12	0.12
H_2O*	1.74	1.71	1.81	1.69	3.58	3.54	3.47	3.52	3.49	3.45	3.58	3.65
Sum	100.49	100.46	98.49	98.26	98.55	98.19	99.00	98.50	99.92	100.05	100.29	99.83
Number of cations per formula unit based on 23 oxygen					Number of cations per formula unit based on 22 charges							
Si	6.389	6.477	6.587	6.581	5.614	5.746	5.817	5.786	5.743	5.592	5.693	5.704
Ti	0.183	0.174	0.210	0.182	0.408	0.334	0.289	0.301	0.329	0.346	0.174	0.277
Al	1.952	1.882	1.708	1.715	2.798	2.636	2.626	2.688	2.793	3.080	3.039	2.997
Fe^{+3}	0.483	0.586	0.169	0.383	-	-	-	-				
Fe^{+2}	1.911	1.905	2.498	2.297	2.698	2.852	2.897	2.869	2.725	2.618	2.914	2.864
Mg	2.001	1.902	1.743	1.769	2.056	2.037	1.924	1.921	1.922	1.922	1.775	1.717
Mn	0.059	0.059	0.066	0.059	0.036	0.032	0.044	0.041	0.033	0.037	0.037	0.032
Ca	1.822	1.723	1.948	1.844	0.003	0.000	0.005	0.005	0.016	0.014	0.000	0.008
Na	0.474	0.507	0.356	0.405	0.022	0.034	0.080	0.024	0.038	0.035	0.029	0.018
K	0.269	0.251	0.245	0.256	1.910	1.895	1.878	1.891	1.901	1.794	1.935	1.825
F	0.212	0.240	0.091	0.206	0.039	0.048	0.069	0.063	0.240	0.327	0.205	0.124
Cl	0.025	0.021	0.031	0.026	0.089	0.097	0.134	0.108	0.065	0.061	0.031	0.031
XMg (Mg/(Fe+Mg)	0.50	0.51	0.41	0.42	0.43	0.42	0.40	0.40	0.41	0.42	0.38	0.37

Table S 3. Representative compositions of titanite and epidote from the Alto Rio Preto granite.

Mineral	Titanite								Epidote			
Facies	ABMzG				BGrd				ABMzG		BGrd	
Sample	AA-76		AA-12		AA-45		AA-46		AA-12		AA-46	
Analyses	C3.22	C4.1	C2.2	C2.3	C1.2	C1.3	C1.4	C1.5	C1.3	C1.4	C5.2	C5.3
SiO_2	29.80	29.40	30.35	30.07	30.01	30.14	30.69	28.92	37.34	37.70	37.63	37.04
TiO_2	37.92	37.95	37.50	36.61	36.51	36.64	37.02	35.18	0.00	0.04	0.23	0.14
Al_2O_3	1.74	1.81	2.06	2.23	1.61	2.13	1.47	2.39	21.38	22.20	22.31	22.55
V_2O_3	0.34	0.21	0.26	0.29	0.35	0.30	0.39	0.40	-	-	0.03	0.00
La_2O_3	0.04	0.00	0.00	0.02	0.00	0.03	0.02	0.00	0.00	0.00	0.00	0.01
Ce_2O_3	0.37	0.25	0.16	0.21	0.00	0.00	0.00	0.00	0.03	0.00	0.02	0.00
Nd_2O_3	0.11	0.08	0.04	0.05	0.00	0.00	0.01	0.03	-	-	0.00	0.00
FeO	1.10	0.59	0.96	1.04	0.71	2.21	0.84	2.05	13.87	12.87	12.69	12.19
MgO	0.02	0.00	0.06	0.07	0.01	0.32	0.01	0.05	0.01	0.00	0.02	0.01
MnO	0.07	0.09	0.00	0.04	0.05	0.14	0.02	0.14	0.17	0.17	0.00	0.02
CaO	26.72	28.14	27.52	26.91	27.09	28.01	26.98	27.09	22.63	22.84	24.19	24.23
Na_2O	0.06	0.01	0.01	0.04	0.00	0.06	0.09	0.60	0.04	0.03	0.02	0.05
K_2O	0.00	0.00	0.02	0.00	0.03	0.20	0.01	0.73	0.01	0.02	0.04	0.03
F	0.452	1.05	0.58	0.50	0.57	0.60	0.63	0.84	-	-	0.10	0.18
Cl	0	0.001	0.01	0.00	0.02	0.01	0.01	0.14	0.00	0.00	0.02	0.00
H_2O *	0.86	0.90	0.87	0.89	0.86	0.84	0.85	0.68	1.85	1.86	1.90	1.88
Sum	99.15	100.26	99.53	98.05	97.81	101.64	99.04	99.25	97.82	97.97	99.19	98.33
	Number of cations per formula unit based on 4 atoms								Number of cations per formula unit based on 8 atoms			
Si	4.000	4.000	4.000	4.000	4.000	4.000	4.000	4.000	3.022	3.033	2.964	2.961
Ti	3.829	3.884	3.718	3.664	3.661	3.658	3.629	3.661	0.000	0.002	0.014	0.009
Al	0.275	0.291	0.319	0.349	0.252	0.333	0.225	0.390	2.040	2.104	2.071	2.125
V	0.036	0.023	0.028	0.030	0.038	0.032	0.041	0.045	-	-	0.002	0.000
La	0.002	0.000	0.000	0.001	0.000	0.002	0.001	0.000	0.000	0.000	0.000	0.000
Ce	0.012	0.003	0.008	0.010	0.000	0.000	0.000	0.000	0.001	0.000	0.001	0.000
Nd	0.004	0.001	0.002	0.002	0.000	0.000	0.000	0.002	-	-	0.000	0.000
Fe	0.123	0.067	0.106	0.115	0.002	0.063	0.001	0.010	0.939	0.866	0.836	0.815
Mg	0.000	0.003	0.001	0.007	0.006	0.016	0.002	0.016	0.001	0.000	0.002	0.001
Mn	0.008	0.010	0.007	0.008	3.869	3.982	3.767	4.015	0.012	0.012	0.000	0.002
Ca	3.843	4.102	3.885	3.834	0.079	0.246	0.092	0.237	1.962	1.968	2.042	2.075
Na	0.016	0.003	0.003	0.010	0.000	0.015	0.023	0.161	0.007	0.005	0.002	0.008

K	0.001	0.000	0.003	0.000	0.005	0.034	0.002	0.128	0.001	0.002	0.004	0.003
F	0.192	0.452	0.240	0.211	0.240	0.253	0.261	0.369	-	-	-	-
Al/Fe	2.24	4.34	3.01	3.03	3.19	1.35	2.45	1.65	-	-	-	-
Pistacite	-	-	-	-	-	-	-	-	32	29	29	28

Pistacite = $[Fe^{3+}/(Fe^{3+}+Al)]*100$

Table S 4. Representative plagioclase compositions of the Alto Rio Preto granite.

Facies	ABMzG				BGrd			
Sample	AA-76		AA-12		AA-45		AA-46	
Analyses	C2.1	C2.2	C2.1	C2.2	C2.2	C2.3	C2.2	C2.3
Texture	rim	core	rim	core	rim	core	rim	core
SiO_2	60.36	59.42	59.48	58.95	60.34	61.02	62.16	61.94
TiO_2	0.03	0.01	0.04	0.00	0.01	0.00	0.00	0.18
Al_2O_3	24.89	25.45	24.81	25.45	23.88	24.16	23.41	23.65
Fe_2O_3	0.07	0.11	0.06	0.07	0.10	0.06	0.04	0.04
MgO	0.00	0.02	0.01	0.00	0.01	0.03	0.02	0.00
MnO	0.19	0.00	0.00	0.01	6.06	5.66	5.21	5.21
CaO	6.22	6.88	6.97	7.30	0.08	0.01	0.00	0.09
Na_2O	8.21	7.57	7.71	7.35	8.17	8.44	8.85	8.67
K_2O	0.14	0.32	0.20	0.25	0.25	0.31	0.17	0.11
Sum	100.15	99.79	99.39	99.48	98.98	100.25	100.06	100.21
Number of cations per formula unit based on 8 oxygen								
Si	2.686	2.657	2.671	2.646	2.716	2.717	2.759	2.748
Ti	0.001	0.000	0.001	0.000	0.000	0.000	0.000	0.006
Al	1.305	1.341	1.313	1.346	1.267	1.268	1.224	1.236
Fe^{3+}	0.002	0.004	0.002	0.002	0.003	0.002	0.001	0.001
Mg	0.000	0.001	0.001	0.000	0.000	0.002	0.001	0.000
Mn	0.007	0.000	0.000	0.000	0.003	0.000	0.000	0.003
Ca	0.296	0.330	0.335	0.351	0.292	0.270	0.248	0.248
Na	0.708	0.656	0.671	0.639	0.713	0.729	0.762	0.746
K	0.008	0.018	0.011	0.014	0.014	0.018	0.010	0.006
An	0.29	0.33	0.33	0.35	0.29	0.27	0.24	0.25

An = Ca/(Ca+Na+K)

Table S 5. Normalized molar proportions used for crystallization phase equilibria modeling of the Alto Rio Preto magmas.

Facies	Sample	Pseudosection	Oxygen fugacity	H_2O (wt%)	SiO_2	TiO_2	Al_2O_3	FeO	MgO	CaO	K_2O	Na_2O	H_2O	O
Amphibole-biotite Monzogranite	AA-76	P-T	NNO + 1	4	63.68	0.47	8.23	3.75	2.53	3.42	2.05	2.97	12.71	0.20
		T/P-M(H_2O)	NNO +1	6	60.04	0.47	7.74	3.53	2.38	3.22	1.93	2.79	17.93	0.18
			NNO +1	1	70.59	0.52	9.10	4.15	2.80	3.78	2.27	3.28	3.51	0.41
			NNO +1	9	55.10	0.41	7.10	3.24	2.18	2.95	1.77	2.56	24.68	0.14
			NNO-1.5	3	60.04	0.47	7.74	3.53	2.38	3.22	1.93	2.79	17.93	0.04
		T/P-M(O)	NNO+2.5	3	60.04	0.47	7.74	3.53	2.38	3.22	1.93	2.79	17.93	0.39

Table S 6. whole-rock geochemistry used for calculating the viscosity in the Alto Rio Preto magmas (compiled from Neri et al, submitted a, b).

Facies	ABMzG			BGrd	
Sample	AA-76	AA-12	AA-13	AA-76	AA-12
SiO_2	67	67.9	SiO_2	67	67.9
TiO_2	0.66	0.37	TiO_2	0.66	0.37
Al_2O_3	14.65	17.2	Al_2O_3	14.65	17.2
FeO	4.71	2.80	FeO	4.71	2.80
MnO	0.07	0.05	MnO	0.07	0.05
MgO	1.78	0.8	MgO	1.78	0.8
CaO	3.35	3.63	CaO	3.35	3.63
Na_2O	3.21	3.82	Na_2O	3.21	3.82
K_2O	3.38	3.81	K_2O	3.38	3.81
P_2O_5	0.17	0.1	P_2O_5	0.17	0.1
H_2O	6.0	6.0	H_2O	6.0	6.0

Table S 7. Viscosity of the Alto Rio Preto magmas from liquid to solid temperatures calculated using the Giordano et al. (2008) model.

Facies	ABMzG			BGrd	
Sample	AA-76	AA-12	AA-13	AA-45	AA-46
Temperature (ºC)	Viscosity (10^x Pa s)				
960	2.9			4.7	
950	3.0			4.8	
940	3.1		3.4	4.9	
930	3.1		3.5	5.0	
920	3.2		3.6	5.1	
910	3.3		3.6	5.2	
900	3.4		3.7	5.3	
890	3.4		3.8	5.4	
880	3.5	3.5	3.9	5.5	5.7
870	3.6	3.6	3.9	5.6	5.8
860	3.7	3.7	4.0	5.7	5.9
850	3.8	3.8	4.1	5.8	6.0
840	3.9	3.9	4.2	5.9	6.1
830	3.9	4.0	4.3	6.0	6.3
820	4.0	4.0	4.4	6.1	6.4
810	4.1	4.1	4.4	6.3	6.5
800	4.2	4.2	4.5	6.4	6.6
790	4.3	4.3	4.6	6.5	6.7
780	4.4	4.4	4.7	6.6	6.9
770	4.5	4.5	4.8	6.8	7.0
760	4.6	4.6	4.9	6.9	7.1
750	4.7	4.7	5.0	7.0	7.3
740	4.8	4.8	5.1	7.2	7.4
730	4.9	4.9	5.2	7.3	7.5
720	5.0	5.0	5.3	7.5	7.7
710	5.2	5.2	5.4	7.6	7.8
700	5.3	5.3	5.6	7.8	8.0
690	5.4	5.4	5.7	7.9	8.1
680	5.5	5.5	5.8	8.1	8.3
670	5.6	5.6	5.9	8.3	8.5
660	5.8	5.8	6.0	8.4	8.6
650	5.9	5.9	6.2	8.6	8.8
640	6.0	6.0	6.3	8.8	9.0
630	6.2	6.1	6.4	9.0	9.2
620	6.3	6.3	6.6	9.2	9.3

SUPPLEMENTARY MATERIAL 2 - FIGURES

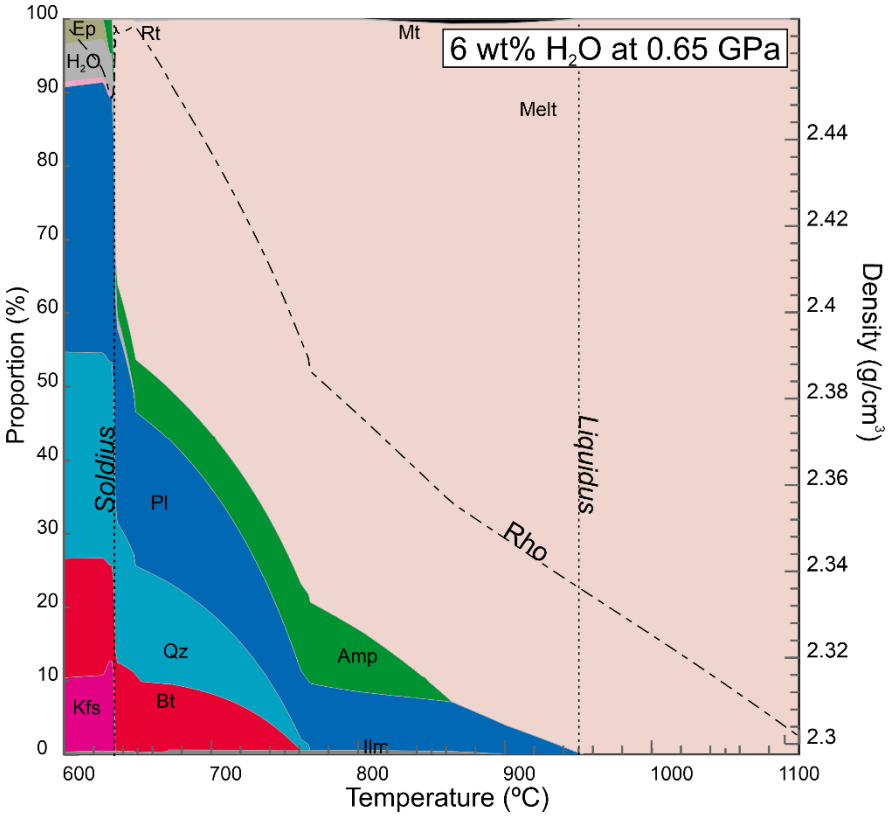


Fig. S 1. Phase proportions calculated for sample AA-76 at 0.65 GPa (6wt% H_2O). Striped, black line represents the density of the system (ρ).

SUPPLEMENTARY MATERIAL 3 – EPIDOTE DISSOLUTION METHODOLOGY

Methodological criteria for calculation of epidote dissolution kinetics proposed by Sial et al. (2008):

(1) Selection of idiomorphic to subdiomorphic magmatic epidotes, these crystals allow a better definition of their original shape, which is why they are used for the estimation of the dissolution degree. In the absence of isolated epidote crystals, epidote crystals involving allanite cores in epitaxial growth can be used.

(3) The pistacite content of the selected epidote crystals should fall within the magmatic field (Ps: 25–35 mol%; Liou, 1973);

(4) The intensity of crystal corrosion must be based on the maximum extent of dissolution, and the measurements must be perpendicular to the crystal faces affected by corrosion.

(5) The estimation of the corrosion time is calculated using the minimum apparent diffusion coefficient between tonalitic magma and epidote (5×10- 17 m2 s-1 for Si, Al, Ca, and F) at 750ºC. This diffusion coefficient has been successfully applied to other granitoid magmas. The estimation is based on the equations proposed by Brandon et al. (1996):

$$d_z = \left[\left(D_{app} \text{ x } t \right)^{1/2} \right]$$

$$t = d_z^2 / (5 \text{ x } 10^{-17})$$

- dz = dissolution zone width (m);
- D_{app} = apparent diffusion coefficient (5×10^{-17} m^2 s^{-1});
- t = partial epidote dissolution time (s)

(6) The magma emplacement depth is estimated using the Al-in-hornblend geobarometers (Tab. 1). The magma generation depth is generally deduced from petrological criteria.

(7) The magma transport rate is calculated using the ratio between the path length (difference between magma generation and emplacement depths) and the average corrosion time of the epidote exposed to melt. The path length corresponds to the difference between 10 kbar (1.0 GPa), initial epidote crystallization pressure, and emplacement depth (Brandon et al., 1996):

$$Tr = L_r / t$$

- Tr = transport rate (m/yr).
- Lr = path length (m), defined by the equation:

$$L_r = \frac{(10 - P_e) 10^3}{3 \text{ (m)}}$$

- P_e = emplacement pressure (kbar).
- t = partial dissolution time do epidote (yr)

Based on these criteria, the dimensions and length of maximum dissolutions of epidote crystals were measured on representative thin sections of the Alto Rio Preto granite (Fig. 11). Afterwards, the arithmetic mean of the obtained values was assumed to represent the average epidote dissolution and transport rate of the magmas (Tab. 2).

REFERENCES

Brandon AD, Creaser RA, Chacko T (1996) Constraints on Rates of Granitic Magma Transport from Epidote Dissolution Kinetics. Science (1979) 271:1845–1848. https://doi.org/10.1126/science.271.5257.1845

Sial AN, Vasconcelos PM, Ferreira VP, et al (2008) Geochronological and mineralogical constraints on depth of emplacement and ascencion rates of epidote-bearing magmas from northeastern Brazil. Lithos 105:225–238. https://doi.org/10.1016/j.lithos.2008.04.002

4 DEHYDRATION MELTING OF BASALTIC CRUST GENERATES RHYACIAN HIGH-K CALC-ALKALINE GRANITES IN THE BACAJÁ DOMAIN, SE AMAZONIAN CRATON

Arthur Santos da Silva Neri

Roberto Dall'Agnol

José de Arimatéia Costa de Almeida

Gilmara Regina Lima Feio

Submetido à *Journal of the Geological Society* como *Research article* em 15/07/2025.

Respeitando as normas da revista *Journal of the Geological Society.*, a formatação, citações e referências bibliográficas desta seção seguem o padrão requerido pela revista.



Gmail — Arthur Neri <santosarthursilvaa@gmail.com>

A manuscript number has been assigned to Melting of basaltic crust, SE Amazonian Craton

1 mensagem

JGS <em@editorialmanager.com> 15 de julho de 2025 às 09:55
Responder a: JGS <jgs@geolsoc.org.uk>
Para: Arthur Santos da Silva Neri <santosarthursilvaa@gmail.com>

Dear Mr. Neri,

Thank you for your submission entitled "Dehydration melting of basaltic crust generates Rhyacian high-K calc-alkaline granites in the Bacajá Domain, SE Amazonian Craton" to Journal of the Geological Society. It has been been assigned the following article number: jgs2025-147. The Journal Manager will now perform an initial quality check and contact you if there are any problems.

You will be able to check on the progress of your submission by logging on to Editorial Manager as an author. Please note that only the corresponding author is able to check the status of the submission. The URL is https://www.editorialmanager.com/jgsl/.

If you have posted a version of this submission to a preprint server, please ensure that it is updated according to the GSL preprint policy

Kind regards,
Bethan

Bethan Littley
Journal Development Editor
Journal of the Geological Society

Dehydration melting of basaltic crust generates Rhyacian high-K calc-alkaline granites in the Bacajá Domain, SE Amazonian Craton

Arthur S. S. Neri [a, b*], Roberto Dall'Agnol [a, b, c], Gilmara R. L. Feio [d, e], José A. C. Almeida [a, b]

[a] Programa de pós-graduação em Geologia e Geoquímica, IG – UFPA

[b] Grupo de Pesquisa Petrologia de Granitoides, Instituto de Geociências (IG), Universidade Federal do Pará (UFPA), Rua Augusto Corrêa, 01, Belém-PA, Brazil. CEP 66075-110.

[c] Instituto tecnológico Vale, Belém-PA, Brazil.

[d] Grupo de Mineralogia e Petrologia, Instituto de Geociências e Engenharias (IGE), Universidade Federal do Sul e Sudeste do Pará (Unifesspa), Marabá-PA, Brazil.

[e] Programa de Pós-Graduação em Propriedade Intelectual e Transferência de Tecnologia para a Inovação (Unifesspa).

[*] Corresponding author

ABSTRACT: Rhyacian granitoids of diverse compositions and ages are widely distributed across the Bacajá Domain, offering critical insights into the evolution of the Transamazonian Orogeny. The Alto Rio Preto granite is a WNW-elongated intrusion (~250 km²) emplaced immediately south of the Misteriosa transcurrent shear zone. It comprises three distinct facies: amphibole-biotite monzogranite to biotite monzogranite, and an independent biotite granodiorite-tonalite. Although derived from separate magma batches, all facies are cogenetic. Late-magmatic to solid-state deformational features define a structural framework marked by WNW-ESE to NW-SE foliation planes with moderate to subvertical dips to NE and SW, accompanied by a shallow-plunging mineral stretching lineation. The granite is metaluminous to slightly peraluminous, magnesian, and exhibits calc-alkaline to high-K calc-alkaline character. Zircon U-Pb suggest minimum crystallization ages at 2067±4.9 Ma and 2098±11 Ma, while titanite U-Pb dating yielded ages of 2067±9.3 Ma and 2068.6±9.9 Ma, for BGrd and ABMzG facies respectively, interpreted as magmatic crystallization ages. Thermodynamic-geochemical modeling indicates that the parental magma of the mozogranitic facies was generated through dehydration melting of basaltic crust at 0.99 GPa and 865 ºC. The Alto Rio Preto granite represents a classic high-K calc-alkaline granite derived from the partial melting of lower mafic crust in a collisional setting.

4.1 INTRODUCTION

During the Paleoproterozoic era (2500-1600 Ma), especially during the Rhyacian to Orosirian (2300-1800 Ma), major orogenic belts were developed on a global scale during the Columbia assembly (Zhao *et al.* 2002; Meert and Santosh 2017; Brown and Johnson 2018; Grenholm *et al.* 2019). In these belts, either of collisional or accretionary origin, granitoids generated throughout the orogenic process, from pre-collisional to post-collisional stages are a ubiquitous feature. (Klein et al. 2012; Klaver et al. 2015; Eglinger et al. 2017; Wu et al. 2022; Barros et al. 2023; Shi et al. 2025). In this context, the definition of granite petrogenesis can provide significant insights into the evolution of collisional zones and is widely used to better understand the processes that lead to crustal reworking and growth in collisional orogens (Costa *et al.* 2018; Sun *et al.* 2019).

Crustal reworking is the modification of pre-existing crustal material led by processes such as partial melting, metamorphism, magmatism, and fluid-rock interaction (Hawkesworth and Kemp 2006; Hawkesworth *et al.* 2010, 2019; Dhuime *et al.* 2015). To better understand the crustal reworking in collisional orogens, it is necessary to assess its geodynamic setting and formation processes and magma sources of granitoids. In the early stages of collision, the magmatism is likely induced by slab rollback or *syn*-exhumation (Ma *et al.* 2017; Hao *et al.* 2019), while during the post-collisional stage it is related to delamination or slab breakoff (Eglinger et al. 2017; Wane et al. 2018; Marangoanha et al. 2020; Gamaleldien et al. 2022), or by mantle plume within the craton (Gamal El Dien *et al.* 2021). The formation of granitoid in these zones is primarily controlled by two mechanisms: (i) partial melting of the pre-existing continental or oceanic crust (Chappell and Stephens, 1988; Clemens and Stevens, 2016a; Collins et al., 2020, 2016), and (ii) fractional crystallization of mantle-derived mafic magmas with or without crustal contamination (DePaolo 1981; Vogel *et al.* 2008; Bucholz *et al.* 2014; Walker *et al.* 2015).

This article presents new field, petrographic, geochemical, and geochronological data of the Rhyacian high-K calc-alkaline Alto Rio Preto granite occurring in the Bacajá Domain, SE Amazonian craton. These data clarify the petrogenetic and emplacement processes of high-K calc-alkaline granites in collisional orogens, as well as provide insights into crustal reworking mechanisms these settings.

4.2 GEOLOGICAL SETTING

The Maroní-Itacaiúnas Province is the main province established during the Paleoproterozoic (Rhyacian-Orosirian) in the Amazonian Craton (Tassinari and

Macambira 2004; Santos *et al.* 2006). The Bacajá Domain (Fig. 1b) is the southern extension of the Maroní-Itacaiúnas province in the Brazil Central shield. This domain is composed of Archean and Siderian fragments reworked during the Transamazonian Orogeny between ca. 2.26 and 1.99 Ga (Hurley *et al.* 1967; Cordani *et al.* 2000), and Rhyacian to Orosirian granitoids related to orogenic magmatism (Vasquez et al. 2005, 2008; Vasquez and Rosa-Costa 2008; Macambira et al. 2009, 2022; Barros et al. 2023; Magalhães et al. 2023). The Bacajá basement is represented by two lithotectonic associations: (i) Archean metamorphic complexes composed of granulites and orthogneiss with Mesoarchean (3000±2 Ma and 2943±4 Ma, (Macambira *et al.* 2007; Vasquez and Rosa-Costa 2008) and Neoarchean (2671±3 Ma, Vasquez and Rosa-Costa 2008) protoliths; and (ii) a late Neoarchean orthoderived granite-gneiss-migmatite association (2503±10 Ma; Macambira et al. 2003, 2004; Vieira et al. 2022). Associated with this basement, Siderian juvenile greenstone belts containing acid volcanic rocks crystallized at 2452±3 Ma to 2359±3 Ma crop out (Macambira et al. 2003, 2009; Vasquez 2006; Macambira and Amireault 2025).

As proposed by Vasquez and Rosa-Costa (2008 and references therein), the Paleoproterozoic orogenic magmatism records several events: (i) pre-collisional magmatism dated from 2215±2 Ma to 2133±10 Ma; (ii) the syn- to late-collisional magmatism dated from 2114±3 Ma to 2102±3 Ma; (iii) late- to post-collisional magmatism dated from 2086±5 Ma to 2069±6 Ma; and (iv) the post-collisional magmatism dated at 1986±5 Ma.

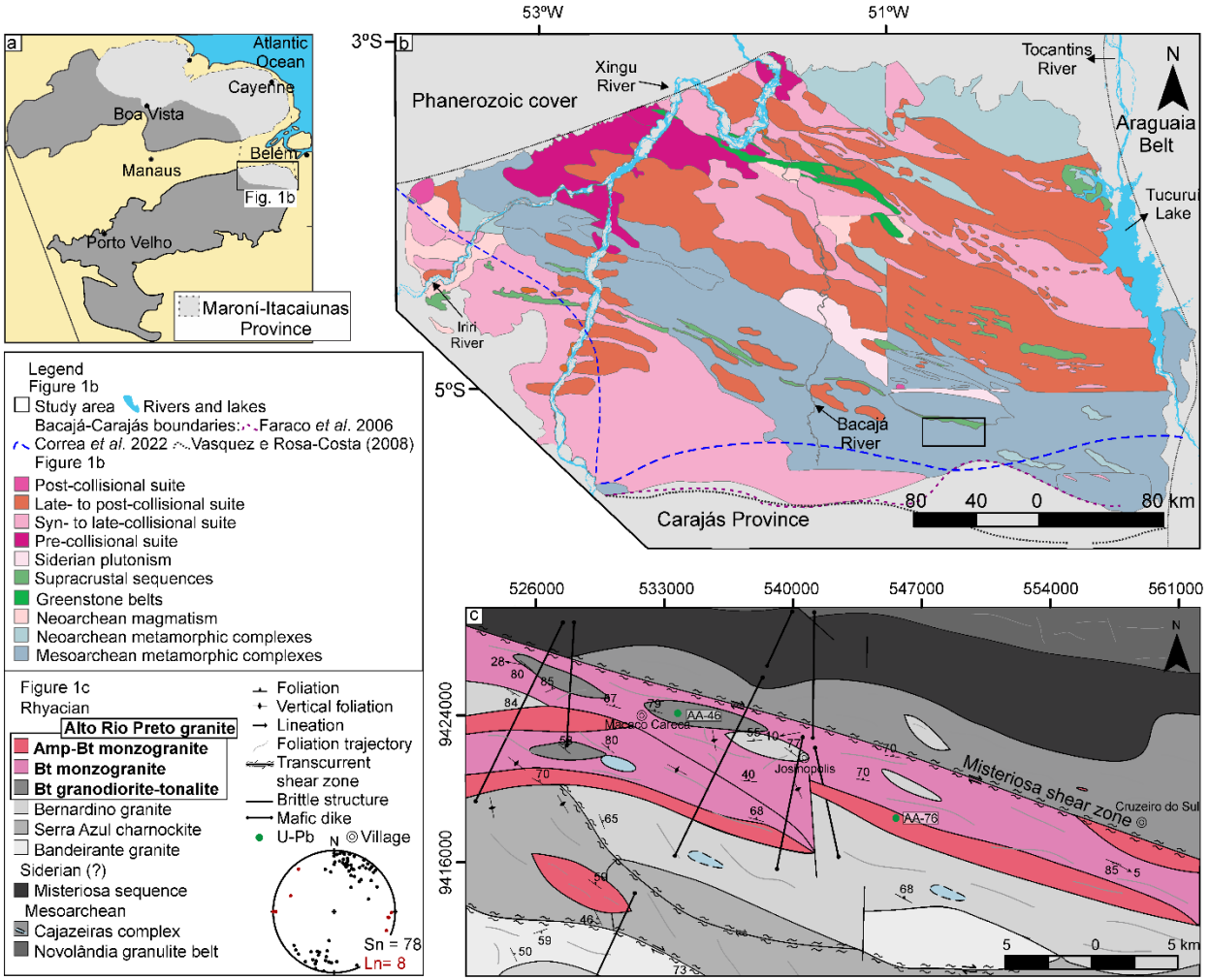


Fig. 1. (**a**) Amazonian craton and the location of the Bacajá Domain in the Maroni-Itacaiúnas Province (Tassinari and Macambira, 2004); (**b**) simplified geological map of the Bacajá Domain (Barros *et al.* 2007; Vasquez and Rosa-Costa 2008; Macambira *et al.* 2009; Besser and Barros 2015; Macambira and Ricci 2015); (**c**) Geological map of the studied area (Neri et al., submitted).

4.3 METHODS

4.3.1 Fieldwork and petrography

Fieldwork in the study area covered 1600 km² at a scale of 1:100.000. The work was carried out in four campaigns from 2019 to 2023 to investigate the structural pattern and stratigraphic relations between the distinct lithological associations that outcrop in that area. Petrographic, geochemistry, geophysical, and geochronological surveys supported geological mapping.

Petrography was performed using an Axio Imager.A2M Zeiss microscope. Modal analysis was conducted using an automatic point counter (Stageled) coupled with the Hardlegde software by Endeeper. A total of ~1800-2000 points were counted per thin section in a grid of 0.4 mm (Tab. S1), which were then used to classify the rock samples according to the Subcommission on the Systematics of Igneous Rocks of the International Union of Geological Sciences (Le Maitre 2002). Magmatic and deformational microtextures/structures were described according to Passchier and Trouw (2005) and Trouw *et al*. (2009). Mineral abbreviations follow Whitney and Evans (2010).

4.3.2 Geochemistry

Approximately 0.5–2 kg of fourteen fresh samples were crushed for whole-rock chemical analysis at the Oficina de Preparação de Amostras, Federal University of Pará (OPA-UFPA), Brazil using jaw crushers, and the obtained material was powdered in an agate swing mill until it reached a particle size of <10 μm at the laboratories of IG-UFPA. The chemical analyses were performed by inductively coupled plasma atomic emission spectroscopy (ICP-AES) for major and minor elements, and ICP mass spectrometry (ICP-MS) for trace elements (including the rare earth elements) at the ALS Geochemistry Laboratory, Geochemical diagrams were generated by using the GCDkit software (Janoušek et al., 2003). More detailed information about analytical procedures can be found at https://www.alsglobal.com.

4.3.3 Thermodynamic and trace element modelling

The thermodynamic modeling was performed using the Software GeoPs version 3.5 (Xiang and Connolly 2022) combined with dataset and a-X models of Holland et al., 2018) of the system KNCFMASHTO (K_2O-Na_2O-CaO-FeO-MgO-Al_2O_3-SiO_2-H_2O-TiO_2-Fe_2O_3).

The melt composition was calculated using Excel spreadsheets provided by the modeling software. To evaluate the best fit for our study, we considered the isolines compositions of SiO_2 and MgO in the liquid (Semprich et al., 2015), which are considered

indicative of magmatic differentiation, to select the melt composition more adequate to be representative of the parental magma in a range of ±2 wt% using Visual Basic for Applications (VBA) programming. After finding the best match, we extracted the composition of all phases, their modes, and the volume percentage of melt in a specific P-T point, which was then used in the trace element modeling.

The trace element modeling was performed using Excel spreadsheets based on an equilibrium partial melting equation (Wilson 1989):

$$\frac{CL}{C0} = \frac{1}{D(1-f)}\left(\frac{1}{D} - 1\right)$$

Where C_L and C_O are the trace element concentrations in the melt and in the source, respectively; f is the weight fraction of melt and D is the bulk distribution coefficient for the residual solids when melt is removed from the system. The mineral/liquid partition coefficients (Kd) used in the modeling were obtained from the online database https://kdd.earthref.org/KdD/.

4.3.4 Zircon and titanite U-Pb geochronology

Zircon and titanite were separated using standard rock crushing and heavy mineral separation techniques. Grains were individually selected, picked, and mounted in epoxy resin. Grain mounts were polished to expose the grain centers. Backscatter electron images (BSE) and cathodoluminescence (CL) for zircon were performed with a scanning electron microscope (SEM) at Centro de Pesquisas Geocronológicas (CPGeo) from the University of São Paulo (USP).

The zircon analyses were performed at GeoLab/USP with a SHRIMP IIe system, which consists of a mass spectrometer coupled to an ion microprobe with high sensitivity and resolution that uses a collimated and accelerated beam of primary ions (O^{2-}) to reach a target where secondary ions are generated from a 30 μm spot. The secondary ions are accelerated through the equipment, and the $^{254}UO^+$, $^{206}Pb^+$, $^{207}Pb^+$, $^{208}Pb^+$, $^{238}U^+$, $^{254}ThO^{+,}$, and $^{196}Zr_2O^+$ isotopes generated by the sample are measured successively. Its instrumental performance and analytical procedures are documented by Sato et al. (2014) and references therein: (i) primary beam → Kohler aperture = 120 μm; spot size = 30 μm; beam density of O^{2-} ions = 2.5–7.0 ηA (depending on brightness aperture); (ii) secondary beam → source aperture = 80 μm; mass resolutions for $^{196}Zr_2O$, ^{206}Pb, ^{207}Pb, ^{208}Pb, ^{238}U, ^{248}ThO, and ^{254}UO ranging from 5,000 to 5,500 (1%), and residuals <0.025. The corrections required by the technique are made by analyzing unknown materials and reference materials to determine specific calibration factors (Black *et al.* 2004). Thus,

during execution, for every five analyses on material of unknown age, one analysis is performed on the reference standard.

The Temora-2 reference zircon (416.78 ± 0.33 Ma; Black et al., 2004) was used for standard isotopic ratios, and the SL13 zircon (238 ppm; Sato et al., 2014) was used for reference of the concentration of U. The corrections for common lead were performed with ^{204}Pb, according to the isotopic evolution model of Stacey and Kramers (1975). Data reduction was performed in SQUID 1.6 software(Ludwig 2009).

The U-Pb analyses on titanite were done at Centro de Pesquisas Geocronológicas (CPGeo) from the University of São Paulo (USP). The analysis was performed using a Neptune ICP-MS and Analyte Excite excimer laser. Instrument setup parameters were 8.55 J/m^2 laser fluence, 6 Hz, ~25 μm spot size. Each analysis comprised 40 sequential measurements, with an integration time of approximately 1 second per measurement. The first 10 measurements were conducted with the laser ablation turned off to determine the instrumental blank, while the remaining 30 measurements were taken under the "Analyte Excite" excimer laser.

Seven isotopic signals were measured simultaneously. Four isotopes (^{206}Pb, ^{208}Pb, ^{232}Th, and ^{238}U) were analyzed using Faraday cups, which provide higher signal amplitudes, while three isotopes (^{202}Hg, ^{204}Pb, and ^{207}Pb) were measured using Multiple Ion Counters (MICs), which offer higher sensitivity. To ensure accurate measurements, the averaged value of the instrumental blank was subtracted from each of the seven isotopic signals at the end of each sequence.

Since the ^{235}U isotope was not directly measured, its signal was mathematically derived by dividing the ^{238}U signal by the known $^{238}U/^{235}U$ relative abundance (137.88). The contribution of mercury (Hg) to the ^{204}Pb signal was corrected by subtracting the quotient of the ^{202}Hg signal divided by the known $^{202}Hg/^{204}Hg$ relative abundance (4.355).

The age estimations were calculated using U-Pb ratios ($^{206}Pb/^{238}U$, $^{207}Pb/^{235}U$, and $^{208}Pb/^{232}Th$) in conjunction with the Stacey-Kramers model to determine the relative abundances of $^{206}Pb/^{204}Pb$, $^{207}Pb/^{204}Pb$, and $^{208}Pb/^{204}Pb$, which vary according to geological age. To account for the presence of non-radiogenic "common Pb," the ^{204}Pb signal was used to correct the measured ^{206}Pb, ^{207}Pb, and ^{208}Pb signals by subtracting the respective ^{204}Pb signal multiplied by the calculated relative abundances.

To mitigate instrumental drift and systematic errors, the BLR-1 primary standard (1047 ± 0.7 Ma, Aleinikoff *et al.* 2007) was analyzed approximately every 10 minutes, the secondary standard was Khan (522.2 ± 2.2 Ma, Heaman 2009). Comparisons between

measured and tabulated BLR-1 values allowed for the determination of multiplicative coefficients to convert total signals of Pb ($^{204}Pb+^{206}Pb+^{207}Pb+^{208}Pb$), Th ($^{232}Th$), and U ($^{235}U+^{238}U$) into concentration values (ppm units), as well as fractionation correction factors for the isotope ratios ($^{206}Pb/^{238}U$, $^{207}Pb/^{235}U$, $^{207}Pb/^{206}Pb$, and $^{208}Pb/^{232}Th$), which were applied before final age calculations. This analytical approach ensured precision and accuracy in the determination of isotopic compositions and age estimations, providing reliable geochronological data. Data processing and diagram generation were carried out in Isoplot 4.15 (Ludwig 2003). The errors of the isotope ratios were 1σ (absolute), and those of the age ellipses were 2σ (absolute).

4.4 RESULTS

4.4.1 Geological and structural aspects

The Alto Rio Preto granite is a WNW–ESE-elongated intrusion covering an area of approximately 250 km², consisting of two coalescent plutons, with a minor stock also present in the southeastern portion of the study area (Fig. 1c). It is primarily composed of granites, with subordinate granodiorites and tonalites, and its contacts with the Cajazeiras Complex and the Misteriosa sequence are entirely controlled by the Serra Misteriosa transcurrent shear zone. To the south, the contacts are more diffuse and characterized by alternate occurrences of it with other Paleoproterozoic granitoids (Fig. 1c). The Alto Rio Preto granite contains rare mafic microgranular enclaves (MME) (Fig. 2a) and lenses of high-pressure aluminous granulites (Fig. 1c), confirming the intrusive nature of the granitoid in the Archean rocks. Additionally, sparse leucogranitic veins, oriented parallel to the regional foliation, are observed (Fig. 2b). The Alto Rio Preto granite is intruded by the peraluminous Bernardino Granite and crosscut by N–S and NE–SW mafic dikes.

Field observations indicate a consistent structural pattern imprinted on the Alto Rio Preto granite defined by a WNW–ESE to NW–SE moderate (40–68°) to steeply inclined (70–89°) foliation, concordant with the major axes of the plutons, dipping predominantly towards the NE and subordinately towards the SW. This foliation is associated with a shallow (0–25°) plunging mineral stretching lineation, mostly oriented to the East (Fig. 2c). At the map scale, the foliation trajectories and shear zones define dominant WNW–ESE and subordinate NW–SE trends. From south to north, an increase in strain intensity is observed toward the Misteriosa shear zone. In low-strain domains (southwestern portion), the granites preserve primary magmatic fabrics, displaying an isotropic character (Fig. 2d) or a weakly oriented alignment of euhedral feldspar phenocrysts, defining a magmatic flow fabric trending WNW–ESE with steep dips (Fig.

2e). In medium-strain domains, the igneous fabric is partially overprinted, and solid-state deformation features become dominant, characterized by shear bands (Fig. 2f), S-C foliations parallel to the magmatic fabrics (Fig. 2g), and oval-shaped feldspar crystals (Fig. 2h). In high-strain domains, the magmatic fabrics are completely obliterated, and the rocks exhibit tectonic banding with a mylonitic to ultramylonitic character (Fig. 2h, i).



Fig. 2. Field aspects of the Alto Rio Preto granite. (**a**) oval-shaped mafic enclaves in the contact zone between the granite and the Serra Azul charnockite; (**b**) late granitic veins concordant with the regional foliation; (**c**) low plunge mineral stretching lineation; (d) isotropic biotite monzogranite; (e) alignment of K-feldspars phenocrystals indicating structures of magmatic flow; (**f**) centimetric shear-bands developed in the granite; (**g**) sinistral S-C shear structures; (**h**) plagioclase σ-porphyroclasts indicating dextral shear in mylonitic granitoid; (**i**) tectonic banding juxtaposing mylonites and ultramylonites.

4.4.2 Petrography

4.4.2.1 Modal classification

The rocks consist of varying proportions of quartz, K-feldspar, and plagioclase, with biotite ± amphibole as the main mafic minerals. Titanite, allanite, epidote[1], zircon, and opaque minerals occur as primary accessories, while muscovite, chlorite, and epidote[2] are secondary phases (Tab. S1).

Based on modal classification (Fig. 3), three distinct facies have been identified: (i) amphibole-biotite monzogranite to granodiorite (ABMzG), (ii) biotite monzogranite (BMzG), and (iii) biotite granodiorite to tonalite (BGrd). These rocks are predominantly leucocratic (M' = 11.95–21.4), with rare occurrences of hololeucocratic varieties (M' = 4.8) (Fig. 3).

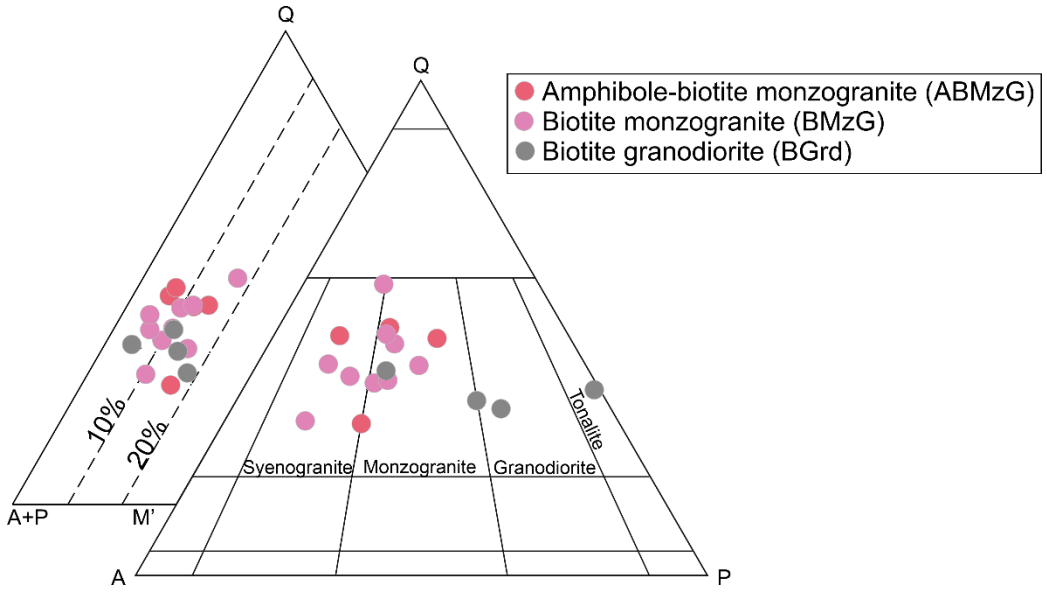


Fig. 3. QAP and Q-A+P-M' diagrams (Le maitre 2002) for samples of the Alto Rio Preto granite.

4.4.2.2 Microtextural and microstructural features

The studied rocks are predominantly medium-grained, with local occurrences of coarse-grained varieties. They display equigranular to heterogranular textures, with occasional porphyroclastic features. Most rocks are strongly foliated, as evidenced by the alignment of mafic and felsic minerals. Magmatic textures are preserved in the extreme southwest of the area, transitioning progressively to protomylonites and ultramylonites toward the Misteriosa shear zone.

4.4.2.3 Deformational Aspects

The northern boundary of the granite body is defined by the regional Misteriosa shear zone (Fig. 1c). Therefore, an analysis of the microstructures and textures of the granitoids was conducted to determine the deformation patterns these rocks underwent. According to the mylonite classification of (Trouw *et al.* 2009), these rocks were divided

into two domains: (i) a low-grade domain and (ii) a medium-grade domain.

Despite this subdivision, both domains have some features in common, including the alignment of mafic and felsic minerals, including feldspar porphyroclasts, quartz, biotite, and amphibole, which define a foliation, forming a disjunctive and spaced structure. The cleavage domains range from irregular to smooth forms, and are oriented parallel to one another, with a gradual transition between cleavage domains and microlithons. The microlithons are composed of quartz and feldspar, whereas the mafic-enriched domains consist of biotite, amphibole, and primary accessory minerals.

4.4.2.3.1 Low-grade domain

The low grade is domain is very restricted, occurring only far from the shear zones, mostly in the southeastern portion of the granite. It consists of rocks with partially preserved igneous textures, where crystals retain euhedral to subhedral shapes (Fig. 4a). They show progressive transition to mylonite as they approach the main shear zone. Feldspar deformation occurs primarily through fracturing (Fig. 4b), although some evidence of crystal-plastic deformation is observed, including undulose extinction and comminution into small new grains (Fig. 4c). Recovery processes are ubiquitous, particularly in quartz, which commonly exhibits undulose extinction (Fig. 4d). Locally, bulging recrystallization is observed in deformed quartz grains (Fig. 4e).

4.4.2.3.2 Medium-grade domain

The medium grade domain occurs near and within the shear zones and occupies the largest areas of the granite. It is characterized by plastic deformation in feldspars, evidenced by undulose extinction and twinning deformation (Fig. 4f). The increasing temperature provides the necessary heat for feldspar to recrystallize via bulging, which is marked by core-mantle structures (Fig. 4g) and flame-perthite in K-feldspar (Fig. 4h). Quartz is fully recrystallized through subgrain rotation with local grain boundary migration (Fig. 4i)..

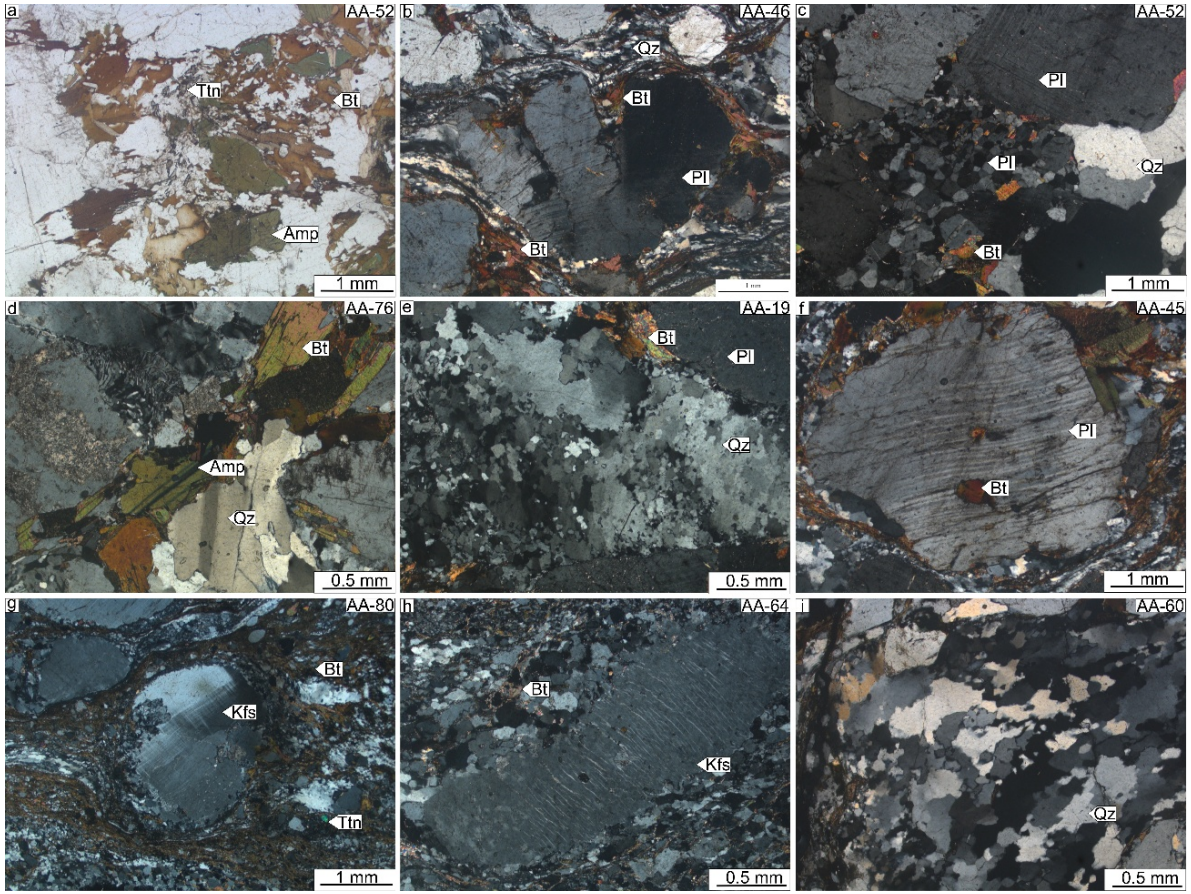


Fig. 4. Microstructural features of the Alto Rio Preto granite: low-grade (**a–e**) and medium-grade (**f–i**) mylonites. (**a**) Idiomorphic to subidiomorphic aggregates of amphibole, biotite, and titanite; (**b**) late-magmatic fractures in plagioclase; (**c**) crystal-plastic deformation in plagioclase, evidenced by comminution into tiny new grains; (**d**) quartz with undulose extinction, highlighting the recovery process; (**e**) deformed quartz with undulose extinction and lobate contacts, showing incipient recrystallization by bulging; (**f**) Plagioclase porphyroclast exhibiting deformation by "kinking"; (**g**) core-mantle structures in K-feldspar porphyroclasts formed by bulging recrystallization; (**h**) Flame-perthite in K-feldspar; (**i**) Quartz recrystallized by subgrain rotation.

4.4.3 Whole-rock geochemistry

4.4.3.1 Major and trace elements

Representative chemical compositions of the Alto Rio Preto granite are presented in Tab. 1 (compiled from Neri *et al.* submitted). The granitoids exhibit a broad range of silica contents (67.0 to 76.1 wt.%) and moderate Al_2O_3 concentrations (12.9 to 15.2 wt.%, with an outlier value of 17.2 wt.%). They show moderate K_2O contents, with the highest value recorded in the BMzG facies (4.52 wt.%) and the lowest in a tonalite of the granodioritic facies (2.5 wt.%). In contrast, Na_2O shows an inverse trend, reaching its maximum in the granodioritic facies (4.2 wt.%) and its minimum in the ABMzG facies (2.96 wt.%). Most of major oxides, including TiO_2, Al_2O_3, FeO_t, MgO, CaO, and P_2O_5, display negative correlations with silica, whereas K_2O and Na_2O do not define clear correlation trends with silica (Fig. 5). In rocks of similar silica contents, the ABMzG are enriched in CaO compared to the BMzG. The rocks exhibit moderate Mg# values (23–41) that in general show negative correlation with silica.

Trace element compositions reveal variable LILE contents with high Ba (782–1305 ppm, median = 1020.5, with an anomalous value of 1775 ppm), moderate Sr (155.5–465, ppm, median = 328.5, with Ba + Sr = 957.5–2240 ppm, median = 1336.5) and significantly lower Rb (100.5–195.5 ppm, median = 131). Regarding high-field strength elements (HFSE), the granite is characterized by low Zr (111–256 ppm, median = 178.5) and Nb (3.03–11.95 ppm, median = 7.78), as well as variable but generally low Y contents (2.8–30.8 ppm, median = 13.2). The Sr/Y ratios are low to moderate (6.6–68.6, median, 19, with one outlier at 129.7).

The Alto Rio Preto granitoids share similar rare earth elements (REE) patterns, although variations in $(La/Yb)_N$ ratios, heavy REE (HREE) concentrations, and Eu anomalies are observed. In the amphibole-bearing facies (Fig. 7a), two distinct patterns are identified, both showing similar $(La/Yb)_N$ (22.48–33.06; Tab. 1): (i) samples with higher REE concentrations and pronounced negative Eu anomalies; (ii) samples with lower REE content, and either subtle negative or positive Eu anomalies. In the BMzG facies (Fig. 7c), two trends are also recognized: (1) samples with higher REE contents, $(La/Yb)_N$ ratios of 22.47–23.88, and negative Eu anomalies (Eu/Eu* = 0.80–0.52); (2) samples with higher $(La/Yb)_N$ ratios of 40.45-63.67, pronounced MREE depletion ($(Gd/Yb)_N$ = 2.77–3.93), and negative to slightly positive Eu anomalies (Eu/Eu* = 0.74–1.21). Similarly, two patterns are identified in the BGrd facies (Fig. 7e): (1) samples with higher REE contents, $(La/Yb)_N$ ratios of 18.76–44.98, and negative Eu anomalies (Eu/Eu*

= 0.44-0.69, Tab. 1); (2) an isolated tonalitic sample (AA-16) with lower REE content, higher (La/Yb)N ratio (127.30), strong MREE depletion ($(Gd/Yb)_N$ = 9.78), and a slightly negative Eu anomaly (Eu/Eu* = 0.83).

Multi-element patterns (Fig. 7b, d, f) are consistent across all samples, characterized by pronounced negative anomalies in Nb, P, and Ti, as well as slightly negative Ba and Sr anomalies. The Nb depletion is typical of crustal melts or magmas influenced by crustal contamination. The negative P and Ti anomalies suggest the removal of one or more mineral phases that selectively incorporated these elements without significantly affecting other HFSE. Additionally, the mildly negative anomalies in Ba and Sr observed in most samples indicate feldspar fractionation and/or its presence as a residual phase.

Table 1. Whole-rock chemical composition of representative samples of the Alto Rio Preto granite.

Sample	AA-76	AA-52	AA-12	AA-63A	AA-60	AA-23	AA-21	AA-13	AA-61	AA-14A	AA-45	AA-16	AA-46	AA-19
Lithology	ABMzG	ABMzG	ABMzG	BMzG	BMzG	BMzG	ABMzG	ABMzG	BMzG	BMzG	BGrd	Bton	BGrd	BGrd
SiO_2	67	67.4	67.9	71.2	72.5	74.2	73.1	73.4	75.9	76.1	70.2	72.1	72.2	73.3
TiO_2	0.66	0.55	0.37	0.34	0.3	0.18	0.35	0.38	0.13	0.2	0.44	0.28	0.26	0.29
Al_2O_3	14.65	14.3	17.2	15.2	14.25	12.95	13.85	14.3	12.9	13.4	14.3	14.9	14.55	14.85
FeO	4.71	3.91	2.80	2.59	2.06	1.58	2.47	2.80	1.46	2.34	3.34	2.59	2.07	2.29
MnO	0.07	0.06	0.05	0.03	0.03	0.04	0.06	0.06	0.03	0.03	0.06	0.02	0.03	0.04
MgO	1.78	1.38	0.8	0.59	0.7	0.3	0.87	0.95	0.24	0.55	1.18	0.98	0.49	0.51
CaO	3.35	3.01	3.63	2.06	2.1	1.16	2.21	2.5	1.12	1.32	2.41	2.43	2.18	2.52
Na_2O	3.21	3.13	3.82	3.81	3.7	3.32	2.96	3.18	3.44	3.47	3.52	4.2	4.07	4.03
K_2O	3.38	3.9	3.81	4.52	3.62	4.45	4.44	4.32	4.51	4.27	3.6	2.5	3.12	2.81
P_2O_5	0.17	0.14	0.1	0.08	0.03	0.04	0.09	0.1	0.03	0.05	0.15	0.07	0.06	0.04
LOI	0.94	0.94	0.69	0.45	0.89	0.6	0.95	0.79	0.53	0.63	0.82	0.83	0.67	0.9
Total	100.6	99.35	101.74	101.33	100.55	99.12	101.79	>102.00	100.55	>102.00	100.54	101.34	100.1	101.98
Ba	996	1305	1775	1080	796	919	1175	1155	802	782	1045	865	1100	898
Rb	128	147.5	112.5	123	110	195.5	135	157.5	134	163.5	161	113	121	100.5
Sr	321	352	465	340	336	178.5	291	298	155.5	259	311	380	449	393
Zr	250	242	256	187	176	143	150	145	111	140	181	187	175	192
Nb	11.95	9.72	7.49	7.15	6.06	8.21	5.49	5.97	3.03	6.72	9.5	8.1	8.48	10.2
Y	30.8	19.6	24.7	6.8	4.9	14	12	11.5	23.5	5.2	22.1	2.8	12.4	20.2
Hf	6.31	6.38	6.59	5.13	4.94	4.57	4.03	3.99	3.44	4.1	4.94	4.78	4.75	5.37
Ta	0.8	0.7	0.8	0.6	0.5	0.8	0.4	0.8	0.4	0.5	0.9	1.1	1.2	0.6
Ga	19.6	18.3	19.8	18.3	16.6	14.4	16.2	16.1	16.3	16.5	20.6	18.4	19.6	17.9
Cs	1.76	1.38	1.44	1.37	0.72	1.99	0.89	1.66	1.68	1.16	2.94	2.13	1.45	1.05
Sn	2	2.6	1.7	1.3	1.4	2.5	1.3	1.7	1.8	0.8	2.2	2.8	1.5	0.9
Th	22.3	25.9	16.5	22.4	43.8	25.3	5.24	18.6	14.8	38.2	13.6	12.55	25.6	34.8
U	1.41	1.53	1.45	1.76	3.93	3.69	1.19	2	3.84	8.12	2.37	1.2	3.25	2.73
V	75	54	36	32	26	11	32	38	15	19	48	25	14	15
W	57.5	86.7	18	80.8	50.4	43.4	1.8	2.6	22.5	39.4	22.1	32.9	101	36.8
Cr	26	30	12	16	53	9	68	38	9	137	30	54	12	9
La	82.7	80.6	68.1	45.5	42.5	46	30.4	42.4	64.1	27.6	53.1	32.1	48.7	67.9

Ce	166	159	122.5	79.6	79.5	82.2	51.9	82.1	72.9	54.9	98.6	58.7	88.7	125
Pr	18.2	16.45	13.6	7.84	8.39	8.63	5.36	8.84	12.1	5.84	11.4	5.99	9.07	13.45
Nd	65.1	57.9	50.6	26.3	28	28.7	18.6	30.1	40.7	21.1	37.9	19.7	30.2	45.6
Sm	11.7	9.35	8.76	3.17	3.69	4.53	3.01	4.43	6.32	3.36	7.32	3.21	4.57	7.78
Eu	1.3	1.22	1.49	0.99	0.68	0.66	1.05	1.03	1.47	0.67	1.12	0.7	0.9	0.95
Gd	9.26	6.49	6.79	1.99	2.16	3.28	2.46	3.25	5.02	2.24	5.51	2.06	3.49	5.65
Tb	1.2	0.78	0.93	0.21	0.21	0.46	0.3	0.39	0.75	0.23	0.89	0.2	0.5	0.68
Dy	6.91	4.21	5.28	0.97	1.08	2.84	1.62	2.17	3.64	1.07	4.52	0.66	2.34	3.51
Ho	1.21	0.72	0.83	0.21	0.18	0.5	0.32	0.42	0.78	0.18	0.86	0.1	0.5	0.68
Er	2.97	1.84	2.49	0.59	0.48	1.36	0.71	1.13	2.22	0.57	2.18	0.16	1.02	2.14
Tm	0.37	0.25	0.3	0.05	0.06	0.18	0.12	0.11	0.32	0.05	0.25	<0.01	0.14	0.37
Yb	1.88	1.72	2.48	0.58	0.45	1.38	0.62	1.05	1.81	0.46	1.42	0.17	0.73	2.44
Lu	0.31	0.23	0.25	0.12	0.06	0.17	0.09	0.12	0.24	0.09	0.2	0.03	0.12	0.41
$(La/Yb)_N$	22.48	31.59	24.42	52.89	63.67	22.47	33.06	27.22	23.88	40.45	25.21	127.30	44.98	18.76
Eu/Eu*	0.38	0.48	0.59	1.21	0.74	0.52	1.18	0.83	0.80	0.75	0.54	0.83	0.69	0.44
Mg#	40	39	34	29	38	25	39	38	23	30	39	40	30	28
Ba+Sr	1317	1657	2240	1420	1132	1097.5	1466	1453	957.5	1041	1356	1245	1549	1291
Sr/Y	10	18	19	50	69	24	26	13	7	50	14	136	36	19

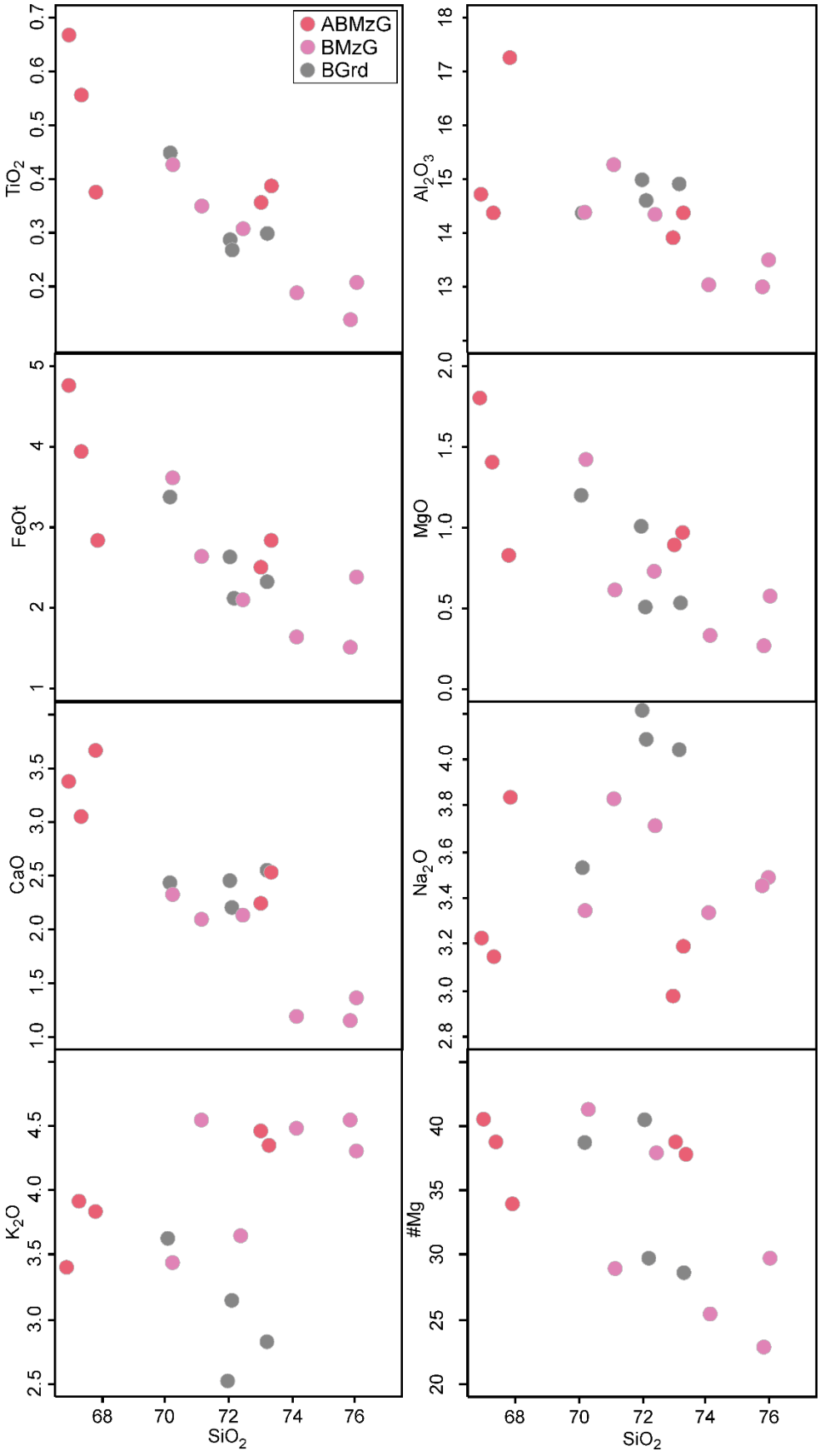


Fig. 5. Harker diagram (SiO_2 vs major elements) of the Alto Rio Preto granite.

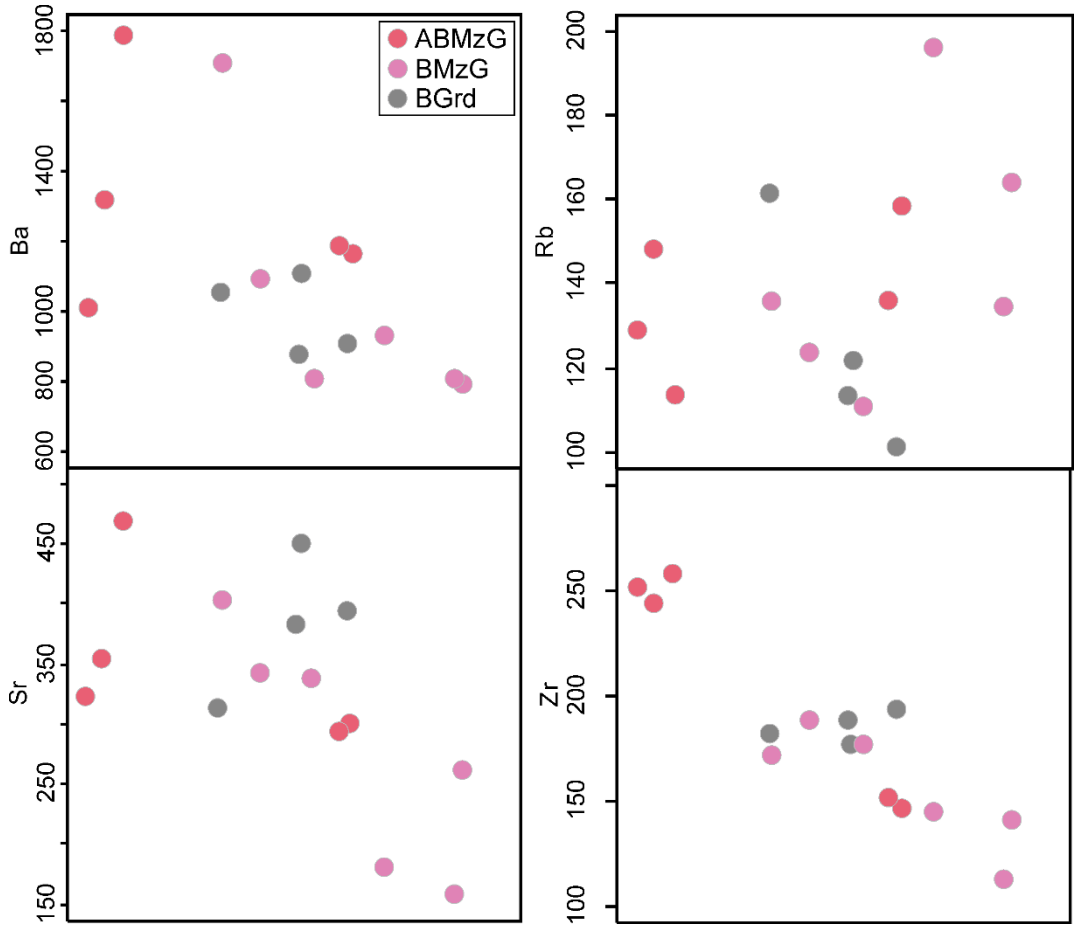


Fig. 6. Harker diagram (SiO_2 vs trace elements) of the Alto Rio Preto granite.

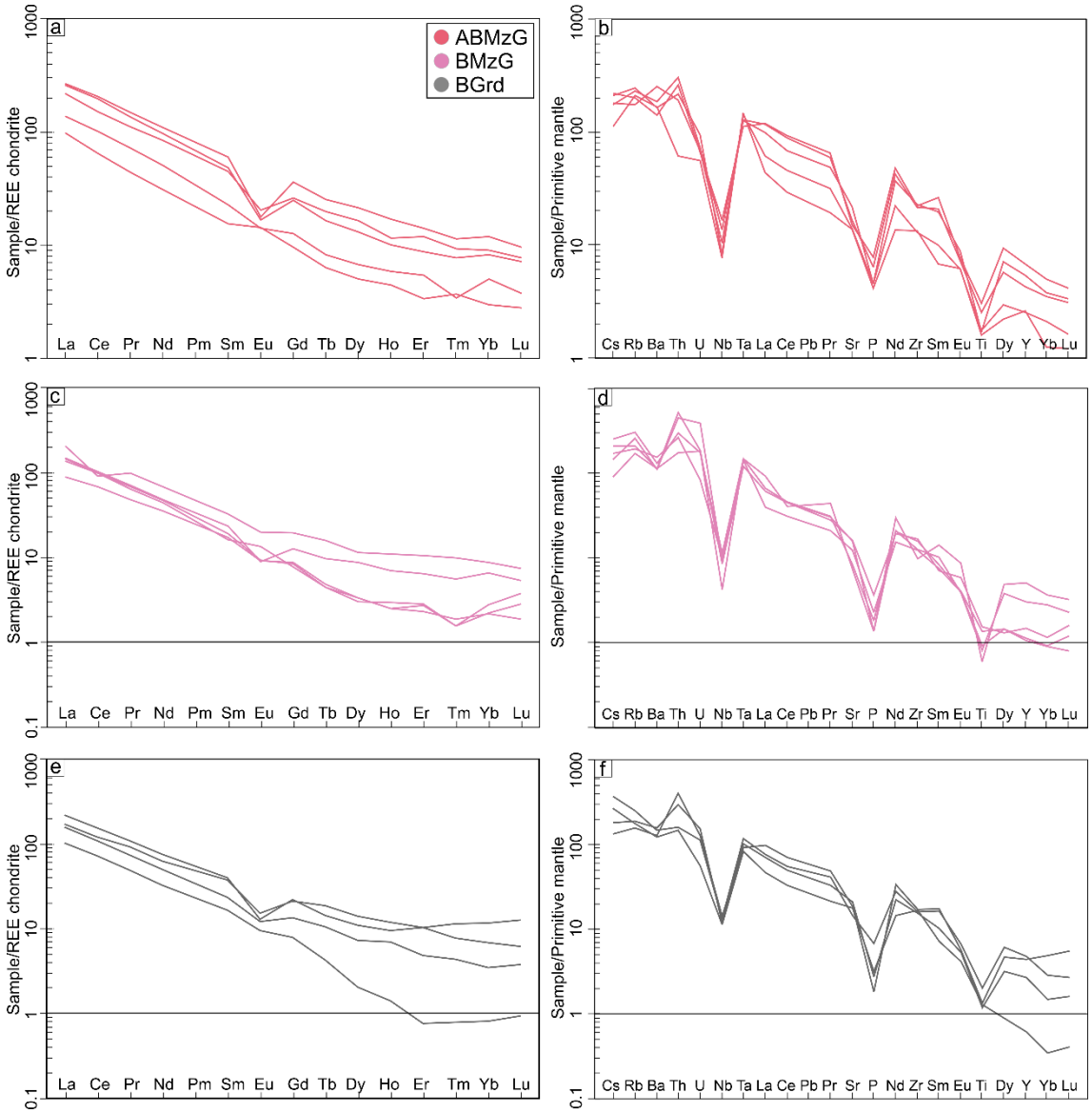


Fig. 7. Chondrite normalized REE patterns (Boynton, 1984) and normalized multielement patterns (McDonough and Sun, 1995) of the distinct facies of the Alto Rio Preto granite. (**a-b**) ABMzG, (**c-d**) BMzG, (**e-f**) BGrd.

4.4.3.2 Geochemical classififcation and magmatic series

In the P-Q diagram (Fig. 7a, fields of Debon and Le Fort, 1983), the Alto Rio Preto granitoids are classified as monzogranites or granodiorites. In the A/CNK vs. A/NK (Fig. 7b, the amphibole-bearing facies are metaluminous, whereas the biotite-facies without amphibole are slightly peraluminous. The granitoids predominantly plot in the calc-alkaline field (Fig. 7c) in the modified alkali-lime index (MALI) diagram (Frost *et al.* 2001).

In the SiO_2 vs. Fe-index diagram (Frost *et al.* 2001), most samples fall within the magnesian field (Fig. 7d), with a few silica-rich samples plotting in the ferroan field. The SiO_2 vs. K_2O diagram (Peccerillo and Taylor 1976) shows that all granite samples have high-K calc-alkaline character (Fig. 7e), while most of the granodiorite facies are

calc-alkaline. Finally, in the tectonic discrimination diagram of Rb vs. Y+Nb (Pearce et al. 1984), the samples plot in the transition between the syn-collisional and volcanic arc granites (Fig. 8f).

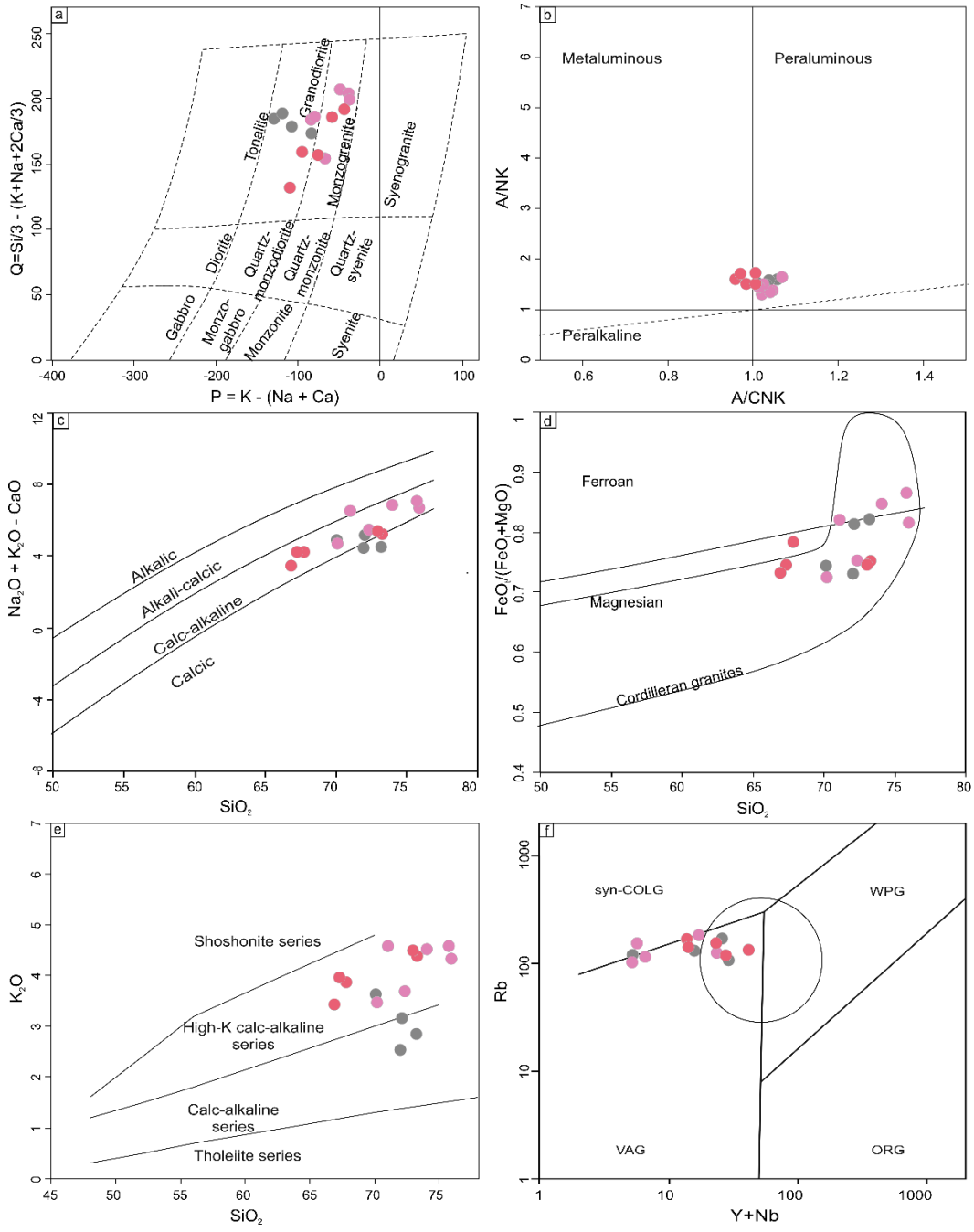


Fig. 8. Geochemical classification and magmatic series of the Alto Rio Preto granite. (**a**) P-Q diagram (Debon and Fort, 1983); (**b**) A/NK vs. A/CNK (Shand 1943); (**c**) SiO_2 vs Na_2O+K_2O – CaO diagram (Frost *et al.* 2001); (**d**) SiO_2 vs FeOt/(FeOt+MgO) diagram (*Frost et al.* 2001); (**e**) K_2O vs. SiO_2 (Peccerillo and Taylor 1976); (**f**) Rb vs. Y+Nb (Pearce *et al.* 1984).

4.4.4 U-Pb geochronology

We selected representative samples from the ABMzG and BGrd facies of the Alto Rio Preto granite for dating. For both samples titanite and zircon were dated. U-Pb data are found in Tab. S2.

The zircon grains from sample AA-46, a biotite monzogranite related to the granodiorite facies, are pale to dark brown, euhedral, short to long prismatic, with lengths between 100 to 330 μm. CL images typically show low luminescence associated with regular oscillatory zoning. Some zircon grains display high-luminescence cores and low luminescence rims. Minor opaque and apatite inclusions are common (Fig. 9). For sample AA-46, eighteen spot analyses show strong discordance (Fig. 10a). Seven spots defined an upper intercept at 2067±4.9 Ma (Fig. 10c, MSWD = 2.1) and a lower intercept of 452±10 Ma (MSWD = 2.1). Th/U ratios varies from 0.03 to 0.72. Two older $^{207}Pb/^{206}Pb$ apparent ages 2589±6 Ma and 3215± 37 Ma.

Titanite grains from this sample are euhedral to subhedral and display a dark brown color. BSE imaging indicates that most titanite grains have complex BSE responses with dark cores and light rims, or even multiple truncated BSE responses, oscillatory zoning can also be found (Fig. 9). A total of 35 spot analyses were conducted on 31 titanite grains, 14 analyses provided a concordia age of 2067.1±9.3 Ma (Fig. 10b). This age overlaps withing errors with zircon age from this sample (Fig. 10d)

For sample AA-76, an amphibole-biotite monzogranite, zircon U-Pb SHRIMP data is presented in Neri et al. (submitted). Its zircon grains display similar features of zircons from sample AA-46 (Fig. 9). Upper intercept ages indicated minimum crystallization ages at 2098±11 Ma (Fig. 10c, MSWD = 1.9)

Titanite grains from this sample are also euhedral to subhedral, ranging in color from light to dark brown. BSE images reveal that most titanite exhibits complex BSE responses with truncated light and dark domains, homogenous grains are also common, while oscillatory zoning is rare (Fig. 9). A total of 35 spot analyses were performed on 29 titanite grains, 14 spot analyses defined a concordia age of 2068.8±9.9 Ma (Fig. 10d). This age is slightly younger (ca. 8 Ma) than zircon ages from the same sample (Fig. 10f).

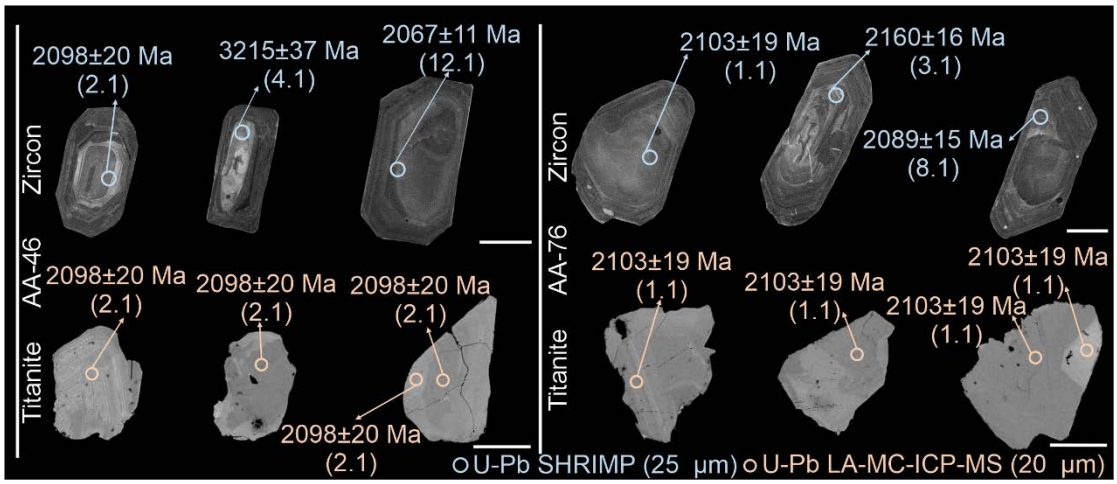


Fig. 9. Representative CL images for zircon and BSE images for titanite from of the Alto Rio Preto granite. Zircon CL images for sample AA-76 are from Neri et al. (submitted).

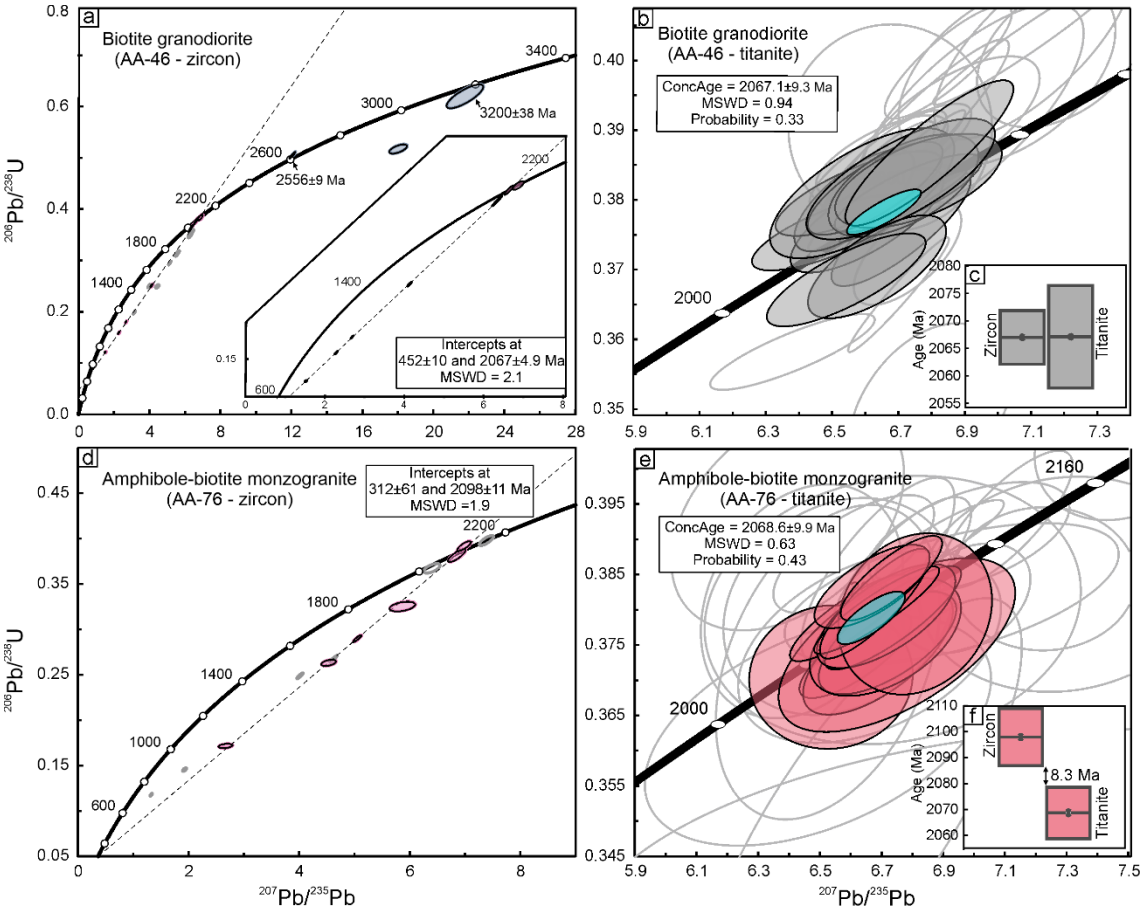


Fig. 10. (**a**) SHRIMP U-Pb concordia plots for zircon from sample AA-46. (**b**) LA-ICP-MS U-Pb concordia diagram for titanite from sample AA-46. (**c**) Comparison of zircon and titanite U-Pb ages from sample AA-46. (**d**) SHRIMP U-Pb concordia plots for zircon from sample AA-76 (Neri et al., submitted). (**e**) LA-ICP-MS U-Pb concordia diagram for titanite from sample AA-76. (**f**) Comparison of zircon and titanite U-Pb ages from sample AA-76.

4.5 DISCUSSION

4.5.1 Meaning of U-Pb ages

The zircon upper intercept ages 2067±4.9 Ma and 2098±11 Ma are interpreted as a minimum crystallization age for the granite, due to its high discordance. The older ages at 2589±6 Ma and 3202±28 Ma are interpreted as xenocrystals, probably incorporated from wall-rocks during ascent and emplacement.

Titanite is a robust mineral for U-Pb dating, capable of recording multiple stages of magmatic and post-magmatic processes, as well as deformational and metamorphic events (Broska et al., 2007; Holder et al., 2019; Papapavlou et al., 2017; Słaby et al., 2021; Spencer et al., 2013). In our samples, titanite is in the late crystallizing phase (Neri et al., in prep). Although some crystals may present typical igneous oscillatory zoning (Fig. 9), titanite major element composition suggests and inherited igneous and/or recrystallized origin (Neri et al., in prep).

For sample AA-46, the overlapping ages of titanite and zircon suggest that these minerals crystallized during the same event. The major element affinity with inherited igneous titanite suggests that the titanite ages likely record the magmatic crystallization.

For sample AA-76, titanite ages are slightly younger (ca. 8 Ma) than the zircon upper intercept ages. Some possibilities arise analyzing the data from this sample. (i) This sample is slightly older compared to the other granite facies, and zircon ages represent crystallization and the titanite ages late deformational stages. (ii) Zircon data is slightly overestimated, given the high MWSD and highly discordant analyses, there are even younger concordant zircons analyses in this sample at 2048±26 Ma (Fig. 10). In this scenario, titanite ages would better represent the granite crystallization. (iii) Titanite crystallized at late magmatic stages, shortly after zircon crystallization. Given that the sample is far from the shear zone (Fig. 2c), preserve primary magmatic fabrics and titanite chemistry suggest an inherited igneous or recrystallized composition, the titanite ages at 2068.8±9.9 Ma most likely represent crystallization age.

4.5.2 Petrogenesis

4.5.2.1 Assessment of element mobility

Multiple deformation and metamorphic events, reaching up to granulite facies, have affected the study area and its surroundings (Silva 2021). Therefore, before using whole-rock geochemical data to constrain the granite's petrogenesis and tectonic setting, it is essential to evaluate the impact of late post-magmatic alteration on the available chemical compositions.

Polat *et al.* (2002) and Polat and Hofmann (2003) suggest that a low loss on ignition (LOI: 0.45–0.95 wt%) and the absence of distinct Ce anomalies (δCe, calculated as $Ce_N/\sqrt{(La_N \times Pr_N)}$: 0.63-1.05) indicate that the granite's primary chemical signature has remained largely unaltered during post-magmatic processes.

Furthermore, Zr is generally regarded as one of the least mobile elements and can therefore serve as an alteration-independent index of geochemical variation (Polat et al. 2002). The analyzed samples exhibit linear correlations between Zr and REE, HFSE (Y, Nb, Ta, Ti, and Hf), and LILE (Ba, Rb, Sr, and Th) (Fig. S1), suggesting that these elements remained essentially immobile and can be reliably used to constrain the petrogenesis and tectonic setting of the granite.

4.5.2.2 Magma source

Several models have been proposed to explain the origin of high-K calc-alkaline granites, most of which involve the partial melting of lower to middle crustal material, typically influenced by underplated mafic magmas from the lithospheric mantle (Ghoneim *et al.* 2022). In general, I-type granites can be derived from the melting of metaluminous basaltic to andesitic rocks (Roberts and Clemens 1993; Wolf and Wyllie 1994; Nandedkar et al. 2014). The genetic processes are often complex and may involve partial melting, fractional crystallization, magma mixing, or interactions between these processes (Petford 1995; Schiano et al. 2010; Brown 2013; Clemens and Stevens 2016).

The Alto Rio Preto granite comprises two distinct magmatic assemblages: (1) amphibole-biotite monzogranite and biotite monzogranite facies; and (2) biotite granodiorite facies. Both assemblages display similar geochemical and isotopic signatures, indicating a common source and suggesting they are cogenetic. However, their petrographic and geochemical differences indicate that they are not co-magmatic.

Field, geochemical, geochronological, and isotopic evidence suggest that the Alto Rio Preto granite formed from dominantly crustal melts, without significant input from mantle-derived magmas. The scarcity of mafic enclaves, that are observed only in a few outcrops, (Fig. 3a) is a primary indicator limited mantle-derived melt contribution (Roberts and Clemens, 1993). The biotite composition, characterized by low MgO is consistent with derivation from crustal sources (Neri et al., in prep). Additionally, the high silica content (up to 76.1 wt%) and moderate #Mg (<0.41) are typical of crustal melts (Rapp and Watson 1995; Moyen 2009). The enrichment in large-ion lithophile elements (LILE) and light rare earth elements (LREE), coupled with depletion in HFSE and pronounced negative Nb, P, and Ti anomalies in chondrite-normalized trace element

patterns, further support a crustal source. The presence of inherited Archean to Paleoproterozoic zircon grains and strongly negative $\varepsilon Nd_{(t)}$ and $\varepsilon Hf_{(t)}$ values (Neri et al., submitted) also corroborates a dominant crustal origin.

The calc-alkaline to high-K calc-alkaline affinity of the Alto Rio Preto granite can be explained by the partial melting of hydrous mafic to intermediate metaigneous rocks in the middle to lower crust (Roberts and Clemens 1993; Patiño Douce 1999). In the Al_2O_3/(FeOt+MgO) vs. 3CaO vs. 5(K_2O/Na_2O) source diagram, Fig. 11a; fields of Laurent et al., 2014), most samples plot within the field of granitoids derived from high-K mafic rocks, with some plotting in the border between the tonalite and metasediments fields. On the CaO + FeOt +MgO + TiO_2 vs. CaO/ (FeOt + MgO + TiO_2) plot (Fig. 11b; fields of Patiño Douce 1999) most samples plot in the field of melts derived from amphibolites and basalts, reinforcing a mafic source. However, some samples plot in the field of melts derived from metagraywackes, suggesting a possible sedimentary source or potential assimilation of metasedimentary material during magma ascent. This interpretation is consistent with the presence of metasedimentary rocks and S-type granites in the region (Neri at al., submitted). On the diagram FeOt + MgO vs. Nb+ Zr + Y (Fig. 11b; fields of Laurent *et al.* 2014), all samples plot within the field of crustal derived melts, further supporting a crustal origin.

The depth of magma generation can be inferred based on the Sr and Yb contents in whole-rock geochemistry (Zhang *et al.* 2006). At lower pressures (<1.5 GPa), plagioclase remains stable in the source, retaining Sr. However, at higher pressures (>1.5 GPa, e.g., (Almeida *et al.* 2011), plagioclase becomes unstable, releasing Sr into the melt. The presence of discrete to strongly negative Eu anomalies in REE patterns suggests that plagioclase was retained in the source, indicating melting at pressures below 1.5 GPa. The Sr/Y and $(La/Yb)_N$ ratios are also commonly used to estimate pressure conditions during partial melting (Zhang *et al.* 2010; He *et al.* 2011). In this context, high Sr/Y and (La/Yb)N ratios are often associated with high-pressure melting in the garnet stability field, but they can also result from sources that were initially enriched in Sr/Y (Moyen 2009) and that hypothesis was contested by Smithies et al. (2019). Most Alto Rio Preto granite samples exhibit low (6.6–25.9) to intermediate (36.2–68.6) Sr/Y ratios, with only one outlier (135.7). These values and discussed geochemical evidence suggest that the Alto Rio Preto granite magmas were derived from the partial melting of high-K mafic sources at pressures below 1.5 GPa, leaving plagioclase as a residual phase. The weak to moderate negative Eu anomalies further support the presence of residual plagioclase or

the occurrence of plagioclase fractional crystallization or both. Additionally, the concave-upward REE patterns displayed by a few samples indicate fractionation of amphibole during crystallization or its retention in the source.

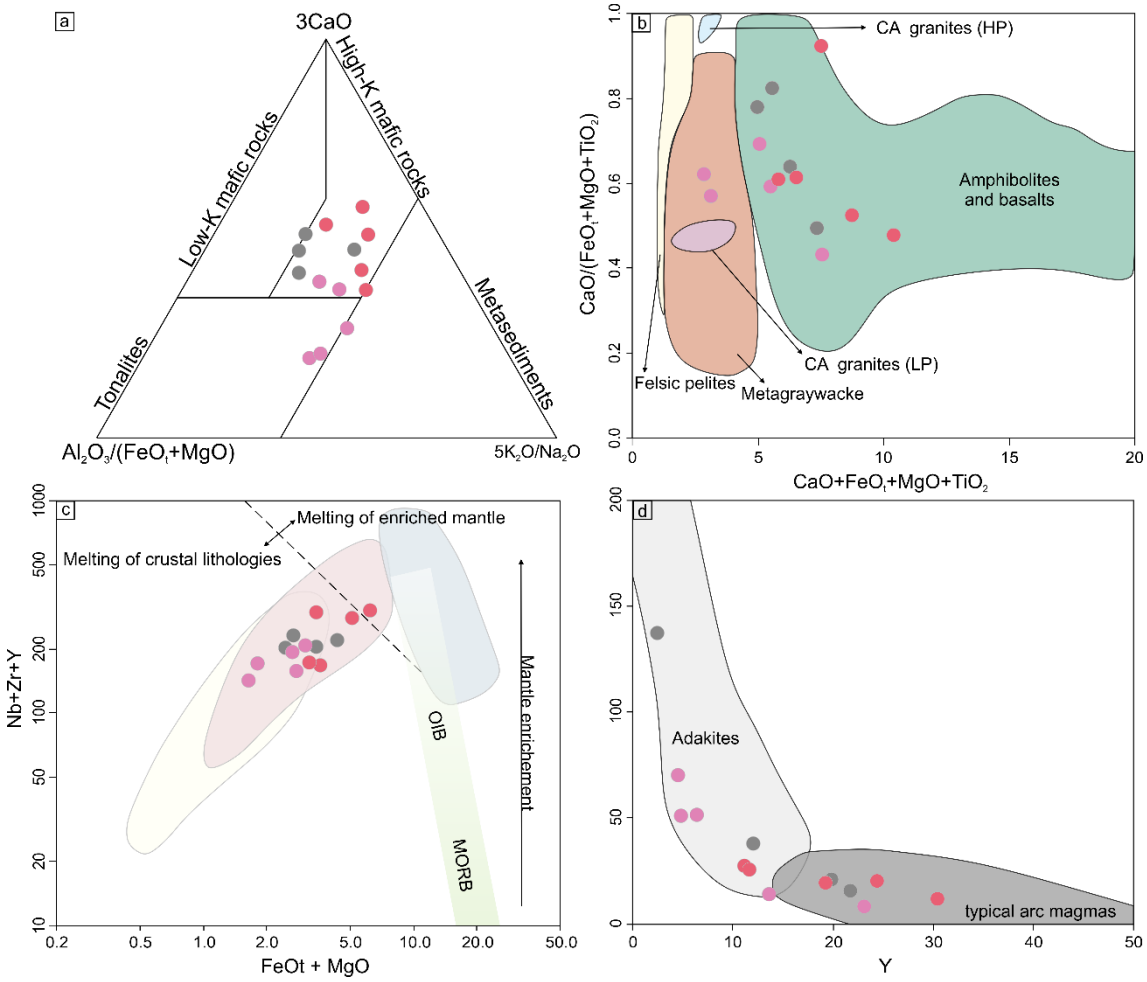


Fig. 11. Geochemical insights into the petrogenesis of the Alto Rio Preto granite. (**a**) diagram Al_2O_3/(FeOt+MgO) vs. 3CaO vs. 5(K_2O/Na_2O) for magma source (Laurent et al., 2014); (**b**) CaO + FeOt +MgO + TiO_2 vs. CaO/ (FeOt + MgO + TiO_2) (Patiño Douce 1999); (**c**) FeOt + MgO vs. Nb + Zr + Y (Laurent *et al.* 2014); (**d**) Y vs. Sr/Y.

4.5.2.3 Phase equilibria and trace element modeling

Partial melting in the crust can occur through two primary mechanisms: (i) dehydration melting and (ii) fluid-assisted melting (Wolf and Wyllie 1994; Rapp and Watson 1995; Collins et al. 2016, 2020). Both processes can generate granitic melts, but certain geochemical and mineralogical features can help infer the most probable melting mechanism responsible for granitoid magma formation.

Dehydration melting occurs when the breakdown of hydrous minerals, such as micas and amphiboles, releases water into the system, reducing the temperature of stability of anhydrous minerals. This process occurs at high temperatures (>800 ºC) and pressures, and it is common in subduction zones or orogenic belts. It is a key mechanism in the deep crust, particularly during amphibolite-to-granulite facies transitions, playing

a crucial role in generating felsic magmas in orogenic settings(Wolf and Wyllie 1994; Rapp and Watson 1995), but is observed also in within plate settings (Dall'Agnol *et al.* 1999; Teixeira *et al.* 2019).

Conversely, fluid-assisted melting occurs when water-rich fluids infiltrate water unsaturated rocks, lowering the melting temperature of minerals. This mechanism is widespread in subduction zones and the continental crust, often producing basaltic and andesitic magmas. Compared to dehydration melting, fluid-assisted melting generally occurs at lower temperatures (700–750 ºC) (Robertson and Wyllie 1971; Sawyer 1999; Collins et al. 2016, 2020).

In the study area, a late- to post-collisional setting has been identified (Neri et al., submitted). The generation in it of Rhyacian granites was most likely driven by a delamination process that provided the necessary heat to induce crustal melting. This aspect, combined with the absence of subduction-related rock assemblages (Neri et al., submitted), suggests that the primary mechanism responsible for the formation of the Alto Rio Preto granitoids was dehydration melting of the lower crust.

Given that a high-K mafic rock (amphibolite or basalt) was indicated as the probable source of the Alto Rio Preto granite magmas, we selected an average middle Proterozoic basalt composition (Condie 1993) as a representative source for its parental magmas, and performed thermodynamic modeling using the Software GeoPs version 3.5 (Xiang and Connolly 2022) combined with the dataset and a-X models of Holland et al. (2018), for the system KNCFMASHTO (K_2O-Na_2O-CaO-FeO-MgO-Al_2O_3-SiO_2-H_2O-TiO_2-Fe_2O_3). The results are presented in a pseudosection (Fig. 12) constructed for a P-T range of 0.3–1.2 GPa and 750–1000 ºC, incorporating isopleths of SiO_2 and MgO in the generated melt, along with isolines representing melt volume. A water content of 1.5 wt% was assumed to model dehydration melting of the admitted basaltic source (Ge et al., 2022), and the $Fe^{3+}/(Fe^{2+}+Fe^{3+})$ ratio was set at 0.15, consistent with the predominantly oxidized nature of the early crust (Palin *et al.* 2016; Ge *et al.* 2023). These parameters align with the geochemical indicators commonly used as proxies for magma genesis (see section 5.2.2) and with the thermobarometric constraints established through mineral chemistry and thermodynamic modeling (Neri et al. in prep).

In the pseudosection, amphibole remains stable across most of the P-T range, becoming unstable only at extremely high temperatures (>970 ºC) and moderate to low pressure (<0.6 GPa). Orthopyroxene stability strongly depends on pressure and temperature, crystallizing at high temperatures (≥ 820° C) and variable pressures (0.3 to

1.1 GPa). Garnet is stable only above ~1.04 GPa and ~840 ºC.

The SiO_2 isolines are primarily pressure-dependent, whereas MgO and melt volume are temperature-dependent. These constraints were used to select the most appropriate P-T conditions for extracting the melt composition.

Given the similar geochemical, geochronological and isotopic behavior of the ABMzG + BMzG and BGrd facies, although they are not co-magmatic, it is assumed that they are derived from similar sources (co-genetic) and originated through similar processes. Therefore, the modeling is focused on the ABMzG facies, because it's the more primitive facies in the granite (lower SiO_2 and higher MgO, Tab. 1).

Partial melting in the crust can occur through two primary mechanisms: (i) dehydration melting and (ii) fluid-assisted melting (Collins et al., 2020, 2016; Rapp and Watson, 1995; Wolf and Wyllie, 1994). Both processes can generate granitic melts, but certain geochemical and mineralogical features can help infer the most probable melting mechanism responsible for granitoid formation.

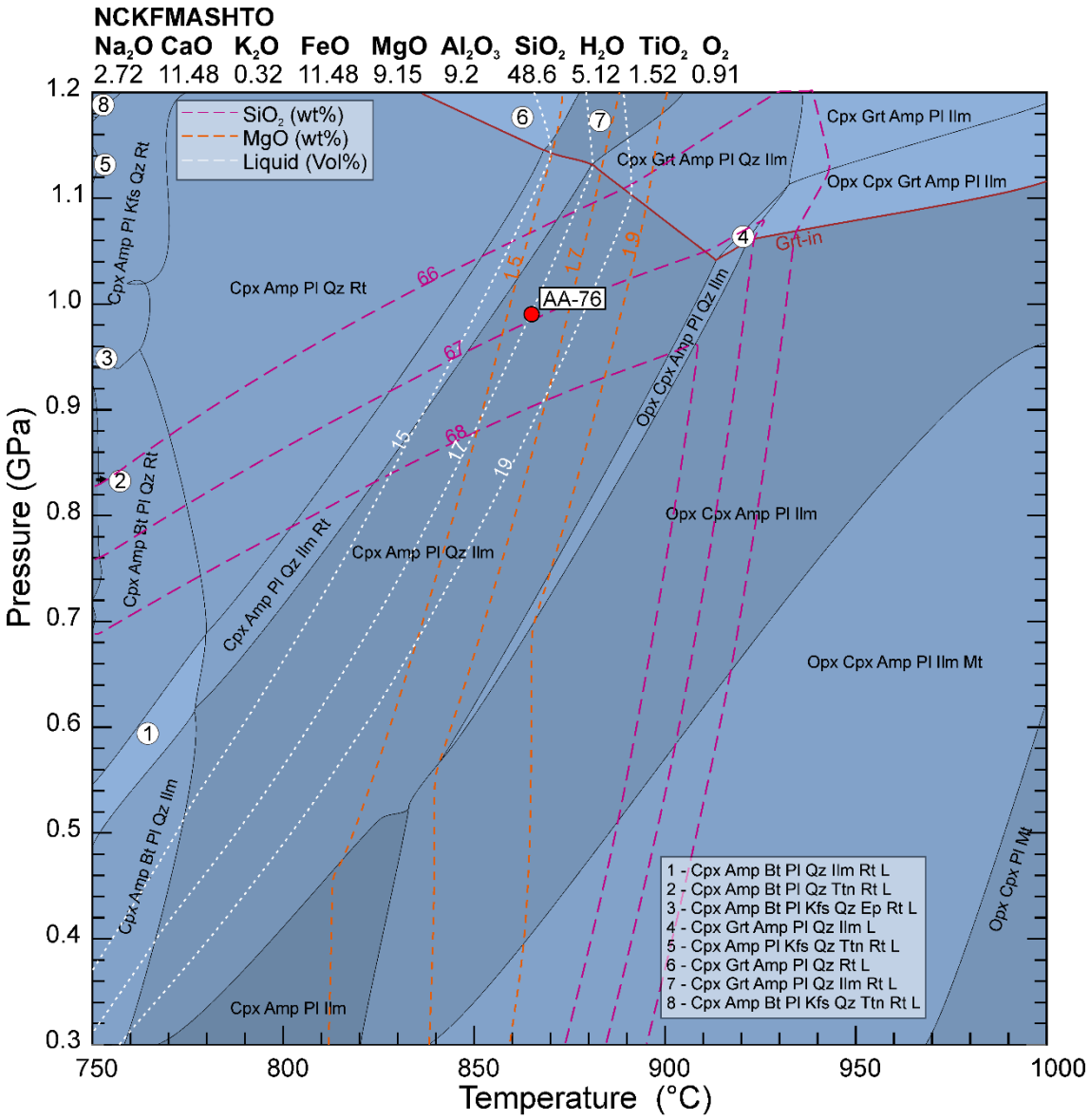


Fig. 12. Pseudosection of an average basalt composition (Condie 1993) obtained by thermodynamic modeling. The red circle represents the assumed P-T conditions at which melt composition was extracted and the trace elements were calculated.

To test the hypothesis of dehydration melting as the main process responsible for the origin of the Alto Rio Preto magma, the sample AA-76 (amphibole-biotite monzogranite) was selected to represent the composition of its primary magma. The calculated melt composition that most closely resembles the original magma was generated at 0.99 GPa and 865 ºC, resulting 16.9% of melt (melt fraction). The residual assemblage consists of amphibole (49.28%), plagioclase (27.42%), clinopyroxene (13.70%), ilmenite (0.96%), and quartz (8.64%)(Table 2, Fig. 13).

These conditions suggest that dehydration melting was governed by the following reaction:

$$Ca_2(Mg,Fe)_4Al(Si_7Al)O_{22}(OH)_2 + SiO_2 \rightarrow Ca(Mg,Fe)Si_2O_6 + CaAl_2Si_2O_8 + L \quad (1)$$

Hornblend + quartz → clinopyroxene + plagioclase + liquid

Table 2 - Modeling of major and trace elements for the generation of Rhyacian granites via dehydration melting of basaltic crust.

Source rock		Residual		Calculated	Modeled sample
Average metabasalt (C_0)[a]		Mineralogy	Vol (%)	magma (C_L)	AA-76
Major elements (wt.%)					
SiO_2	50.2	Amphibole	49.28	66.9	67
TiO_2	1.5	Plagioclase	27.42	0.89	0.66
Al_2O_3	15.5	Clinopyroxene	13.70	12.68	14.65
FeO	9.4	Ilmenite	0.96	3.15	4.71
MgO	6.6	Quartz	8.64	1.57	1.78
CaO	9.5			2.44	3.35
Na_2O	2.7			2.98	3.21
K_2O	0.84			4.37	3.38
Trace Elements (ppm)					
Ba	315	Melting conditions		1243	996
Rb	28	F = 16.9%		140	128
Sr	236	P = 0.99 GPa		341	321
Y	33	T = 865 ºC		35.3	30.8
Zr	130			276	250
Nb	4			12.87	11.95
La	12			53.9	82.7
Ce	30			131	166
Nd	15			51.1	65.1
Sm	3.7			10.0	11.7
Eu	1.2			1.5	1.3
Gd	4.03			8.44	9.26
Yb	2.6			2.37	2.48
Lu	0.45			0.34	0.31

[a]Condie (1993)

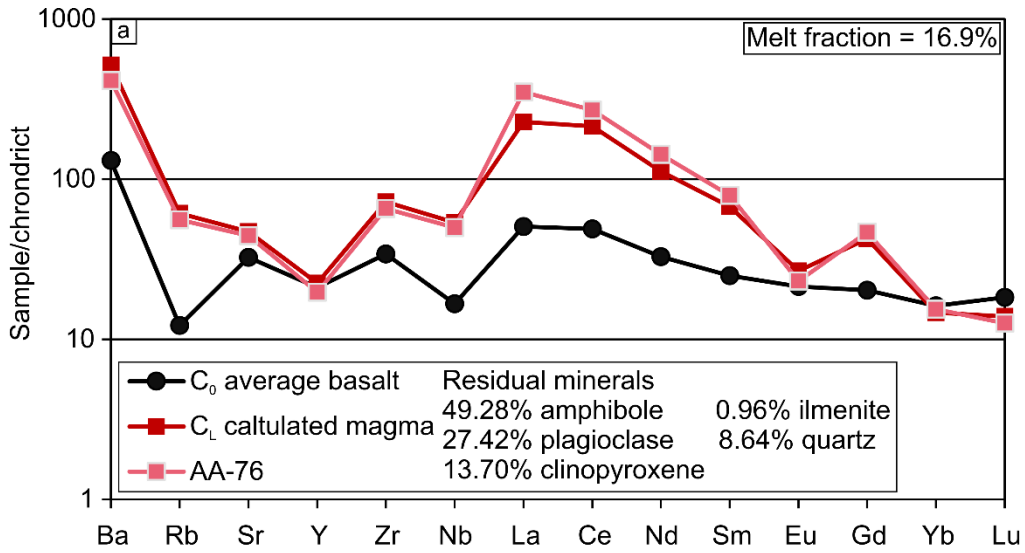


Fig. 13. Trace element modeling for the generation of the Alto Rio Preto granite magmas. (**a**) Amphibole-biotite monzogranite (AA-76).

4.5.2.4 Thermodynamic-geochemical modeling uncertanties

The integration of thermodynamic and geochemical modeling provides a powerful tool to investigate petrogenesis of igneous rocks. In this study, the compilation of these two methods aligned with petrographical, mineralogical and geochemical data were used to infer the partial melting conditions of the source rocks of the Alto Rio Preto magma. Similar approaches have been successfully employed to evaluate the melting conditions for the origin of diversified igneous rocks (Semprich et al. 2015; Ge et al. 2018, 2022, 2023), highlighting the reliability of this approach in refining petrogenesis of igneous rocks.

Despite their utility, this approach carries inherent uncertainties. Limitations in the thermodynamic database, given the simplifications in solution models (Holland *et al.* 2018b), although these limitations are mitigated using an internally consistent database like the one used in this work. The assumption of equilibrium and closed system adopted here may not reflect in full the natural processes. Moreover, mineral modes and modeled melt compositions rely on a complex interaction between bulk-rock composition, redox state, water activity and trace element partition coefficients, many of which are estimated rather than directly measured.

Dealing with these limitations requires careful examination of the petrographic, mineralogical and geochemical data, compiling this data with previous studies that use similar approaches (e.g., Semprich *et al.* 2015). The modeling results obtained in this study show an internal consistency that aligned with whole-rock geochemical data and thermobarometric constrains (Neri *et al.* submitted), supporting a reliable petrogenetic

model.

4.5.3 Magmatic evolution

Fractional crystallization appears to have played a crucial role in magmatic evolution of the two independent magmas that constitute the Alto Rio Preto granite. Amphibole-biotite monzogranites seem to have evolved to biotite monzogranites, while biotite granodiorites also seem to have evolved through similar processes to more evolved components within the facies. This is evidenced by the horizontal trends observed in the plots of highly and moderately incompatible elements, particularly in the La vs. La/Sm and Th vs. Th/Nd diagrams (Fig. 14a, b).

Negative correlations between SiO_2 and MgO, CaO, TiO_2, FeO, Al_2O_3, P_2O_5, Sr, and Zr (Figs. 5 and 6), the two latter specially in ABMzG to BMzG, indicate that the fractionating mineral assemblage consisted of biotite, amphibole, plagioclase, apatite, zircon, and Fe–Ti oxides.

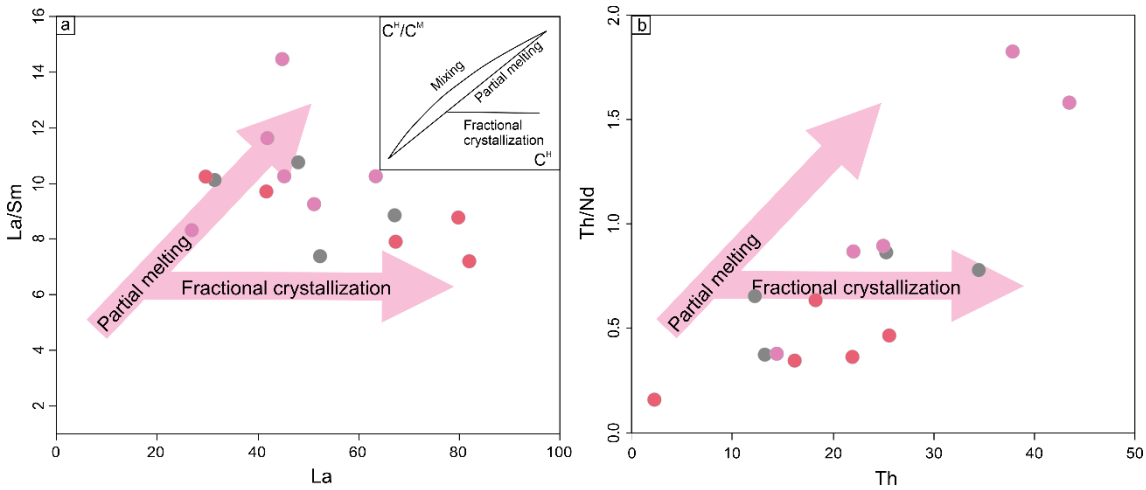


Fig. 14. (**a**) La vs. La/Sm, (**b**) Th vs. Th/Nd diagrams for the Alto Rio Preto granite with trends for partial melting and fractional crystallization defined by (Schiano *et al.* 2010).

4.5.4 Magma emplacement and deformation

The Bacajá Domain is characterized by an extensive transcurrent regime, with megastructures controlled by large-scale shear zones (Barros et al. 2007, 2023; Macambira and Ricci 2015). These zones are closely associated with extensive syn-tectonic orogenic magmatism and acted as conduits that facilitated magma ascent and emplacement (Barros et al., 2023).

The Alto Rio Preto granite is an elongated intrusion, with its length significantly exceeding its width, a typical feature of syn-tectonic granitoids (Neves 2012). The pluton is bounded to the north by the transcurrent Misteriosa Shear Zone, which extends beyond

the limits of the studied area (Oliveira *et al.* 1994), suggesting a strong tectonic control over its emplacement (Neves 2012).

The parallel alignment between magmatic and mylonitic foliations proves that deformation began during the magmatic stage (Castro 1987; Vernon *et al.* 1989; Paterson *et al.* 1998; Passarelli *et al.* 2010). Additionally, the occurrence at the microscopic scale of magmatic fractures in feldspars filled with remnant melt (Fig. 2b), confirm that deformation initiated while a liquid phase was still present in the system. Similar features have been documented in other Rhyacian granitoids of the Bacajá Domain (Barros et al. 2007, 2023; de Sousa 2008).

The identified microstructures provide insights into the temperatures at which deformation occurred (Trouw *et al.* 2009). In the low-grade mylonitic domain, quartz predominantly exhibits undulose extinction, indicative of deformation through the recovery process, with local occurrences of bulging recrystallization. These microtextures suggest deformation temperatures ranging from 250 to 500 °C (Trouw *et al.* 2009). In the medium-grade mylonitic domain, quartz deformation is primarily characterized by bulging and subgrain rotation recrystallization, while feldspars exhibit deformation twinning, undulose extinction, and core-mantle structures formed by bulging recrystallization, features typical of mylonites formed at temperatures between 500 and 650 °C and possibly higher (Trouw *et al.* 2009). Feldspar crystals are also deformed, displaying magmatic microfractures that indicate temperatures above the solidus for the initial stages of deformation.

4.5.5 Implications for magmatism in collisional settings

Crustal reworking and continental growth are key processes for understanding the geochemical and isotopic characteristics of the continental crust (Brown and Rushmer 2008; Zheng *et al.* 2015). Collisional zones provide unique environments to study these processes, as both can occur at different stages of collision. In these settings, granitoids can form through two primary mechanisms (Moyen 2020 and references therein): (i) partial melting of continental crust, resulting in the reworking of pre-existing material, in which case the generated granitoid does not contribute to net continental crustal growth (e.g., Chappell and White 2001; Eglinger et al. 2017; Marangoanha et al. 2019). (ii) Partial melting of oceanic crust or fractional crystallization of mafic magmas, leading to the addition of juvenile material and net crustal growth (Jagoutz and Kelemen 2015; Jagoutz and Klein 2018). Therefore, whether collisional granitoids contribute to crustal growth depends on their petrogenetic origin.

The Bacajá Domain formed through the collision during the Paleoproterozoic between the basement and pre-collisional island arcs of Bacajá with the Carajás province (Barros et al., 2023; Macambira et al., 2022, 2009; Magalhães et al., 2023). Hence, the collisional zone between these domains offers an excellent opportunity to investigate the mechanisms of crustal reworking and maturation.

Magmatic rocks in the Bacajá Domain record a range of geodynamic environments. In the north, they reflect two-sided subduction with significant input from mantle-derived melts (Barros et al. 2023; Magalhães et al. 2023). In contrast, magmatism in the southern part of the domain, particularly in the study area, records a collisional to post-collisional setting associated with lithospheric delamination (Neri *et al.* submitted).

The Alto Rio Preto granite magmas were derived from Archean, basaltic lower crustal sources that underwent partial melting, with limited or no significant interaction with mantle-derived melts. Geochemical data indicate that the magmas evolved through fractional crystallization, likely during ascent and emplacement. These characteristics suggest that the Alto Rio Preto granite formed through reworking of pre-existing continental crust, without contributing to significant net crustal growth in the collisional zone between the Bacajá and Carajás domains. The geochemical data is further supported by zircon grains and strongly negative $\varepsilon Nd_{(t)}$ and $\varepsilon Hf_{(t)}$ values (Neri et al., submitted) also corroborates a dominant crustal origin. Thus, the Alto Rio Preto granite represents a classical example of granite related to crustal reworking in a collisional zone under a post-collisional delamination regime.

4.6 CONCLUSIONS

Considering the data present in this work, the main conclusions are:

1. The deformation initiated when there was still liquid in the system and progressed to a solid-state deformation. characterizing the granite as a syn-tectonic intrusion.
2. Zircon and titanite ages suggest that the granite crystallized between 2098 ± 11 and 2067.1±9.3 Ma.
3. The Alto Rio Preto granitoids are magnesian, vary from metaluminous to slightly peraluminous, and have affinities with calc-alkaline to high-K calc-alkaline series.
4. The parental magma was generated through dehydration melting of a basaltic crust at 0.99 GPa and 865 ºC (monzogranitic facies), leaving an amphibolite residue (amphibole, plagioclase, ilmenite, and quartz).

5. The Alto Rio Preto granite is an example of typical high-K calc-alkaline granite formed by reworking of pre-existing crustal material in a collisional to post-collisional setting.

ACKNOWLEDGMENTS

This paper is part of the first author's PhD thesis developed at the Instituto de Geociências, UFPA. The authors acknowledge UNIFESSPA students and staff for their previous work in the studied area and for shared information. We are also grateful to K. Sato for assistance during the acquisition of zircon U–Pb SHRIMP data at the Laboratório de Geologia de Alta Resolução (Universidade de São Paulo-USP) and C. Passareli for her assistance in titanite U-Pb LA-ICP-MS at the Centro de Pesquisas em Geocronologia e Geoquímica Isotópica (USP).

FUNDING INFORMATION

This research received financial support from CNPq (R. D.– 304648-2019-1; G.R.L. F. - 408396/2023-7) and FAPESPA (G.R.L.F. E-2024/2285715). This study was also financed in part by the Coordenação de Aperfeiçoamento de Pessoal de Nível Superior - Brasil (CAPES) - Finance Code 001 (A.S.S. N. - No. 88887.643812/2021-00).

REFERENCES

Aleinikoff, J.N., Wintsch, R.P., Tollo, R.P., Unruh, D.M., Fanning, C.M. and Schmitz, M.D. 2007. Ages and origins of rocks of the Killingworth dome, south-central Connecticut: Implications for the tectonic evolution of southern New England. *American Journal of Science*, **307**, 63–118, https://doi.org/10.2475/01.2007.04.

Almeida, J. de A.C., Dall'Agnol, R., et al. 2011. Zircon geochronology, geochemistry and origin of the TTG suites of the Rio Maria granite-greenstone terrane: Implications for the growth of the Archean crust of the Carajás province, Brazil. *Precambrian Research*, **187**, 201–221, https://doi.org/10.1016/j.precamres.2011.03.004.

Barros, C.E. de M., Macambira, M.J.B., Santos, M.C. da C., Silva, D.C.C., Palmeira, L.C.M. and Sousa, M.M. 2007. Estruturas sinmagmáticas e idade de zircão de granitos (evaporação de Pb) paleoproterozóicos da parte leste do domínio Bacajá, Província Maroni-Itacaiúnas. *Revista Brasileira de Geociências*, **37**, 293–304, https://doi.org/10.25249/0375-7536.2007373293304.

Barros, C.E. de M., Besser, M.L. and Gouvêa Vasconcellos, E.M. 2023. Voluminous

Paleoproterozoic plutonic belt of the Bacajá Domain in Amazon Craton: Petrology, geotectonic setting and Pb–Pb zircon evaporation ages. *Journal of South American Earth Sciences*, **130**, 104491, https://doi.org/10.1016/j.jsames.2023.104491.

Besser, M.L. and Barros, C.E.M. 2015. *Geologia e Recursos Minerais Da Folha Rio Bacajá - SA.22-Y-D-VI, Estado Do Pará*.

Black, L.P., Kamo, S.L., et al. 2004. Improved 206Pb/238U microprobe geochronology by the monitoring of a trace-element-related matrix effect; SHRIMP, ID–TIMS, ELA–ICP–MS and oxygen isotope documentation for a series of zircon standards. *Chemical Geology*, **205**, 115–140, https://doi.org/10.1016/j.chemgeo.2004.01.003.

Boynton, W. V. 1984. Cosmochemistry of the Rare Earth Elements: Meteorite Studies. 63–114, https://doi.org/10.1016/B978-0-444-42148-7.50008-3.

Broska, I., Harlov, D., Tropper, P. and Siman, P. 2007. Formation of magmatic titanite and titanite–ilmenite phase relations during granite alteration in the Tribeč Mountains, Western Carpathians, Slovakia. *Lithos*, **95**, 58–71, https://doi.org/10.1016/j.lithos.2006.07.012.

Brown, M. 2013. Granite: From genesis to emplacement. *Geological Society of America Bulletin*, **125**, 1079–1113, https://doi.org/10.1130/B30877.1.

Brown, M. and Johnson, T. 2018. Secular change in metamorphism and the onset of global plate tectonics. *American Mineralogist*, **103**, 181–196, https://doi.org/10.2138/am-2018-6166.

Brown, M. and Rushmer, T. 2008. *Evolution and Differentiation of the Continental Crust*, 1st ed.

Bucholz, C.E., Jagoutz, O., Schmidt, M.W. and Sambuu, O. 2014. Phlogopite- and clinopyroxene-dominated fractional crystallization of an alkaline primitive melt: petrology and mineral chemistry of the Dariv Igneous Complex, Western Mongolia. *Contributions to Mineralogy and Petrology*, **167**, 994, https://doi.org/10.1007/s00410-014-0994-6.

Castro, A. 1987. On granitoid emplacement and related structures. A review. *Geologische Rundschau*, **76**, 101–124, https://doi.org/10.1007/BF01820576.

Chappell, B.W. and Stephens, W.E. 1988. Origin of infracrustal (I-type) granite magmas. *Earth and Environmental Science Transactions of the Royal Society of Edinburgh*, **79**, 71–86, https://doi.org/10.1017/S0263593300014139.

Chappell, B.W. and White, A.J.R. 2001. Two contrasting granite types: 25 years later. *Australian Journal of Earth Sciences*, **48**, 489–499, https://doi.org/10.1046/j.1440-

0952.2001.00882.x.

Clemens, J.D. and Stevens, G. 2016. Melt segregation and magma interactions during crustal melting: Breaking out of the matrix. *Earth-Science Reviews*, **160**, 333–349, https://doi.org/10.1016/j.earscirev.2016.07.012.

Collins, W.J., Huang, H.-Q. and Jiang, X. 2016. Water-fluxed crustal melting produces Cordilleran batholiths. *Geology*, **44**, 143–146, https://doi.org/10.1130/G37398.1.

Collins, W.J., Murphy, J.B., Johnson, T.E. and Huang, H.-Q. 2020. Critical role of water in the formation of continental crust. *Nature Geoscience*, **13**, 331–338, https://doi.org/10.1038/s41561-020-0573-6.

Condie, K.C. 1993. Chemical composition and evolution of the upper continental crust: Contrasting results from surface samples and shales. *Chemical Geology*, **104**, 1–37, https://doi.org/10.1016/0009-2541(93)90140-E.

Cordani, U.G., Sato, K., Teixeira, W., Tassinari, C.G. and Basei, M.A.S. 2000. Crustal evolution of the South American Platform. *Tectonic Evolution of South America*, 19–40.

Costa, F.G., Klein, E.L., et al. 2018. Geochemistry and U–Pb–Hf zircon data for plutonic rocks of the Troia Massif, Borborema Province, NE Brazil: Evidence for reworking of Archean and juvenile Paleoproterozoic crust during Rhyacian accretionary and collisional tectonics. *Precambrian Research*, **311**, 167–194, https://doi.org/10.1016/j.precamres.2018.04.008.

Dall'Agnol, R., Scaillet, B. and Pichavant, M. 1999. An Experimental Study of a Lower Proterozoic A-type Granite from theEastern Amazonian Craton, Brazil. *Journal of Petrology*, **40**, 1673–1698, https://doi.org/10.1093/petrology/40.11.1673.

de Sousa, C.S. 2008. *Petrologia, Geologia Estrutural e Aerogeofísica Da Porção Leste Do Domínio Bacajá, Província Maroni-Itacaiúnas*. Universidade Federal do Pará.

Debon, F. and Le Fort, P. 1983. A chemical–mineralogical classification of common plutonic rocks and associations. *Transactions of the Royal Society of Edinburgh: Earth Sciences*, **73**, 135–149, https://doi.org/10.1017/S0263593300010117.

DePaolo, D.J. 1981. Trace element and isotopic effects of combined wallrock assimilation and fractional crystallization. *Earth and Planetary Science Letters*, **53**, 189–202, https://doi.org/10.1016/0012-821X(81)90153-9.

Dhuime, B., Wuestefeld, A. and Hawkesworth, C.J. 2015. Emergence of modern continental crust about 3 billion years ago. *Nature Geoscience*, **8**, 552–555, https://doi.org/10.1038/ngeo2466.

Eglinger, A., Thébaud, N., et al. 2017. New insights into the crustal growth of the Paleoproterozoic margin of the Archean Kéména-Man domain, West African craton (Guinea): Implications for gold mineral system. *Precambrian Research*, **292**, 258–289, https://doi.org/10.1016/j.precamres.2016.11.012.

Frost, B.R., Barnes, C.G., COLLINS, W.J., ARCULUS, R.J., ELLIS, D.J. and FROST, C.D. 2001. A Geochemical Classification for Granitic Rocks. *Journal of Petrology*, **42**, 2033–2048, https://doi.org/10.1093/petrology/42.11.2033.

Gamal El Dien, H., Li, Z.-X., et al. 2021. Two-stage crustal growth in the Arabian-Nubian shield: Initial arc accretion followed by plume-induced crustal reworking. *Precambrian Research*, **359**, 106211, https://doi.org/10.1016/j.precamres.2021.106211.

Gamaleldien, H., Li, Z.-X., Abu Anbar, M., Murphy, J.B. and Doucet, L.S. 2022. Geochronological and isotopic constraints on Neoproterozoic crustal growth in the Egyptian Nubian Shield: Review and synthesis. *Earth-Science Reviews*, **235**, 104244, https://doi.org/10.1016/j.earscirev.2022.104244.

Ge, R., Zhu, W., Wilde, S.A. and Wu, H. 2018. Remnants of Eoarchean continental crust derived from a subducted proto-arc. *Science Advances*, **4**, https://doi.org/10.1126/sciadv.aao3159.

Ge, R., Wilde, S.A., Zhu, W., Zhou, T. and Si, Y. 2022. Formation and evolution of Archean continental crust: A thermodynamic – geochemical perspective of granitoids from the Tarim Craton, NW China. *Earth-Science Reviews*, **234**, 104219, https://doi.org/10.1016/j.earscirev.2022.104219.

Ge, R.-F., Wilde, S.A., Zhu, W.-B. and Wang, X.-L. 2023. Earth's early continental crust formed from wet and oxidizing arc magmas. *Nature*, **623**, 334–339, https://doi.org/10.1038/s41586-023-06552-0.

Ghoneim, M.F., Abdel-Karim, A.-A.M., Anbar, M.M.A., Nageib, A. and El-Shafei, S.A. 2022. Petrogenesis of Postcollisional High-K Calc-Alkaline and Alkaline Magmatism in Southern Sinai, Egypt: The Role of Crustal Anatexis Combined with Convective Diffusion. *The Journal of Geology*, **130**, 111–132, https://doi.org/10.1086/718832.

Grenholm, M., Jessell, M. and Thébaud, N. 2019. A geodynamic model for the Paleoproterozoic (ca. 2.27–1.96 Ga) Birimian Orogen of the southern West African Craton – Insights into an evolving accretionary-collisional orogenic system. *Earth-Science Reviews*, **192**, 138–193, https://doi.org/10.1016/j.earscirev.2019.02.006.

Hao, L.-L., Wang, Q., Wyman, D.A., Yang, J.-H., Huang, F. and Ma, L. 2019. Crust-mantle mixing and crustal reworking of southern Tibet during Indian continental subduction: Evidence from Miocene high-silica potassic rocks in Central Lhasa block. *Lithos*, **342–343**, 407–419, https://doi.org/10.1016/j.lithos.2019.05.035.

Hawkesworth, C., Cawood, P.A. and Dhuime, B. 2019. Rates of generation and growth of the continental crust. *Geoscience Frontiers*, **10**, 165–173, https://doi.org/10.1016/j.gsf.2018.02.004.

Hawkesworth, C.J. and Kemp, A.I.S. 2006. Evolution of the continental crust. *Nature*, **443**, 811–817, https://doi.org/10.1038/nature05191.

Hawkesworth, C.J., Dhuime, B., Pietranik, A.B., Cawood, P.A., Kemp, A.I.S. and Storey, C.D. 2010. The generation and evolution of the continental crust. *Journal of the Geological Society*, **167**, 229–248, https://doi.org/10.1144/0016-76492009-072.

He, Y., Li, S., Hoefs, J., Huang, F., Liu, S.-A. and Hou, Z. 2011. Post-collisional granitoids from the Dabie orogen: New evidence for partial melting of a thickened continental crust. *Geochimica et Cosmochimica Acta*, **75**, 3815–3838, https://doi.org/10.1016/j.gca.2011.04.011.

Heaman, L.M., 2009. The application of U–Pb geochronology to mafic, ultramafic and alkaline rocks: An evaluation of three mineral standards. *Chemical Geology* **261**, 43–52. https://doi.org/10.1016/j.chemgeo.2008.10.021

Holder, R.M., Hacker, B.R., Seward, G.G.E. and Kylander-Clark, A.R.C. 2019. Interpreting titanite U–Pb dates and Zr thermobarometry in high-grade rocks: empirical constraints on elemental diffusivities of Pb, Al, Fe, Zr, Nb, and Ce. *Contributions to Mineralogy and Petrology*, **174**, 42, https://doi.org/10.1007/s00410-019-1578-2.

Holland, T.J.B., Green, E.C.R. and Powell, R. 2018. Melting of Peridotites through to Granites: A Simple Thermodynamic Model in the System KNCFMASHTOCr. *Journal of Petrology*, **59**, 881–900, https://doi.org/10.1093/petrology/egy048.

Hurley, P.M., Almeida, F.F.M., et al. 1967. Test of continental drift by means of radiometric ages. *Science*, 495–500.

Jagoutz, O. and Kelemen, P.B. 2015. Role of Arc Processes in the Formation of Continental Crust. *Annual Review of Earth and Planetary Sciences*, **43**, 363–404, https://doi.org/10.1146/annurev-earth-040809-152345.

Jagoutz, O. and Klein, B. 2018. On the importance of crystallization-differentiation for the generation of SiO_2-rich melts and the compositional build-up of arc (and

continental) crust. *American Journal of Science*, **318**, 29–63, https://doi.org/10.2475/01.2018.03.

Klaver, M., de Roever, E.W.F., Nanne, J.A.M., Mason, P.R.D. and Davies, G.R. 2015. Charnockites and UHT metamorphism in the Bakhuis Granulite Belt, western Suriname: Evidence for two separate UHT events. *Precambrian Research*, **262**, 1–19, https://doi.org/10.1016/j.precamres.2015.02.014.

Klein, E.L., Rodrigues, J.B., Lopes, E.C.S. and Soledade, G.L. 2012. Diversity of Rhyacian granitoids in the basement of the Neoproterozoic-Early Cambrian Gurupi Belt, northern Brazil: Geochemistry, U–Pb zircon geochronology, and Nd isotope constraints on the Paleoproterozoic magmatic and crustal evolution. *Precambrian Research*, **220–221**, 192–216, https://doi.org/10.1016/j.precamres.2012.08.007.

Laurent, O., Martin, H., Moyen, J.F. and Doucelance, R. 2014. The diversity and evolution of late-Archean granitoids: Evidence for the onset of "modern-style" plate tectonics between 3.0 and 2.5Ga. *Lithos*, **205**, 208–235, https://doi.org/10.1016/j.lithos.2014.06.012.

Le Maitre, R.W. 2002. *Igneous Rocks: A Classification and Glossary of Terms*. Le Maitre, R. W., Streckeisen, A., Zanettin, B., Le Bas, M. J., Bonin, B. and Bateman, P. (eds), https://doi.org/10.1017/CBO9780511535581.

Ludwig, K. 2009. Squid 2: a user's manual. *Berkeley Geochronology Center Special Publication No. 5*.

Ludwig, K.R. 2003. isoplot Excell version 3.0. A geochronological toolkit for Microsoft Excel,.

Ma, L., Wang, Q., et al. 2017. Paleocene (c. 62 Ma) Leucogranites in Southern Lhasa, Tibet: Products of Syn-collisional Crustal Anatexis during Slab Roll-back? *Journal of Petrology*, **58**, 2089–2114, https://doi.org/10.1093/petrology/egy001.

Macambira, E.M.B. and Ricci, P.S.F. 2015. *Geologia e Recursos Minerais Da Folha Tucuruí – SA.22-Z-C, Estado Do Pará*, 1st ed.

Macambira, M.J.B., Silva, D.C.C., Barros, C.E.M. and Scheller, T. 2003. New isotope evidences confirming the existence of a paleoproterozoic terrain in the region at the north of the Carajas Mineral Province. *In*: *IV South American Symposium on Isotope Geology*. 205–206.

Macambira, M.J.B., Silva, D.C.C., Vasquez, M.L. and Barros, C.E.M. 2004. Investigação do limite Arqueano-Paleoproterozoico ao norte da Província Carajás, Amazônia Oriental. *In*: *42º Congresso Brasileiro de Geologia*.

Macambira, M.J.B., Pinheiro, V.L. and Armstrong, R.A. 2007. A fronteira Arqueano-Paleoproterozoico no SE do Cráton Amazônico: abrupta no tempo, suave na tectônica? *In*: *X Simpósio de Geologia Da Amazônia*. 97–100.

Macambira, M.J.B., Vasquez, M.L., Silva, D.C.C. da, Galarza, M.A., Barros, C.E. de M. and Camelo, J. de F. 2009. Crustal growth of the central-eastern Paleoproterozoic domain, SW Amazonian craton: Juvenile accretion vs. reworking. *Journal of South American Earth Sciences*, **27**, 235–246, https://doi.org/10.1016/j.jsames.2009.02.001.

Macambira, M.J.B., Vasquez, M.L., Monteiro, P.C. and Armstrong, R.A. 2022. Neoarchean to Rhyacian crustal records along the Middle Xingu River area, Amazonian craton. *Brazilian Journal of Geology*, **52**, https://doi.org/10.1590/2317-4889202220220017.

Macambira, M.J.B. and Amireault, S. 2025. Isotopic study (U Pb, Sm Nd, and Pb Pb) of rocks and auriferous mineralizations from the Volta Grande do Xingu deposits, Bacajá Domain, Amazonian craton. *Journal of Geochemical Exploration*, **274**, 107767, https://doi.org/10.1016/j.gexplo.2025.107767.

Magalhães, L.B., Macambira, M.J.B., Macambira, E.M.B. and Ricci, P. dos S.F. 2023a. Crustal growth in the northeast portion of the Rhyacian Bacajá Domain, SE Amazonian craton, based on U-Pb, Lu-Hf, and Sm-Nd data. *Brazilian Journal of Geology*, **53**, https://doi.org/10.1590/2317-4889202320220068.

Marangoanha, B., de Oliveira, D.C. and Dall'Agnol, R. 2019. The Archean granulite-enderbite complex of the northern Carajás province, Amazonian craton (Brazil): Origin and implications for crustal growth and cratonization. *Lithos*, **350–351**, 105275, https://doi.org/10.1016/j.lithos.2019.105275.

Marangoanha, B., de Oliveira, D.C., Galarza, M.A. and Marques, G.T. 2020. Crustal anatexis and mantle-derived magmas forming Neoarchean A-type granitoids in Carajás Province, northern Brazil: Petrological evidence and tectonic control. *Precambrian Research*, **338**, https://doi.org/10.1016/j.precamres.2019.105585.

McDonough, W.F. and Sun, S. -s. 1995. The composition of the Earth. *Chemical Geology*, **120**, 223–253, https://doi.org/10.1016/0009-2541(94)00140-4.

Meert, J.G. and Santosh, M. 2017. The Columbia supercontinent revisited. *Gondwana Research*, **50**, 67–83, https://doi.org/10.1016/j.gr.2017.04.011.

Moyen, J.-F. 2009. High Sr/Y and La/Yb ratios: The meaning of the "adakitic signature". *Lithos*, **112**, 556–574, https://doi.org/10.1016/j.lithos.2009.04.001.

Moyen, J.-F. 2020. Granites and crustal heat budget. *Geological Society, London, Special Publications*, **491**, 77–100, https://doi.org/10.1144/SP491-2018-148.

Nandedkar, R.H., Ulmer, P. and Müntener, O. 2014. Fractional crystallization of primitive, hydrous arc magmas: an experimental study at 0.7 GPa. *Contributions to Mineralogy and Petrology*, **167**, 1015, https://doi.org/10.1007/s00410-014-1015-5.

Neves, S.P. 2012. *Granitos Orogênicos - Da Geração Dos Magmas à Intrusão e Deformação*, 1st ed. Gama, J. (ed.).

Neri, A.S.S., Dall'Agnol, R., Dantas, E.L., Feio, G.R.L., Almeida, J.A.C., Galarza, M.A., Rhyacian magmatism in the southern Bacajá Domain: Implications for the crustal evolution of SE Amazonian Craton, Brazil. *Precambrian Research*, manuscript submitted for publication.

Oliveira, J.R., Neto, C.S.S. and Costa, E.J. de S. 1994. *Programas Levantamentos Geoóligocs Do Brasil: Serra Pelada (Folha SB.22-X-C) Estado Do Pará*, 1st ed.

Palin, R.M., White, R.W., Green, E.C.R., Diener, J.F.A., Powell, R. and Holland, T.J.B. 2016. High-grade metamorphism and partial melting of basic and intermediate rocks. *Journal of Metamorphic Geology*, **34**, 871–892, https://doi.org/10.1111/jmg.12212.

Papapavlou, K., Darling, J.R., Storey, C.D., Lightfoot, P.C., Moser, D.E. and Lasalle, S. 2017. Dating shear zones with plastically deformed titanite: New insights into the orogenic evolution of the Sudbury impact structure (Ontario, Canada). *Precambrian Research*, **291**, 220–235, https://doi.org/10.1016/j.precamres.2017.01.007.

Passarelli, C.R., Basei, M.A.S., Siga, O., Reath, I.M. and Campos Neto, M. da C. 2010. Deformation and geochronology of syntectonic granitoids emplaced in the Major Gercino Shear Zone, southeastern South America. *Gondwana Research*, **17**, 688–703, https://doi.org/10.1016/j.gr.2009.09.013.

Passchier, C.W. and Trouw, R.A.J. 2005. *Microtectonics*, https://doi.org/10.1007/3-540-29359-0.

Paterson, S.R., Fowler, T.K., Schmidt, K.L., Yoshinobu, A.S., Yuan, E.S. and Miller, R.B. 1998. Interpreting magmatic fabric patterns in plutons. *Lithos*, **44**, 53–82, https://doi.org/10.1016/S0024-4937(98)00022-X.

Patiño Douce, A.E. 1999. What do experiments tell us about the relative contributions of crust and mantle to the origin of granitic magmas? *Geological Society, London, Special Publications*, **168**, 55–75, https://doi.org/10.1144/GSL.SP.1999.168.01.05.

Pearce, J.A., Harris, N.B.W. and Tindle, A.G. 1984. Trace Element Discrimination Diagrams for the Tectonic Interpretation of Granitic Rocks. *Journal of Petrology*, **25**, 956–983, https://doi.org/10.1093/petrology/25.4.956.

Peccerillo, A. and Taylor, S.R. 1976. Geochemistry of eocene calc-alkaline volcanic rocks from the Kastamonu area, Northern Turkey. *Contributions to Mineralogy and Petrology*, **58**, 63–81, https://doi.org/10.1007/BF00384745.

Petford, N. 1995. W. S. Pitcher, 1993. The Nature and Origin of Granite. xiii + 321 pp. London, Glasgow, New York, Tokyo, Melbourne, Madras: Blackie Academic & Professional. Price £39.95 (hard covers). ISBN 0 7514 0800 7. *Geological Magazine*, **132**, 245–245, https://doi.org/10.1017/S001675680001195X.

Polat, A. and Hofmann, A.W. 2003. Alteration and geochemical patterns in the 3.7–3.8 Ga Isua greenstone belt, West Greenland. *Precambrian Research*, **126**, 197–218, https://doi.org/10.1016/S0301-9268(03)00095-0.

Polat, A., Hofmann, A.W. and Rosing, M.T. 2002. Boninite-like volcanic rocks in the 3.7–3.8 Ga Isua greenstone belt, West Greenland: geochemical evidence for intra-oceanic subduction zone processes in the early Earth. *Chemical Geology*, **184**, 231–254, https://doi.org/10.1016/S0009-2541(01)00363-1.

Rapp, R.P. and Watson, E.B. 1995. Dehydration Melting of Metabasalt at 8-32 kbar: Implications for Continental Growth and Crust-Mantle Recycling. *Journal of Petrology*, **36**, 891–931, https://doi.org/10.1093/petrology/36.4.891.

Roberts, M.P. and Clemens, J.D. 1993. Origin of high-potassium, talc-alkaline, I-type granitoids. *Geology*, **21**, 825, https://doi.org/10.1130/0091-7613(1993)021<0825:OOHPTA>2.3.CO;2.

Robertson, J.K. and Wyllie, P.J. 1971. Experimental Studies on Rocks from the Deboullie Stock, Northern Maine, including Melting Relations in the Water-Deficient Environment. *The Journal of Geology*, **79**, 549–571, https://doi.org/10.1086/627675.

Santos, J.O.S., Hartmann, L.A., Faria, M.S., Riker, S.R., Miguel, M., Almeida, M.E. and Mcnaughton, N.J. 2006. a Compartimentação Do Cráton Amazonas Em Províncias : Avanços Ocorridos No Período 2000-2006. *In*: *IX Simpósio de Geologia Da Amazônica*.

Sato, K., Tassinari, C.C.G., Basei, M.A.S., Siga Júnior, O., Onoe, A.T. and Souza, M.D. de. 2014. Sensitive High Resolution Ion Microprobe (SHRIMP IIe/MC) of the Institute of Geosciences of the University of São Paulo, Brazil: analytical method

and first results. *Geologia USP. Série Científica*, **14**, 3–18, https://doi.org/10.5327/Z1519-874X201400030001.

Sawyer, E.W. 1999. Criteria for the recognition of partial melting. *Physics and Chemistry of the Earth, Part A: Solid Earth and Geodesy*, **24**, 269–279, https://doi.org/10.1016/S1464-1895(99)00029-0.

Schiano, P., Monzier, M., Eissen, J.-P., Martin, H. and Koga, K.T. 2010. Simple mixing as the major control of the evolution of volcanic suites in the Ecuadorian Andes. *Contributions to Mineralogy and Petrology*, **160**, 297–312, https://doi.org/10.1007/s00410-009-0478-2.

Semprich, J., Moreno, J.A. and Oliveira, E.P. 2015. Phase equilibria and trace element modeling of Archean sanukitoid melts. *Precambrian Research*, **269**, 122–138, https://doi.org/10.1016/j.precamres.2015.08.004.

Shand, S.J. 1943. *Eruptive Rocks: Their Genesis, Composition, and Classification, with a Chapter on Meteorites*, 2nd ed.

Shi, Q., Shu, R.-X., et al. 2025. Paleoproterozoic granite in the Khondalite Belt, northern margin of the North China Craton: Response to the assembly of the Columbia supercontinent. *Precambrian Research*, **417**, 107640, https://doi.org/10.1016/j.precamres.2024.107640.

Silva, A.S. 2021. *Metamorfismo de UHT e HP No Domínio Bacajá, Cráton Do Amazonas*. Master's dissertation, Universidade de Brasília.

Słaby, E., Anczkiewicz, R., et al. 2021. High-temperature fluids in granites during the Neoarchaean-Palaeoproterozoic transition: Insight from Closepet titanite chemistry and U-Pb dating (Dharwar craton, India). *Lithos*, **386–387**, 106039, https://doi.org/10.1016/j.lithos.2021.106039.

Smithies, R.H., Lu, Y., et al. 2019. No evidence for high-pressure melting of Earth's crust in the Archean. *Nature Communications*, **10**, 5559, https://doi.org/10.1038/s41467-019-13547-x.

Spencer, K.J., Hacker, B.R., et al. 2013. Campaign-style titanite U–Pb dating by laser-ablation ICP: Implications for crustal flow, phase transformations and titanite closure. *Chemical Geology*, **341**, 84–101, https://doi.org/10.1016/j.chemgeo.2012.11.012.

Stacey, J.S. and Kramers, J.D. 1975. Approximation of terrestrial lead isotope evolution by a two-stage model. *Earth and Planetary Science Letters*, **26**, 207–221, https://doi.org/10.1016/0012-821X(75)90088-6.

Sun, C., Xu, W., Cawood, P.A., Tang, J., Zhao, S., Li, Y. and Zhang, X. 2019. Crustal growth and reworking: A case study from the Erguna Massif, eastern Central Asian Orogenic Belt. *Scientific Reports*, **9**, 17671, https://doi.org/10.1038/s41598-019-54230-x.

Tassinari, C.C.G. and Macambira, M.J.B. 2004. A evolução tectônica do Craton Amazônico. *In*: Mantesso-Neto, V., Bartorelli, A., Carneiro, C. D. R. and Brito Neves, B. B. (eds) *Geologia Do Continente Sul Americano: Evoluc¸ Ão Da Obra de Fernando Flávio Marques Almeida*. 471–486.

Teixeira, M.F.B., Dall'Agnol, R., Santos, J.O.S., Kemp, A. and Evans, N. 2019. Petrogenesis of the Paleoproterozoic (Orosirian) A-type granites of Carajás Province, Amazon Craton, Brazil: Combined in situ Hf O isotopes of zircon. *Lithos*, **332–333**, 1–22, https://doi.org/10.1016/j.lithos.2019.01.024.

Trouw, R.A.J., Passchier, C.W. and Wiersma, D.J. 2009. *Atlas of Mylonites- and Related Microstructures*, https://doi.org/10.1007/978-3-642-03608-8.

Vasquez, M.L. 2006. *Geocronologia Em Zircão, Monazita e Granada e Isótopos de Nd Das Associações Litológicas Da Porção Oeste Do Domínio Bacajá: Evolução Crustal Da Porção Meridional Da Província Maroni-Itacaiúnas – Sudeste Do Cráton Amazônico*. Universidade Federal do Pará.

Vasquez, M.L. and Rosa-Costa, L.T. 2008. *Geologia e Recursos Minerais Do Estado Do Pará : Sistema de Informações Geográficas – SIG : Texto Explicativo Dos Mapas Geológico e Tectônico e de Recursos Minerais Do Estado Do Pará*, 1st ed.

Vasquez, M.L., Macambira, M.J.B. and Galarza, M.A. 2005. Granitoides Transamazônicos da região Iriri-Xingu, Pará – novos dados geológicos e geocronológicos. *In*: *Contribuições a Geologia Da Amazônia*. 16.

Vasquez, M.L., Macambira, M.J.B. and Armstrong, R.A. 2008. Zircon geochronology of granitoids from the western Bacajá Domain, southeastern Amazonian craton, Brazil: Neoarchean to Orosirian evolution. *Precambrian Research*, **161**, 279–302, https://doi.org/10.1016/j.precamres.2007.09.001.

Vernon, R.H., Paterson, S.R. and Geary, E.E. 1989. Evidence for syntectonic intrusion of plutons in the Bear Mountains fault zone, California. *Geology*, **17**, 723, https://doi.org/10.1130/0091-7613(1989)017<0723:EFSIOP>2.3.CO;2.

Vieira, C., Amaral, W. and Holanda, F.S. 2022. Petrography, geochemistry and zircon U-Pb geochronology of the Siderian-Rhyacian granitoids of NW Bacajá Domain, Amazonian Craton. *Journal of the Geological Survey Of Brazil*, **5**,

https://doi.org/10.29396/jgsb.2022.v5.n3.1.

Vogel, T.A., Hidalgo, P.J., Patino, L., Tefend, K.S. and Ehrlich, R. 2008. Evaluation of magma mixing and fractional crystallization using whole-rock chemical analyses: Polytopic vector analyses. *Geochemistry, Geophysics, Geosystems*, **9**, https://doi.org/10.1029/2007GC001790.

Walker, B.A., Bergantz, G.W., Otamendi, J.E., Ducea, M.N. and Cristofolini, E.A. 2015. A MASH Zone Revealed: the Mafic Complex of the Sierra Valle Fértil. *Journal of Petrology*, **56**, 1863–1896, https://doi.org/10.1093/petrology/egv057.

Wane, O., Liégeois, J.-P., Thébaud, N., Miller, J., Metelka, V. and Jessell, M. 2018. The onset of the Eburnean collision with the Kenema-Man craton evidenced by plutonic and volcanosedimentary rock record of the Masssigui region, southern Mali. *Precambrian Research*, **305**, 444–478, https://doi.org/10.1016/j.precamres.2017.11.008.

Whitney, D.L. and Evans, B.W. 2010. Abbreviations for names of rock-forming minerals. *American Mineralogist*, **95**, 185–187, https://doi.org/10.2138/am.2010.3371.

Wilson, M. 1989. *Igneous Petrogenesis*, 1st ed. Wilson, M. (ed.), https://doi.org/10.1007/978-1-4020-6788-4.

Wolf, M.B. and Wyllie, P.J. 1994. Dehydration-melting of amphibolite at 10 kbar: the effects of temperature and time. *Contributions to Mineralogy and Petrology*, **115**, 369–383, https://doi.org/10.1007/BF00320972.

Wu, B., Long, X., Lan, C., Zhang, S., Zuo, R. and Wang, J. 2022. Paleoproterozoic tectonic evolution of the Khondalite Belt in the North China Craton: Constraints from the geochronology and geochemistry of 1.9–2.3 Ga felsic and basic intrusive rocks in the Jining area. *Precambrian Research*, **371**, 106570, https://doi.org/10.1016/j.precamres.2022.106570.

Xiang, H. and Connolly, J.A.D. 2022. GeoPS: An interactive visual computing tool for thermodynamic modelling of phase equilibria. *Journal of Metamorphic Geology*, **40**, 243–255, https://doi.org/10.1111/jmg.12626.

Zhang, H., Harris, N., Guo, L. and Xu, W. 2010. The significance of Cenozoic magmatism from the western margin of the eastern syntaxis, southeast Tibet. *Contributions to Mineralogy and Petrology*, **160**, 83–98, https://doi.org/10.1007/s00410-009-0467-5.

Zhang, Q., Wang, C.Y.W., Li, C.D., Wang, Y.L., Jin, W.J. and Jia, X.Q. 2006. Granite classification on the basis of Sr and Yb contents and its implications. *Acta*

Petrologica Sinica, **22**, 2249–2269.

Zhao, G., Cawood, P.A., Wilde, S.A. and Sun, M. 2002. Review of global 2.1-1.8 Ga orogens: Implications for a pre-Rodinia supercontinent. *Earth-Science Reviews*, **59**, 125–162, https://doi.org/10.1016/S0012-8252(02)00073-9.

Zheng, Y., Chen, Y., Dai, L. and Zhao, Z. 2015. Developing plate tectonics theory from oceanic subduction zones to collisional orogens. *Science China Earth Sciences*, **58**, 1045–1069, https://doi.org/10.1007/s11430-015-5097-3.

SUPPELEMENTARY MATERIAL 1 - MODAL ANALYSES

Table S 1. Modal analyses of the Alto Rio Preto granite samples.

	Amphibole-biotite monzogranite					Amphibole-biotite monzogranite							BGrd-tonalite			
Lithology	ABMzG	ABSG	ABMzG	ABMzG	ABMzG	BMzG	BMzG	BMzG	BMzG	BSG	BSG	BSG	Bton	BMzG	BGrd	BMzG
Samples	AA-12	AA-13	AA-21	AA-52	AA-76	AA-14A	AA-24A	AA-63A	AA-64	AA-23	AA-61	AA-62	AA-16	AA-19	AA-45	AA-46
Quartz	23.17	37.55	41.5	26.65	38.85	39.5	39.7	30	42.05	35.6	38.55	25.45	29.95	31.5	25.72	34.25
Plagioclase	35.06	10.25	20.3	29.95	16.45	20	17.4	19.95	11.25	17.05	12.75	13.15	50.3	40.35	36.78	19.4
K-feldspar	20.06	31.6	26.75	32.9	23.95	26.85	26.5	28.05	19.65	38.3	41.3	46	1.9	20	16.06	31.45
Amphibole	5.39	3.7	0.3	1.35	2.85	-	-	-	-	-	-	-	-	-	-	-
Biotite	15.28	11.6	8.5	7.85	16	12.65	15.25	20.2	22.1	8.35	6.75	13.45	15.9	4.95	21.28	11.6
Muscovite	-	-	-	-	-	0.2	0.25	-	-	-	0.05	-	0.55	-	-	0.25
Titanite	0.06	0.45	-	0.05	0.4	-	0.15	0.25	0.7	0.05	-	-	-	-	0.06	0.2
Allanite	0.39	x	-	-	0.15	0.05	0.05	x	0.2	0.15	-	-	-	-	-	0.2
Epidote	0.17	0.2	x	0.15*	0.15	0.05	0.1	x	0.15	0.05	-	-	-	x	-	0.2
Zircon	0.06	x	x	0.05	x	x	0.05	0.2	0.15	0.05	0.05	0.05	0.15	0.05	0.06	0.05
Opaque	0.17	0.1	0.05	0.05	0.15	0.05	0.15	0.45	0.61	0.05	0.15	0.2	0.25	0.1	0.06	0.05
Apatite	0.06	0.15	-	0.3	0.25	0.3	0.15	0.35	0.05	0.25	0.3	0.1	0.05	x	x	0.3
Clorite	0.06	x		x	0.15	0.1	0.05	0.1	1.1	0.05	0.15	0.25	x	0.1	x	0.5
Sericite	0.11	3.85	1.40	0.65	0.65	0.15	0.2	0.25	2.85	x	0.1	1.35	0.75	2.8	x	1.55
Carbonate	-	0.10	-	0.05	0.15	-	-	0.05	0.05	-	-	0.05	0.3	0.1	-	-
F Minerals	78.69	83.55	89.95	90.15	79.9	86.7	84.05	78.25	75.8	90.95	92.75	85.8	83.5	94.65	78.62	86.9
M minerals	21.35	15.95	8.8	9.45	19.6	12.85	15.6	20.7	23.4	8.65	6.85	13.6	16.6	5	21.4	12.25
100%																
Q	29.60	47.29	46.87	49.02	49.02	45.74	47.50	38.47	57.64	39.15	41.64	30.08	36.46	34.30	32.74	40.25
A	44.78	39.80	22.92	30.22	30.22	31.09	31.69	35.96	26.93	42.11	44.59	54.37	61.23	24.01	20.44	36.96
P	25.62	12.91	30.21	20.76	20.76	23.16	20.81	25.57	15.43	18.74	13.77	15.54	2.31	41.69	46.82	22.80
M'	21.29	15.75	8.75	9.00	19.35	12.6	15.2	20.25	22.75	8.6	6.7	13.45	15.7	4.8	21.4	11.95

- not observed in the thin section; x -observed, but not counted

SUPPLEMENTARY MAETRIAL 2- U-Pb GEOCHRONOLOGY

Table S 2. U-Pb SHRIMP data on zircon for sample AA-46.

Location - 533536/9424188					Isotopic ratios									Apparent ages				
Spot	U (ppm)	Th (ppm)	Th/U	^{206}Pbc (%)	^{238}U/^{206}Pb	1σ (%)	^{207}U/^{206}Pb	1σ (%)	^{207}Pb/^{235}U	1σ (%)	^{206}Pb/^{238}U	1s (%)	ρ	^{207}Pb/^{206}Pb	1σ (%)	^{206}Pb/^{208}U	1σ (%)	%conc
AA-46-15.1	312	162	0.52	0.14	1.98	1.1	0.173	0.36	12.1	1.1	0.505	1.1	0.95	2589	±6	2637	±23	-2
AA-46-10.2	62	19	0.30	1.94	1.93	1.4	0.253	1.77	18.0	2.3	0.517	1.4	0.62	3202	±28	2688	±31	+20
AA-46-4.1	116	30	0.26	1.12	1.61	3.1	0.255	2.36	21.8	3.9	0.620	3.1	0.79	3215	±37	3111	±76	+4
AA-46-1.1	925	234	0.25	0.40	5.04	1.3	0.115	0.63	3.1	1.5	0.199	1.3	0.90	1879	±11	1167	±14	+41
AA-46-2.1	164	117	0.72	1.02	2.61	1.2	0.130	1.14	6.9	1.7	0.384	1.2	0.73	2098	±20	2094	±22	+0
AA-46-3.1	399	53	0.13	1.39	3.19	1.5	0.129	0.92	5.6	1.7	0.314	1.5	0.85	2080	±16	1759	±23	+18
AA-46-5.1	279	136	0.49	1.33	2.87	1.1	0.131	0.92	6.3	1.5	0.349	1.1	0.77	2107	±16	1929	±19	+10
AA-46-6.1	347	216	0.62	1.31	2.81	1.1	0.130	1.05	6.4	1.5	0.356	1.1	0.72	2097	±18	1962	±19	+7
AA-46-7.1	948	37	0.04	2.73	8.26	1.1	0.092	1.58	1.5	1.9	0.121	1.1	0.55	1458	±30	736	±7	+52
AA-46-8.1	690	102	0.15	0.45	3.98	1.1	0.120	0.59	4.1	1.2	0.251	1.1	0.87	1950	±11	1445	±14	+29
AA-46-10.1	982	113	0.12	0.43	5.56	1.0	0.109	0.58	2.7	1.2	0.180	1.0	0.87	1775	±11	1067	±10	+43
AA-46-12.1	222	75	0.34	0.29	2.65	1.3	0.128	0.62	6.7	1.5	0.378	1.3	0.91	2067	±11	2065	±24	+0
AA-46-13.1	1077	36	0.03	1.28	3.40	1.0	0.127	0.50	5.1	1.1	0.295	1.0	0.90	2051	±9	1664	±15	+21
AA-46-16.1	867	107	0.12	1.06	6.29	1.3	0.105	0.81	2.3	1.6	0.159	1.3	0.86	1706	±15	952	±12	+48
AA-46-2.2	704	177	0.25	0.32	4.00	1.1	0.115	0.55	4.0	1.2	0.250	1.1	0.89	1881	±10	1438	±14	+26
AA-46-9.1	402	90	0.22	4.09	4.01	1.1	0.129	1.48	4.4	1.8	0.249	1.1	0.60	2086	±26	1435	±14	+35
AA-46-14.1	673	181	0.27	0.12	2.74	1.0	0.127	0.35	6.4	1.1	0.365	1.0	0.95	2055	±6	2008	±18	+3
AA-46-11.1	646	133	0.21	0.15	2.77	1.1	0.127	0.39	6.3	1.1	0.361	1.1	0.94	2055	±7	1986	±18	+4

Table S 3. LA-ICP-MS titanite data for sample AA-46.

Location - 533536/9424188		Isotopic ratios											Pb total	Pb rad	Th	U	Th/U	Apparent ages						
SPOT		207/235	1σ	206/238	1 σ	coef. corr	238/206	1 σ	207/206	1 σ	208/206	1 σ						$T_{206/238}$	1 σ	$T_{207/235}$	1 σ	$T_{207/206}$	1 σ	Conc.
20.1	U	6.7086	0.1388	0.3759	0.0054	0.83	2.6603	0.0384	0.1294	0.0030	0.1863	0.0352	8.61	13	6	27	0.22	2057	26	2074	18	2090	40	99
28.1	U	6.4949	0.1562	0.3753	0.0036	0.76	2.6643	0.0253	0.1255	0.0033	0.0901	0.0136	5.68	13	5	29	0.19	2054	17	2045	21	2036	46	100
22.1	U	6.6058	0.1525	0.3771	0.0050	0.75	2.6517	0.0348	0.1270	0.0028	0.1346	0.0056	3.17	27	24	62	0.38	2063	23	2060	21	2058	39	100
19.1	U	6.5669	0.1194	0.3800	0.0048	0.72	2.6320	0.0333	0.1254	0.0024	0.0989	0.0125	6.30	23	10	53	0.19	2076	22	2055	16	2034	32	101
29.1	U	6.5803	0.1656	0.3810	0.0040	0.76	2.6250	0.0276	0.1253	0.0035	0.0848	0.0189	6.75	13	3	29	0.09	2081	19	2057	22	2033	50	101
24.1	U	6.5911	0.1839	0.3810	0.0062	0.68	2.6246	0.0424	0.1255	0.0032	0.0645	0.0106	5.87	13	2	29	0.08	2081	29	2058	25	2035	45	101
26.1	U	6.7300	0.1467	0.3810	0.0037	0.81	2.6245	0.0254	0.1281	0.0030	0.1141	0.0126	5.29	12	7	27	0.27	2081	17	2077	19	2072	42	100
32.1	U	6.7144	0.1266	0.3792	0.0034	0.97	2.6375	0.0237	0.1284	0.0025	0.5984	0.1451	0.00	62	14	91	0.16	2072	16	2075	16	2077	34	99
33.1	U	6.7158	0.1496	0.3821	0.0049	0.58	2.6171	0.0333	0.1275	0.0033	0.0960	0.0254	7.22	13	5	30	0.17	2086	23	2075	20	2063	45	100
5.1	U	6.6648	0.1569	0.3828	0.0067	0.97	2.6126	0.0455	0.1263	0.0026	0.0682	0.0102	3.19	23	8	54	0.14	2089	31	2068	21	2047	36	101
34.1	U	6.7614	0.1662	0.3828	0.0045	0.58	2.6125	0.0304	0.1281	0.0032	0.0804	0.0162	5.99	11	2	24	0.10	2089	21	2081	22	2072	44	100
25.1	U	6.7077	0.1882	0.3830	0.0057	0.74	2.6107	0.0390	0.1270	0.0032	0.1047	0.0119	4.67	15	9	33	0.27	2090	27	2074	25	2057	45	100
13.1	U	6.6362	0.1378	0.3705	0.0049	0.69	2.6994	0.0356	0.1299	0.0030	0.0756	0.0146	7.03	9	3	20	0.13	2032	23	2064	19	2097	41	98
30.1	U	6.5430	0.1584	0.3686	0.0044	0.79	2.7132	0.0325	0.1288	0.0035	0.0710	0.0159	6.58	9	1	22	0.06	2023	21	2052	22	2081	49	98
31.1	D	6.6306	0.1344	0.3817	0.0044	0.78	2.6199	0.0302	0.1260	0.0030	0.1126	0.0070	3.43	18	13	42	0.32	2084	21	2063	18	2043	41	101
4.1	D	6.7942	0.1676	0.3868	0.0069	0.88	2.5855	0.0460	0.1274	0.0025	0.0749	0.0076	4.70	15	5	33	0.16	2108	32	2085	22	2063	35	101
17.1	D	6.6360	0.1148	0.3837	0.0050	0.89	2.6066	0.0342	0.1254	0.0023	0.1058	0.0378	3.99	23	11	53	0.21	2093	23	2064	15	2035	33	101
16.1	D	6.6686	0.1166	0.3859	0.0046	0.83	2.5915	0.0309	0.1253	0.0024	0.0909	0.0114	7.89	29	7	66	0.11	2104	21	2069	15	2034	33	101
23.1	D	6.6759	0.1610	0.3861	0.0051	0.82	2.5902	0.0342	0.1254	0.0028	0.1105	0.0192	4.44	17	10	38	0.26	2105	24	2069	21	2035	39	101
35.1	D	6.6503	0.1313	0.3864	0.0038	0.72	2.5879	0.0252	0.1248	0.0027	0.0982	0.0080	4.13	23	13	53	0.25	2106	18	2066	18	2026	38	101
3.1	D	6.8582	0.1768	0.3910	0.0063	0.67	2.5573	0.0412	0.1272	0.0025	0.1134	0.0097	6.51	17	8	37	0.20	2128	29	2093	23	2060	35	101
9.1	D	6.7444	0.1910	0.3893	0.0091	0.93	2.5688	0.0598	0.1257	0.0020	0.0877	0.0085	4.26	29	11	67	0.17	2120	42	2079	25	2038	29	101
6.1	D	6.6753	0.2027	0.3903	0.0098	0.01	2.5621	0.0644	0.1240	0.0026	0.1234	0.1252	7.92	14	4	33	0.13	2124	46	2069	26	2015	37	102
10.1	D	6.9114	0.2296	0.3924	0.0104	0.73	2.5483	0.0673	0.1277	0.0028	0.0972	0.0150	7.07	9	3	21	0.15	2134	48	2100	29	2067	40	101
21.1	D	7.0276	0.2162	0.3981	0.0088	0.47	2.5120	0.0556	0.1280	0.0043	0.5216	0.0677	5.78	11	29	17	1.67	2160	41	2115	28	2071	61	102
18.1	D	6.8502	0.1266	0.3998	0.0054	0.85	2.5014	0.0336	0.1243	0.0023	0.1945	0.0072	5.61	24	8	47	0.17	2168	25	2092	16	2019	32	103
8.1	D	7.1058	0.1968	0.4024	0.0090	0.73	2.4849	0.0558	0.1281	0.0021	0.1092	0.0296	10.42	18	6	40	0.15	2180	42	2125	25	2072	29	102
2.1	D	7.0900	0.1887	0.4030	0.0062	0.97	2.4811	0.0382	0.1276	0.0026	0.0627	0.0137	4.07	16	4	37	0.11	2183	29	2123	24	2065	36	102
1.1	D	7.1903	0.1672	0.4012	0.0071	0.40	2.4923	0.0443	0.1300	0.0026	0.2785	0.1092	75.84	22	4	38	0.10	2175	33	2135	21	2098	35	101
7.1	D	7.7533	0.2396	0.4429	0.0116	1.00	2.2579	0.0592	0.1270	0.0023	0.8231	0.6043	194.38	87	14	76	0.18	2364	51	2203	26	2056	31	107
11.1	D	6.7276	0.1071	0.3723	0.0049	0.65	2.6862	0.0350	0.1311	0.0027	0.2430	0.0754	14.28	17	7	31	0.23	2040	23	2076	14	2112	36	98
12.1	D	6.7897	0.1608	0.3488	0.0089	0.36	2.8667	0.0730	0.1412	0.0052	0.2758	0.0405	19.46	5	2	9	0.26	1929	42	2084	22	2242	71	92
14.1	D	6.7004	0.1005	0.3664	0.0054	0.97	2.7292	0.0404	0.1326	0.0028	0.3774	0.1227	73.11	30	7	54	0.14	2012	26	2073	13	2133	38	97

15.1	D	26.3019	0.2209	1.8837	0.0192	0.92	0.5309	0.0054	0.1013	0.0016	1.9341	0.0656	115.08	295	52	60	0.88	6827	47	3358	10	1648	26	203
27.1	D	6.3802	0.1641	0.3582	0.0036	0.85	2.7917	0.0280	0.1292	0.0037	0.3200	0.1293	11.27	15	4	29	0.15	1974	17	2030	23	2087	51	97

Standard Titanite BLR-1 data on 06/16/2025 — Khan secondary standard on 06/16/2025

Concordia Age =1047.8 ± 3.2 Ma — Concordia Age = 520.4 ± 2.5 Ma

U = used for age calculations

D = discarded for age calculations

Table S 3. LA-ICP-MS titanite data for sample AA-76.

Location - 545527/9418493		Isotopic ratios																AGES						
SPOT		207/235	1σ	206/238	1 σ	coef. corr	238/206	1 σ	207/206	1 σ	208/206	1 σ	Pb total	Pb rad	Th	U	Th/U	$T_{206/238}$	1 σ	$T_{207/235}$	1 σ	$T_{207/206}$	1 σ	Conc.
22.1	U	6.5343	0.1749	0.3705	0.0067	0.04	2.6991	0.0490	0.1279	0.0036	0.2399	0.0262	10.73	7	8	14	0.56	2032	32	2051	24	2070	51	99
9.1	U	6.6134	0.1198	0.3735	0.0040	0.78	2.6772	0.0285	0.1284	0.0025	0.1620	0.0352	6.45	14	12	32	0.36	2046	19	2061	16	2076	34	99
27.1	U	6.6864	0.1603	0.3740	0.0058	0.66	2.6739	0.0418	0.1297	0.0029	0.4368	0.0245	8.86	7	18	13	1.38	2048	27	2071	21	2094	39	98
6.1	U	6.7479	0.2531	0.3750	0.0082	0.60	2.6664	0.0579	0.1305	0.0056	0.9588	0.0311	9.32	8	30	11	2.79	2053	38	2079	34	2105	76	98
26.1	U	6.7173	0.1472	0.3753	0.0048	0.66	2.6645	0.0341	0.1298	0.0024	0.3137	0.0215	6.04	15	29	30	0.95	2054	23	2075	20	2095	33	99
16.1	U	6.7105	0.1617	0.3762	0.0055	0.49	2.6583	0.0391	0.1294	0.0029	0.1282	0.0143	8.73	9	4	20	0.20	2058	26	2074	22	2090	39	99
10.1	U	6.5946	0.1276	0.3789	0.0041	0.86	2.6392	0.0283	0.1262	0.0025	0.1185	0.0118	8.16	11	5	26	0.18	2071	19	2059	17	2046	35	100
17.1	U	6.7353	0.1456	0.3789	0.0049	0.85	2.6392	0.0338	0.1289	0.0027	0.3078	0.0063	5.40	22	43	43	0.99	2071	23	2077	19	2083	37	99
14.1	U	6.7130	0.1482	0.3792	0.0049	0.67	2.6375	0.0340	0.1284	0.0030	0.0975	0.0225	8.49	10	3	23	0.11	2072	23	2074	20	2076	41	99
34.1	U	6.8068	0.1645	0.3795	0.0076	0.17	2.6353	0.0525	0.1301	0.0032	0.3387	0.0367	10.67	12	20	21	0.92	2074	35	2087	22	2099	44	99
8.1	U	6.6822	0.1340	0.3800	0.0041	0.91	2.6315	0.0283	0.1275	0.0025	0.3835	0.0077	3.21	27	59	51	1.16	2076	19	2070	18	2064	35	100
21.1	U	6.6761	0.1175	0.3809	0.0052	0.85	2.6252	0.0355	0.1271	0.0024	0.3927	0.0192	3.54	24	58	44	1.32	2081	24	2070	15	2058	33	100
31.1	U	6.6676	0.1234	0.3834	0.0039	0.70	2.6086	0.0266	0.1261	0.0016	0.1625	0.1139	2.63	86	66	199	0.33	2092	18	2068	16	2045	22	101
24.1	U	6.7300	0.1086	0.3845	0.0040	0.82	2.6006	0.0269	0.1269	0.0020	0.0608	0.0035	2.81	33	11	78	0.15	2097	19	2077	14	2056	27	101
20.1	D	6.6099	0.1720	0.3879	0.0055	0.68	2.5779	0.0368	0.1236	0.0029	0.1108	0.0127	8.24	10	5	23	0.24	2113	26	2061	23	2009	40	102
28.1	D	6.8887	0.1375	0.3900	0.0037	0.90	2.5641	0.0243	0.1281	0.0016	0.0826	0.0043	4.12	32	15	73	0.20	2123	17	2097	18	2072	22	101
1.1	D	7.5021	0.2017	0.4047	0.0079	0.24	2.4713	0.0481	0.1345	0.0044	0.2393	0.0569	17.04	4	2	7	0.28	2190	36	2173	25	2157	56	100
2.1	D	6.4936	0.3706	0.3628	0.0107	0.46	2.7566	0.0815	0.1298	0.0080	0.2317	0.0478	19.09	3	1	7	0.15	1995	50	2045	49	2096	104	97
3.1	D	7.0705	0.8787	0.3409	0.0146	0.31	2.9337	0.1260	0.1504	0.0207	0.4571	0.0991	46.22	2	0	3	0.14	1891	72	2120	108	2351	232	89
4.1	D	6.6304	0.3460	0.3501	0.0208	0.78	2.8562	0.1697	0.1374	0.0103	0.6845	0.0809	15.82	5	12	7	1.82	1935	99	2063	46	2194	135	93
5.1	D	6.7362	0.4027	0.3800	0.0126	0.14	2.6318	0.0870	0.1286	0.0095	0.7529	0.1161	20.68	5	12	6	1.83	2076	59	2077	53	2079	128	99
7.1	D	6.6882	0.1642	0.3855	0.0087	0.77	2.5937	0.0587	0.1258	0.0042	0.1697	0.0388	11.34	6	3	13	0.21	2102	40	2071	21	2040	57	101
11.1	D	6.7646	0.1490	0.3857	0.0068	0.78	2.5927	0.0457	0.1272	0.0030	0.2568	0.0186	11.68	11	12	21	0.57	2103	32	2081	19	2060	41	101
12.1	D	6.4421	0.2165	0.3812	0.0110	0.26	2.6233	0.0754	0.1226	0.0062	0.1637	0.0367	24.07	4	1	9	0.07	2082	51	2038	30	1994	90	102
13.1	D	6.5262	0.2399	0.3726	0.0147	0.38	2.6841	0.1062	0.1270	0.0070	0.2347	0.0302	16.90	4	3	8	0.35	2041	70	2049	34	2058	101	99

15.1	D	6.3958	0.2489	0.3931	0.0106	0.39	2.5437	0.0686	0.1180	0.0037	0.2648	0.0512	18.03	3	1	5	0.18	2137	49	2032	32	1926	53	105
18.1	D	6.9275	0.3577	0.3823	0.0066	0.56	2.6159	0.0452	0.1314	0.0068	0.1927	0.0355	16.80	4	2	8	0.21	2087	31	2102	45	2117	92	99
19.1	D	7.2916	0.3108	0.3836	0.0101	0.10	2.6068	0.0685	0.1379	0.0061	0.2244	0.0525	17.92	3	1	6	0.18	2093	47	2148	40	2200	79	97
23.1	D	7.1039	0.1426	0.3928	0.0065	0.79	2.5458	0.0418	0.1312	0.0035	0.3193	0.0525	13.18	10	14	18	0.78	2136	30	2125	18	2114	47	100
25.1	D	6.5626	0.2477	0.3805	0.0102	0.21	2.6283	0.0702	0.1251	0.0054	0.3762	0.0676	17.33	5	6	8	0.76	2079	47	2054	33	2030	77	101
29.1	D	8.0682	0.2907	0.4078	0.0107	0.70	2.4521	0.0641	0.1435	0.0046	0.8200	0.1596	66.91	9	2	8	0.20	2205	49	2239	32	2270	55	98
30.1	D	7.2260	0.1973	0.3844	0.0067	0.01	2.6015	0.0454	0.1363	0.0038	1.0561	0.5882	84.66	38	8	28	0.27	2097	31	2140	25	2181	49	97
32.1	D	6.9747	0.1373	0.3816	0.0051	0.35	2.6203	0.0353	0.1325	0.0020	0.5068	0.1691	21.60	20	31	31	1.01	2084	24	2108	18	2132	27	98
33.1	D	6.6612	0.2812	0.3747	0.0090	0.41	2.6687	0.0640	0.1289	0.0054	0.2158	0.0377	12.46	6	5	13	0.42	2052	42	2068	36	2083	75	99
35.1	D	6.9836	0.2150	0.3903	0.0052	0.54	2.5621	0.0339	0.1298	0.0031	0.3464	0.0467	13.03	9	13	16	0.84	2124	24	2109	28	2095	42	100

Standard Titanite BLR-1 data on 06/16/2025

Concordia Age =1048.7 ± 3.2 Ma

Khan secondary standard on 06/16/2025

Concordia Age = 523.8 ± 2.9 Ma

U = used for age calculations

D = discarded for age calculations

SUPPLEMENTARY MATERIAL 3 - FIGURES

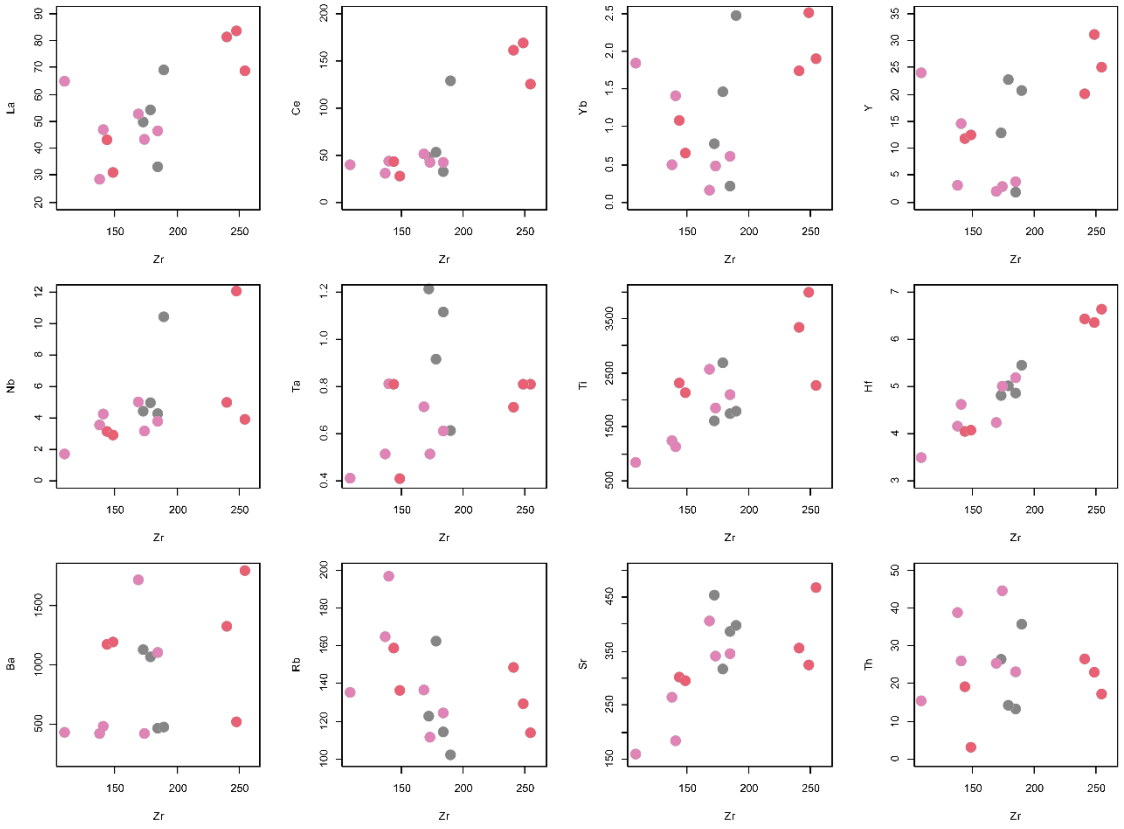


Fig. S 2. Harker diagram Zr vs. major and trace elements.

5 WATER, REDOX, AND COMPOSITIONAL CONTROLS ON ORTHOPYROXENE AND FAYALITE STABILITY IN RHYACIAN IGNEOUS CHARNOCKITES, BACAJÁ DOMAIN, SE AMAZONIAN CRATON: INSIGHTS FROM MINERAL CHEMISTRY AND THERMODYNAMIC MODELING

Arthur Santos da Silva Neri

Roberto Dall'Agnol

Gilmara Regina Lima Feio

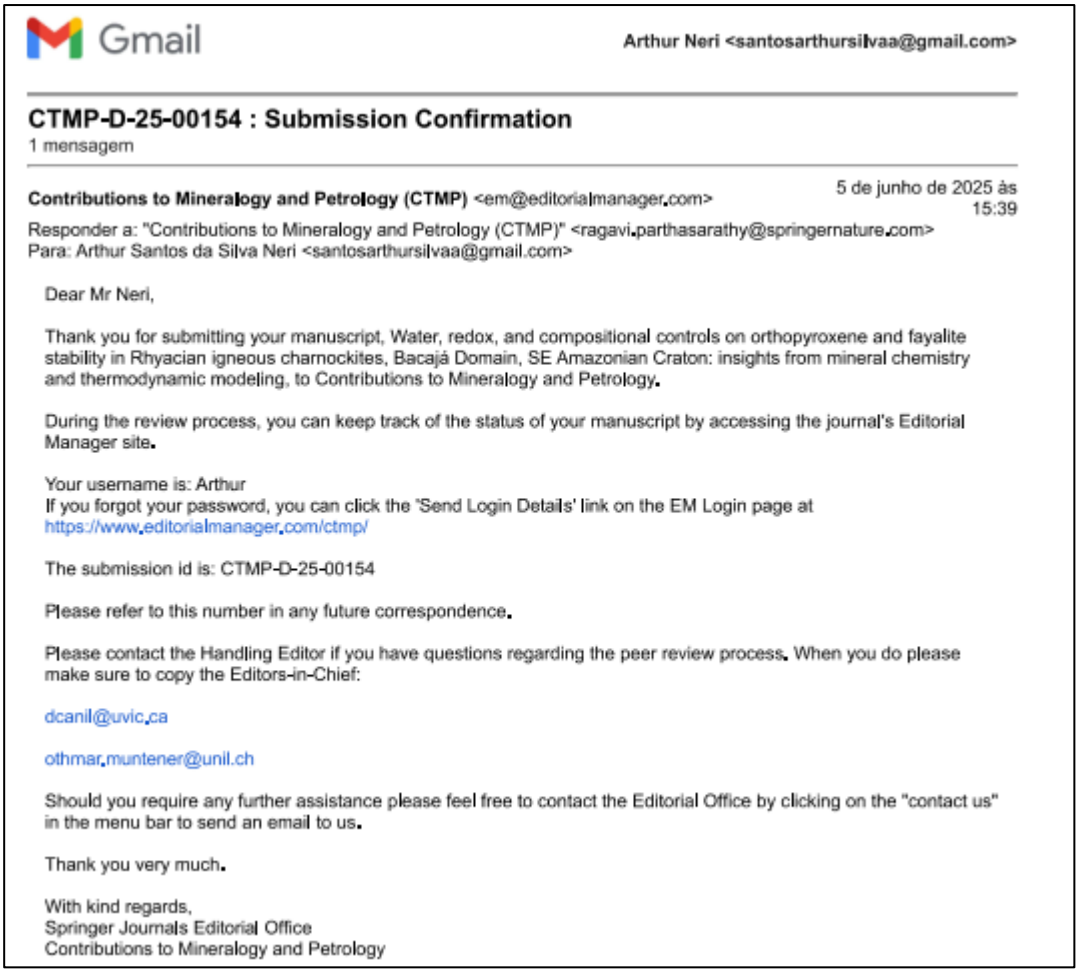
Caio José Mesquita Soares

Ingrid Roberta Viana da Cunha

José de Arimatéia Costa de Almeida

Submetido à *Contributions to Mineralogy and Petrology* como *research article* em 05/06/2025 e em processo de revisão em 23/06/2025.

Respeitando as normas da revista *Contributions to Mineralogy and Petrology*, a formatação, citações e referências bibliográficas desta seção seguem o padrão requerido pela revista.



Gmail — Arthur Neri <santosarthursilvaa@gmail.com>

CTMP-D-25-00154 : Submission Confirmation

1 mensagem

Contributions to Mineralogy and Petrology (CTMP) <em@editorialmanager.com> — 5 de junho de 2025 às 15:39

Responder a: "Contributions to Mineralogy and Petrology (CTMP)" <ragavi.parthasarathy@springernature.com>
Para: Arthur Santos da Silva Neri <santosarthursilvaa@gmail.com>

Dear Mr Neri,

Thank you for submitting your manuscript, Water, redox, and compositional controls on orthopyroxene and fayalite stability in Rhyacian igneous charnockites, Bacajá Domain, SE Amazonian Craton: insights from mineral chemistry and thermodynamic modeling, to Contributions to Mineralogy and Petrology.

During the review process, you can keep track of the status of your manuscript by accessing the journal's Editorial Manager site.

Your username is: Arthur
If you forgot your password, you can click the 'Send Login Details' link on the EM Login page at
https://www.editorialmanager.com/ctmp/

The submission id is: CTMP-D-25-00154

Please refer to this number in any future correspondence.

Please contact the Handling Editor if you have questions regarding the peer review process. When you do please make sure to copy the Editors-in-Chief:

dcanil@uvic.ca

othmar.muntener@unil.ch

Should you require any further assistance please feel free to contact the Editorial Office by clicking on the "contact us" in the menu bar to send an email to us.

Thank you very much.

With kind regards,
Springer Journals Editorial Office
Contributions to Mineralogy and Petrology

Water, redox, and compositional controls on orthopyroxene and fayalite stability in Rhyacian igneous charnockites, Bacajá Domain, SE Amazonian Craton: insights from mineral chemistry and thermodynamic modeling

Arthur Santos da Silva Neri [a, b *], Roberto Dall'Agnol [a, b, c], Gilmara Regina Lima Feio [d, e], Caio José Mesquita Soares [a, b], Ingrid Roberta Viana da Cunha [a, b], José de Arimatéia Costa de Almeida [a, b]

[a] Programa de pós-graduação em Geologia e Geoquímica, Instituto de Geociências (IG), Universidade Federal do Pará (UFPA), Rua Augusto Corrêa, 01, Belém-PA, Brazil. CEP 66075-110.

[b] Grupo de Pesquisa Petrologia de Granitoides IG – UFPA.

[c] Instituto Tecnológico Vale, Belém-PA, Brazil.

[d] Grupo de Mineralogia e Petrologia, Instituto de Geociências e Engenharias (IGE), Universidade Federal do Sul e Sudeste do Pará (UNIFESSPA), Marabá, PA, CEP 68505080, Brazil.

[e] Programa de Pós-Graduação em Propriedade Intelectual e Transferência de Tecnologia para a Inovação (Unifesspa).

ABSTRACT: The crystallization conditions of orthopyroxene and fayalite-bearing granitoids remain critical for understanding the evolution of charnockitic magmas. This study integrates petrography, mineral chemistry, thermobarometry, and thermodynamic modeling to evaluate the P-T-fO_2-H_2O conditions during the crystallization of two contrasting Rhyacian igneous charnockites: the Maravilha (2.09 Ga) and Serra Azul (2.06 Ga) plutons, located in the Bacajá Domain, SE Amazonian Craton. The Maravilha charnockite comprises (i) fayalite- and (ii) pyroxene-bearing granites, whereas Serra Azul is dominated by pyroxene-bearing tonalites and granodiorites. Fayalite-bearing rocks evolved under reduced conditions (FMQ±0.5), with initial water content of ≤3 wt%, while the pyroxene-bearing association evolved under more oxidizing conditions (NNO±0.5), with ~4 wt% initial water. Both associations were emplaced at ~0.3-0.6 GPa. Serra Azul charnockites crystallized under oxidizing conditions (NNO±0.7 to NNO+2), with initial H_2O of ~2-3 wt% and pressures between 0.3-0.6 GPa. Thermodynamic modeling indicates that fayalite and orthopyroxene can crystallize in moderately hydrous melts, ranging from 2.3 to 6 wt% H_2O for fayalite (possibly up to 9 wt%), and ~5-6 wt% for orthopyroxene. Fayalite is restricted to reduced conditions (FMQ-1 to FMQ-0.6) and low pressures (≤0.3 GPa), whereas orthopyroxene is stable from reduced to moderately

oxidizing conditions (FMQ-2 to NNO+1.1) and over wider pressure range. These findings highlight that crystallization of fayalite and orthopyroxene is not restricted to low-water conditions, but instead reflect a complex interaction among water content, melt pressure, redox state, and melt composition.

Keywords: Orthopyroxene, fayalite, thermodynamic modeling, igneous charnockites; GeoPs;

5.1 INTRODUCTION

Charnockites represent an orthopyroxene-and/or fayalite-bearing granitoid that is clearly of igneous and intrusive origin or an orthopyroxene-bearing orthogneiss within a granulite terrane (Frost and Frost 2008). They have been the subject of research during the past century because they are an essential part of high-grade terranes and have played a crucial role in the growth and differentiation of the continental crust (Janasi 2002; Anderson et al. 2003; Rajesh et al. 2014; Zhao et al. 2018; Peng et al. 2019; Marangoanha et al. 2020; Felix et al. 2020).

Most igneous charnockites are metaluminous to weakly peraluminous, geochemically akin to I and A-type granites, with rare strongly peraluminous occurrences that approach S-type granites (Zhao et al., 2023 and references therein). In different kind of charnockites, the preservation of orthopyroxene and/or fayalite relies on complex geological processes that involve either: the presence of CO_2-rich fluids that reduce the water activity in the melt, and raise the solidus temperature expanding the field of stability of orthopyroxene; or the extraction of hydrous melts from an orthopyroxene/fayalite-bearing mush that prevents peritetic back-reactions of these minerals and residual liquid during decrease of temperature and progressive crystallization (Zhao et al. 2023).

Experimental data reveals that orthopyroxene crystallizes in metaluminous to peraluminous granitic compositions at temperatures from 700 to 1100 ºC and pressures from 0.1 to 1.0 GPa and melt H_2O contents of <7 wt.% (Naney 1983; Dall'Agnol et al. 1999; Huang et al. 2019; Gómez-Frutos and Castro 2022). In natural systems, with dacitic to rhyolitic composition, the crystallization of orthopyroxene has been inferred to have mostly occurred at high to moderately high temperatures (mostly above 800 °C) and at low water activity (Scaillet et al. 2016).

Experimental petrology studies, yet time-consuming and expensive, can provide precise insights on P-T-fO_2-H_2O conditions during crystallization of magmatic systems (e.g., Naney 1983; Dall'Agnol et al. 1999; Scaillet et al. 2016; Zhao et al. 2017, 2018; Huang et al. 2019). In contrast, thermodynamic modeling (Connolly 2005; De Capitani

and Petrakakis 2010; Gualda et al. 2012; Xiang and Connolly 2022) provides an alternative and faster approach to determine crystallization conditions. GeoPs is a program that offer results similar to those of other softwares (Xiang and Connolly 2022) and can be used to calculate diverse pseudosections of petrologic interest. Coupled with the thermodynamic dataset designed for igneous systems provided by Holland et al. (2018), GeoPs can be used to model crystallization conditions of igneous systems from peridotite to granite compositions in a wide range of pressure and temperature conditions.

In this sense, this study presents estimation of the crystallization conditions of two contrasting Rhyacian charnockite units from the Bacajá Domain, SE Amazonian craton. The integrated results based on conventional mineral thermobarometry and thermodynamic modeling allowed us to infer the P-T-fO_2-H_2O conditions during the crystallization of the studied rocks. They provided valuable insights into the stability of mineral phases with changing water and redox conditions and a better understanding of the magmatic evolution of igneous charnockites.

5.2 GEOLOGICAL SETTING OF STUDIED CHARNOCKITES

The Bacajá Domain (Fig. 1) is located at the eastern edge of the Amazonian Craton (Fig. 1a) in the southeasternmost portion of the Maroní-Itacaiúnas province (Fig. 1b; Tassinari and Macambira 2004). It comprises Archean (3.0-2.5 Ga) and Siderian (2.45-2.36 Ga) fragments (Vasquez 2006; Macambira et al. 2009; Cristo 2018; Vieira et al. 2022) reworked during a Paleoproterozoic (2.26-1.99 Ga) collisional orogeny (Hurley et al. 1967; Cordani et al. 2000; Kroonenberg et al. 2016). An extensive and geochemically diverse Rhyacian orogenic magmatism took place in the domain at 2.21-2.05 Ga with coeval high-grade metamorphism (Vasquez 2006; Vasquez and Rosa-Costa 2008; Vasquez et al. 2008; Macambira et al. 2009, 2022; Macambira and Ricci 2015; Magalhães et al. 2023; Barros et al. 2023).(Vasquez 2006; Vasquez and Rosa-Costa 2008; Vasquez et al. 2008; Macambira et al. 2009, 2022; Macambira and Ricci 2015; Magalhães et al. 2023; Barros et al. 2023).

The studied charnockites outcrop in the southern Bacajá Domain near its boundary with the Carajás domain (Fig. 1b). These charnockites comprise orthopyroxene- and fayalite-bearing rocks and orthopyroxene-free granitoids intruded into Mesoarchean high-grade metamorphic rocks. The Maravilha charnockite forms an extensive batholith in the southwest of the studied area (Fig. 1c), it comprises isotropic rocks and rocks with preserved primary magmatic structures defined by aligned K-feldspar megaphenocrystals (Fig. 2a, b, c). It may contain enclaves of aluminous granulites or, more rarely, of mafic

rocks. In contrast, the Serra Azul charnockite occurs as elongated stripes near the center of the mapped area and is strongly affected by transcurrent WNW-ESE shear zones (Fig. 1c), which locally obliterate primary textures and originate a mylonitic fabric (Fig. 2d, e, f).

Petrographically, the Maravilha charnockite is composed of (quartz) monzonites to syenites, charnockites, and granites with ferroan or A-type affinity (Rajesh et al. 2011; Zhao et al. 2023). The Serra Azul is composed of enderbites, charnoenderbites, and rare granites with magnesian or I-type affinity (Rajesh et al. 2011; Zhao et al. 2023). U-Pb SHRIMP zircon ages indicate Rhyacian crystallization ages at ca. 2.09 Ga and at ca. 2.07 Ga for Maravilha and Serra Azul charnockites, respectively (Neri et al., submitted). The Nd-Hf isotopes indicate derivation from Paleo- to Mesoarchean crustal sources with no significant input of mantle-derived magmas (Neri et al., submitted). The integration of field, geochemical, and isotopic data suggests that the charnockites were formed in a continental collision setting at the border of the Archean Carajás domain (Neri et al., submitted)

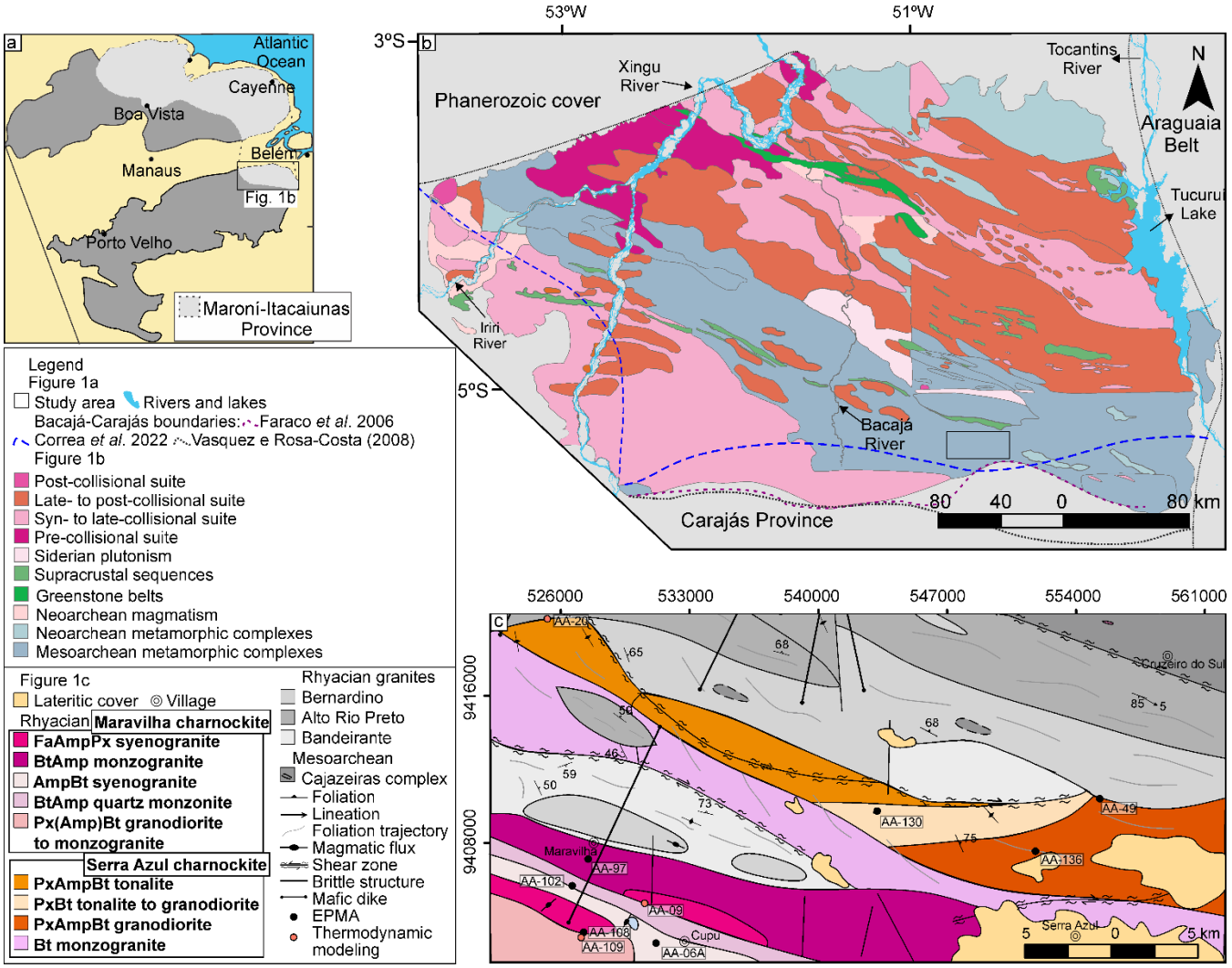


Fig. 1 a The Amazonian craton, highlighting the Maroní-Itacaiúnas Province. **b** regional map of the Bacajá Domain (modified after (Vasquez and Rosa-Costa 2008; Macambira and Ricci 2015; Barros et al. 2023). **c** geological map of the studied area with the location of the studied samples (modified from Neri et al. submitted)



Fig. 2 Field aspects of the Maravilha **a-c** and Serra Azul **d-f** charnockites. **a** isotropic biotite-amphibole quartz monzonite. **b** coarse-grained fayalite-pyroxene-amphibole syenogranite. **c** equigranular medium-grained pyroxene-amphibole-biotite granodiorite (sample AA-109; cf. modeling). **d** medium-grained pyroxene-amphibole-biotite tonalite (sample AA-20;cf. modeling). **e** alignment of mafic minerals in the clinopyroxene-biotite tonalite. **f** alignment of mafic minerals in the biotite monzogranite facies

5.3 ANALYTICAL METHODS

Modal analyses were done using the software Endeeper Hardlege, and ~1800-2000 points were counted in a thin section of each sample (Tab. S1, Fig. 3). Representative samples of each facies were selected for mineral chemistry analyses; six samples of the Maravilha charnockite and four of the Serra Azul charnockite (cf. Tab. S1). Olivine, pyroxenes, amphibole, biotite, and plagioclase were analyzed. Polished thin sections were submitted to wavelength dispersive spectroscopy (WDS) quantitative analyses at the

Laboratório de Microssonda (LABSON) from Universidade de Brasília (UnB), using a JEOL JXA-8230 electron microprobe analyzer. Analyses were performed under the following operating conditions: a column accelerating voltage of 15 kV, a current of 10 nA, an analysis time of 10 s, and a spot size of 1-5 μm. The standards used for instrument calibration were andradite (Ca and Fe), microcline (Si, Al, and K), olivine (Mg), albite (Na), pyrophanite (Ti and Mn), vanadinite (V and Cl), nickel oxide (Ni), chromium trioxide (Cr), and Celestine (Sr). Mineral abbreviations follows Whitney and Evans (2010).

5.4 RESULTS

5.4.1 Petrography and mineral chemistry

5.4.1.1 Maravilha charnockite

Based on modal compositions (Tab. S1), six varieties were recognized and grouped into two major associations (Fig. 3). The first comprises the following facies: biotite-amphibole quartz monzonite to quartz syenite (BAQMzn), biotite-amphibole monzogranite (BAMzG), amphibole-biotite syenogranite (ABSG), and fayalite-amphibole-pyroxene syenogranite (FAPSG). The second includes the pyroxene-amphibole-biotite granodiorite to monzogranite (PABGrd) and pyroxene-biotite monzogranite (PBMzG).

The Maravilha charnockite preserves primary magmatic structures and shows medium to coarse-grained equigranular to heterogranular texture, commonly with porphyritic to megaporphyritic textures. Its rocks are leucocratic (M' = 9.35-22.6%) and vary in color from light to dark gray and pinkish (Fig. 2a-c). Main mafic phases include fayalite, orthopyroxene, clinopyroxene, amphibole, and biotite. Accessory phases are zircon, apatite, ilmenite ± magnetite ± allanite; whereas grunerite, epidote, sericite, and chlorite are the secondary ones.

The fayalite occurs as xenomorphic crystals in contact with quartz, commonly rimmed by amphibole (Fig. 4a) and altered to iddingsite, or in aggregates with pyroxenes and amphibole (Fig. 4b). Its composition is close to the fayalite end member (Fig. 5a, Fa_{93}; Tab. S2).

In the fayalite-bearing samples, orthopyroxene forms subdiomorphic, medium to coarse-grained crystals usually rimmed by amphibole; and commonly shows clinopyroxene lamellae intergrowths (Fig. 4b). In fayalite-absent facies, it appears either as subdiomorphic medium- to fine-grained isolated crystals in the matrix or rimmed by amphibole/biotite (Fig 4e, f). Clinopyroxene is restricted to the FPASG and PABGrd

facies, it is fine-grained and occurs associated with orthopyroxene. All orthopyroxene analyzed crystals are classified as ferrosilite. Its XMg is lower in fayalite-bearing facies (0.16-0.20) than in the fayalite-free ones (XMg = 0.22-0.36) (Fig. 5b, Tab. S2). Clinopyroxene lamellae range from augite to hedenbergite, with rare pigeonites (Fig. 5b, Tab. S2).

In facies where it is the main mafic phase, amphibole forms idiomorphic to subdiomorphic medium- to coarse grained crystals (Fig. 4c, d). In contrast, in pyroxene and fayalite-bearing samples, it occurs commonly in mafic clots enveloping those phases (Fig. 4b, c). It is calcic ($^{B}Ca/^{B}(Ca+Na) \geq 0.75$) and classified dominantly as hastingsite with minor ferro-edenite (Leake et al., 1997). (Fig. 5c, Tab. S2). In the sample AA-109, amphibole shows higher Si and $Mg/(Mg+Fe^{2+})$ and classify exclusively as ferro-edenite. In samples AA-06B, AA-97, and AA-102, some amphiboles are less enriched in alkalis [$(Na+K)A < 0.50$] and classified as ferrohornblende and ferrotschermakite (Fig. 5d). Secondary amphibole also occurs in some facies (Fig. 4d) and is classified as grunerite (Fig. S1, Tab. S3).

Biotite shows two main textural aspects. In samples with dominant amphibole (AA-97 and AA-102), it forms symplectic intergrowths with quartz, suggesting transformation of amphibole (Fig. 4c), and it is often altered to chlorite. In samples with dominant biotite (AA-06A, AA-08B, and AA-109), it occurs as individual idiomorphic to xenomorphic or as xenomorphic crystals forming rims around orthopyroxene (Fig. 4f). Most biotite is Fe-rich [$Fe/(Fe+Mg) > 0.6$], except in sample AA-109 ($Fe/(Fe+Mg) < 0.6$, Tab. S4, Fig. 6a, b), and varies from subalkaline to alkaline (Fig. 6c). All distinct types fall within the field of magmatic biotite (Fig. 6d).

Plagioclase and K-feldspar are generally subdiomorphic to xenomorphic and range from 0.5 to 4 mm; however, in porphyritic and very-coarse-grained facies, it forms idiomorphic crystals that can attain centimetric size. Plagioclase composition varies little between facies and range from calcic oligoclase to sodic andesine (An_{28-35}) with rare labradorite cores (An_{51}, Tab 3, Fig. 6e). They are also often zoned displaying normal zoning with An-richer cores and An-poorer rims (Tab. S5).

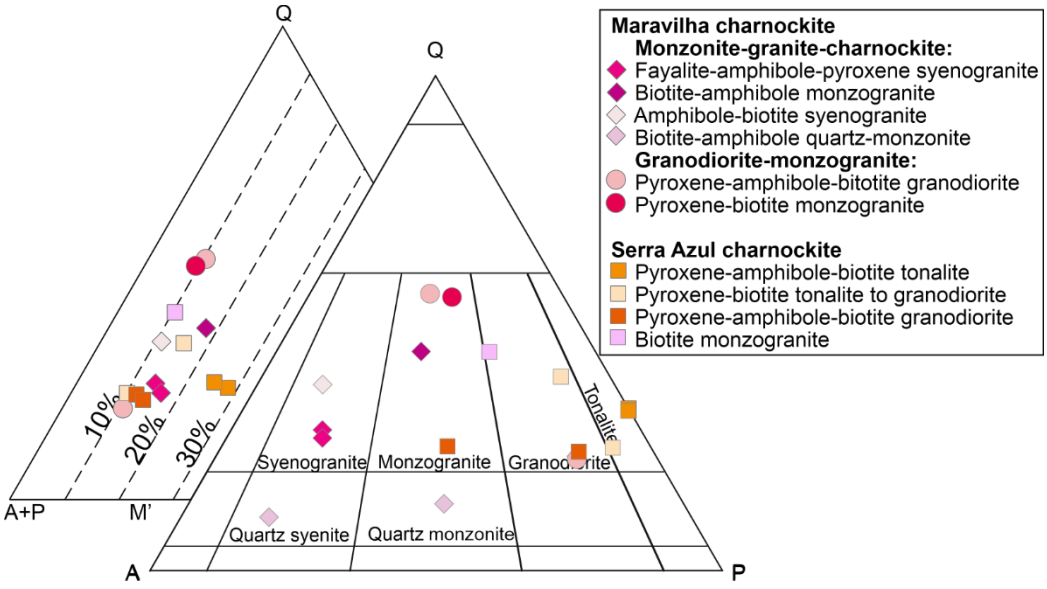


Fig. 3 QAP and Q-A+P-M' diagrams for representative samples of the Maravilha and Serra Azul charnockites (Fields of Le Maitre et al., 2002)

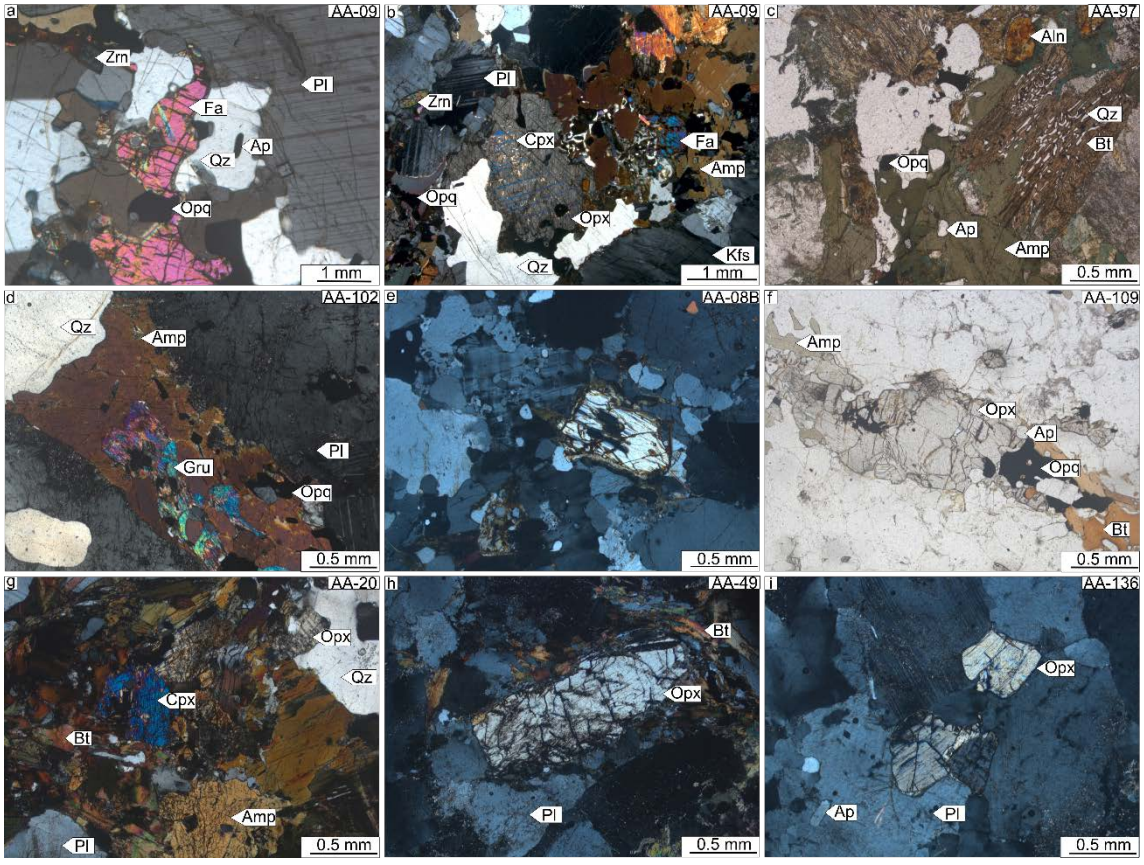


Fig. 4 Microscopic features of the Maravilha **a-f** and Serra Azul **g-i** charnockites. **a** fayalite with straight contacts with quartz and rimmed by amphibole in FAPSG. **b** mafic clot in FAPSG composed of amphibole, fayalite, and inverted pigeonite. **c** symplectic intergrowth of biotite + quartz after amphibole in BAMz. **d** grunerite enclosed by hastingsitic amphibole in BAMz. **e** idiomorphic orthopyroxene in straight contact with quartz and feldspars in the matrix of BPMzG. **f** elongated orthopyroxene accompanied by amphibole and biotite in BPMzG. **g** amphibole associated with biotite and orthopyroxene in PABTn. **h** subidiomorphic orthopyroxene crystal surrounded by late-magmatic biotite in PABGrd; **i** subidiomorphic orthopyroxene crystals associated with plagioclase in the matrix.

5.4.1.2 Serra Azul charnockite

Four petrographic varieties were recognized in the Serra Azul charnockite (Fig. 3): pyroxene-amphibole-biotite tonalite (PABTon), pyroxene-biotite tonalite to granodiorite (PBTnGrd), pyroxene-amphibole-biotite granodiorite (PABGrd), and biotite monzogranite (BMzG).

Primary magmatic textures are largely overprinted by mylonitic fabrics and barely preserved, resulting in an oriented and often banded structure. The rocks are greyish to pinkish (Fig. 2d-f), leucocratic (M' = 11.6-39.6%), and typically show equigranular to heterogranular medium-grained or, locally, coarse-grained texture.

Orthopyroxene forms fine- to medium-grained idiomorphic to subdiomorphic crystals, commonly oriented and rimmed by amphibole and biotite (Fig. 4 g, h). Clinopyroxene is fine- to medium-grained, subdiomorphic to xenomorphic, and typically aligned with biotite-rich layers. Where both pyroxenes coexist, clinopyroxene is consistently finer grained than orthopyroxene. Orthopyroxene is generally ferrosilite (Tab. S6, Fig. 5b) with moderate XMg (0.35-0.46), but in one sample (AA-136, Fig. 5b), it is classified as enstatite (XMg = 0.51-0.54). Clinopyroxene compositions are dominantly augite, with subordinate diopside and rare pigeonite (Tab. S6, Fig. 5b).

Amphibole occurs as two main textural types: (i) subdiomorphic crystals aligned to the foliation together with biotite and (ii) xenomorphic medium-grained rims around pyroxene crystals (Fig. 4g). Both types have similar compositions. Amphibole is calcic ($^{B}Ca/^{B}(Ca+Na) \geq 0.75$) and classified mostly as magnesiohornblende and ferrohornblende, with rare ferrotschermakite (Tab. S7, Fig. 5d, Leake; et al. 1997). Compared to Maravilha charnockite amphibole, those from Serra Azul are enriched in Si and have higher $Mg/(Mg+Fe^{2+})$.

Biotite exhibits three distinct textural types: (i) subdiomorphic to idiomorphic single crystals in the matrix, (ii) together with amphibole in mafic clots, or (iii) replacing ortho- and clinopyroxene crystals (Fig. 4g, h). It is dominantly magnesian biotite, with $Fe/(Fe+Mg) < 0.6$ in most samples, except for AA-49 (Fig. 6a, b; Tab. S7). Biotite composition spans from calc-alkaline to subalkaline (Fig. 6c) and falls entirely within the magmatic biotite field (Fig. 6f).

Plagioclase and K-feldspar are subdiomorphic to idiomorphic, fine- to medium-grained crystals often oriented parallel to foliation. Plagioclase composition ranges from

oligoclase to andesine (An_{21-36}) and commonly displays normal zoning, with An-richer cores and An-poorer rims (Tab. S8).

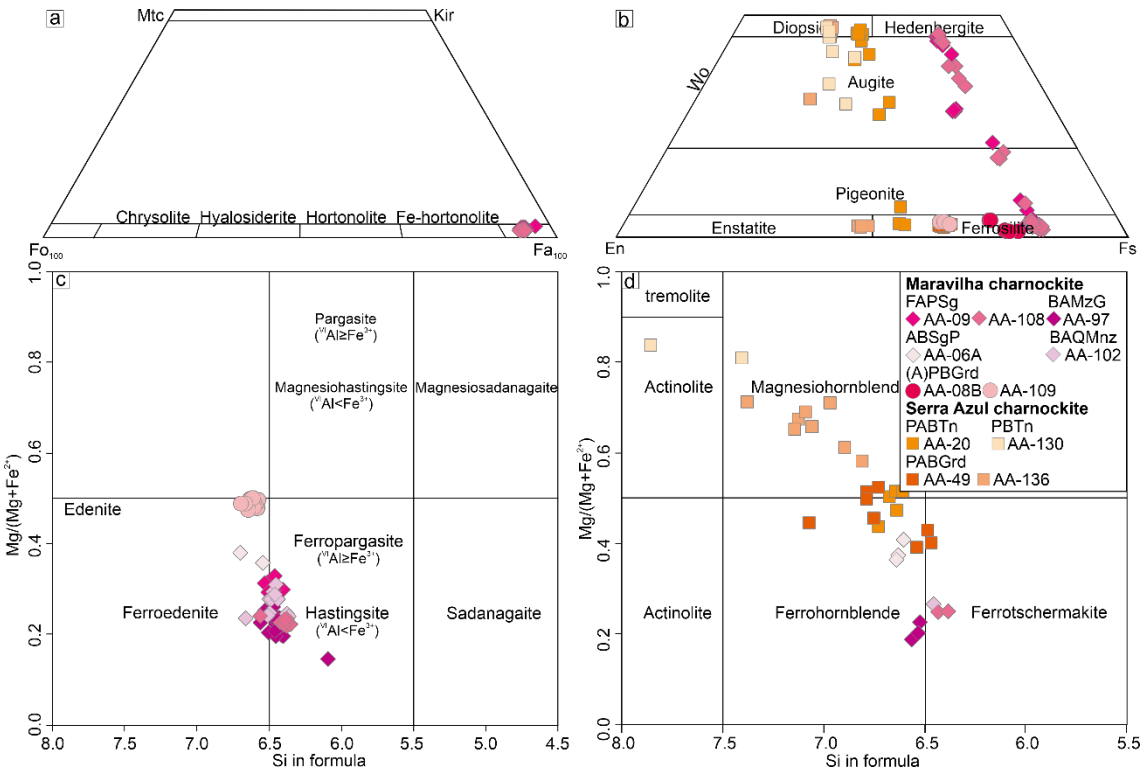


Fig. 5 Classification diagrams for olivine, pyroxenes and amphiboles from Maravilha and Serra Azul charnockites. **a** Olivine composition plotted in the Fo-Lrn-Fa diagram. **b** Pyroxene compositions plotted in the En-Wo-Fs classification diagram (fields after Morimoto *et al*. 1988) **c** Mg/(Mg + Fe^{2+}) versus Si diagram for amphiboles with $Ca_B \geq 1.50$, (Na + K)A ≥ 0.50, and Ti < 0.50. **d** Mg/(Mg + Fe^{2+}) versus Si diagram for amphiboles with $Ca_B \geq 1.50$, (Na + K)A < 0.50, and $Ca_A < 0.50$

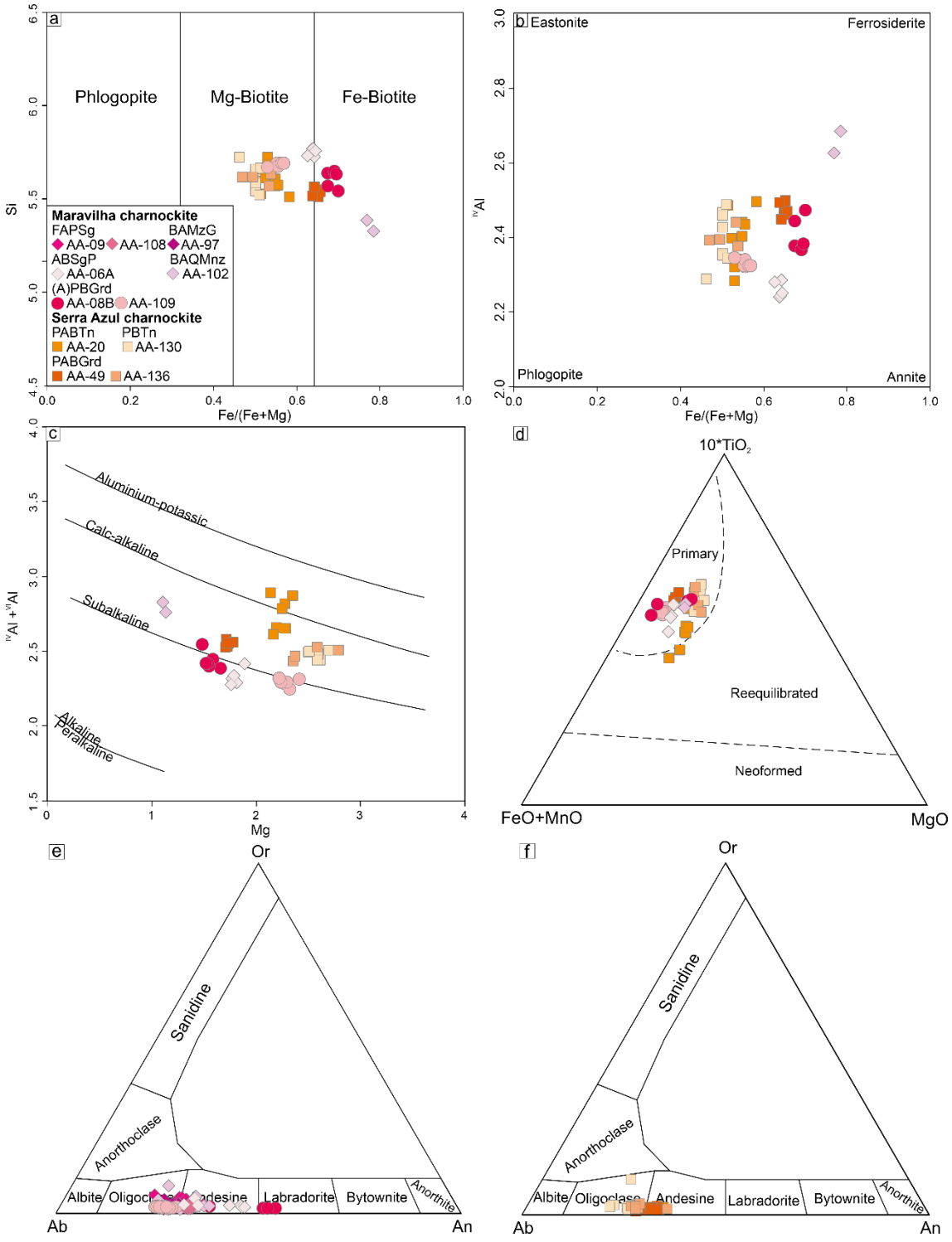


Fig. 6 Classification diagrams for biotite and plagioclase from Maravilha and Serra Azul charnockites. **a** Si vs. Fe/(Fe + Mg) diagram (Deer et al., 2013). **b** Fe/(Fe + Mg) x Al^{IV} diagram (Deer et al., 1992). **c** Mg x Alt diagram (Nachit, 1985); (d) (FeO + MnO)-(10*TiO2)-MgO diagram with fields from Nachit et al. (2005); **e** and **f** Ab-An-Or diagram for feldspars (Deer et al., 2013)

5.4.2 Crystallization phase equilibria

5.4.2.1 Experimental constraints on orthopyroxene and fayalite stability

Experimental studies demonstrate that orthopyroxene crystallization in metaluminous felsic to intermediate magmas is sensitive to melt composition, temperature, melt H_2O content, and oxygen fugacity. In metaluminous silicic magmas, orthopyroxene crystallizes between 750-890 ºC and H_2O contents ranging from 1.3 wt% to 6.8 wt% (e.g., Naney 1983; Dall'Agnol et al. 1999; Bogaerts et al. 2006; Scaillet et al. 2016; Huang et al. 2019). Under reduced conditions (NNO-1.5), it is stable in the temperature interval of ~950°C to ~750 ºC at variable H_2O contents (~3 to 8 wt%), while in oxidized systems (NNO+2.5), it is stable only at >850 ºC and <5 wt% H_2O (Dall'Agnol et al. 1999).

Fayalite crystallization is less well constrained experimentally. In syenogranitic composition, Cunha (2023) reported that fayalite crystallizes at temperatures between 700 and 800 ºC and 6-9 wt% H_2O in the melt (low water contents were not investigated in the experiments), under reduced conditions (NNO-1.3) at 0.2-0.4 GPa. Fayalite was not observed at 0.8 GPa or under oxidized conditions (NNO+2.4). These results suggest that fayalite is sensitive to pressure and oxygen fugacity, being restricted to low-pressure and reduced conditions. Moreover, they indicate also that fayalite can crystallize in moderately to strongly hydrous environments. This differs from most studies that suggest fayalite crystallization only at low water content (Frost et al. 1999; Anderson et al. 2003; Guo et al. 2016). However, different studies are convergent about fayalite crystallization only in reduced environments.

5.4.2.2 Modeling strategy and parameters

Thermodynamic modeling was performed with the GeoPS 3.5 (Xiang and Connolly 2022) and the internally consistent dataset and activity-composition (a-X) models of Holland (2018) in the KNCFMASHTO system (K_2O–Na_2O–CaO–FeO–MgO–Al_2O_3–SiO_2–H_2O–TiO_2–Fe_2O_3) designed for igneous rocks in dry and wet environments, using whole-rock compositions compiled from Neri et al. (submitted). The oxidation state of the magma was determined using the software fO_2Melt (Holland et al. 2018), considering the calculated $\log fO_2$ estimated from amphibole and biotite compositions (Ridolfi et al. 2010). For each unit (Maravilha and Serra Azul charnockites), we selected for each facies the probably least evolved sample with the lowest SiO_2 and highest MgO, showing the best-preserved mineral assemblage. The normalized molar proportions used in the modeling are available in Tab. S9.

The pseudosections were computed under water-undersaturated conditions with variable initial H_2O content (1-4 wt%) for the selected samples. Pressure and temperature ranges were 0.1-0.6 GPa and 600ºC to 1100-1200ºC, consistent with mineral thermobarometry (section 5.2), and experimental data for magmatic systems with similar compositions (Dall'Agnol et al. 1999; Scaillet et al. 2016).

To evaluate the influence of changing water and redox state on orthopyroxene and fayalite stability and their relationship with other phases we also calculated T/P-M_{H2O} and T/P-$M_{O(log\,fO2)}$ diagrams (Fig. 8, 10, 12). T-M_{H2O} diagrams were calculated at 0.5 GPa for oxidized samples (Maravilha and Serra Azul), and at 0.2 GPa for the Reduced Maravilha sample. P-$M_{H2O/(log\,fO2)}$ diagrams were calculated at 800 ºC (oxidized) and 820 ºC (reduced) for Maravilha charnockite and at 850 ºC for Serra Azul charnockites, matching the conditions where key phases are stable. T-$M_{O(log\,fO2)}$ diagrams were calculated using fixed water contents of 3 to 4 wt% in the system, which provided the best fit between the natural samples and modeling.

5.4.2.3 Reduced Maravilha charnockite

The sample AA-09 is a fayalite-amphibole-pyroxene syenogranite. The predicted liquidus and phase relations vary with temperature, H_2O content, and pressure (Fig. 7). The liquidus temperature decreases systematically from 1050 ºC (at 1 wt% H_2O) to 900 ºC (at 4 wt%), while the solidus temperature remains at ~680 ºC at 0.1 GPa for all investigated water contents and tends to decrease with increased pressure. In all diagrams, plagioclase is the liquidus phase, followed by ilmenite and magnetite. The calculated composition of plagioclase at first saturation is more calcic (An ~0.68-71) than the most calcic composition detected in the natural sample (An = 0.36-0.29). Plagioclase with this composition could crystallize at ~800 ºC to 700 ºC for 2 and 3 wt% initial water, respectively (Fig. 7b, c).

Fayalite is the first ferromagnesian silicate to crystallize under low-pressureconditions. Its appearance shifts to lower temperatures with an increasing initial H_2O (from 860 ºC for1 wt%to 810 ºC for 3 wt%), while its temperature of disequilibrium remains at 680 ºC for all water contents. Contrasting behavior is observed concerning pressure for fayalite, which stability gradually increases with H_2O from 0.18 GPa (1 wt%) to 0.3 GPa (4 wt%). The crystallization onset temperatures of orthopyroxene are similar to those of fayalite, but with increasing water and lower pressures, its crystallization temperatures tend to be lower. However, the orthopyroxene differs of fayalite because it remains stable at pressures higher than 0.3 GPa. The XMg of orthopyroxene suggests

crystallization between ~750 to 760 ºC in systems with 2 wt% or 3 wt% of initial water, respectively. (Fig. 7b, c).

Clinopyroxene is the next ferromagnesian silicate to crystallize. It has a progressively narrower stability field in water rich-systems, until being stable in a short P-T range at 4 wt% H_2O (Fig. 7d). Amphibole is the latest ferromagnesian phase to crystallize, with its stability field expanding towards more water enriched systems (e.g., 700 ºC at 0.2 GPa -1 wt% H_2O; 720 ºC at 0.2 GPa – 4 wt%). The amphibole in curve is situated between the clinopyroxene in and clinopyroxene out curves suggesting a possible reaction involving clinopyroxene with liquid to form amphibole.

The crystallization of quartz and alkali feldspar is highly sensitive to water content, both shift to lower temperature with increasing H_2O content and decrease of pressure (Fig. 7a-d). Another remarkable aspect is the appearance of alkali feldspar at temperatures similar or even higher than those of orthopyroxene.

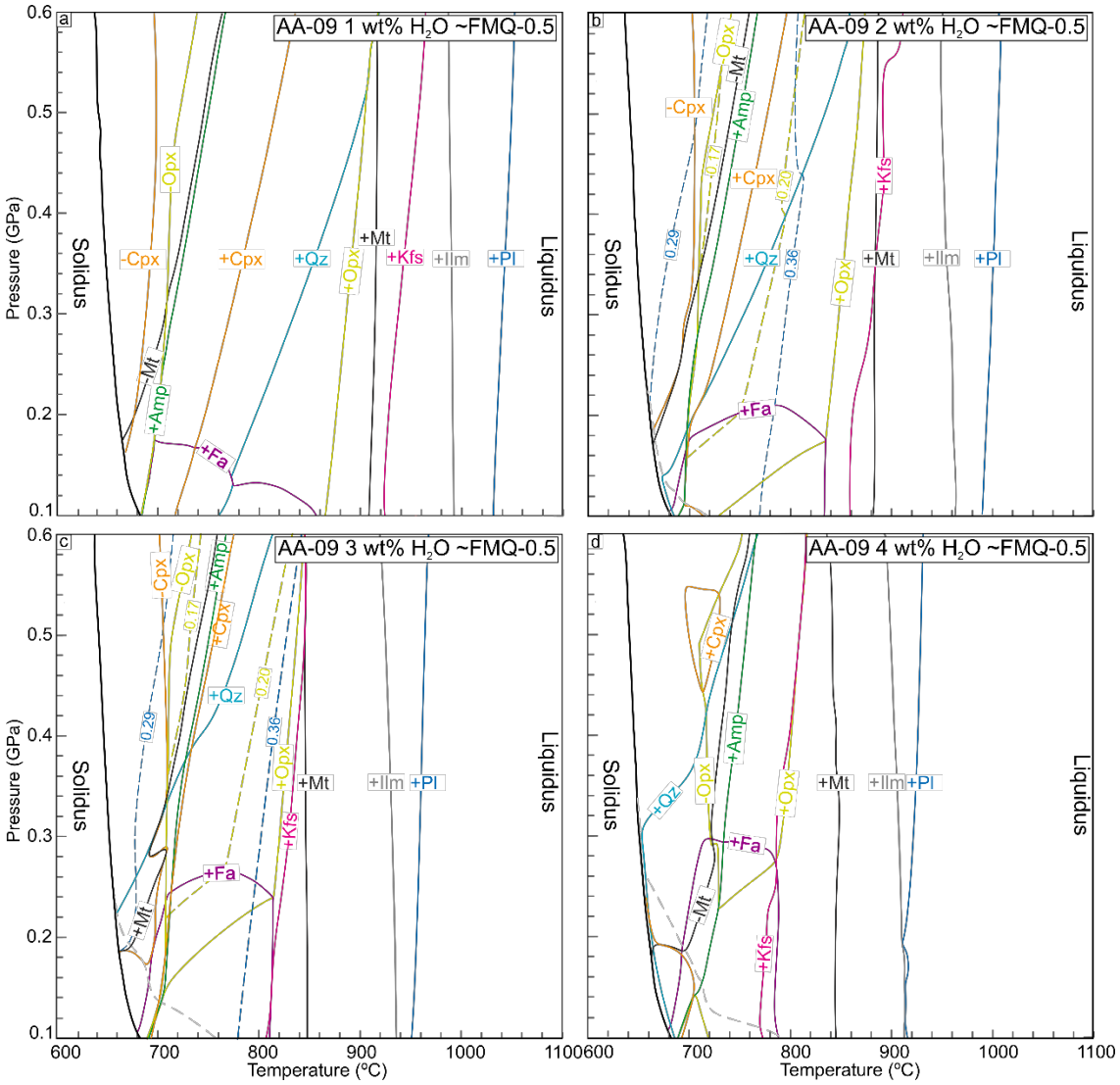


Fig. 7 P-T pseudosection for the reduced variety of the Maravilha charnockite at (**a**) 1 wt%, (**b**) 2 wt%, (**c**) 3 wt%, and (**d**) 4 wt% of initial H_2O in the system. Solid lines mark each phase stability field; the beginning of crystallization is marked with the symbol (+) and its end with (-). (**d**) dashed lines mark the XMg of orthopyroxene (yellow) and XAn in plagioclase (blue). The light grey dashed lines indicate water saturation.

The T-M_{H2O} and P-M_{H2O} pseudosections for sample AA-09 (Fig. 8a-d), reveal phase relations consistent with the P-T diagram. At 0.2 GPa and reduced conditions (~FMQ-0.5), plagioclase remains the liquidus phase up to 4.5 wt% H_2O, followed by ilmenite and magnetite.

Orthopyroxene is stable from ~870 to 700 ºC at 1 wt% H_2O, with its stability shrinking as H_2O increases, becoming unstable above ~4.5 wt% H_2O in the melt (Fig. 8a). Fayalite is stable between 815 and 700 ºC for >2.3 wt% H_2O and its stability field decrease until ~6 wt% in the melt, when it becomes unstable. Under water-saturated conditions, its stability expands between 700–720 ºC (2.4–9 wt%) and even at higher temperatures (880–740 °C at 4.5–9 wt%, Fig. 8a). However, these portions of its

calculated stability remain inconclusive, as indicated by the dashed lines in Fig. 8a, probably due to overlapping phase equilibria or limited model resolution under specific P–T–fO_2–H_2O conditions. In the P-M_{H2O} diagram, fayalite stability increases with both pressure and H_2O contents, reaching up to 0.5 GPa at 9 wt% H_2O. Similarly, orthopyroxene is stable across the modeled pressure range, becoming unstable after ~5 wt%. As observed in fayalite, orthopyroxene fields also display minor areas of uncertainty that suggest it its stable up to 9 wt% H_2O 9Fig. 8b), which should be interpreted with caution. Clinopyroxene is low temperature phase (~740 ºC at 1 wt%) and becomes unstable at > 4 wt% H_2O.

At 2 wt% H_2O (Fig. 8a), amphibole, ilmenite, and K-feldspar are stable throughout the modeled water range, suggesting that their stability does not rely on water contents in the melt. However, their crystallization temperatures vary with water content: amphibole appears at higher temperatures as H_2O increases (e.g., from ~700 ºC at 1 wt% and ~740 ºC at 4 wt%), while K-feldspar stability shifts to lower temperatures with increasing H_2O.

Redox conditions exert a major control on the stability of Fe-Mg silicates (Dall'Agnol et al. 1999). Changing the oxygen fugacity from reduced (FMQ-2) to oxidized (FMQ+2) (Fig. 8c, d), plagioclase, ilmenite, quartz, amphibole and K-feldspar remain stable across all redox conditions in the modeled range. On the other hand, the stability of magnetite, fayalite, orthopyroxene, and clinopyroxene strongly depends on the redox condition (Fig. 8c). Magnetite does not crystallize at any pressure (Fig. 8d) in extremely reduced conditions (FMQ-2), and ilmenite is the only Fe-Ti oxide under these conditions.

Orthopyroxene is stable from ~FMQ-2 to ~FMQ+0.9, when it becomes unstable. with maximum stability at ~FMQ-0.7 (~800-700 ºC temperature interval). At 800 ºC, its pressure stability increases with increasing fO_2, peaking at ~0.72 GPa and FMQ+1.3. Fayalite, on the other hand, is restricted to reduced conditions between ~FMQ-2 to FMQ-0.6, when it becomes unstable. Its maximum stability (820 to 680 ºC) is at the most reduced conditions FMQ-2. At 800 ºC (Fig. 8d), it is evident the strong dependence of fayalite stability of pressure and fO_2 (unstable above 0.3 GPa and fO_2 > FMQ-0.1). Fayalite and orthopyroxene coexist in a restricted P interval from 0.22 to 0.3 GPa in

reduced environments. Clinopyroxene is a low temperature phase, crystallizing at 680 ºC at FMQ-2, and becomes unstable at the solidus (~660 ºC) at FMQ-1.4.

Clinopyroxene, garnet, and amphibole are pressure-dependent phases, appearing only at ≥ 0.7, ≥ 0.68 and ≥ 0.72 GPa.

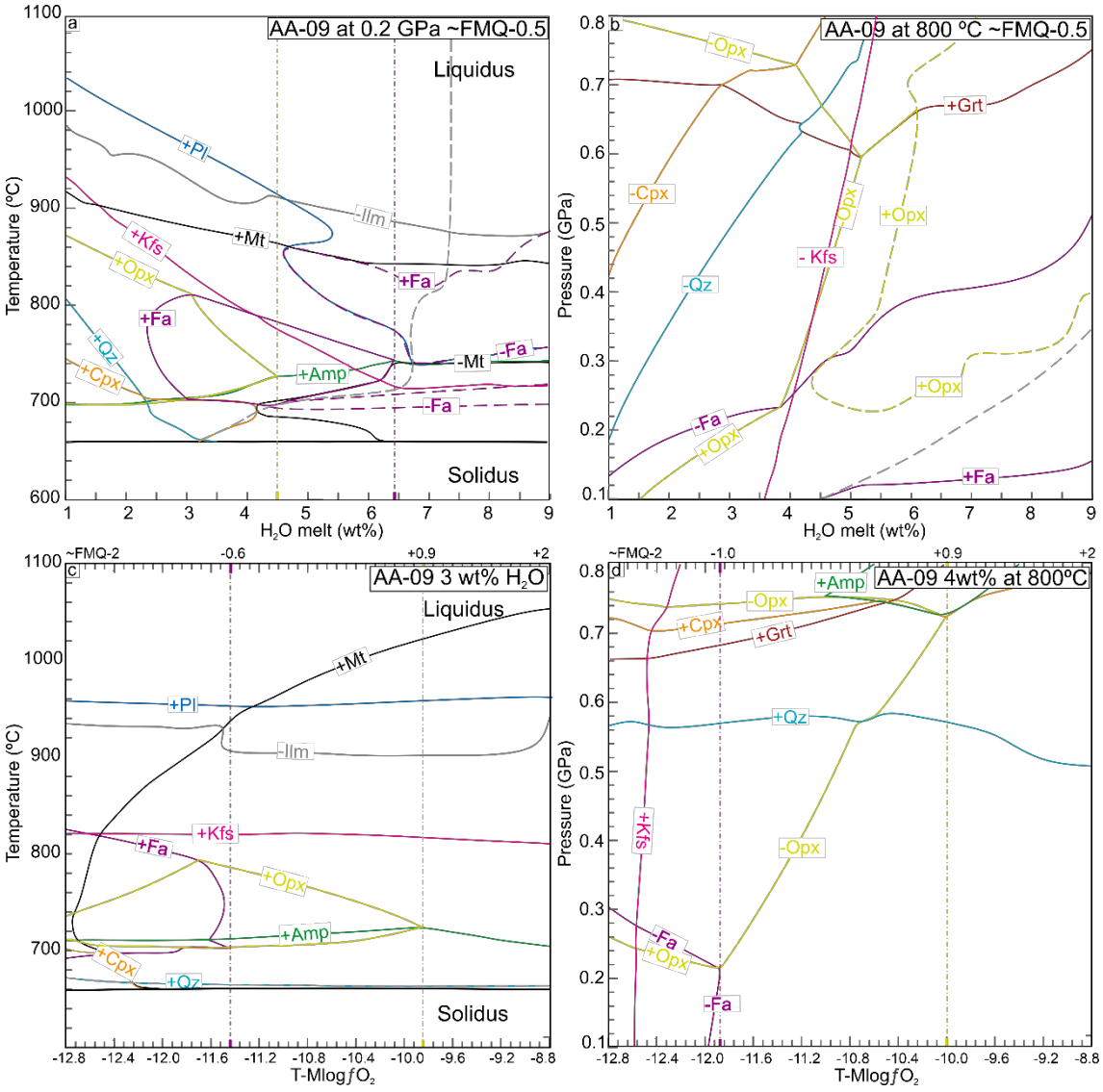


Fig. 8 T/P-M_{H2O} and T/P-M_{logfO2} for the reduced Maravilha charnockite (sample AA-09). **a** T-M_{H2O} at 0.5 GPa and ~NNO. **b** P-M_{H2O} at 820ºC and ~NNO. **c** T-M_{logfO2} for 4 wt% H_2O. **d** P-M_{logfO2} for 4 wt% H_2O at 820ºC. The plus (+) symbol marks the appearance of the phase, and the minus (-) its disappearance. The vertical striped lines mark the upper limit of fayalite and orthopyroxene stability. Dashed areas indicate inconclusive stability fields for fayalite and orthopyroxene. These uncertain domains probably reflect limitations in the thermodynamic dataset resolution, and should be interpreted with caution. The P-$M_{H2O/logfO2}$ must be read from the left to the right and from the bottom to the top

5.4.2.4 Oxidized Maravilha charnockite

Pseudosections for sample AA-109 (Fig. 9a-d), a pyroxene-amphibole-biotite granodiorite, indicate that crystallization is controlled primarily by melt H_2O and temperature, with pressure exerting a minor influence. The liquidus temperatures are

higher at 1-2 wt% H_2O (> 1100 ºC), decreasing to ~1070 ºC and ~1050 °C at 3 and 4wt.% of initial H_2O, respectively. Regardless of the initial water content, plagioclase is the liquidus phase, followed by ilmenite and magnetite. The calculated composition of plagioclase at first saturation is more calcic (An ~86) than the most calcic composition detected in the natural sample (An ~ 30).

Orthopyroxene is consistently the first ferromagnesian silicate to crystallize, with its appearance shifting to lower temperatures with increasing H_2O, from: ~920 °C (1 wt%, Fig. 9a), over 885 °C (2 wt%, Fig. 9b) and 860 °C (3 wt%, Fig. 9c) to ~850 °C (4 wt%, Fig. 9d), whereas its temperature of disequilibrium (Opx-out) remains around 750 °C, for all systems at 0.1 GPa. The XMg (0.44-0.41) of orthopyroxene in the 4 wt% H_2O suggests crystallization between ~840-780 ºC (Fig. 9d). For different water contents, the proximity of the Opx-out curve with the beginning of biotite crystallization is evident. At 4 wt% H_2O, the Opx-out curve coincides closely with the onset of biotite and amphibole crystallization (Fig. 9d).

Biotite is the second ferromagnesian silicate to crystallize and remain stable down to the solidus. Its onset temperature does not significantly diverge with the water content (760 ºC, 1 wt%, Fig. 7a; ~780 ºC, 2-4 wt %, Fig. 9b, c, d). At 4 wt%, the XMg in biotite (0.43-0.45) indicates initial crystallization at ~770-780ºC. Clinopyroxene follows an it occurs in all compositions at temperatures lower or near those of biotite, becoming unstable at pressures below ~0.2 GPa

Amphibole is absent for low water contents, occurs only for the composition with 3 wt% in a restricted temperature field (760~780ºC) at >0.55 GPa and with 4 wt%, it is only stable between ~780-700 ºC and above ~0.22 GPa.

Quartz and K-feldspar show strong dependence of melt water content, with their stability shifting to lower temperature with increasing H_2O and for ≥ 3 wt% H_2O (Fig. 9c, d), K-feldspar becomes stable only near the solidus. For all considered water contents, titanite crystallizes near the solidus.

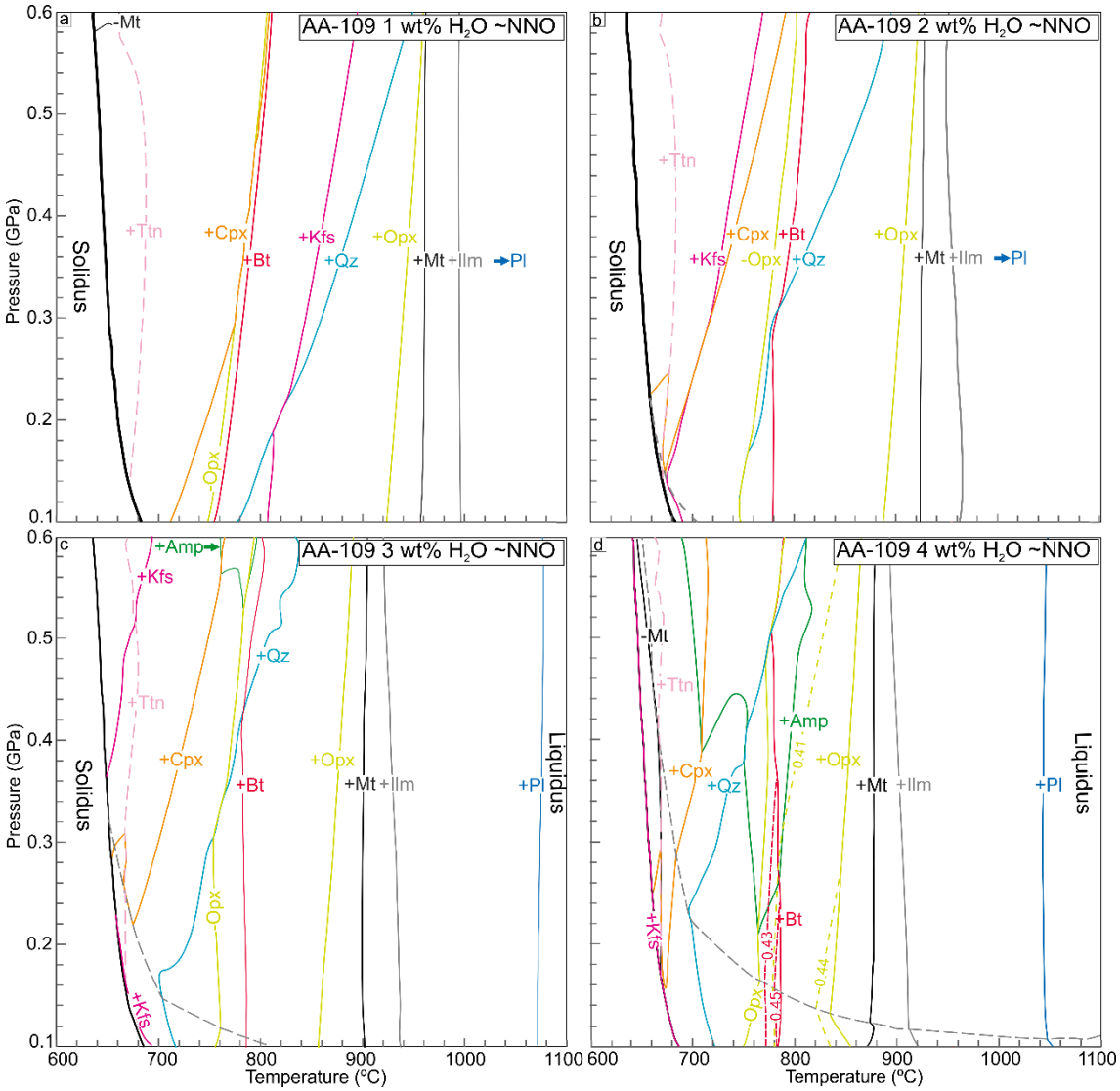


Fig. 9 P-T pseudosection for the oxidized variety of the Maravilha charnockite at (**a**) 1 wt%, (**b**) 2 wt%, (**c**) 3 wt%, and (**d**) 4 wt% of initial H_2O in the system. Solid lines mark each phase stability field; the beginning of crystallization is marked with the symbol (+) and its end with (-); and the dashed light-pink line represents the limit of titanite, experimental phase not observed in natural samples. (**d**) dashed lines mark the XMg of orthopyroxene (yellow) and biotite (red). The light grey dashed lines indicate water saturation.

T-M_{H2O} and P-M_{H2O} pseudosections under oxidizing conditions (~NNO) reveal a crystallization sequence that looks consistent with observed petrographic aspects (Fig. 10a-d). At 0.5 GPa, plagioclase is the liquidus phase across all water contents, followed by ilmenite, magnetite, and orthopyroxene. Orthopyroxene crystallized between ~950-800 ºC at 1 wt% H_2O, and its stability field progressively shrinks with increasing water and becomes unstable (Opx-out) above ~5.3 wt% H_2O (Fig. 10a). This feature is reinforced in the P-M_{H2O} section at 820 ºC (Fig. 10b), where orthopyroxene is stable between 0.3-0.78 and up to ~5.3 wt% H_2O.

Amphibole becomes stable only above ~4 wt% H_2O in the range of ~840-660 ºC (Fig. 10a), consistent with experimental data (Dall'Agnol et al. 1999). Its stability fields oppose those of orthopyroxene, suggesting that both phases rarely coexist under equilibrium in the modeled range, although limited overlap occurs between 0.3-0.8 GPa and 1-5.3 wt% H_2O. This observation suggest that amphibole-orthopyroxene assemblages observed in natural samples likely crystallized at ≤ 4 wt H_2O. Garnet appears only in pressures higher than ~0.8 GPa (Fig. 10b).

Quartz, biotite, clinopyroxene, titanite, and quartz are stable throughout the modeled range of water, indicating that their stability do not rely on water contents in the melt; though their crystallization temperature decreases towards more wet conditions (e.g., biotite at 1 wt% crystallizes at 800ºC and at ~735º C at 9 wt%). K-feldspar shows a more accentuated decrease of temperature with increasing water, becoming unstable above ~4 wt%.

Changing the oxygen fugacity from reduced (NNO-1.5) to strongly oxidized (NNO+2.5) (Fig. 10c, d), plagioclase, ilmenite, quartz, biotite, amphibole, clinopyroxene, and titanite remain stable from reduced to oxidizing conditions. On the other hand, the stability of magnetite, orthopyroxene, and K-feldspar is sensitive to changing in redox condition (Fig. 10c). Magnetite does not crystallize in extremely reduced conditions (NNO<-1.4) at any pressure (Fig. 10d), and ilmenite is the only Fe-Ti oxide under these conditions.

Orthopyroxene is stable between NNO-1.5 to NNO+1.1, crystallizing in the temperature interval of 770-860 ºC at ~NNO-1.5. Its stability field decrease towards more oxidizing conditions, until its disappearance at NNO+1.1. This is further confirmed in the P-M $_{logfO2}$ section at 820 ºC (Fig. 10d), where its stability field peaks at 0.47 GPa and ~NNO+1.1. Towards more oxidizing conditions, only amphibole is stable. Garnet appears only above 0.72 GPa, which defines an upper-pressure limit.

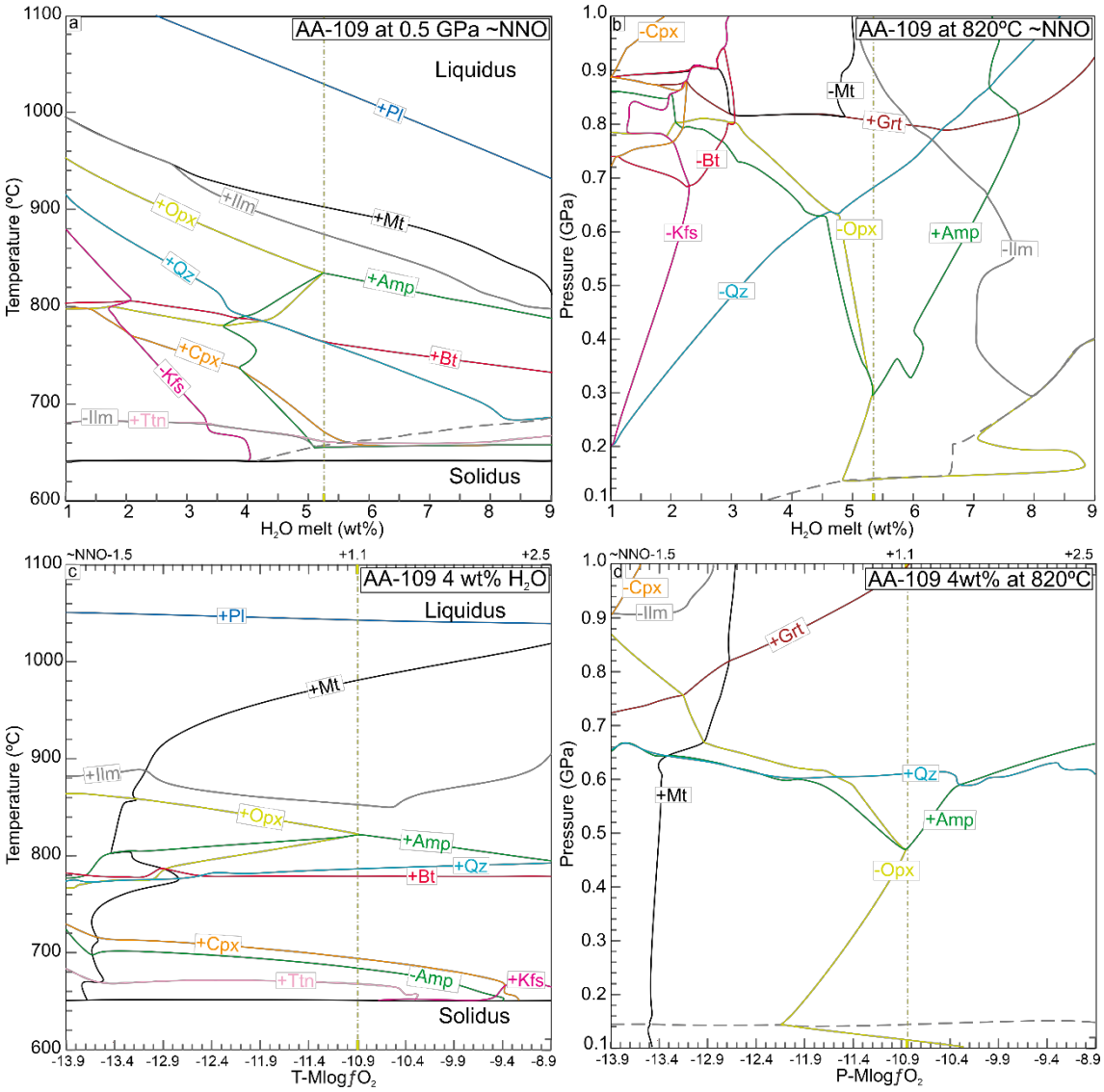


Fig. 10 T/P-M_{H2O} and T/P-M_{logfO2} for the oxidized Maravilha charnockite (sample AA-109). **a** T-M_{H2O} at 0.5 GPa and ~NNO. **b** P-M_{H2O} at 820ºC and ~NNO. **c** T-M_{logfO2} for 4 wt% H_2O. **d** P-M_{logfO2} for 4 wt% H_2O at 820ºC. The plus (+) symbol marks the appearance of the phase, and the minus (-) its disappearance. The vertical striped lines mark the upper limit of orthopyroxene stability. The P-$M_{H2O/logfO2}$ must be read from the left to the right and from the bottom to the top.

5.4.2.5 Serra Azul charnockite

Pseudosections for sample AA-20 (Fig. 11a-d), a pyroxene-amphibole-biotite tonalite. The liquidus temperatures decrease with increasing initial H_2O content, from ~1145 ºC at 1 wt% H_2O to ~1080 ºC at 4 wt%. Plagioclase is the liquidus phase across all models, followed by ilmenite and magnetite. The modeled plagioclase compositions at first saturation (An = ~81 – 2wt%; ~84 at 3 wt%) is significantly more calcic than that observed in the natural sample (An = 35-29). Plagioclase with an An ~35 crystallize at 790°C in the 2 wt.% H_2O model (Fig. 11b) and at 720 ºC in the 3 wt% model (Fig. 11c).

Orthopyroxene is the first ferromagnesian silicate to crystallize, followed by clinopyroxene. Its stability field shrinks with increasing H_2O and pressure, from ~1060

(1 wt%, Fig. 8a), 985 °C (2 wt%, Fig. 8b) and 960 °C (3 wt%, Fig. 8c) to ~950 °C (4 wt%, Fig. 8d), with a similar Opx-out temperature at ca. 720 ºC for all systems. The XMg (0.50-0.51) of orthopyroxene indicates crystallization temperatures of ~870-765 ºC at 2wt% (Fig. 11b) and 890-800 ºC at 3 wt% (Fig. 11c). At higher water contents, the field of orthopyroxene and amphibole coexistence tends to enlarge, while clinopyroxene becomes restricted to lower pressures (<0.14 GPa at 4 wt%).

Amphibole is generally the third ferromagnesian silicate to crystallize. Its stability expands with increasing water and pressure, from ~730-810- ºC at 1 wt% (Fig. 8a) to ~725-920- ºC at 4 wt% (Fig. 11d) being stable until the solidus The XMg (0.51-0.44) of the amphibole suggest crystallization temperatures at ~820-700 ºC (2 wt%) and ~880-720 ºC (3 wt%). Biotite is the next phase to crystallize, initiating near ~800 ºC and remaining stable down to the solidus in all models. The XMg of the mica (0.44-0.45) indicates crystallization between ~760-670 ºC (2 wt%) and 780-670 ºC (3 wt%).

Quartz stability is highly dependent to H_2O content and is less affected by pressure changes, shifting to lower temperatures with increasing water content. K-feldspar is restricted to low initial water contents (1 wt%, Fig. 11a), in a restricted temperature interval (~800-825 ºC), above ~0.42 GPa. Although not observed in natural samples, titanite crystallizes in the modeling at near-solidus temperature above ~0.3 GPa.

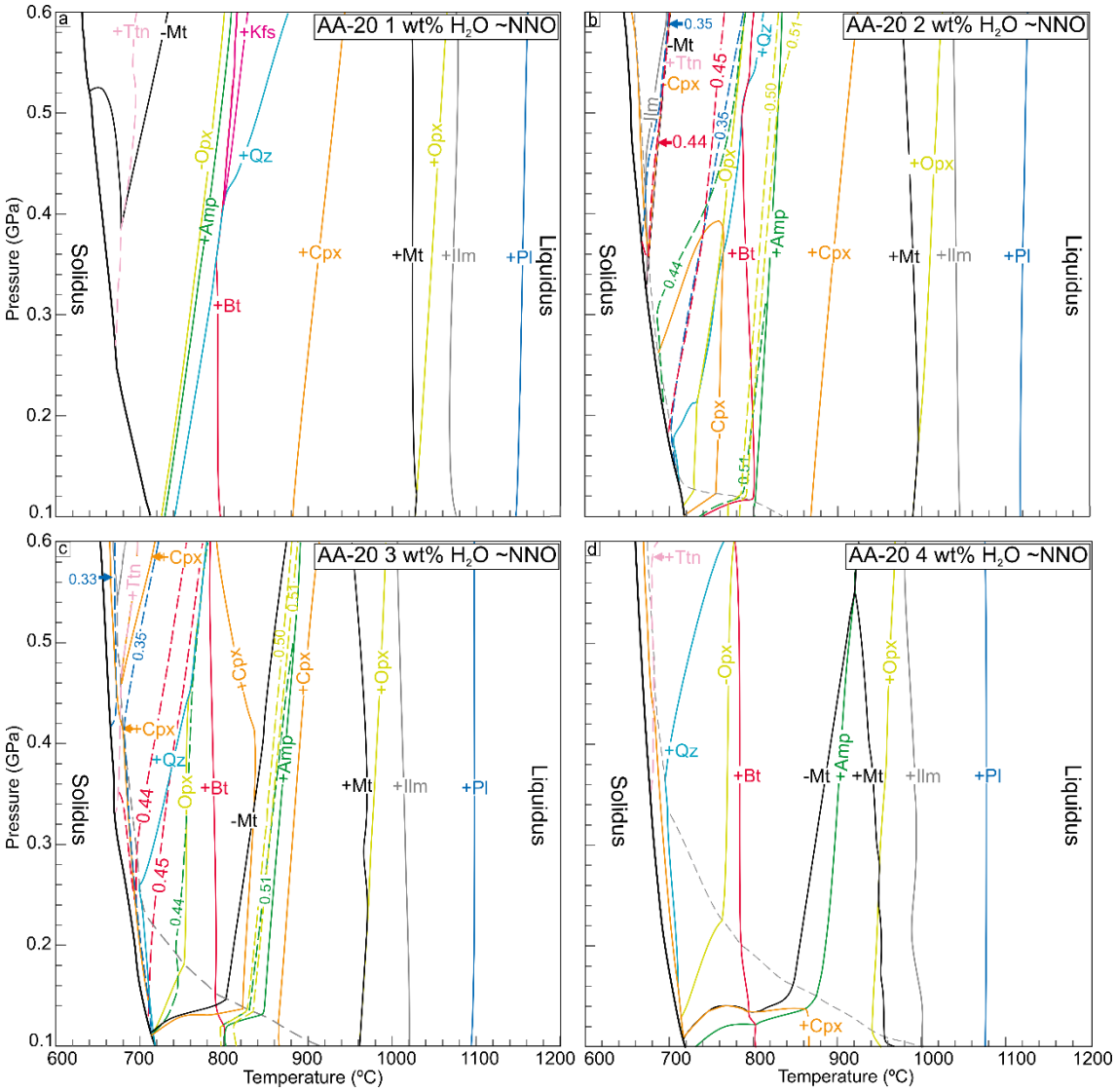


Fig. 11 P-T pseudosection of the Serra Azul charnockite at (**a**) 1 wt%, (**b**) 2 wt%, (**c**) 3wt%, and (**d**) 4 wt% of initial H_2O in the system. Solid lines mark each phase stability field; the beginning of crystallization is marked with the symbol (+) and its end with (-); the dashed light-pink line represents the limit of titanite, experimental phase not observed in natural samples. (**b, c**) dashed lines mark the XMg of orthopyroxene (yellow), green (amphibole), and biotite (red). The light grey dashed lines indicate water saturation

Under oxidizing conditions (~NNO), the T-M_{H2O} diagram for sample AA-20 (Fig. 12a) shows a crystallization sequence coherent with petrographic features. Plagioclase is the liquidus phase and is followed by ilmenite, magnetite, and, in lower water compositions, orthopyroxene (Fig. 12a, b). At 1 wt% H_2O, orthopyroxene crystalizes between ~1050-760 ºC, but its stability field progressively narrows with increasing water and disappears (Opx-out) at ~6 wt% H_2O. The Opx-out curve in the P-M_{H2O} diagram. at 850 ºC (Fig. 12b) indicates that the stability field of Opx is enlarged with decreasing pressure.

Clinopyroxene crystallizes at ~920ºC and remains stable until the solidus. Both pyroxenes could coexist between 920-780 ºC, with a maximum of 3.2 wt% H_2O (Fig.

12a). Similar conditions for their coexistence are observed with changing pressure, extending to > 3.3 wt% H_2O at 0.5 GPa (Fig. 12b). The integration of T-P M_{H2O} defined an upper H_2O (3.2-3.3 wt%) for their coexistence.

Amphibole is stable from 1 to 9 wt% H_2O, indicating limited H_2O influence in the modeled Ca-Fe-Mg rich compositions (Fig. 12a). However, pressure exerts a stronger influence in amphibole stability (Fig. 12b); it is stable at pressures >0.12 GPa, but its stability field diminishes toward dryer compositions with increasing pressure (e.g., ~0.9 GPa for 1 wt% H_2O). Amphibole could coexist with orthopyroxene in a broader temperature and pressure interval (920-780 ºC at 0.5 GPa, Fig. 12a; 0.12to 0.9 GPa at 850 ºC, Fig. 12b) and in a more restricted one with clinopyroxene (880-780 ºC at 0.5 GPa, Fig. 11a; 0.12 to 0.9 GPa Fig. 12b).

The water content does not strongly influence plagioclase, ilmenite, magnetite, biotite, quartz, and titanite as they remain stable in the range of the modeled water content, but, except for titanite, their crystallization temperature decreases with increasing water. Garnet and K-feldspar are limited to pressures higher than 0.93 and 0.78 GPa (Fig. 12b), respectively.

Changing the redox conditions at fixed water content and varying temperature (Fig. 12c) or fixing temperature and varying pressure (Fig. 12d), plagioclase, ilmenite, amphibole, biotite, and quartz are not severely affected, being stable throughout the modeled range. Amphibole crystallization temperature increases toward more oxidizing conditions, from ~835 ºC at NNO -1.5 to ~950ºC at NNO +2.5 (Fig. 12c). Other phases are directly affected by the oxidation state of the magma. Magnetite does not crystallize below NNO-1.2 and its stability field increases towards more oxidizing conditions. Orthopyroxene is stable throughout the modeled range; however, its stability field decreases significantly towards more oxidizing conditions (Fig. 12c). At 850 ºC, its stability field enlarges towards lower pressures and higher oxygen fugacity, peaking at at 0.12 GPa and NNO+1.5 in an undersaturated-water environment (Fig. 12d).

Two pyroxenes and amphibole could coexist in the magma in a short temperature interval (740~900 ºC) until NNO+0.7 (Fig. 11c). The P-M_{logfO2} diagram (Fig. 12d) indicates that at 850ºC, they can coexist from 0.12 to 0.8 GPa up to NNO-0.1.

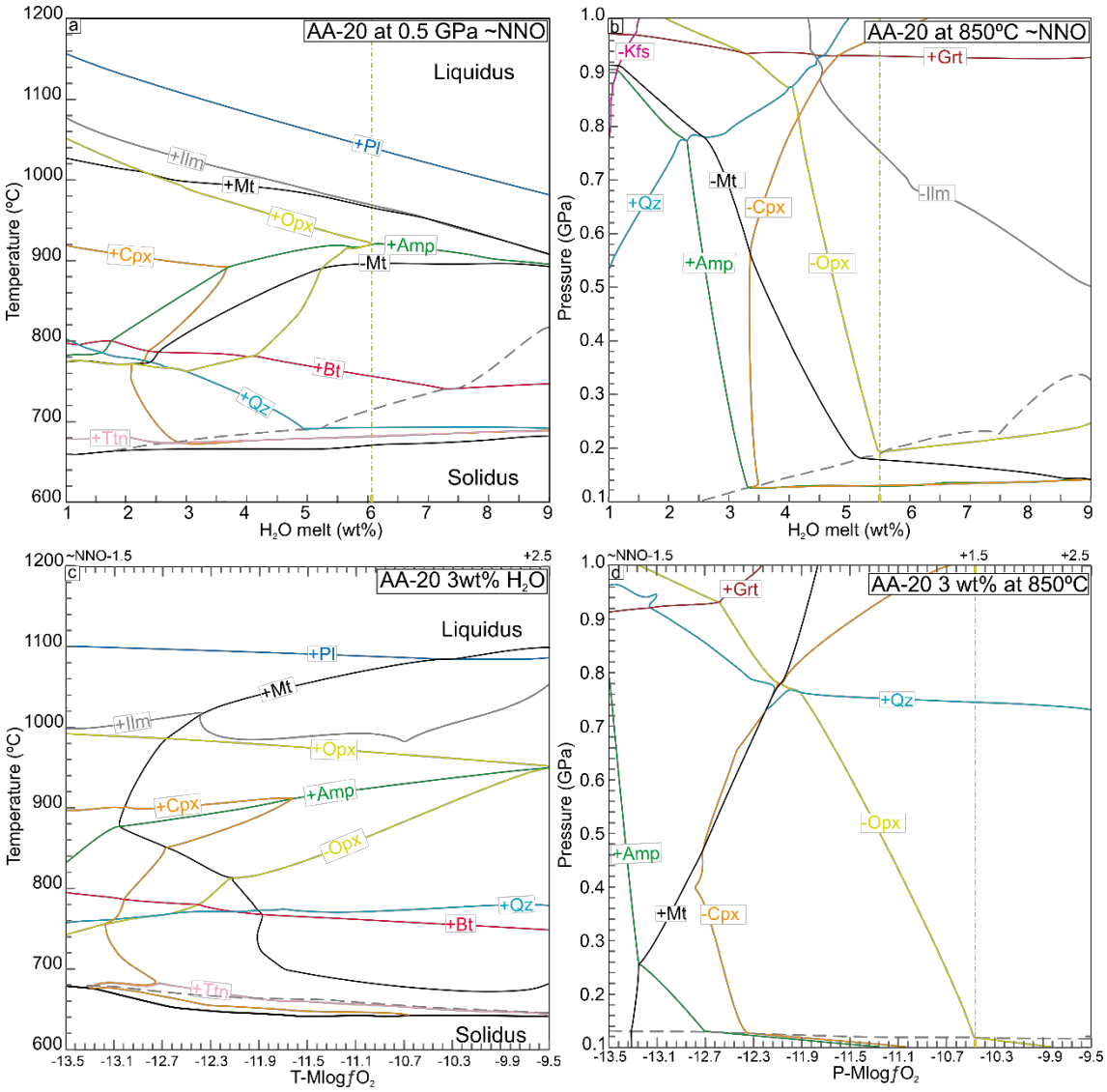


Fig. 12 T/P-M_{H2O} and T/P-M_{logfO2} for the Serra Azul charnockite (sample AA-20). **a** T-M_{H2O} at 0.5 GPa and ~NNO. (**b**) P-M_{H2O} at 850ºC and ~NNO. (**c**) T-M_{logfO2} at 3 wt% H_2O. (**d**) P-M_{logfO2} at 3 wt% H_2O and 850ºC. The plus (+) symbol marks the appearance of the phase, and the minus (-) is the disappearance. The vertical striped lines mark the upper limit of orthopyroxene stability. The P-$M_{H2O/logfO2}$ must be read from the left to the right and from the bottom to the top

5.5 DISCUSSION

5.5.1 Characteristics of orthopyroxene and fayalite and origin of the studied charnockites

Given that charnockites can be formed in both magmatic or metamorphic settings (Frost and Frost 2008; Touret and Huizenga 2012), a proper evaluation of the crystallization sequences requires establishing their origin. In this context, clarifying the origin of fayalite and orthopyroxene is crucial, as they are the diagnostic minerals of charnockitic sequences (Frost and Frost 2008). Overall, four mechanisms have been proposed to account for their origin, namely:

(i) Biotite and/or amphibole breakdown reactions:

$Bt + Qz \rightarrow Opx + Kfs + H_2O$ (1, Bucher e Grapes 2011, Harlov 2012)

$Amp + Qz \rightarrow Opx + Cpx + H_2O$ (2, Tsunogae et al. 2003)

These reactions occur in temperatures below the solidus and are typical of metamorphic settings. However, the subdiomorphic to idiomorphic textures of fayalite and orthopyroxene, the absence of biotite and/or amphibole inclusions, as well as the presence of biotite and amphibole crystals enveloping partial or entirely fayalite and orthopyroxene suggest that the latter are early magmatic phases. In contrast, biotite and amphibole crystallized later, possibly through peritetic magmatic reactions. Therefore, the reactions (1) and (2) do not adequately explain the formation of orthopyroxene and fayalite.

(ii) Feldspar and quartz metasomatism induced by fluids or melts that are enriched in ferrous iron (Fe^{2+}) (Oyawoye 1965; Schilling et al. 2011). This hypothesis is mainly supported by the presence of residual inclusions of quartz and/or feldspar within orthopyroxene and fayalite, but they are absent in the studied charnockites.

(iii) Antecrystic origin from mantle-derived sources (Xie et al. 2023). This model is not supported in the studied units, as the low Cr_2O_3 in both fayalite and orthopyroxene is incompatible with a mantle origin.

(iv) Fractional crystallization from water-poor magmas (Collins et al. 1982; Shellnutt and Zhou 2008; Vásquez et al. 2009; Guo et al. 2016; Zhao et al. 2023a; Liu et al. 2024). This mechanism best explains the textures and compositions of both fayalite and orthopyroxene. They occur in mafic aggregates, surrounded by late-magmatic amphibole and biotite, and exhibit subdiomorphic to idiomorphic textures. Orthopyroxene also shows low Al_2O_3 contents (Fig. 13d, Tab. 1,Zhao et al. 2023a; Liu et al. 2024), consistent with crystallization from metaluminous to slightly peraluminous magmas.

Besides the aspects related to orthopyroxene and fayalite characteristics, several lines of argument point to a magmatic origin of Maravilha and Serra Azul charnockites: (i) their occurrence as large intrusive bodies (Fig. 1); (ii) K-feldspar megaphenocrysts are present in some facies, particularly in the Maravilha charnockite (Fig. 2a, b), showing textures indicative of crystallization in the presence of melt (Wang et al., 2018); (iii) Zircon crystals displaying typical features of magmatic acidic–intermediate rocks (Koschek, 1993; Corfu et al., 2003); (iv) U-Pb SHRIMP zircon ages of 2.09 Ga and 2.06

Ga, for the Maravilha and Serra Azul charnockites, respectively (Neri et al., submitted), coincident with the main magmatic events in the Bacajá Domain.

Taken together, the petrographic, geochemical, and geochronological evidence supports the interpretation that the Maravilha and Serra Azul charnockite are of igneous origin.

5.5.2 Thermodynamic modeling: limitations and reliability

Before drawing further interpretation from the thermodynamic modeling results, it is necessary to understand the inherent uncertainties of the method. Zhao et al. (2017) conduced detailed modeling on peraluminous igneous charnockites and compared their results with experimental using the dataset of Holland and Powell (2011). They concluded that the modeling is appropriate for igneous systems with low initial water (~1-2 wt%) at moderately low to low pressures (0.1 to 0.3 GPa).

However, the new dataset by Holland et al. (2018) significantly expanded the applicability of thermodynamic modeling to a broader range of bulk-rock compositions, from peridotite to granite under a wide range of P-T conditions from 0.0001 to 7.0 GPa and temperatures varying from 650º C to peridotite liquidus, and from nearly dry (0.8 wt% H_2O) to water-saturated systems (up to15 wt% H_2O). Further comparative studies performed by García-Arias (2020), using both natural and synthetic compositions, demonstrated that the a-X models in Holland et al. (2018), provided consistent results when compared to the experimental data.

Despite these advances, a perfect agreement when comparing thermodynamic models with experimental data should not be expected, given the complexity of natural systems and some simplified assumptions adopted in the models. Mesquita et al. (2025) reported some inconsistencies in the modeling of compositionally complex A-type granites, such as the presence of mineral phases absent in natural sample, stability curves incompatible with magmatic evolution and limitations in computing reactions between mineral phases. Despite these inconsistencies, those authors concluded that the modeling yielded results reasonably consistent with natural samples. These limitations are not only restricted to thermodynamic modeling but also have been reported in experimental studies (Bogaerts et al. 2006; Cunha 2023).

In the present study, some diagrams may present inconclusive stability fields (Fig. 8a, b) for fayalite and orthopyroxene. These uncertainties might be related to overlapping stability domains under specific conditions, limited resolution of the thermodynamic dataset for these phases, or even numerical issues during modelling with GeoPS (Zhao et

al. 2017, 2023; Holland et al. 2018). These inconclusive areas preclude a precise definition of mineral boundaries, yet they do not invalidate the broader thermodynamic set. When integrated with petrographic and mineral chemistry data, the modeling outputs remain consistent with natural observations.

Nonetheless, it is possible to affirm that thermodynamic modeling using the database of Holland et al. (2018) provides meaningful geological insights into igneous rocks crystallization/melting conditions within the parameters considered in this work.

5.5.3 Crystallization parameters

Crystallization parameters were estimated using whole-rock geochemistry (Neri et al. submitted), mineral chemistry of selected phases (pyroxenes, amphiboles, biotite, and plagioclase; this study) and thermodynamic modelling. Estimated temperature and pressure for pyroxenes and amphiboles were obtained using the WinPyrox (Yavuz 2013) and WinAmptb programs (Yavuz and Döner 2017). A summary of P-T-fO_2-X_{H2O} obtained by mineral chemistry data is given in Tab. 1.

5.5.3.1 Temperature

For the Maravilha charnockite, apatite saturation thermometry (Harrison and Watson 1984) yielded high temperatures from 840 to 940 ºC (Tab. 1), attaining its maximum in the fayalite-bearing sample (947 ºC – AA-09) and its minimum in a fayalite-absent facies (840 ºC – AA-06B). These results are similar to the values via machine learning using whole rock compositions (802-944°C; Weber and Blundy, 2024). Zircon saturation thermometry (Watson and Harrison 1983) generally provides lower values (779-861 ºC) except for sample AA-97 (BAMzG), which reached 941ºC (Tab. 1). Considering that apatite and zircon are early crystallized phases in these rocks, these values are indicative of near liquidus temperatures.

Amphibole-based thermometry yielded lower temperatures, consistent with amphibole crystallizing later than apatite and zircon. The calibration by Ridolfi et al. (2010) provided higher values than that of Putirka (2016). Minimum values, 784-894 ºC (Ridolfi et al. 2010) and 662-756°C (Putirka, 2016), were obtained in sample AA-97 (BAMzG). Maximum values occurred in sample AA-06A (ABSGP facies): 1031-1044°C (Ridolfi et al. 2010), and 857-866°C (Putirka 2016), although those values diverge from the overall behavior of the other samples and are most likely overestimated. Aside from sample AA-06A, most of other samples approach the minimum temperature range (Tab. 1). The biotite thermometer (Li and Zhang, 2022) furnished temperatures of 784-809 ºC, which overlap with those resulting from the amphibole calibrations.

For the Serra Azul charnockite, apatite-saturation (Harrison and Watson 1984), and whole-rock (Weber and Blundy 2024) thermometry provided high temperature ranges of 796-927 ºC and 899-979°C, respectively, with a trend toward lower temperatures from tonalitic to granodioritic facies (Tab. 1). Zircon saturation temperatures are consistently lower (781-842ºC). The two-pyroxene thermometer by Wood and Banno (1973) provided higher values (938-1019 ºC; Tab. 1) than those indicated by the previously discussed methods, which are higher or superposed with the temperatures (766-1078 ºC and 755-983 ºC) defined using, respectively, the ones by Putirka (2008) and Ágreda-López et al. (2024). Amphibole-based thermometers gave lower temperatures (679-774 ºC, Putirka 2016). Finally, the biotite thermometer by Li and Zhang (2022) provides temperatures (776-841 ºC) that overlaps with the amphibole's temperatures.

5.5.3.2 Pressure

Estimating emplacement pressure for Maravilha charnockite using conventional mineral thermobarometry is challenging due to its dominantly reduced character (cf. Anderson and Smith, 1995), which contrasts with the oxidized conditions under which the Al-in-geobarometer was initially calibrated (Hammarstrom and Zen 1986; Hollister et al. 1987; Schmidt 1992). In contrast, barometers based on whole-rock and biotite compositions using machine learning (Li and Zhang 2022; Weber and Blundy 2024; Ágreda-López et al. 2024) are not limited by redox conditions, as they were calibrated for temperatures close to the solidus and over a large pressure range and could be applied to a wide range of granitoid rocks. Hence, they can give valuable insights into pressure conditions for the Maravilha charnockite.

For the monzonite-granite-charnockite association, machine learning barometers indicate pressures of 0.43-0.51 GPa (biotite compositions; Li et al., 2022) and 0.55-0.68 GPa (whole-rock compositions, Weber and Blundy 2024). Thermodynamic modelling, however, places fayalite crystallization at low pressures (<0.3 GPa) (Fig. 7). For the granodiorite-monzogranite association, which has an oxidizing character (section 5.2.3), machine-learning barometers yielded similar to slightly higher pressures: 0.48 to 0.6 GPa (biotite compositions; Li et al., 2022) and 0.54 to 0.64 GPa (whole-rock compositions, Weber and Blundy 2024). Al-in-amphibole geobarometers provided consistent, but generally lower estimates of 0.33-0.47 GPa (Hammarstrom and Zen 1986; Hollister et al. 1987; Schmidt 1992), 0.30-0.35 GPa (Mutch et al. 2016), and 0.15-0.19 GPa (Ridolfi et al. 2010).

Modeling sets an upper pressure limit of 0.6-0.68 GPa for the reduced facies, where garnet, absent in the natural sample, appears (Fig. 8b, d). In contrast, fayalite crystallizes only at low pressures (<0.3 GPa at 3 wt% H_2O). The mineral and whole-rock barometers provided significantly higher pressures from 0.43 to 0.68 GPa (Tab. 1), likely reflecting early crystallization pressures, while the lower values from modeling should represent late-stage emplacement. This suggests that the reduced facies crystallize at ca. 0.3-0.6 GPa.

For the oxidized facies, thermodynamic data also defines an upper pressure limit of ~0.8 GPa, which marks the garnet crystallization, a phase not observed in the natural sample. Machine learning barometers indicate higher pressures (0.54-0.6 GPa), interpreted as initial crystallization pressures, while Al-in-amphibole provided consistent values of 0.2-0.45 GPa, interpreted as final emplacement pressures. In summary, both associations crystallized at ca. 0.3-0.6 GPa.

In the Serra Azul charnockite, Al-in-amphibole barometers (Hammarstrom and Zen 1986; Hollister et al. 1987; Schmidt 1992) yielded 0.40-0.45 GPa for tonalitic facies and more variable (0.12-0.52 GPa) for granodioritic ones. The calibration of Mutch et al. (2016) furnished slightly lower values (0.35 GPa - PABTn; 0.2-0.42 GPa -PABGrd, Tab. 1), while that of Ridolfi et al. (2010) yielded the lowest pressures (0.09-0.25 GPa) for both tonalitic and granodioritic facies. In contrast, barometers using biotite and whole-rock compositions (Li and Zhang 2022; Ágreda-López et al. 2024) provided the highest values (PABTn: 0.55-0.6 GPa; PBTn: 0.45-0.76 GPa; PABGrd: 0.34-0.60 GPa; Tab. 8). A noticeable feature is that pressure decreases from tonalitic to granodioritic facies (Tab.1).

Thermodynamic modelling provides additional constraints. The appearance of garnet and K-feldspar, not observed in the natural sample, sets upper pressure limits of 0.93 and 0.78 GPa, respectively. Data from mineral and whole rock barometry suggest initial pressures of crystallization of 0.58 to 0.76 GPa and final emplacement pressure at 0.2 to 0.4 GPa. An interval of 0.3 to 0.6 GPa similar to Maravilha charnockite seems reasonable for this unit.

5.5.3.3 Oxygen fugacity

The oxygen fugacity conditions during the crystallization of the Maravilha and Serra Azul charnockites were estimated using Fe/(Fe+Mg) in amphibole and biotite, as these minerals become progressively enriched in Mg with increasing fO_2 (e.g., Anderson

and Smith 1995; Anderson et al. 2008; Cunha et al. 2016; Dall'Agnol et al. 2017; Silva et al. 2020; Mesquita et al. 2025)

The contrasting oxygen fugacity of the studied charnockites is highlighted in the Fe/(Fe+Mg) vs Al^{iv} diagram (Fig. 13a), where the amphiboles of the Maravilha charnockite plot mainly in the transition between the intermediate and low fO_2 fields, with the exception of the AA-109 sample that falls in the high fO_2 field, approaching the samples of Serra Azul charnockite that show higher oxygen fugacity compared to the dominant rocks of Maravilha charnockite.

In the Fe/(Fe+Mg) vs. total Al diagram (Fig. 13b), the biotites from Maravilha charnockite plot int the transition between the magnetite and ilmenite granite fields, except for the sample with more oxidized amphiboles that falls in the magnetite field. The biotite data from the Serra Azul charnockite falls exclusively on the magnetite-series granite field (Fig. 13b).

The diagram Log fO_2 vs temperature (Fig. 13c), based on Ridolfi et al. (2010) estimates, also highlights this redox dichotomy. Most Maravilha samples plot on or near the FMQ buffer, while AA-109 plots slightly above the NNO. In contrast, all samples of Serra Azul charnockite show comparatively higher fO_2 varying from NNO to NNO+2.

The combination of mineral chemistry and thermodynamic modelling indicates that the Maravilha charnockite crystallized under variable redox conditions (Fig. 13a, b, c). Most of the suite formed under reduced conditions at FMQ±0.5, while a subordinate variety of APBGrd (AA-109) crystallized in more oxidized conditions at NNO±0.5. On the other hand, the Serra Azul charnockite crystallized only in oxidizing conditions at NNO±0.7 and even reaching NNO+2 (AA-136).

5.5.3.4 Water content

Experimental data suggest that 5 wt.% H_2O at 0.4 GPa, or 7–9 wt.% H_2O at 0.96 GPa, are required for amphibole to be the silicic liquidus phase and suppress pyroxene crystallization (Naney 1983; Prouteau and Scaillet 2003). Admitting that the studied charnockites were emplaced between 0.3-0.6 GPa (Tab. 1), the occurrence as early crystallizing phases of pyroxenes and, in some cases, fayalite indicates that initial water content in the magma was likely lower than 5 wt%.

To further constrain H_2O contents during crystallization, we estimated melt water concentrations at the time of amphibole growth using the hygrometer of Ridolfi et al. (2010, Tab. 1). In the Maravilha charnockite, the fayalite-bearing samples yielded values of 4.6-7.4 wt%, while pyroxene-bearing varieties showed slightly lower values

(3.6-4.3 wt%). Amphibole-bearing samples lacking these indicative minerals provided higher values from 5.5 to 9.1 wt%. For the Serra Azul charnockite, values range from 5.6 to 7.9 wt% (Tab. 1).

As water tends to increase during crystallization, the value obtained from amphibole chemistry must represent the amount of water at the moment of its crystallization. As amphibole is not the earliest phase to crystallize, the initial water content must have been lower than the value obtained by the hygrometer.

Integrating the mineral data with thermodynamic modeling results, the estimated initial water contents were approximately 3-4 wt% H_2O for the reduced and oxidized varieties of the Maravilha charnockite, and 2-3 wt% for the Serra Azul charnockite.

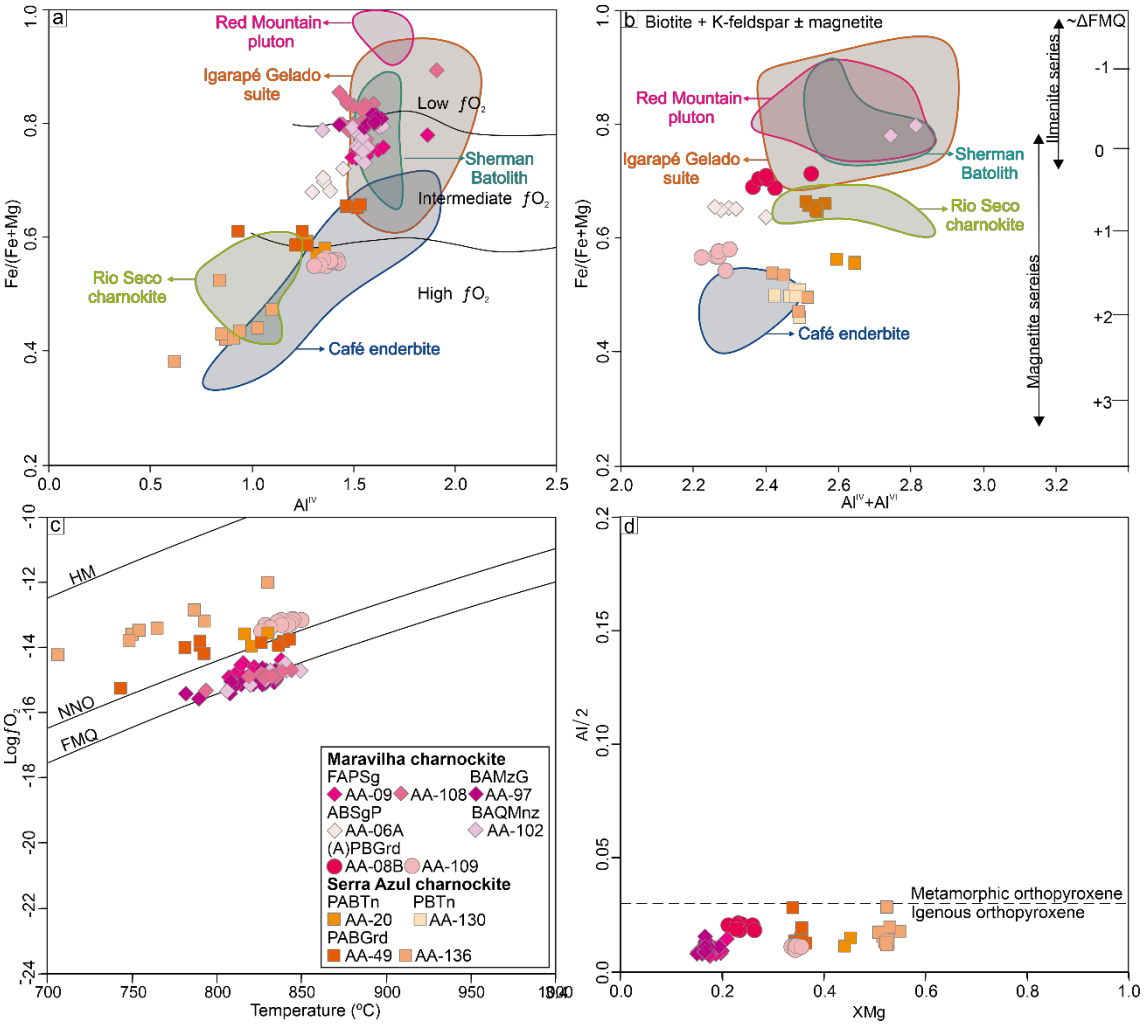


Fig. 13 Estimative of crystallization parameters from Maravilha and Serra Azul charnockites. **a** Fe/(Fe+Mg) vs. AlI^V diagram showing the compositional variation of amphibole (fields after Anderson and Smith 1995). **b** Fe/(Fe+ Mg) vs. Al^{IV} + Al^{VI} diagram showing the compositional variation of biotites (ilmenite and magnetite series according to Anderson et al. 2008). **c** LogfO_2 vs. temperature based on amphibole composition (Ridolfi et al. 2010). **d** XMg vs. Al/2 in orthopyroxene; fields of igneous and metamorphic pyroxenes are after Zhao et al. (2023). Fields for comparison in **a** and **b** are from Red Mountain Pluton (Anderson et al. 2003), Sherman batholith (Frost et al. 1999), Rio Seco charnockite (Felix et al. 2020); Café enderbite (Marangoanha et al., 2022); and Igarapé Gelado suite (Mesquita et al., 2025)

Table 1 Summary of P-T conditions for studied charnockites based on conventional and machine learning thermobarometry

Unit	Maravilha charnockite							Serra Azul charnockite			
Facies	FAPSg		BAMzG	ABSgP	BAQMz	BPMzG	APBGrd	PABTn	PBTn	PABGrd	
Sample	AA-09	AA-108	AA-97	AA-06A	AA-102	AA-08B	AA-109	AA-20	AA-130	AA-49	AA-136
Temperature (ºC)											
Harrison and Watson (1984) Apatite	947	-	870	840	894	904	903	898	927	796	-
Watson and Harrison (1983) Zircon	861	-	941	832	884	779	785	781	842	824	-
Weber and Blundy (2024) WR	944	-	802	941	908	806	918	979	914	899	
Agreda Lópes (2024) Cpx	949-1052	930-996	-	-	-	-	-	771-889	758-883	-	755-968
Putirka (2008) Opx-Cpx	-	-	-	-	-	-	-	838-1078	-	-	766-901
Wood and Bano (1973) Opx-Cpx	-	-	-	-	-	-	-	938-1013	-	-	1012-1019
Putirka (2016) Amp	725-675	693-753	662-756	857-866	707-772	-	793-818	754-760		679-774	711-742
Ridolfi et al. (2010) Amp	809-845	796-846	784-894	1031-1044	808-852	-	828-852	819-832	-	745-844	750-794
Li (2022) Bt	-	-	-	790-809	783-790	784-796	765-775	786-841	776-812	786-835	793-818
Pressure (GPa)											
Hammartson and Zen (1986) Amp	0.44-0.55	0.49-0.57	0.5-0.58	0.35-0.39	0.47-0.55	-	0.33-0.41	0.40	-	0.22-0.5	0.23-0.37
Hollister (1987) Amp	0.45-0.58	0.49-0.55	0.5-0.58	0.36-0.39	0.49-0.58		0.33-0.42	0.41	-	0.29-0.52	0.12-0.29
Schmidt (1992) Amp	0.49-0.59	0.53-0.59	0.54-0.62	0.4-0.43	0.52-0.59		0.38-0.47	0.45	-	0.38-0.49	0.24-0.34
Ridolfi et al. (2010) Amp	0.21-0.27	0.24-0.28	0.24-0.31	0.14-0.15	0.23-0.28		0.15-0.19	0.18	-	0.14-0.25	0.09-0.14
Mutch et al. (2016) Amp	0.38-0.46	0.41-0.48	0.42-0.49	0.32-0.34	0.4-0.46	-	0.30-0.35	0.35		0.27-0.42	0.2-0.28
Li (2022) Bt	-	-	-	0.43-0.51	-	0.57-0.6	0.48-0.56	0.49-0.59	0.45-0.58	0.34-0.6	0.38-0.49
Weber and Blundy (2024) WR	0.55	-	0.56	0.55	0.68	0.54	0.64	0.60	0.76	0.52	-
Oxygen fugacity											
Ridolfi et al. (2010) $\log fO_2$	-14.9 to -13.7	-15.4 to 14.8	-15.6 to -14.7	-12.60 to -12.47	-15.3 to -14.5	-	-13.6 to -13.2	-14.02 to -13.6	-	-15.3 to -13.8	-13.9 to -12.9
Water content											
Ridolfi et al. (2010)	4.6-6.3	6.2-7.4	5.8-9.1	6.56-6.72	5.5-8.1	-	3.6-4.3	6.0-7.1	-	5.8-7.9	5.6-6.9

5.5.4 The effects of P-T-fO_2-H_2O and melt composition on orthopyroxene and fayalite stability in metaluminous magmas

Crystallization experiments have demonstrated that orthopyroxene can crystallize in metaluminous magmas at temperatures from 750 to 900 ºC, under reduced (NNO-1.5) to oxidized conditions (NNO+2.5), and at melt water contents up to ≤.8 wt% (Naney 1983; Dall'Agnol et al. 1999; Scaillet et al. 2016; Zhao et al. 2017, 2018; Huang et al. 2019). Its stability is favored under reduced conditions, where it may crystallize at lower temperatures (~750 ºC) and under higher water content (8 wt%; Dall'Agnol et al. 1999).

The thermodynamic data obtained in this study broadly agrees with the previous experimental results. Orthopyroxene crystallizes at high temperatures in oxidizing conditions (960-850 ºC), and under reduced conditions, its stability extends to lower temperatures (e.g., 810 ºC at 3 wt% H_2O Maravilha charnockite). Pressure does not appear to exert significant influence in orthopyroxene stability, as it remains stable across the modeled pressure range, provided that water content and redox conditions are favorable (section 4). Orthopyroxene may crystallize in water-rich conditions (4.5 and possibily up to 9 wt% H_2O) if the melt is sufficiently ferroan and reduced, as observed in the reduced facies of the Maravilha charnockite. Toward more oxidizing conditions, as seen in the oxidized variety of the Maravilha and in the Serra Azul charnockites, orthopyroxene remains stable at moderate water contents (~5.2 to 6 wt%).

A comparison between the oxidized Maravilha and Serra Azul charnockites, both crystallized under similar redox conditions (near the NNO buffer), reveals that the higher FeOt and MgO in the latter (Tab. S8) favor a broader temperature window for orthopyroxene crystallization at equivalent H_2O in the melt (e.g., 780-1060 ºC at 1 wt% H_2O - Serra Azul; 800-960 ºC at 1 wt% H_2O - oxidized Maravilha). These compositional and redox variations are also highlighted by natural mineral compositions. Orthopyroxene from reduced Maravilha samples shows lower XMg and coexists with fayalite, whereas in oxidized facies and in the Serra Azul charnockite, when present, it has a higher XMg and occurs alongside with amphibole and biotite.

Experimental data on fayalite are limited, but Cunha (2023) showed that fayalite can crystallize in syenogranitic melts with moderate to high water contents (6 to 9 wt% H_2O) under reduced conditions (NNO-1.3) and low-pressure regimes 0.2-0.4 GPa.

The thermodynamic data of the reduced Maravilha charnockite also broadly agree with experimental data. In our modeling, fayalite is a low-pressure phase, stable only below ~0.3 GPa, in a temperature range from 700 to 820 ºC (at 0.2 GPa). Fayalite can

crystallize from water-poor (2.3 wt%) to water rich conditions (6.5 wt%), including water-saturated environments in low temperatures (680-700 ºC, up to 9wt%). A direct relationship between water content and the pressure stability fields is observed, with fayalite stabilizing at higher pressures as water content increases, reaching a maximum of 0.5 GPa at 9 wt% H_2O. Nevertheless, fayalite remains restricted to reduced environments, crystallizing only between FMQ -0.6 to FMQ -1.0. Even in compositions enriched in FeOt, fayalite does not crystallize in oxidizing conditions (e.g., near NNO).

Taken together, the thermodynamic data suggests that orthopyroxene stability is less sensitive to variations in P-T-fO_2-H_2O than fayalite. Orthopyroxene can crystallize from reduced to oxidizing conditions, in either ferroan or magnesian metaluminous magmas. In contrast, fayalite is restricted to reduced conditions, in ferroan metaluminous magmas. These relatively narrow and strict conditions required for the coexistence of fayalite + quartz in charnockites may explain why such assemblages are relatively rare in the geological record (Zhao et al., 2022) compared to the more common orthopyroxene-bearing charnockites.

5.5.5 Comparison with other igneous charnockites

We selected representative igneous charnockites for comparison. Although most lack thermodynamic modeling data, expect for a few examples of peraluminous charnockites with S-type affinity (Zhao et al. 2017; Wang et al. 2023), and a single metaluminous with A-type affinity (Mesquita et al., 2025), crystallization parameters for many charnockites have been defined based on whole-rock and mineral chemistry data, as also employed in this study (section 5.2). The selected charnockites include: the Sherman batholith (Frost et al. 1999) and Red Mountain pluton (Anderson et al. 2003), from the USA; the Rio Seco charnockite (Felix et al. 2020), Café enderbite (Marangoanha et al. 2022), Igarapé Gelado suite (Mesquita et al., 2025) from Carajás Province, Brazil (Tab. 2).

The Sherman batholith (1.43 Ga) comprises distinct facies that may or may not contain fayalite and orthopyroxene. It is classified as metaluminous, ilmenite-series, and A-type granites. Orthopyroxene is ferrosilite; clinopyroxene is dominantly augite, with subordinate pigeonite. Olivine is rich in the fayalite molecule (Fa_{94-98}). Amphibole is hornblende, and biotite is highly ferroan (XFe > 0.75). Fayalite-bearing facies crystallized at > 900 ºC, and pressures of ~0.25 GPa under low water activity and reduced conditions

(FMQ -0.1 to FMQ -0.5) while fayalite-absent facies crystallized at lower temperatures (750 ºC) and under more oxidizing conditions (FMQ +0.5).

The Red Mountain pluton (1.43 Ga), part of the Laramie anorthosite complex, also displays diverse facies from fayalite monzonite to biotite-hornblende granite that may contain fayalite and clinopyroxene. It is a metaluminous, ilmenite-series, A-type granite. Olivine is Fe-rich (Fa_{93-95}). Clinopyroxene is ferroaugite. Amphibole composition varies from hastingsite to ferrohastingsite (XFe_{92-99}). Biotite also has high XFe (0.90-0.99). Fayalite monzonite crystallized at ca. 1000 ºC under extremely reduced conditions (FMQ -1 to FMQ -2), while biotite-hornblende quartz syenite crystallized near or slightly below FMQ. Both facies were emplaced at ~0.3 GPa, under water-unsaturated conditions.

The charnockites from Carajás province include several plutons crystallized between 2.72 and 2.76 Ga (Marangoanha et al. 2019). They comprise granites associated granodiorites and tonalites, and gabbronorites in the case of the Rio Seco charnockite (Felix et al. 2020). The Café and Rio Seco charnockites are metaluminous, magnetite-series, metaluminous, and have a magnesian affinity. In contrast, the Igarapé Gelado suite consists of moderatly oxidized ferroan charnockites with A-type affinity (Mesquita et al., 2025). The pyroxenes are mostly ferrosilite with rare enstatite, while clinopyroxene is augite with restricted diopside. Amphibole is hastingisite and magnesiohornblende. Biotite becomes progressively enriched in Fe from the Rio Seco, Café, and Igarapé Gelado charnockites. These charnockites crystallized at high temperatures (<1000 ºC) and their magmas should had significant water contents (mostly above 4 wt% H_2O – amphibole hygrometer), redox conditions vary from oxidizing (Rio Seco charnockite: NNO ± 0.5 to +1; Café enderbite: NNO+1.7) to reduced (Café enderbite: FMQ; Igarapé Gelado suite: FMQ ± 0.5 to -1). Emplacement pressures range from low (Rio Seco; 0.31-0.19 GPa), to moderate (Igarapé Gelado suite, ~0.55 GPa), to high (Café enderbite, 0.75-0.60 GPa).

The charnockites from Bacajá Domain reveal contrasting behavior concerning mineral chemistry and crystallization parameters but share similarities with other igneous charnockites worldwide. The reduced Maravilha charnockite closely resembles Sherman and Red Mountain plutons in terms of petrography, mineral composition, and crystallization conditions. They crystallized at high temperatures, low pressures, and from relatively dry magmas in reduced conditions. However, the mentioned plutons from the USA are far more reduced (FMQ down to -2) than the Maravilha charnockite (FMQ±0.5). Despite some differences in petrographic features, the reduced Maravilha and Igarapé

Gelado share similar mineral compositions and T–fO_2 conditions, both crystallizing at high temperatures (up to 1000 ºC), under reduced conditions (Maravilha, FMQ ±0.5; Igarapé Gelado, FMQ+0.5).

The oxidized facies of the Maravilha Charnockite crystallized at high temperatures, similar pressures (~0.3-0.6 GPa), and with 4 wt% H_2O of initial water, under more oxidizing conditions (near or slightly above NNO±0.5). It shows contrasts with the reduced association of the Sherman and Red Mountain rocks and is more similar to the Café enderbite in petrography, mineral chemistry and crystallization conditions.

The Serra Azul charnockite share similarities with both Café enderbite and Rio Seco charnockite, particularly in terms of petrography, mineral chemistry and crystallization conditions. They crystallized under high-temperature conditions (above 1000 ºC) in oxidizing conditions (near NNO to NNO +1). The Rio Seco charnockite was emplaced at lower pressures (<0.19 GPa), the Café enderbite at higher pressures (0.75-0.6), and the Serra Azul charnockite in moderate pressure (0.2-0.4 GPa). Initial water content is estimated at 2-3 wt% for Serra Azul charnockite, but the early crystallization of anhydrous phases and the incompatible behavior of water promote an increase in the melt water content in the residual liquid with continuous crystallization. At the time of amphibole crystallization, for a 2 wt % of initial H_2O, it was higher than 4 wt% and possibly reaching ~6-7 wt% (Tab. 1). Similarly, amphibole hygrometry from the Carajás charnockites indicates melt H_2O contents above 4 wt%, reaching up to 5.8 wt% at the time of amphibole crystallization.

Table 2 Comparison between the main crystallization parameters of selected charnockites

	Temperature (ºC)				Pressure (GPa)				fO_2	H_2O activity/content	Reference
Maravilha charnockite reduced	832-941[1]	840-947[2]	662-866[3]	784-894[4]	0.43-0.54[a]	0.55-0.68[b]			Reduced FMQ ±0.5	<4 wt%	this study
Maravilha charnockite oxidized	779-785[1]	904-903[2]	793-818[3]	828-852[4]	0.48-0.6[c]	0.54-0.64[b]	0.15-0.19[c]	0.30-0.35[d]	Oxidized NNO	4 wt%	this study
Serra Azul charnockite	781-842[1]	796-898[2]	679-760[3]	745-844[4]	0.34-0.60[a]	0.52-0.76[b]	0.09-0.25[c]	0.3-0.42[d]	Oxidized NNO to NNO+2	2-3wt%	this work
Sherman Batholith	968-869[5]				0.20-0.38[e]	0.18[f]			Reduced FMQ -0.1 to 0.5	0.7 (4.9 wt.%)	Frost et al. (1999)
Red Mountain pluton	>1000[6]				0.30[g]				Reduced FMQ-1.25 to -2.25	0.2 (2.5 wt.%)	Anderson et al. (2003)
Rio Seco charnockite	800-713[1]	766-666[3]			0.19-0.31[d]				Oxidized NNO	>4 wt%	Felix et al. (2020)
Café enderbite	912-833[1]	817-782[3]			0.28-0.44[c]	0.34-0.60[d]			Oxidized FMQ to NNO+1.7	4.8-5.6 w%	Marangoanha et al (2022)
Igarapé Gelado suite	937–852[1]	899–852[4]	777–720[3]		0.30-0.58[c]	0.47-0.70[d]			Reduced FMQ +0.5	5-6 wt%	Mesquita et al. (2025)

Geothermometers: [1] Watson and Harrison (1983) – Zircon; [2] Watson and Harrison (1983) – Apatite; [3] Putirka (2016) – Amphibole; [4] Ridolfi et al. (2010)- amphibole; [5]QUILF (Andersen et al. 1993); [6] SOLVCALC (Wen and Nekvasil 1994) – ternary feldspar;

Barometers: [a] Li (2022) -Biotite; [b] Weber and Blundy (2024)- whole-rock; [c] Ridolfi et al. (2010) – amphibole; [d] Mutch (2016) – amphibole; [e]QUILF (Andersen et al. 1993) – olivine and pyroxene; [f] Anderson and Smith (1995))- amphibole; [g]Geological evidence;

5.5.6 Global implications for charnockite magmatism

Igneous charnockites are an important constituent of high-grade terranes, where they played a significant role in crustal growth and reworking (e.g., Anderson et al. 2003; Rajesh et al. 2014; Zhao et al. 2018; Peng et al. 2019; Marangoanha et al. 2020). Several studies over the years have reported crystallization conditions based on mineral thermobarometry and experimental petrology (e.g., Naney 1983; Dall'Agnol et al. 1999; Frost et al. 1999; Bogaerts et al. 2006; Mesquita et al. 2025). These studies usually converge that charnockites are derived from water-poor magmas under reduced to mildly oxidized conditions that are necessary for the occurrence of orthopyroxene and fayalite in these rocks.

In this study, the integration of mineral thermobarometry and thermodynamic modeling performed on igneous charnockites from Bacajá Domain, carries a broader implication for understanding the conditions that control the crystallization of orthopyroxene and fayalite. The results presented here challenge the paradigm that metaluminous charnockites are restricted to dry conditions. As demonstrated by thermodynamic modelling, orthopyroxene and fayalite can crystallize from hydrous magmas at mid-crustal pressures, if melt compositions and redox conditions are favorable. The obtained results put in evidence that crystallization of orthopyroxene and fayalite is not solely a product of extreme dry conditions, but rather a complex interaction between melt composition, water content, oxygen fugacity, and pressure.

In a broader perspective, the presence of fayalite and orthopyroxene in metaluminous granitoids must be evaluated with caution, combining effects of redox buffering, melt composition, pressure and water content to better understand the parameters that control their stability. In this sense, thermodynamic modelling is a valuable tool providing the necessary framework to understand the formation of metaluminous charnockitic magmas.

5.6 CONCLUSIONS

The integration of petrography, mineral chemistry, crystallization parameters, and thermodynamic modeling on igneous charnockites from the Bacajá Domain, Amazonian craton, led to the following conclusions:

1. The distinct facies of the Maravilha charnockite evolved in different conditions. The monzonite-granite-charnockite association evolved under reduced conditions (FMQ±0.5). The initial water content was probably ~3 wt%. The

granodiorite-monzogranite facies crystallized under oxidizing conditions (NNO±0.5). The magma's initial water content was likely ~4 wt%. Both associations crystallized below 0.7 GPa, most probably between 0.3-0.6 GPa.

2. The Serra Azul charnockite evolved under oxidizing conditions close to or above the NNO buffer (NNO±0.7). The magma's initial water content was probably 2-3 wt%, and it crystallized below ~0.9 GPa, most probably between 0.3-0.6 GPa.

3. Fayalite stability is constrained to reduced conditions (at or bellow FMQ) and low-pressure environments (≤0.3 GPa), but is not limited to dry melts, crystallizing from moderately to hydrous magmas (possibly up to 9 25).

4. Orthopyroxene exhibits broader crystallization stability, forming under both reduced and oxidized conditions (FMQ-2 to NNO+2.5) and across a wide pressure range, and moderately hydrous magmas (up to 6 wt%). Melts more enriched in FeO and MgO expands the stability of orthopyroxene.

5. These findings challenge the prevailing paradigm that orthopyroxene- and fayalite-bearing charnockite form exclusively under dry conditions. Instead, they support a model where a complex interaction between P-T-fO_2-H_2O parameters controls the phases stability, thereby redefining the conditions under which charnockites can be formed.

ACKNOWLEDGMENTS

This paper is part of the first author's PhD thesis developed at the Instituto de Geociências, UFPA. The authors acknowledge UNIFESSPA staff and students for their previous work in the studied area and for shared information; N.F Botelho, G. Fernandes for their assistance with EPMA analyses. This research received financial support from Conselho Nacional de Desenvolvimento científico e Técnológico (CNPq - R. Dall'Agnol, 304648- 2019-1; G.R.L. Feio - 408396/2023-7) and Fundação Amazônia de Amparo a Estudos e Pesquisas do Estado do Pará (FAPESPA, G.R.L. Feio, E-2024/2285715). This study was also financed in part by the Coordenação de Aperfeiçoamento de Pessoal de Nível Superior - Brasil (CAPES) - Finance Code 001 (A.S.S. Neri - No. 88887.643812/2021-00).

REFERENCES

Ágreda-López M, Parodi V, Musu A, et al (2024) Enhancing machine learning thermobarometry for clinopyroxene-bearing magmas. Comput Geosci 193:105707. https://doi.org/10.1016/j.cageo.2024.105707

Andersen DJ, Lindsley DH, Davidson PM (1993) QUILF: A pascal program to assess equilibria among Fe□Mg□Mn□Ti oxides, pyroxenes, olivine, and quartz. Comput Geosci 19:1333–1350. https://doi.org/10.1016/0098-3004(93)90033-2

Anderson IC, Frost CD, Frost BR (2003) Petrogenesis of the Red Mountain pluton, Laramie anorthosite complex, Wyoming: implications for the origin of A-type granite. Precambrian Res 124:243–267. https://doi.org/10.1016/S0301-9268(03)00088-3

Anderson JL, Barth AP, Wooden JL, Mazdab F (2008) Thermometers and Thermobarometers in Granitic Systems. Rev Mineral Geochem 69:121–142. https://doi.org/10.2138/rmg.2008.69.4

Anderson JL, Smith DR (1995) The effects of temperature and fO2 on the Al-in-hornblende barometer. American Mineralogist 80:549–559. https://doi.org/10.2138/am-1995-5-614

Barros CE de M, Besser ML, Gouvêa Vasconcellos EM (2023) Voluminous Paleoproterozoic plutonic belt of the Bacajá Domain in Amazon Craton: Petrology, geotectonic setting and Pb–Pb zircon evaporation ages. J South Am Earth Sci 130:104491. https://doi.org/10.1016/j.jsames.2023.104491

Bogaerts M, Scaillet B, Auwera J V. (2006) Phase Equilibria of the Lyngdal Granodiorite (Norway): Implications for the Origin of Metaluminous Ferroan Granitoids. Journal of Petrology 47:2405–2431. https://doi.org/10.1093/petrology/egl049

Bucher K, Grapes R (2011) Petrogenesis of Metamorphic Rocks. Springer Berlin Heidelberg, Berlin, Heidelberg

Collins WJ, Beams SD, White AJR, Chappell BW (1982) Nature and origin of A-type granites with particular reference to southeastern Australia. Contributions to Mineralogy and Petrology 80:189–200. https://doi.org/10.1007/BF00374895

Connolly JAD (2005) Computation of phase equilibria by linear programming: A tool for geodynamic modeling and its application to subduction zone decarbonation. Earth Planet Sci Lett 236:524–541. https://doi.org/10.1016/j.epsl.2005.04.033

Cordani UG, Sato K, Teixeira W, et al (2000) Crustal evolution of the South American Platform. Tectonic Evolution of South America 19–40

Cristo LCF (2018) Estudo petrográfico e isotópico (Pb-Pb, U-Pb e Sm-Nd) de rochas metavulcânicas, mineralizações auríferas e rochas granitoides relacionadas ao greenstone belt Três Palmeiras, Volta Grande do Xingu, Domínio Bacajá. Universidade Federal do Pará

Cunha IRV da, Dall'Agnol R, Feio GRL (2016) Mineral chemistry and magnetic petrology of the Archean Planalto Suite, Carajás Province – Amazonian Craton: Implications for the evolution of ferroan Archean granites. J South Am Earth Sci 67:100–121. https://doi.org/10.1016/j.jsames.2016.01.007

Cunha IRV (2023) Petrologia experimental e química mineral das suítes neoarqueanas Vila Jussara e Planalto, Província Carajás, Amazônia, Brasil. PhD Thesis, Universidade Federal do Pará.

Dall'Agnol R, da Cunha IRV, Guimarães FV, et al (2017) Mineralogy, geochemistry, and petrology of Neoarchean ferroan to magnesian granites of Carajás Province, Amazonian Craton: The origin of hydrated granites associated with charnockites. Lithos 277:3–32. https://doi.org/10.1016/j.lithos.2016.09.032

Dall'Agnol R, Scaillet B, Pichavant M (1999) An Experimental Study of a Lower Proterozoic A-type Granite from theEastern Amazonian Craton, Brazil. Journal of Petrology 40:1673–1698. https://doi.org/10.1093/petrology/40.11.1673

De Capitani C, Petrakakis K (2010) The computation of equilibrium assemblage diagrams with Theriak/Domino software. American Mineralogist 95:1006–1016. https://doi.org/10.2138/am.2010.3354

Felix WQ, Oliveira DC, Silva LR, Silva FF (2020) Charnockites from Carajás Province, SE Amazonian Craton (Brazil): Petrogenetic constraints and intensive crystallization parameters. J South Am Earth Sci 101:102598. https://doi.org/10.1016/j.jsames.2020.102598

Frost BR, Frost CD (2008) On charnockites. Gondwana Research 13:30–44. https://doi.org/10.1016/j.gr.2007.07.006

Frost CD, Frost BR, Chamberlain KR, Edwards BR (1999) Petrogenesis of the 1.43 Ga Sherman Batholith, SE Wyoming, USA: a Reduced, Rapakivi-type Anorogenic Granite. Journal of Petrology 40:1771–1802. https://doi.org/10.1093/petroj/40.12.1771

García-Arias M (2020) Consistency of the activity–composition models of Holland, Green, and Powell (2018) with experiments on natural and synthetic compositions:

A comparative study. Journal of Metamorphic Geology 38:993–1010. https://doi.org/10.1111/jmg.12557

Gómez-Frutos D, Castro A (2022) Sanukitoid crystallization relations at 1.0 and 0.3 GPa. Lithos 414–415:106632. https://doi.org/10.1016/j.lithos.2022.106632

Gualda GAR, Ghiorso MS, Lemons R V., Carley TL (2012) Rhyolite-MELTS: a Modified Calibration of MELTS Optimized for Silica-rich, Fluid-bearing Magmatic Systems. Journal of Petrology 53:875–890. https://doi.org/10.1093/petrology/egr080

Guo C, Zeng L, Li Q, et al (2016) Hybrid genesis of Jurassic fayalite-bearing felsic subvolcanic rocks in South China: Inspired by petrography, geochronology, and Sr–Nd–O–Hf isotopes. Lithos 264:175–188. https://doi.org/10.1016/j.lithos.2016.08.020

Hammarstrom JM, Zen E (1986) Aluminum in hornblende: An empirical igneous geobarometer. American Mineralogy 71:

Harlov DE (2012) The potential role of fluids during regional granulite-facies dehydration in the lower crust. Geoscience Frontiers 3:813–827. https://doi.org/10.1016/j.gsf.2012.03.007

Harrison TM, Watson EB (1984) The behavior of apatite during crustal anatexis: Equilibrium and kinetic considerations. Geochim Cosmochim Acta 48:1467–1477. https://doi.org/10.1016/0016-7037(84)90403-4

Holland TJB, Green ECR, Powell R (2018) Melting of Peridotites through to Granites: A Simple Thermodynamic Model in the System KNCFMASHTOCr. Journal of Petrology 59:881–900. https://doi.org/10.1093/petrology/egy048

Holland TJB, Powell R (2011) An improved and extended internally consistent thermodynamic dataset for phases of petrological interest, involving a new equation of state for solids. Journal of Metamorphic Geology 29:333–383. https://doi.org/10.1111/j.1525-1314.2010.00923.x

Hollister LS, Grissom GC, Peters EK, et al (1987) Confirmation of the empirical correlation of Al in hornblende with pressure of solidification of calc-alkaline plutons. American Mineralogist 72:231–239

Huang F, Scaillet B, Wang R, et al (2019) Experimental Constraints on Intensive Crystallization Parameters and Fractionation in A-Type Granites: A Case Study on the Qitianling Pluton, South China. J Geophys Res Solid Earth 124:10132–10152. https://doi.org/10.1029/2019JB017490

Hurley PM, Almeida FFM, Melcher GC, et al (1967) Test of continental drift by means of radiometric ages. Science (1979) 495–500

Janasi V de A (2002) Elemental and Sr–Nd isotope geochemistry of two Neoproterozoic mangerite suites in SE Brazil: implications for the origin of the mangerite–charnockite–granite series. Precambrian Res 119:301–327. https://doi.org/10.1016/S0301-9268(02)00127-4

Kroonenberg SB, De Roever EWF, Fraga LM, et al (2016) Paleoproterozoic evolution of the Guiana Shield in Suriname: A revised model. Geologie en Mijnbouw/Netherlands Journal of Geosciences 95:491–522. https://doi.org/10.1017/njg.2016.10

Leake; BE, Woolley; AR, Arps; CES, et al (1997) Nomenclature of amphiboles; Report of the Subcommittee on Amphiboles of the International Mineralogical Association, Commission on New Minerals and Mineral Name. American Mineralogist 82:1019–1037.

Li X, Zhang C (2022) Machine Learning Thermobarometry for Biotite-Bearing Magmas. J Geophys Res Solid Earth 127:. https://doi.org/10.1029/2022JB024137

Liu X, Wang Q, Liu X-J, et al (2024) Early Cretaceous fayalite-, ferrosilite-, and biotite-bearing rhyolitic porphyries in the Baishuizhai area, South China: Formation by fractional crystallization in the shallow crust. Lithos 482–483:107694. https://doi.org/10.1016/j.lithos.2024.107694

Macambira EMB, Ricci PSF (2015) Geologia e recursos minerais da Folha Tucuruí – SA.22-Z-C, Estado do Pará, 1st edn. CPRM, Belém

Macambira MJB, Vasquez ML, Monteiro PC, Armstrong RA (2022) Neoarchean to Rhyacian crustal records along the Middle Xingu River area, Amazonian craton. Brazilian Journal of Geology 52:. https://doi.org/10.1590/2317-4889202220220017

Macambira MJB, Vasquez ML, Silva DCC, et al (2009) Crustal growth of the central-eastern Paleoproterozoic domain, SW Amazonian craton: Juvenile accretion vs. reworking. J South Am Earth Sci 27:235–246. https://doi.org/10.1016/j.jsames.2009.02.001

Magalhães LB, Macambira MJB, Macambira EMB, Ricci P dos SF (2023) Crustal growth in the northeast portion of the Rhyacian Bacajá Domain, SE Amazonian craton, based on U-Pb, Lu-Hf, and Sm-Nd data. Brazilian Journal of Geology 53:. https://doi.org/10.1590/2317-4889202320220068

Marangoanha B, de Oliveira DC, Galarza MA, Marques GT (2020) Crustal anatexis and mantle-derived magmas forming Neoarchean A-type granitoids in Carajás Province, northern Brazil: Petrological evidence and tectonic control. Precambrian Res 338:. https://doi.org/10.1016/j.precamres.2019.105585

Marangoanha B, Oliveira DC de, Dall'Agnol R (2019) The Archean granulite-enderbite complex of the northern Carajás province, Amazonian craton (Brazil): Origin and implications for crustal growth and cratonization. Lithos 350–351:. https://doi.org/10.1016/j.lithos.2019.105275

Marangoanha B, Oliveira DC de, Lamarão CN, et al (2022) Geothermobarometry and geochemical modeling of Archean charnockites from Carajás Province, Amazonian craton, Brazil. Brazilian Journal of Geology 52:. https://doi.org/10.1590/2317-4889202220210092

Mesquita CJS, Dall'Agnol R, Neri AS da S, et al (2025) Crystallization parameters and thermodynamic modeling of the Igarapé Gelado suite: Implications for the Neoarchean magmatism of the Carajás province, Brazil. J South Am Earth Sci 153:105357. https://doi.org/10.1016/j.jsames.2025.105357

Neri, A.S.S., Dall'Agnol, R., Dantas, E.L., Feio, G.R.L., Almeida, J.A.C., Galarza, M.A., Rhyacian magmatism in the southern Bacajá Domain: Implications for the crustal evolution of SE Amazonian Craton, Brazil. Precambrian Researc*h*, manuscript submitted for publication.

Naney MT (1983) Phase equilibria of rock-forming ferromagnesian silicates in graniic systems. Am J Sci 283:993–1033

Oyawoye MO (1965) Bauchite : a New Variety in the Quartz Monzonitic Series. Nature 205:689–689. https://doi.org/10.1038/205689a0

Peng P, Qin Z, Sun F, et al (2019) Nature of charnockite and Closepet granite in the Dharwar Craton: Implications for the architecture of the Archean crust. Precambrian Res 334:105478. https://doi.org/10.1016/j.precamres.2019.105478

Prouteau G, Scaillet B (2003) Experimental Constraints on the Origin of the 1991 Pinatubo Dacite. Journal of Petrology 44:2203–2241. https://doi.org/10.1093/petrology/egg075

Putirka K (2016) Amphibole thermometers and barometers for igneous systems and some implications for eruption mechanisms of felsic magmas at arc volcanoes. American Mineralogist 101:841–858. https://doi.org/10.2138/am-2016-5506

Putirka KD (2008) Thermometers and Barometers for Volcanic Systems. Rev Mineral Geochem 69:61–120. https://doi.org/10.2138/rmg.2008.69.3

Rajesh HM, Santosh M, Wan Y, et al (2014) Ultrahigh temperature granulites and magnesian charnockites: Evidence for Neoarchean accretion along the northern margin of the Kaapvaal Craton. Precambrian Res 246:150–159. https://doi.org/10.1016/j.precamres.2014.03.001

Rajesh HM, Santosh M, Yoshikura S (2011) The Nagercoil Charnockite: a Magnesian, Calcic to Calc-alkalic Granitoid Dehydrated during a Granulite-facies Metamorphic Event. Journal of Petrology 52:375–400. https://doi.org/10.1093/petrology/egq084

Ridolfi F, Renzulli A, Puerini M (2010) Stability and chemical equilibrium of amphibole in calc-alkaline magmas: an overview, new thermobarometric formulations and application to subduction-related volcanoes. Contributions to

Santos JOS, Hartmann LA, Faria MS, et al (2006) a Compartimentação Do Cráton Amazonas Em Províncias : Avanços Ocorridos No Período 2000-2006. In: IX Simpósio de Geologia da Amazônica. Sociedade Brasileira de Geologia, Belém

Scaillet B, Holtz F, Pichavant M (2016) Experimental Constraints on the Formation of Silicic Magmas. Elements 12:109–114. https://doi.org/10.2113/gselements.12.2.109

Schilling J, Frost BR, Marks MAW, et al (2011) Fe-Ti oxide-silicate (QUIlF-type) equilibria in feldspathoid-bearing systems. American Mineralogist 96:100–110. https://doi.org/10.2138/am.2011.3596

Schmidt MW (1992) Amphibole composition in tonalite as a function of pressure: an experimental calibration of the Al-in-hornblende barometer. Contributions to Mineralogy and Petrology 110:304–310. https://doi.org/10.1007/BF00310745

Shellnutt JG, Zhou M-F (2008) Permian, rifting related fayalite syenite in the Panxi region, SW China. Lithos 101:54–73. https://doi.org/10.1016/j.lithos.2007.07.007

Silva AS da, Feio GRL, Alves JPS, et al (2020) Mineralogy, petrology, and origin of the Pedra Branca Suite: a tonalitic-trondhjemitic association with high Zr, Ti and Y, Carajás Province, Amazonian Craton. Brazilian Journal of Geology 50:. https://doi.org/10.1590/2317-4889202020190093

Tassinari CCG, Macambira MJB (2004) A evolução tectônica do Craton Amazônico. In: Mantesso-Neto V, Bartorelli A, Carneiro CDR, Brito Neves BB (eds) Geologia do Continente Sul Americano: Evoluc¸ ão da obra de Fernando Flávio Marques Almeida. São Paulo, pp 471–486

Touret JLR, Huizenga JM (2012) Charnockite microstructures: From magmatic to metamorphic. Geoscience Frontiers 3:745–753. https://doi.org/10.1016/j.gsf.2012.05.004

Tsunogae T, Osanai Y, Owada M, et al (2003) High fluorine pargasites in ultrahigh temperature granulites from Tonagh Island in the Archean Napier Complex, East Antarctica. Lithos 70:21–38. https://doi.org/10.1016/S0024-4937(03)00087-2

Vasquez ML (2006) Geocronologia em zircão, monazita e granada e isótopos de Nd das associações litológicas da porção oeste do Domínio Bacajá: evolução crustal da porção meridional da Província Maroni-Itacaiúnas – Sudeste Do Cráton Amazônico. Universidade Federal do Pará

Vasquez ML, Macambira MJB, Armstrong RA (2008) Zircon geochronology of granitoids from the western Bacajá Domain, southeastern Amazonian craton, Brazil: Neoarchean to Orosirian evolution. Precambrian Res 161:279–302. https://doi.org/10.1016/j.precamres.2007.09.001

Vasquez ML;, Rosa-Costa LT; (2008) Geologia e Recursos Minerais do Estado do Pará : Sistema de Informações Geográficas – SIG : texto explicativo dos mapas Geológico e Tectônico e de Recursos Minerais do Estado do Pará, 1st edn. Brazilian Geological Service, CPRM, Belém

Vásquez P, Glodny J, Franz G, et al (2009) Origin of fayalite granitoids: New insights from the Cobquecura Pluton, Chile, and its metapelitic xenoliths. Lithos 110:181–198. https://doi.org/10.1016/j.lithos.2009.01.001

Vieira C, Amaral W, Holanda Santos F (2022) Petrography, geochemistry and zircon U-Pb geochronology of the Siderian-Rhyacian granitoids of NW Bacajá Domain, Amazonian Craton. Journal of the Geological Survey Of Brazil 5:. https://doi.org/10.29396/jgsb.2022.v5.n3.1

Wang B, Wei C, Tian W (2023) Ultrahigh-Temperature Anatexis of Greywackic Granulites Generates Peraluminous Charnockites in the Jining Complex, North China Craton. Journal of Petrology 64:. https://doi.org/10.1093/petrology/egad030

Watson EB, Harrison TM (1983) Zircon saturation revisited: temperature and composition effects in a variety of crustal magma types. Earth Planet Sci Lett 64:295–304. https://doi.org/10.1016/0012-821X(83)90211-X

Weber G, Blundy J (2024) A Machine Learning-Based Thermobarometer for Magmatic Liquids. Journal of Petrology 65:. https://doi.org/10.1093/petrology/egae020

Wen S, Nekvasil H (1994) SOLVALC: An interactive graphics program package for calculating the ternary feldspar solvus and for two-feldspar geothermometry. Comput Geosci 20:1025–1040. https://doi.org/10.1016/0098-3004(94)90039-6

Whitney, D.L. and Evans, B.W. 2010. Abbreviations for names of rock-forming minerals. American Mineralogist, 95, 185–187, https://doi.org/10.2138/am.2010.3371

Wood BJ, Banno S (1973) Garnet-orthopyroxene and orthopyroxene-clinopyroxene relationships in simple and complex systems. Contributions to Mineralogy and Petrology 42:109–124. https://doi.org/10.1007/BF00371501

Xiang H, Connolly JAD (2022) GeoPS: An interactive visual computing tool for thermodynamic modelling of phase equilibria. Journal of Metamorphic Geology 40:243–255. https://doi.org/10.1111/jmg.12626

Xie Y, Li X, Mo X, et al (2023) The effects of the source composition on the origin of orthopyroxene-bearing adakitic granitoid in West Qinling, Central China. Geoscience Frontiers 14:101554. https://doi.org/10.1016/j.gsf.2023.101554

Yavuz F (2013) WinPyrox: A Windows program for pyroxene calculation classification and thermobarometry. American Mineralogist 98:1338–1359. https://doi.org/10.2138/am.2013.4292

Yavuz F, Döner Z (2017) WinAmptb : A Windows program for calcic amphibole thermobarometry. Periodico di Mineralogia 86:. https://doi.org/https://doi.org/10.2451/2017PM710

Zhao K, Xu X, Erdmann S (2018) Thermodynamic modeling for an incrementally fractionated granite magma system: Implications for the origin of igneous charnockite. Earth Planet Sci Lett 499:230–242. https://doi.org/10.1016/j.epsl.2018.07.039

Zhao K, Xu X, Erdmann S (2017) Crystallization conditions of peraluminous charnockites: constraints from mineral thermometry and thermodynamic modelling. Contributions to Mineralogy and Petrology 172:26. https://doi.org/10.1007/s00410-017-1344-2

Zhao K, Xu X, Klemd R, et al (2023) A review of the genetic mechanisms generating igneous charnockite: CO2 flushing and crystal-melt segregation in mushy reservoirs. Earth Sci Rev 237:104295. https://doi.org/10.1016/j.earscirev.2022.104295

SUPPLEMENTARY MATERIAL 1 - TABLES

Table S 1 Representative modal compositions from Maravilha and Serra Azul charnockites

Unit	Maravilha Charnockite									Serra Azul charnockite						
Facies	FPASG		BAMzG	ABSG	BAQMz	BAQS	PABGrdMzG		PBMzG	PABTon		PBTonGrd		PABGd		BMzG
Sample	AA-09	**AA-108**	**AA-97**	**AA-06A**	**AA-102**	AA-119A	**AA-109**	AA-08D	**AA-08B**	AA-15	**AA-20**	**AA-130**	AA-02	**AA-49**	**AA-136**	AA-50
Quartz	22.9	20.7	33.6	30.9	10.1	8.5	19.2	44.2	49.05	19.11	17.55	22.1	32.1	20.4	20.1	39.3
Plagioclase	12.9	13.1	20.4	11.5	35.2	12.8	56.1	16.1	10.8	40.95	46.55	62.2	42.4	53.9	53.1	32.5
K-feldspar	46.9	45.9	23.4	43	34.8	65.2	12.3	17.7	23.9	-	-	5.7	6.6	9	11.5	17.2
Fayalite	3.5	4.1	-	-	-	-	-	-	-	-	-	-	-	-		-
Orthopyroxene	3.8	5.3	-	-	-	-	2.6	-	1.4	-	2.45	-	1	1.9	1.8	-
Clinopyroxene	3.1	3.5	-	-	-	-	2.1	1.2	-	-	0.65	2.1	-	0.1	2.2	-
Amphibole	6.6	6.9	10.1	0.5	9.1	6.3	2.1	4.85	-	17.11	15.55		-	1.9	3.8	-
Biotite	-	-	7.1	12.95	6.1	3.5	5.5	5.3	6.8	22.04	15.8	8.9	15	11	7.1	11.4
Zircon	x	x	x	x			x	x	x	-	x		0.1	x	x	0.1
Allanite	-	-	0.9	0.05	0.8	0.7	-	0.1	-	-	x	-	-	-	-	-
Apatite	x	x	x	0.5	x	x	X	0.35	0.3	x	0.45	x	0.2	0.2	x	0.2
Opaque minerals	0.3	0.5	0.5	0.35	0.4	0.5	0.4	0.35	0.1	0.22	0.15	0.2	0.2	0.7	0.2	x
Chlorite	-	-	-	0.6	x	x	-	x	0.55	x	0.3	x	0.4	0.6	x	-
Secondary amphibole	-	-	4	-	2.3	2.4	-	-	-	-	-	0.2	2	0.3	0.2	0.3
Q	27.69	25.97	43.41	36.82	12.61	9.83	21.92	56.667	44.43	32.27	32.39	24.56	39.58	24.57	23.73	44.16
A	56.71	57.59	30.23	51.26	43.45	75.38	14.04	22.692	15.99	0	0	6.33	8.14	36.15	13.58	36.52
P	15.6	16.44	26.36	11.92	43.94	14.79	64.04	20.641	216,534	67.73	67.61	69.11	52.28	39.28	62.69	19.33
M'	17.3	20.03	22.6	12.95	19.9	13.5	12.7	11.2	9.35	39.56	34.15	11.8	17.9	13	15.3	11.6

x – found in the thin section, but not counted; - absent in the thin section. The samples in bold were analyzed via EPMA

Table S 1 Representative compositions of fayalite, orthopyroxene and clinopyroxene from the Maravilha charnockite

	Fayalite				orthopyroxene								Clinopyroxene			
Sample	AA-09		AA-108		AA-09		AA-108		BPMzG		APBGrd		AA-09		AA-108	
Facies	FAPSg				FAPSg				AA-08B		AA-109		FAPSg			
Analyses	C2.6	C1.5	C1.4	C1.9	C2.1	C2.7	C2.1	C4.3	C4.1	C4.2	C2.2	C1.1	C1.1	C1.3	C1.4	C2.1[
Texture	core	rim	core	rim	core	rim	rim	core	rim	core	core	core	lamellae	lamellae	lamellae	lamellae
SiO_2	29.20	29.66	29.53	29.66	48.47	46.64	46.90	47.27	46.88	47.28	48.56	48.57	49.58	50.15	49.18	49.17
TiO_2	0.00	0.00	0.03	0.08	0.08	0.25	0.00	0.17	0.13	0.15	0.19	0.13	0.17	0.15	0.07	0.17
Al_2O_3	0.00	0.00	0.00	0.00	0.50	0.25	0.28	0.43	0.77	0.77	0.38	0.37	0.65	0.77	0.81	0.72
Fe_2O_3	-	-	-	-	0.42	1.49	0.51	0.00	0.00	0.00	0.00	0.24	0.92	0.23	0.55	1.73
FeO	66.54	66.24	66.16	66.37	35.29	42.95	44.52	44.10	41.66	41.46	37.05	36.52	23.02	23.29	26.56	23.07
MgO	2.07	2.41	2.24	1.99	5.06	5.39	5.18	5.24	7.29	7.47	11.00	11.21	4.95	4.95	4.68	4.61
MnO	0.04	0.11	0.01	0.03	0.34	1.05	0.91	1.20	0.33	0.35	1.10	1.06	0.45	0.35	0.54	0.51
CaO	1.14	1.06	1.11	1.22	0.67	0.97	0.95	0.84	1.01	1.05	0.74	0.79	20.32	20.59	17.41	20.17
Na_2O	0.03	0.02	0.00	0.00	0.15	0.03	0.02	0.02	0.00	0.07	0.01	0.05	0.24	0.26	0.23	0.27
K_2O	0.00	0.00	0.01	0.00	0.00	0.00	0.01	0.00	0.00	0.00	0.01	0.01	0.00	0.01	0.00	0.01
Sum	99.03	99.51	99.08	99.34	99.97	99.03	99.27	99.27	98.07	98.59	99.02	98.94	100.30	100.74	100.04	100.42
	Formulae recalculated on the basis of 4 oxygens				Formulae recalculated on the basis of 6 oxygen											
Si	0.987	0.993	0.995	0.997	1.990	1.981	1.989	1.993	1.977	1.978	1.978	1.978	1.974	1.983	1.979	1.962
Ti	-	-	-	-	0.002	0.008	0.000	0.005	0.004	0.005	0.006	0.004	0.005	0.004	0.002	0.005
Al	-	-	-	-	0.024	0.013	0.014	0.021	0.038	0.038	0.018	0.018	0.031	0.036	0.039	0.034
Fe^{3+}	-	-	-	-	0.013	0.048	0.016	0.000	0.000	0.000	0.000	0.007	0.028	0.007	0.016	0.052
Fe^{2+}	1.882	1.854	1.863	1.865	1.212	1.526	1.579	1.555	1.469	1.451	1.262	1.244	0.766	0.770	0.894	0.770
Mn	0.033	0.030	0.032	0.035	0.310	0.341	0.327	0.329	0.458	0.466	0.668	0.680	0.015	0.012	0.019	0.017
Mg	0.105	0.120	0.112	0.100	0.023	0.035	0.034	0.030	0.036	0.037	0.026	0.027	0.294	0.292	0.281	0.274
Ca	0.001	0.004	0.000	0.001	0.411	0.048	0.041	0.054	0.015	0.016	0.048	0.046	0.867	0.872	0.751	0.862
Na	-	-	-	-	0.012	0.003	0.001	0.001	0.000	0.005	0.001	0.004	0.019	0.020	0.018	0.021
K	-	-	-	-	0.000	0.000	0.000	0.000	0.000	0.000	0.001	0.000	0.000	0.001	0.000	0.001
Fa(%)	0.93	0.93	0.93	0.93	-	-	-	-	-	-	-	-	-	-	-	-
XMg	-	-	-	-	0.20	0.18	0.17	0.18	0.24	0.24	0.35	0.35	0.27	0.27	0.24	0.25

Fa(%)=Fe/(Fe+Mg)*100; XMg = Mg/(Mg+Fe^{2+})

Table S 2 Representative chemical composition of amphibole and biotite of the Maravilha charnockite

	Amphibole												Biotite					
Sample	AA-09		AA-108		AA-97		AA-06		AA-102		APBGrd		ABSgP		BPMzG		APBGrd	
Facies	FAPSg				BAMzG		ABSgP		BAQMz		AA-109		AA-06		AA-08B		AA-109	
Analyses	C1.2	C1.5	C1.2	C1.1	C4.3	C1.3	C3.4	C3.1	C4.2	C4.3	C2.1	C2.3	C1.1	C1.2	C4.1	C4.2	C2.2	C1.2
Texture	core	rim	core	rim	core	rim	core	rim	core	rim	rim	core	core	rim	core	rim	core	core
SiO_2	41.38	41.14	40.19	40.65	41.06	39.48	42.80	42.66	40.93	40.91	43.16	42.60	36.23	36.76	34.88	34.98	35.98	36.16
TiO_2	1.91	1.14	2.11	1.58	1.91	1.68	0.72	0.77	2.36	2.08	1.85	2.10	4.25	3.80	3.93	3.80	4.30	4.28
Al_2O_3	8.34	8.93	9.72	9.98	8.91	9.76	8.57	8.53	9.56	9.19	8.02	8.76	12.39	12.35	12.54	12.69	12.00	12.31
Fe_2O_3*	5.09	7.08	5.00	5.41	4.60	3.73	5.90	7.73	3.58	3.51	3.81	2.20	-	-	-	-	-	-
FeO*	21.25	19.96	22.70	21.89	22.78	24.32	19.59	17.52	21.41	22.55	16.69	17.53	24.95	25.18	26.73	26.79	22.35	22.74
MgO	5.28	5.35	3.87	4.02	4.19	3.21	6.03	6.59	5.24	4.71	9.18	8.87	7.61	7.83	6.54	6.52	9.93	9.65
MnO	0.26	0.20	0.23	0.26	0.22	0.23	0.60	0.49	0.27	0.21	0.16	0.18	0.21	0.28	0.16	0.19	0.00	0.12
CaO	10.43	10.41	10.48	10.58	10.59	10.73	10.93	10.61	10.70	10.88	11.07	11.14	0.02	0.02	0.01	0.03	0.02	0.05
Na_2O	1.63	1.73	1.60	1.36	1.48	1.50	1.37	1.39	1.49	1.39	1.80	1.87	0.15	0.15	0.05	0.05	0.09	0.06
K_2O	1.51	1.40	1.44	1.29	1.24	1.51	1.29	1.20	1.58	1.47	1.25	1.35	9.50	9.58	9.43	9.43	9.47	9.18
F	1.45	1.65	1.58	1.63	0.53	0.43	1.58	1.60	1.72	1.65	0.00	0.00	0.15	0.22	1.58	1.78	0.02	0.01
Cl	0.10	0.08	0.60	0.49	0.04	0.05	0.08	0.02	0.34	0.46	0.83	0.71	1.80	1.82	0.07	0.05	1.32	1.02
H2O*	1.18	1.09	0.04	0.04	1.61	1.62	1.18	1.16	0.07	0.03	1.73	1.76	3.18	3.17	2.87	2.79	3.38	3.48
Sum	98.25	98.43	97.38	97.08	98.60	97.77	98.95	98.64	97.17	96.94	98.73	98.34	98.48	99.12	97.13	97.27	97.53	98.02
	Formulae recalculated on the basis of 23 oxygen												Formulae recalculated on the basis of 22 oxygens					
Si	6.524	6.459	6.369	6.427	6.508	6.381	6.635	6.596	6.430	6.474	6.612	6.563	5.719	5.764	5.636	5.638	5.683	5.719
Ti	0.226	0.134	0.252	0.188	0.228	0.204	0.084	0.090	0.279	0.248	0.213	0.243	0.505	0.448	0.478	0.461	0.511	0.505
Al	1.549	1.652	1.815	1.859	1.665	1.859	1.565	1.554	1.769	1.713	1.448	1.590	2.305	2.282	2.388	2.411	2.234	2.305
Fe^{3+}	0.604	0.837	0.596	0.644	0.549	0.453	0.688	0.899	0.423	0.418	0.439	0.255	0.000	0.000	0.000	0.000	0.000	0.000
Fe^{2+}	2.802	2.620	3.008	2.895	3.019	3.287	2.540	2.265	2.813	2.984	2.139	2.258	3.294	3.302	3.612	3.611	2.952	3.294
Mg	1.242	1.252	0.915	0.948	0.991	0.774	1.395	1.520	1.226	1.112	2.097	2.038	1.791	1.830	1.575	1.567	2.338	1.791
Mn	0.034	0.027	0.031	0.035	0.030	0.032	0.079	0.064	0.035	0.029	0.021	0.024	0.028	0.037	0.022	0.026	0.000	0.028
Ca	1.762	1.750	1.779	1.792	1.799	1.858	1.816	1.758	1.801	1.844	1.817	1.839	0.003	0.003	0.002	0.005	0.003	0.003
Na	0.500	0.527	0.490	0.418	0.454	0.470	0.410	0.416	0.455	0.425	0.535	0.559	0.046	0.046	0.016	0.016	0.028	0.046
K	0.303	0.281	0.291	0.261	0.251	0.311	0.254	0.237	0.316	0.298	0.244	0.265	1.913	1.916	1.944	1.939	1.908	1.913
F	0.722	0.818	0.302	0.245	0.263	0.221	0.037	0.012	0.168	0.229	0.000	0.000	0.075	0.109	0.807	0.907	0.010	0.075
Cl	0.026	0.021	0.011	0.010	0.012	0.013	0.309	0.305	0.019	0.009	0.216	0.186	0.248	0.248	0.010	0.007	0.181	0.139
XMg	0.31	0.32	0.23	0.25	0.25	0.19	0.35	0.40	0.30	0.27	0.50	0.47	0.35	0.36	0.30	0.30	0.44	0.35

XMg = $Mg/(Mg+Fe^{2+})$

T**able S 4** Representative chemical compositions of secondary amphibole from the Serra Azul charnockite

Sample	AA-97		AA-102	
Facies	BAMzG		BAQMz	
Analyses	C2.8	C2.9	C3.3	c3.4
Texture	core	rim	core	rim
SiO_2	48.81	49.30	49.85	50.18
TiO_2	0.00	0.00	0.00	0.11
Al_2O_3	0.50	0.33	0.45	0.45
Fe^2O_3*	0.00	0.00	0.00	0.00
FeO*	39.41	39.34	36.40	37.85
MgO	5.54	5.67	6.90	6.77
MnO	0.81	0.87	0.72	0.65
CaO	0.95	0.76	1.77	1.24
Na_2O	0.06	0.05	0.04	0.04
K_2O	0.04	0.00	0.01	0.01
F	1.77	1.77	1.78	1.86
Cl	0.15	0.17	0.21	0.07
H_2O*	0.01	0.00	0.00	0.00
Sum	98.09	98.23	98.11	99.24
Si	7.924	7.974	7.971	7.957
Ti	0.000	0.000	0.000	0.013
Al	0.096	0.062	0.085	0.084
Fe^{3+}	0.000	0.000	0.000	0.000
Fe^{2+}	5.350	5.321	4.868	5.018
Mg	1.342	1.367	1.644	1.601
Mn	0.111	0.119	0.097	0.087
Ca	0.165	0.131	0.304	0.210
Na	0.020	0.016	0.013	0.014
K	0.008	0.001	0.002	0.001
F	0.077	0.089	0.104	0.035
Cl	0.002	0.000	0.000	0.001
XMg	0.20	0.20	0.25	0.24

XMg = $Mg/(Mg+Fe^{2+})$

Table S 5 Representative chemical composition of plagioclase of the Maravilha charnockite

Sample	AA-09		AA-108		AA-97		AA-06		AA-102		BPMzG		APBGrd	
Facies	FAPSg				BAMzG		ABSgP		BAQMz		AA-08B		AA-109	
Analyses	C2.2	C2.8	C1.1	C1.2	C1.10	C1.16	C4.7	C4.3	C4.1	c5.4	C3.1	C3.4	C2.4	C2.8
Texture	rim	core	rim	core	rim	core	rim	core	rim	core	rim	core	rim	core
SiO_2	59.63	59.13	60.05	59.81	60.62	59.78	59.82	55.76	60.31	59.77	59.74	54.89	60.24	58.82
TiO_2	0.07	0.00	0.00	0.00	0.01	0.03	0.00	0.00	0.00	0.00	0.03	0.13	0.00	0.00
Al_2O_3	24.37	25.19	25.33	25.02	24.16	24.48	24.62	27.65	25.06	25.33	24.60	28.20	24.16	25.13
Fe_2O_3	0.35	0.08	0.09	0.15	0.12	0.06	0.10	0.11	0.12	0.06	0.04	0.06	0.10	0.10
MgO	0.03	0.00	0.00	0.01	0.00	0.02	0.00	0.01	0.00	0.01	0.00	0.01	0.00	0.01
MnO	0.02	0.00	0.00	0.03	0.00	0.00	0.00	0.00	0.00	0.00	0.00	0.00	0.01	0.02
CaO	6.18	7.38	6.82	7.08	5.93	6.53	6.73	10.01	6.70	7.24	6.49	10.63	6.03	7.13
Na_2O	8.01	7.17	7.74	7.85	8.40	7.99	8.03	6.24	7.87	7.32	8.00	5.62	10.09	9.23
K_2O	0.38	0.33	0.18	0.23	0.26	0.33	0.31	0.16	0.23	0.26	0.21	0.16	0.29	0.28
Sum	99.06	99.27	100.20	100.17	99.51	99.23	99.61	99.94	100.30	100.00	99.12	99.70	100.91	100.71
Formulae recalculated on the basis of 8 oxygen														
Si	2.686	2.657	2.670	2.666	2.712	2.688	2.681	2.514	2.680	2.664	2.686	2.483	2.681	2.629
Ti	0.002	0.000	0.000	0.000	0.000	0.001	0.000	0.000	0.000	0.000	0.001	0.004	0.000	0.000
Al	1.294	1.334	1.327	1.315	1.274	1.297	1.300	1.469	1.312	1.330	1.304	1.503	1.267	1.324
Fe^{3+}	0.012	0.003	0.003	0.005	0.004	0.002	0.003	0.004	0.004	0.002	0.001	0.002	0.003	0.003
Mg	0.002	0.000	0.000	0.000	0.000	0.001	0.000	0.001	0.000	0.001	0.000	0.001	0.000	0.000
Mn	0.001	0.000	0.000	0.001	0.000	0.000	0.000	0.000	0.000	0.000	0.000	0.000	0.000	0.001
Ca	0.298	0.355	0.325	0.338	0.284	0.315	0.323	0.484	0.319	0.346	0.313	0.515	0.287	0.342
Na	0.700	0.624	0.667	0.679	0.729	0.696	0.698	0.545	0.677	0.633	0.697	0.493	0.870	0.799
K	0.022	0.019	0.010	0.013	0.015	0.019	0.018	0.009	0.013	0.015	0.012	0.009	0.016	0.016
An	29	36	32	33	28	31	31	47	32	35	31	51	26	30

*An(%) = (Ca/(Na+K+Ca))*100

Table S 6 Representative chemical compositions of ortho- and clinopyroxene from the Serra Azul charnockite

	Orthopyroxene						Clinopyroxene					
Sample	AA-20		AA-49		AA-136		AA-20		AA-130		AA-136	
Facies	PABTn		PABGrd		PABGrd		PABTn		PBTn		PABGrd	
Analyses	C2.1	C2.2	C1.2	C5.1	C1.1	C7.1	C3.2	C3.1	C1.1	C1.3	C5.6	C6.8
Texture	rim	core	core	rim	core	rim	core	rim	rim	core	core	rim
SiO_2	52.97	52.44	48.72	48.84	50.36	50.32	51.62	51.34	49.37	51.63	51.47	51.37
TiO_2	0.05	0.00	0.10	0.00	0.18	0.12	0.20	0.21	0.25	0.34	0.07	0.13
Al_2O_3	0.59	0.45	0.53	0.50	0.69	0.79	1.09	0.94	1.23	1.23	0.81	0.95
Fe2O3	0.00	0.00	0.33	0.37	0.00	0.00	0.26	0.70	6.43	0.89	0.00	0.00
FeO	27.65	28.70	35.96	35.06	27.90	26.34	13.99	16.45	10.54	11.80	11.28	11.16
MgO	13.03	12.94	10.93	11.64	16.49	16.97	10.26	10.26	11.77	12.62	12.02	11.76
MnO	1.49	1.55	1.44	1.16	0.99	0.94	0.66	0.74	0.52	0.64	0.48	0.35
CaO	1.03	1.00	1.09	1.09	0.99	0.94	21.41	19.15	19.69	19.62	20.87	20.91
MnO	1.49	1.55	1.45	1.16	0.86	0.92	0.66	0.74	0.52	0.64	0.48	0.35
Na2O	0.10	0.13	0.03	0.04	0.04	0.06	0.32	0.34	0.43	0.43	0.34	0.43
K2O	0.14	0.00	0.00	0.01	0.00	0.05	0.01	0.00	0.01	0.00	0.00	0.01
Sum	97.20	97.32	99.24	98.75	97.53	96.58	99.85	100.23	100.39	99.29	97.52	97.22
	Number of cations per formula unit based on 6 oxygen											
Si	2.088	2.076	1.980	1.984	1.988	1.993	1.978	1.974	1.887	1.965	1.992	1.994
Ti	0.001	0.000	0.003	0.000	0.005	0.003	0.006	0.006	0.007	0.010	0.002	0.004
Al	0.027	0.021	0.025	0.024	0.032	0.037	0.049	0.043	0.055	0.055	0.037	0.044
Fe^{3+}	0.000	0.000	0.010	0.011	0.000	0.000	0.007	0.020	0.185	0.025	0.000	0.000
Fe^{2+}	0.912	0.950	1.222	1.191	0.921	0.872	0.448	0.529	0.337	0.376	0.365	0.362
Mg	0.766	0.764	0.662	0.704	0.970	1.002	0.586	0.588	0.671	0.716	0.693	0.680
Mn	0.050	0.052	0.050	0.040	0.29	0.031	0.021	0.024	0.017	0.021	0.016	0.011
Ca	0.044	0.042	0.048	0.048	0.042	0.040	0.879	0.788	0.806	0.800	0.865	0.869
Na	0.008	0.010	0.002	0.003	0.003	0.005	0.024	0.025	0.032	0.032	0.025	0.032
K	0.007	0.000	0.000	0.000	0.000	0.003	0.000	0.000	0.000	0.000	0.000	0.001
XMg*	0.46	0.45	0.35	0.37	0.51	0.54	0.56	0.52	0.56	0.64	0.66	0.65

*$XMg = Mg/(Mg+Fe^{2+})$

Table S 7 Representative chemical compositions of amphibole and biotite of the Serra Azul charnockite

	Amphibole						Biotite							
Sample	AA-20		AA-49		AA-136		AA-20		AA-130		AA-49		AA-136	
Facies	PABTn		PABGrd		PABGrd		PABTn		PBTn		PABGrd		PABGrd	
Analyses	C1.1	C1.2	C6.2	C6.3	C1.2	C1.1	C1.1	C1.2	C1.1	C2.1	C1.1	C4.2	C1.2	C4.1
Texture	rim	core	rim	core	core	rim	core	core	rim	core	core	rim	core	rim
SiO_2	44.02	43.51	42.08	42.08	47.46	45.14	36.56	36.16	36.01	35.63	35.18	34.97	34.75	35.05
TiO_2	1.59	1.71	2.01	1.90	0.48	0.71	3.93	4.29	3.87	4.90	4.64	4.88	4.85	4.55
Al_2O_3	8.80	8.90	9.72	9.09	5.98	7.56	14.68	14.33	13.15	13.24	13.74	13.73	13.01	12.82
Fe_2O_3*	5.15	3.73	3.76	6.87	5.35	4.97	-	-	-	-	-	-	-	-
FeO*	15.53	16.97	18.62	16.95	10.84	12.45	21.20	21.57	19.63	19.62	25.07	24.44	19.96	20.00
MgO	8.67	8.39	6.62	7.04	12.28	10.81	9.66	9.53	11.12	11.08	7.46	7.64	9.90	9.76
MnO	0.41	0.48	0.37	0.39	0.40	0.33	0.21	0.21	0.17	0.17	0.17	0.16	0.19	0.15
CaO	11.25	11.34	10.94	10.59	11.25	11.24	0.01	0.02	0.01	0.05	0.02	0.04	0.04	0.02
Na_2O	0.91	1.29	0.95	1.25	0.90	0.99	0.11	0.08	0.10	0.09	0.11	0.10	0.09	0.08
K_2O	1.07	1.14	1.38	1.28	0.55	0.79	9.72	9.72	9.40	9.55	9.39	9.31	9.22	9.31
F	0.22	0.19	0.00	0.01	0.21	0.21	3.55	0.58	0.60	0.61	0.00	0.00	0.32	0.19
Cl	0.06	0.06	0.13	0.10	0.07	0.11	0.54	0.08	0.27	0.25	0.29	0.23	0.22	0.31
H_2O*	1.84	1.85	1.88	1.89	1.86	1.81	0.07	3.51	3.40	3.42	3.66	3.66	3.45	3.48
Sum	99.54	99.61	98.75	99.65	97.56	97.07	100.29	100.17	98.14	99.07	100.19	99.83	96.26	95.97
	Number of cations per formula unit based on 23 oxygen						Number of cations per formula unit based on 22 charges							
Si	6.669	6.630	6.522	6.467	7.120	6.890	1.217	1.204	1.199	1.186	1.171	1.164	1.157	1.167
Ti	0.181	0.196	0.234	0.219	0.055	0.081	0.098	0.107	0.097	0.123	0.116	0.122	0.121	0.114
Al	1.571	1.598	1.775	1.647	1.057	1.361	0.432	0.422	0.387	0.390	0.404	0.404	0.383	0.377
Fe^{3+}	0.587	0.428	0.438	0.795	0.603	0.570	-	-	-	-	-	-	-	-
Fe^{2+}	1.967	2.163	2.413	2.179	1.361	1.589	0.295	0.300	0.273	0.273	0.349	0.340	0.278	0.278
Mg	1.958	1.907	1.528	1.613	2.748	2.459	0.240	0.236	0.276	0.275	0.185	0.190	0.246	0.242
Mn	0.052	0.062	0.051	0.049	0.051	0.043	0.003	0.003	0.002	0.002	0.002	0.002	0.003	0.002
Ca	1.826	1.851	1.817	1.743	1.808	1.837	0.000	0.000	0.000	0.001	0.000	0.001	0.001	0.000
Na	0.268	0.381	0.285	0.371	0.261	0.293	0.002	0.001	0.002	0.001	0.002	0.002	0.001	0.001
K	0.207	0.221	0.273	0.251	0.106	0.153	0.103	0.103	0.100	0.101	0.100	0.099	0.098	0.099
F	0.105	0.089	0.001	0.003	0.101	0.102	0.187	0.031	0.032	0.032	0.000	0.000	0.017	0.010
Cl	0.016	0.015	0.034	0.025	0.018	0.028	0.015	0.002	0.008	0.007	0.008	0.006	0.006	0.009
XMg*	0.5	0.47	0.39	0.43	0.67	0.61	0.45	0.44	0.50	0.50	0.35	0.36	0.47	0.47

*$XMg = Mg/(Mg+Fe^{2+})$

Table S 8 Representative chemical composition of plagioclase of the Serra Azul charnockite

Sample	AA-20		AA-130		AA-49		AA-136	
Facies	PABTn		PBTn		PABGrd		PABGrd	
Analyses	C4.4	C1.4	C1.1	C1.3	C6.3	C4.5	C1.1	C7.1
Texture	rim	core	rim	rim	rim	core	rim	core
SiO_2	60.52	59.30	60.22	59.57	59.31	60.85	60.26	58.34
TiO_2	0.01	0.01	0.00	0.09	0.00	0.00	0.00	0.00
Al_2O_3	24.95	25.39	24.50	25.69	25.37	23.97	23.95	25.23
Fe_2O_3	0.02	0.13	0.04	0.16	0.18	0.16	0.07	0.07
MgO	0.00	0.01	0.00	0.00	0.03	0.02	0.00	0.03
CaO	6.34	7.27	5.93	7.19	4.64	5.82	5.91	7.30
Na_2O	8.08	7.43	8.14	7.64	7.73	8.13	8.08	7.19
K_2O	0.20	0.28	0.11	0.28	1.66	0.39	0.24	0.17
Sum	100.22	99.85	99.05	100.64	99.00	99.52	98.56	98.39
	Number of cations per formula unit based on 8 oxygen							
Si	2.689	2.653	2.703	2.645	2.676	2.723	2.718	2.645
Ti	0.000	0.000	0.000	0.003	0.000	0.000	0.000	0.000
Al	1.307	1.338	1.296	1.344	1.349	1.264	1.273	1.348
FeI^{3+}	0.001	0.004	0.002	0.005	0.006	0.005	0.002	0.003
Mg	0.000	0.001	0.000	0.000	0.002	0.001	0.000	0.002
Ca	0.302	0.348	0.285	0.342	0.224	0.279	0.285	0.355
Na	0.696	0.644	0.709	0.657	0.676	0.705	0.707	0.632
K	0.011	0.016	0.006	0.016	0.096	0.022	0.014	0.010
An (%)*	30	35	28	34	23	28	28	36

*An(%) = (Ca/(Na+K+Ca))*100

Table S 9 - Normalized molar proportions used for crystallization phase equilibria modeling

Unit	Sample	Pseudosection	Oxygen fugacity	H_2O (wt%)	SiO_2	TiO_2	Al_2O_3	FeO	MgO	CaO	Na_2O	K_2O	H_2O	O
Maravilha charnockite	Whole-rock composition in wt%				69.9	0.44	15.25	3.89	1.12	3.49	3.54	3.04		
	AA-09 (reduced)	P-T	FMQ-0.5	1	73.42	0.40	9.08	3.46	0.67	2.58	3.23	3.59	3.50	0.12
			FMQ-0.5	2	70.94	0.39	8.78	3.35	0.65	2.50	3.12	3.47	6.76	0.10
			FMQ-0.5	3	68.62	0.38	8.49	3.24	0.63	2.42	3.01	3.36	9.81	0.08
			FMQ-0.5	4	66.44	0.36	8.22	3.14	0.61	2.34	2.93	3.25	12.66	0.08
		T/P-M(H_2O)	FMQ-0.5	1	73.42	0.40	9.08	3.46	0.67	2.58	3.23	3.59	3.50	0.12
			FMQ-0.5	9	57.36	0.31	7.10	2.71	0.53	2.02	2.53	2.81	24.60.	0.06
		T/P-M(O)	FMQ-2.0	3	68.62	0.38	8.49	3.24	0.63	2.42	3.01	3.36	9.81	0.04
			FMQ+2.0	3	68.62	0.38	8.49	3.24	0.63	2.42	3.01	3.36	9.81	0.38
	Whole-rock composition in wt%				70	0.51	14.7	3.95	0.43	2.3	3.18	5.73		
	AA-109 (oxidized)	P-T	NNO	1	72.33	0.34	9.30	3.37	1.73	3.87	3.55	2.01	3.45	0.17
			NNO	2	69.92	0.33	8.99	3.25	1.67	3.74	3.43	1.94	6.67	0.13
			NNO	3	67.66	0.32	8.70	3.15	1.62	3.62	3.32	1.88	9.68	0.11
			NNO	4	65.54	0.31	8.43	3.05	1.57	3.51	3.22	1.82	12.51	0.09
		T/P-M(H_2O)	NNO	1	72.33	0.34	9.30	3.37	1.73	3.87	3.55	2.01	3.45	0.17
			NNO	9	56.68	0.27	7.29	2.64	1.35	3.03	2.78	1.57	24.34	0.06
		T/P-M(O)	NNO-1.5	4	65.54	0.31	8.43	3.05	1.57	3.51	3.22	1.82	12.51	0.04
			NNO+2.5	4	65.54	0.31	8.43	3.05	1.57	3.51	3.22	1.82	12.51	0.39
Serra Azul charnockite	Whole-rock composition in wt%				60.4	0.82	16	6.51	2.76	5	3.84	2.01		
	AA-20	P-T	NNO	1	64.46	0.66	10.06	5.81	4.39	5.72	3.97	1.37	3.56	0.32
			NNO	2	62.25	0.64	9.72	5.61	4.24	5.52	3.84	1.32	6.87	0.25
			NNO	3	60.18	0.61	9.39	5.42	4.1	5.34	3.71	1.28	9.97	0.21
			NNO	4	58.24	0.59	9.09	5.25	3.97	5.17	3.59	1.24	12.86	0.17
		T/P-M(H_2O)	NNO	1	64.46	0.66	10.06	5.81	4.39	5.72	3.97	1.37	3.56	0.21
			NNO	9	50.17	0.51	7.83	4.52	3.42	4.45	3.09	1.06	24.93	0.10
		T/P-M(O)	NNO-1.5	3	60.18	0.61	9.39	5.42	4.1	5.34	3.71	1.28	9.97	0.08
			NNO+2.5	3	60.18	0.61	9.39	5.42	4.1	5.34	3.71	1.28	9.97	0.82

SUPPLEMENTARY MATERIAL 2 - FIGURES

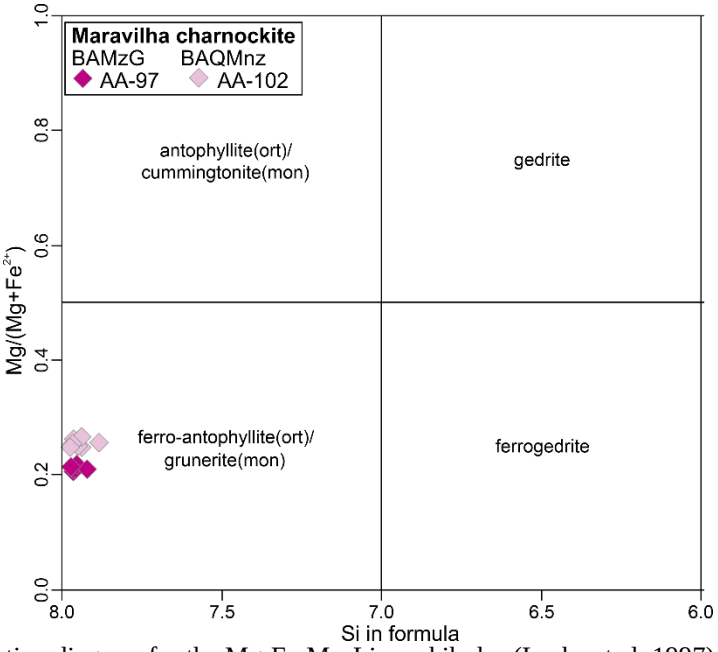


Fig. S1 Classification diagram for the Mg-Fe-Mn-Li amphiboles (Leake et al. 1997) of the Maravilha charnockite

6 THE OLDEST SANUKITOID *s.l.* MAGMATISM IN THE AMAZONIAN CRATON REVEALS MANTLE-CRUST INTERACTIONS DURING THE MESOARCHEAN IN THE BACAJÁ DOMAIN

Arthur Santos da Silva Neri

Roberto Dall'Agnol

Elton Luiz Dantas

Gilmara Regina Lima Feio

José de Arimatéia Costa de Almeida

Marco Antonio Galarza

Submetido à *Gondwana Research* como *short communication article* em 11/07/2025 e em processo de revisão em 14/07/2025.

Devido aos direitos autorais da *Gondwana Research*, a formatação, citações e referências bibliográficas desta seção seguem o padrão requerido pela revista.



Gmail — Arthur Neri <santosarthursilvaa@gmail.com>

Submission Confirmation
1 mensagem

Gondwana Research <em@editorialmanager.com> 11 de julho de 2025 às 17:22
Responder a: Gondwana Research <santosh@cugb.edu.cn>
Para: Arthur Santos da Silva Neri <santosarthursilvaa@gmail.com>

Article Type:GR Letter

Dear Arthur,

Your submission entitled "The oldest sanukitoid s.l. magmatism in the Amazonian Craton reveals mantle-crust interactions during the Mesoarchean in the Bacajá domain" has been received by Gondwana Research

You may check on the progress of your paper by logging on to the Editorial Manager as an author. The URL is https://www.editorialmanager.com/gwr/.

Your username is: Arthur

If you need to retrieve password details, please go to:
https://www.editorialmanager.com/gwr/l.asp?i=370524&l=48MD3AIY

Your manuscript will be given a reference number once an Editor has been assigned.

Thank you for submitting your work to this journal.

Kind regards,

Editorial Manager
Gondwana Research

The oldest sanukitoid *s.l.* magmatism in the Amazonian Craton reveals mantle-crust interactions during the Mesoarchean in the Bacajá Domain

Arthur Santos da Silva Neri [a, b*], Roberto Dall'Agnol [a, b, c], Elton Luiz Dantas [d], Gilmara Regina Lima Feio [e], José de Arimatéia Costa de Almeida [a, b], [a, f] Marco Antonio Galarza [a]

[a] Programa de pós-graduação em Geologia e Geoquímica, IG – UFPA

[b] Grupo de Pesquisa Petrologia de Granitoides, Instituto de Geociências (IG), Universidade Federal do Pará (UFPA), Rua Augusto Corrêa, 01, Belém-PA, Brazil. CEP 66075-110.

[c] Instituto tecnológico Vale, Belém-PA, Brazil.

[d] Laboratório de Estudos Geocronológicos, Geodinâmicos e Ambientais, Universidade de Brasília, Brasília-DF, Brazil**.** CEP 70910-900.

[e] Grupo de Mineralogia e Petrologia, Instituto de Geociências e Engenharias (IGE), Universidade Federal do Sul e Sudeste do Pará (Unifesspa), Marabá-PA, Brazil

[f] Laboratório de Geologia Isotópica (Pará-Iso), IG-UFPA.

ABSTRACT:

Sanukitoids are key rocks to understanding the geodynamics of the Archean. Mesoarchean sanukitoids *s.l.* have been identified as basement inliers in the Paleoproterozoic Bacajá Domain, SE Amazonian Craton, Brazil. This basement is composed of tonalitic to granodioritic orthogneisses, amphibolites and minor paragnaisses. The orthogneisses and amphibolites are chemically similar to sanukitoids *s.l.;* they are calc-alkaline, metaluminous to slightly peraluminous, potassic (K_2O > 1.77 wt%), and enriched in ferromagnesian oxides. They have high concentrations of Ba + Sr >1400 ppm) and transitional metals (V ≥ 40 ppm, Cr ≥ 39 ppm). Zircon U-Pb data yield igneous crystallization ages at 2.97 Ga to 2.94 Ga, and additional ages at ca. 2.81 Ga (Pb-lost/metamorphism?) and ca. 2.09-1.96 Ga (metamorphism). Magmatic zircon cores yielded positive $\varepsilon Hf_{(t)}$ (+0.5 to +2.5), while the metamorphic rims provided negative $\varepsilon Hf_{(t)}$ (-8.4 to -8.3), both with Mesoarchean model ages (3.18 to 3.20 Ga). Whole-rock Nd isotope analyses furnished positive to negative $\varepsilon Nd_{(t)}$ (+2.96 to -4.20) and late Paleoarchean to early Mesoarchean model ages (3.23 to 2.97 Ga). These results provide the earliest evidence of sanukitoid *s.l.* magmatism in the Amazonian Craton and one of

the oldest worldwide. The isotopic and geochemical data support the role of TTG-derived melts in metasomatizing the mantle source. These findings offer new constraints for understanding the nature of mantle-crust interactions during early crustal evolution and contribute to global models of late Archean magmatic regimes across ancient cratonic nuclei.

KEYWORDS: Mantle-crust interactions, sanukitoids *s.l.*, Mesoarchean, Amazonian craton;

6.1 INTRODUCTION

Most of the continental crust was formed in the Archean era, primarily in the late Archean (3.0-2.5 Ga) (Hawkesworth et al., 2019, 2013). Thus, understanding the evolution and reworking of the Archean continental crust is crucial for reconstructing Earth's early evolution. Systematically, the Archean record comprises three main groups: (i) early low-K granitoids of tonalite-trondhjemite-granodiorite (TTG) series (Almeida et al., 2011; Joshi et al., 2022; Moyen and Martin, 2012) (ii) supracrustal (meta-volcanic and meta-sedimentary rocks) compositing the greenstone belts (Anhaeusser, 2014; de Souza et al., 2001); (iii) late high-K granitoid rocks, including sanukitoids, biotite granites, two-mica granites, and alkaline granites, and typically intrude the older lithologies (Almeida et al., 2013; da Silva et al., 2025; Dall'Agnol et al., 2017; Feio et al., 2012; Laurent et al., 2014; Oliveira et al., 2011).

Sanukitoids *sensu lato* (*s.l.*) are minor yet widespread components of late Archean terranes. They encompass various granitoids with contrasting compositions but share similar petrogenesis (Dey and Moyen, 2020; Peng et al., 2019; Ribeiro-Silva et al., 2023). These rocks originate from interactions between mantle peridotite and an incompatible-element-rich component in subduction-collision or intraplate settings (Laurent et al., 2014 and references therein). Therefore, understanding their origin provides insight into the tectonic setting where mantle and crustal components interacted. Most sanukitoids *s.l* crystallized in the Neoarchean, with rare Mesoarchean occurrences, including the Carajás province (2.92-2.86 Ga Nascimento et al., 2025; Ribeiro-Silva et al., 2023), the Ukrainian shield (2.92-2.86 Ga; Bibikova et al., 2008), the Pilbara craton (2.95 Ga; Smithies and Champion, 2000), and the oldest in Greenland (3.04 Ga; Garde, 1997; Steenfelt et al., 2005). The geodynamic significance of sanukitoid magmatism extends beyond their local occurrence, as its generation marks a transition from TTG crust formation to enriched-mantle derived magmatism (e.g., Ribeiro-Silva et al., 2023). Therefore, documenting their presence in distinct cratons provides essential insights into the early Archean

geodynamics.

This study presents the whole-rock geochemistry, zircon U-Pb-Hf isotopes, and whole-rock Nd isotopes of a Mesoarchean basement inlier within the Paleoproterozoic Bacajá Domain, composed predominantly of sanukitoids *s.l.* Our findings identify this magmatism as the oldest sanukitoid *s.l.* magmatism in the Amazonian Craton and the second oldest worldwide.

6.2 GEOLOGICAL SETTING

The Bacajá Domain is part of the Maroni-Itacaiúnas Province (Fig. 1a, b), a large province established during the Paleoproterozoic in the northern Amazonian craton (Santos et al., 2006; Tassinari and Macambira, 2004). It comprises Archean and Siderian fragments intensely reworked during a Rhyacian (2.26-1.99 Ga) collisional orogeny (Cordani et al., 2000; Hurley et al., 1967), accompanied by extensive orogenic magmatism (Macambira et al., 2009; Magalhães et al., 2023; Vasquez and Rosa-Costa, 2008; Vasquez et al., 2008).

The Archean remnants of the Bacajá Domain include metamorphic complexes with Mesoarchean (3.0-2.94 Ga) granulites and orthogneisses, as well as late Neoarchean (2.63-2.50 Ga) orthogneisses and granitoids (Macambira et al., 2022, 2007; Magalhães et al., 2023; Vasquez and Rosa-Costa, 2008). Siderian (2.45-2.36 Ga) greenstone belts and related rocks are also present (Macambira and Amireault, 2025; Macambira et al., 2009; Vasquez, 2006). The extensive Rhyacian orogenic magmatism is diverse and occurred at 2.21-2.05 Ga, coincident with high-grade metamorphism (Barros et al., 2007; Macambira et al., 2009, 2004, 2003; Magalhães et al., 2023; Vasquez, 2006; Vieira et al., 2022; Neri et al., submitted).

6.3 RESULTS

Supplementary material 1 summarizes analytical methods. Whole-rock geochemistry, assessment of element mobility, U-Pb ages, and Hf isotope data are in Supplementary material S2, S3, S4, and S5, respectively.

6.3.1 Field aspects and petrography

Our study focuses on a basement inlier within the Bacajá Domain, attributed to the to the Archean Cajazeiras complex, which is widespread throughout the domain, particularly in its southern portion (Fig. 1b). In the study area (Fig. 1c), this inlier is bounded to the north by the supracrustal Serra Misteriosa sequence, composed of quartzites and mica-schists, and to the south by the Misteriosa transcurrent shear zone, which juxtaposes the Mesoarchean complex with Rhyacian granitoids.

The complex comprises non-migmatitic to metatexitic orthogneisses with tonalitic to granodioritic compositions (Fig. 2). These orthogneisses often contain mafic enclaves (Fig. 2c) and millimetric to centimetric stromatic granitic leucosomes, which generally run parallel to the foliation (Fig. 2a, d). Minor occurrences of paragnaisses are also present.

A well-developed foliation is imprinted in the orthogneisses, primarily defined by the alignment of interlayered mafic and felsic layers (Fig. 2a), gneissic banding (Fig. 2a, b) and deformed mafic enclaves (Fig. 2c). This foliation trends WNW-ESE to NW-SE with moderate (49º-69º) to steep (70º-90º) dips, towards both NE and SW. It is associated with a shallow plunging mineral (10º-12º) stretching lineation towards W (Fig. 1c).

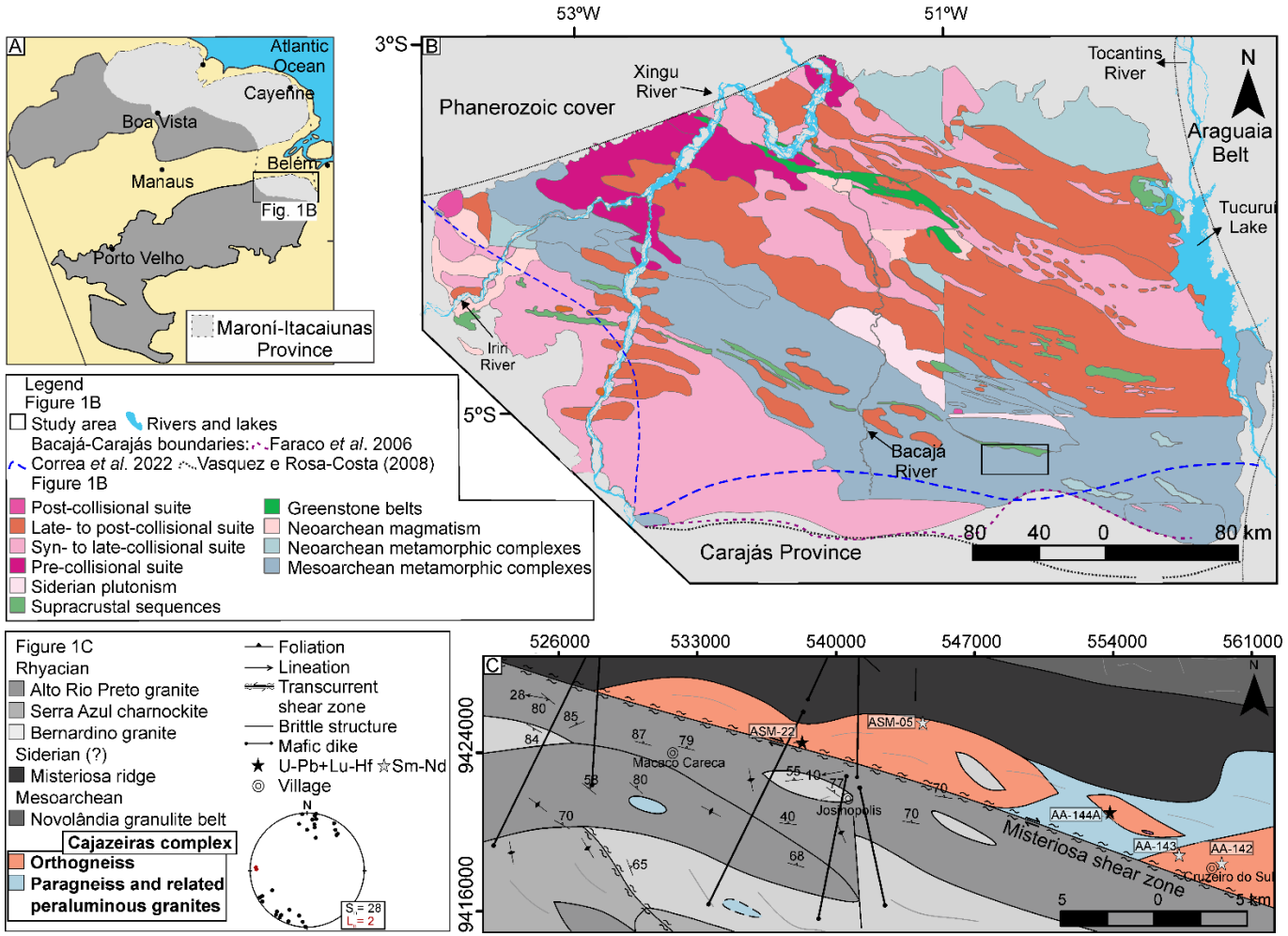


Figure 1 - (A) Amazonian craton and the location of the Bacajá Domain in the Maroni-Itacaiúnas Province (Tassinari and Macambira, 2004). (B) simplified geological map of the Bacajá Domain (Barros et al., 2007; Besser and Barros, 2015; Macambira and Ricci, 2015; Macambira et al., 2009; Vasquez and Rosa-Costa, 2008). (C) Geological map of the studied area (modified from Neri et al., submitted). The white star symbol near the Cruzeiro do Sul village (AA-142) represents the 3.01 Ga orthogneiss dated by Macambira et al. (2007).

The rock samples comprise clinopyroxene-amphibole-biotite and (amphibole)-biotite orthogneisses that are coarse- to medium-grained, with local porphyroclastic occurrences. They are marked by typical banding highlighted by the intercalation of quartz-felspathic granoblastic and mafic nematoblastic levels. Common accessory minerals are allanite, zircon, magnetite, apatite, ilmenite, and pyrite. The mafic rocks are classified as amphibolites and have a medium-grained nematoblastic texture. Accessories minerals are apatite, zircon, titanite, and Fe-Ti oxides.



Figure 2 - Field (A to D) and microscopic (E, F) aspects of the Cajazeiras complex. (a) compositional layering parallel to stromatic leucosomes; (b) foliation highlighted by the alignment of mafic and felsic minerals; (c) amphibolite enclave in metatexitic orthogneiss. Leucosome accumulation at the enclave's border; (d) centimetric injected granitic leucosome; (E) interlayered levels of aligned ferromagnesian minerals alternated with quartz-feldspathic levels; (F) coronitic texture of clinopyroxene (core) and amphibole (rim). Abbreviations follows Whitney and Evans (2010).

6.3.2 Geochemistry

Major element compositions (Tab. S1) indicate a restricted silica range for most analyzed rocks (66.1-66.6 wt%), except for an outlier (72.2 wt%) and a mafic sample (55.2 wt%). These rocks are calc-alkaline, metaluminous to slightly peraluminous, and predominantly magnesian (Fig. 3a, b, c). The granitoids contain moderate MgO (0.81-1.6 wt%), K_2O ($K_2O/Na_2O > 0.38$), and are enriched ferromagnesian oxides (FeO_t + MgO + MnO + TiO_2 > 4wt%, Fig. 3d) and CaO (2.47-4.22 wt%).

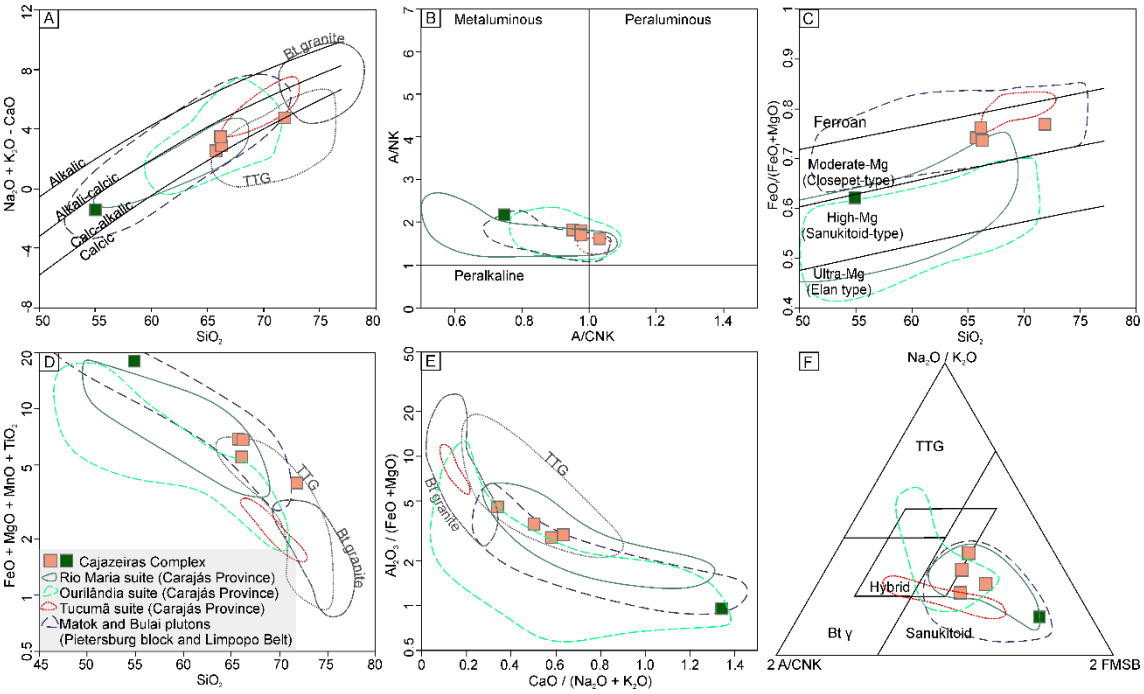


Figure 3 - Major-element geochemistry of the orthogneisses of the Cajazeiras Complex. (A) MALI index ([Na_2O + K_2O] – CaO) vs. SiO2 diagram (Frost et al. 2001); (B) A/CNK vs. A/NK; (C) FeOt / (FeOt + Mg) vs. SiO_2 (Frost et al. 2001, modified by Terentiev and Santosh, 2018); (D) sum of "mafic" oxides (FeOt + MgO + MnO + TiO2) vs. SiO2; (E) Al_2O_3/(FeOt + MgO) vs. CaO/(Na_2O + K_2O); (F) Ternary source diagram 2A/CNK vs. Na_2O/K_2O vs. 2FMSB,fields are the same as Laurent et al. (2014 and references therein). For comparison are shown the fields of Amazonian craton sanukitoids (Rio Maria suite, Oliveira et al., 2011; Ourilândia and Tucumã suites, Ribeiro-Silva et al., 2023), sanukitoids *s.l.* , TTG and Bt-granite from Pietersburg block and Limpopo belt (Laurent et al., 2014).

In terms of trace elements, these rocks are enriched in Ba and Sr (Ba + Sr =1478-3528 ppm), while exhibiting low Rb (48.2-96.1 ppm) and Y (7.3-15 ppm), resulting in high Ba/Rb (12.29-18.63 in the granitoids, and a lower value of 9.65 ppm in the amphibolite sample; Fig. 4a) and high Sr/Y ratios (31.67-69.25, outlier 16.62). They are also enriched in transitional metals (Fig. 4b, V ≥ 40 ppm, Cr ≥39 ppm), while displaying relatively low HFSE contents (Fig. 4b, e.g., Zr = 158-281 ppm).

REE patterns (Fig. 4c; Tab. S1) show moderate to high fractionation $(La/Yb)_N$ = 30.95-91.53 in the granitoids), with weak to moderate negative Eu anomalies (Eu/Eu* = 0.51-0.85), except for one strongly positive value (1.46). Primitive-mantle-normalized

multielement patterns (Fig. 4d) reveal negative Nb-Ta-P-Ti anomalies. These geochemical characteristics collectively classify these rocks as sanukitoid *s.l.* (Laurent et al., 2014).

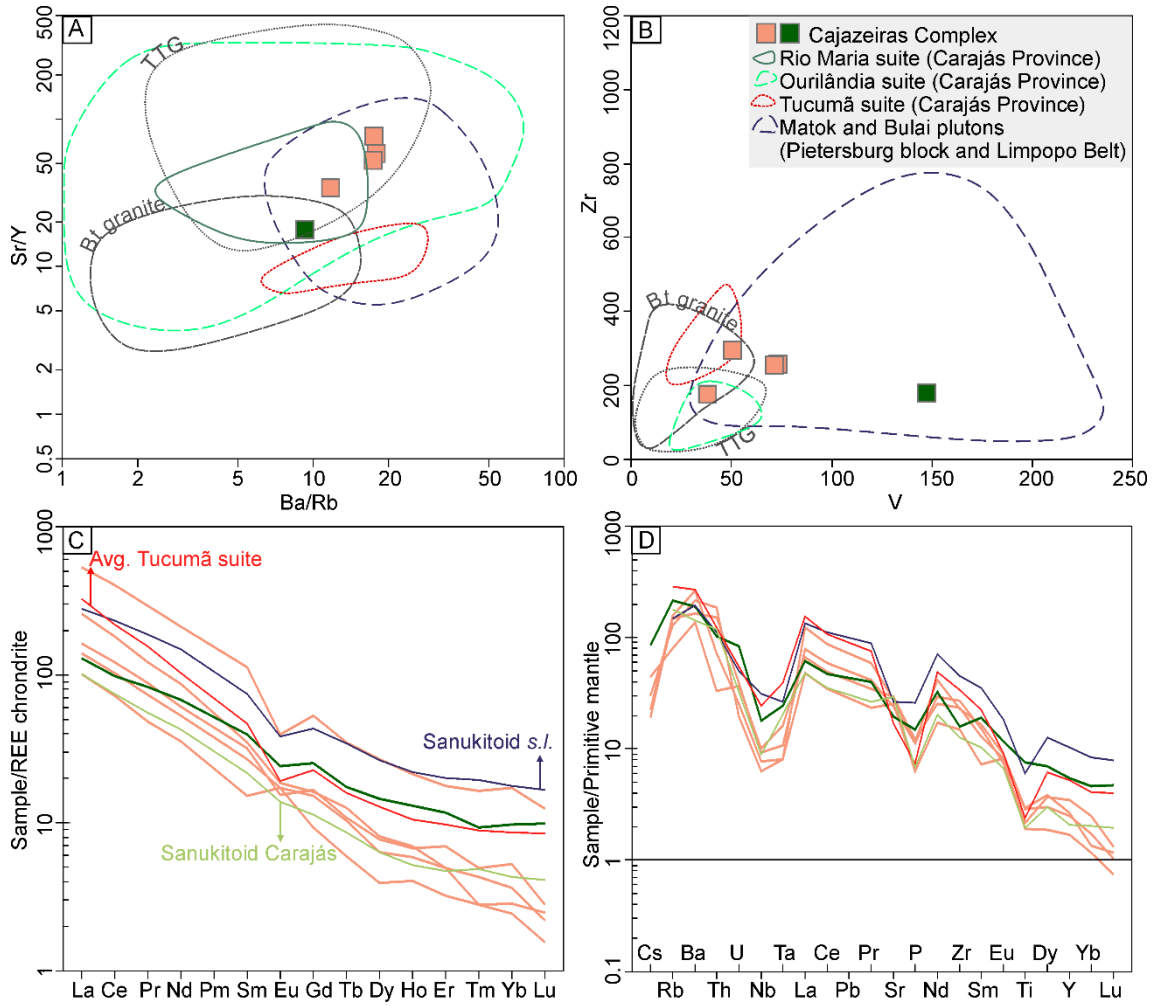


Figure 4 - Trace-element geochemistry of the Cajazeiras complex. (A) Sr/Y vs. Ba/Rb ratios; (B) HFSE (represented by Zr) vs. transition element (represented by V) concentrations; (C) REE patterns normalized according to Boynton (1984); (D) multi-element patterns normalized according to McDonough and Sun (1995).

6.3.3 Zircon U-Pb-Hf isotopes

Zircon grains from two orthogneisses, a tonalitic sample (ASM-22) and granodioritic sample (AA-144A), were analyzed via LA-ICP-MS.

For ASM-22 (Fig. 5a, Tab. S2), forty analyses were performed on twenty-one zircons. The magmatic cores yield two ages: (i) an upper intercept age of 2970.4±9.2 Ma (2σ, n =11, MSWD = 1.2) with Th/U ratios between 0.75-4.79; (ii) a younger upper intercept age at 2812±12 Ma (2σ, n= 4, MSWD = 1.4) with Th/U ratios of 0.92-2.06. Ages from the metamorphic rims are scattered along the concordia, ranging from 2136±14 to 2074±14 Ma (n = 14, $^{207}Pb/^{206}Pb$ age) with Th/U ratios between 0.09-1.82. A subset of these analyses yields a weighted average age of 2095±6 Ma (2σ, n =7, MSWD

= 1.4). Additionally, a single zircon crystal records an age of 2210±13 Ma.

Hf isotope analyses of five core domains reveal initial $^{176}Hf/^{177}Hf$ ratios between 0.280951 to 0.281038, slightly positive εHf(t) values (+0.5 to +2.6), and two-stage model ages (T_{DM}^{C}) varying from 3.18 to 3.20 Ga. Six rim analyses show initial Hf ratios between 0.281217 and 0.281227, negative εHf(t) values (−8.1 to -8.4), and similar T_{DM}^{C} ages (3.18 to 3.20 Ga) (Fig. 5c, Tab. S4).

For AA-144A (Fig. 5b, Tab. S3), Forty-five analyses were conducted on twenty-one zircons. Most of the analyses are highly discordant, but the magmatic cores provide two main age groups: (i) an upper intercept at 2939.5±6.1 Ma (2σ, n = 5, MSWD = 0.66) with Th/U ratios between 0.48-1.53; and (ii) and 2811±13 Ma (2σ, n=6, MSWD = 1.4) with Th/U ratios between 0.54-1.50. Metamorphic rims yielded an upper intercept of 1962±5.9 Ma (2σ, n= 3, MSWD = 0.055).

The older ages of 2970.4±9.2 Ma (ASM-22) and 2939.5±6.1 Ma(AA-144A) are interpreted as crystallization ages of the orthogneiss protolith (Whitehouse and Kemp, 2010). The younger ages obtained in core domains (2812±12 Ma – ASM-22; 2811±13 Ma – AA-144A) could result of Pb-lost or might represent an unprecedented metamorphic event. The Rhyacian ages recorded in the rims are interpreted as the imprint of the later metamorphic event widespread across the Bacajá Domain (Macambira et al., 2022 and references therein).

6.3.4 Nd isotopes

Nd isotopes obtained from five orthogneiss samples, reveal late Paleoarchean to early Mesoarchean model ages ranging from 3.23 to 2.97 Ga, with εNd(t) values varying from positive (+2.96 to +0.65) to negative (-4.20 to -1.66). The proximity between crystallization and model ages suggest relatively short crustal residence times, and the mostly positive εNd(t) reinforces a juvenile contributions to the orthogneisses protoliths. In contrast, samples with negative εNd(t) suggest a crustal contribution, which might be related to minor crustal contamination during the magmatic evolution or to minor leucosome contribution in these samples.

Table 1 - Nd isotopes data from the studied orthogneisses.

Sample	Sm (ppm)	Nd (ppm)	$^{147}Sm/^{144}Nd$	$^{143}Nd/^{144}Nd$ (±2SE)	f(Sm/Nd)	εNd(0)	T(Ga)	εNd(t)	T_{DM} (Ga)	T_{DM2} (Ga)
AA-142	5.97	46.24	0.0780	0.510429(7)	-0.60	-43.09	3.01*	2.96	2.97	
AA-143	5.62	35.87	0.0947	0.510652(7)	-0.52	-38.75	3.01*	0.80	3.10	
AA-144A	3.29	19.68	0.1012	0.510570(7)	-0.49	-40.35	2.94	-4.20	3.41	3.23
ASM-05	5.007	21.522	0.1406	0.511453 (4)	-0.29	-23.12	2.97	-1.66	3.40	3.06
ASM-22	4.427	27.392	0.0977	0.510726(8)	-0.50	-37.30	2.97	0.65	3.08	

*Age from Macambira et al. (2007).

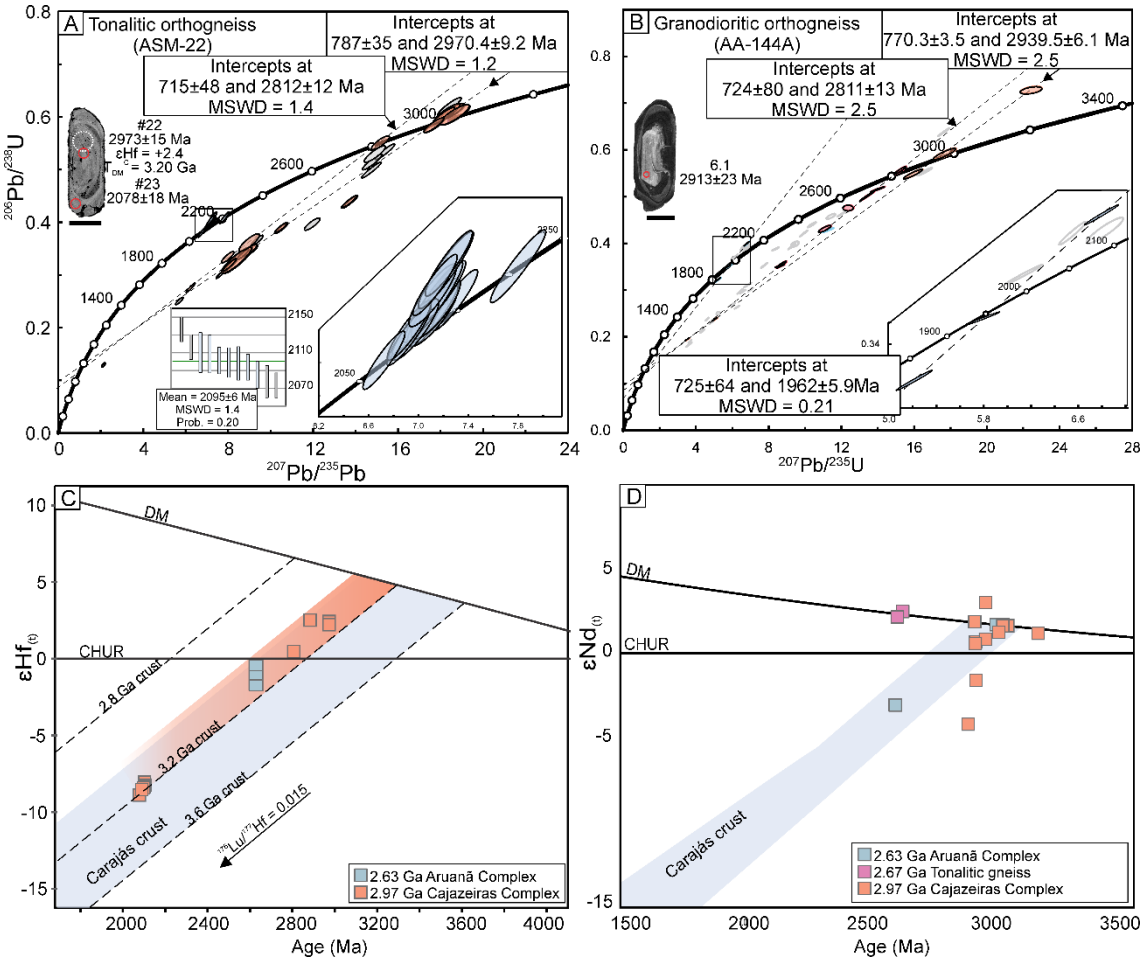


Figure 5 - (A) concordia diagram of the sample ASM-22 (tonalitic orthogneiss); (B) concordia diagram for sample AA-144A (granodioritic orthogneiss), zircon scale bar is 100 µm; (C) εHf(t) vs T (Ma).; (D) εNd(t) vs. T(Ga). Data from the Aruanã complex are from Magalhães et al. (2023) and those of the tonalitic gneiss from Macambira et al. (2009). The fields of Carajás Crust in (C) are summarized from Marangoanha et al. (2019) and Ribeiro-Silva et al. (2023); and in (D) are from Feio et al. (2013).

6.4 DISCUSSION

6.4.1 Petrogenesis

Sanukitoids *s.l* are generally thought to form through partial melting of a metasomatized mantle or via interaction between crustal melt and mantle peridotite (Heilimo et al., 2010; Lobach-Zhuchenko et al., 2005; Oliveira et al., 2011; Qian and Hermann, 2010; Semprich et al., 2015).

The Cajazeiras orthogneisses plot within the enriched mantle source field in the ternary diagram Er vs. Ba+Sr/1000 vs. 1/Er (Fig. 7a, Heilimo et al., 2010) and predominantly at the intersection of low- and high-K mafic rocks fields in the source diagram of Laurent et al. (2014) (Fig. 7b). These characteristics, combined with high transitional metals contents (V and Cr), relatively low Nb/La ratios (Fig. 7c), and positive

εHf(t) and εNd(t) of the Cajazeiras orthogneisses support a significant mantle influence in their genesis. However, their high LILE concentrations (Ba+Sr > 1400ppm) indicate a strong crustal contribution. These geochemical signatures align well established petrogenetic models for sanukitoids *s.l.* formation (Laurent et al., 2014).

A melt-related metasomatizing agent is suggested by the relatively high La/Yb and Nb/Y ratios (Fig. 7d) and further confirmed by the $(Hf/Sm)_N$ (0.81–1.77; >1.0 in the orthogneisses; Fig. 7e), with most samples plotting in the field of melt-related metasomatism. The metasomatic agent of the mantle was probably derived from a slab-derived melt, as indicated by the relatively low Nb/Zr and Nb/Ta ratios of the orthogneisses (Plank and Langmuir, 1998; Sun et al., 2020), which suggest a mix between TTG-melts and depleted mantle (Fig. 6f).

The relatively low to moderate Mg# (36 to 40 with an anomalous value of 24 in the granitoids; 53 in the amphibolite) are atypical for mantle-derived magmas (Moyen, 2009). This feature could reflect a more significant enrichment in the mantle, subsequent mixing with crustal-derived magmas, assimilation of older crustal lithologies, or even differentiation from a more primitive magma.

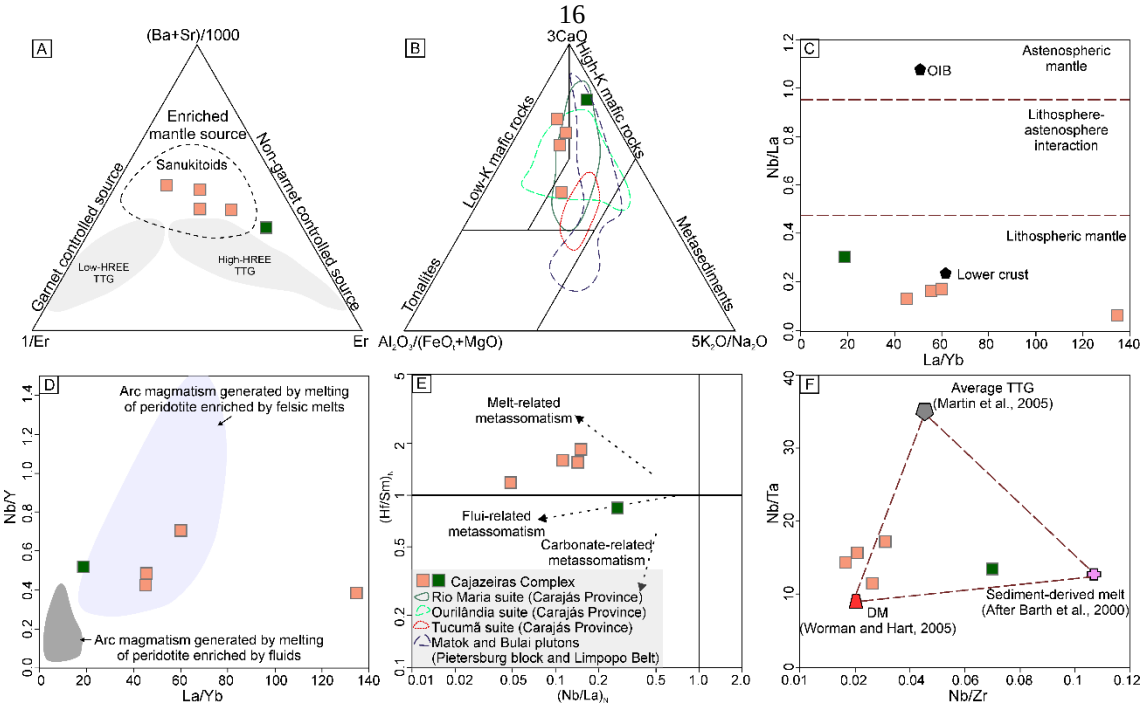


Figure 6 - Petrogenetic diagrams for the orthogneisses of the Cajazeiras Complex. (A) Ternary 1/Er vs. (Ba+Sr)/1000 vs. Er discriminant source (Heilimo *et al.*, 2010); (B) Source discriminant diagram for Archean granitoids (Laurent et al., 2014); (C) Nb/La vs. La/Yb diagram (after Smith et al., 1999); (D) discriminant Nb/Y vs. La/Yb diagram of mantle metasomatism agents (Martin *et al.*, 2009); (E) $(Hf/Sm)_N$ versus $(Nb/La)_N$ diagram (after La Flèche et al., 1998); (F) Nb/Ta vs. Nb/Zr diagram (Sun et al., 2020). Depleted-mantle (DM, Workman and Hart, 2005), average-TTG (Martin et al., 2005), sediment-derived melts (Barth et al., 2000).

6.4.2 Tectonic setting and regional implications

Two geodynamic models to advocate the origin of late Archean granitoids, including sanukitoids *s.l.*: (i) a terrane accretion event (i.e. continental collision), where crustal thickening followed by slab breakoff, retreat, or lithospheric delamination provides the required heat source for melting (Ribeiro-Silva et al., 2023; Semprich et al., 2015); or (ii) an intraplate setting, where the lithosphere experiences a thermal event such as plume upwelling (Costa et al., 2020; Jayananda et al., 2000) or rifting and break up of a stable continent (Smithies and Champion, 2000). Defining the tectonic setting in Archean rocks is challenging, mainly because the primary relationship between sanukitoids and other rock types may be obscured by later deformation and metamorphism. As a result, determining the setting typically relies on integrating geochemical, isotopic, and geophysical data (Costa et al., 2020; Spencer et al., 2024; Zhang et al., 2021).

In the Cajazeiras complex, the primary relationship between the sanukitoids and other lithotypes has been erased due to Paleoproterozoic deformation and metamorphism. Therefore, geochemical and isotopic signatures are key to inferring the tectonic setting of their formation. Using the multidimensional discrimination diagrams of Verma et al., (2013), all samples plot within the collisional and continental arc fields (Fig 7a, b), suggesting a collision-related setting or possibly in a transitional setting from a continental arc to a collisional regime. This interpretation aligns with most tectonic models proposed for sanukitoids origin (Laurent et al., 2014 and references therein). Therefore, the geochemical and isotopic data indicate that the sanukitoids *s.l.* from the Bacajá Domain originated from the partial melting of a mantle metasomatized by a TTG-like melt, most likely in a collisional setting. Further studies based on Ti-Pb-Sr isotopes (Spencer et al., 2024), along with geophysical data, should provide additional insights into the tectonic setting of their formation.

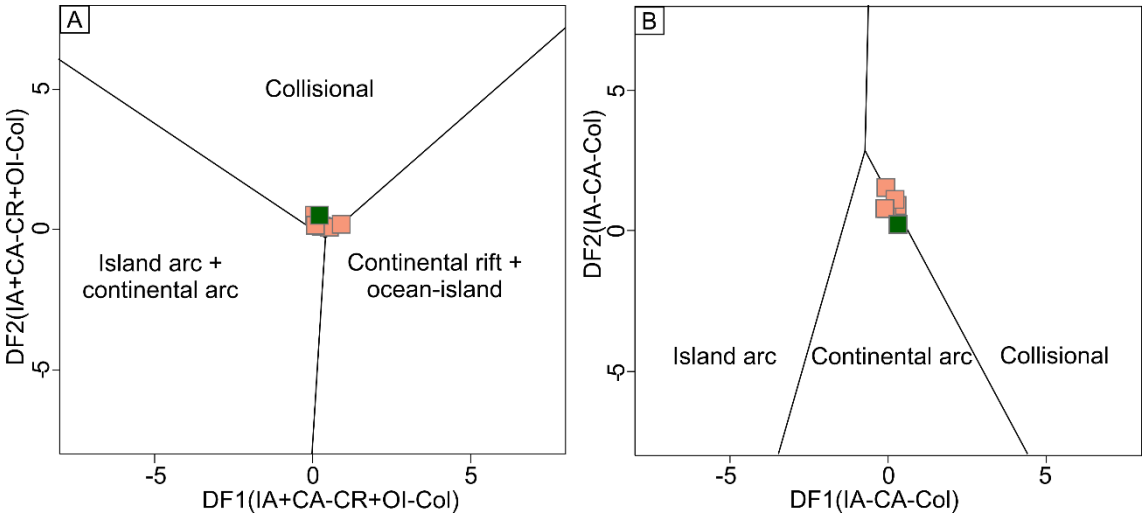


Figure 7 - Multi-dimensional diagrams based on ln-transformed ratios of immobile trace elements for the discrimination of acid rocks (Verma et al., 2013). (A) DF1 vs. DF2., (B) DF1 vs. DF2.

The sanukitoids described in this study are 2.97-2.94 Ga old. Additionally, a 3.0 Ga old sample was previously dated in the same area (Macambira et al., 2007), making these rocks the oldest sanukitoid *s.l* identified in the Amazonian craton and the second oldest worldwide, younger only than the sanukitoids from West Greenland that crystalized at 3.04 Ga (Garde, 1997). It is widely accepted that sanukitoid *s.l*. magmatism represents a secondary magmatic stage following TTG magmatism in several Archean cratons worldwide (Laurent et al., 2014 and references therein). Given that the mantle source of the studied samples was likely enriched by TTG melts (Fig. 7f), it is plausible that TTG rocks older than 3.0 Ga remain undiscovered in the Bacajá basement.

A comparison with the adjacent Archean crust of the Carajás Province suggests similarities in Nd-T_{DM} ages (Fig. 5d). However, while Hf-T_{DM}^{C} ages indicate that the Carajás crust dates back to the Paleoarchean (Fig. 5c), the Bacajá basement Hf-T_{DM}^{C} ages are restricted to the Mesoarchean. Between 3.0 and 2.95 Ga, Carajás Province experienced extensive TTG magmatism, accompanied by subordinate granitic magmatism in the Rio Maria and Sapucaia domains (Almeida et al., 2011; Alves, 2020; Feio et al., 2013; Feio and Dall'Agnol, 2012; Ribeiro-Silva et al., 2023). In contrast, the Canaã dos Carajás domain and Carajás basin granites *s.s.* (2.88-2.83 Ga) are dominant over TTG rocks. Sanukitoid magmatism in the Carajás Province occurred later, at ca. 2.87 Ga, with a single older occurrence dated at 2.92 Ga old in the Ourillândia area (Oliveira et al., 2011; Ribeiro-Silva et al., 2023 and references therein).

Despite some overlap in Nd-T_{DM} and Hf-T_{DM}^{C} model ages between the Mesoarchean Bacajá Domain and the Carajás province, which points to reservoirs with similar ages, several key differences (cf. Neri et al., submitted) suggest distinct

evolutionary histories. These contrasts challenge the hypothesis that the southern Bacajá Domain represents a direct extension of the Carajás province basement (Motta et al., 2019). The Archean history between the two domains is still unclear, as highlighted by Motta et al. (2019). However, the overlapping ages in modified zircon cores in the Cajazeiras orthogneiss and granites *s.s.* in the Carajás Province could suggest that the two domains were juxtaposed at 2.84-2.80 Ga.

6.4.3 Mantle metasomatism and crustal growth in the Archean

The role of mantle metasomatism in Archean crustal growth has been widely recognized as key processes in transition from TTG crust formation to enriched mantle derived magmatism, like sanukitoids (Almeida et al., 2011; Joshi et al., 2022; Hawkesworth et al., 2019, 2013; Moyen and Martin, 2012).

The discovery of Mesoarchean sanukitods in the Bacajá Domain suggest that mantle metasomatism by TTG-like melts was already active in the Amazonian Craton by 3.0 Ga. Although the tectonic mechanism that led to these processes remains to be solved, these observations reflect a widespread process that contributed to late-stage Archean crustal growth and lithospheric stabilization (Laurent et al., 2014; Oliveira et al., 2011; Joshi et al., 2022 and references therein).

6.5 CONCLUSIONS

We identified 2.97-2.94 Ga old sanukitoid *s.l.* magmatism in the Bacajá Domain, SE Amazonian Craton. They represent the oldest sanukitoid *s.l* magmatism in the Amazonian Craton and the second oldest worldwide. These rocks were derived from the partial melting of a mantle source metasomatized by a TTG melt, most probably in a collision to subduction setting.

The discovery of early sanukitoids *s.l.* in the Bacajá Domain expands the global inventory of such rocks and provide insights into the mechanisms of crustal growth and mantle metasomatism in the Archean. These processes most likely played a key role in the stabilization of the Amazonian craton.

ACKNOWLEDGMENTS

This paper is part of the first author's PhD thesis developed at the Instituto de Geociências, UFPA. The authors acknowledge UNIFESSPA students and staff for their previous work in the studied area. RD acknowledges CNPq (Proc. 3006767/2019-8). GRL acknowledgs CNPq and FAPESPA (Proc. 408396/2023-7, E-2024/2285715). This study was financed in part by the Coordenação de Aperfeiçoamento de Pessoal de Nível

Superior - Brasil (CAPES) - Finance Code 001 (No. 88887.643812/2021-00).

REFERENCES

Almeida, J. de A.C. de, Dall'Agnol, R., Leite, A.A. da S., 2013. Geochemistry and zircon geochronology of the Archean granite suites of the Rio Maria granite-greenstone terrane, Carajás Province, Brazil. J. South Am. Earth Sci. 42, 103–126. https://doi.org/10.1016/j.jsames.2012.10.008

Almeida, J. de A.C., Dall'Agnol, R., de Oliveira, M.A., Macambira, M.J.B., Pimentel, M.M., Rämö, O.T., Guimarães, F.V., Leite, A.A. da S., 2011. Zircon geochronology, geochemistry and origin of the TTG suites of the Rio Maria granite-greenstone terrane: Implications for the growth of the Archean crust of the Carajás province, Brazil. Precambrian Res. 187, 201–221. https://doi.org/10.1016/j.precamres.2011.03.004

Alves, J.P.S., 2020. A relação entre o Domínio Bacajá e o Domínio Carajás, sudeste do Cratón Amazônico, com base em geologia isotópica e química mineral. Master dissertation. Instituto de Geociências, Belém.

Anhaeusser, C.R., 2014. Archaean greenstone belts and associated granitic rocks – A review. J. African Earth Sci. 100, 684–732. https://doi.org/10.1016/j.jafrearsci.2014.07.019

Barros, C.E. de M., Macambira, M.J.B., Santos, M.C. da C., Silva, D.C.C., Palmeira, L.C.M., Sousa, M.M., 2007. Estruturas sinmagmáticas e idade de zircão de granitos (evaporação de Pb) paleoproterozóicos da parte leste do Domínio Bacajá, Província Maroni-Itacaiúnas. Rev. Bras. Geociências 37, 293–304. https://doi.org/10.25249/0375-7536.2007373293304

Barth, M.G., McDonough, W.F., Rudnick, R.L., 2000. Tracking the budget of Nb and Ta in the continental crust. Chem. Geol. 165, 197–213. https://doi.org/10.1016/S0009-2541(99)00173-4

Besser, M.L., Barros, C.E.M., 2015. Geologia e recursos minerais da Folha Rio Bacajá - SA.22-Y-D-VI, Estado do Pará. CPRM, Belém.

Bibikova, E. V., Lobach-Zhuchenko, S.B., Artemenko, G. V., Claesson, S., Kovalenko, A. V., Krylov, I.N., 2008. Late Archean magmatic complexes of the Azov terrane, Ukrainian Shield: Geological setting, isotopic age, and sources of material. Petrology 16, 211–231. https://doi.org/10.1134/S0869591108030016

Boynton, W. V., 1984. Cosmochemistry of the Rare Earth Elements: Meteorite Studies.

pp. 63–114. https://doi.org/10.1016/B978-0-444-42148-7.50008-3

Cordani, U.G., Sato, K., Teixeira, W., Tassinari, C.G., Basei, M.A.S., 2000. Crustal evolution of the South American Platform. Tecton. Evol. South Am. 19–40.

Costa, F.G., Santos, P.A. dos, Serafim, I.C.C. de O., Costa, I.S.L., Roopnarain, S., 2020. From Mesoarchean drips to modern–style tectonics in the Carajás Province, Amazonian Craton. J. South Am. Earth Sci. 104, 102817. https://doi.org/10.1016/j.jsames.2020.102817

Cristo, L.C.F., 2018. Estudo petrográfico e isotópico (Pb-Pb, U-Pb e Sm-Nd) de rochas metavulcânicas, mineralizações auríferas e rochas granitoides relacionadas ao greenstone belt Três Palmeiras, Volta Grande do Xingu, Domínio Bacajá. Universidade Federal do Pará.

da Silva, F.F., de Oliveira, D.C., Dall'Agnol, R., Schneider Santos, J.O., Galarza, M.A., Guimarães, F.V., de Sousa, L.A.M., 2025. Petrogenesis and tectonic settings of the Neoarchean A-type granitoid complex from the Carajás Province, Amazonian craton: constraints from geochemistry, SHRIMP U–Pb zircon geochronology and Hf–Nd isotopes. J. Geol. Soc. London. 182. https://doi.org/10.1144/jgs2024-109

Dall'Agnol, R., Cunha, I.R.V. da, Guimarães, F.V., Oliveira, D.C. de, Teixeira, M.F.B., Feio, G.R.L., Lamarão, C.N., 2017. Mineralogy, geochemistry, and petrology of Neoarchean ferroan to magnesian granites of Carajás Province, Amazonian Craton: The origin of hydrated granites associated with charnockites. Lithos 277, 3–32. https://doi.org/10.1016/j.lithos.2016.09.032

de Souza, Z.S., Potrel, A., Lafon, J.-M., Althoff, F.J., Martins Pimentel, M., Dall'Agnol, R., de Oliveira, C.G., 2001. Nd, Pb and Sr isotopes in the Identidade Belt, an Archaean greenstone belt of the Rio Maria region (Carajás Province, Brazil): implications for the Archaean geodynamic evolution of the Amazonian Craton. Precambrian Res. 109, 293–315. https://doi.org/10.1016/S0301-9268(01)00164-4

Dey, S., Moyen, J.-F., 2020. Archean granitoids of India: windows into early Earth tectonics – an introduction. Geol. Soc. London, Spec. Publ. 489, 1–13. https://doi.org/10.1144/SP489-2020-155

Feio, G.R.L., Dall'Agnol, R., 2012. Geochemistry and petrogenesis of the Mesoarchean granites from the Canaã dos Carajás area, Carajás Province, Brazil: Implications for the origin of Archean granites. Lithos 154, 33–52. https://doi.org/10.1016/j.lithos.2012.06.022

Feio, G.R.L., Dall'Agnol, R., Dantas, E.L., Macambira, M.J.B., Gomes, A.C.B.,

Sardinha, A.S., Oliveira, D.C., Santos, R.D., Santos, P.A., 2012. Geochemistry, geochronology, and origin of the Neoarchean Planalto Granite suite, Carajás, Amazonian craton: A-type or hydrated charnockitic granites? Lithos 151, 57–73. https://doi.org/10.1016/j.lithos.2012.02.020

Feio, G.R.L., Dall'Agnol, R., Dantas, E.L., Macambira, M.J.B., Santos, J.O.S., Althoff, F.J., Soares, J.E.B., 2013. Archean granitoid magmatism in the Canaã dos Carajás area: Implications for crustal evolution of the Carajás province, Amazonian craton, Brazil. Precambrian Res. 227, 157–185. https://doi.org/10.1016/j.precamres.2012.04.007

Garde, A.A., 1997. Accretion and evolution of an Archaean high-grade grey gneiss – amphibolite complex: the Fiskefjord area, southern West Greenland. Geology of Greenland Survey Bulletin, Copenhagen.

Hawkesworth, C., Cawood, P., Dhuime, B., 2013. Continental growth and the crustal record. Tectonophysics 609, 651–660. https://doi.org/10.1016/j.tecto.2013.08.013

Hawkesworth, C., Cawood, P.A., Dhuime, B., 2019. Rates of generation and growth of the continental crust. Geosci. Front. 10, 165–173. https://doi.org/10.1016/j.gsf.2018.02.004

Heilimo, E., Halla, J., Hölttä, P., 2010. Discrimination and origin of the sanukitoid series: Geochemical constraints from the Neoarchean western Karelian Province (Finland). Lithos 115, 27–39. https://doi.org/10.1016/j.lithos.2009.11.001

Hurley, P.., Almeida, F.F.., Melcher, G.., Cordani, U.., Rand, J., Kawashita, K., Vandoros, P., Pinson, W.., Fairbairn, H.., 1967. Test of continental drift by means of radiometric ages. Science (80-.). 495–500.

Jayananda, M., Moyen, J.-F., Martin, H., Peucat, J.-J., Auvray, B., Mahabaleswar, B., 2000. Late Archaean (2550–2520 Ma) juvenile magmatism in the Eastern Dharwar craton, southern India: constraints from geochronology, Nd–Sr isotopes and whole rock geochemistry. Precambrian Res. 99, 225–254. https://doi.org/10.1016/S0301-9268(99)00063-7

Joshi, K.B., Singh, S.K., Halla, J., Ahmad, T., Rai, V.K., 2022. Neodymium Isotope Constraints on the Origin of TTGs and High-K Granitoids in the Bundelkhand Craton, Central India: Implications for Archaean Crustal Evolution. Lithosphere 2022. https://doi.org/10.2113/2022/6956845

La Flèche, M.R., Camiré, G., Jenner, G.A., 1998. Geochemistry of post-Acadian, Carboniferous continental intraplate basalts from the Maritimes Basin, Magdalen

Islands, Québec, Canada. Chem. Geol. 148, 115–136. https://doi.org/10.1016/S0009-2541(98)00002-3

Laurent, O., Martin, H., Moyen, J.F., Doucelance, R., 2014. The diversity and evolution of late-Archean granitoids: Evidence for the onset of “modern-style” plate tectonics between 3.0 and 2.5Ga. Lithos 205, 208–235. https://doi.org/10.1016/j.lithos.2014.06.012

Lobach-Zhuchenko, S.B., Rollinson, H.R., Chekulaev, V.P., Arestova, N.A., Kovalenko, A.V., Ivanikov, V.V., Guseva, N.S., Sergeev, S.A., Matukov, D.I., Jarvis, K.E., 2005. The Archaean sanukitoid series of the Baltic Shield: geological setting, geochemical characteristics and implications for their origin. Lithos 79, 107–128. https://doi.org/10.1016/j.lithos.2004.04.052

Macambira, E.M.B., Ricci, P.S.F., 2015. Geologia e recursos minerais da Folha Tucuruí – SA.22-Z-C, Estado do Pará, 1st ed. CPRM, Belém.

Macambira, M.J.B., Amireault, S., 2025. Isotopic study (U Pb, Sm Nd, and Pb Pb) of rocks and auriferous mineralizations from the Volta Grande do Xingu deposits, Bacajá Domain, Amazonian craton. J Geochem Explor 274, 107767. https://doi.org/10.1016/j.gexplo.2025.107767

Macambira, M.J.B., Pinheiro, V.L., Armstrong, R.A., 2007. A fronteira Arqueano-Paleoproterozoico no SE do Cráton Amazônico: abrupta no tempo, suave na tectônica?, in: X Simpósio de Geologia Da Amazônia. pp. 97–100.

Macambira, M.J.B., Silva, D.C.C., Barros, C.E.M., Scheller, T., 2003. New isotope evidences confirming the existence of a paleoproterozoic terrain in the region at the north of the Carajas Mineral Province, in: IV South American Symposium on Isotope Geology. Salvadaro, Brazil, pp. 205–206.

Macambira, M.J.B., Silva, D.C.C., Vasquez, M.L., Barros, C.E.M., 2004. Investigação do limite Arqueano-Paleoproterozoico ao norte da Província Carajás, Amazônia Oriental, in: 42º Congresso Brasileiro de Geologia. Araxá.

Macambira, M.J.B., Vasquez, M.L., Monteiro, P.C., Armstrong, R.A., 2022. Neoarchean to Rhyacian crustal records along the Middle Xingu River area, Amazonian craton. Brazilian J. Geol. 52. https://doi.org/10.1590/2317-4889202220220017

Macambira, M.J.B., Vasquez, M.L., Silva, D.C.C., Galarza, M.A., Barros, C.E.M., Camelo, J.F., 2009. Crustal growth of the central-eastern Paleoproterozoic domain, SW Amazonian craton: Juvenile accretion vs. reworking. J. South Am. Earth Sci. 27, 235–246. https://doi.org/10.1016/j.jsames.2009.02.001

Magalhães, L.B., Macambira, M.J.B., Macambira, E.M.B., Ricci, P. dos S.F., 2023. Crustal growth in the northeast portion of the Rhyacian Bacajá Domain, SE Amazonian craton, based on U-Pb, Lu-Hf, and Sm-Nd data. Brazilian J. Geol. 53. https://doi.org/10.1590/2317-4889202320220068

Marangoanha, B., Oliveira, D.C. de, Dall'Agnol, R., 2019. The Archean granulite-enderbite complex of the northern Carajás province, Amazonian craton (Brazil): Origin and implications for crustal growth and cratonization. Lithos 350–351. https://doi.org/10.1016/j.lithos.2019.105275

Martin, H., Smithies, R.H., Rapp, R., Moyen, J.-F., Champion, D., 2005. An overview of adakite, tonalite–trondhjemite–granodiorite (TTG), and sanukitoid: relationships and some implications for crustal evolution. Lithos 79, 1–24. https://doi.org/10.1016/j.lithos.2004.04.048

McDonough, W.F., Sun, S. -s., 1995. The composition of the Earth. Chem. Geol. 120, 223–253. https://doi.org/10.1016/0009-2541(94)00140-4

Moyen, J.-F., Martin, H., 2012. Forty years of TTG research. Lithos 148, 312–336. https://doi.org/10.1016/j.lithos.2012.06.010

Nascimento, A.C. do, Oliveira, D.C. de, Gabriel, E.O., Leite-Santos, P.J., 2025. Geology, geochemistry and zircon SHRIMP U–Pb geochronology of Mesoarchean high-Mg granitoids: constraints on petrogenesis, emplacement timing and deformation of the Água Limpa suite in the Carajás Province, SE Amazonian Craton. J. Geol. Soc. London. 182. https://doi.org/10.1144/jgs2024-098

Neri, A.S.S., Dall'Agnol, R., Dantas, E.L., Feio, G.R.L., Almeida, J.A.C., Galarza, M.A., Rhyacian magmatism in the southern Bacajá Domain: Implications for the crustal evolution of SE Amazonian Craton, Brazil. *Precambrian Research*, manuscript submitted for publication.

Oliveira, M.A. de, Dall'Agnol, R., Almeida, J. de A.C. de, 2011. Petrology of the Mesoarchean Rio Maria suite and the discrimination of sanukitoid series. Lithos 127, 192–209. https://doi.org/10.1016/j.lithos.2011.08.017

Peng, P., Qin, Z., Sun, F., Zhou, X., Guo, J., Zhai, M., Ernst, R.E., 2019. Nature of charnockite and Closepet granite in the Dharwar Craton: Implications for the architecture of the Archean crust. Precambrian Res. 334, 105478. https://doi.org/10.1016/j.precamres.2019.105478

Plank, T., Langmuir, C.H., 1998. The chemical composition of subducting sediment and its consequences for the crust and mantle. Chem. Geol. 145, 325–394.

https://doi.org/10.1016/S0009-2541(97)00150-2

Qian, Q., Hermann, J., 2010. Formation of High-Mg Diorites through Assimilation of Peridotite by Monzodiorite Magma at Crustal Depths. J. Petrol. 51, 1381–1416. https://doi.org/10.1093/petrology/egq023

Ribeiro-Silva, L., Oliveira, D.C., Toro, M.A.G., Nascimento, A.C. do, Marangoanha, B., Marques, G.T., 2023. Zircon U–Pb–Hf isotope and geochemical constraints on the petrogenesis and tectonic setting of Mesoarchean granitoids from the Carajás province, Amazonian craton, Brazil. Precambrian Res. 398, 107204. https://doi.org/10.1016/j.precamres.2023.107204

Santos, J.O.S., Hartmann, L.A., Faria, M.S., Riker, S.R., Miguel, M., Almeida, M.E., Mcnaughton, N.J., 2006. a Compartimentação Do Cráton Amazonas Em Províncias : Avanços Ocorridos No Período 2000-2006, in: IX Simpósio de Geologia Da Amazônica. Sociedade Brasileira de Geologia, Belém.

Semprich, J., Moreno, J.A., Oliveira, E.P., 2015. Phase equilibria and trace element modeling of Archean sanukitoid melts. Precambrian Res. 269, 122–138. https://doi.org/10.1016/j.precamres.2015.08.004

Smithies, R.H., Champion, D.C., 2000. The Archaean High-Mg Diorite Suite: Links to Tonalite-Trondhjemite-Granodiorite Magmatism and Implications for Early Archaean Crustal Growth. J. Petrol. 41, 1653–1671. https://doi.org/10.1093/petrology/41.12.1653

Spencer, L.M., Albert, C., Williams, H.M., Nebel, O., Parkinson, I.J., Smithies, R.H., Bruno, H., Fowler, M., Moreira, H., Lissenberg, C.J., Millet, M.-A., 2024. Tracing hydrous eclogite melts in the source of sanukitoids. Earth Planet. Sci. Lett. 648, 119067. https://doi.org/10.1016/j.epsl.2024.119067

Steenfelt, A., Garde, A.A., Moyen, J.-F., 2005. Mantle wedge involvement in the petrogenesis of Archaean grey gneisses in West Greenland. Lithos 79, 207–228. https://doi.org/10.1016/j.lithos.2004.04.054

Sun, G., Liu, S., Wang, M., Bao, H., Teng, G., 2020. Complex Neoarchean mantle metasomatism: Evidence from sanukitoid diorites-monzodiorites-granodiorites in the northeastern North China Craton. Precambrian Res. 342, 105692. https://doi.org/10.1016/j.precamres.2020.105692

Tassinari, C.C.G., Macambira, M.J.., 2004. A evolução tectônica do Craton Amazônico, in: Mantesso-Neto, V., Bartorelli, A., Carneiro, C.D.R., Brito Neves, B.B. (Eds.), Geologia Do Continente Sul Americano: Evoluc¸ Ão Da Obra de Fernando Flávio

Marques Almeida. São Paulo, pp. 471–486.

Vasquez, M.L.., Rosa-Costa, L.T.., 2008. Geologia e Recursos Minerais do Estado do Pará : Sistema de Informações Geográficas – SIG : texto explicativo dos mapas Geológico e Tectônico e de Recursos Minerais do Estado do Pará, 1st ed. Brazilian Geological Service, CPRM, Belém.

Vasquez, M.L., 2006. Geocronologia em zircão, monazita e granada e isótopos de Nd das associações litológicas da porção oeste do Domínio Bacajá: evolução crustal da porção meridional da Província Maroni-Itacaiúnas – Sudeste Do Cráton Amazônico. Universidade Federal do Pará.

Vasquez, M.L., Macambira, M.J.B., Armstrong, R.A., 2008. Zircon geochronology of granitoids from the western Bacajá Domain, southeastern Amazonian craton, Brazil: Neoarchean to Orosirian evolution. Precambrian Res. 161, 279–302. https://doi.org/10.1016/j.precamres.2007.09.001

Verma, S.P., Pandarinath, K., Verma, S.K., Agrawal, S., 2013. Fifteen new discriminant-function-based multi-dimensional robust diagrams for acid rocks and their application to Precambrian rocks. Lithos 168–169, 113–123. https://doi.org/10.1016/j.lithos.2013.01.014

Vieira, C., Amaral, W., Holanda Santos, F., 2022. Petrography, geochemistry and zircon U-Pb geochronology of the Siderian-Rhyacian granitoids of NW Bacajá Domain, Amazonian Craton. J. Geol. Surv. Brazil 5. https://doi.org/10.29396/jgsb.2022.v5.n3.1

Whitehouse, M.J., Kemp, A.I.S., 2010. On the difficulty of assigning crustal residence, magmatic protolith and metamorphic ages to Lewisian granulites: Constraints from combined in situ U-Pb and Lu-Hf isotopes. Geol. Soc. Spec. Publ. 335, 81–101. https://doi.org/10.1144/SP335.5

Whitney, D.L., Evans, B.W., 2010. Abbreviations for names of rock-forming minerals. Am. Mineral. 95, 185–187. https://doi.org/10.2138/am.2010.3371

Workman, R.K., Hart, S.R., 2005. Major and trace element composition of the depleted MORB mantle (DMM). Earth Planet. Sci. Lett. 231, 53–72. https://doi.org/10.1016/j.epsl.2004.12.005

Zhang, Zhiguo, Liu, X., Xiao, W., Xu, J.-F., Shi, Y., Gong, X., Hu, R., Liu, P., Song, Y., Xiao, Y., Zhang, Zhaoqi, Li, R., Li, D., 2021. Geochemistry and Sr–Nd–Hf–Pb isotope systematics of late Carboniferous sanukitoids in northern West Junggar, NW China: Implications for initiation of ridge-subduction. Gondwana Res. 99, 204–218.

https://doi.org/10.1016/j.gr.2021.07.008

SUPPLEMENTARY MATERIAL 1 - METHODS

GEOLOGICAL MAPPING AND PETROGRAPHY

Geological mapping was undertaken in the southern Bacajá Domain area in three campaigns from 2019 to 2023. Petrographic, geophysical, and geochemical surveys supported geological mapping. The petrography was done at the Microscopy Laboratory of the Instituto de Geociências of Universidade Federal do Pará, Brazil.

GEOCHEMISTRY

Six chemical analyses of representative samples from the studied rocks (five orthogneisses and one amphibolite) were conducted at ALS laboratories. These analyses were comprehensive, with major element concentrations determined using inductively coupled plasma emission spectrometry (ICP-AES), and trace and rare earth elements analyzed by inductively coupled plasma–mass spectrometry (ICP–MS). Information regarding the description of the methods and the detection limits is available at https://www.alsglobal.com.

ZIRCON U-Pb AND Hf ISOTOPES

Zircon was separated using standard rock crushing and heavy mineral separation techniques. Grains were individually selected, picked, and mounted in epoxy resin. Grain mounts were polished to expose the grain centers.

For sample ASM-22 backscatter electron images for zircon were performed with a QUANTA 450 – FEI scanning electron microscope (SEM) at the Laboratório de Estudos Geodinâmicos, Geocronológicos e Ambientais (LEGGA, from Brasília University – UnB) with the following conditions: 10 nA, 20kV, 13.8 mm working distance. The sample ASM-22 was analyzed at LEGGA-UnB; the analyses follow the laboratory's standard procedures (Bühn et al., 2009). The analyses in zircon were carried out using the Neptune Series High-Resolution Multicollector ICP-MS coupled with laser ablation system Nd-YAG 213nm NewWave. Instrument setup parameters were 3,81 laser fluence, 10 Hz, ~25 μm spot size. U-Pb zircon data were standardized using GJ-1 (reference 609 Ma, Jackson et al., 2004)) as a primary standard and tested using the zircon 91500 (reference 1065 Ma, Wiedenbeck et al., 1995) as a secondary standard. External errors were calculated with the error propagation of individual measurements of GJ-1 and each spot's measurements. Data reduction was made using the software Iolite v4.0 (Paton et al., 2011), and VisualAge (Petrus and Kamber, 2012)

For sample AA-144A, the U-Pb analyses on zircon were done at Centro de Pesquisas Geocronológicas (CPGeo) from the University of São Paulo (USP). The analysis was performed using a Neptune ICP-MS and Analyte Excite excimer laser. Instrument setup

parameters were 0.89 J/cm^2 laser fluence, 6 Hz, ~20 μm spot size. The procedure consisted of 40 sequential measurements, with an integration time of about 1 second each. The first 10 measurements were made with the laser off to obtain the instrumental blank, followed by 30 measurements with the laser on. Seven isotopic signals were measured simultaneously: 206, 208, 232, and 238 in Faraday cups, and 202, 204, and 207 in Multiple Ion Counters. The instrumental blank value was subtracted from each isotopic signal after every sequence. The 235 isotope was not directly measured but was calculated by dividing the 238 signal by the U $^{238/235}$ relative abundance (137.88). The contribution of Hg in the 204 signal was corrected by subtracting the quotient of the 202 signal divided by the Hg $^{202/204}$ relative abundance (4.355). Using the U/Pb ratios (206/238, 207/235, and 208/232), relative abundances of 206/204, 207/204, and 208/204 were calculated using Stacey-Kramers equations. The common Pb fraction of 206, 207, and 208 was subtracted by removing the 204 signal multiplied by the respective relative abundances. The GJ-1 1 (reference 609 Ma, Jackson et al., 2004) standard was periodically re-measured (approximately every 10 minutes) to correct for instrumental variations and tested the Pleošovice zircon (reference 337 Ma, Sláma et al., 2008), was used as secondary standard. This allowed the calculation of the multiplicative coefficients used to convert Pb, Th, and U signals into ppm units and the correction factors for the four ratios (206/238, 207/235, 207/206, and 208/232) used in age calculation. Concordia diagrams and density plots were done using Isoplot/Ex (Ludwig, 2003).

The Lu-Hf analyses on zircon were performed using a LA–MC–ICP–MS at the Pará-Iso (UFPA). The laboratory procedures are described in Milhomem Neto and Lafon (2019). The laser-induced elemental fractionation and instrumental mass discrimination were corrected using the isotopic ratios of the GJ-1 zircon (608.5 ± 1.5 Ma; Jackson et al., 2004), while the Mud Tank zircon (732 ± 1 Ma; Horstwood et al., 2016) was analyzed as a secondary reference material.

The Lu, Hf, and Yb isotopes were concomitantly measured from isotope ratios $^{173}Yb/^{171}Yb$, $^{179}Hf/^{177}Hf$, $^{175}Lu/^{177}Hf$, and $^{176}Hf/^{177}Hf$ (spot size of 40-50 μm). The isobaric interferences of ^{176}Lu and ^{176}Yb were corrected using an equation that involved a mass fractionation factor (β) for Lu and Yb and the intensity of the signals observed in the interference-free isotopes ^{175}Lu and ^{173}Yb, normalized from their isotopic abundances $^{176}Lu/^{175}Lu = 0.026549$ (Chu et al., 2002) and $^{176}Yb/^{173}Yb = 0.786956$ (Thirlwall and Anczkiewicz, 2004). For the correction of the isotopic fractionation caused by the equipment during the analyses, according to the exponential law (Russell et al., 1978),

the Yb isotope ratios were normalized assuming a value of 1.12346 for $^{173}Yb/^{171}Yb$ (Thirlwall and Anczkiewicz, 2004), and the Hf isotope ratios were normalized using a value of 0.7325 for $^{179}Hf/^{177}Hf$ (Patchett and Tatsumoto, 1981). The mass bias behavior of Lu was assumed to be identical to that of Yb. To perform these correction calculations and obtain the corrected $^{176}Hf/^{177}Hf$ and $^{176}Lu/^{177}Hf$ ratios of each analyzed spot, the raw data were processed with a Microsoft Excel macro (Milhomem Neto and Lafon, 2019).

The calculations of ƐHf(t) and two-stage model ages (Hf-T_{DM}^{C}) used the decay constant λ_{176Lu} of $1.867x10^{-11}$ $years^{-1}$ (Söderlund et al., 2004), as well as a $^{176}Lu/^{177}Hf$ ratio of 0.015 as an average value for continental crust (Griffin et al., 2002). For present-day, $^{176}Lu/^{177}Hf$ of 0.0336 and $^{176}Hf/^{177}Hf$ ratios of 0.282785 for the chondritic uniform reservoir (CHUR) (Bouvier et al., 2008) and $^{176}Lu/^{177}Hf$ ratios of 0.0388 and $^{176}Hf/^{177}Hf$ of 0.28325 for the depleted mantle (DM) (Andersen et al., 2009) were assumed.

WHOLE ROCK Sm-Nd ISOTOPES

Sm-Nd isotopic analyses were performed on two laboratories. Sample ASM-22 and ASM-05 were analyzed at LEGGA -UnB, following the method described by Gioia and Pimentel (2000) using a Finnigan MAT 262 mass spectrometer. Whole-rock powders (~50 mg) were mixed with ^{149}Sm–^{150}Nd spike solution and dissolved in Savillex Digestion Vessels. Sm and Nd extraction of whole-rock samples followed conventional cation exchange chromatography techniques, with Teflon columns containing LN-Spec resin (HDEHP – diethylhexil phosphoric acid supported on PTFE powder). Sm and Nd fractions were loaded on Re evaporation filaments of double filament assemblies, and the isotopic measurements were carried out on a multicollector thermal ionization mass spectrometer in static mode. Uncertainties of Sm/Nd and $^{143}Nd/^{144}Nd$ ratios were better than ±0.1% (2 σ standard error) and ±0.0015% (1σ), respectively, according to repeated analyses of the international rock standard BHVO-1. $^{143}Nd/^{144}Nd$ ratios were normalized to $^{146}Nd/^{144}Nd=0.7219$, and the decay constant used was $6.54x10^{-12}$. The T_{DM} values were calculated using the model of DePaolo (1981).

The other three samples (AA-142, AA-143 and AA-144A) were analyzed at CPGEO-USP following the methodology described by Magdaleno et al. (2024) using a Neptune Plus Thermo Scientific MC-ICP-MS. Prior to analysis, the acids used were purified at low temperatures using sub-boiling distillers (DST-1000® Savillex) and sub-boiling distillation bottles (®Savillex). Approximately 50 mg of powdered rock were dissolved through acid digestion in successive steps using HNO_3 + HF and HCl in a Teflon beaker (®Savillex) at 100°C in a clean box. For each sample, Nd and Sm analyses were

performed through 120 and 45 measurements, respectively, and uncertainties were calculated at the 2σ level. The $^{143}Nd/^{144}Nd$ isotopic ratios were normalized to a $^{146}Nd/^{144}Nd$ value of 0.7219 (DePaolo, 1981).

REFERENCES

Andersen, T., Andersson, U.B., Graham, S., Åberg, G., Simonsen, S.L., 2009. Granitic magmatism by melting of juvenile continental crust: new constraints on the source of Palaeoproterozoic granitoids in Fennoscandia from Hf isotopes in zircon. J. Geol. Soc. London. 166, 233–247. https://doi.org/10.1144/0016-76492007-166

Bouvier, A., Vervoort, J.D., Patchett, P.J., 2008. The Lu–Hf and Sm–Nd isotopic composition of CHUR: Constraints from unequilibrated chondrites and implications for the bulk composition of terrestrial planets. Earth Planet. Sci. Lett. 273, 48–57. https://doi.org/10.1016/j.epsl.2008.06.010

Chu, N.-C., Taylor, R.N., Chavagnac, V., Nesbitt, R.W., Boella, R.M., Milton, J.A., German, C.R., Bayon, G., Burton, K., 2002. Hf isotope ratio analysis using multi-collector inductively coupled plasma mass spectrometry: an evaluation of isobaric interference corrections. J. Anal. At. Spectrom. 17, 1567–1574. https://doi.org/10.1039/b206707b

Gioia, S.M.C.L., Pimentel, M.M., 2000. The Sm-Nd isotopic method in the Geochronology Laboratory of the University of Brasília. An. Acad. Bras. Cienc. 72, 218–245. https://doi.org/10.1590/s0001-37652000000200009

Griffin, W.., Wang, X., Jackson, S.., Pearson, N.., O'Reilly, S.Y., Xu, X., Zhou, X., 2002. Zircon chemistry and magma mixing, SE China: In-situ analysis of Hf isotopes, Tonglu and Pingtan igneous complexes. Lithos 61, 237–269. https://doi.org/10.1016/S0024-4937(02)00082-8

Horstwood, M.S.A., Košler, J., Gehrels, G., Jackson, S.E., McLean, N.M., Paton, C., Pearson, N.J., Sircombe, K., Sylvester, P., Vermeesch, P., Bowring, J.F., Condon, D.J., Schoene, B., 2016. Community-Derived Standards for <scp>LA</scp> - <scp>ICP</scp> - <scp>MS</scp> U-(Th-)Pb Geochronology – Uncertainty Propagation, Age Interpretation and Data Reporting. Geostand. Geoanalytical Res. 40, 311–332. https://doi.org/10.1111/j.1751-908X.2016.00379.x

Jackson, S.E., Pearson, N.J., Griffin, W.L., Belousova, E.A., 2004. The application of laser ablation-inductively coupled plasma-mass spectrometry to in situ U-Pb zircon geochronology. Chem. Geol. 211, 47–69.

https://doi.org/10.1016/j.chemgeo.2004.06.017

Ludwig, K.R., 2003. isoplot Excell version 3.0. A geochronological toolkit for Microsoft Excel,.

Magdaleno, G.B., Petronilho, L.Ap., Ruiz, I.R., Babinski, M., Martins, V.T.S., 2024. Pb-Sr-Nd isotopic characterization of USGS reference materials by TIMS and MC-ICP-MS at CPGeo-USP, in: XIII South American Symposium on Isotope Geology. Búzios, Brazil.

Milhomem Neto, J.M., Lafon, J.M., 2019. Zircon U-Pb and Lu-Hf isotope constraints on Archean crustal evolution in Southeastern Guyana Shield. Geosci. Front. 10, 1477–1506. https://doi.org/10.1016/j.gsf.2018.09.012

Patchett, P.J., Tatsumoto, M., 1981. A routine high-precision method for Lu-Hf isotope geochemistry and chronology. Contrib. to Mineral. Petrol. 75, 263–267. https://doi.org/10.1007/BF01166766

Paton, C., Hellstrom, J., Paul, B., Woodhead, J., Hergt, J., 2011. Iolite: Freeware for the visualisation and processing of mass spectrometric data. J. Anal. At. Spectrom. 26, 2508–2518. https://doi.org/10.1039/c1ja10172b

Petrus, J.A., Kamber, B.S., 2012. VizualAge: A Novel Approach to Laser Ablation ICP-MS U-Pb Geochronology Data Reduction. Geostand. Geoanalytical Res. 36, 247–270. https://doi.org/10.1111/j.1751-908X.2012.00158.x

Russell, W.A., Papanastassiou, D.A., Tombrello, T.A., 1978. Ca isotope fractionation on the Earth and other solar system materials. Geochim. Cosmochim. Acta 42, 1075–1090. https://doi.org/10.1016/0016-7037(78)90105-9

Sláma, J., Košler, J., Condon, D.J., Crowley, J.L., Gerdes, A., Hanchar, J.M., Horstwood, M.S.A., Morris, G.A., Nasdala, L., Norberg, N., Schaltegger, U., Schoene, B., Tubrett, M.N., Whitehouse, M.J., 2008. Plešovice zircon — A new natural reference material for U–Pb and Hf isotopic microanalysis. Chem Geol 249, 1–35. https://doi.org/10.1016/j.chemgeo.2007.11.005

Söderlund, U., Patchett, P.J., Vervoort, J.D., Isachsen, C.E., 2004. The 176Lu decay constant determined by Lu–Hf and U–Pb isotope systematics of Precambrian mafic intrusions. Earth Planet. Sci. Lett. 219, 311–324. https://doi.org/10.1016/S0012-821X(04)00012-3

Thirlwall, M.F., Anczkiewicz, R., 2004. Multidynamic isotope ratio analysis using MC–ICP–MS and the causes of secular drift in Hf, Nd and Pb isotope ratios. Int. J. Mass Spectrom. 235, 59–81. https://doi.org/10.1016/j.ijms.2004.04.002

Wiedenbeck, M., Allé, P., Corfu, F., Griffin, E.L., Meier, M., Oberli, F., Quadt, A.V., Roddick, J.C., Spiegel, W., 1995. Three Natural Zircon Standards for U-Th-Pb, Lu-Hf, Trace Element and Ree Analyses. Geostand. Newsl. 19, 1–23. https://doi.org/10.1111/j.1751-908X.1995.tb00147.x

SUPPLEMENTARY MATERIAL 2 – WHOLE-ROCK GEOCHEMISTRY

Table S 1 - Whole-rock geochemical data for Cajazeiras complex.

Sample	AA-145B	ASM-22	AA-143	AA-142	AA-144A
Lithology	Amph	TnOgn	GrdOgn	TnOgn	GrdOgn
SiO_2	55.2	66.1	66.5	66.6	72.2
TiO_2	1.52	0.58	0.43	0.59	0.38
Al_2O_3	14	16.7	15.85	16.05	14.75
FeO*	9.58	4.34	3.59	4.32	2.59
MgO	6	1.57	1.17	1.6	0.81
MnO	0.17	0.07	0.06	0.04	0.04
CaO	6.5	4.22	3.49	3.83	2.47
Na_2O	2.66	4.71	4.4	4.19	3.89
K_2O	2.14	1.77	2.3	2.22	3.01
P_2O_5	0.31	0.25	0.23	0.24	0.13
LOI	1.31	0.97	1.48	0.92	0.9
Total	100.68	101.93	100.07	101.29	101.71
Ba	1255	898	1095	1410	1730
Rb	130	48.2	89.1	78	95.3
Sr	389	580	475	548	507
Zr	166	245	281	241	158
Nb	11.8	6.63	6.11	4.17	5.03
Y	23.4	10.7	15	11.3	7.3
Hf	4.37	5.42	6.54	5.35	3.63
Ta	0.9	0.6	0.4	0.3	0.3
Ga	19.8	19.7	20.1	20	17.4
Cs	1.8	0.92	0.4	0.63	0.47
Sn	3	1	1.5	0.8	1.6
Th	8.26	2.63	12.1	15	5.79
U	1.67	0.73	0.78	0.39	0.51
V	150	76	53	74	40
Cr	260	41	46	59	39
Ti	0.96	0.37	0.28	0.38	0.24
Sc	19.4	9	7.5	7.6	5.4
La	40	43	50.5	80.1	31.1
Ce	79.5	82.8	98.8	147	58
Pr	10.1	8.87	10.65	14.9	5.91
Nd	40.8	31.8	36.6	51.6	21.3
Sm	7.75	5.26	6.19	6.76	2.95
Eu	1.78	1.27	1.14	1.36	1.27
Gd	6.57	3.95	4.33	4.17	2.39
Tb	0.83	0.49	0.51	0.6	0.28
Dy	4.68	2.03	2.48	2.6	1.26
Ho	0.94	0.42	0.48	0.5	0.29
Er	2.47	1.03	1.45	1.03	0.67
Tm	0.3	0.14	0.16	0.09	0.09
Yb	2.02	0.76	1.1	0.59	0.51
Lu	0.32	0.07	0.09	0.08	0.05
FeO_t+MgO+MnO+TiO_2	17.27	6.56	5.25	6.55	3.82
Mg#	53	39	37	40	36
K_2O/Na_2O	0.80	0.38	0.52	0.53	0.77
Sr/Y	17	54	32	48	69
Ba+Sr	1644	1478	1570	1958	2237
(La/Yb)n	13.35	38.15	30.95	91.53	41.11
Eu/Eu*	0.76	0.85	0.67	0.78	1.46

Amph = amphibolte; Tn = tonalitic; Grd = granodioritic; Ogn = orthogneiss.

SUPPLEMENTARY MATERIAL 3 - ASSESSMENT OF ELEMENT MOBILITY

The Cajazeiras complex was affected by metamorphism, partial melting, and deformation during the Paleoproterozoic. Therefore, assessing the elements' mobility before employing them to constrain the complex's petrogenesis is crucial.

The criteria proposed by Polat and Hofmann (2003) suggest that low loss on ignition (LOI: 0.9-1.48 wt%) and the absence of distinct Ce anomalies (δCe, calculated as $Ce_N/sqrt(La_N \times Pr_N)$: 0.96-1.04) indicate that the complex's primary chemical signature has not significantly changed during post-magmatic processes (Polat et al., 2002; Polat and Hofmann, 2003).

REFERENCES

Polat, A., Hofmann, A.., 2003. Alteration and geochemical patterns in the 3.7–3.8 Ga Isua greenstone belt, West Greenland. Precambrian Res. 126, 197–218. https://doi.org/10.1016/S0301-9268(03)00095-0

Polat, A., Hofmann, A.., Rosing, M.., 2002. Boninite-like volcanic rocks in the 3.7–3.8 Ga Isua greenstone belt, West Greenland: geochemical evidence for intra-oceanic subduction zone processes in the early Earth. Chem. Geol. 184, 231–254. https://doi.org/10.1016/S0009-2541(01)00363-1

SUPPLEMENTARY MATERIAL 4 - U-Pb GEOCHRONOLOGY

Table S 2 - U-Pb LA-ICP-MS data on zircon for sample ASM-22.

Location - 539776/9424268								Data for Wetherill plot[2] (Isotopic ratios)							Ages (Ma)						
Identifier	Spot number	Family	^{206}Pb (mV)	U[1] (ppm)	Th/U	$^{206}Pb/^{204}Pb$	2s (%)	$^{207}Pb/^{235}U$	2s (%)	$^{206}Pb/^{238}U$	2s (%)	Rho	$^{207}Pb/^{206}Pb$	2s (abs)	$^{206}Pb/^{238}U$	2s (abs)	$^{207}Pb/^{235}U$	2s (abs)	$^{207}Pb/^{206}Pb$	2s (abs)	Conc[3] (%)
Core	#36	1a	0.004	36	2.84	12567	17.4	18.5702	2.39	0.6113	2.00	0.84	0.2202	1.31	3075	49	3019	23	2981	21	103.2
Core	#37	1a	0.002	22	3.98	11643	12.3	18.3192	2.71	0.6080	2.39	0.88	0.2187	1.29	3062	58	3007	26	2970	21	103.1
Core	#22	1a	0.050	566	0.75	166448	18.7	18.1531	2.39	0.6026	2.20	0.92	0.2191	0.94	3040	53	2998	23	2973	15	102.3
Core	#33	1a	0.002	25	2.60	6066	18.0	18.6636	3.03	0.6046	2.57	0.85	0.2243	1.60	3048	62	3024	29	3010	26	101.3
Core	#51	1a	0.009	102	1.48	132487	4.0	17.6925	2.17	0.5848	1.94	0.89	0.2202	0.98	2968	46	2973	21	2982	16	99.6
Core	#20	1a	0.007	83	4.79	9066	83.3	13.0161	2.32	0.4560	2.19	0.94	0.2057	0.78	2422	44	2681	22	2871	13	84.4
Core	#47	1a	0.017	256	2.36	12937	58.7	10.4972	2.24	0.3897	2.03	0.91	0.1950	0.93	2121	37	2479	21	2784	15	76.2
Core	#10	1a	0.031	598	2.32	11209	84.0	9.0228	3.10	0.3470	2.62	0.84	0.1889	1.67	1920	43	2340	28	2731	27	70.3
Core	#39	1a	0.009	153	1.61	2577	83.5	8.7175	2.52	0.3395	2.32	0.92	0.1855	0.97	1884	38	2309	23	2702	16	69.7
Core	#09	1a	0.014	237	2.47	473	86.8	8.4100	6.92	0.3281	6.24	0.90	0.1860	2.99	1827	99	2275	64	2703	50	67.6
Core	#26	1a	0.032	642	2.40	4661	15.8	8.0870	3.27	0.3192	3.10	0.95	0.1839	1.04	1785	49	2240	29	2687	17	66.4
Core	#08	1b	0.022	234	1.88	9084	42.6	15.1354	2.28	0.5516	1.92	0.84	0.1982	1.23	2832	44	2824	22	2811	20	100.8
Core	#24	1b	0.012	187	1.92	4965	93.3	8.9646	4.40	0.3621	3.75	0.85	0.1786	2.31	1991	64	2332	38	2638	38	75.5
Core	#19	1b	0.030	601	0.92	4067	13.3	7.9555	2.99	0.3343	2.59	0.87	0.1728	1.48	1859	42	2225	27	2584	25	72.0
Core	#49	1b	0.031	754	2.06	7868	42.7	6.2073	2.80	0.2763	2.67	0.96	0.1635	0.82	1572	37	2005	24	2492	14	63.1
Core	#05	D	0.015	194	2.91	9927	####	11.1673	2.78	0.4120	2.38	0.86	0.1955	1.44	2224	45	2536	25	2787	24	79.8
Core	#41	D	0.044	569	1.87	43152	20.6	14.7173	2.58	0.4998	2.47	0.96	0.2140	0.74	2613	53	2797	25	2935	12	89.0
Core	#34	D	0.035	598	2.57	23652	23.4	9.3478	2.37	0.3665	2.07	0.87	0.1850	1.16	2013	36	2372	22	2698	19	74.6
Core	#38	D	0.013	118	0.89	34406	55.2	18.3845	2.48	0.6202	2.28	0.92	0.2143	0.97	3111	56	3010	24	2938	16	105.9
Core	#13	D	0.032	349	2.33	15003	####	15.3546	2.44	0.5345	2.29	0.94	0.2076	0.83	2760	52	2837	23	2886	13	95.6
Core	#35	D	0.056	731	2.32	14161	51.8	14.7534	2.58	0.5150	2.38	0.92	0.2085	0.99	2678	52	2799	25	2894	16	92.6
Core	#54	D	0.005	51	1.52	3781	68.2	14.8727	2.76	0.5300	2.41	0.87	0.2030	1.33	2741	54	2807	26	2849	22	96.2
Core	#21	D	0.034	755	2.42	12459	60.0	7.5957	2.09	0.3009	1.93	0.93	0.1833	0.79	1696	29	2184	19	2682	13	63.2
Core	#27	D	0.023	610	2.69	3283	51.3	5.6769	2.58	0.2510	2.28	0.88	0.1644	1.21	1443	29	1928	22	2500	20	57.7
Rim	#12	2	0.006	95	0.45	239090	2.8	7.8030	2.33	0.4093	2.20	0.95	0.1386	0.75	2212	41	2208	21	2210	13	100.1
Rim	#11	2	0.008	144	1.32	3224	71.7	7.2943	2.05	0.3990	1.89	0.92	0.1329	0.79	2164	35	2148	18	2136	14	101.3
Rim	#28	2	0.008	139	1.20	20172	25.1	7.1359	2.20	0.3949	2.04	0.93	0.1314	0.80	2146	37	2128	20	2116	14	101.4
Rim	#40	2	0.005	86	1.82	32521	18.4	7.1162	2.34	0.3944	1.96	0.84	0.1310	1.28	2143	36	2126	21	2110	22	101.6
Rim	#25	2	0.008	133	0.31	14550	2.6	7.1406	2.26	0.3964	1.89	0.83	0.1309	1.24	2152	35	2129	20	2109	21	102.1
Rim	#42	2	0.013	212	0.61	60259	17.3	7.1958	2.10	0.4015	1.92	0.91	0.1303	0.86	2176	35	2136	19	2101	15	103.6
Rim	#48	2	0.016	274	0.86	14207	16.2	7.1221	2.70	0.3984	2.53	0.94	0.1302	0.95	2162	47	2127	24	2099	17	103.0
Rim	#55	2	0.014	247	0.76	47008	24.9	6.9763	2.21	0.3901	1.93	0.87	0.1301	1.07	2123	35	2108	20	2098	19	101.2
Rim	#53	2	0.010	184	0.71	51239	15.8	6.9235	2.08	0.3883	1.90	0.92	0.1298	0.83	2115	34	2102	19	2094	15	101.0
Rim	#50	2	0.008	134	1.80	18952	16.7	6.9283	2.08	0.3899	1.90	0.91	0.1291	0.85	2122	34	2102	19	2085	15	101.8
Rim	#23	2	0.021	313	0.09	33029	81.1	7.1164	2.19	0.4004	1.93	0.88	0.1286	1.02	2171	36	2126	20	2078	18	104.5
Rim	#52	2	0.006	108	1.44	91548	4.3	6.7248	2.05	0.3808	1.89	0.92	0.1283	0.79	2080	34	2076	18	2074	14	100.3
Rim	#07	2	0.009	142	1.39	22067	24.5	7.2229	2.51	0.4081	2.34	0.93	0.1285	0.89	2206	44	2139	22	2077	16	106.2
Rim	#06	2	0.024	374	0.86	14146	62.5	7.2459	2.13	0.4101	1.97	0.92	0.1282	0.81	2216	37	2142	19	2073	14	106.9

Rim	#14	2	0.010	163	1.23	44108	6.1	7.1356	2.04	0.4036	1.88	0.92	0.1282	0.79	2185	35	2128	18	2072	14	105.4
Rim	#56	2	0.013	671	0.39	537	93.3	2.1031	3.47	0.1295	2.59	0.75	0.1176	2.31	785	19	1148	23	1917	42	41.0

Following http://www.plasmage.org/recommendations

[1] concentration uncertainty c.20%

[2] data not corrected for common-Pb

[3] Concordance calculated as (^{206}Pb-^{238}U age/^{207}Pb-^{206}Pb age)*100

Decay constants of Jaffey et al. (1971) used

Uncertainties quoted without components related to systematic error unless otherwise stated

Total systematic uncertainties (s_{sys}): ^{206}Pb/^{238}U = 1.0%, ^{207}Pb/^{206}Pb = 0.55% (2s)

U = used in age calculations, D = discarded for age calculations

Table S 3 - U-Pb LA-ICP-MS data on zircon for sample AA-144A.

Location - 555726/9420040								Isotopic ratios							Ages (Ma)						
Spot number	Texture	Family	Common Pb (%)	Pb (ppm)	Th (ppm)	U (ppm)	Th/U	$^{207}Pb/^{235}U$	1s (abs)	$^{206}Pb/^{238}U$	1s (abs)	Rho	$^{207}Pb/^{206}Pb$	1s (abs)	$^{206}Pb/^{238}U$	1s (abs)	$^{207}Pb/^{235}U$	1s (abs)	$^{207}Pb/^{206}Pb$	1s (abs)	Conc. (%)
4.1	core	1a	0.23	89	40	83	0.48	22.4466	0.2472	0.7278	0.0033	0.47	0.2237	0.0023	3525	12	3203	11	3007	17	110
6.1	core	1a	0.10	22	19	26	0.71	15.9527	0.2176	0.5485	0.0043	0.93	0.2109	0.0030	2819	18	2874	13	2913	23	98
15.1	core	1a	0.00	8	12	8	1.53	17.6948	0.2576	0.5917	0.0050	0.89	0.2169	0.0029	2997	20	2973	14	2958	22	100
10.1	core	1a	10.77	211	501	612	0.82	3.5239	0.0438	0.1945	0.0011	0.99	0.1314	0.0012	1146	6	1533	9	2117	15	74
21.1	core	1a	8.62	194	431	398	1.08	5.0485	0.0538	0.2375	0.0014	0.99	0.1542	0.0012	1374	7	1828	8	2393	13	75
40.1	core	1b	0.16	187	265	177	1.50	15.2396	0.1411	0.5563	0.0035	0.95	0.1987	0.0016	2851	15	2830	9	2815	13	100
33.1	core	1b	0.47	152	163	188	0.86	13.4270	0.1697	0.5013	0.0044	0.99	0.1943	0.0026	2619	19	2710	12	2779	22	96
8.1	core	1b	1.59	98	66	121	0.54	14.0042	0.1615	0.5158	0.0024	0.98	0.1969	0.0021	2681	10	2750	11	2801	17	97
42.1	core	1b	0.57	222	225	305	0.74	11.1060	0.1428	0.4313	0.0030	0.84	0.1868	0.0022	2312	13	2532	12	2714	20	91
31.1	core	1b	0.35	208	358	288	1.24	8.7171	0.1128	0.3546	0.0031	0.93	0.1783	0.0023	1957	15	2309	12	2637	22	84
5.1	core	1b	0.71	178	186	312	0.60	8.6298	0.1018	0.3519	0.0015	0.90	0.1779	0.0018	1944	7	2300	11	2633	17	84
24.1	core	1b	0.50	177	173	229	0.76	12.3880	0.1176	0.4759	0.0025	0.91	0.1888	0.0015	2509	11	2634	9	2732	13	95
7.1	core	D	6.58	116	140	241	0.58	8.3728	0.0748	0.3880	0.0014	0.97	0.1565	0.0016	2113	7	2272	10	2418	19	93
17.1	core	D	0.59	221	525	535	0.98	6.0205	0.0522	0.2693	0.0013	0.95	0.1621	0.0012	1537	7	1979	8	2478	13	77
19.1	core	D	1.02	150	112	220	0.51	10.3685	0.0960	0.4397	0.0023	0.94	0.1710	0.0013	2349	10	2468	9	2568	13	95
22.1	core	D	1.21	196	271	255	1.06	11.4210	0.1015	0.4578	0.0023	0.79	0.1809	0.0013	2430	10	2558	8	2662	12	94
23.1	core	D	2.55	192	373	263	1.42	12.0151	0.0976	0.4629	0.0024	0.99	0.1882	0.0014	2453	11	2606	8	2727	13	94
14.1	core	D	8.48	200	583	476	1.23	4.8329	0.0437	0.2306	0.0012	0.99	0.1520	0.0011	1338	6	1791	8	2369	13	74
26.1	core	D	1.01	250	579	501	1.16	6.5761	0.0613	0.2970	0.0016	0.99	0.1606	0.0012	1676	8	2056	8	2462	12	81
27.1	core	D	0.24	92	59	95	0.62	17.6295	0.1336	0.6379	0.0036	0.99	0.2004	0.0016	3181	14	2970	7	2830	13	107
30.1	core	D	4.26	208	525	477	1.10	5.2187	0.0399	0.2499	0.0014	0.26	0.1514	0.0012	1438	7	1856	6	2362	13	77
32.1	core	D	0.83	250	881	773	1.14	4.3345	0.0491	0.2130	0.0016	0.81	0.1476	0.0019	1245	9	1700	9	2318	22	73
34.1	core	D	1.38	181	427	413	1.04	9.9222	0.0860	0.4211	0.0026	0.99	0.1709	0.0022	2266	13	2428	11	2566	22	93
35.1	core	D	1.35	202	451	606	0.74	3.6067	0.0661	0.1832	0.0021	0.99	0.1428	0.0020	1085	11	1551	10	2261	22	69
36.1	core	D	0.55	263	705	564	1.25	7.0003	0.0560	0.3009	0.0017	0.99	0.1688	0.0013	1696	8	2112	7	2545	13	80
37.1	core	D	0.50	205	209	331	0.63	9.2696	0.0830	0.3929	0.0025	0.99	0.1711	0.0013	2136	11	2365	8	2569	13	90
38.1	core	D	10.99	238	415	619	0.67	4.6103	0.0355	0.2379	0.0013	0.99	0.1406	0.0011	1376	7	1751	7	2234	14	78
39.1	core	D	1.06	271	338	398	0.85	9.4378	0.0891	0.3982	0.0025	0.56	0.1719	0.0013	2161	12	2382	9	2576	13	90
41.1	core	D	0.36	223	236	357	0.66	7.7488	0.0732	0.3526	0.0023	0.99	0.1594	0.0012	1947	11	2202	9	2449	13	88
43.1	core	D	0.80	268	505	515	0.98	6.8401	0.0832	0.3106	0.0020	0.99	0.1597	0.0019	1744	10	2091	11	2453	20	83
44.1	core	D	7.39	242	389	472	0.82	6.4238	0.0610	0.2971	0.0021	0.99	0.1568	0.0013	1677	11	2036	9	2422	14	82
45.1	core	D	3.58	288	1057	955	1.11	3.6651	0.0330	0.1902	0.0013	0.97	0.1397	0.0011	1123	7	1564	7	2224	14	71
28.1	core	D	13.28	69	95	56	1.69	14.3025	0.1291	0.5237	0.0031	0.88	0.1981	0.0020	2715	13	2770	8	2811	15	98
1.1	core	D	12.73	146	309	258	1.20	7.0223	0.0950	0.2869	0.0013	0.95	0.1775	0.0021	1626	6	2114	10	2630	18	76
2.1	rim	2	9.53	105	220	208	1.06	5.8045	0.0603	0.3512	0.0013	0.99	0.1199	0.0013	1940	6	1947	10	1954	19	99
12.1	rim	2	5.84	95	132	174	0.76	5.2190	0.0639	0.3222	0.0020	0.99	0.1175	0.0011	1801	10	1856	10	1918	17	97
20.1	rim	2	1.23	115	155	195	0.80	6.8038	0.0611	0.3994	0.0020	0.99	0.1235	0.0010	2166	9	2086	8	2008	14	103
13.1	rim	D	4.33	94	49	183	0.27	6.1482	0.0649	0.3716	0.0019	0.99	0.1200	0.0010	2037	9	1997	10	1956	16	101
29.1	rim	D	0.03	104	115	188	0.61	6.5600	0.0478	0.3908	0.0023	0.97	0.1217	0.0010	2127	10	2054	7	1982	15	103

18.1	rim	D	0.68	64	104	105	0.99	6.8323	0.0646	0.3921	0.0025	0.91	0.1264	0.0012	2132	12	2090	8	2048	17	102
3.1	rim	D	1.55	139	301	179	1.68	11.2664	0.1242	0.4282	0.0019	0.99	0.1908	0.0021	2297	9	2545	11	2750	18	90
9.1	rim	D	1.39	65	111	110	1.01	6.7018	0.0759	0.3904	0.0023	0.99	0.1245	0.0012	2125	11	2073	10	2022	18	102
16.1	rim	D	0.07	53	131	42	3.11	16.5854	0.1695	0.5535	0.0034	0.96	0.2173	0.0019	2840	14	2911	9	2961	14	97
25.1	rim	D	3.19	158	358	367	0.98	6.2637	0.0553	0.2635	0.0013	0.99	0.1724	0.0013	1508	7	2013	8	2581	12	74
11.1	rim	D	15.31	189	352	404	0.87	4.6838	0.0548	0.2391	0.0014	0.91	0.1421	0.0013	1382	7	1764	10	2253	15	78

U = used in age calculations, D = discarded for age calculations

GJ first standard on 19/08/2024
Concordia Age = 602.7 ±1.6 Ma
GJ reference age: 608.5 +/- 0.4 Ma (TIMS) - Jackson et al. 2004.

Pleošovice secondary standard on 19/08/2024
Concordia Age = 337.3 ± 0.92 Ma
Pleošovice reference age: 337.13 +/- 0.37 - Sláma et al, 2008.

SUPPLEMENTARY MATERIAL 5 - Lu-Hf ISOTOPES ON ZIRCON

Table S 3 - Lu-Hf isotopic data on zircon by LA-MC-ICP-MS. *Calculated from the ratio $^{176}Lu/^{177}Hf = 0.015$, the average value of the continental crust (Griffin et al., 2002).

Spot ID	Family	t_{U-Pb} (Ma)	$^{176}Hf/^{177}Hf$	2SE	$^{176}Lu/^{177}Hf$	2SE	$^{176}Yb/^{177}Hf$	2SE	$^{178}Hf/^{177}Hf$	2SE	$\varepsilon_{Hf}(0)$	$^{176}Hf/^{177}Hf_{(t)}$	$\varepsilon_{Hf}(t)$	$\varepsilon_{Hf}(t)$ 2SE	Hf-T_{DM}^{C} (Ga)*
48	2	2095	0.281227	0.000037	0.000281	0.000024	0.011673	0.000331	1.467180	0.000052	-55.1	0.281216	-8.1	0.71	3.18
42	2	2095	0.281219	0.000030	0.000249	0.000010	0.011080	0.000272	1.467172	0.000055	-55.4	0.281209	-8.4	0.36	3.19
52	2	2095	0.281217	0.000024	0.000229	0.000011	0.009477	0.000299	1.467257	0.000048	-55.4	0.281208	-8.4	0.42	3.20
55	2	2095	0.281217	0.000028	0.000222	0.000016	0.009713	0.000385	1.467207	0.000049	-55.5	0.281208	-8.4	0.65	3.20
53	2	2095	0.281217	0.000024	0.000229	0.000011	0.009477	0.000299	1.467257	0.000048	-55.4	0.281208	-8.4	0.42	3.20
50	2	2095	0.281222	0.000025	0.000260	0.000020	0.011047	0.000549	1.467277	0.000038	-55.3	0.281211	-8.3	0.68	3.19
8	1b	2812	0.281029	0.000026	0.000762	0.000058	0.032431	0.001744	1.467244	0.000038	-62.1	0.280988	0.5	0.04	3.20
54	1b	2812	0.281038	0.000017	0.000789	0.000064	0.031216	0.004050	1.467164	0.000054	-61.8	0.280996	0.8	0.13	3.18
10	1b	2975	0.280981	0.000024	0.000760	0.000073	0.033400	0.002538	1.467199	0.000046	-63.8	0.280938	2.6	0.25	3.19
22	1a	2975	0.280951	0.000023	0.000291	0.000058	0.013124	0.001863	1.467182	0.000080	-64.9	0.280934	2.4	0.49	3.20
37	1a	2975	0.280968	0.000030	0.000542	0.000072	0.025133	0.002669	1.467085	0.000042	-64.3	0.280937	2.5	0.34	3.19
33	1a	2975	0.280960	0.000030	0.000501	0.000062	0.020579	0.003888	1.467071	0.000035	-64.5	0.280932	2.3	0.59	3.20

7 TITANITE PETROCHRONOLOGY OF GARNET-FREE ORTHOGNEISSES FROM THE BASEMENT OF BACAJÁ DOMAIN, SE AMAZONIAN CRATON: INSIGHTS INTO METAMORPHIC EVOLUTION WITHOUT GARNET CONTROL

Arthur Santos da Silva Neri

Roberto Dall'Agnol

Alice Cunha da Silva

Vinícius Tieppo Meira

Gilmara Regina Lima Feio

Valdecir de Assis Janasi

Ingrid Roberta Viana da Cunha

Elton Luiz Dantas [f]

A ser submetido à *Lithos* como *regular article.*

Respeitando as normas da revista *Lithos*, a formatação, citações e referências bibliográficas desta seção seguem o padrão requerido pela revista.

Titanite petrochronology of garnet-free orthogneisses from the basement of Bacajá Domain, SE Amazonian Craton: insights into metamorphic evolution without garnet control

Arthur Santos da Silva Neri [a, b*], Roberto Dall'Agnol [a, b, c], Alice Cunha da Silva [d, e], Vinícius Tieppo Meira [e], Gilmara Regina Lima Feio [d, f], Valdecir de Assis Janasi [g], Ingrid Roberta Viana da Cunha [b, h], Elton Luiz Dantas [i]

[a] Programa de pós-graduação em Geologia e Geoquímica, Instituto de Geociências (IG), Universidade Federal do Pará (UFPA), Rua Augusto Corrêa, 01, Belém-PA, Brazil. CEP 66075-110.

[b] Grupo de Pesquisa Petrologia de Granitoides IG – UFPA.

[c] Instituto Tecnológico Vale, Belém-PA, Brazil.

[d] Grupo de Mineralogia e Petrologia, Instituto de Geociências e Engenharias (IGE), Universidade Federal do Sul e Sudeste do Pará (Unifesspa), Marabá-PA, Brazil

[e] Departamento de Geologia e Recursos Naturais, Universidade Estadual de Campinas, Campinas-SP, Brazil, CEP 13083-855.

[f] Programa de Pós-Graduação em Propriedade Intelectual e Transferência de Tecnologia para a Inovação (UNIFESSPA).

[g] Instituto de Geociências, Universidade de São Paulo, Rua do Lago, 562, São Paulo-SP, Brazil, CEP 05508-080.

[h] Present address: Universidade Federal do Oeste do Pará (UFOPA), Rua Ver. José de Sousa Andrade, Juruti - PA, Brazil. CEP 68170-000.

[i] Laboratório de Estudos Geocronológicos, Geodinâmicos e Ambientais, Universidade de Brasília, Brasília-DF, Brazil. CEP 70910-900.

ABSTRACT: Linking titanite ($CaTiSiO_5$) composition and ages to the metamorphic evolution of the host rock provides valuable insights into the P-T-t evolution of orogens. This study presents in-situ titanite U-Pb and trace element data from two upper amphibolite- to granulite-facies orthogneisses of the Cajazeiras Complex, located in the basement of the southern Bacajá Domain, SE Amazonian Craton. The titanite data are integrated with the mineral chemistry of major phases, U-Pb zircon geochronology, pseudosection modeling, and trace element compositions of clinopyroxene and amphibole to investigate the chemical relationships between titanite and major phases in garnet-free rocks and to reconstruct the P-T-t evolution of the complex during

Paleoproterozoic orogenesis. Peak metamorphic conditions are characterized by the assemblage clinopyroxene + amphibole + biotite + plagioclase + K-feldspar + quartz + magnetite + ilmenite + melt, which occurred at ~0.52-0.55 GPa / 760-790ºC around 2210 Ma (?), based on U-Pb zircon rim ages. The cooling to the solidus likely took place between 2100-2076 Ma, as recorded by zircon rim growth. A subsequent retrometamorphic stage is characterized by the assemblage amphibole + biotite + plagioclase + K-feldspar + titanite + quartz + magnetite + ilmenite + H_2O, occurring at 0.40-0.48 GPa/600-650ºC and dated to 2017-2012 Ma based on U-Pb titanite data. Titanite is enriched in REE and has low $(Dy/Yb)_N$, confirming its crystallization in the absence of garnet. Neither clinopyroxene nor amphibole show significant HREE enrichment, displaying flat patterns, suggesting that they did not exert a strong influence on titanite chemistry.

Keywords: Titanite, Amphibole, upper amphibolite-granulite facies; Trace elements; P-T-t paths, Paleoproterozoic.

7.1 INTRODUCTION

Titanite ($CaTiSiO_5$) is a widespread accessory mineral in both metamorphic and igneous rocks (Broska et al., 2007; Kontonikas-Charos et al., 2019; Scibiorski et al., 2019; Scibiorski and Cawood, 2022; Spencer et al., 2013). Depending on the geochemical environment and element availability, various substitutions can occur at the Ti and Ca sites. Ti^{4+} can be replaced by Al, Fe, and high-field-strength elements (HFSE), whereas Ca^{2+} may incorporate rare earth elements (REE), U, Th, and Pb (Kontonikas-Charos et al., 2019; Kowallis et al., 2022). The presence of these elements makes titanite a powerful tool for deciphering the metamorphic evolution of host rock, as its trace element composition is controlled by element availability, P-T conditions, and the presence of other minerals (Cioffi et al., 2019; Scibiorski et al., 2019). These features, combined with its relatively high abundance in orthogneisses of intermediate and moderately calcic compositions (Frost et al., 2001; Kohn, 2017), make titanite a crucial tool for dating such rocks, which often lack other reactive petrochronometers like monazite.

Numerous studies have demonstrated that titanite is an effective petrochronometer in metamorphic rocks because it can record multiple metamorphic stages (Cioffi et al., 2019; Kavanagh-Lepage et al., 2024; Scibiorski et al., 2019; Stearns et al., 2015). The correlation between distinct titanite chemical domains and garnet growth or consumption has become increasingly common in the literature (Cioffi et al., 2019; Garber et al., 2017;

Scibiorski et al., 2019). These studies indicate a strong chemical link between titanite and garnet. However, in garnet-free samples, the relationship between titanite and other phases remains poorly understood. A few studies suggest a possible link between titanite and amphibole (Scibiorski et al., 2019), but this connection has yet to be fully explored.

In this study, we present titanite U-Pb ages and trace element compositions from two garnet-free metatexitic orthogneisses, metamorphosed at upper amphibolite- to granulite-facies conditions, from the basement of the Bacajá Domain, SE Amazonian craton. By integrating petrographic observations, phase equilibria modeling, major-phase chemistry, trace element analysis, and titanite petrochronology, we aim to elucidate titanite behavior in garnet-free orthogneisses and investigate its REE budget in relation to other phases. Our findings provide new insights into the metamorphic evolution of the Bacajá basement.

7.2 GEOLOGICAL SETTING

The Maroní-Itacaiúnas Province (Fig. 1) is the main province established during the Paleoproterozoic (Rhyacian) in the Amazonian craton (Santos et al., 2006; Tassinari and Macambira, 2004). The Bacajá Domain (Fig. 1c) represents an extension of the Maroní-Itacaiúnas province within the Brazil Central shield. This domain comprises Archean and Siderian fragments reworked during the Transamazonian Orogeny between ca. 2.26 and 1.99 Ga (Cordani et al., 2000; Hurley et al., 1967; Kroonenberg et al., 2016), as well as Rhyacian to Orosirian granitoids associated with orogenic magmatism (Macambira et al., 2009; Magalhães et al., 2023; Vasquez and Rosa-Costa, 2008; Vasquez, 2006; Vasquez et al., 2008).

The Bacajá basement consists of two main lithotectonic associations: (i) Archean metamorphic complexes composed of granulites and orthogneisses with Mesoarchean (3000±2 Ma and 2943±4 Ma (Macambira et al., 2007; Vasquez and Rosa-Costa, 2008) and Neoarchean (2671±3 Ma, Vasquez and Rosa-Costa, 2008) protoliths; and (ii) a late Neoarchean granite-gneiss-migmatite association crystallized at 2503±10 Ma (Macambira et al., 2004, 2003; Vieira et al., 2022). Within the first association, restricted aluminous granulites and paragneisses occur as small lenses or enclaves within the Archean orthoderived rocks, with detrital sources ranging from the Mesoarchean to the Paleoproterozoic (3.14-2.47 Ga, Vasquez, 2006). Additionally, Siderian juvenile greenstone belts and associated rocks crop out, with acid volcanic rocks crystallized between 2452±3 Ma and 2359±3 Ma (Macambira et al., 2009; Macambira et al., 2003; Vasquez, 2006).

Paleoproterozoic orogenic magmatism records several events as proposed by Vasquez and Rosa-Costa (2008) (i) pre-collisional magmatism (2215±2 Ma to 2133±10 Ma; (ii) the syn- to late-collisional magmatism (2114±3 Ma to 2102±3 Ma); (iii) late- to post-collisional magmatism (2086±5 Ma to 2069±6 Ma); and (iv) the post-collisional magmatism (1986±5 Ma).

Metamorphic events are temporally associated with orogenic magmatism. Vasquez (2006) identified two major metamorphic events based on monazite U-Pb ages: the first at 2100 Ma, interpreted as peak granulite-facies metamorphism related to the Bacajá-Carajás collision, and the second at 2070 Ma, linked to orogenic collapse. More recent monazite petrochronological data (Corrêa, 2020, Neri et al., 2025) push back the peak granulite metamorphism to 2230-2221 Ma, with retrogressive conditions recorded at 2190 Ma and 2004 Ma

Previous studies suggest that the Cajazeiras Complex represents the most evolved and exhumed portion of the Bacajá basement (Vasquez and Rosa-Costa, 2008). ts protoliths exhibit geochemical affinities with sanukitoids s.l., crystallized at ca. 3.00-2.94 Ga (Neri et al., submitted; Macambira et al., 2007; Vasquez and Rosa-Costa, 2008) and were subsequently reworked between 2.10-2.07 Ga based on zircon U-Pb geochronology. Isotopic data (positive εNd and εHf values) indicate juvenile contributions to their protoliths (Neri et al., submitted).

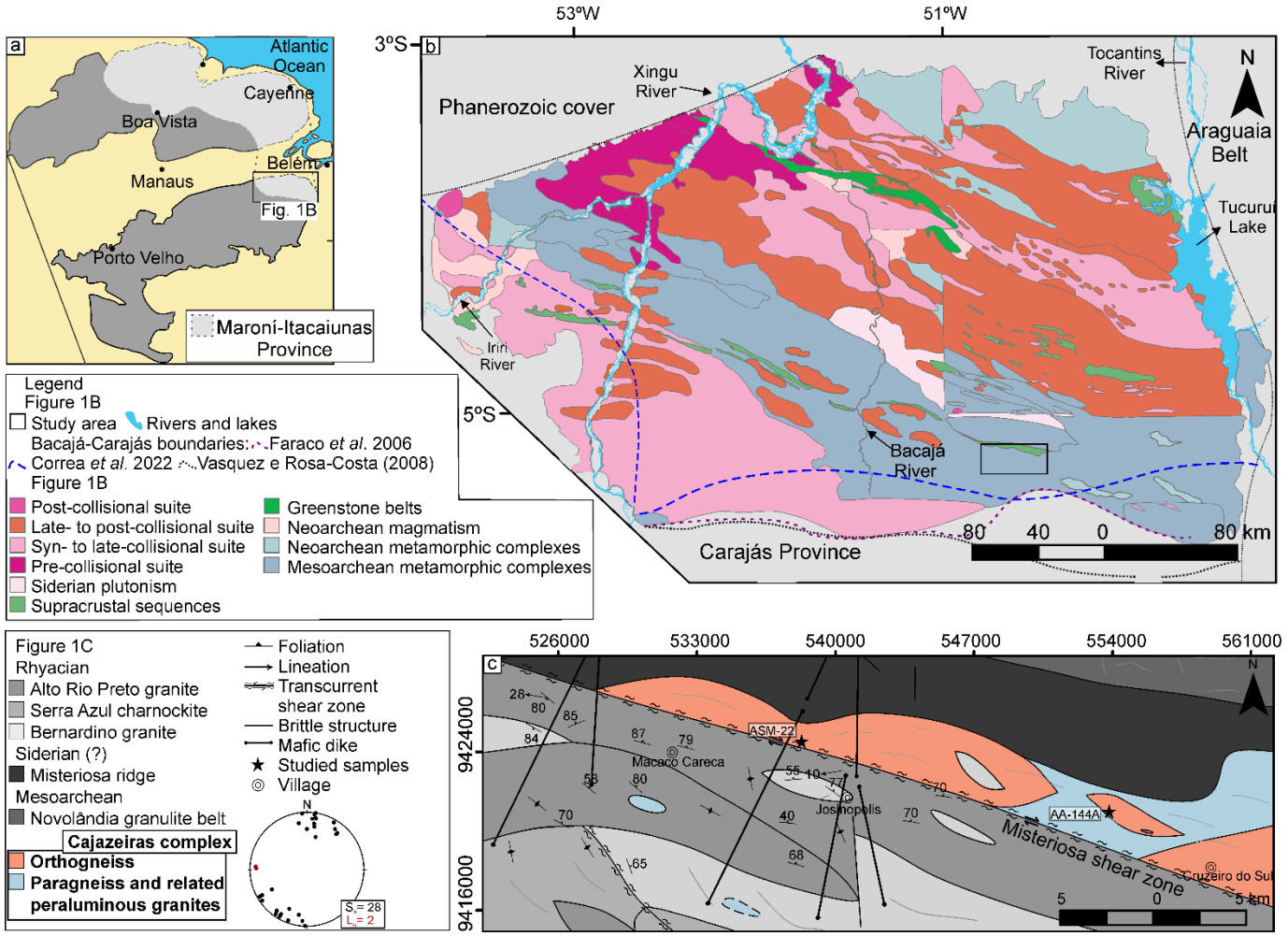


Fig. 1. (a) Amazonian craton and the location of Maroni-Itacaiúnas Province (Tassinari and Macambira, 2004). (b) simplified map of the Bacajá Domain (modified after Barros et al., 2023; Macambira and Ricci, 2015; Macambira et al., 2009; Vasquez and Rosa-Costa, 2008). (b) Geological map of the studied area (modified from Neri et al., submitted). The withe star symbol near the Vila Cruzeiro do Sul represents the orthogneiss crystallized at 3009 ± 27 Ma and metamorphosed at 2074 ± 8 Ma (Macambira et al., 2007).

7.3 ANALYTICAL METHODS

7.3.1 Petrography and mineral chemistry

Two representative samples (AA-144A and ASM-22) were selected for mineral characterization. The analyzed minerals include clinopyroxene, amphibole, biotite, plagioclase, K-feldspar, and titanite. Polished thin sections underwent quantitative wavelength dispersive spectroscopy (WDS) analyses at the Laboratório de Microssonda (LABSON) of the Universidade de Brasília (UnB) using a JEOL JXA-8230 electron microprobe analyzer. Analyses were conducted with an accelerating voltage of 15 kV, a current of 10 nA, an acquisition time of 10 s, and a spot size of 1–5 nm. Instrument calibration was performed using the following standards: andradite (Ca, Fe), microcline (Si, Al, K), olivine (Mg), albite (Na), pyrophanite (Ti, Mn), vanadinite (V, Cl), nickel oxide (Ni), chromium trioxide (Cr), and celestine (Sr). Prior to analysis, all thin sections were carbon-coated. Mineral abbreviations follow Whitney and Evans (2010).

7.3.2 In-situ trace elements LA-ICP-MS

Trace element compositions of titanite, amphibole, and clinopyroxene were determined using a Thermo Scientific Finnigan Element 2 SF-ICP-MS coupled with a CETAC LSX-213 G2+ ultraviolet laser system at the Isotope Geochemistry Laboratory of the University of São Paulo, Brazil. The laser parameters were set to a fluence of 3 J/cm², a frequency of 6 Hz, and a spot size of 25 μm. Data acquisition and reduction were performed in blocks of 120 analyses, using NIST SRM 612 as the primary standard and NIST SRM 610, USGS BCR-1, and USGS BHVO-2G as secondary reference materials. Time-resolved signal data were processed using the software Glitter (Van Achterbergh et al., 2001). Internal standard values for titanite, amphibole, and clinopyroxene were derived from mineral chemistry data. The trace element results are available in Table S4, S5, S6, and S7.

7.3.3 U-Pb geochronology

U-Pb analyses were conducted on polished thin sections at the Centro de Pesquisas Geocronológicas (CPGeo) of the University of São Paulo (USP) using a Neptune ICP-MS coupled with an Analyte Excite excimer laser system. The instrument setup included a laser fluence of 8.55 J/m², a repetition rate of 6 Hz, and a spot size of ~25 μm. Each analysis consisted of 40 sequential measurements, with an integration time of approximately 1 second per measurement. The first 10 measurements were performed with the laser ablation turned off to determine the instrumental blank, while the remaining 30 measurements were taken with the laser active.

Seven isotopic signals were measured simultaneously: four isotopes (^{206}Pb, ^{208}Pb, ^{232}Th, and ^{238}U) were analyzed using Faraday cups to ensure high signal amplitude, while three isotopes (^{202}Hg, ^{204}Pb, and ^{207}Pb) were measured using Multiple Ion Counters (MICs) for higher sensitivity. The instrumental blank average was subtracted from each of the seven isotopic signals at the end of each sequence to correct for background noise.

Since the ^{235}U isotope was not directly measured, its signal was mathematically inferred by dividing the ^{238}U signal by the known $^{238}U/^{235}U$ ratio (137.88). Mercury interference on the ^{204}Pb signal was corrected by subtracting the quotient of the ^{202}Hg signal divided by the known $^{202}Hg/^{204}Hg$ ratio (4.355).

Due to the concordant to near-concordant nature of most analyses, no significant discordance was observed, preventing the calculation of common lead through Tera-Wasserburg intercepts. Instead, age estimations were derived from U-Pb ratios ($^{206}Pb/^{238}U$, $^{207}Pb/^{235}U$, and $^{208}Pb/^{232}Th$) using the Stacey-Kramers model to determine the relative abundances of $^{206}Pb/^{204}Pb$, $^{207}Pb/^{204}Pb$, and $^{208}Pb/^{204}Pb$, which vary as a function of geological age. The measured ^{206}Pb, ^{207}Pb, and ^{208}Pb signals were corrected for common Pb by subtracting the respective ^{204}Pb signal multiplied by the calculated relative abundances.

To mitigate instrumental drift and systematic errors, the BLR-1 standard (1047 ± 0.7 Ma, Aleinikoff et al., 2007) was analyzed approximately every 10 minutes. The secondary standard was Khan (522.2±2.2 Ma, Heaman, 2009). Comparisons between measured and reference BLR-1 values enabled the calculation of multiplicative correction factors for Pb ($^{204}Pb+^{206}Pb+^{207}Pb+^{208}Pb$), Th ($^{232}Th$), and U ($^{235}U+^{238}U$) concentrations (in ppm), as well as fractionation correction factors for isotope ratios ($^{206}Pb/^{238}U$, $^{207}Pb/^{235}U$, $^{207}Pb/^{206}Pb$, and $^{208}Pb/^{232}Th$). These corrections were applied prior to final age calculations to ensure precision and accuracy. Concordia diagrams and density plots were generated using Isoplot/Ex (Ludwig, 2003). U-Pb data are available in table S8 and S9.

7.4 RESULTS

7.4.1 Petrography and mineral chemistry

The samples are classified as clinopyroxene-amphibole-biotite metatexitic orthogneisses with tonalitic (ASM-22) and granodioritic (AA-144A) compositions. They are medium- to coarse-grained with marked banding, highlighted by the intercalation of quartz-feldspathic granoblastic and nematoblastic levels formed by mafic minerals (Fig. 2a, b). They mainly consist of biotite, amphibole, clinopyroxene, quartz, plagioclase, K-

feldspar, and accessory minerals such as titanite, zircon, allanite, apatite, magnetite, and ilmenite.

The clinopyroxene crystals are subdioblastic and nematoblastic, usually containing inclusions of amphibole and biotite (Fig. 2c) and surrounded by them (coronitic texture, Fig. 2c). They are magnesian (XMg = 0.69-0.84) and classified as diopside (Fig. 3a, Tab. S1).

Biotite and amphibole crystals occur in three distinct textural forms: (1) xenoblastic, fine-grained inclusions within clinopyroxene (Amp1, Bt1); (2) xenoblastic, medium-grained coronae surrounding clinopyroxene (Amp2, Bt2); and (3) subdioblastic to xenoblastic, medium- to coarse-grained crystals (Amp3), which compose oriented levels along with reddish biotite (Bt3), usually replacing the former (Fig. 2c, d, e). No significant chemical distinctions were observed among the different textural types. Amphibole has $(Na + K)_A < 0.5$, $Mg/(Mg+Fe^{2+})$ ratios between 0.58 and 0.62, and Ti (a.p.f.u) from 0.14 to 0.20 (Tab. S1). It is classified as magnesiohornblende (Fig. 3b, Leake et al., 1997). The biotites show XMg ratios from 0.56 to 0.51 and Ti (a.p.f.u) between 0.13 and 0.33 (Fig. 3c, Tab. S1).

Titanite occurs as fine-grained subdioblastic to xenoblastic crystals (up to 0.6 mm) that are usually elongated with the foliation (Fig. 2d); small-sized (0.05-0.04 mm) crystals can also occur, accompanying larger crystals. Titanite may also occur as coronae around magnetite. Opaque accessory minerals are mostly magnetite with rare ilmenite intergrowths and can occur as idioblastic to subdioblastic inclusions in different rock-forming minerals or in the matrix.

The plagioclase and K-feldspar crystals occur in two forms: (1) coarse-grained xenoblastic crystals included in a medium-grained matrix (Fig. 2c, d, e); and (2) subdioblastic to xenoblastic crystals composing the matrix (Fig. 2c, d, e). Plagioclase crystals are compositionally homogeneous and classified as oligoclase (An_{25-27}, Fig. 3c, Tab. S3). K-feldspar is classified as sanidine (Fig. 3d). Quartz can occur as fine-grained recrystallized grains in the matrix or as medium to coarse-grained xenoblastic crystals stretched within the foliation with undulatory extinction.

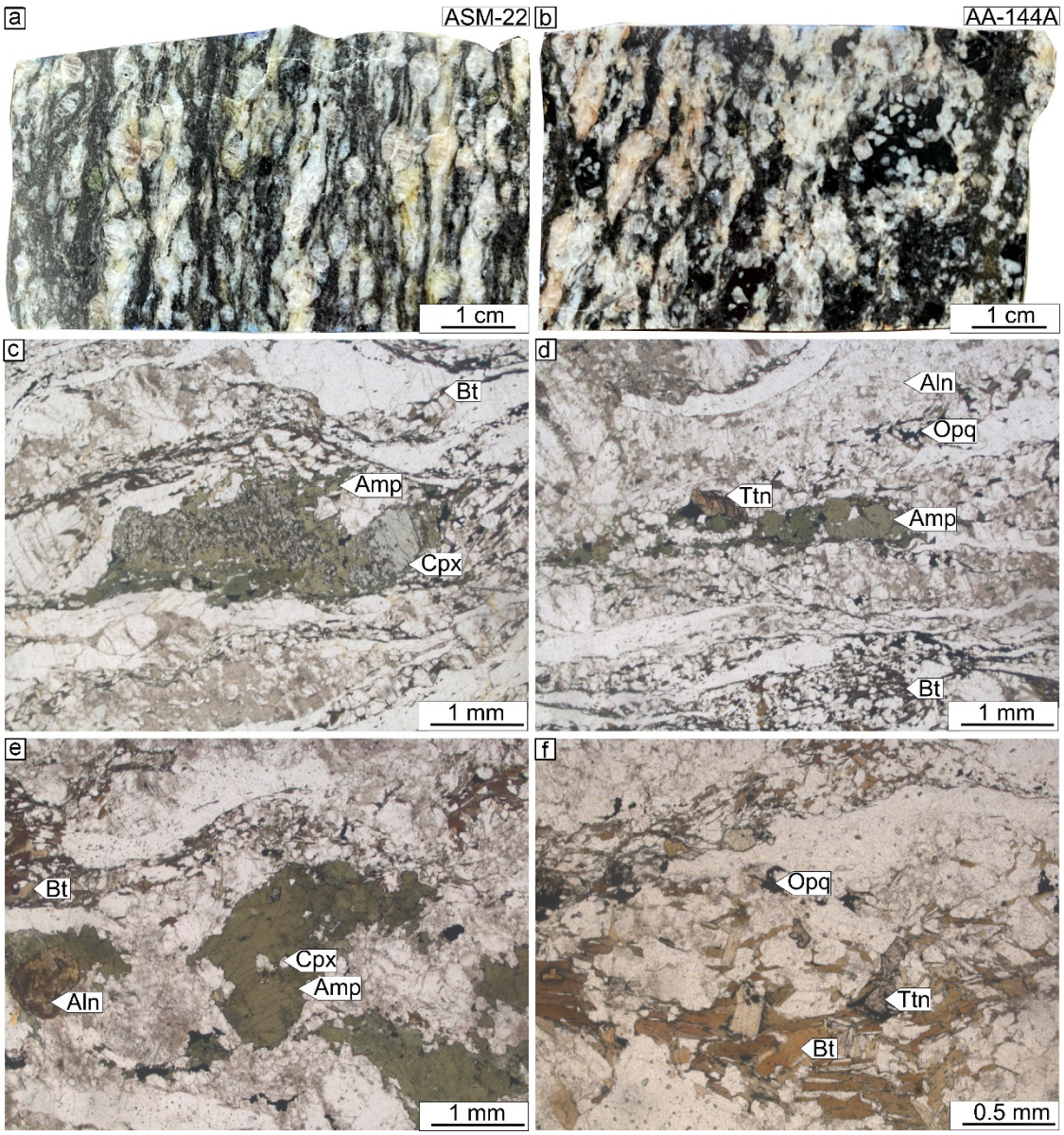


Fig. 2. Hand specimen and plane polarized transmitted light photomicrographs of sample ASM -22 (a, c, d), and AA-144A (b, e, f). (c) amphibole coronas around clinopyroxene; (d) alignment of amphibole in straight contact with titanite alternating with quartz felspathic levels; (e) medium-grained amphibole with clinopyroxene core, associated with medium-grained allanite; (f) association of titanite with biotite.

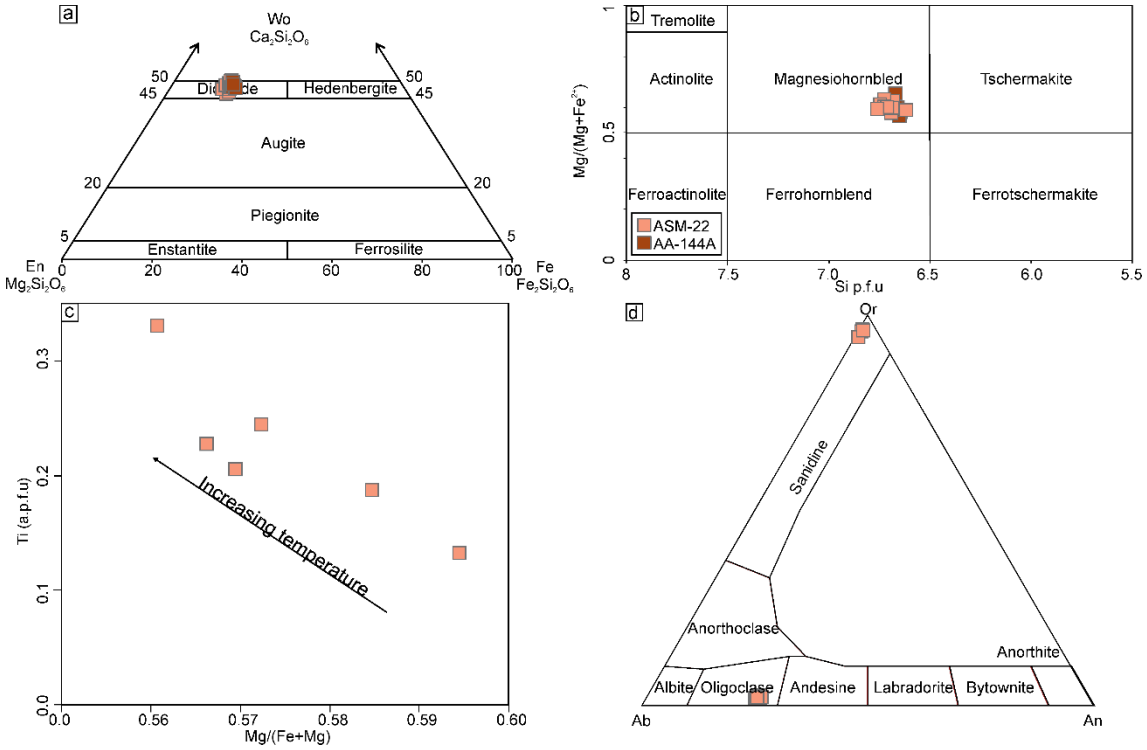


Fig. 3. Classification diagrams for the analyzed mineral phases. (a) Pyroxene compositions showing En-Wo-Fs classification diagram after (Morimoto et al., 1988); (b) amphibole classification (Leake; et al., 1997); Mg/(Mg + Fe^{2+}) versus Si diagram based on $Ca_B \geq 1.50$, (Na + K)A < 0.50, and $Ca_A < 0.50$; (c) Mg/(Mg+Fe) vs Ti (a.p.f.u) diagram for biotite compositions; (f) Ab–An–Or ternary diagram showing the plagioclase compositions

7.4.2 P-T conditions

7.4.2.1 Mineral thermobarometry

7.4.2.1.1 Amphibole

Employing the calibrations of Liao et al. (2021), titanium a.p.f.u in amphibole was used to calculate temperatures . For sample ASM-22, Ti a.p.f.u ranges from 0.14 to 0.20 (Tab. 1, Fig. 4), yielding a peak at 780±26 ºC. For the sample AA-144A, Ti a.p.f.u ranges from 0.16 to 0.21 (Tab. S1, Fig. 4), yielding a peak at 789±23 ºC. Calibration uncertainties for the Ti-Amp thermometer are 70°C (2SE, Liao et al., 2021).

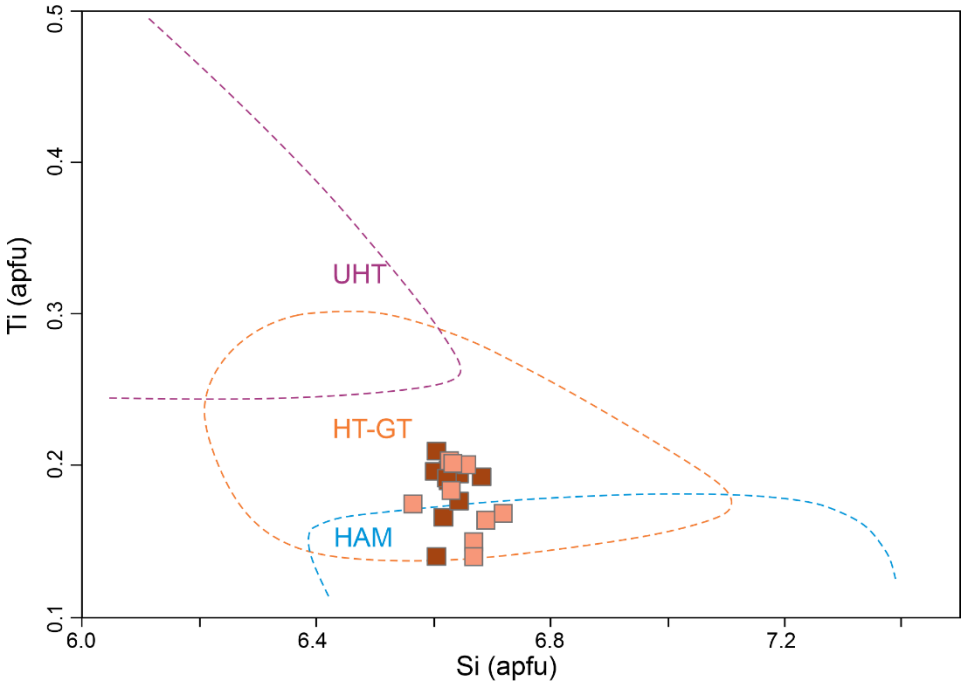


Fig. 4. Si vs. Ti in amphibole diagram with metamorphic facies boundaries (after Liao et al. 2021). Amphibole compositions from Cajazeiras orthogneisses indicate transition from high-temperature amphibolite to granulite facies. Ultra-high temperature granulite facies (UHT); high temperature granulite facies (HT-GT); high-temperature amphibolite facies (HAM).

7.4.2.1.2 Titanite

Titanite does not exhibit clear zoning or marked compositional contrasts between cores and rims in larger grains, displaying similar Zr contents. For sample ASM-22, Zr concentrations are 242 ± 83 ppm (Tab. S4), and for sample AA-144A, they are 314 ± 88 ppm (Tab. S5), which yielded temperatures of 721 ± 10 ºC and 724 ± 19 ºC at 0.46 GPa, respectively (Hayden et al., 2007).

7.4.2.2 Phase equilibria modeling

The phase equilibria modeling of the Cpx-Amp-Bt orthogneiss with tonalitic composition (sample ASM-22) was carried out in the NCKFMASHTO system (Na_2O-CaO-K_2O-FeO-MgO-Al_2O_3-SiO_2-H_2O-TiO_2-O_2) using GeoPs version 3.5 (Xiang and Connolly, 2022) and the internally consistent thermodynamic dataset HP622.DS (Holland and Powell, 2011). The following a-X relations were used: tonalitic melt, augite, hornblende, and sodic-calcic clinopyroxene (Green et al., 2016); garnet, orthopyroxene, biotite, and muscovite (White et al., 2014); epidote (Holland and Powell, 2011); feldspars (Holland and Powell, 2003); spinel-magnetite (White et al., 2002); ilmenite-hematite (White et al., 2002). Pure phases include quartz, rutile, titanite, and water. Titanite is a solid solution (Deer et al., 2013; Franz and Spear, 1985), but since there is no consistent a-X model that fully encompasses titanite's complexities, the fields obtained in the modeling can only approximate its natural stability. The bulk composition used for the

calculations was based on whole-rock analysis obtained by ICP-AES (Neri et al., submitted). The H_2O content was determined using a T-$M_{(H2O)}$ diagram and was fixed at 1.7 mol %. Bulk-rock Fe_2O_3 was fixed to a $Fe^{3+}/(Fe^{2+} + Fe^{3+})$ ratio of 0.15 (Palin et al., 2016).

The P-T pseudosection was calculated within the range of 600-850 °C and 0.3-0.8 GPa (Fig. 5A). The solidus occurs at 665 ºC for a pressure of 0.3 GPa and its temperature decreases gradually with increasing pressure (~630 °C at 0.8 GPa). Orthopyroxene is stable only at high temperatures that increase from ~775 ºC at low pressures (0.3 GPa) to ~840 ºC at 0.8 GPa. The calculated clinopyroxene stability field enlarges with increased T, it being stable in the range of 650 ºC to ~800 °C at pressures varying from 0.3 GPa to ~0.54 GPa; at higher pressures (>0.54 GPa), it is stable at higher temperatures, attaining 850 ºC at 0.78 GPa. Amphibole is stable at variable pressures and temperatures and occurs in almost all conditions considered (Fig. 5) except for the temperatures >~660 °C at low pressures. Biotite is also observed in different temperatures and pressures being absent only in some high temperature paragenesis.

Titanite is stable at temperatures lower than ~700 °C and a maximum pressure of 0.76 GPa, where it coexists with rutile in a restricted P-T interval. Rutile occurs at higher pressures than titanite, usually above ~0.74 GPa, and is also limited to temperatures <~700 °C, suggesting that titanite and rutile do not coexist in equilibrium. In contrast, ilmenite is stable throughout the P-T range, becoming unstable only at lower temperatures (<700 ºC) and pressures (<~0.46 GPa). Magnetite occurs associated with ilmenite in variable conditions of temperature and pressure, but differently of ilmenite it is stable also at low pressures and temperatures.

The metamorphic peak assemblage observed in petrographic investigations consists of clinopyroxene + amphibole + biotite + plagioclase + K-feldspar + quartz + magnetite + ilmenite, which occurs in the range of 0.41-0.56 GPa / 700-805ºC. However, the $XTi_{M)}$ in biotite and amphibole constrains the peak at ~0.52-0.55 GPa / 760-790ºC (Fig. 5B). The disappearance of clinopyroxene marks the post-peak stage, accompanied by the formation of coronitic amphibole around clinopyroxene and the crystallization of titanite, as defined by the assemblage amphibole + biotite + plagioclase + K-feldspar + titanite + quartz + magnetite + ilmenite + H_2O, which occurs at 0.40-0.48 GPa / 600-650ºC.

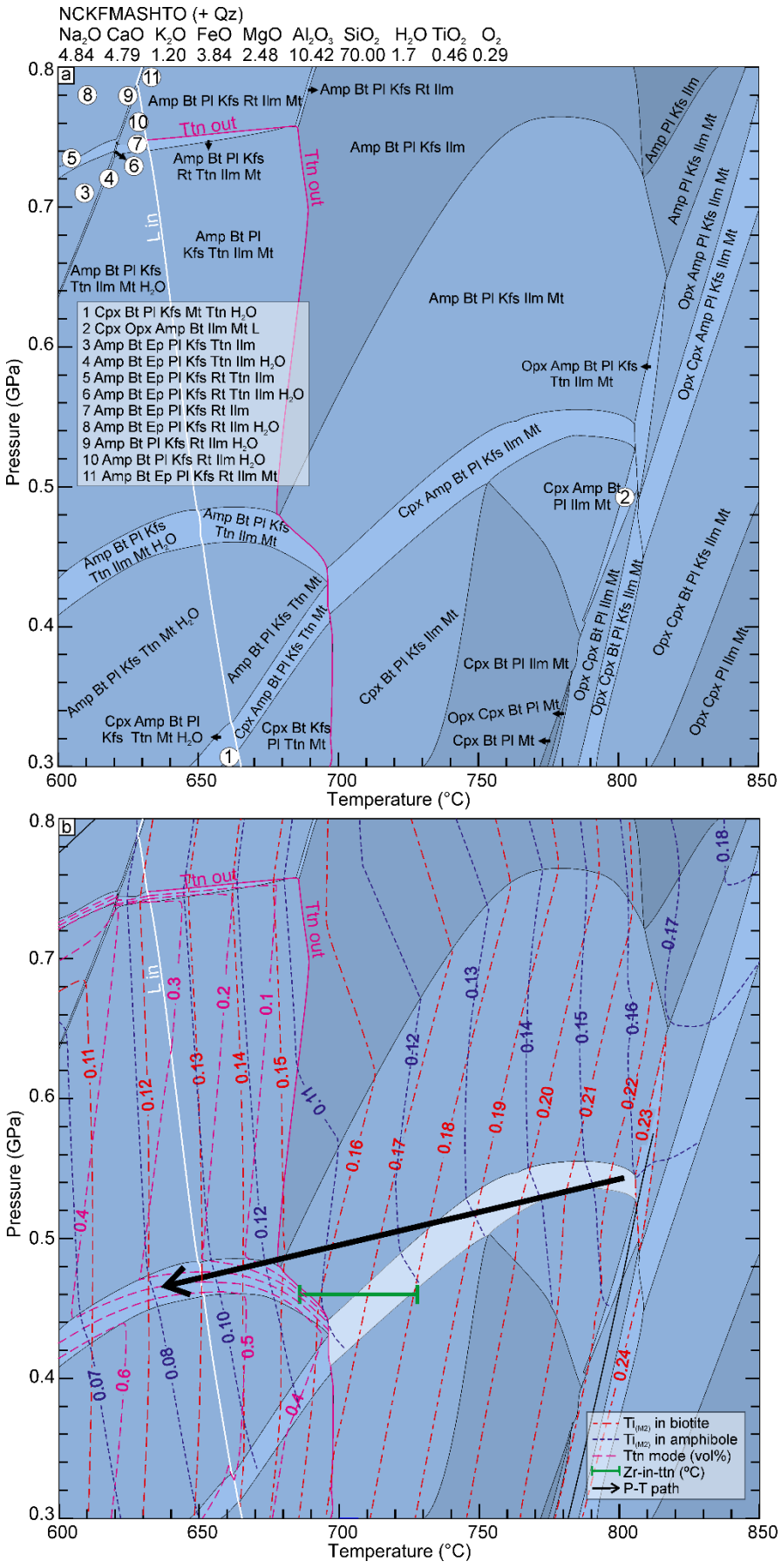


Fig. 5. (a) Pseudosection of sample ASM-22 calculated with GeoPs 3.5 (Xiang and Connolly, 2022); (b) pseudosection contoured by selected mineral isopleths to define a P-T path.

7.4.3 Trace element mineral chemistry of rock-forming minerals

The clinopyroxenes from both samples exhibit similar REE patterns (Fig. 6a, b). They are characterized by low ΣREE values (ASM-22: 96.9-143.6 ppm; AA-144A: 44.5-290.2 ppm) and negative Eu anomalies (Eu/Eu* = 0.39-0.18). They show flat patterns with a smooth LREE-enrichment compared to HREE [$(La/Yb)_N$ = 1.07-6.22, with a few outliers ranging from 0.24-0.66, which occur as inclusions in coarse-grained amphibole].

Amphibole in both samples also shares similar REE patterns (Fig. 6c, d). They are more enriched in ΣREE than clinopyroxene (ASM-22: 262.5-396.3 ppm; AA-144A: 435.9-956.2 ppm) and also exhibit negative Eu anomalies (Eu/Eu* = 0.23-0.46). No clear distinction between cores and rims was observed. There is no significant REE fractionation in sample ASM-22 [$(La/Yb)_N$ = 0.96-1.36], whereas sample AA-144A shows higher (La/Yb)N in the cores (1.44-2.85) compared to the rims (0.44-0.86). Both samples also exhibit high $(Gd/Yb)_N$ ratios (2.08-3.58).

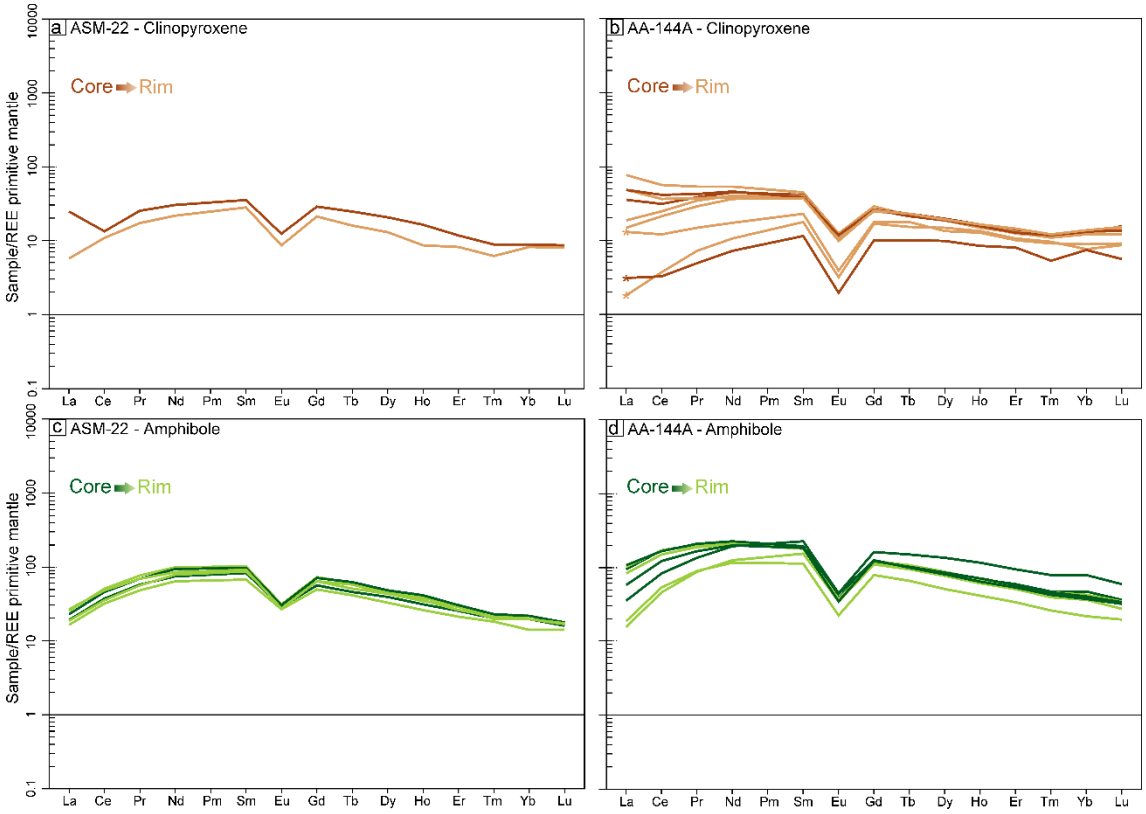


Fig. 6. Chondrite-normalized REE patterns of (a-b) clinopyroxene, (c-d) amphibole, normalized to the chondrite values of McDonough and Sun (1995).

7.4.4 Titanite petrochronology

Back-scattering electron (BSE) images of titanite grains reveal that, in both samples, titanite mostly lacks conspicuous zoning. Some grains show complex BSE responses, but no specific patterns were observed. In chondrite-normalized diagrams,

titanite analyses from the tonalitic orthogneiss (sample ASM-22, Fig. 7A) display positive Eu anomalies (Eu/Eu* = 1.18-3.01), and significant fractionation between LREE and HREE [$(La/Yb)_N$ = 5.9-10.4] and exhibit inclined HREE patterns [$(Gd/Yb)_N$ = 2.6-3.5].

Titanite analyses from the granodioritic orthogneiss (sample AA-144A, Fig. 7B) show marked negative to positive Eu anomalies (Eu/Eu* = 0.36-1.74), discrete fractionation between LREE and HREE [$(La/Yb)_N$ = 2.56-5.78], and display sub-horizontal to mildly inclined HREE patterns [$(Gd/Yb)_N$ = 0.99-2.7].

When comparing both samples, the titanite of the tonalitic sample (ASM-22) is impoverished in Y compared to that of the granodioritic sample (AA-144A), with the latter providing lower Sr/Y ratios (avg. 0.03) compared to the former (avg. 0.05). As noted, titanite does not show coherent zoning, although some regions may exhibit higher BSE responses, corresponding to slightly higher REE+Y contents in sample AA-144A. Overall, the titanite of the tonalitic sample (ASM-22) is impoverished in REE+ compared to that of the granodioritic sample (AA-144A), as shown in the REE diagrams (Fig. 7A, B), and also in Y (Fig. 7C). The low $(Dy/Yb)_N$ further supports that the titanites crystallized in the absence of garnet (Fig. 7c, Scibiorski et al., 2019). Titanite in both samples has low Th/U rations (0.38-0.64 – ASM-22; 0.18-1.08 – AA-144A, Tab. S1).

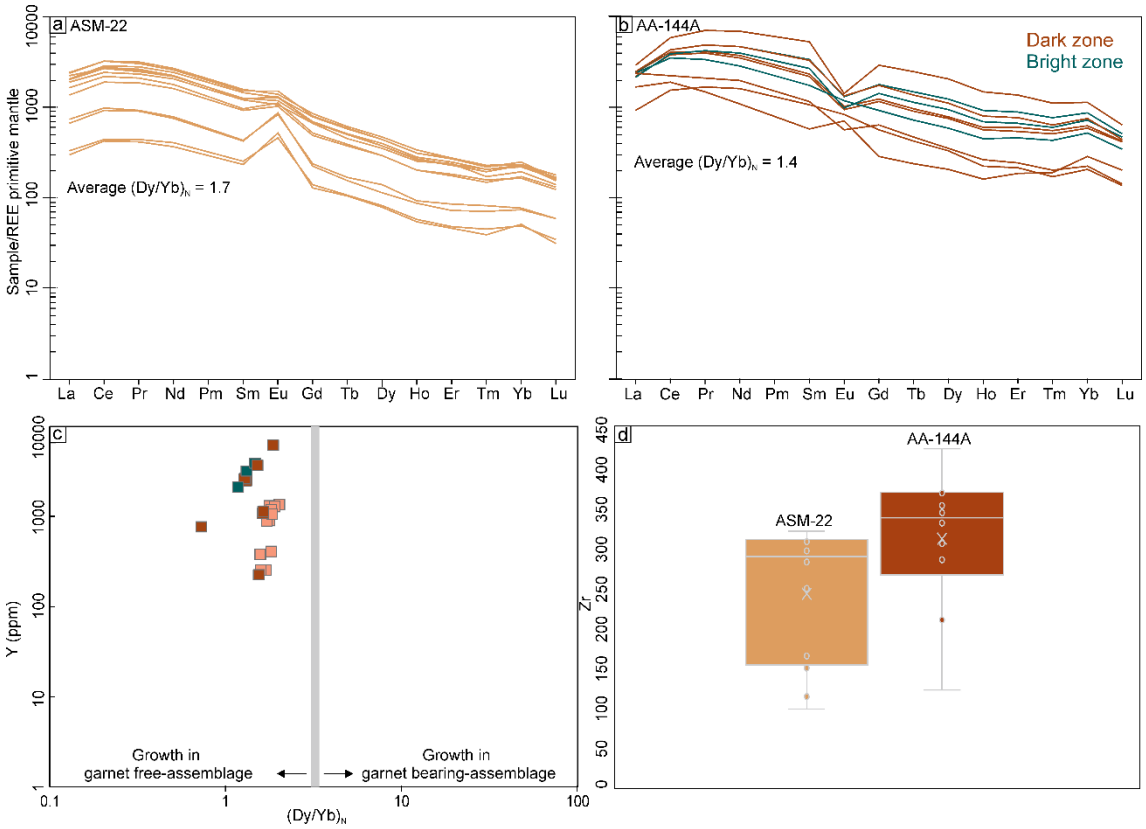


Fig. 7. Chondrite-normalized REE patterns titanite from sample ASM-22 (a) and AA-144A (b); (c) Sr vs. Y diagram for both samples; (d) box plot of Zr concentration in both samples. Normalized to the chondrite values after McDonough and Sun (1995).

Thirty U-Pb isotopic analyses were performed on titanites from the sample ASM-22 (Fig. 8A, Tab. S2). All analyses are concordant to near-concordant; discarding the spots with high common Pb, we obtained an upper intercept age of 2017±16 (MSWD = 0.76). Th/U ratios range from 0.3 to 0.8.

Thirty-two isotopic analyses were performed on titanites from the sample AA-144A (Fig. 8B, Tab. S2); all analyses are concordant to near-concordant. Discarding the spots with high common Pb, we obtained an upper intercept age of 2012±9.2 (MSWD = 1.4). Th/U ratios range from 0.1 to 1.2.

Neri et al. (submitted) presented zircon U-Pb data from the sample ASM-22. Here, we summarize their results. The metamorphic rims from sample ASM-22 are scattered on the concordia and give ages on the range from 2136±14 to 2074±14 Ma (n = 14, $^{207}Pb/^{206}Pb$ age), with Th/U ratios between 0.09 and 1.82. A single outlier at 2210±13 Ma was registered (Fig. 8C, D).

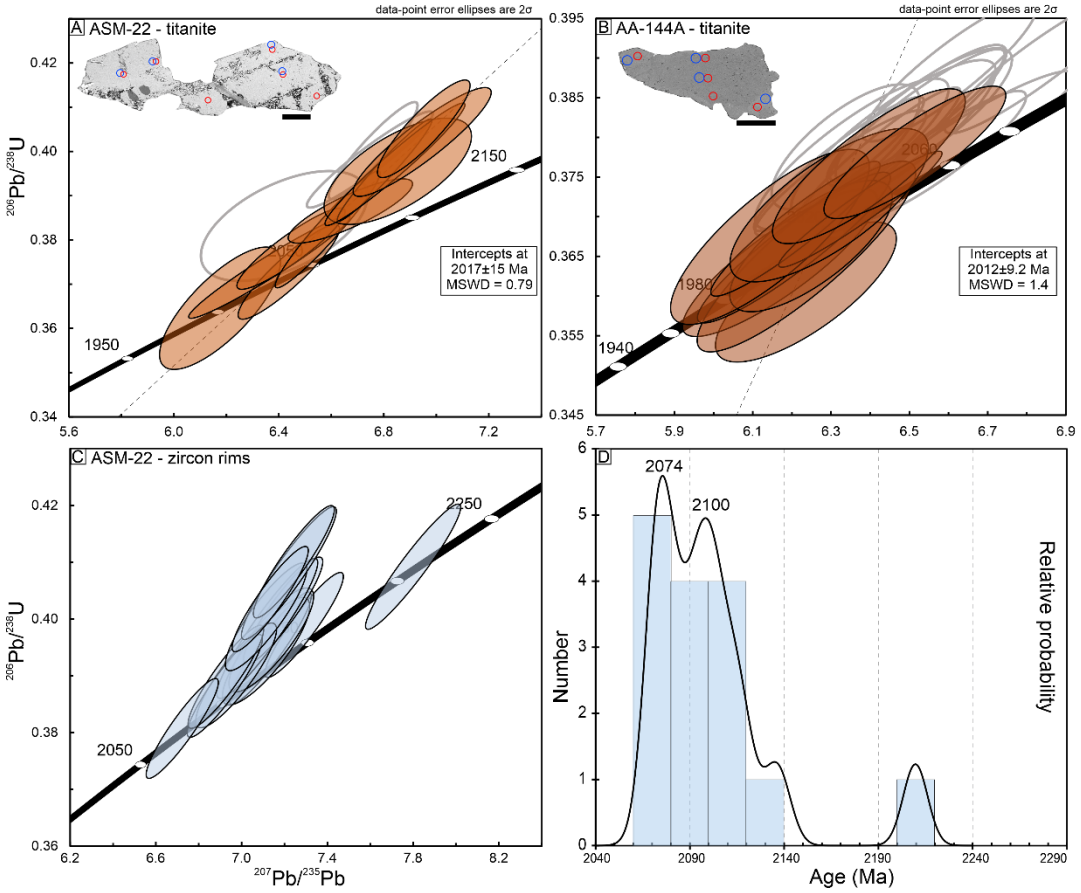


Fig. 8. U-Pb wheterill plots for titanite data from samples ASM-22 (a), and AA-144A (b); (c) U-Pb and REE data of zircon rims from sample ASM-22; (d) U-Pb from sample AA-144A. gray ellipses were discarded for age calculations. Scale bar in figura a and b are 100 μm; blue circles indicate REE spots (25 μm), and red circles U-Pb spots (20 μm).

7.5 DISCUSSION

7.5.1 Significance of REE patterns, trace elements, and U-Pb ages

Titanite's major and trace element behavior strongly depends on element availability, compatibility, and local bulk composition during crystallization (e.g., Gao et al., 2012; Smith et al., 2009). Therefore, tracing variations in trace element signatures can provide valuable insights into the crystallization conditions of titanite and its relationship with other rock-forming and accessory minerals (Cioffi et al., 2019; Gao et al., 2012; Kavanagh-Lepage et al., 2024; Papapavlou et al., 2017; Scibiorski et al., 2019; Scibiorski and Cawood, 2022; Storey et al., 2007).

Titanite has a higher partition coefficient (Kd) for MREE over LREE and HREE, meaning that titanite preferentially incorporates MREE over the other REE (Prowatke and Klemme, 2006; Tiepolo et al., 2002). In contrast, garnet, zircon, and to a lesser extent amphibole, strongly prefer HREE (Bottazzi et al., 1999; Rocha et al., 2018; Siegel et al., 2017; Smit et al., 2024). Therefore, titanite that grows concomitant with or after garnet growth tends to be HREE-depleted, showing high $(Dy/Yb)_N$, as any available HREE is preferentially incorporated by garnet and zircon. On the other hand, titanite that grew in the absence of garnet is relatively enriched in HREE and shows low $(Dy/Yb)_N$ (Scibiorski et al., 2019). A similar behavior is observed concerning LREE. If titanite crystallizes after allanite, monazite, and/or apatite, minerals with high Kd for LREE, it will be LREE-depleted (Papapavlou et al., 2017). Therefore, understanding trace element behavior in titanite is a challenging task requiring knowledge of the REE budget of associated minerals, the local bulk composition, and the P-T conditions of titanite formation.

The titanite trace element compositions of the studied samples (Fig. 7) share striking similarities with minor differences that will be highlighted. Titanites reveal relatively flat REE patterns with enrichment in LREE and small impoverishment in HREE (Fig. 7a, b; cf. $(La/Yb)_N$). The enrichment in LREE in both samples suggests titanite crystallization in an environment where allanite and apatite had not yet crystallized. The absence of garnet in both samples plays a crucial role in REE distribution since garnets preferentially incorporate HREE, so its absence results in the relatively high contents of HREE in titanite and limited fractionation of HREE (Fig. 7a, b). This feature is highlighted by the low $(Dy/Yb)_N$ in titanite (avg. 1.7, ASM-22; and 1.5, AA-144A). Other studies suggest a correlation between titanite and amphibole, where amphibole breakdown should release HREE that titanite would incorporate during its crystallization (Cioffi et al., 2019; Kavanagh-Lepage et al., 2024). In the Cajazeiras orthogneisses, amphibole crystallizes concomitant with titanite (Fig. 4). No strong evidence of

amphibole breakdown to other phases like biotite or epidote was observed in petrographic analyses (Fig. 2). In sample ASM-22, the REE patterns of amphibole are flat with no significant HREE enrichment [$(La/Yb)_N$ = 0.96-1.36], whereas in sample AA-144A there is a slight enrichment, mainly in the core [(La/Yb)N core 1.44-2.85; rims 0.44-0.86]. The lack of strong enrichment in HREE in both amphibole and clinopyroxene suggests that these minerals did not exert a strong influence on titanite chemistry and, therefore, that titanite, together with zircon, is the mineral that retains most of the HREE+Y in garnet-free rocks.

Concerning the U-Pb ages, the two samples provided titanite ages that overlap within errors: 2017±15 Ma (ASM-22) and 2012±9.2 Ma (AA-144A). Still, these ages are significantly younger than those obtained in zircon rims in sample ASM-22, that scatter along the concordia from 2136±14 to 2074±14 Ma, with an outlier at 2210±13 Ma ($^{207}Pb/^{206}Pb$ age) (Neri et al., submitted). The age gap between U-Pb data from titanite and zircon in our samples suggests that the titanite ages most likely record cooling ages. The titanite REE patterns in each sample do not show significant differences, which suggests that titanite was formed in the same environment and that the obtained ages most likely result from volume diffusion of Pb above the closure temperature (Scibiorski et al., 2019).

7.5.2 Zr-in-titanite temperatures

The lack of rutile in our samples leads us to assume a TiO_2 activity of 0.75, as suggested by previous studies (Chambers and Kohn, 2012; Kapp et al., 2009; Kohn, 2017). However, these temperatures are significantly inconsistent with the predicted temperatures of titanite stability based on pseudosection modeling (Fig. 4). This discrepancy suggests that the Zr-in-titanite temperatures are overestimated, likely due to disequilibrium partitioning of Zr into titanite during crystallization in the retrograde stage. This disequilibrium could result from slow diffusion rates of Zr at lower temperatures, leading to an imbalance between titanite and zircon (Cioffi et al., 2019). Similar cases of retrograde crystallization or low-temperature (re)crystallization of titanite have been documented in other localities (Cioffi et al., 2019; Cruz-Uribe et al., 2018; Holder et al., 2019). An alternative possibility, although less likely, is that the absence of zirconium in the modeling could shrink the stability fields of titanite to lower temperatures.

7.5.3 P-T-t evolution and regional implications

The southern basement of the Bacajá Domain underwent significant reworking during the Transamazonian orogeny (Macambira et al., 2007; Neri et al., submitted; Vasquez and Rosa-Costa, 2008). The peak metamorphic conditions in the Cajazeiras complex were achieved at ~0.52-0.55 GPa/760-790ºC and were accompanied by partial melting. U-Pb zircon dating

indicates that these conditions were reached around 2210 Ma (?). Retrogressive conditions occurred at 0.43-0.48 GPa/650-695ºC, marked by the disappearance of clinopyroxene and the formation of titanite. U-Pb data from titanite suggest these conditions were attained between ca. 2017 and 2012 Ma (Tab. 1).

The oldest metamorphic zircon age points to the initiation of Paleoproterozoic metamorphism around ~2210 Ma (Fig. 8c, d, 9). However, this should be treated with caution, because other meanings for this isolated age are possible. However, recent monazite petrochronology performed on nearby aluminous granulites indicates that the earliest metamorphic stages occurred at ~2230-2210 Ma (Neri et al., in press) which aligns with the zircon rim data, reinforcing that the earliest metamorphism in the Cajazeiras complex took place effectively around ~2210 Ma. The subsequent zircon peak at 2100 Ma is followed by another at 2074 Ma, which corresponds to the crystallization ages of granites and charnockites occurring in the region, and is also coincident with the age obtained in zircon rims of a granodioritic gneiss in the study area (Barros et al., 2023; Macambira et al., 2009; Magalhães et al., 2023, Neri et al., submitted).

Table 1 - Summary of petrography, geochronology, and metamorphic conditions of the Cajazeiras gneisses.

Sample	Lithology	UTM coordinate		Mineral assemblage		Protolith age (Ma)	Metamorphism age (Ma)		P-T conditions	
		X	Y	Major	Accessories	Zircon	Zircon	Titanite	Peak	retrograde
ASM-22	Cpx-Amp-Bt tonalitic gneiss	539252	942279	Bt + Amp + Cpx + Pl + Qz + Kfs	Ttn + Aln + Zrn + Mt + Ilm +Py	2970.4 ± 9.2[1]	2136 ± 14 to 2074 ±14[1]	2017±15	0.52-0.55 GPa 760-790ºC	0.43-0.48 GPa 650-695ºC
AA-144A	Cpx-Bt-Amp granodioritic gneiss	555726	9420040	Amp +Bt + Cpx + Pl + Qz + Kfs	Ttn + Aln + Zrn + Mt + Ilm +Py	2940 ± 9.2[1]	1962 ± 11[1]	2012±9.2	-	-
MJ-21[2]	Granodioritic gneiss[2]	557714[2]	9419277[2]	-	-	3009 ± 27[2]	2074 ± 8[2]	-	-	-

[1]Data from Neri et al. (submitted), [2]Macambira et al (2007)

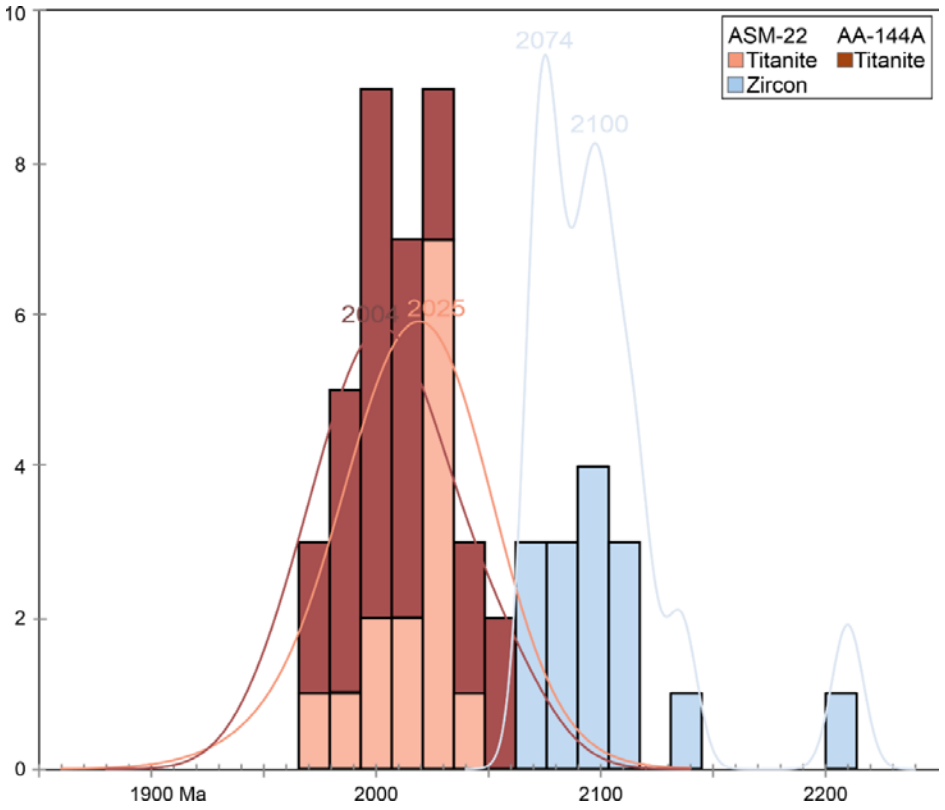


Fig. 9. Summary of titanite and zircon U-Pb data from the Cajazeiras orthogneiss.

The P-T-t paths derived from the Cajazeiras complex contrast with the high-pressure granulite metamorphism recorded in aluminous granulites from the studied area (Fig. 1 and 10), indicating that these rocks were located at different depths in the crust but were later brought together during late-orogenic processes. Despite their distinct metamorphic histories, their time evolution occurred in the late Paleoproterozoic, in agreement with data from other regions within the Bacajá Domain (Vasquez, 2006).

The geological history of the southern Bacajá Domain is notably complex (Neri et al., submitted). To the south of the Misteriosa transcurrent shear zone, the dominant rock types are Rhyacian granites and igneous charnockites, with sparse paragneisses occurring as restricted lenses within the granitoid bodies (Neri et al., submitted). In contrast, to the north of the shear zone, metamorphic rocks derived from igneous and sedimentary protoliths, with facies ranging from upper amphibolite to ultra-high temperature granulites are exposed (Silva, 2021). The Misteriosa shear zone seems to mark a boundary between two geologically distinct blocks, each with its own unique geological history. Within this context, the orthogneisses of the Cajazeiras complex represent the Mesoarchean basement of the Bacajá Domain, which was extensively reworked during the Paleoproterozoic collision between the Bacajá Domain and Carajás province.

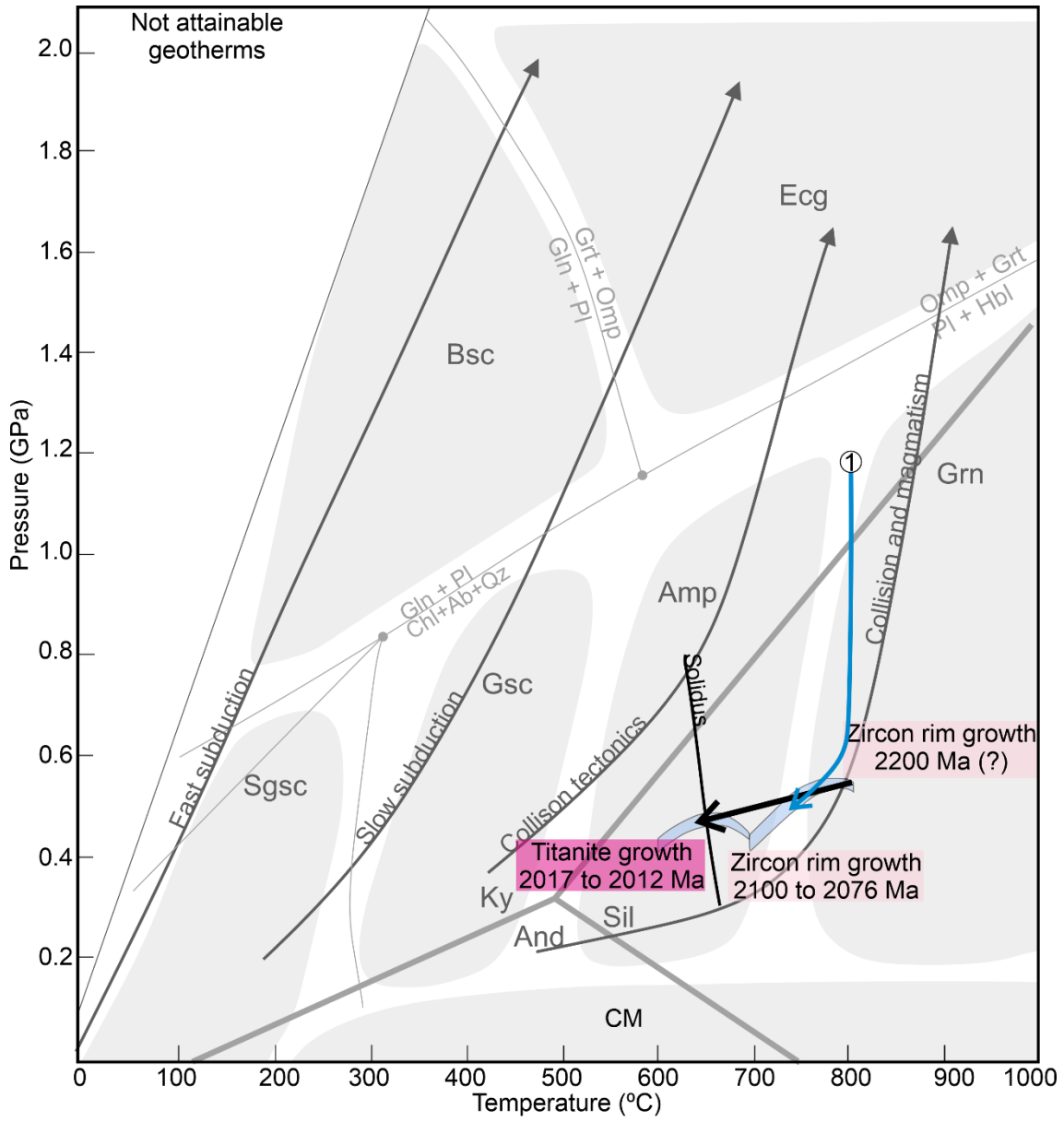


Fig. 10. P-T-t trajectories (black arrow) for the clinopyroxene-amphibole-biotite tonalitic orthogneiss (ASM-22). The titanite ages are from the two analyzed samples in this study. (1) P-T path from high-pressure aluminous granulite from the studied area (Neri et al., in press). Metamorphic facies grid for metabasaltic rocks and geothermal gradients from Bucher and Frey (2002); CM – Contact metamorphism, Grn – Granulite, Amp – Amphibolite, Gsc – Greenschist, Sgsc – Subgreenschist, Bsc – Blueschist, Ecg – eclogite.

The definition of the boundary between distinct geological domains is a challenging task that usually relies on the integration of multiple datasets, including geochronology, geochemistry, structural geology, and geophysics (Cordani et al., 2000; Santos et al., 2006; Tassinari and Macambira, 2004). The boundary between the northern Carajás province and the southern Bacajá Domain has been a subject of debate for decades (Cordani et al., 1984; Correa et al., 2022; Faraco et al., 2006; Macambira et al., 2007; Motta et al., 2019; Vasquez and Rosa-Costa, 2008).

Earlier interpretations, based on satellite-borne gravity and seismic data, suggest that no clear distinction exists between the crust from the northern Carajás province and the southern Bacajá Domain, raising the possibility that the Bacajá Domain could represent and exhumed portion of the Carajás province (Motta et al., 2019). However, more recent airborne magnetic data on the Bacajá Domain was used to define the depth of the bottom of the local magnetic layer. It resulted in a newly proposed boundary further north than previously established (Fig. 1b, Correa et al., 2022). This interpretation challenges prior models (Faraco et al., 2006; Vasquez and Rosa-Costa, 2008) and suggests a more complex geological transition between the Bacajá Domain and the Carajás province.

Neri et al. (submitted) highlighted key differences between the southern Bacajá Domain and northern Carajás province. They highlighted the widespread occurrence of Rhyacian magmatism in the study area; a feature absent in Carajás. However, the knowledge on the Archean fragments in the Bacajá Domain is still limited and a direct metamorphic comparison between the two domains has not been conducted, leaving room for further investigation into the tectonic and metamorphic evolution of these regions.

In the study area, the Cajazeiras complex is characterized by orthogneisses with sanukitoid *s.l.* affinities that crystallized at 3.0 to 2.94 Ga (Macambira et al., 2007; Neri et al., submitted; Vasquez and Rosa-Costa, 2008) and recorded a Pb-loss/metamorphism at 2.80-2.81 Ga (modified zircon cores; Neri et al., submitted). The complex experienced upper-amphibolite to granulite facies metamorphism with associated partial melting that took place in the Rhyacian at 2.21 to 2.01 Ga. On the other hand, the metamorphic record in the basement of the adjacent Carajás domain is characterized by orthogneiss and granulites with TTG affinities. These rocks crystallized at 3.06 to 2.93 Ga and were metamorphosed under ultra-high-temperature granulite facies with associated partial melting between 2.89 and 2.84 Ga (Delinardo-Silva et al., 2025; Marangoanha et al., 2019; Silva et al., 2021). This metamorphic event is coincident with emplacement of mixed crustal-juvenile leucogranites/orthogneisses in the Carajás province. In the northern Carajás region, these orthogneisses also experienced a metamorphic event at 2.75-2.70, probably related to the intrusion of A-type granites and charnockites in Carajás (Alves, 2020), that was not registered in the Bacajá Domain so far.

Although these domains might share an Archean history, prior to the Rhyacian Orogeny in the Bacajá Domain (Motta et al., 2019), their Archean evolution is not fully constrained so far. However, the available geochemical, isotopic, and metamorphic data point to distinct processes leading to the origin and evolution of their basements. These differences suggest that distinct tectonic histories and metamorphic events have shaped each domain.

7.6 CONCLUSIONS

The integration of petrography, mineral chemistry, and titanite petrochronology has led to the following conclusions:

1. Amphibole and clinopyroxene did not exert a strong influence on titanite geochemistry.
2. Titanite and zircon are the main reservoirs of HREE in garnet-free rocks.
3. The Zr-in-titanite temperatures derived from crystals that crystallized in the retrograde path should be carefully assessed, as they may be likely overestimated.
4. Titanite crystalized only during the retrograde path, providing a valuable tool for elucidating exhumation histories.
5. The Complex records peak metamorphic conditions at upper amphibolite facies at 0.52-0.55 GPa and 760–790 °C at ~2210 Ma (?), with cooling to the solidus at 2100-2076 Ma, and underwent retrograde re-equilibration to 0.43-0.48 GPa and 600-650ºC at ~2017-2012 Ma.

ACKNOWLEDGMENTS

This paper is part of the first author's PhD thesis developed at the Instituto de Geociências, UFPA. The authors acknowledge UNIFESSPA students and staff for their previous work in the studied area and shared information. N.F Botelho, G. Fernandes for their assistance with EPMA analyses. C. Passareli for her assistamce with U-Pb analyses. R. Dall'Agnol acknowledges the CNPq fellowship (Proc. 304648- 2019-1). G. R. L. Feio acknowledges CNPQ and FAPESPA funding (Proc. 304648- 2019-1, E-2024/2285715). This study was financed in part by the Coordenação de Aperfeiçoamento de Pessoal de Nível Superior - Brasil (CAPES) - Finance Code 001 (No. 88887.643812/2021-00).

REFERENCES

Aleinikoff, J.N., Wintsch, R.P., Tollo, R.P., Unruh, D.M., Fanning, C.M., Schmitz, M.D., 2007. Ages and origins of rocks of the Killingworth dome, south-central Connecticut: Implications for the tectonic evolution of southern New England. Am. J. Sci. 307, 63–118. https://doi.org/10.2475/01.2007.04

Alves, J.P.S., 2020. A relação entre o Domínio Bacajá e o Domínio Carajás, sudeste do Cratón Amazônico, com base em geologia isotópica e química mineral. (Master dissertation). Instituto de Geociências, Belém.

Barros, C.E. de M., Besser, M.L., Gouvêa Vasconcellos, E.M., 2023. Voluminous Paleoproterozoic plutonic belt of the Bacajá Domain in Amazon Craton: Petrology,

geotectonic setting and Pb–Pb zircon evaporation ages. J. South Am. Earth Sci. 130, 104491. https://doi.org/10.1016/j.jsames.2023.104491

Bottazzi, P., Tiepolo, M., Vannucci, R., Zanetti, A., Brumm, R., Foley, S.F., Oberti, R., 1999. Distinct site preferences for heavy and light REE in amphibole and the prediction of Amph/L D REE. Contrib. to Mineral. Petrol. 137, 36–45. https://doi.org/10.1007/s004100050580

Broska, I., Harlov, D., Tropper, P., Siman, P., 2007. Formation of magmatic titanite and titanite–ilmenite phase relations during granite alteration in the Tribeč Mountains, Western Carpathians, Slovakia. Lithos 95, 58–71. https://doi.org/10.1016/j.lithos.2006.07.012

Chambers, J.A., Kohn, M.J., 2012. Titanium in muscovite, biotite, and hornblende: Modeling, thermometry, and rutile activities of metapelites and amphibolites. Am. Mineral. 97, 543–555. https://doi.org/10.2138/am.2012.3890

Cioffi, C.R., Campos Neto, M. da C., Möller, A., Rocha, B.C., 2019. Titanite petrochronology of the southern Brasília Orogen basement: Effects of retrograde net-transfer reactions on titanite trace element compositions. Lithos 344–345, 393–408. https://doi.org/10.1016/j.lithos.2019.06.035

Cordani, U., Tassinari, C.C.G., Kawashita, K., 1984. A Serra dos Carajás como região limitrofe entre províncias tectônicas. Ciências da Terra 9, 6–11.

Cordani, U.G., Sato, K., Teixeira, W., Tassinari, C.G., Basei, M.A.S., 2000. Crustal evolution of the South American Platform. Tecton. Evol. South Am. 19–40.

Corrêa, L.S., 2020. Petrochronology of paragneisses of Bacajá Domain, Amazon Craton. Universidade de Campinas.

Correa, R.T., Vidotti, R.M., Guedes, V.J.C.B., Scandolara, J.E., 2022. Mapping the Thermal Structure of the Amazon Craton to Constrain the Tectonic Domains. J. Geophys. Res. Solid Earth 127. https://doi.org/10.1029/2021JB023025

Cruz-Uribe, A.M., Feineman, M.D., Zack, T., Jacob, D.E., 2018. Assessing trace element (dis)equilibrium and the application of single element thermometers in metamorphic rocks. Lithos 314–315, 1–15. https://doi.org/10.1016/j.lithos.2018.05.007

Deer, W.A., Howie, R.A., Zussman, J., 2013. An Introduction to the Rock-Forming Minerals. Mineralogical Society of Great Britain and Ireland. https://doi.org/10.1180/DHZ

Delinardo-Silva, M.A., Monteiro, L.V.S., Moreto, C.P.N., Faustinoni, J., Santos, T.J.S., Sousa, S.D., Xavier, R.P., 2025. From Source to Sink: U-Pb Geochronology and Lithochemistry Unraveling the Missing Link Between Mesoarchean Anatexis and Magmatism in the Carajás Province, Brazil. Minerals 15, 265. https://doi.org/10.3390/min15030265

Faraco, M.T.L., Vale, A.G., Santos, J.O.S., Luzardo, R., Ferreira, A. l., Oliveira, M.A., Marinho, P.A.C., 2006. Levantamento geológico da região ao norte da Província Carajás in: Souza, in: Souza, Valmir; Horbe, A.C. (Ed.), Contribuições a Geologia Da Amazônia. Sociedade Brasileira de Geologia, Belém, pp. 32–44.

Franz, G., Spear, F.S., 1985. Aluminous titanite (sphene) from the Eclogite Zone, south-central Tauern Window, Austria. Chem. Geol. 50, 33–46. https://doi.org/10.1016/0009-2541(85)90110-X

Frost, B.R., Chamberlain, K.R., Schumacher, J.C., 2001. Sphene (titanite): phase relations and role as a geochronometer. Chem. Geol. 172, 131–148. https://doi.org/10.1016/S0009-2541(00)00240-0

Gao, X.-Y., Zheng, Y.-F., Chen, Y.-X., Guo, J., 2012. Geochemical and U–Pb age constraints on the occurrence of polygenetic titanites in UHP metagranite in the Dabie orogen. Lithos 136–139, 93–108. https://doi.org/10.1016/j.lithos.2011.03.020

Garber, J.M., Hacker, B.R., Kylander-Clark, A.R.C., Stearns, M., Seward, G., 2017. Controls on Trace Element Uptake in Metamorphic Titanite: Implications for Petrochronology. J. Petrol. 58, 1031–1057. https://doi.org/10.1093/petrology/egx046

Green, E.C.R., White, R.W., Diener, J.F.A., Powell, R., Holland, T.J.B., Palin, R.M., 2016. Activity–composition relations for the calculation of partial melting equilibria in metabasic rocks. J. Metamorph. Geol. 34, 845–869. https://doi.org/10.1111/jmg.12211

Heaman, L.M., 2009. The application of U–Pb geochronology to mafic, ultramafic and alkaline rocks: An evaluation of three mineral standards. Chem Geol 261, 43–52. https://doi.org/10.1016/j.chemgeo.2008.10.021

Holder, R.M., Hacker, B.R., Seward, G.G.E., Kylander-Clark, A.R.C., 2019. Interpreting titanite U–Pb dates and Zr thermobarometry in high-grade rocks: empirical constraints on elemental diffusivities of Pb, Al, Fe, Zr, Nb, and Ce. Contrib. to Mineral. Petrol. 174, 42. https://doi.org/10.1007/s00410-019-1578-2

Holland, T., Powell, R., 2003. Activity-compositions relations for phases in petrological calculations: An asymetric multicomponent formulation. Contrib. to Mineral. Petrol. 145, 492–501. https://doi.org/10.1007/s00410-003-0464-z

Holland, T.J.B., Powell, R., 2011. An improved and extended internally consistent thermodynamic dataset for phases of petrological interest, involving a new equation of state for solids. J. Metamorph. Geol. 29, 333–383. https://doi.org/10.1111/j.1525-1314.2010.00923.x

Hurley, P.., Almeida, F.F.., Melcher, G.., Cordani, U.., Rand, J., Kawashita, K., Vandoros, P.,

Pinson, W.., Fairbairn, H.., 1967. Test of continental drift by means of radiometric ages. Science (80-.). 495–500.

Kapp, P., Manning, C.E., Tropper, P., 2009. Phase-equilibrium constraints on titanite and rutile activities in mafic epidote amphibolites and geobarometry using titanite–rutile equilibria. J. Metamorph. Geol. 27, 509–521. https://doi.org/10.1111/j.1525-1314.2009.00836.x

Kavanagh-Lepage, C., Gervais, F., Larson, K., Crowley, J., Moukhsil, A., 2024. Titanite petrochronology, phase equilibria modelling and the role of amphibole during decompression: Insights from the Shabogamo Domain, central Grenville Province. Precambrian Res. 413, 107571. https://doi.org/10.1016/j.precamres.2024.107571

Kohn, M.J., 2017. Titanite Petrochronology. Rev. Mineral. Geochemistry 83, 419–441. https://doi.org/10.2138/rmg.2017.83.13

Kontonikas-Charos, A., Ehrig, K., Cook, N.J., Ciobanu, C.L., 2019. Crystal chemistry of titanite from the Roxby Downs Granite, South Australia: insights into petrogenesis, subsolidus evolution and hydrothermal alteration. Contrib. to Mineral. Petrol. 174, 59. https://doi.org/10.1007/s00410-019-1594-2

Kowallis, B.J., Christiansen, E.H., Dorais, M.J., Winkel, A., Henze, P., Franzen, L., Mosher, H., 2022. Variation of Fe, Al, and F Substitution in Titanite (Sphene). Geosciences 12, 229. https://doi.org/10.3390/geosciences12060229

Kroonenberg, S.B., De Roever, E.W.F., Fraga, L.M., Reis, N.J., Faraco, T., Lafon, J.M., Cordani, U., Wong, T.E., 2016. Paleoproterozoic evolution of the Guiana Shield in Suriname: A revised model. Geol. en Mijnbouw/Netherlands J. Geosci. 95, 491–522. https://doi.org/10.1017/njg.2016.10

Leake;, B.E., Woolley;, A.R., Arps;, C.E.S., Birch;, W.D., Gilbert;, M.C., Grice;, J.D., Hawthorne;, F.C., Kato;, A., Kisch;, H.J., Krivovichev;, V.G., Linthout;, K., Laird;, J., Mandarino;, J.A., Maresch;, W. V., Nickel;, E.H., Rock;, N.M.S., Youzhi, Schumacher;, J.C., Smith;, D.C., Stephenson;, N.C.N., Ungaretti;, L., Whittaker;, E.J.W., Guo, Y., 1997. Nomenclature of amphiboles; Report of the Subcommittee on Amphiboles of the International Mineralogical Association, Commission on New Minerals and Mineral Name. Am. Mineral. 82, 1019–1037.

Liao, Y., Wei, C., Rehman, H.U., 2021. Titanium in calcium amphibole: Behavior and thermometry. Am. Mineral. 106, 180–191. https://doi.org/10.2138/am-2020-7409

Ludwig, K.R., 2003. isoplot Excell version 3.0. A geochronological toolkit for Microsoft Excel,.

Macambira, E.M.B., Ricci, P.S.F., 2015. Geologia e recursos minerais da Folha Tucuruí – SA.22-Z-C, Estado do Pará, 1st ed. CPRM, Belém.

Macambira, M.J.B., Pinheiro, V.L., Armstrong, R.A., 2007. A fronteira Arqueano-Paleoproterozoico no SE do Cráton Amazônico: abrupta no tempo, suave na tectônica?, in: X Simpósio de Geologia Da Amazônia. pp. 97–100.

Macambira, M.J.B., Silva, D.C.C., Barros, C.E.M., Scheller, T., 2003. New isotope evidences confirming the existence of a paleoproterozoic terrain in the region at the north of the Carajas Mineral Province, in: IV South American Symposium on Isotope Geology. Salvadaro, Brazil, pp. 205–206.

Macambira, M.J.B., Silva, D.C.C., Vasquez, M.L., Barros, C.E.M., 2004. Investigação do limite Arqueano-Paleoproterozoico ao norte da Província Carajás, Amazônia Oriental, in: 42º Congresso Brasileiro de Geologia. Araxá.

Macambira, M.J.B., Vasquez, M.L., Silva, D.C.C. da, Galarza, M.A., Barros, C.E. de M., Camelo, J. de F., 2009. Crustal growth of the central-eastern Paleoproterozoic domain, SW Amazonian craton: Juvenile accretion vs. reworking. J. South Am. Earth Sci. 27, 235–246. https://doi.org/10.1016/j.jsames.2009.02.001

Magalhães, L.B., Macambira, M.J.B., Macambira, E.M.B., Ricci, P. dos S.F., 2023. Crustal growth in the northeast portion of the Rhyacian Bacajá Domain, SE Amazonian craton, based on U-Pb, Lu-Hf, and Sm-Nd data. Brazilian J. Geol. 53. https://doi.org/10.1590/2317-4889202320220068

Marangoanha, B., Oliveira, D.C. de, Dall'Agnol, R., 2019. The Archean granulite-enderbite complex of the northern Carajás province, Amazonian craton (Brazil): Origin and implications for crustal growth and cratonization. Lithos 350–351, 105275. https://doi.org/10.1016/j.lithos.2019.105275

Morimoto, N., Fabries, J., Ferguson, A.K., Ginzburg, I. V., Ross, M., Seifert, F.A., Zussman, J., Aoki, K., Gottardi, G., 1988. Nomenclature of Pyroxenes. Mineral. Mag. 52, 535–550. https://doi.org/10.1180/minmag.1988.052.367.15

Motta, J.G., Souza Filho, C.R. d., Carranza, E.J.M., Braitenberg, C., 2019. Archean crust and metallogenic zones in the Amazonian Craton sensed by satellite gravity data. Sci. Rep. 9. https://doi.org/10.1038/s41598-019-39171-9

Neri, A.S.S., Dall'Agnol, R., Dantas, E.L., Feio, G.R.L., Almeida, J.A.C., Galarza, M.A., Rhyacian magmatism in the southern Bacajá Domain: Implications for the crustal evolution of SE Amazonian Craton, Brazil. *Precambrian Research*, manuscript submitted for publication.

Palin, R.M., White, R.W., Green, E.C.R., Diener, J.F.A., Powell, R., Holland, T.J.B., 2016. High-grade metamorphism and partial melting of basic and intermediate rocks. J.

Metamorph. Geol. 34, 871–892. https://doi.org/10.1111/jmg.12212

Papapavlou, K., Darling, J.R., Storey, C.D., Lightfoot, P.C., Moser, D.E., Lasalle, S., 2017. Dating shear zones with plastically deformed titanite: New insights into the orogenic evolution of the Sudbury impact structure (Ontario, Canada). Precambrian Res. 291, 220–235. https://doi.org/10.1016/j.precamres.2017.01.007

Prowatke, S., Klemme, S., 2006. Rare earth element partitioning between titanite and silicate melts: Henry's law revisited. Geochim. Cosmochim. Acta 70, 4997–5012. https://doi.org/10.1016/j.gca.2006.07.016

Rocha, B.C., Moraes, R., Möller, A., Cioffi, C.R., 2018. Magmatic inheritance vs. UHT metamorphism: Zircon petrochronology of granulites and petrogenesis of charnockitic leucosomes of the Socorro–Guaxupé nappe, SE Brazil. Lithos 314–315, 16–39. https://doi.org/10.1016/j.lithos.2018.05.014

Santos, J.O.S., Hartmann, L.A., Faria, M.S., Riker, S.R., Miguel, M., Almeida, M.E., Mcnaughton, N.J., 2006. a Compartimentação Do Cráton Amazonas Em Províncias : Avanços Ocorridos No Período 2000-2006, in: IX Simpósio de Geologia Da Amazônica. Sociedade Brasileira de Geologia, Belém.

Scibiorski, E., Kirkland, C.L., Kemp, A.I.S., Tohver, E., Evans, N.J., 2019. Trace elements in titanite: A potential tool to constrain polygenetic growth processes and timing. Chem. Geol. 509, 1–19. https://doi.org/10.1016/j.chemgeo.2019.01.006

Scibiorski, E.A., Cawood, P.A., 2022. Titanite as a petrogenetic indicator. Terra Nov. 34, 177–183. https://doi.org/10.1111/ter.12574

Siegel, K., Williams-Jones, A.E., van Hinsberg, V.J., 2017. The amphiboles of the REE-rich A-type peralkaline Strange Lake pluton – fingerprints of magma evolution. Lithos 288–289, 156–174. https://doi.org/10.1016/j.lithos.2017.07.012

Silva, A.S. da, 2021. Metamorfismo de UHT e HP no Domínio Bacajá, Cráton do Amazonas. Universidade de Brasília (UnB).

Silva, M.A.D., Monteiro, L.V.S., Santos, T.J.S., Moreto, C.P.N., Sousa, S.D., Faustinoni, J.M., Melo, G.H.C., Xavier, R.P., Toledo, B.A.M., 2021. Mesoarchean migmatites of the Carajás Province: From intra-arc melting to collision. Lithos 388–389, 106078. https://doi.org/10.1016/j.lithos.2021.106078

Smit, M.A., Vrijmoed, J.C., Scherer, E.E., Mezger, K., Kooijman, E., Schmitt-Kielman, M., Tual, L., Guilmette, C., Ratschbacher, L., 2024. Retentiveness of rare earth elements in garnet with implications for garnet Lu-Hf chronology. J. Metamorph. Geol. 42, 703–727. https://doi.org/10.1111/jmg.12769

Smith, M.P., Storey, C.D., Jeffries, T.E., Ryan, C., 2009. In Situ U-Pb and Trace Element Analysis of Accessory Minerals in the Kiruna District, Norrbotten, Sweden: New Constraints on the Timing and Origin of Mineralization. J. Petrol. 50, 2063–2094. https://doi.org/10.1093/petrology/egp069

Spencer, K.J., Hacker, B.R., Kylander-Clark, A.R.C., Andersen, T.B., Cottle, J.M., Stearns, M.A., Poletti, J.E., Seward, G.G.E., 2013. Campaign-style titanite U–Pb dating by laser-ablation ICP: Implications for crustal flow, phase transformations and titanite closure. Chem. Geol. 341, 84–101. https://doi.org/10.1016/j.chemgeo.2012.11.012

Stearns, M.A., Hacker, B.R., Ratschbacher, L., Rutte, D., Kylander-Clark, A.R.C., 2015. Titanite petrochronology of the Pamir gneiss domes: Implications for middle to deep crust exhumation and titanite closure to Pb and Zr diffusion. Tectonics 34, 784–802. https://doi.org/10.1002/2014TC003774

Storey, C.D., Smith, M.P., Jeffries, T.E., 2007. In situ LA-ICP-MS U–Pb dating of metavolcanics of Norrbotten, Sweden: Records of extended geological histories in complex titanite grains. Chem. Geol. 240, 163–181. https://doi.org/10.1016/j.chemgeo.2007.02.004

Tassinari, C.C.G., Macambira, M.J.., 2004. A evolução tectônica do Craton Amazônico, in: Mantesso-Neto, V., Bartorelli, A., Carneiro, C.D.R., Brito Neves, B.B. (Eds.), Geologia Do Continente Sul Americano: Evoluc¸ Ão Da Obra de Fernando Flávio Marques Almeida. São Paulo, pp. 471–486.

Tiepolo, M., Oberti, R., Vannucci, R., 2002. Trace-element incorporation in titanite: constraints from experimentally determined solid/liquid partition coefficients. Chem. Geol. 191, 105–119. https://doi.org/10.1016/S0009-2541(02)00151-1

Van Achterbergh, E., Ryan, C.G., Jackson, S.E., Griffin, W.., 2001. Data reduction software for LA-ICP-MS: appendix, in: Sylvester, P.J. (Ed.), Laser Ablation-ICP-Mass Spectrometry in the Earth Sciences: Principles and Applications. Mineralog. Assoc. Canada (MAC) Short Course Series, Ottawa, Ontario, Canada, pp. 239 – 243.

Vasquez, M.L.., Rosa-Costa, L.T.., 2008. Geologia e Recursos Minerais do Estado do Pará : Sistema de Informações Geográficas – SIG : texto explicativo dos mapas Geológico e Tectônico e de Recursos Minerais do Estado do Pará, 1st ed. Brazilian Geological Service, CPRM, Belém.

Vasquez, M.L., 2006. Geocronologia em zircão, monazita e granada e isótopos de Nd das associações litológicas da porção oeste do Domínio Bacajá: evolução crustal da porção meridional da Província Maroni-Itacaiúnas – Sudeste Do Cráton Amazônico. Universidade

Federal do Pará.

Vasquez, M.L., Macambira, M.J.B., Armstrong, R.A., 2008. Zircon geochronology of granitoids from the western Bacajá Domain, southeastern Amazonian craton, Brazil: Neoarchean to Orosirian evolution. Precambrian Res. 161, 279–302. https://doi.org/10.1016/j.precamres.2007.09.001

Vieira, C., Amaral, W., Holanda Santos, F., 2022. Petrography, geochemistry and zircon U-Pb geochronology of the Siderian-Rhyacian granitoids of NW Bacajá Domain, Amazonian Craton. J. Geol. Surv. Brazil 5. https://doi.org/10.29396/jgsb.2022.v5.n3.1

Whitney, D.L. and Evans, B.W. 2010. Abbreviations for names of rock-forming minerals. American Mineralogist, 95, 185–187, https://doi.org/10.2138/am.2010.3371

White, R.W., Powell, R., Clarke, G.L., 2002. The interpretation of reaction textures in Fe-rich metapelitic granulites of the Musgrave Block, Central Australia: Constraints from mineral equilibria calculations in the system. J. Metamorph. Geol. 20, 41–55. https://doi.org/10.1046/j.0263-4929.2001.00349.x

White, R.W., Powell, R., Holland, T.J.B., Johnson, T.E., Green, E.C.R., 2014. New mineral activity–composition relations for thermodynamic calculations in metapelitic systems. J. Metamorph. Geol. 32, 261–286. https://doi.org/10.1111/jmg.12071

Xiang, H., Connolly, J.A.D., 2022. GeoPS: An interactive visual computing tool for thermodynamic modelling of phase equilibria. J. Metamorph. Geol. 40, 243–255. https://doi.org/10.1111/jmg.12626

SUPPLEMENTARY MATERIAL 1 - MINERAL CHEMISTRY

Table S 1 - representative compositions of clinopyroxene, amphibole and biotite from the studied orthogneisses

Mineral	Clinopyroxene				Amphibole				Biotite	
Sample	ASM-22		AA-144A		ASM-22		AA-144A		ASM-22	
Analyses	C2.1	C2.2	C4.3	C9.2	C9.1	C9.4	C4.3	C9.2	C1.5	C6.1
Texture	Rim	core	rim	core	rim	core	rim	core	rim	core
SiO_2	52.51	53.09	52.88	52.61	44.56	45.04	44.25	43.92	35.69	36.33
TiO_2	0.05	0.15	0.01	0.09	1.77	1.32	1.68	1.83	3.00	4.21
Al_2O_3	0.93	0.84	0.58	0.94	8.74	8.61	8.70	9.15	15.55	13.76
Fe_2O_3*	1.55	1.40	1.76	2.00	3.58	5.39	4.04	2.73	2.75	0.00
FeO*	7.65	7.66	6.97	7.21	12.83	11.24	12.07	13.22	17.70	16.87
MgO	12.58	12.90	12.84	12.86	11.33	11.82	11.62	11.20	13.43	12.69
MnO	0.80	0.79	0.72	0.71	0.41	0.51	0.59	0.51	0.25	0.36
CaO	22.78	23.12	23.86	22.57	11.82	11.71	11.57	11.74	0.00	0.39
Na_2O	0.61	0.54	0.46	0.70	1.14	1.20	1.46	1.39	0.08	0.08
K_2O	0.00	0.00	0.01	0.00	1.08	0.99	1.21	1.22	9.47	9.73
F	0.00	0.00	0.00	0.00	0.11	0.11	0.29	0.39	0.12	0.43
Cl	0.01	0.01	0.00	0.01	0.09	0.06	0.20	0.22	0.09	0.08
H_2O*	-	-	-	-	1.92	1.93	1.79	1.74	3.83	3.60
Sum	99.55	100.58	100.18	99.84	99.46	99.91	99.41	99.11	99.14	98.42
	Formulae based on 6 oxygens				Formulae based on 23 oxygens				Formulae based on 11 oxygens	
Si	1.977	1.977	1.977	1.972	6.662	6.674	6.628	6.612	2.736	2.854
Ti	0.001	0.004	0.000	0.003	0.199	0.148	0.189	0.207	0.173	0.249
Al	0.041	0.037	0.025	0.041	1.541	1.504	1.535	1.623	1.405	1.274
Fe^{3+}	0.044	0.039	0.050	0.056	0.403	0.601	0.455	0.309	-	-
Fe^{2+}	0.241	0.239	0.218	0.226	1.604	1.392	1.512	1.664	1.135	1.108
Mg	0.706	0.716	0.715	0.719	2.525	2.611	2.596	2.513	1.535	1.486
Mn	0.026	0.025	0.023	0.022	0.052	0.064	0.074	0.065	0.016	0.024
Ca	0.919	0.922	0.956	0.906	1.894	1.859	1.857	1.894	0.000	0.002
0	0.044	0.039	0.033	0.051	0.332	0.344	0.424	0.405	0.012	0.012
K	0.000	0.000	0.000	0.000	0.206	0.186	0.230	0.234	0.926	0.976
F	-	-	-	-	0.050	0.052	0.138	0.187	0.030	0.106
Cl	-	-	-	-	0.022	0.014	0.051	0.057	0.012	0.010
XMg	0.71	0.72	0.73	0.72	0.61	0.65	0.71	0.60	0.57	0.57

Table S 2 - Representative chemical compositions of titanite from the studied orthogneisses

Sample	ASM-22				AA-144A			
Analyses	C8.1	C8.4	C7.3	C5.3	C3.8	C3.11	C5.3	C5.4
Texture	unzoned	unzoned	unzoned	unzoned	unzoned	unzoned	unzoned	unzoned
SiO_2	30.12	29.97	29.92	30.54	30.14	30.30	30.47	29.96
TiO_2	36.45	38.05	36.53	36.72	37.38	35.80	36.60	36.58
Al_2O_3	1.14	0.94	1.26	1.31	1.05	1.31	1.08	1.16
V_2O_3	0.30	0.32	0.32	0.33	0.28	0.31	0.28	0.27
Y_2O_3	0.09	0.11	0.19	0.14	0.06	0.08	0.13	0.15
La_2O_3	0.03	0.13	0.06	0.05	0.11	0.08	0.09	0.14
Ce_2O_3	0.29	0.34	0.56	0.39	0.48	0.20	0.63	0.68
Nd_2O_3	0.08	0.11	0.18	0.13	0.18	0.10	0.16	0.23
FeO	1.17	0.58	1.22	1.57	1.11	1.32	1.04	1.22
MgO	0.00	0.00	0.00	0.03	0.01	0.02	0.03	0.03
MnO	0.16	0.10	0.16	0.10	0.12	0.15	0.05	0.12
CaO	28.22	27.39	27.68	28.13	27.76	28.14	27.92	27.50
Na_2O	0.02	0.04	0.01	0.05	0.00	0.02	0.02	0.03
K_2O	0.00	0.01	0.01	0.13	0.03	0.00	0.00	0.00
F	0.21	0.15	0.24	0.34	0.38	0.37	0.43	0.34
Cl	0.00	0.00	0.00	0.00	0.02	0.00	0.00	0.01
H_2O *	1.03	1.05	1.01	0.99	0.95	0.96	0.94	0.96
	Number of cations per formula unit based on 4 atoms							
Sum	99.37	99.49	99.45	100.98	100.14	99.24	99.92	99.43
Si	4.000	4.000	4.000	4.000	4.000	4.000	4.000	4.000
Ti	3.641	3.820	3.674	3.618	3.732	3.555	3.614	3.674
Al	0.179	0.147	0.199	0.202	0.165	0.204	0.166	0.182
V	0.032	0.035	0.034	0.035	0.029	0.033	0.029	0.029
Y	0.007	0.007	0.014	0.010	0.004	0.006	0.009	0.011
La	0.001	0.006	0.003	0.002	0.005	0.004	0.004	0.007
Ce	0.014	0.017	0.027	0.019	0.023	0.010	0.030	0.033
Nd	0.004	0.005	0.009	0.006	0.008	0.005	0.008	0.011

Fe^{2+}	0.130	0.064	0.137	0.172	0.123	0.146	0.114	0.136
Mg	0.000	0.000	0.000	0.006	0.002	0.004	0.005	0.005
Mn	0.018	0.011	0.019	0.011	0.014	0.016	0.006	0.014
Ca	4.015	3.917	3.965	3.948	3.947	3.980	3.927	3.934
Na	0.006	0.011	0.004	0.012	0.000	0.005	0.006	0.007
K	0.001	0.001	0.002	0.021	0.005	0.000	0.001	0.000
F	0.089	0.062	0.103	0.139	0.158	0.152	0.177	0.143

Table S 3- Representative analyses plagioclase and K-feldspar from the sample ASM-22

Mineral	Plagioclase		K-feldspar	
Analyses	C9.7	C2.15	C2.1	C2.2
Texture	rim	core	rim	core
SiO_2	61.92	60.63	63.65	63.20
TiO_2	0.04	0.03	0.00	0.00
Al_2O_3	24.01	25.01	19.29	19.49
Fe_2O_3*	0.12	0.17	0.12	0.04
MgO	0.01	0.01	0.00	0.00
MnO	0.01	0.01	0.00	0.02
CaO	5.41	5.55	0.00	0.00
Na_2O	8.61	8.35	0.47	0.53
K_2O	0.20	0.22	15.35	15.44
Sum	100.40	100.08	99.01	98.71
Number of cations per formula unit based on 8 oxygens				
Si	2.74	2.696	2.964	2.952
Ti	0.001	0.001	0.000	0.000
Al	1.252	1.311	1.059	1.073
Fe^{3+}	0.004	0.006	0.004	0.001
Mg	0	0.001	0.000	0.000
Mn	0	0	0.000	0.001
Ca	0.256	0.265	0.000	0.000
Na	0.739	0.72	0.043	0.048
K	0.012	0.012	0.912	0.920
An	0.25	0.27	0.00	0.00
Or	0.01	0.01	0.955	0.95

SUPPLEMENTARY MATERIAL 1 - TRACE ELEMENT DATA

Table S 4 - Titanite trace element data for sample ASM-22

Sample	ASM-22												
Spot	C8Ttn1.1	C8Ttn1.2	C8Ttn2.1	C8Ttn2.2	C3Ttn1.2	C3ttn2.1	C7Ttn1.1	C7Ttn1.2	C8Ttn1.3	C8Ttn1.4	C7Ttn1.5	C7Ttn1.6	C7Ttn1.7
Texture	core	rim	rim	core	rim	rim	rim	core	rim	rim	rim	core	rim
Sr	25.22	29.52	31.11	30.52	21.49	23.44	32.65	31.67	31.88	31.24	40.35	72.44	106.3
Y	379.96	408.34	896.97	892.04	252.47	251.28	1352.19	1142.68	1094.49	1306.68	1289.53	1171.76	1060.31
Zr	151.5	166.47	313.57	251.25	99.69	115.51	303.52	298.49	284.4	316.88	323.24	309.95	287.2
Nb	619.2	659.95	1423.87	1172.85	332.98	412.69	1762.95	1166.48	1137.43	1108.7	1710.89	1369.08	1654.37
La	436.55	476.62	1072.4	890.85	215.21	194.95	1558.39	1331.3	1317.24	1346.44	1590.42	1447.27	1230.24
Ce	1567.02	1645.32	3671.11	3180.72	748.18	705.43	5449.75	4606.29	4560.63	4833.77	5465.89	4504.39	4085.15
Pr	229.29	237.54	539.73	470.63	112.5	106.1	802.17	666.81	663.75	709.32	772.06	631.24	594.55
Nd	938.32	985.66	2245.45	2016.92	508.42	462.46	3366.24	2803.88	2824.05	3072.55	3265.48	2719.94	2606.26
Sm	172.1	176.37	390.67	376.86	102.49	94.1	637.42	505.09	498.75	595.17	611.47	511.41	494.41
Eu	134.33	128.46	170.31	158.04	71.56	80.59	213.91	197.16	202.47	196.38	234.1	184	164.12
Gd	120.97	130.56	284.61	264.81	76.85	70.72	461.4	375.44	368.33	425.09	435.36	371.31	365.74
Tb	15.32	16.62	38.98	37.02	10.64	10.34	60.51	50.17	49.44	57.69	58.16	50.7	44.59
Dy	77.04	93.82	195.82	198.06	55.7	53.61	314.97	253.17	252.34	296.28	298.53	267.53	238.89
Ho	12.89	13.82	30.37	30.49	8.54	8.12	50.08	40.03	39.5	46.9	46.79	41.75	37.56
Er	31.79	37.76	80.76	77.46	21.2	20.1	121.35	101.85	99.59	118.54	120.29	108.55	104.96
Tm	4.81	5.59	10.7	10.16	3.09	2.64	15.62	14.21	13.35	14.92	15.19	14.02	11.71
Yb	32.42	34.19	73.41	76.57	21.76	22.39	103.26	101.42	100.94	110.65	103.73	97.76	85.87
Lu	4.04	3.99	8.4	8.89	2.37	2.11	11.36	10.79	10.52	11.3	12.1	11.06	9.59
Hf	4.49	7.08	13.56	9.55	3.28	4.36	17.07	13.75	14.63	12.97	15.44	13.78	13.38
Ta	18.58	19.58	69.1	40.13	12.97	13.39	118.91	55.28	49.91	46.01	81.01	71.27	105.78
Th	17.5	18.41	54.28	41.9	1.61	1.21	122.77	125.06	73.33	96.24	105.07	89.42	97.27
U	34.7	40.77	113.28	109.72	11.43	12.89	238.91	196.89	194.95	206.11	197.02	210.89	129.12
T °C	690	694	727	715	670	677	725	725	722	728	729	727	722
Zr_in_titanite*													

Table S 5 - Titanite trace element for sample AA-144A

Sample	AA-144A										
Spot	C7Ttn1.1	C7Ttn1.2	C7Ttn1.3	C7Ttn1.4	C6Ttn1.1	C6Ttn1.2	C6Ttn1.3	C6Ttn3.1	C6Ttn4.1	C9Ttn1.1	C9Ttn2.1
Texture	rim	core	rim	brim	bright core	rim	bright core	core	bright core	core	core
Sr	28.71	35.28	97.82	31.36	65.48	69.5	52.34	40.77	282.53	105.25	86.98
Y	2456.34	2589.38	6078.18	3152.11	2086.9	756.48	3855.26	3630.52	1060.14	1121.05	222.33
Zr	373.4	426.73	371.15	346.19	307.57	211.68	355.3	333.43	94.79	123.77	59.86
Nb	1193.99	1576.13	2228.6	966.86	819.69	347.1	1528.37	725.03	201.87	369.59	181.56
La	1422.68	1561.86	1886.46	1385.39	1537.87	1082.15	1580.99	1603.52	1555.51	594.84	324.05
Ce	6403.37	6818.99	9845.06	6550.68	5843.43	3217.8	7269.16	7300.65	3769.11	2601.69	1102.49
Pr	1011.58	1063.3	1784.52	1085.98	850.67	379.76	1247.51	1230.82	535.75	423.39	142.71

Nd	4386.35	4665.38	8671.98	4988.88	3570.77	1378.23	5877.25	5863.06	2482.01	2032.68	568.11
Sm	889.08	938.88	2146.51	1086.79	718.2	232.62	1368.27	1335.09	474.4	436.02	89.07
Eu	145.01	159.17	218.45	152.75	183.24	108.58	203.7	208.18	87.07	129.32	75.76
Gd	634.58	678.53	1597.99	775.25	506.39	155.28	971.44	961.38	346.66	307.03	67.42
Tb	89.45	95.92	245.81	113.62	71.38	23.5	146.3	136.44	46.48	42.15	7.98
Dy	504.84	529.87	1391.11	632.5	401.54	138.1	841.57	752.31	238.65	223.82	42.64
Ho	83.73	90.63	220.05	103.67	67.34	23.87	139	118.52	39.09	33.21	6.39
Er	239.31	264.33	596.99	294.48	200.64	80.97	391.65	338.04	107.26	94.16	19.27
Tm	34.44	37.54	76.43	41.02	29.7	13.01	52.3	43.93	13.71	11.81	2.44
Yb	258.75	276.55	499.92	322.78	229	127.28	382.44	332.84	98.41	91.52	18.48
Lu	28.23	28.91	43.34	32.04	23.56	13.76	35.04	30.22	9.64	9.26	2.15
Hf	25.07	36.22	31.71	19.93	19.02	12.52	26.84	24.74	6.28	7.4	<1.24
Ta	52.46	75.33	239.73	37.47	19.41	3.71	103.16	14.55	3.72	5.19	0.87
Th	176.47	217.2	261.85	163.66	84.19	38.86	204.18	105.42	22.38	17.08	5.55
U	236.32	251.37	241.63	271.68	209.44	136.71	289.51	241.36	67.96	91.97	31.44
T°C Zr_in_titanite*	737	744	736	732	726	707	734	730	667	680	646

Table S 6 - Clinopyroxene trace element data for samples ASM-22 and AA-144A

Sample	ASM-22		AA-144A								
Spot	C1Px1.2	C1Px1.3	C2Px1.1	C2Px1.2	C2Px1.3	C2Px2.1	C2Px2.2	C2Px23	C7Px1.1	C7Px1.2	C7Px1.3
Texture	core	rim	core	rim	core	rim	core	rim	rim	core	rim
Ti	1461.06	960.8	668.97	690.87	654.64	1643.41	734.56	759.24	515.16	337.96	532.62
Sr	33.83	17.74	42.04	31.03	28.41	22.21	29.25	20.44	8.22	6.61	12.72
Y	51.52	34.37	55.86	59.85	55.74	57.2	59.27	58.21	48.08	32.55	46.93
Zr	19.07	15.9	18.71	21.59	25.34	19.95	28.43	23.87	12.32	9.71	11.84
Nb	2.31	1.14	0.157	0.709	0.124	4.14	0.329	0.089	0.226	0.149	0.6
La	15.92	3.67	49.37	22.66	31.32	12.1	31.6	9.6	1.18	2	8.47
Ce	22.5	18.07	94.8	52.29	61.53	41.81	69.39	35.15	6.15	5.5	19.94
Pr	6.48	4.37	13.56	9.61	9.39	8.74	10.73	7.24	1.84	1.25	3.74
Nd	37.73	27.43	67.01	56.08	48.13	50.27	56.81	45.15	13.21	8.96	21.34
Sm	14.29	11.53	18.11	16.61	15.34	16.19	15.46	15.15	7.24	4.63	9.4
Eu	1.9	1.32	1.9	1.68	1.52	1.69	1.79	1.55	0.49	0.301	0.6
Gd	15.74	11.4	15.73	14.21	13.71	13.5	14.26	13.75	9.07	5.52	9.59
Tb	2.45	1.58	2.13	2.27	2.22	2.21	2.12	2.29	1.5	1	1.76
Dy	13.84	8.72	12.78	13.21	12.97	12.59	12.6	12.97	9.92	6.65	8.96
Ho	2.44	1.29	2.31	2.46	2.35	2.18	2.32	2.45	2	1.25	1.87
Er	5.18	3.58	5.39	6	5.76	5.57	5.61	6.31	4.69	3.47	4.43

Tm	0.599	0.423	0.766	0.735	0.805	0.747	0.804	0.812	0.656	0.361	0.619
Yb	3.95	3.61	5.39	5.63	6.08	5.34	6	6.11	3.35	3.25	3.89
Lu	0.581	0.547	0.96	1.047	0.937	0.818	0.903	1.022	0.589	0.383	0.625
Hf	1.46	1.39	1.66	1.94	2.15	1.78	2.08	1.99	1.44	1.05	1.26
Ta	0.17	0.079	<0.029	0.04	<0.023	0.19	<0.027	0.033	0.045	<0.038	0.055
Th	0.093	0.007	0.136	0.052	0.076	0.102	6.66	0.0303	0.035	0.043	0.137
U	0.023	0.056	0.293	0.158	0.304	0.271	0.424	0.055	0.036	0.031	0.148

Table S 7 - Amphibole trace element data for samples ASM-22 and AA-144A

Sample	ASM-22						AA-144A							
Spot	C9Amp1.1	C9Amp1.2	C9Amp1.3	C9Amp2.1	C9Amp2.2	C9Amp2.3	C4Amp1.1	C4amp1.2	C4amp1.3	C7Amp1.1	C7Amp1.2	C7Amp1.3	C7Amp1.4	C7Amp1.5
Texture	rim	core	rim	rim	core	rim	rim	core	rim	rim	core	core	rim	core
Ti	6598.52	7232.06	7662.41	9429.09	7226.92	8043.62	9091.48	9208.61	6824.36	8232.43	8106.07	7341.73	13271.66	9352.6
Sr	25.94	29.13	27.07	36.82	30.5	31.89	31.81	37	24.54	40.09	36.51	75.1	34.8	34.91
Y	93.3	109.89	123.24	134.94	136.18	120.95	227.74	256.54	147.76	242.58	257.12	240.93	407.01	249.42
Zr	20.21	22.63	22.94	29.45	33.14	29.25	47.7	60.23	35.3	53.48	55.86	40.56	74.05	50.86
Nb	21.04	24.66	26.36	35.42	27.85	32.49	41.01	45.05	25.09	47.2	43.21	35.6	79.89	43.67
La	10.57	12.52	12.15	16.5	14.86	17.41	10.17	60.54	12.19	53.98	65.63	69.49	22.68	37.74
Ce	53.81	63.12	58.93	83.94	75.99	80.85	77.18	282.64	88.95	251.65	286.38	277.47	137	205.88
Pr	12.39	14.79	14.45	19.51	17.34	17.7	22.04	51.6	22.62	48.02	50.57	52.57	34.18	42.24
Nd	80.15	92.73	98.97	122.33	118.44	106.3	155.78	280.31	145.54	255.73	266.31	283.74	243.09	245.73
Sm	27.11	33.95	35.62	41.29	39.17	37.54	61.91	74.35	46.15	73.02	74.74	79.04	92	74.12
Eu	4.08	4.49	4.67	4.83	4.62	4.21	5.31	5.87	3.44	5.75	5.26	6.75	6.91	5.33
Gd	26.94	30.97	34.46	39.11	38.22	34.87	59.53	64.52	42.77	62.24	65.47	67.95	88.24	65.46
Tb	4.11	4.56	5.72	5.95	6.12	5.07	9.38	9.93	6.53	9.93	10.5	9.86	14.91	10.13
Dy	21.9	26.12	29.57	32	32.22	29.34	51.2	56.76	34.05	53.04	58.03	54.83	89.74	56.91
Ho	3.89	4.6	5.15	5.68	6.15	5.34	9.1	10.25	6.22	10.02	10.25	9.58	17.03	10.46
Er	9.24	11.07	12.63	12.95	13.34	11.31	22.45	25.97	14.72	24.79	25.2	23.39	41.34	25.25
Tm	1.23	1.38	1.33	1.39	1.55	1.44	2.65	3.18	1.75	3.15	2.95	2.86	5.29	3.13
Yb	6.15	8.54	8.58	9.65	9.64	8.72	15.82	20.61	9.67	18.77	18.16	16.54	34.39	17.82
Lu	0.95	1.1	1.15	1.14	1.2	1.16	1.85	2.44	1.34	2.33	2.18	2.15	4.01	2.31
Hf	1.24	1.48	1.61	2.12	2.18	2.06	4.61	4.44	3.03	4.18	4.17	3.58	6.14	3.78
Ta	0.87	0.97	0.99	1.5	1.2	1.46	1.52	1.4	0.887	1.56	1.43	1.19	2.6	1.4
Th	0.026	0.036	<0.0206	0.0178	0.035	0.031	0.017	0.076	0.0385	0.125	0.36	0.045	0.051	0.035
U	0.056	0.032	0.085	0.099	0.045	0.075	0.098	0.325	0.338	0.27	0.301	0.483	0.853	0.404

SUPPLEMENTARY MATERIAL 3 - U-Pb GEOCHRONOLOGY

Table S 8 – LA-ICP-MS titanite data for sample ASM-22

Location - 539776/9424268	Isotopic ratios																Apparent ages						
SPOT	207/235	1σ (abs)	206/238	1 σ (abs)	coef. corr	238/206	1 σ (abs)	207/206	1 σ (abs)	208/206	1 σ (abs)	Common Pb (%)	Pb rad (ppm)	Th (ppm)	U (ppm)	Th/U	$T_{206/238}$	1 σ (abs)	$T_{207/235}$	1 σ (abs)	$T_{207/206}$	1 σ (abs)	Conc.
C4_7.3	6.1772	0.0962	0.3646	0.0058	0.76	2.7427	0.0434	0.1229	0.0029	0.2068	0.0158	7.7	10	12	23	0.5	2004	27	2001	14	1998	42	100
C4_4.2	6.4396	0.0806	0.3728	0.0045	0.91	2.6822	0.0321	0.1253	0.0023	0.2791	0.0091	6.4	27	45	57	0.8	2043	21	2038	11	2033	33	100
C4_7.2	6.3654	0.1283	0.3739	0.0048	0.97	2.6743	0.0345	0.1235	0.0031	0.2468	0.0363	7.2	14	19	29	0.6	2048	23	2028	18	2007	44	101
C4_7.1	6.4478	0.0860	0.3781	0.0038	0.91	2.6450	0.0268	0.1237	0.0021	0.2544	0.0122	5.7	14	22	29	0.8	2067	18	2039	12	2010	30	101
C4_4.1	6.5879	0.0834	0.3824	0.0055	0.96	2.6148	0.0377	0.1249	0.0026	0.2975	0.0974	8.0	14	19	29	0.7	2088	26	2058	11	2028	37	101
C4_3.2	6.6745	0.0989	0.3866	0.0030	0.84	2.5867	0.0203	0.1252	0.0018	0.2113	0.0241	2.0	54	82	111	0.7	2107	14	2069	13	2032	26	101
C8_2.3	6.8553	0.1172	0.3956	0.0050	0.66	2.5280	0.0320	0.1257	0.0018	0.0574	0.0054	3.2	19	6	45	0.1	2149	23	2093	15	2039	26	102
C7_2.1	6.8051	0.0753	0.3959	0.0048	0.97	2.5262	0.0308	0.1247	0.0017	0.1563	0.0118	1.8	48	54	102	0.5	2150	22	2086	10	2024	24	103
C8_2.1	6.8446	0.1113	0.3972	0.0058	0.97	2.5179	0.0366	0.1250	0.0018	0.2824	0.0891	5.7	29	38	55	0.7	2156	27	2092	14	2029	25	103
C8_2.2	6.9484	0.1098	0.4022	0.0051	0.91	2.4863	0.0317	0.1253	0.0017	0.1171	0.0065	5.4	20	13	44	0.3	2179	24	2105	15	2033	25	103
C7_3.1	6.9545	0.0737	0.4052	0.0046	0.89	2.4681	0.0280	0.1245	0.0016	0.2544	0.1600	9.2	54	50	108	0.5	2193	21	2106	10	2022	23	104
C7_1.1	6.7465	0.1001	0.3982	0.0045	0.95	2.5115	0.0286	0.1229	0.0014	0.1326	0.0063	2.5	47	45	100	0.4	2161	21	2079	13	1999	20	103
C7_1.2	6.7592	0.0707	0.4002	0.0046	0.93	2.4987	0.0285	0.1225	0.0016	0.0988	0.0034	1.3	71	51	161	0.3	2170	21	2080	9	1993	23	104
C8_1.2	6.4199	0.1322	0.3831	0.0052	0.54	2.6100	0.0353	0.1215	0.0022	0.1756	0.0129	7.8	9	9	18	0.5	2091	24	2035	18	1979	32	102
C3_2.1	6.0187	0.1457	0.3424	0.0042	0.61	2.9208	0.0361	0.1275	0.0026	0.2190	0.2396	19.7	7	1	15	0.1	1898	20	1979	21	2064	37	95
C3_1.3	6.2239	0.1838	0.3454	0.0108	0.08	2.8955	0.0909	0.1307	0.0048	0.1993	0.0378	29.3	4	1	7	0.1	1912	51	2008	27	2107	68	95
C3_1.2	6.3216	0.2319	0.3635	0.0133	0.19	2.7510	0.1008	0.1261	0.0056	0.2857	0.0534	37.4	4	1	7	0.1	1999	64	2022	34	2045	82	98
C3_1.1	6.0447	0.2257	0.3661	0.0075	0.47	2.7314	0.0558	0.1197	0.0050	0.3352	0.2013	31.5	3	1	6	0.1	2011	35	1982	31	1952	74	101
C3_1.4	5.8029	0.1781	0.3708	0.0111	0.01	2.6969	0.0810	0.1135	0.0052	0.1579	0.0317	26.1	4	1	7	0.1	2033	53	1947	27	1856	86	104
C4_5.1	6.5529	0.0823	0.3760	0.0039	0.45	2.6599	0.0277	0.1264	0.0022	0.5961	0.3436	37.2	51	49	59	0.8	2057	18	2053	11	2049	30	100
C4_3.1	6.7845	0.1028	0.3799	0.0035	0.27	2.6326	0.0243	0.1295	0.0020	0.4830	0.1291	24.8	72	63	101	0.6	2076	16	2084	13	2092	28	99
C8_1.1	6.5977	0.1373	0.3852	0.0060	0.36	2.5958	0.0404	0.1242	0.0022	0.2362	0.0157	14.8	8	7	14	0.5	2101	28	2059	18	2018	31	102
C7_1.5	6.8151	0.0776	0.3927	0.0050	0.81	2.5466	0.0322	0.1259	0.0018	0.3079	0.0965	21.7	49	36	84	0.4	2135	23	2088	10	2041	25	102
C4_6.1	6.8069	0.0758	0.3935	0.0036	0.95	2.5415	0.0234	0.1255	0.0019	0.4913	0.1160	20.2	42	81	68	1.2	2139	17	2087	10	2035	27	102
C7_1.4	6.8470	0.0702	0.3965	0.0049	0.92	2.5219	0.0314	0.1252	0.0017	0.2438	0.0812	11.5	55	49	109	0.4	2153	23	2092	9	2032	25	102
C7_1.3	6.8150	0.0745	0.3975	0.0050	0.87	2.5158	0.0318	0.1243	0.0017	0.3733	0.0298	25.4	63	41	98	0.4	2158	23	2088	10	2020	24	103
C8_1.3	6.9452	0.1279	0.3983	0.0057	0.98	2.5109	0.0359	0.1265	0.0019	0.1464	0.0493	11.0	14	6	26	0.2	2161	26	2105	17	2050	27	102
C4_2.1	7.0742	0.1161	0.4051	0.0046	0.94	2.4683	0.0279	0.1266	0.0023	0.6406	0.1316	27.9	56	35	54	0.6	2193	21	2121	14	2052	31	103
C7_1.6	6.6687	0.0710	0.4058	0.0049	0.83	2.4646	0.0297	0.1192	0.0016	0.2834	0.0583	19.6	94	57	159	0.4	2196	22	2069	9	1944	23	106
C4_1.1	7.2849	0.0860	0.4113	0.0047	0.27	2.4312	0.0279	0.1285	0.0017	0.6236	0.1160	30.3	63	86	81	1.1	2221	21	2147	11	2077	24	103

Standard Titanite BLR-1 data on 25/06/2024
Concordia Age =1047.2 ± 1.5 Ma
BLR-1 reference age: 1047.1 +/- 0.4 Ma (TIMS) - Aleinikoff et al, 2007.

Khan secondary standard on 25/06/2024
Concordia Age = 520.4 ± 1.2 Ma
Khan reference age: 522.2 +/- 2.2 Ma – Heaman L. ,2009.

Table S 9 – LA-ICP-MS titanite data for sample AA-144A

Location - 555726/9420040	Isotopic ratios															Apparent ages						
SPOT	207/235	1σ (abs)	206/238	1 σ (abs)	coef. corr	238/206	1 σ (abs)	207/206	1 σ (abs)	208/206	1 σ (abs)	Pb total (%)	Pb rad (ppm)	Th (ppm)	U (ppm)	Th/U	$T_{206/238}$	1 σ (abs)	$T_{207/235}$	1 σ (abs)	$T_{207/206}$	1 σ (abs)	Conc.
C3_1.1	6.2367	0.0962	0.3605	0.0037	0.76	2.7736	0.0283	0.1255	0.0019	0.3920	0.2292	10.8	19	24	39	0.6	1985	17	2010	13	2035	26	98
C5_1.3	6.1698	0.1036	0.3642	0.0039	0.86	2.7457	0.0292	0.1229	0.0019	0.1436	0.0176	9.8	36	18	79	0.2	2002	18	2000	15	1998	28	100
C6_2.3	6.2380	0.1163	0.3650	0.0050	0.88	2.7397	0.0376	0.1239	0.0016	0.1618	0.0076	8.2	18	13	37	0.4	2006	24	2010	16	2014	24	99
C5_1.1	6.2060	0.1027	0.3661	0.0040	0.93	2.7312	0.0295	0.1229	0.0019	0.1919	0.0276	2.7	57	79	122	0.6	2011	19	2005	14	1999	27	100
C9_1.1	6.2496	0.0865	0.3663	0.0035	0.74	2.7298	0.0257	0.1237	0.0016	0.0731	0.0066	2.3	22	9	54	0.2	2012	16	2011	12	2011	23	100
C6_4.1	6.1447	0.1057	0.3675	0.0046	0.81	2.7212	0.0341	0.1213	0.0014	0.1482	0.0243	2.4	46	45	102	0.4	2018	22	1997	15	1975	21	101
C6_3.2	6.2100	0.0901	0.3685	0.0035	0.94	2.7136	0.0261	0.1222	0.0016	0.1727	0.0178	4.9	47	51	101	0.5	2022	17	2006	13	1989	23	100
C9_3.1	6.3757	0.0869	0.3710	0.0031	0.96	2.6956	0.0221	0.1246	0.0016	0.0583	0.0071	3.8	19	4	43	0.1	2034	14	2029	12	2024	23	100
C5_2.2	6.2961	0.1055	0.3715	0.0040	0.75	2.6919	0.0292	0.1229	0.0019	0.1072	0.0081	1.1	52	43	120	0.4	2036	19	2018	15	1999	28	100
C6_1.1	6.3974	0.1026	0.3764	0.0041	0.84	2.6567	0.0287	0.1233	0.0019	0.1142	0.0142	1.9	52	40	117	0.3	2060	19	2032	14	2004	27	101
C3_5.2	6.5148	0.0968	0.3781	0.0035	0.86	2.6445	0.0243	0.1250	0.0016	0.0904	0.0057	4.7	17	8	38	0.2	2068	16	2048	13	2028	23	100
C7_1.5	6.5203	0.0931	0.3828	0.0035	0.92	2.6126	0.0238	0.1235	0.0015	0.2289	0.0060	1.3	51	83	104	0.8	2089	16	2049	13	2008	22	101
C3_4.1	6.8270	0.0987	0.3892	0.0036	0.93	2.5691	0.0241	0.1272	0.0015	0.1404	0.0076	2.6	23	20	50	0.4	2119	17	2089	13	2060	21	101
C7_1.4	6.6032	0.0926	0.3883	0.0037	0.90	2.5750	0.0245	0.1233	0.0015	0.2287	0.0068	3.1	45	68	90	0.7	2115	17	2060	12	2005	22	102
C9_5.1	6.3369	0.0787	0.3788	0.0033	0.74	2.6399	0.0229	0.1213	0.0014	0.0948	0.0209	2.7	46	22	105	0.2	2071	15	2024	11	1976	21	102
C7_1.1	6.5367	0.0940	0.3827	0.0036	0.83	2.6131	0.0243	0.1239	0.0015	0.1929	0.0029	2.0	44	57	93	0.6	2089	17	2051	13	2013	22	101
C7_1.2	6.5189	0.0955	0.3827	0.0037	0.89	2.6128	0.0253	0.1235	0.0016	0.2163	0.0082	2.0	50	72	102	0.7	2089	17	2049	13	2008	23	101
C3_3.1	6.6778	0.1023	0.3809	0.0031	0.92	2.6255	0.0214	0.1272	0.0015	0.1166	0.0058	5.8	23	13	50	0.3	2080	14	2070	13	2059	21	100
C3_5.1	6.5707	0.0949	0.3776	0.0034	0.91	2.6483	0.0241	0.1262	0.0015	0.0928	0.0049	3.2	20	11	48	0.2	2065	16	2055	13	2046	21	100
C6_4.2	6.3243	0.0911	0.3755	0.0033	0.92	2.6630	0.0233	0.1221	0.0015	0.1705	0.0360	4.8	55	56	119	0.5	2055	16	2022	13	1988	21	101
C6_3.1	6.3203	0.0905	0.3766	0.0035	0.94	2.6551	0.0248	0.1217	0.0015	0.1855	0.0258	7.2	50	47	105	0.4	2061	17	2021	13	1981	22	101
C7_1.3	6.4219	0.0869	0.3777	0.0036	0.94	2.6479	0.0251	0.1233	0.0015	0.3825	0.0240	7.0	62	130	111	1.2	2065	17	2035	12	2005	22	101
C5_2.1	6.3533	0.1030	0.3779	0.0040	0.86	2.6462	0.0277	0.1219	0.0018	0.2185	0.0056	1.0	66	107	138	0.8	2067	18	2026	14	1985	27	102
C5_1.2	6.4595	0.1088	0.3798	0.0041	0.86	2.6327	0.0286	0.1233	0.0019	0.0750	0.0030	1.5	45	24	105	0.2	2076	19	2040	15	2005	28	101
C3_2.1	6.4739	0.0977	0.3717	0.0035	0.80	2.6903	0.0255	0.1263	0.0016	0.3120	0.0744	18.3	32	25	56	0.4	2037	17	2042	13	2047	22	99
C6_5.1	5.9679	0.1149	0.3329	0.0055	0.59	3.0036	0.0497	0.1300	0.0019	0.3985	0.0437	25.4	13	6	21	0.3	1853	27	1971	17	2098	25	93
C9_4.1	5.5099	0.0698	0.3458	0.0033	0.99	2.8919	0.0273	0.1156	0.0014	0.5281	0.1225	83.8	55	17	87	0.2	1915	16	1902	11	1889	23	100

C6_2.2	6.0965	0.1212	0.3477	0.0048	0.89	2.8763	0.0393	0.1272	0.0018	0.3637	0.0566	25.9	24	16	37	0.4	1924	23	1990	17	2059	26	96
C6_1.3	5.9283	0.0963	0.3576	0.0043	0.98	2.7965	0.0337	0.1202	0.0014	0.3520	0.0783	13.8	46	79	86	0.9	1971	21	1965	15	1960	21	100
C9_2.1	6.2970	0.1198	0.3642	0.0044	0.92	2.7461	0.0331	0.1254	0.0024	0.1373	0.0247	12.1	9	2	20	0.1	2002	21	2018	17	2035	34	99
C6_1.2	6.6168	0.1083	0.3809	0.0041	0.97	2.6255	0.0282	0.1260	0.0020	0.2019	0.0261	12.3	39	28	78	0.4	2080	19	2062	15	2043	28	100
C6_2.1	7.1147	0.1202	0.3951	0.0050	0.95	2.5313	0.0323	0.1306	0.0016	0.3828	0.1067	26.3	24	15	32	0.4	2146	23	2126	16	2106	22	100

Standard Titanite BLR-1 data on 06/25/2024
Concordia Age =1047.2 ± 1.5 Ma
BLR-1 reference age: 1047.1 +/- 0.4 Ma (TIMS) - Aleinikoff et al, 2007.

Khan secondary standard on 06/25/2024
Concordia Age = 520.4 ± 1.2 Ma
Khan reference age: 522.2 +/- 2.2 Ma - Heaman,2009.

8 ATIVIDADES FUTURAS

Com os dados remanescentes que foram obtidos durante o período de doutoramento e não foram apresentados neste volume, estão sendo elaborados mais dois manuscritos. São eles:

Origin of orthopyroxene-bearing magmatic and metamorphic rocks: an example from the Bacajá Domain, SE Amazonian Craton, Brazil. Neste artigo serão discutidos dados de campo, petrografia, geoquímica, química mineral (elementos maiores, menores, traço e ETR), modelamento termodinâmico e geoquímico, geocronologia e isótopos (Nd-Hf) dos granulitos félsicos e charnockitos ígneos aflorantes na área de estudo, a fim de elucidar a origem das rochas portadoras de ortopiroxênio em ambientes ígneos e metamórficos e as implicações disso para a evolução da crosta inferior durante o Pré-Cambriano.

Ultra-high temperature recorded in mafic and felsic granulites from southern Bacajá Domain, SE Amazonian Craton. Neste artigo serão discutidos aspectos de campo, petrográficos, mineralógicos, condições P-T e geocronologia dos granulitos máficos e félsicos do Cinturão Granulítico Novolândia. Os dados serão integrados para determinar as condições de metamorfismo registradas nessas rochas, bem como as idades de cristalização de seus protólitos e metamorfismo e avaliar os motores do metamorfismo granulítico que atingiu a região.

9 CONCLUSÕES

A integração de dados de campo, petrográficos, mineralógicos, geoquímicos, geocronológicos e isotópicos permitiu aprofundar o conhecimento sobre a geologia da área de estudo, localizada na porção sul do Domínio Bacajá, em sua região limítrofe com a Província Carajás. Os principais eventos registrados na área estão sumarizados na figura 1.

Foram identificadas novas unidades riacianas de rochas granitoides e charnockíticas previamente englobadas no Complexo Cajazeiras que foram cristalizadas durante um longo período de atividade magmática que durou cerca de 70 Ma. Neste período foram cristalizados os granitos Bandeirante, Alto Rio Preto e Bernardino e os charnockitos Maravilha e Serra Azul. As unidades são em sua maioria cálcio-alcalinas e magnesianas, mas podem variar para cálcicas ou álcali-cálcicas e ferrosas. A integração de isótopos de Nd-Hf sugere que a crosta riaciana da região de estudo resulta do intenso retrabalhamento crustal de fontes majoritariamente arqueanas com pouca ou nenhuma contribuição mantélica. Essas rochas foram formadas em um ambiente colisional a pós-colisional, sendo sua origem provavelmente desencadeada pela delaminação da crosta espessada, durante um evento orogenético paleoproterozoico (Orogenia Transamazônica). O Domínio Bacajá e outros domínios no Escudo das Guianas e Cráton Oeste Africano apresentam semelhanças nos padrões geocronológicos e isotópicos, reforçando hipóteses prévias que eles estavam justapostos durante a amalgamação do supercontinente Columbia.

O Granito Alto Rio Preto é composto por granitos e granodioritos-tonalitos que podem conter epidoto magmático como mineral acessório. O granito foi colocado em pressões entre 0,45 e 0,7 GPa, temperaturas entre 949 e ~640 ºC, sob condições oxidantes (NNO±0,5 a ±1) e moderado a altos conteúdos de água nos magmas (~6 % em peso nos monzogranitos; < 4 % em peso, nos granodioritos). A preservação de epidoto magmático nessas rochas resulta de um processo complexo que dependeu de altas pressões, condições oxidantes e quantidade de água no magma, combinadas a baixa densidade e viscosidade que permitiram a rápida ascensão do magma na crosta (4-5 km/ano e taxa de dissolução 2-3 ano para epidoto) impedindo a total dissolução do epidoto. As semelhanças com outros granitos portadores de epidoto magmático de diferentes idades e formados em ambiente tectônicos distintos, localizados na Província Borborema e Índia, indicam que esse mineral é um excelente marcador das condições de cristalização e também fornece informações valiosas sobre processos profundos da crosta.

As rochas que compões o Granito Alto Rio Preto são variavelmente deformadas a depender da proximidade da zona de cisalhamento Misteriosa. São milonitos de baixo a médio grau, cuja deformação foi iniciada ainda no estágio magmático e perdurou até a solidificação completa

dos magmas, caracterizando uma intrusão sintectônica. A sobreposição entre as idades de zircão e titanita e a química dos cristais de titanita sugerem que ambos os minerais foram formados durante o mesmo evento magmático. Essa unidade apresenta afinidade geoquímica com granitos cálcio-alcalinos a cálcio-alcalinos de alto K, com baixas a médias razões Sr/Y. O magma parental da fácies monzogranítica foi gerado via fusão por desidratação da crosta máfica de composição semelhante a basaltos paleoproterozoicos a 1,0 GPa e 865 ºC deixando resíduo de fusão de composição anfibolítica. As idades U-Pb em zircão e titanita sugerindo origem durante o mesmo evento magmático, sem modificações significativas após a cristalização. Esse granito representa um típico exemplo de granito derivado de fontes crustais com pouca ou nenhuma contribuição mantélica e, portanto, não contribuiu significativamente para o crescimento crustal na zona de interface entre o Domínio Bacajá e a Província Carajás.

Os charnockitos Maravilhas e Serra Azul são de origem ígnea e podem ou não conter ortopiroxênio e/ou faialita + quartzo. No Charnockito Maravilha, duas associações petrográficas foram identificadas: (i) monzonito-granito-charnockito e (ii) granodiorito-monzogranito, enquanto o Charnockito Serra Azul é composto por tonalitos e granodioritos com raros monzogranitos. A fácies (i) do Charnockito Maravilha cristalizou em temperaturas entre 1052 e ~680 ºC, evoluiu em condições reduzidas (FMQ±0,5), com conteúdo inicial de água no magma ≤3 wt%. Por outro lado, a fácies (ii) cristalizou em temperaturas entre 1050 e ~680 ºC evoluiu sob condições oxidantes (NNO±0,5) e com água inicial do magma de ~4 wt%. As duas associações foram colocadas a pressões entre 0,3 e 0,6 GPa. O charnockito Serra Azul foi colocado a pressões entre 0,3 e 0,6 GPa, temperaturas entre 1078 e ~700 ºC, evoluiu sob condições oxidantes (NNO±0,7) e a água inicial do magma era provavelmente de 2-3 % em peso. A integração dos dados de composições minerais, termobarometria convencional, por *machine learning*, e modelamento termodinâmico permitiram visualizar como a interação complexa entre composição do líquido magmático, quantidade de água no magma, pressão e fugacidade de oxigênio controlaram as condições de cristalização de ortopiroxênio e faialita. Faialita é uma fase estável em baixas pressões (<0.3 GPa), condições reduzidas e que pode ocorrer em líquidos moderadamente enriquecidos em água (2-6 wt%); Por outro lado, o ortopiroxênio é estável em um maior intervalor de pressão (até 0.9 GPa), ocorre desde condições reduzidas (FMQ-2) até oxidantes (NNO+2.5) e em líquidos moderadamente enriquecidos em água (até ~6 wt%), além disso, composições mais ricas em FeOt e MgO expandem os campos de estabilidade do ortopiroxênio. Os dados termodinâmicos trazem novas perspectivas sobre o magmatismo charnockítico que historicamente é considerado restrito a condições anidras, porém, modelamento com base em dados recentes, mostra que a cristalização dessas rochas

pode ocorrer em condições mais variadas do que previamente inferido.

A aplicação de diversos diagramas de modelagem termodinâmica para compreensão de processos de cristalização e fusão em sistemas ígneos representa uma contribuição original e inédita para o Domínio Bacajá e, de modo mais amplo, para o Cráton Amazônico. Antes do presente trabalho existiam apenas dois estudos utilizando metodologias semelhantes realizados na Província Carajás (Mesquita *et al.* 2025, Semprich *et al.* 2015). A aplicação dessa metodologia abre uma nova fronteira para a compreensão de processos em sistemas magmáticos de diferentes composições e submetidos a distintas condições de P-T-fO_2-H_2O durante a cristalização.

O Complexo Cajazeiras é composto por ortognaisses tonalíticos a monzograníticos que foram cristalizados entre 3,01 e 2,94 Ga e posteriormente retrabalhados/metamorfisados em 2,81-2,80 Ga e 2,21-2,01 Ga durante a Orogenia Transamazônica. A litogeoquímica dos ortognaisses indica afinidades com rochas sanukitoids *s.l.* devido à dicotomia entre a alta concentração de metais de transição como V e Cr e, ao mesmo tempo, enriquecimento em Ba e Sr (LILE). Os isótopos de Hf-Nd indicam fonte com contribuição juvenil para o protólito dos ortognaisses que foi derivado da fusão parcial de um manto enriquecido por fundidos de composição semelhante a TTG. Essas rochas representam os sanukitoides mais antigos do Cráton Amazônico e o segundo mais antigo do mundo. A descoberta dessas rochas abre precedente para presença de outras associações arqueanas típicas ainda mais antigas, como os TTG, no embasamento do Domínio Bacajá. Além disso, elas indicam que processos de metassomatismo do manto já estavam ativos em 3,0 Ga ou até antes disso no Cráton Amazônico.

Os ortognaisses do complexo Cajazeiras foram metamorfisados em fácies anfibolito superior a granulito. Registram pico metamórfico em 0,52-0,55 GPa/760–790 °C que ocorreu a 2,21 Ga (?), com resfriamento em direção ao *solidus* entre 2,10 e 2,08 Ga e retrometamorfismo em 0,43-0,48 GPa/600-650 °C em 2.01 Ga. A petrocronologia de titanita indica que anfibólio e clinopiroxênio não exercem grande influência nos padrões de ETR da titanita e ainda que, em rochas com ausência de granada, titanita e zircão são os principais portadores de elementos terras raras pesados.

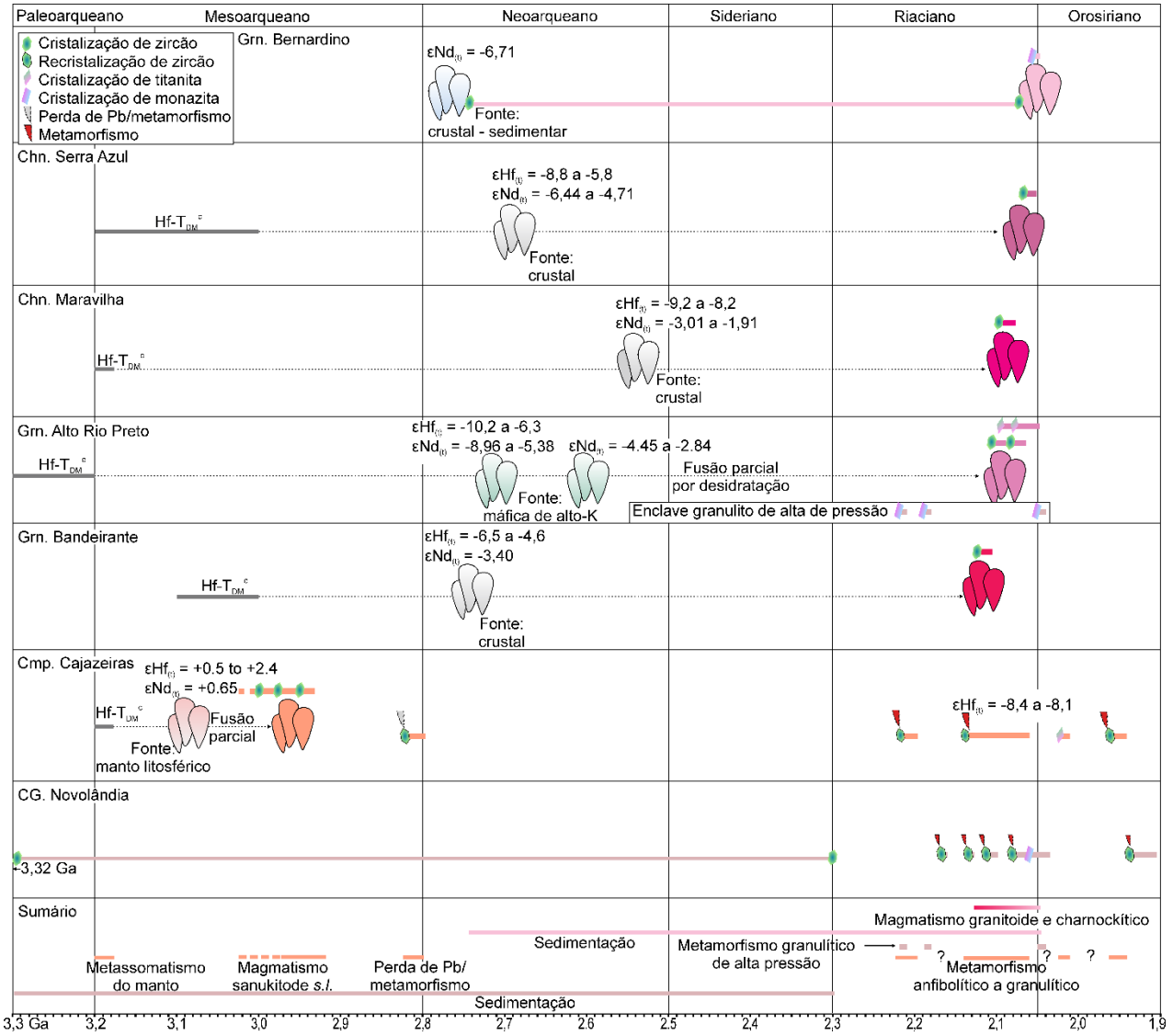


Figura 1 – Sumário dos eventos magmáticos e metamórficos registrados na área de estudo (utilizando dados de Silva 2021, Macambira *et al.* 2007, acrescidos dos dados de Neri *et al.* submetido, e dados não publicados do autor). CG = cinturão granulítico, Cmp= complexo; Grn = granito; Chn = charnockito.

Em uma análise integrada de todos os resultados obtidos nesta tese, acrescidos de dados da literatura, é notória a complexidade geológica da região sul do Domínio Bacajá. A região apresenta registros geológicos que vão desde o Mesoarqueano até a transição Riaciano-Orosiriano, totalizando cerca de 1 bilhão de anos (Fig. 1). Essa história se inicia no Mesoarqueano com a cristalização entre 3,01 e 2,94 Ga (Fig. 1a) dos protólitos dos sanukitoides *s.l.* mais antigos do Cráton Amazônico, agrupados no Complexo Cajazeiras. Apesar do processo que metassomatizou o manto ainda não ter sido definido, essa descoberta indica que esse processo já estava ativo no Mesoarqueano no cráton.

A relação entre a crosta arqueana do Domínio Bacajá e Província Carajás ainda é incerta, como destacado por Motta *et al.* (2019), porém estima-se que em torno de 2,80-2,83 esses segmentos do cráton poderiam estar ligados, tendo em vista a idade coincidente entre o evento de perda de chumbo/metamorfismo registrado nos sanukitoides e a cristalização de ortognaisses no extremo norte da Província Carajás (Alves 2020, Fig. 1b). Este evento deve ter gerado aumento de temperatura e poderia ter sido responsável pela perturbação registrada no sistema isotópico dos ortognaisses.

Posteriormente a isso, o registro neoarqueano nos dois domínios mostra rochas com idade de cristalização entre 2,6 e 2,5 Ga em ambos os domínios, sugerindo um grande evento térmico regional capaz de gerar rochas desde o extremo norte e oeste do Domínio Bacajá (Macambira *et al.* 2009, Magalhães *et al.* 2023, Vasquez & Rosa-Costa 2008, Vieira *et al.* 2022) até a porção norte da Provincia Carajás (Salgado *et al.* 2019 e referências contidas nele). Porém, são notórios os contrastes geoquímicos e isotópicos entre rochas de idade semelhantes nos dois domínios (Salgado *et al.* 2019, Vieira *et al.* 2022), sugerindo que, mesmo tendo havido formação de rochas no mesmo período nos dois segmentos, elas são muito provavelmente oriundas de fontes e processos significativamente distintos.

Rochas siderianas são comuns na porção norte do Domínio Bacajá, mas, até o momento, não foram registradas na porção sul do domínio. Entretanto idades siderianas são comuns em rochas de origem sedimentar (Salgado *et al.* 2019, Silva 2021), sugerindo contribuição de rochas siderianas nos sedimentos.

A maior parte de eventos magmáticos e metamórficos no Domínio Bacajá está concentrada no Riaciano, período em que foram registrados os primeiros indícios de metamorfismo de alta pressão e alta temperatura, bem como magmatismo de arco entre 2,23 e 2,16 Ga (Barros *et al.* 2023, Corrêa, 2020, Vieira *et al.* 2022, Fig. 3a). Estima-se que a colisão entre o Domínio Bacajá e a Província Carajás possa ter ocorrido entre 2,12 e 2,10 Ga com extenso magmatismo colisional associado (Fig. 3b). Por fim, entre 2,10 e 2,06 Ga (Fig. 3c), ocorreu o colapso do

orógeno marcado pelo vasto magmatismo tardi- a pós-colisional provavelmente gerado por delaminação crustal (Barros *et al.* 2023, Macambira & Ricci 2015, Magalhães *et al.* 2023, Vasquez, 2006, Vasquez *et al.* 2008, Vasquez & Rosa-Costa, 2008).

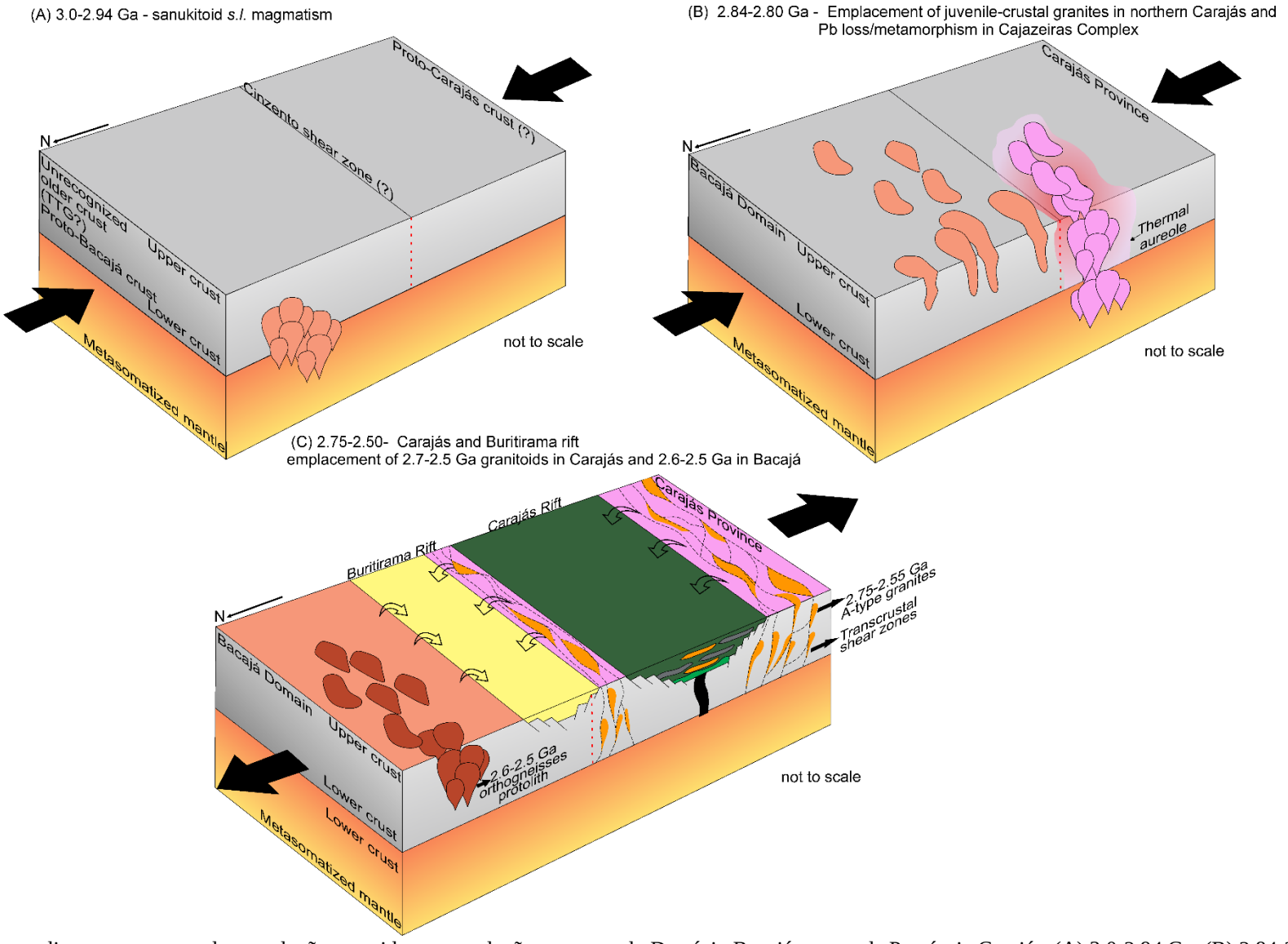


Figura 2 - Blocos diagramas mostrando a evolução sugerida para evolução arqueana do Domínio Bacajá e norte da Província Carajás. (A) 3,0-2,94 Ga; (B) 2,84-2,80 Ga; (C) 2,75-2,50 Ga (sem escala).

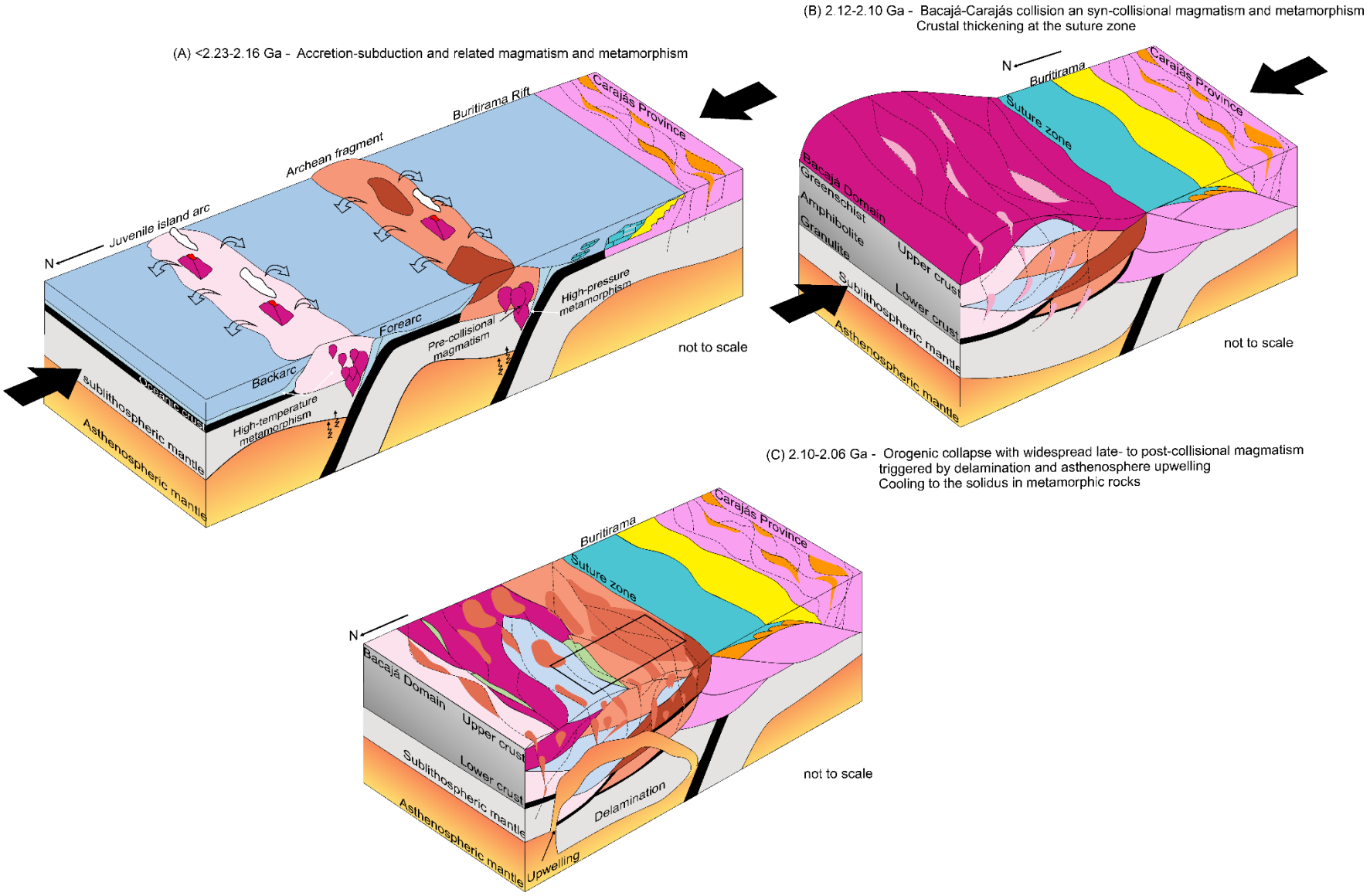


Figura 3 - Blocos diagramas mostrando a evolução sugerida para evolução Riaciana do sul do Domínio Bacajá e norte da Província Carajás. (A) 2,23-2,16 Ga; (B)2,12-2,10 Ga; (C) 2,10-2,06 Ga (sem escala). O retângulo destacado em (C) representa a área de estudo.

REFERÊNCIAS

Aleinikoff J.N., Wintsch R.P., Tollo R.P., Unruh D.M., Fanning C.M., Schmitz M.D. 2007. Ages and origins of rocks of the Killingworth dome, south-central Connecticut: Implications for the tectonic evolution of southern New England. *American Journal of Science,* **307**(1): 63–118. https://doi.org/10.2475/01.2007.04.

Almeida J.A.C., Feio G.R.L., Félix-Silva A.D., Junior M.F. 2016. Caracterização Geológica do Complexo Cajazeiras, Vila Cruzeiro do Sul, Domínio Bacajá, Cráton Amazônico, *In* SBG, 48º Congresso Brasileiro de Geologia, Porto Alegre. *Anais*[...].

Alves J.P.S., 2020. *A relação entre o Domínio Bacajá e o Domínio Carajás, sudeste do Cratón Amazônico, com base em geologia isotópica e química mineral.* MS Dissertation, Universidade Federal do Pará, Belém, 90 p.

Andersen T., Andersson U.B., Graham S., Aberg G., Simonsen S.L. 2009. Granitic magmatism by melting of juvenile continental crust: new constraints on the source of Palaeoproterozoic granitoids in Fennoscandia from Hf isotopes in zircon. *Journal of the Geology Society London*, **166:** 233-247. https://doi.org/10.1144/0016-76492007-166.

Barbosa C.H.T., Almeida J.A.C., Feio G.R.L. 2016. Petrografia das rochas do Complexo Cajazeiras, Vila Cruzeiro do Sul, Domínio Bacajá, Cráton Amazônico, *In:* 48º Congresso Brasileiro de Geologia. *Sociedade Brasileira de Geologia*, Porto Alegre.

Barros C.E.M., Besser M.L., Gouvêa V.E.M. 2023. Voluminous Paleoproterozoic plutonic belt of the Bacajá Domain in Amazon Craton: Petrology, geotectonic setting and Pb-Pb zircon evaporation ages. *Journal of South America. Earth Sciences.* **130**: 104491. https://doi.org/10.1016/j.jsames.2023.104491.

Barros C.E.M., Macambira M.J.B., Santos M.C.C., Silva D.C.C., Palmeira L.C.M., Sousa M.M. 2007. Estruturas sin-magmáticas e idade de zircão de granitos (evaporação de Pb) paleoproterozóicos da parte leste do Domínio Bacajá, Província Maroni-Itacaiúnas. *Revista Brasileira de Geociências,* **37**(2): 293-304. https://doi.org/10.25249/0375-7536.2007373293304.

Besser M.L. & Barros C.E.M. (ed.). 2015. *Geologia e recursos minerais da Folha Rio Bacajá - SA.22-Y-D-VI, Estado do Pará*. Belém, CPRM, 102 p.

Black L.P., Kamo S.L., Allen C.M., Davis D.W., Aleinikoff J.N., Valley J.W., Mundil R., Campbell I.H., Korsch R.J., Williams, I.S., Foudoulis, C. 2004. Improved $^{206}Pb/^{238}U$ microprobe geochronology by the monitoring of a trace-element-related matrix effect; SHRIMP, ID-TIMS, ELA-ICP-MS and oxygen isotope documentation for a series of

zircon standards. *Chemical Geolology*, **205**(1-2): 115-140. https://doi.org/10.1016/j.chemgeo.2004.01.003.

Bonamici, C.E., Fanning, C.M., Kozdon, R., Fournelle, J.H., Valley, J.W., 2015. Combined oxygen-isotope and U-Pb zoning studies of titanite: New criteria for age preservation. *Chemical Geology*, **398**: 70–84. https://doi.org/10.1016/j.chemgeo.2015.02.002.

Bouvier A., Vervoort J.D., Patchett P.J. 2008. The Lu-Hf and Sm-Nd isotopic composition of CHUR: Constraints from unequilibrated chondrites and implications for the bulk composition of terrestrial planets. *Earth and Planetary Science Letters*, **273**(1-2): 48-57. https://doi.org/10.1016/j.epsl.2008.06.010.

Chu N.-C., Taylor R.N., Chavagnac V., Nesbitt R.W., Boella R.M., Milton J.A., German C.R., Bayon G., Burton K. 2002. Hf isotope ratio analysis using multi-collector inductively coupled plasma mass spectrometry: an evaluation of isobaric interference corrections. *Journal of Analytical Atomic Spectrometry*, **17**(12): 1567-1574. https://doi.org/10.1039/b206707b.

Corrêa L.C., Meira V.T., Vasquez M.L. 2019. Metamorfismo dos paragnaisses da região oeste do Domínio Bacajá, Estado do Pará: Dados preliminares, *In*: SBG, 16º Simpósio de Geologia da Amazonia, Manaus. *Resumos expandidos*, p. 626-630.

Corrêa L. S. 2020. *Petrochronology of paragneisses of Bacajá Domain, Amazon Craton*. MS Dissertation, Universidade de Campinas, São Paulo. 120p.

Correa R.T., Vidotti R.M., Guedes V.J.C.B., Scandolara J.E. 2022. Mapping the Thermal Structure of the Amazon Craton to Constrain the Tectonic Domains. *Journal of Geophysical Research: Solid Earth*. **127**(1): e2021JB023025. https://doi.org/10.1029/2021JB023025.

Costa F., Santos P., Serafim I., Costa I., Roopnarain S. 2020. From Mesoarchean drips to modern-style tectonics in the Carajás Province, Amazonian Craton. *Journal of South America Earth Science*, **104**. https://doi.org/10.1016/j.jsames.2020.102817.

Cristo L.C.F. 2018. *Estudo petrográfico e isotópico (Pb-Pb, U-Pb e Sm-Nd) de rochas metavulcânicas, mineralizações auríferas e rochas granitoides relacionadas ao greenstone belt Três Palmeiras, Volta Grande do Xingu, Domínio Bacajá*. MS Dissertation, Universidade Federal do Pará, Belém, 65p.

Del Lama E.A., Sato K., Basei M.A.S., Siga Júnior O., Sproesser W.M., Passarelli C.R. 2008. Novas técnicas aplicadas ao método U-Pb no CPGeo - IGc/USP: avanços na digestão química, espectrometria de massa (TIMS) e exemplos de aplicação integrada

com SHRIMP. *Geologia USP. Série Científica,* **8**(2): 76-99. https://doi.org/10.5327/Z1519-874X2008000200006.

Delor C., Lahondère D., Egal E., Lafon J.M., Cocherie A., Guerrot C., Rossi P., Trufert C., Theveniaut H., Phillips D., Avelar V.G. (ed.) 2003. Transamazonian crustal growth and reworking as revealed by the 1:500,000-scale geological map of French Guiana, *In: Geology of France and Surrounding Areas*, p. 5-57.

DePaolo D.J. 1981. Trace element and isotopic effects of combined wallrock assimilation and fractional crystallization. *Earth and Planetary Science Letters*, **53**(2): 189-202. https://doi.org/10.1016/0012-821X(81)90153-9.

Faraco M.T.L., Vale A.G., Santos J.O.S., Luzardo R., Ferreira A.L., Oliveira M.A., Marinho P.A.C. 2006. Levantamento geológico da região ao norte da Província Carajás. *In:* Souza V. S. & Horbe A.C. (ed.). *Contribuições a Geologia Da Amazônia*. Belém, SBG, p. 32–44.

Feio G.R.L., Sousa J.T., Almeida J.A.C. 2016. Geotermobarometria de granulitos do Complexo Novolândia, porção sul do Domínio Bacajá, Província Tranzamazonas. *In* SBG, 48º Congresso Brasileiro de Geologia, Porto Alegre. *Anais*[...].

Félix-Silva A D., Almeida J.A.C., Feio G.R.L. 2016. Mapa e banco de dados geológicos da Vila Cruzeiro do Sul, porção sul do Domínio Bacajá. *In* SBG, 48º Congresso Brasileiro de Geologia, Porto Alegre. *Anais*[...].

Fettes D., Desmons J., Reis Neto M. 2014. *Rochas Metamórficas:* Classificação e Glossário. 1 ed. São Paulo, Oficina de texto, 313 p.

Gioia S.M.C.L. & Pimentel M.M. 2000. The Sm-Nd isotopic method in the Geochronology Laboratory of the University of Brasília. *Anais da Academia Brasileira de Ciências,* **72**(2): 218-245. https://doi.org/10.1590/s0001-37652000000200009.

Gonçalves G.O., Lana C., Scholz R., Buick I.S., Gerdes A., Kamo S.L., Corfu F., Marinho M.M., Chaves A.O., Valeriano C., Nalini H.A. 2016. An assessment of monazite from the Itambé pegmatite district for use as U-Pb isotope reference material for microanalysis and implications for the origin of the "Moacyr" monazite. *Chemical Geology*, **424:** 30-50. https://doi.org/10.1016/j.chemgeo.2015.12.019.

Grenholm M., Jessell M., Thébaud N. 2019. A geodynamic model for the Paleoproterozoic (ca. 2.27–1.96 Ga) Birimian Orogen of the southern West African Craton - Insights into an evolving accretionary-collisional orogenic system. *Earth and Space Science*, **192**: 138-193. https://doi.org/10.1016/j.earscirev.2019.02.006.

Griffin W.L., Powell W.J., Pearson N.J., O'reilly S.Y. (ed.). 2008. Appendix A2: Glitter:

Data reduction software for laser ablation ICP–MS. *In*: Sylvester P. (ed.). *Laser Ablation ICP-MS in the Earth Sciences: Current Practices and Outstanding Issues*. Canada, Mineralogical Association of Canada, p. 307-311. https://doi.org/10.3749/9780921294801.app02.

Griffin W.L., Wang X., Jackson S.E., Pearson N.J., O'Reilly S.Y., Xu X., Zhou X. 2002. Zircon chemistry and magma mixing, SE China: In-situ analysis of Hf isotopes, Tonglu and Pingtan igneous complexes. *Lithos*, **61**(3-4): 237-269. https://doi.org/10.1016/S0024-4937(02)00082-8.

Heaman L.M., 2009. The application of U–Pb geochronology to mafic, ultramafic and alkaline rocks: An evaluation of three mineral standards. *Chemical Geology*, **261**: 43–52. https://doi.org/10.1016/j.chemgeo.2008.10.021

Holland T., Green E., Powell R. 2018. Melting of peridotites through to granites: A simple thermodynamic model in the system KNCFMASHTOCr. *Journal of Petrology* **59**(5): 881-900. https://doi.org/10.1093/petrology/egy048.

Holland T.J.B. & Powell R. 2011. An improved and extended internally consistent thermodynamic dataset for phases of petrological interest, involving a new equation of state for solids. *Journal of metamorphic Geology*, **29**(3): 333-383.

Horstwood M.S.A., Košler J., Gehrels G., Jackson S.E., McLean N.M., Paton C., Pearson N.J., Sircombe K., Sylvester P., Vermeesch P., Bowring J.F., Condon D.J., Schoene B. 2016. Community-Derived Standards for LA-ICP-MS U-(Th-)Pb Geochronology - Uncertainty Propagation, Age Interpretation and Data Reporting. *Geostandards and Geoanalytical Research*, **40**(3): 311-332. https://doi.org/10.1111/j.1751-908X.2016.00379.x.

Hurley P.M., Almeida F.F.M., Melcher G.C., Cordani U.G., Rand J., Kawashita K., Vandoros P., Pinson W.H., Fairbairn H.W. 1967. Test of continental drift by means of radiometric ages. *Science*, **157**(3788): 495-500. https://doi.org/10.1126/science.157.3788.495.

Jackson S.E., Pearson N.J., Griffin W.L., Belousova E.A. 2004. The application of laser ablation-inductively coupled plasma-mass spectrometry to in situ U-Pb zircon geochronology. *Chemical Geology*, **211**(1-2): 47-69. https://doi.org/10.1016/j.chemgeo.2004.06.017.

João X.S.J. & Vale A.G. (ed.). 1987. *Folha Altamira - A.22-Y-D: Texto explicativo*. Brasília, DF, CPRM, 51 p.

Johansson Å., Bingen B., Huhma H., Waight T., Vestergaard R., Soesoo A., Skridlaite G.,

Krzeminska E., Shumlyanskyy L., Holland M.E., Holm-Denoma C., Teixeira W., Faleiros F.M., Ribeiro B.V, Jacobs J., Wang C., Thomas R.J., Macey P.H., Kirkland C.L., Hartnady M.I.H., Eglington B.M., Puetz S.J., Condie K.C. 2022. A geochronological review of magmatism along the external margin of Columbia and in the Grenville-age orogens forming the core of Rodinia. *Precambrian Research*, **371**: 106463. https://doi.org/10.1016/j.precamres.2021.106463

Knoper M., Armstrong RA., Andreoli MAG., Ashwal LD. 2000. The Steenkampskraal monazite vein: a subhorizontal stretching shear zone indicating extensional collapse of Namaqualand at 1033 Ma?. *Journal of African Earth Sciences*, **1:** 38-38.

Kowallis B.J., Christiansen E.H., Dorais M.J., Winkel A., Henze P., Franzen L., Mosher H. 2022. Variation of Fe, Al, and F Substitution in Titanite (Sphene). *Geosciences (Basel)*, **1**2 229. https://doi.org/10.3390/geosciences12060229.

Kroonenberg S.B. 2019. The Proterozoic Basement of the Western Guiana Shield and the Northern Andes *In*: Cediel, F. & Shaw, R.P. (ed.). *Geology and Tectonics of Northwestern South America*. *Frontiers in Earth Sciences*. Springer Cham, p. 115-192. https://doi.org/10.1007/978-3-319-76132-9_3.

Kroonenberg S.B., Roever E.W.F., Fraga L.M., Reis N.J., Faraco T., Lafon J.-M., Cordani U., Wong T.E. 2016. Paleoproterozoic evolution of the Guiana Shield in Suriname: A revised model. *Netherlands Journal of Geosciences - Geologie en Mijnbouw*, **95**(4): 491-522. https://doi.org/10.1017/njg.2016.10.

Le Maitre R.W. (ed.). 2002. Igneous Rocks: A Classification and Glossary of Terms, Geological Magazine. Cambridge, Cambridge University Press. 236 p. https://doi.org/10.1017/CBO9780511535581.

Ludwig K. 2009. *SQUID 2: A User's Manual*. Berkeley, Berkeley Geochronology Center, (Special Publication, 5).

Ludwig KR. (ed.). 2008. *User's manual for Isoplot 3.6: a geochronological toolkit for Microsoft Center*. Berkeley, Berkeley Geochronology Center, 78 p. (Special Publication, 4).

Macambira E.M.B., Ricci P.D.F., Anjos G.A. (ed.). 2019. *Geologia e recursos minerais da Folha Repartimento - SB.22-X-A*. Belém, CPRM, 107p.

Macambira E.M.B. & Ricci P.S.F. (ed.). 2015. *Geologia e recursos minerais da Folha Tucuruí – SA.22-Z-C, Estado do Pará*. Belém, CPRM, 213p.

Macambira M.J.B., Barros C.E., Cristina D., Silva C., Santos C.C. 2001. Novos dados geológicos e geocronológicos para a região ao norte da Província de Carajás;

evidências para o estabelecimento do limite Arqueano-Paleoproterozóico no sudeste do Cráton Amazônico, *In*: SBG, VII Simpósio de Geologia Da Amazônia, Belém. *Resumos expandidos.* p. 818-821.

Macambira M.J.B., Pinheiro V.L., Armstrong R.A. 2007. A fronteira Arqueano-Paleoproterozoico no SE do Cráton Amazônico: abrupta no tempo, suave na tectônica?. *In:* SBG, X Simpósio de Geologia Da Amazônia, Roraima. *Resumos expandidos.* p. 97-100.

Macambira M.J.B., Silva D.C.C., Barros C.E.M., Scheller T. 2003. New isotope evidences confirming the existence of a paleoproterozoic terrain in the region at the north of the Carajas Mineral Province. *In*: IV South American Symposium on Isotope Geology. Salvador. *Anais*[...]. p. 205–206.

Macambira M. J. B., Silva D.C.C., Vasquez M.L., Barros C.E.M. 2004. Investigação do limite Arqueano-Paleoproterozoico ao norte da Província Carajás, Amazônia Oriental, *In:* SBG, 42º Congresso Brasileiro de Geologia. Araxá. *Anais*[...]

Macambira M.J.B., Teixeira W., Vasquez M.L. 2020. O Cráton Amazônico e suas províncias geocronológicas: o legado de Umberto Cordani. *In:* Bartorelli A., Teixeira W., Neves, B. B. B (ed.). *Geocronologia e evolução tectônica do Continente Sul-Americano: a contribuição de Umberto Giuseppe Cordani*. São Paulo, Solaris Edições Culturais. p. 47-62.

Macambira M.J.B., Vasquez M.L., Silva D.C.C. Galarza M.A., Barros C.E.M., Camelo J.F. 2009. Crustal growth of the central-eastern Paleoproterozoic domain, SW Amazonian craton: Juvenile accretion vs. reworking. *Journal of South American Earth Sciences*, **27**(4): 235-246. https://doi.org/10.1016/J.JSAMES.2009.02.001.

Macambira M.J.B., Vasquez M.L., Monteiro P.C., Armstrong R.A. 2022. Neoarchean to Rhyacian crustal records along the Middle Xingu River area, Amazonian craton. *Brazilian Journal of Geology*, **52**(4): 1-20. https://doi.org/10.1590/2317-4889202220220017.

Macambira M.J.B. & Amireault S. 2022. Isotopic study (U Pb, Sm Nd, and Pb Pb) of rocks and auriferous mineralizations from the Volta Grande do Xingu deposits, Bacajá Domain, Amazonian craton. *Journal of Geochemical* Exploration, **284**: 107767. https://doi.org/10.1016/j.gexplo.2025.107767

Magalhães L.B., Macambira M.J.B., Macambira E.M.B., Ricci, P.S.F. 2023. Crustal growth in the northeast portion of the Rhyacian Bacajá Domain, SE Amazonian craton, based on U-Pb, Lu-Hf, and Sm-Nd data. *Brazilian Journal of Geology*, **53**(2):

1-18. https://doi.org/10.1590/2317-4889202320220068.

Meert J.G. & Santosh M. 2017. The Columbia supercontinent revisited. *Gondwana Research*, **50**: 67-83. https://doi.org/10.1016/j.gr.2017.04.011.

Mesquita C.J.S., Dall'Agnol R., Neri A.S.S., Cunha I.R.V., Almeida J.A.C., Oliveira J.K.M. 2025. Crystallization parameters and thermodynamic modeling of the Igarapé Gelado suite: Implications for the Neoarchean magmatism of the Carajás Province, Brazil. *Journal of South America Earth Sciences*, **153**. https://doi.org/10.1016/j.jsames.2025.105357.

Milhomem Neto J.M. & Lafon J.-M. 2019. Zircon U-Pb and Lu-Hf isotope constraints on Archean crustal evolution in Southeastern Guyana Shield. *Geoscience Frontiers*, **10**(4): 1477-1506. https://doi.org/10.1016/j.gsf.2018.09.012.

Milhomem-Neto J.M. & Lafon J.-M. 2020. Crustal growth and reworking of Archean crust within the Rhyacian domains of the southeastern Guiana Shield, Brazil: Evidence from zircon U-Pb-Hf and whole-rock Sm-Nd geochronology. *Journal of South American Earth Sciences*, **103**: 102740. https://doi.org/10.1016/j.jsames.2020.102740.

Monteiro P.C. 2006. Investigação do limite entre os domínios geocronológicos da região do Médio Xingu, Sudeste do Cráton Amazônico. MS Dissertation, Universidade Federal do Pará, Pará. 104p.

Motta J.G., Filho C.R.S., Carranza E.J.M., Braitenberg C. 2019. Archean crust and metallogenic zones in the Amazonian Craton sensed by satellite gravity data. *Scientific Reports*, **9**: 2565. https://doi.org/10.1038/s41598-019-39171-9.

Neri A.S.S., Dantas E.L., Peixoto E.I.N., Fuck R.A., Feio G.R.L., Luvizotto G.L., Silva A.C., Almeida J.A.C. 2025. The missing record of high-pressure granulite metamorphism in the Amazonian Craton. *Terra Nova*. Submitted

Oliveira J.R., Neto C.S.S., Souza C.E.J. (ed.). 1994. *Programas Levantamentos Gelógicos do Brasil: Serra Pelada (Folha SB.22-X-C) Estado do Pará*. Belém, CPRM, 238 p.

Passchier C.W. & Trouw R.A.J. 2005. *Microtectonics*. 1 ed. Heidelberg, Springer Berlin. 366 p.

Patchett P.J. & Tatsumoto M. 1980. Hafnium isotope variations in oceanic basalts. *Geophysical Research Letters*, **7**(1): 1077-1080. https://doi.org/10.1029/GL007i012p01077.

Paton C., Hellstrom J., Paul B., Woodhead J., Hergt J. 2011. Iolite: Freeware for the visualisation and processing of mass spectrometric data. *Journal of Analytical Atomic*

Spectrometry, **26**(12): 2508-2518. https://doi.org/10.1039/c1ja10172b

Petrus J.A. & Kamber B.S. 2012. VizualAge: A Novel Approach to Laser Ablation ICP-MS U-Pb Geochronology Data Reduction. *Geostandards and Geoanalytical Research*, **36**: 247-270. https://doi.org/10.1111/j.1751-908X.2012.00158.x

Ricci P.S.F. 2006a. Most of the "Xingu Complex" previously mapped in the Bacajá High-Grade Block (Pará) comprises retrograded granulites as yet unsuspected from a petrological standpoint. *In:* SBG, 43 º Congresso Brasileiro de Geologia. Aracajú. *Anais*[...]

Ricci P.S.F. 2006b. Mineralogically bizarre charnockitoids of the Bacajá High-Grade Block (Pará): discharnockitized and reemplaced plutons mistakenly confused with granitoids crystallized at shallower crustal levels. *In:* SBG, X Simpósio de Geologia da Amazônia, 9. *Resumos expandidos* v. 9, p. 189-192.

Rosa-Costa L.T., Lafon J.M., Delor C. 2006. Zircon geochronology and Sm–Nd isotopic study: Further constraints for the Archean and Paleoproterozoic geodynamical evolution of the southeastern Guiana Shield, north of Amazonian Craton, Brazil. *Gondwana Research*, **10**(3-4): 277–300. https://doi.org/10.1016/j.gr.2006.02.012.

Rosa-Costa L.T., Lafon J.-M., Milhomem Neto J.M., Pinto J.A.E. 2025. An overview of Rhyacian continental magmatic arcs of the southeastern Guiana Shield, Amazonian Craton. *Journal of South America Earth Sciences*, **159**. https://doi.org/10.1016/j.jsames.2025.105504.

Russell W.A., Papanastassiou D.A., Tombrello T.A. 1978. Ca isotope fractionation on the Earth and other solar system materials. *Geochimica et Cosmochimica Acta*, **42**(8): 1075-1090. https://doi.org/10.1016/0016-7037(78)90105-9

Salgado S.S., Caxito, F. A., Silva R.C.F., Lana C., 2019. Provenance of the Buritirama Formation reveals the Paleoproterozoic assembly of the Bacajá and Carajás blocks (Amazon Craton) and the chronocorrelation of Mn-deposits in the Transamazonian/Birimian system of northern Brazil/West Africa. *Journal of South America Earth Sciences*, **96**. https://doi.org/10.1016/j.jsames.2019.102364

Sláma J., Košler J., Condon D.J., Crowley J.L., Gerdes A., Hanchar J.M., Horstwood M.S.A., Morris G.A., Nasdala, L., Norberg N., Schaltegger U., Schoene B., Tubrett M.N., Whitehouse M.J., 2008. Plešovice zircon — A new natural reference material for U–Pb and Hf isotopic microanalysis. *Chemical Geology*, **249**: 1–35. https://doi.org/10.1016/j.chemgeo.2007.11.005

Santos J.O.S. 2003. Geotectônica dos Escudos das Guianas e Brasil-Central, in: Bizzi,

L.A., Schobbenhaus, C., Vidotti, R.M., Gonçalves, J.H. (ed.). *Geologia, Tectônica e Recursos Minerais Do Brasil*. CPRM, Brasília, p. 169-195.

Santos J.O.S., Hartmann L.A., Faria M.S., Riker S.R., Miguel M., Almeida M.E., Mcnaughton N.J. 2006. A Compartimentação do Cráton Amazonas em Províncias: Avanços Ocorridos no Período 2000-2006. *In:* SBG, IX Simpósio de Geologia da Amazônia, Belém. *Anais*[...]. p. 156-159

Sato K., Tassinari C.C.G., Basei M.A.S., Siga Júnior O., Onoe A.T., Souza M.D. 2014. Sensitive High Resolution Ion Microprobe (SHRIMP IIe/MC) of the Institute of Geosciences of the University of São Paulo, Brazil: analytical method and first results. *Geologia USP. Série Científica*, **14** (3): 3-18. https://doi.org/10.5327/Z1519-874X201400030001

Sawyer E.W. (ed.) 2008. Atlas of migmatites. Canada, The Canadian Mineralogist. 371 p. (Special Publication, 9). https://doi.org/10.1139/9780660197876

Scibiorski E.A., Cawood P.A. 2022. Titanite as a petrogenetic indicator. *Terra Nova*, **34**(3): 177-183. https://doi.org/10.1111/ter.12574

Semblano F.R.D, Pereira N.C.S, Vasquez M.L, Macambira M.J.B. 2016. Novos dados geológicos e isotópicos para o Domínio Iriri-Xingu, Província Amazônia Central: implicações para a idade do Grupo Iriri. *Geologia USP Série Científica*, **16** (3): 19-38. https://doi.org/10.11606/issn.2316-9095.v16i3p19-38.

Semprich J., Moreno J.A., Oliveira E.P. 2015. Phase equilibria and trace element modeling of Archean sanukitoid melts. *Precambrian Research*, **269**: 122-138.

Silva A.S. 2021. *Metamorfismo de UHT e HP no Domínio Bacajá, Cráton do Amazonas*. MS Dissertation, Universidade de Brasília, Brasília, 131 p.

Silva M.A.D., Monteiro L.V.S., Santos T.J.S., Moreto C.P.N., Sousa S.D., Faustinoni J.M., Melo G.H.C., Xavier R.P., Toledo B.A.M. 2021. Mesoarchean migmatites of the Carajás Province: From intra-arc melting to collision. *Lithos*, **388-389**: 106078 https://doi.org/10.1016/j.lithos.2021.106078.

Söderlund U., Patchett P.J., Vervoort J.D., Isachsen C.E. 2004. The ^{176}Lu decay constant determined by Lu-Hf and U-Pb isotope systematics of Precambrian mafic intrusions. *Earth Planet Science Letter*, **219**(3-4): 311-324. https://doi.org/10.1016/S0012-821X(04)00012-3.

Sousa J.T., Feio G.R.L., Almeida J.A.C., Ribeiro A.A.S., Andrade P.T.S.R. 2016. Química mineral em biotita de granulito máfico e kinzigito da área de vila Cruzeiro Do Sul, Domínio Bacajá, Província Transamazonas. *In:* SBG, 48º Congresso Brasileiro de

Geologia. Porto Alegre. *Anais*[...].

Souza V.S. 1995. *Geologia e mineralizações auríferas da área do garimpo do Manelão região do Bacajá - PA*. MS Dissertation, Universidade Federal do Pará, Belém.

Souza V.S. & Kotschoubey B. 2005. Geologia e mineralizações auríferas do garimpo do Manelão, Região do Médio Rio Bacajá (PA). *In:* Horbe A.M.C. & Souza V.S. (ed.). *Contribuições à geologia da Amazônia*. p. 152-164.

Souza V.S., Macambira M.J.B., Kotschoubey B. 2003. Idade de zircão do granito Felício Turvo, graimpo de ouro do Manelão, região do Bacajá (PA): implicações tectônicas. *In:* SBG, VIII Simpósio de Geologia Da Amazônia, Manaus. *Resumos expandidos*, p. 153-156.

Stern R.A. 1998. High resolution SIMS determination of radiogenic trace isotope ratios in minerals. *In:* Cabri L.J, Vaughan D.J (ed.) *Modern approaches to ore and environmental mineralogy*. Canada, Mineralogical Association of Canada, p. 241-268.

Tassinari C. C. G. & Macambira M.J.B. 2004. A evolução tectônica do Craton Amazônico. In: Mantesso-Neto, V., Bartorelli, A., Carneiro, C.D.R., Brito Neves, B.B. (ed.), *Geologia do Continente Sul Americano: Evolução da obra de Fernando Flávio Marques Almeida*. São Paulo, Beca, p. 471-486.

Tavares, F.M., 2015. *Evolução geotêctonica do nordeste da Província Carajás*. PhD Thesis, Universidade Federal do Rio de Janeiro, Rio de Janeiro, 130p.

Tavares, F.M. & Silva C.M.G. 2015. *Carta Geológica da Folha Serra Pelada - SB.22-X-C-VI*. Belém, CPRM.

Thirlwall M.F. & Anczkiewicz R. 2004. Multidynamic isotope ratio analysis using MC-ICP-MS and the causes of secular drift in Hf, Nd and Pb isotope ratios. *International Journal of Mass Spectrometry*, **235**(1): 59-81. https://doi.org/10.1016/j.ijms.2004.04.002

Trouw R.A.J. Passchier C.W., Wiersma D.J. 2009. *Atlas of Mylonites - and related microstructures*. 1 ed. Heidelberg, Springer Berlin, 322 p.

Vanderhaeghe O., Ledru P., Thiéblemont D., Egal E., Cocherie A., Tegyey M., Milési J.-P. 1998. Contrasting mechanism of crustal growth. *Precambrian Research*, **92**(1): 165-193. https://doi.org/10.1016/S0301-9268(98)00074-6.

Vasquez L.V. & Rosa-Costa L.R., 2008. Geologia e Recursos Minerais do Estado do Pará: Sistema de Informações Geográficas - SIG: texto explicativo dos mapas Geológico e Tectônico e de Recursos Minerais do Estado do Pará. Belém, CPRM, 329 p.

Vasquez M.L. 2006. *Geocronologia em zircão, monazita e granada e isótopos de Nd das associações litológicas da porção oeste do Domínio Bacajá: evolução crustal da porção meridional da Província Maroni-Itacaiúnas - Sudeste Do Cráton Amazônico*. PhD Thesis, Universidade Federal do Pará, Pará, 220 p.

Vasquez M.L., Macambira M.J.B., Armstrong R.A. 2008. Zircon geochronology of granitoids from the western Bacajá Domain, southeastern Amazonian craton, Brazil: Neoarchean to Orosirian evolution. *Precambrian Research*, **161**(3-4): 279-302. https://doi.org/10.1016/j.precamres.2007.09.001.

Vasquez M. L., Macambira M.J.B., Galarza M.A. 2005. Granitoides Transamazônicos da região Iriri-Xingu, Pará – novos dados geológicos e geocronológicos. In: Horbe A.M.C. & Souza V. S. (ed.). *Contribuições a Geologia Da Amazônia*. Belém, SBG. p. 16-31.

Vernon R.H. (ed.). 2005. *A practical guide to rock microstructure*. Cambridge, Cambridge University Press. 594 p. https://doi.org/10.1017/CBO9780511807206.

Vieira C., Amaral W., Holanda F.S. 2022. Petrography, geochemistry and zircon U-Pb geochronology of the Siderian-Rhyacian granitoids of NW Bacajá Domain, Amazonian Craton. *Journal of the Geological Survey of Brazil*, **5**(3): 145-76. https://doi.org/10.29396/jgsb.2022.v5.n3.1.

Wiedenbeck M., Allé P., Corfu F., Griffin E.L., Meier M., Oberli F., Quadt A. V, Roddick J.C., Spiegel W. 1995. Three Natural Zircon Standards for U-Th-Pb, Lu-Hf, Trace Element and Ree Analyses. *Geostandards Newsletter*, **19**(1): 1-23. https://doi.org/10.1111/j.1751-908X.1995.tb00147.x.

Williams I.S. 1997. U-Th-Pb Geochronology by Ion Microprobe. *In:* Michael A. McKibben, W.C. Shanks, III, W. Ian Ridley. (ed.). *Applications of Microanalytical Techniques to Understanding Mineralizing Processes*. Society of Economic Geologists, p. 1-35. https://doi.org/10.5382/Rev.07.

Wilson M. (ed.). 1989. *Igneous Petrogenesis. A global tectonic approach*. London, Springer Dordrecht. 466 p. https://doi.org/10.1007/978-1-4020-6788-4.

Xiang H. & Connolly J.A.D, 2022. GeoPS: An interactive visual computing tool for thermodynamic modelling of phase equilibria. *Journal of Metamorphic Geology*. **40**(2): 243-255. https://doi.org/10.1111/jmg.12626.

Zhao G., Cawood P.A., Wilde S.A., Sun M. 2002. Review of global 2.1-1.8 Ga orogens: Implications for a pre-Rodinia supercontinent. *Earth-Science Reviews*, **59**: 125-162. https://doi.org/10.1016/S0012-8252(02)00073-9.

Zhao K., Xu X., Erdmann S. 2017. Crystallization conditions of peraluminous charnockites: constraints from mineral thermometry and thermodynamic modelling. *Contributions to Mineralogy and Petrology*, **172**: 26. https://doi.org/10.1007/s00410-017-1344-2.

APÊNDICE A – RESUMOS PUBLICADOS NOS ANAIS DO 51 º CONGRESSO BRASILEIRO DE GEOLOGIA

REWORKING OF MESOARCHEAN BASEMENT DURING PALEOPROTEROZOIC OROGENESIS IN THE SOUTHERN BACAJÁ DOMAIN, SE AMAZONIAN CRATON

Neri, ASS[1], Dall'Agnol, R[1,2], Dantas, EL[3], Feio, GRL[4], Almeida, JAC[1], Galarza, MAT[1]
[1]Programa de Pós-graduação em Geologia e Geoquímica, Instituto de Geociências, UFPA,
[2] Instituto Tecnológico Vale, [3] Laboratório de estudos geodinâmicos e ambientais, UnB,
[4] Universidade Federal do Sul e Sudeste do Pará

ABSTRACT: The Bacajá Domain is situated in the Maroni-Itacaiúnas province in the SE portion of the Amazonian Craton. It is related to a Rhyacian collisional event that took place during the Transamazonian Orogeny (ca. 2.2-1.95 Ga), which reworked minor Mesoarchean to Neoarchean and Siderian crust and induced significant crustal growth during the Rhyacian. New fieldwork, associated with additional petrographic, geochronologic, and Nd-Hf isotopes data on the Mesoarchean basement of the southern portion of the Bacajá Domain, near its boundary with the Carajás Province, allowed us to better understand the diversity and evolution of the Archean basement of the domain. The Mesoarchean basement of the southern Bacajá Domain was designated as the Cajazeiras Complex and comprises mainly clinopyroxene-amphibole-biotite and amphibole-biotite tonalitic to granodioritic orthogneisses with lenses and boudins of metamafic rocks. Minor paragnaisses also occur. A well-developed penetrative foliation, displaying a WNW-ESE to NW-SE trend with moderate to steep dips towards both NE and SW associated with shallow plunging mineral stretching lineation towards W is imprinted in these rocks. Zircon U-Pb geochronology (LA-ICP-MS) in the zircon cores furnished a minimum crystallization age for the igneous protolith of 2975±9 Ma. The ages obtained in the rims of zircon crystals, interpreted as formed during a metamorphic event, spread along the concordia and range from 2136±14 to 2074±14 Ma (apparent $^{207}Pb/^{206}Pb$ age). Lu-Hf isotopes on zircon magmatic cores reveal positive εHf(t) values of +0.5 to +3.1 and Mesoarchean two-stage model ages (Hf-T_{DM}^{c}) varying from 3.11 to 3.19 Ga, while data from the metamorphic rims provided negative εHf(t) values between −8.9 and -8.0, and Mesoarchean Hf-T_{DM}^{c} from 3.14 to 3.17 Ga. Nd whole-rock isotopes provided positive εNd(t) values (+0.64) and Mesoarchean T_{DM} ages (3.06 Ga). The absence of orthopyroxene in the orthogneisses precludes granulite facies conditions and suggests a metamorphic peak at upper amphibolite facies. Previous data coupled with our new data reveals that the Archean basement of the Bacajá Domain is diverse in age and isotopic behavior. Four Archean age sets were recognized: (1) at 2.5 Ga (São José complex), (2) at 2.60-2.63 Ga [εNd(t) = -3.08 to -2.95, εHf(t) = -1.7 to -0.3, Aruanã complex], (3) at 2.67 Ga [εNd(t) = +2.66, tonalitic gneiss from Manelão area], and (4) at 3.0-2.97 [εNd(t) = +0.64, εHf(t) = +0.5 to +3.1, Cajazeiras complex]. The rocks of the two younger Neoarchean age groups show crustal signatures and are concentrated in the northern and western sectors of the studied area. In contrast, the groups with older Neoarchean and Mesoarchean ages display juvenile signatures and are located in its central and southern portions, near the boundary of the Bacajá Domain with the Carajás Province.

Keywords: U-Pb Geochronology, Nd-Hf isotopes, Archean basement, Amphibolite facies,

RHYACIAN MAGMATISM IN THE SOUTHERN BACAJÁ DOMAIN NEAR CARAJÁS PROVINCE BOUNDARY, SE AMAZONIAN CRATON

Neri, ASS[1], Dall'Agnol, R[1,2], Dantas, EL[3], Feio, GRL[4], Almeida, JAC[1]

[1]Programa de Pós-graduação em Geologia e Geoquímica, Instituto de Geociências, UFPA, [2]Instituto Tecnológico Vale, [3] Laboratório de estudos geodinâmicos e ambientais, UNB,

[4]Universidade Federal do Sul e Sudeste do Pará.

ABSTRACT:

The Bacajá Domain is in the Maroni-Itacaiúnas Province, SE Amazonian Craton. It is related to a Rhyacian collisional event developed during the Transamazonian Orogeny (ca. 2.2-1.95 Ga), which reworked the Archean and Siderian crust and provided significant crustal growth during the Paleoproterozoic. The southern portion of the domain is situated near the proposed boundary between it and the Carajás Province and has not been heavily studied so far. Detailed geological mapping, petrography, whole-rock geochemistry, U-Pb geochronology, and Nd isotopes undertaken in that portion of the Bacajá Domain allow us to identify new distinct Paleoproterozoic granitic and charnockitic units previously encompassed in the Mesoarchean Cajazeiras Complex. The granitic units encompass calc-alkaline amphibole-biotite and biotite monzogranites to syenogranites and rare biotite granodiorites and tonalites (Rio Preto granitic complex), calc-alkaline amphibole monzogranites to leucogranites (Bandeirante granite) and calc-alkaline and strongly peraluminous garnet-bearing granites to granodiorites (Bernardino granite). The charnockitic units consist of calc-alkaline orthopyroxene-bearing and orthopyroxene-free tonalites and granodiorites with rare monzogranites (Serra Azul charnockite) and shoshonitic to high-K calc-alkaline fayalite-bearing granites, orthopyroxene-bearing granodiorites, with rare gabbros, monzonites, quartz-monzonites (Maravilha charnockite). Three major periods of magmatism at 2.12-2.10 Ga, 2.09-2.06 Ga, and 2.05 Ga were recognized. The crystallization of the amphibole-bearing varieties of the Rio Preto granitic complex and Bandeirante granite marks the older event. It is followed by the crystallization of the biotite-bearing varieties of the Rio Preto Complex and Maravilha and Serra Azul charnockites. The crystallization of the Bernardino granite marks the younger event. The Nd isotopes of the different units reveal moderate to highly negative $\varepsilon Nd_{(t)}$ (from -1.91 to -8.96) with Mesoarchean to early Siderian (2.90 to 2.48 Ga) T_{DM} ages. The $\varepsilon Nd_{(t)}$ indicates that the Paleoproterozoic crust from southern Bacajá is neither juvenile nor heavily influenced by mantle sources in its origin. The gap between crystallization ages and T_{DM} ages (400 to 830 Ma) suggests long periods of crustal residence. The Paleoproterozoic magmatic units that are dominant in the studied area are not akin in geochemistry, age, and isotopic behavior to the Archean units present in northern Carajás, which implies that the southern region of the Bacajá Domain does not represent an exhumated crust from Carajás but rather an extension of the Paleoproterozoic crust from northern Bacajá.

Keywords: Geochemistry, Nd isotopes, Crustal evolution, Rhyacian granitoids.

UNIVERSIDADE FEDERAL DO PARÁ
INSTITUTO DE GEOCIÊNCIAS
PROGRAMA DE PÓS-GRADUAÇÃO EM GEOLOGIA E GEOQUÍMICA

UNIVERSIDADE FEDERAL DO PARÁ
PROGRAMA DE PÓS-GRADUAÇÃO EM GEOLOGIA E GEOQUÍMICA
TESE APROVADA COM DISTINÇÃO
Instituto de Geociências

PARECER

Sobre a Defesa Pública da Tese de Doutorado de ARTHUR SANTOS DA SILVA NERI

A banca examinadora da Tese de Doutorado de **ARTHUR SANTOS DA SILVA NERI** orientando do Prof. Dr. Roberto Dall'Agnol (UFPA), e composta pelos professores doutores Maria de Lourdes da Silva Rosa (Membro-UFS), Lucia Travassos da Rosa-Costa (Membro-CPRM), Elson Paiva de Oliveira (Membro-UNICAMP), Moacir José Buenano Macambira (Membro-UFPA) após apresentação da sua tese intitulada "**PETROLOGIA E EVOLUÇÃO CRUSTAL DA PORÇÃO SUL DO DOMÍNIO BACAJÁ, CRÁTON AMAZÔNICO: EVOLUÇÃO POLICÍCLICA DO MESOARQUEANO AO RIACIANO**", emite seguinte parecer:

O candidato realizou sua apresentação de forma clara, bem organizada e segura, no tempo estipulado. Na arguição mostrou domínio da temática abordada e respondeu às perguntas formuladas pela banca. O trabalho escrito foi apresentado na forma de cinco artigos submetidos em periódicos de impacto internacional, e um sexto manuscrito a ser submetido. Dessa forma, todos os artigos atendem às exigências básicas para uma tese de doutorado.

Por cumprir com todas as exigências, a banca examinadora decidiu por unanimidade **APROVAR a Tese de Doutorado, com DISTINÇÃO**.

Belém, 13 de agosto de 2025.

Prof. Dr. Roberto Dall'Agnol (Orientador-UFPA)

Profa. Dra. Maria de Lourdes da Silva Rosa (Membro-UFS)

Profa. Dra. Lucia Travassos da Rosa-Costa (Membro-CPRM)

Prof. Dr. Elson Paiva de Oliveira (Membro-UNICAMP)

Prof. Dr. Moacir José Buenano Macambira (Membro-UFPA)